CRYSTAL ARCHIVES OF MAGMATIC PROCESSES

EDITED BY: Teresa Ubide, David A. Neave, Maurizio Petrelli and Marc-Antoine Longpré
PUBLISHED IN: Frontiers in Earth Science

frontiers Research Topics

frontiers

ISSN 1664-8714
ISBN 978-2-88971-469-8
DOI 10.3389/978-2-88971-469-8

About Frontiers

Frontiers is more than just an open-access publisher of scholarly articles: it is a pioneering approach to the world of academia, radically improving the way scholarly research is managed. The grand vision of Frontiers is a world where all people have an equal opportunity to seek, share and generate knowledge. Frontiers provides immediate and permanent online open access to all its publications, but this alone is not enough to realize our grand goals.

Frontiers Journal Series

The Frontiers Journal Series is a multi-tier and interdisciplinary set of open-access, online journals, promising a paradigm shift from the current review, selection and dissemination processes in academic publishing. All Frontiers journals are driven by researchers for researchers; therefore, they constitute a service to the scholarly community. At the same time, the Frontiers Journal Series operates on a revolutionary invention, the tiered publishing system, initially addressing specific communities of scholars, and gradually climbing up to broader public understanding, thus serving the interests of the lay society, too.

Dedication to Quality

Each Frontiers article is a landmark of the highest quality, thanks to genuinely collaborative interactions between authors and review editors, who include some of the world's best academicians. Research must be certified by peers before entering a stream of knowledge that may eventually reach the public - and shape society; therefore, Frontiers only applies the most rigorous and unbiased reviews.
Frontiers revolutionizes research publishing by freely delivering the most outstanding research, evaluated with no bias from both the academic and social point of view. By applying the most advanced information technologies, Frontiers is catapulting scholarly publishing into a new generation.

What are Frontiers Research Topics?

Frontiers Research Topics are very popular trademarks of the Frontiers Journals Series: they are collections of at least ten articles, all centered on a particular subject. With their unique mix of varied contributions from Original Research to Review Articles, Frontiers Research Topics unify the most influential researchers, the latest key findings and historical advances in a hot research area! Find out more on how to host your own Frontiers Research Topic or contribute to one as an author by contacting the Frontiers Editorial Office: frontiersin.org/about/contact

CRYSTAL ARCHIVES OF MAGMATIC PROCESSES

Topic Editors:
Teresa Ubide, The University of Queensvland, Australia
David A. Neave, The University of Manchester, United Kingdom
Maurizio Petrelli, University of Perugia, Italy
Marc-Antoine Longpré, Queens College (CUNY), United States

Citation: Ubide, T., Neave, D. A., Petrelli, M., Longpré, M.-A., eds. (2021). Crystal Archives of Magmatic Processes. Lausanne: Frontiers Media SA.
doi: 10.3389/978-2-88971-469-8

Table of Contents

frontiers in Earth Science

EDITORIAL
published: 20 August 2021
doi: 10.3389/feart.2021.749100

Editorial: Crystal Archives of Magmatic Processes

Teresa Ubide[1]*, *David A. Neave*[2], *Maurizio Petrelli*[3] and *Marc-Antoine Longpré*[4,5]

[1]School of Earth and Environmental Sciences, The University of Queensland, Brisbane, QLD, Australia, [2]Department of Earth and Environmental Sciences, The University of Manchester, Manchester, United Kingdom, [3]Department of Physics and Geology, University of Perugia, Perugia, Italy, [4]School of Earth and Environmental Sciences, Queens College, City University of New York, Queens, NY, United States, [5]Earth and Environmental Sciences, The Graduate Center, City University of New York, New York, NY, United States

Keywords: crystal zoning, magma transport, magma storage, timescales, volcano plumbing system

Editorial on the Research Topic

Crystal Archives of Magmatic Processes

Crystals are direct witnesses of intricate journeys of magma transfer and storage through Earth's mantle and crust. Crystals thus provide windows into processes that are physically inaccessible yet control volcanic behaviour, ore mineralisation and crustal growth (Maclennan et al., 2001; Davidson et al., 2007; Streck, 2008; Cashman et al., 2017; Ubide and Kamber, 2018; Edmonds et al., 2019; Hepworth et al., 2020). However, unravelling crystal archives requires a detailed understanding of how magmatic information is both recorded during crystal growth and then preserved during subsequent storage and transport.

The sensitivity of crystal morphology and zonation to magmatic conditions varies between minerals, and their melt inclusions. High resolution geochemistry resolves ever increasing intracrystal complexities (Davidson et al., 2007; Oeser et al., 2015; Till et al., 2015; Ubide et al., 2015; Neave et al., 2017; Cao et al., 2019). Experimental observations help us link crystal textures and compositions with geological processes, and thereby reconstruct the structure and dynamics of magma storage regions in ways that can be eventually integrated with geophysical data (Hammer, 2008; Putirka 2008; Gualda et al., 2012; Neave and Putirka 2017; Mollo et al., 2018). The diffusive overprinting of chemical zoning may erase precious records and complicate the integration of plutonic and volcanic archives, but it also enables us to quantify timescales of magma storage and transport, informing volcano monitoring efforts (Kahl et al., 2011; Longpré et al., 2014; Petrone et al., 2016; Rasmussen et al., 2018; Mutch et al., 2019; Costa et al., 2020; Petrelli and Zellmer, 2020).

This Research Topic aims to bring new insights into our understanding of how crystal archives can be used to reconstruct the dynamics of magmatic systems. Thirteen original research articles exploit the crystal-eye to magmatic processes by applying novel petrological and geochemical approaches to a range of natural and experimental case studies that access different portions of magma plumbing systems (**Figure 1**). The articles in this Research Topic demonstrate how overcoming the challenges related to the study of crystal archives can open new opportunities for understanding otherwise cryptic magma pathways from source to eruption.

MAKING CRYSTAL ARCHIVES

As magmas crystallise, growing minerals respond to melt compositions and magmatic conditions via their textural characteristics, chemistry and style of compositional zoning (**Figure 1A**). Large crystals have traditionally been considered to grow in a tree-ring fashion, with concentric zones forming sequentially from core to rim, and compositional zoning reflecting sequential changes in the

OPEN ACCESS

Edited and reviewed by:
Catherine Jeanne Annen, Institute of Geophysics (ASCR), Czechia

***Correspondence:**
Teresa Ubide
t.ubide@uq.edu.au

Specialty section:
This article was submitted to Petrology, a section of the journal Frontiers in Earth Science

Received: *29 July 2021*
Accepted: *06 August 2021*
Published: *20 August 2021*

Citation:
Ubide T, Neave DA, Petrelli M and Longpré M-A (2021) Editorial: Crystal Archives of Magmatic Processes. Front. Earth Sci. 9:749100. doi: 10.3389/feart.2021.749100

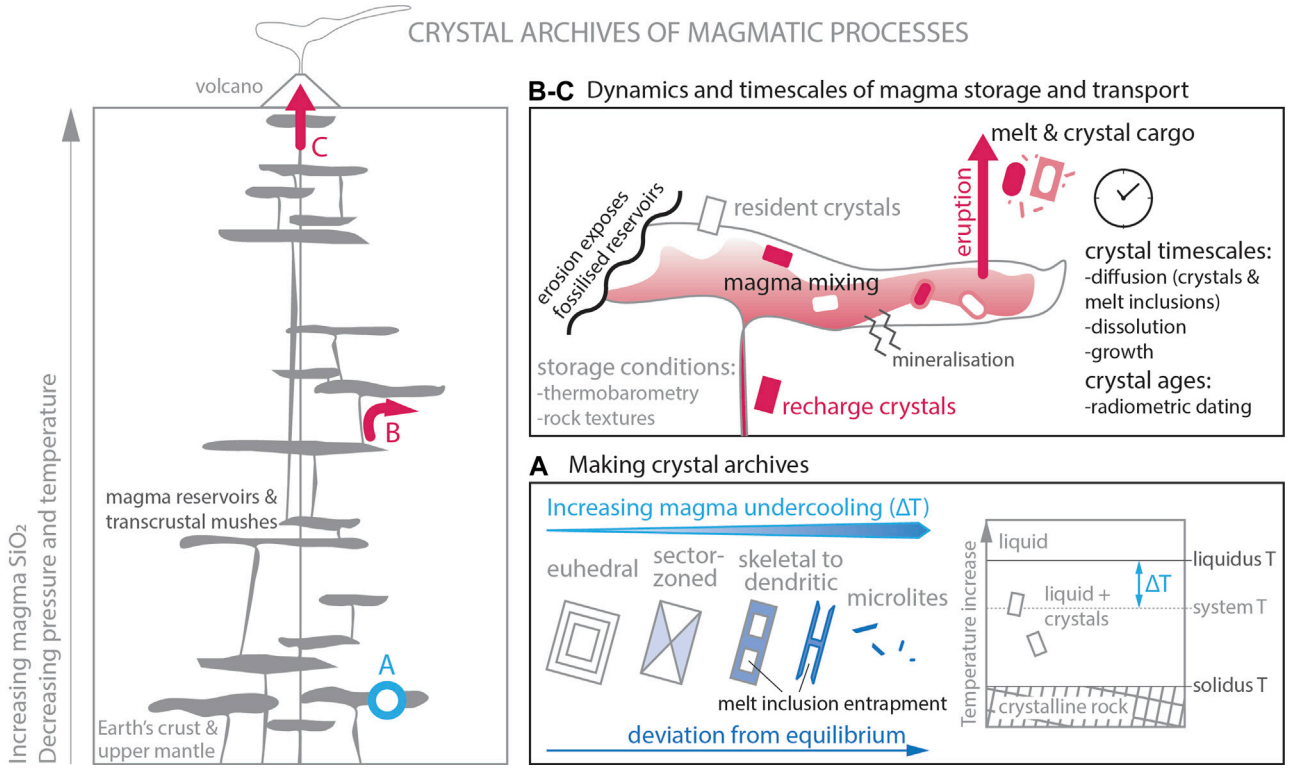

FIGURE 1 | The crystal-eye on magma plumbing systems. Crystal archives unveil the processes, depths and timescales of magma transport and storage from source to eruption. The present Research Topic explores frontiers in magmatic processes exploiting crystal and melt inclusion records. **(A)** Making crystal archives. Variations in crystal morphology, zoning style and entrapment of melt inclusions with the increase in magma undercooling. The degree of magma undercooling (ΔT) increases if the temperature of the system decreases (e.g., due to cooling at the reservoir margin) or if the liquidus temperature increases (e.g., due to degassing). **(B)** Crystals record the dynamics of magma storage and transport between reservoirs, including magma fractionation, recharge, mixing, assimilation, degassing and mush remobilisation. Erupted magmas carry an assortment of crystals (phenocrysts, antecrysts, xenocrysts) that attest to complex pre-eruptive histories. Fossilised magma chambers enable direct observation of crystal records of magmatic processes, and their potential link to mineralisation. **(C)** Crystals act as time capsules of reservoir growth and eruption onset. A variety of timescales can be retrieved applying constraints on the kinetics of crystal growth, dissolution and diffusive re-equilibration in minerals and their melt inclusions.

magmatic environment through time. However, rapid growth at moderate to high degrees of undercooling ($\Delta T = T_{liquidus} - T_{crystallisation}$) generates skeletal to dendritic crystals that grow in a snow-flake fashion with disequilibrium compositions, and can be later infilled via concentric growth, complicating crystal records (Faure et al., 2003; Welsch et al., 2014; Shea et al., 2015; Salas et al., 2021). At low degrees of undercooling, polyhedral crystals can develop sector zoning, where sectors growing coevally along different crystallographic directions have distinct compositions, further complicating crystal archives (Hollister and Gancarz, 1971; Kouchi et al., 1983; Ubide et al., 2019a; Masotta et al., 2020). Conversely, recognising kinetic effects can provide invaluable information about the thermal pathways of magma crystallisation (Bouvet de Maisonneuve et al., 2016; Welsch et al., 2016; Ubide et al., 2019a, Ubide et., 2019b; Neave et al., 2019; Shea et al., 2019; Di Stefano et al., 2020). In addition, diffusive re-equilibration of compositional gradients can generate or modify chemical profiles across crystals, and diffusion modelling can retrieve a wide range of timescales across magmatic plumbing systems (Costa et al., 2020).

To constrain the effects of undercooling and time on olivine growth and zoning, **Mourey and Shea** perform experiments on a Hawaiian tholeiite, and investigate resulting crystals with three-dimensional X-ray micro-tomography. Estimated 3D growth rates (10^{-7} m/s) are almost an order of magnitude higher than those calculated using 2D sections of the same experiments, highlighting the benefit of their novel 3D approach. At ΔT = 40°C, growth rates approach their maxima while nucleation rates remain low, so this may represent a thermal "sweet spot" for the formation of large crystals in dry basalts. A magma chamber can thus generate large crystals within a few hours of thermal perturbations induced, for example, by magma mixing. Crystal growth is initially rapid, and the crystal skeleton forms at a faster pace than diffusion of both moderate (Fe–Mg) and fast (Li) diffusing elements, which complies with a necessary assumption for the application of diffusion chronometry (Costa et al., 2008; Costa et al., 2020). In contrast, subsequent maturation to large polyhedral crystals is comparatively slow, and gradual compositional changes are controlled by diffusive re-equilibration. The initial, rapid formation of an outer crystal

shell enhances the confinement of melt inclusions, which are common in olivine.

Melt inclusions trapped by growing crystals provide distinct records of magmatic evolution (Kent et al., 2010). An important assumption is that entrapped melts are representative of the bulk environment and not liquid boundary layers created during fast crystal growth (Baker, 2008; Longpré et al., 2020). Moreover, the effects of post-entrapment crystallisation within inclusions need to be carefully assessed, as well as the effects of experimentally reheating inclusions prior to microanalysis (Nielsen, 2011). In this context, Lewis et al. undertake an experimental study on the homogenisation of plagioclase-hosted melt inclusions, testing changes in the major and trace element chemistry of glass with pressure and duration of experiments. They find that the best approach for recovering compositions at the time of entrapment is to homogenise the inclusions for short times at low pressure (melt inclusions up to 500 microns in diameter homogenize in 30 min or less), or at the pressure of entrapment (calculated according to CO_2 contents). The authors provide detailed recommendations to reverse post-entrapment processes and thereby reconstruct pre-eruptive magma evolution.

DYNAMICS OF MAGMA STORAGE

The complex nature of subvolcanic plumbing systems reflects magma evolution by a succession of dynamic processes involving magma fractionation, recharge, mixing, assimilation and degassing, which may occur in numerous reservoirs and during magma transfer through crystal mushes (Bergantz et al., 2015; Cashman et al., 2017; Edmonds et al., 2019). This translates into the occurrence of crystal populations with disparate origins at the scale of individual crystals, thin sections and outcrops (equilibrium phenocrysts/autocrysts, cogenetic antecrysts, accidental xenocrysts; Davidson et al., 2007; Kahl et al., 2015). Interrogating the crystal cargo erupted during volcanism or fossilised in intrusions provides a forensic means to access the inner workings of magmatic systems (**Figure 1B**).

To disentangle crystal populations and discern their origins, Caricchi et al. apply machine learning methods to clinopyroxenes erupted during the 2014–2015 Bárðarbunga–Holuhraun eruption in Iceland, where lateral draining of the magma reservoir induced progressive caldera collapse (Gudmundsson et al., 2016). Hierarchical clustering of clinopyroxene major and trace element datasets distinguishes hourglass and prism sectors, as well as concentrically zoned mantles and overgrowth rims, which together respond to thermal variations and associated kinetic effects. Results unveil a sequence of pre-eruptive processes that had not been captured in previous whole rock and melt inclusion studies, including mixing of hot magma with colder resident magma during lateral transport across the feeder dyke. Variations in crystal populations throughout the 6 months of the eruption indicate a decrease in magma mixing with time, which the authors suggest could be linked to the thermal maturation of the dyke. Combined with monitoring data, statistical assessments of crystal zoning provide powerful means to track pre- and syn-eruptive pathways of magma movement towards the surface.

Locating pockets of magma storage prior to eruption is critical in the surveillance of volcanoes across tectonic settings. Klügel et al. investigate crystal and melt records in a chronologically-controlled sample sequence of the 2014–15 eruption at Fogo, Cape Verde, as a natural laboratory to reconstruct magma plumbing in an ocean island setting. Clinopyroxene-melt barometry on carefully filtered equilibrium pairs of rims and groundmass indicates magma storage at upper mantle levels. Clinopyroxene rims are sector-zoned and formed during the eruption, due to H_2O-loss that might have been driven by CO_2-flushing from deeper reservoirs. Microthermometry of CO_2-dominated fluid inclusions in clinopyroxene indicates the ascending magma stalled briefly at the Moho, and diffusion modelling of olivine rims indicates final ascent was fast (on the order of hours). In contrast with other documented eruptions of ocean island basalts, the majority of seismic events precursory to the Fogo eruption were relatively shallow compared to the depths of magma stagnation indicated by barometry. The authors suggest this might be due to short recurrence intervals and small erupted volumes resulting in mostly aseismic magma ascent, which could help inform the monitoring of future volcanic activity at Fogo.

In alkaline continental systems, explosive monogenetic centers can erupt unusual cargoes of crystals and lithics (Irving and Frey, 1984), which may provide valuable constraints on magma source, ascent and eruption. In addition, the unpredictability and abundance of monogenetic volcanoes underline the importance of improving our understanding of their source to surface feeding mechanisms (Smith and Németh, 2017; Brenna et al., 2021). Villaseca et al. investigate spectacular megacryst and cumulate cargoes in the Cenozoic Calatrava volcanic field in central Spain. Trace element signatures in clinopyroxene, amphibole and phlogopite, combined with Sr-Nd isotope systematics in minerals and whole rocks, indicate the disparate cargoes share a common origin. Green Fe-Na-rich clinopyroxenes are interpreted as high-pressure precipitates from highly fractionated liquids, cogenetic with the less fractionated melts that formed colourless clinopyroxenes. Crucially, trace element data serve to test the origin of green clinopyroxenes as cognate vs. xenocrystic cargo, as highlighted in other alkaline settings (Ubide et al., 2014; Jankovics et al., 2016). Results support the notion that alkaline monogenetic fields are fed by deep magmatic systems governed by melt accumulation, fractionation and contamination at variable mantle depths, and in which volatile saturation ultimately triggers mush disaggregation and rapid magma ascent.

Shallow crustal storage is often well developed above deep mafic mushes in arc settings (Annen et al., 2006). Nicotra et al. link plagioclase records with eruptive styles across the volcano stratigraphy of small caldera-forming eruptions at Vulcano (Aeolian Islands, Italy). The authors propose the re-activation of caldera ring-faults may induce decompression of shoshonitic magma and its crystal cargo stored at shallow depths, as well as basaltic, volatile-rich magma with more primitive crystals stored below the level of water exsolution. Decompression of plagioclase

from the shallow reservoir creates sieve textures rich in melt inclusions, overgrowing finely oscillatory zoned cores formed under quiescent conditions. Ascending primitive magma carries resorbed plagioclases, and mixing between recharge and resident magmas results in further resorption. Interestingly, the establishment of magma mixing in the shallow reservoir may follow the transition from phreatomagmatic explosions at the onset of volcanism to sustained lava fountaining, whereby progressive tapping of primitive basalts leads to a shift in eruptive style from Strombolian to Hawaiian. Ring-faults and fractures play a crucial role in channelising rapid magma ascent, leading to partial reservoir emptying and caldera collapse.

Knafelc et al. show that even crystal-poor rhyolites may carry mixed crystal cargoes. In a multi-mineral investigation of the Havre 2012 large submarine eruption in the southwest Pacific, including pumice raft collected along the east coast of Australia and Fiji, as well as samples of seafloor giant pumice and lava flows from the eruption site, the authors show that the mineral assemblage comprises both equilibrium autocrysts and recycled antecrysts. Importantly, they focus only on the autocrysts (plagioclase, orthopyroxene and Fe-Ti oxides) to constrain the pressure, temperature, water content and oxidation state of carrier melts immediately before eruption. Thermodynamic modelling indicates that clinopyroxene and quartz antecrysts are inherited from cold, silicic mush zones. Resorbed high-An plagioclase cores may be sourced from more mafic-intermediate magma. The study highlights the need of careful textural and compositional assessment of mineral-melt equilibrium to reconstruct pre-eruptive processes and architecture across magma compositions and eruptive styles.

Plutonic Perspectives

While mineral assemblages in volcanic rocks preserve complex zoning records due to fast cooling upon eruption, they represent only a portion of crystals processed within magmatic plumbing systems. Plutonic complexes provide direct access to fossilised plumbing systems and the processes occurring during magma solidification that are not necessarily reflected in volcanic records. Holness et al. quantify plagioclase shapes and fabrics in oriented thin sections of troctolitic cumulate bodies from the Layered Series of the Skaergaard intrusion, and the Rum Eastern Layered Intrusion, to assess crystal mobilization, transport and accumulation. Plagioclase foliation becomes stronger as grains become more tabular with increasing cooling rates and corresponding crystal growth rates. The authors link foliations to magmatic currents, tectonic disruptions of poorly consolidated mush, or post-accumulation overgrowths. Upward increases in foliation strength provide detailed records of progressive magma chamber inflation. In turn, frequent replenishment events favour textural equilibration during slow sub-solidus cooling, modifying igneous microstructures. The authors observe a correlation between the standard deviation of dihedral angles at plagioclase triple junctions and the average grain shape, and suggest future research should explore such variation as a means to quantify cumulate thermal histories.

Olivine- and pyroxene-rich cumulates can host Ni-Cu-(platinum group element-PGE) sulphide deposits. Schoneveld et al. explore the potential of pyroxene zoning to record the processes that lead to mineralisation. The authors examine mineralised and barren intrusions across the globe via X-ray fluorescence imaging, which reveals crystal zoning patterns across entire thin sections. Pyroxene zoning is particularly well preserved for slow-diffusing Cr, enhanced in compositional maps obtained at low energy of synchrotron X-rays (Barnes et al., 2020). Interestingly, pyroxene zoning is widespread across mafic intrusions and the zonation styles vary between mineralised and barren bodies. Strongly mineralized intrusions contain pyroxenes with complex Cr variations, including abrupt and sector zoning in orthopyroxenes that contain olivine inclusions. The authors interpret these features as reactive transport of olivine and orthopyroxene crystals within high-flux, dynamic conduit systems where wall rock assimilation induces fluctuations in magmatic conditions and leads to Ni-Cu sulphide mineralization (Barnes et al., 2016). This study grows an exciting line of research on the potential of zoned crystals as fertility indicators for the exploration of ore deposits.

TIMESCALES OF MAGMA ASCENT TO ERUPTION

Crystals act as chronometers that enable the reconstruction of magma transport and storage through time (Cooper and Kent, 2014; Costa et al., 2020; **Figure 1C**). Olivine is extensively exploited for diffusion chronometry in basaltic systems, partly because slow- (e.g., P), moderate- (e.g., Fe-Mg) and fast- (e.g., Li) diffusing elements resolve a wide range of magmatic timescales (Lynn et al., 2018; Costa et al., 2020). Increasing interest in syn-eruptive processes such as magma ascent and degassing has promoted studies focused on fast-diffusing Li. However, charge balancing the incorporation of pentavalent P by monovalent Li during rapid olivine growth (Mallmann et al., 2009) calls for careful assessment of the origin of Li concentration gradients.

To untangle Li records of growth and diffusion, Lynn et al. target trace element zoning in carefully oriented and sectioned olivines from Hawaii, using a combination of electron microprobe, laser ablation mass spectrometry and nanoscale secondary ion mass spectrometry. Li variations can be grouped into two types: 1) broad core-rim zoning that is not coupled with P; 2) fine Li enrichments that are coupled with P and only resolved quantitatively via sub-micrometre analysis. The authors link the non-coupled Li variations to diffusion after magma mixing, which can be modelled to retrieve short timescales (hours to days) of magma intrusion and transport to eruption. In contrast, coupled Li enrichments reflect early rapid growth along branches rich in P and cannot be reliably modelled due to complications arising from multi-component diffusion, poorly constrained initial conditions and analytical challenges associated with resolving fine variations. The authors conclude that only broad zoning of non-coupled Li should be modelled for timescales of magmatic processes, and

provide detailed recommendations on selecting Li profiles for diffusion modelling.

Steinnmann et al. approach the issue of crystal growth vs. diffusion by combining Li elemental and isotope zoning in olivines from the Massif Central in France. The authors measure Li isotope variations via femtosecond laser ablation multi-collector mass spectrometry, previously used to obtain Fe-Mg isotope profiles across the same olivines (Oeser et al., 2015). The isotopic composition of the melt is assumed to be constant during fractional crystallisation, and significant increases in both Li and δ^7Li from olivine cores to rims are interpreted as resulting from diffusion into initially homogeneous olivine grains during magma differentiation. Such zoning broadly correlates with Fe-Mg variations, which are used to retrieve timescale information. In addition, Li shoulders at crystal rims reveal a second diffusion event (Li loss) that is not recorded by Mg–Fe exchange and may reflect degassing during magma ascent or eruption. Importantly, integrated elemental and isotope profiles of Fe-Mg and Li resolve the origin of olivine compositional variations and help unravel multi-stage magma evolution, including cooling, magma mixing and degassing.

The thermal history of magmas during final ascent is crucial to investigate the explosivity of eruptions and help interpret volcano degassing records (La Spina et al., 2015; Oppenheimer et al., 2018). Newcombe et al. explore magma pressure-temperature-time (P-T-t) paths immediately before basaltic eruptions from arc and ocean island volcanoes of different explosivity and magma water content. They combine thermal histories (T-t) from MgO diffusion profiles in olivine-hosted melt inclusions with decompression histories (P-t) previously determined from volatile data. Results indicate a negative correlation between syn-eruptive magma decompression rates and cooling rates; rapidly ascending gas-bearing magmas (subplinian volcanism) experience slower cooling during ascent and eruption than slowly ascending magmas (lava-fountaining). Thermal histories of hydrous arc magmas are not accurately modelled by isentropic magma ascent, where adiabatic expansion of the gas phase is the dominant driver of cooling in the conduit. This may be due to open-system degassing and/or degassing-driven crystallisation, which produces latent heat (Blundy et al., 2006), and argues against the use of isentropic conduit models for arc magmas. The proposed syn-eruptive ascent thermo-chronometer offers a new approach for constraining conduit processes, including magma stalling, magma mixing, open- and closed-system degassing, vapour fluxing, and vapour accumulation during the seconds to hours preceding mafic eruptions.

Water-poor magmas in mid ocean ridge settings pose a challenge for decompression rates based on degassing records. Neave and Maclennan combine experimental constraints on clinopyroxene dissolution with barometric estimates to calculate decompression rates from a wehrlite nodule from the primitive Borgarhraun lava flow in Iceland. Crystal cores have Al-rich compositions consistent with crystallisation at Moho levels. Crystal rims and inclusions have Al-poor compositions that formed at or near the surface. Crucially, rims and inclusions are interpreted as the crystallised remnants of boundary layers formed by the dissolution of high-Al cores during magma ascent, providing a means to calculate ascent timescales. The model returns mantle-to-surface transport durations on the order of days, implying limited unrest may precede some Icelandic eruptions. Results are faster than previous estimates based on olivine diffusion chronometry (Mutch et al., 2019), suggesting that magmas accelerate close to the surface. Interestingly, results are similar to those obtained in arc settings, indicating that magma ascent rates may not correlate simply with magma water contents (Cassidy et al., 2018). The proposed decompression-meter provides a way to estimate decompression rates of water-poor magmas, and highlights the benefits of integrating timescale information from different geospeedometers.

SUMMARY AND FUTURE OUTLOOK

Crystals can help locate regions of magma storage at depth, identify the processes that govern magma ascent and provide time constraints on the triggers of volcanic eruptions. Outstanding challenges include a precise understanding on the complex and overlapping magmatic processes and timescales different minerals are able to record, and preserve, and a careful assessment of the applicability of petrological calibrations established in experimental conditions to natural systems where equilibrium conditions rarely apply. Fortunately, these difficulties are increasingly overcome by exciting developments in experimental, analytical and numerical approaches that bring new perspectives to crystal archives, as highlighted by this Research Topic.

Crystal textures can now be quantified with greater precision and accuracy than ever before. While advanced methods such as the non-destructive 3D X-ray microtomography used by Mourey and Shea are providing previously unattainable insights into rock microstructures, Holness et al. demonstrate that optical microscopy still has a central role to play in advancing our understanding of magma reservoir processes. Technological advances like those exploited by Neave and Maclennan and Schoneveld et al. now make it possible to map compositional variations over whole thin sections, explicitly integrating textural and chemical information and highlighting previously missed features, even in comprehensively studied samples. Future challenges are likely to involve rethinking how the enormous volumes of data generated by such approaches can be presented in transparent yet digestible ways. Although high-precision geochemical microanalyses like the fs-LA-MC-ICP-MS used by Steinmann et al. and the nanoSIMS used by Lynn et al. and Newcombe et al. are now well established tools for reconstructing magmatic histories from crystal zoning, applications to geological systems are still relatively few in number, and many new discoveries can be expected in the years ahead as these techniques mature further. Finally, the ever larger datasets now generated are fueling the growth of quantitative petrology, and statistical approaches like that presented by Caricchi et al. offer exciting new opportunities for better understanding crystal archives of magmatic processes.

AUTHOR CONTRIBUTIONS

TU drafted the first version of the text and figure, with input from DAN. All authors contributed to the final version of the article.

FUNDING

TU was supported by a Foundation Research Excellence Award from The University of Queensland (UQ-FREA RM2019001828), the Advance Queensland Women's Research Assistance Program from the Queensland Government (WRAP109-2019RD1 and RM2020002371), and the Australian Research Council (DP190100814 and DP200101566). DAN was supported by a Presidential Fellowship from the University of Manchester and a NERC Independent Research Fellowship (NE/T011106/1). MP acknowledges the Engage FRB2019 project by Perugia University. MAL acknowledges support from NSF awards # 1650379, 1819053 and 1944723, and the Paula and Jeffrey Gural Endowed Professorship in Geology at Queens College.

ACKNOWLEDGMENTS

We thank all contributing authors, reviewers and additional editors for sharing their science, insights and time, making this Research Topic an exciting collection that reflects current understanding and novel approaches to the study of crystal archives. We thank Camilla Imarisio, Ursula Rabar and Roshan Patel from the Frontiers in Earth Science team for the invitation to submit the Research Topic proposal, and the support through the editorial process.

REFERENCES

Annen, C., Blundy, J. D., and Sparks, R. S. J. (2006). The Genesis of Intermediate and Silicic Magmas in Deep Crustal Hot Zones. *J. Petrol.* 47, 505–539. doi:10.1093/petrology/egi084

Baker, D. R. (2008). The Fidelity of Melt Inclusions as Records of Melt Composition. *Contrib. Mineral. Petrol.* 156, 377–395. doi:10.1007/s00410-008-0291-3

Barnes, S. J., Mole, D. R., Le Vaillant, M., Campbell, M. J., Verrall, M. R., Roberts, M. P., et al. (2016). Poikilitic Textures, Heteradcumulates and Zoned Orthopyroxenes in the Ntaka Ultramafic Complex, Tanzania: Implications for Crystallization Mechanisms of Oikocrysts. *J. Petrol.* 57, 1171–1198. doi:10.1093/petrology/egw036

Barnes, S. J., Paterson, D., Ubide, T., Schoneveld, L. E., Ryan, C., and Le Vaillant, M. (2020). Imaging Trace-Element Zoning in Pyroxenes Using Synchrotron XRF Mapping with the Maia Detector Array: Benefit of Low-Incident Energy. *Am. Mineral.* 105, 136–140. doi:10.2138/am-2020-7228

Bergantz, G. W., Schleicher, J. M., and Burgisser, A. (2015). Open-system Dynamics and Mixing in Magma Mushes. *Nat. Geosci.* 8, 793–796. doi:10.1038/ngeo2534

Blundy, J., Cashman, K., and Humphreys, M. (2006). Magma Heating by Decompression-Driven Crystallization beneath Andesite Volcanoes. *Nature* 443, 76–80. doi:10.1038/nature05100

Brenna, M., Ubide, T., Nichols, A. R. L., Mollo, S., and Pontesilli, A. (2021). "Anatomy of Intraplate Monogenetic Alkaline Basaltic Magmatism," in *Crustal Magmatic System Evolution: Anatomy, Architecture, and Physico-Chemical Processes*. *AGU Geophysical Monograph*. Editors M. Masotta, C. Beier, and S. Mollo, 264, 79–103. doi:10.1002/9781119564485.ch4

Cao, M., Evans, N. J., Reddy, S. M., Fougerouse, D., Hollings, P., Saxey, D. W., et al. (2019). Micro- and Nano-Scale Textural and Compositional Zonation in Plagioclase at the Black Mountain Porphyry Cu deposit: Implications for Magmatic Processes. *Am. Mineral.* 104, 391–402. doi:10.2138/am-2019-6609

Cashman, K. V., Sparks, R. S. J., and Blundy, J. D. (2017). Vertically Extensive and Unstable Magmatic Systems: a Unified View of Igneous Processes. *Science* 355, eaag3055. doi:10.1126/science.aag3055

Cassidy, M., Manga, M., Cashman, K., and Bachmann, O. (2018). Controls on Explosive-Effusive Volcanic Eruption Styles. *Nat. Commun.* 9, 2839. doi:10.1038/s41467-018-05293-3

Cooper, K. M., and Kent, A. J. R. (2014). Rapid Remobilization of Magmatic Crystals Kept in Cold Storage. *Nature* 506, 480–483. doi:10.1038/nature12991

Costa, F., Dohmen, R., and Chakraborty, S. (2008). Time Scales of Magmatic Processes from Modeling the Zoning Patterns of Crystals. *Rev. Mineral. Geochem.* 69, 545–594. doi:10.2138/rmg.2008.69.14

Costa, F., Shea, T., and Ubide, T. (2020). Diffusion Chronometry and the Timescales of Magmatic Processes. *Nat. Rev. Earth Environ.* 1, 201–214. doi:10.1038/s43017-020-0038-x

Davidson, J. P., Morgan, D. J., Charlier, B. L. A., Harlou, R., and Hora, J. M. (2007). Microsampling and Isotopic Analysis of Igneous Rocks: Implications for the Study of Magmatic Systems. *Annu. Rev. Earth Planet. Sci.* 35, 273–311. doi:10.1146/annurev.earth.35.031306.140211

de Maisonneuve, C. B., Costa, F., Huber, C., Vonlanthen, P., Bachmann, O., and Dungan, M. A. (2016). How Do Olivines Record Magmatic Events? Insights from Major and Trace Element Zoning. *Contrib. Mineral. Petrol.* 171, 56. doi:10.1007/s00410-016-1264-6

Di Stefano, F., Mollo, S., Ubide, T., Petrone, C. M., Caulfield, J., Scarlato, P., et al. (2020). Mush Cannibalism and Disruption Recorded by Clinopyroxene Phenocrysts at Stromboli Volcano: New Insights from Recent 2003-2017 Activity. *Lithos* 360-361, 105440. doi:10.1016/j.lithos.2020.105440

Edmonds, M., Cashman, K. V., Holness, M., and Jackson, M. (2019). Architecture and Dynamics of Magma Reservoirs. *Phil. Trans. R. Soc. A.* 377, 20180298. doi:10.1098/rsta.2018.0298

Faure, F., Trolliard, G., Nicollet, C., and Montel, J. M. (2003). A Developmental Model of Olivine Morphology as a Function of the Cooling Rate and the Degree of Undercooling. *Contrib. Mineral. Petrol.* 145, 251–263. doi:10.1007/s00410-003-0449-y

Gualda, G. A. R., Ghiorso, M. S., Lemons, R. V., and Carley, T. L. (2012). Rhyolite-MELTS: a Modified Calibration of MELTS Optimized for Silica-Rich, Fluid-Bearing Magmatic Systems. *J. Petrol.* 53, 875–890. doi:10.1093/petrology/egr080

Gudmundsson, M. T., Jónsdóttir, K., Hooper, A., Holohan, E. P., Halldórsson, S. A., Ófeigsson, B. G., et al. (2016). Gradual Caldera Collapse at Bárdarbunga Volcano, Iceland, Regulated by Lateral Magma Outflow. *Science* 353, aaf8988. doi:10.1126/science.aaf8988

Hammer, J. E. (2008). Experimental Studies of the Kinetics and Energetics of Magma Crystallization. *Rev. Mineralogy Geochem.* 69 (1), 9–59. doi:10.2138/rmg.2008.69.2

Hepworth, L. N., Daly, J. S., Gertisser, R., Johnson, C. G., Emeleus, C. H., and O'Driscoll, B. (2020). Rapid Crystallization of Precious-Metal-Mineralized Layers in Mafic Magmatic Systems. *Nat. Geosci.* 13, 375–381. doi:10.1038/s41561-020-0568-3

Hollister, L. S., and Gancarz, A. J. (1971). Compositional Sector-Zoning in Clinopyroxene from the Narce Area. *Italy. Am. Mineral.* 56, 959.

Irving, A. J., and Frey, F. A. (1984). Trace Element Abundances in Megacrysts and Their Host Basalts: Constraints on Partition Coefficients and Megacryst Genesis. *Geochim. Cosmochim. Acta* 48, 1201–1221. doi:10.1016/0016-7037(84)90056-5

Jankovics, M. É., Taracsák, Z., Dobosi, G., Embey-Isztin, A., Batki, A., Harangi, S., et al. (2016). Clinopyroxene with Diverse Origins in Alkaline Basalts from the Western Pannonian Basin: Implications from Trace Element Characteristics. *Lithos* 262, 120–134. doi:10.1016/j.lithos.2016.06.030

Kahl, M., Chakraborty, S., Costa, F., and Pompilio, M. (2011). Dynamic Plumbing System beneath Volcanoes Revealed by Kinetic Modeling, and the Connection

to Monitoring Data: an Example from Mt. Etna. *Earth Planet. Sci. Lett.* 308 (1–2), 11–22. doi:10.1016/j.epsl.2011.05.008

Kahl, M., Chakraborty, S., Pompilio, M., and Costa, F. (2015). Constraints on the Nature and Evolution of the Magma Plumbing System of Mt. Etna Volcano (1991-2008) from a Combined Thermodynamic and Kinetic Modelling of the Compositional Record of Minerals. *J. Petrol.* 56, 2025–2068. doi:10.1093/petrology/egv063

Kent, A. J. R., Darr, C., Koleszar, A. M., Salisbury, M. J., and Cooper, K. M. (2010). Preferential Eruption of Andesitic Magmas through Recharge Filtering. *Nat. Geosci.* 3, 631–636. doi:10.1038/ngeo924

Kouchi, A., Sugawara, Y., Kashima, K., and Sunagawa, I. (1983). Laboratory Growth of Sector Zoned Clinopyroxenes in the System CaMgSi2O6-CaTiAl2O6. *Contr. Mineral. Petrol.* 83, 177–184. doi:10.1007/BF00373091

La Spina, G., Burton, M., de' Michieli Vitturi, M., and Vitturi, M. (2015). Temperature Evolution during Magma Ascent in Basaltic Effusive Eruptions: a Numerical Application to Stromboli Volcano. *Earth Planet. Sci. Lett.* 426, 89–100. doi:10.1016/j.epsl.2015.06.015

Longpré, M.-A., Klügel, A., Diehl, A., and Stix, J. (2014). Mixing in Mantle Magma Reservoirs Prior to and during the 2011-2012 Eruption at El Hierro, Canary Islands. *Geology* 42 (4), 315–318. doi:10.1130/G35165.1

Longpré, M. A., Stix, J., and Shimizu, N. (2020). "Boundary-Layer Melts Entrapped as Melt Inclusions? The Case of Phosphorus- and CO_2-Rich Spinel-Hosted Melt Inclusions from El Hierro, Canary Islands," in *Dynamic Magma Evolution, Geophysical Monograph Series*. Editor F. Vetere (Hoboken, NJ: AGU), 254, 43–60. doi:10.1002/9781119521143.ch2

Lynn, K. J., Shea, T., Garcia, M. O., Costa, F., and Norman, M. D. (2018). Lithium Diffusion in Olivine Records Magmatic Priming of Explosive Basaltic Eruptions. *Earth Planet. Sci. Lett.* 500, 127–135. doi:10.1016/j.epsl.2018.08.002

Maclennan, J., McKenzie, D., Gronvöld, K., and Slater, L. (2001). Crustal Accretion under Northern Iceland. *Earth Planet. Sci. Lett.* 191, 295–310. doi:10.1016/S0012-821X(01)00420-4

Mallmann, G., O'Neill, H. S. C., and Klemme, S. (2009). Heterogeneous Distribution of Phosphorus in Olivine from Otherwise Well-Equilibrated Spinel Peridotite Xenoliths and its Implications for the Mantle Geochemistry of Lithium. *Contrib. Mineral. Petrol.* 158, 485–504. doi:10.1007/s00410-009-0393-6

Masotta, M., Pontesilli, A., Mollo, S., Armienti, P., Ubide, T., Nazzari, M., et al. (2020). The Role of Undercooling during Clinopyroxene Growth in Trachybasaltic Magmas: Insights on Magma Decompression and Cooling at Mt. Etna Volcano. *Geochim. Cosmochim. Acta* 268, 258–276. doi:10.1016/j.gca.2019.10.009

Mollo, S., Blundy, J., Scarlato, P., De Cristofaro, S. P., Tecchiato, V., Di Stefano, F., et al. (2018). An Integrated P-T-H2o-Lattice Strain Model to Quantify the Role of Clinopyroxene Fractionation on REE+Y and HFSE Patterns of Mafic Alkaline Magmas: Application to Eruptions at Mt. Etna. *Earth-Science Rev.* 185, 32–56. doi:10.1016/j.earscirev.2018.05.014

Mutch, E. J. F., Maclennan, J., Shorttle, O., Edmonds, M., and Rudge, J. F. (2019). Rapid Transcrustal Magma Movement under Iceland. *Nat. Geosci.* 12, 569–574. doi:10.1038/s41561-019-0376-9

Neave, D. A., and Putirka, K. D. (2017). A New Clinopyroxene-Liquid Barometer, and Implications for Magma Storage Pressures under Icelandic Rift Zones. *Am. Mineral.* 102, 777–794. doi:10.2138/am-2017-5968

Neave, D. A., Buisman, I., and Maclennan, J. (2017). Continuous Mush Disaggregation during the Long-Lasting Laki Fissure Eruption, Iceland. *Am. Mineral.* 102, 2007–2021. doi:10.2138/am-2017-6015CCBY

Neave, D. A., Bali, E., Guðfinnsson, G. H., Halldórsson, S. A., Kahl, M., Schmidt, A.-S., et al. (2019). Clinopyroxene-Liquid Equilibria and Geothermobarometry in Natural and Experimental Tholeiites: the 2014-2015 Holuhraun Eruption, Iceland. *J. Petrol.* 60, 1653–1680. doi:10.1093/petrology/egz042

Nielsen, R. L. (2011). The Effects of Re-homogenization on Plagioclase Hosted Melt Inclusions. *Geochem. Geophys. Geosyst.* 12, a–n. doi:10.1029/2011GC003822

Oeser, M., Dohmen, R., Horn, I., Schuth, S., and Weyer, S. (2015). Processes and Time Scales of Magmatic Evolution as Revealed by Fe-Mg Chemical and Isotopic Zoning in Natural Olivines. *Geochim. Cosmochim. Acta* 154, 130–150. doi:10.1016/j.gca.2015.01.025

Oppenheimer, C., Scaillet, B., Woods, A., Sutton, A. J., Elias, T., and Moussallam, Y. (2018). Influence of Eruptive Style on Volcanic Gas Emission Chemistry and Temperature. *Nat. Geosci* 11, 678–681. doi:10.1038/s41561-018-0194-5

Petrelli, M., Zellmer, G. F., and Vetere, F. (2020). "Rates and Timescales of Magma Transfer, Storage, Emplacement, and Eruption," in *Dynamic Magma Evolution. Geophysical Monograph Series*, 1–41. doi:10.1002/9781119521143.ch1

Petrone, C. M., Bugatti, G., Braschi, E., and Tommasini, S. (2016). Pre-eruptive Magmatic Processes Re-timed Using a Non-isothermal Approach to Magma Chamber Dynamics. *Nat. Commun.* 7, 12946. doi:10.1038/ncomms12946

Putirka, K. D. (2008). 3. Thermometers and Barometers for Volcanic Systems. *Rev. Mineral. Geochem.* 69, 61–120. doi:10.1515/9781501508486-004

Rasmussen, D. J., Plank, T. A., Roman, D. C., Power, J. A., Bodnar, R. J., and Hauri, E. H. (2018). When Does Eruption Run-Up Begin? Multidisciplinary Insight from the 1999 Eruption of Shishaldin Volcano. *Earth Planet. Sci. Lett.* 486, 1–14. doi:10.1016/j.epsl.2018.01.001

Salas, P., Ruprecht, P., and Hernández, L. (2021). Out-of-Sequence Skeletal Growth Causing Oscillatory Zoning in arc Olivines. *Nat. Commun.* 12, 4069. doi:10.1038/s41467-021-24275-6

Shea, T., Lynn, K. J., and Garcia, M. O. (2015). Cracking the Olivine Zoning Code: Distinguishing between crystal Growth and Diffusion. *Geology* 43, 935–938. doi:10.1130/G37082.1

Shea, T., Hammer, J. E., Hellebrand, E., Mourey, A. J., Costa, F., First, E. C., , et al. Lynn, K. J., Melnik, O. (2019). Phosphorus and aluminum zoning in Oolivine: contrasting behavior of two nominally incompatible trace elements. *Contrib. Mineral.* doi:10.1007/s00410-019-1618-710.1007/s00410-019-1618-y

Smith, I. E. M., and Németh, K. (2017). "Source to Surface Model of Monogenetic Volcanism: a Critical Review," in *Monogenetic Volcanism*. Editors K. Németh, G. Carrasco-Nuñez, J. J. Aranda-Gómez, and I. E. M. Smith (London, UK: Geological Society of London Special Publication), 446, 1–28. doi:10.1144/sp446.14

Streck, M. J. (2008). Mineral Textures and Zoning as Evidence for Open System Processes. *Rev. Mineral. Geochem.* 69, 595–622. doi:10.2138/rmg.2008.69.15

Till, C. B., Vazquez, J. A., and Boyce, J. W. (2015). Months between Rejuvenation and Volcanic Eruption at Yellowstone Caldera, Wyoming. *Geology* 43, 695–698. doi:10.1130/g36862.1

Ubide, T., and Kamber, B. S. (2018). Volcanic Crystals as Time Capsules of Eruption History. *Nat. Commun.* 9 (1), 326. doi:10.1038/s41467-017-02274-w

Ubide, T., Gale, C., Larrea, P., Arranz, E., and Lago, M. (2014). Antecrysts and Their Effect on Rock Compositions: the Cretaceous Lamprophyre Suite in the Catalonian Coastal Ranges (NE Spain). *Lithos 206–* 207, 214–233.

Ubide, T., McKenna, C. A., Chew, D. M., and Kamber, B. S. (2015). High-resolution LA-ICP-MS Trace Element Mapping of Igneous Minerals: In Search of Magma Histories. *Chem. Geol.* 409, 157–168. doi:10.1016/j.chemgeo.2015.05.020

Ubide, T., Mollo, S., Zhao, J. X., Nazzari, M., and Scarlato, P. (2019a). Sector-zoned Clinopyroxene as a Recorder of Magma History, Eruption Triggers, and Ascent Rates. *Geochim. Cosmochim. Acta* 251, 265–283. doi:10.1016/j.gca.2019.02.021

Ubide, T., Caulfield, J., Brandt, C., Bussweiler, Y., Mollo, S., Di Stefano, F., et al. (2019b). Deep Magma Storage Revealed by Multi-Method Elemental Mapping of Clinopyroxene Megacrysts at Stromboli Volcano. *Front. Earth Sci.* 7, 239. doi:10.3389/feart.2019.00239

Welsch, B., Hammer, J., and Hellebrand, E. (2014). Phosphorus Zoning Reveals Dendritic Architecture of Olivine. *Geology* 42, 867–870. doi:10.1130/G35691.1

Welsch, B., Hammer, J., Baronnet, A., Jacob, S., Hellebrand, E., and Sinton, J. (2016). Clinopyroxene in Postshield Haleakala Ankaramite: 2. Texture, Compositional Zoning and Supersaturation in the Magma. *Contrib. Mineral. Petrol.* 171, 6. https://doi.org/10.1007/s00410-015-1213-9.

Conflict of Interest: The authors declare that the research was conducted in the absence of any commercial or financial relationships that could be construed as a potential conflict of interest.

Publisher's Note: All claims expressed in this article are solely those of the authors and do not necessarily represent those of their affiliated organizations, or those of the publisher, the editors and the reviewers. Any product that may be evaluated in this article, or claim that may be made by its manufacturer, is not guaranteed or endorsed by the publisher.

frontiers in Earth Science

ORIGINAL RESEARCH
published: 15 November 2019
doi: 10.3389/feart.2019.00300

Forming Olivine Phenocrysts in Basalt: A 3D Characterization of Growth Rates in Laboratory Experiments

Adrien J. Mourey and Thomas Shea*

Department of Earth Sciences, University of Hawai'i at Mānoa, Honolulu, HI, United States

Our current knowledge of the genesis, ascent, storage, and eruption of mafic magmas is intimately linked with olivine, its primary crystal cargo. Recent claims that phenocryst-size crystals can grow rapidly and non-concentrically are challenging our perception of what olivine zoning represents (e.g., controlled by growth and/or diffusion), and whether accurate magma crystallization and diffusion timescales can be retrieved. A series of cooling experiments using a dry basalt was carried out in order to quantify the kinetics of olivine growth as a function of the degree of undercooling, and to characterize morphological changes occurring with time. After a 24 h equilibration step at 1290°C (10°C above the olivine liquidus), experiments were rapidly cooled to final temperatures T_f = 1270, 1255, 1240, or 1220°C (imposing undercoolings of $-\Delta T$ = 10, 25, 40, and 60°C, respectively). Growth rates estimated via 3D microtomography renderings of experimental crystals attain 10^{-7} m/s, and are found to be almost an order of magnitude higher than those calculated using 2D sections of the same experiments. We show that mm-sized crystals similar to those found in natural Kīlauea samples can be produced after a few hours under moderate undercooling conditions (25–60°C). Growth rates decrease faintly with time, accompanying transitions between skeletal/hopper and more polyhedral morphologies. Growth rates generally increase until $-\Delta T$ = 40°C, and decrease slightly at $-\Delta T$ = 60°C as rates of nucleation likely increase. The $-\Delta T$ = 40°C vicinity may therefore represent a thermal "sweet spot" for the formation of phenocrysts in dry basalt. Olivine overgrowths on crystals that survived initial dissolution grow slower than homogeneously nucleated crystals, illustrating how new and old crystals in natural magmas likely respond differently to a thermal perturbation. We suggest that the main growth direction of natural olivine (a- or c-axis) may be a sensitive function of undercooling and the presence of a pre-existing growth substrate. Olivine grows faster along the *a*-axis under moderate to high undercooling conditions, while preferred development along the *c*-axis likely occurs under lower undercooling conditions and/or as rims grow around existing crystals. The early history of skeletal olivine crystals is controlled by diffusion in the melt (diffusion-controlled growth regime), while their long-term compositional zoning history is mainly controlled by diffusive re-equilibration.

Keywords: olivine, growth rates, 3D morphology, diffusion, basalt

OPEN ACCESS

Edited by:
Teresa Ubide,
The University of Queensland, Australia

Reviewed by:
Philipp Ruprecht,
University of Nevada, Reno, United States
Takeshi Kuritani,
Hokkaido University, Japan
Silvio Mollo,
Sapienza University of Rome, Italy

****Correspondence:***
Adrien J. Mourey
amourey@hawaii.edu

Specialty section:
This article was submitted to Petrology, a section of the journal Frontiers in Earth Science

Received: *24 July 2019*
Accepted: *31 October 2019*
Published: *15 November 2019*

Citation:
Mourey AJ and Shea T (2019) Forming Olivine Phenocrysts in Basalt: A 3D Characterization of Growth Rates in Laboratory Experiments. Front. Earth Sci. 7:300. doi: 10.3389/feart.2019.00300

INTRODUCTION: OVERVIEW OF OLIVINE GROWTH RATES AND MORPHOLOGY

Olivine is a widespread mineral in ultramafic to intermediate volcanic and igneous rocks (e.g., basalt to andesite, shoshonite, komatiite, boninite, peridotite, or gabbro) representative of various tectonic settings (Pearce and Cann, 1973). In primitive ocean island basalt, for instance, olivine is the only crystallizing phase and thus the main record for a number of given magmatic processes (fractionation, magma mixing, magma degassing, magma transport). Olivine is also common in extraterrestrial rocks like on the Moon. In fact, the early history of lunar rocks is inferred from the kinetics of solidification of the "magma ocean," where olivine was the first crystallizing phase (e.g., Isaacson et al., 2011). Olivine is also a primary phase in Martian basalt, and its composition yields key insights on the evolution of volcanism on Mars (e.g., Ody et al., 2013). For petrologists working on mafic magmas in terrestrial or extraterrestrial rocks, comparing experimental and natural olivine morphologies is crucial in order to retrieve the disequilibrium conditions and cooling history during a magmatic event (First and Hammer, 2016).

The crystallization kinetics of olivine can provide quantitative information about timescales of magma storage and differentiation. The crystal size distribution (CSD) method, where measured crystal dimensions are linked to duration based on available growth rate estimates (e.g., Vinet and Higgins, 2010), is one example. Growth rates are usually assumed to be lower in deep reservoirs where magmas crystallize close to equilibrium, and higher during magma ascent and rapid cooling (Armienti et al., 1994). Knowledge of growth rates is also crucial to characterize the competition between growth and diffusion kinetics under variable magma temperature conditions. Applications of geospeedometry generally require crystallization to be much faster than diffusion, meaning that growth-induced compositional zoning can be effectively discarded from diffusion models and timescale extraction (Costa et al., 2008). Quantification of olivine growth rates is therefore needed to discriminate between chemical zoning resulting from growth vs. diffusion (Shea et al., 2015b). Diffusion modeling is rapidly becoming a central theme for petrological interpretations based on olivine compositions (Lynn et al., 2017), and verifying underlying assumption about growth rates is now imperative. Improving the accuracy of growth rate and morphological development models for olivine could also provide valuable information about the rate of entrapment of olivine-hosted melt inclusions and their fidelity in preserving original melt compositions (Faure et al., 2003, 2007). If growth is fast compared to diffusive re-equilibration of elements in the surrounding melt, boundary layers can form and compromise the interpretation of melt inclusion compositions (Faure and Schiano, 2005). Timescales for the formation of the boundary layers therefore also require robust estimates of growth rates.

Much of our knowledge of the morphological development, reaction rates, thermodynamics of crystallization in silicate melts comes from early experimental work on lunar basalt (e.g., Lofgren et al., 1974; Walker et al., 1976). Donaldson (1976) focused on the crystallization of olivine in lunar and other basaltic–picritic–peridotitic rocks, showing that its morphology depends primarily on the degree of undercooling (i.e., $\Delta T = T_{liq} - T$; the time-independent thermodynamic driving force expressed as the difference between the olivine liquidus and the temperature considered). Four growth morphologies are usually associated with different growth conditions (Donaldson, 1976): polyhedral, tabular, skeletal/hopper, and dendritic by order of increasing growth rate. At relatively low $-\Delta T$ (∼10–40°C), olivine is well-faceted ("polyhedral") morphologies, whereas crystals grown at higher $-\Delta$T (∼40–150°C) exhibit hopper cavities and/or skeletal to dendritic branching (Donaldson, 1976). Although transitions between different morphologies are poorly constrained and may depend on melt composition, polyhedral, tabular, and hopper morphologies are typically representative of low undercooling ($-\Delta$T < 60°C) and dendrites are formed at $-\Delta T > 60$°C (Faure et al., 2003). Thus, undercooling controls olivine growth rate, and thereby the final crystal morphology (Faure et al., 2003). The formation of hopper olivine, a morphology prone to entrapment of melt inclusions, has been notably associated with preferential faster growth along the *a*-axis direction (e.g., Faure et al., 2003).

Because olivine phenocrysts usually exhibit polyhedral morphologies in magmas, they are canonically viewed as having grown slowly at low degrees of undercooling and in a concentric "tree-ring" fashion (e.g., Clark et al., 1986). Thus, studies using olivine to interpret magmatic processes have largely assumed near-equilibrium conditions for phenocryst crystallization and element partitioning (Pearce, 1984). The assumption that polyhedral olivine grows slowly under near-equilibrium conditions has been contested by Welsch et al. (2014), who showed that even large polyhedral olivine phenocrysts can preserve morphological remnants (e.g., stepped hopper cavities) of an early rapid growth. They hypothesized that olivine initially grows rapidly, forming a skeletal olivine framework that is progressively infilled as undercooling and growth rates decrease. Experimental studies have also demonstrated that mineral growth rates also depend on the delay in nucleation (cf. Hammer, 2008 and references therein). The delay in nucleation increases with lower undercooling or lower olivine content (Donaldson, 1979), and nucleation controls growth rate by forcing distribution of the crystalizing mass around few or numerous crystals – i.e., lower nucleation density corresponding to higher growth rate (e.g., Swanson, 1977).

Despite being one of the most studied minerals, the growth rate of olivine is poorly constrained. Early estimates of growth rates relevant to the development of skeletal crystals based on a diffusion-limited aggregation model (Fowler et al., 1989), diffusion coefficients measurements (Donaldson, 1975), or apparent size distribution density (Armienti et al., 1991) all hovered around $\sim 10^{-9}$ m/s. A more thorough, systematic quantification of growth rates as a function of undercooling was carried out by Jambon et al. (1992), who crystallized olivine within feldspar melt inclusions in a tholeiite basalt. Despite the clever experimental setup designed to avoid olivine crystallization on melt inclusion walls, the small size of olivine crystals formed ($\leq$50 μm), coupled with difficulties in estimating the dimensions

of complex 3D skeletal crystals in a 2D section, imply substantial uncertainty in the growth-rate data. Their results showed that lower growth rates (10^{-10}–10^{-9} m/s) yielded polyhedral crystals at $-\Delta T$ = 15–35°C, whereas higher growth rates ($\sim 10^{-8}$–10^{-7} m/s) produce skeletal morphologies at $-\Delta T$ = 56–150°C. Melt inclusion migration experiments performed at very low undercoolings also yielded very slow olivine growth rates around 10^{-9} m/s (Schiano et al., 2006). These two studies are currently the only available sources for olivine growth-rate vs. undercooling data for natural magma compositions.

Growth-rate experiments addressing the complexities of 3D morphologies in a natural basalt using new imaging techniques are thus urgently needed. In order to quantify the preferred interfacial direction of growth, the evolution of these 3D morphologies need to be considered as a function of undercooling. This study focuses on the effects of undercooling and time on olivine growth rate, after a small-to-moderate temperature perturbation (10–60°C), using a 3D quantitative approach. The 3D textural attributes of olivine yield new insights on the undercooling required for phenocryst crystallization, their growth rates, the origin of skeletal olivine in mafic rocks, the evolution of olivine morphologies and its framework as a function of undercooling and time. We also discuss the implications of these results for discriminating growth vs. diffusion induced zoning.

MATERIALS AND METHODS

Experimental Protocol

A natural parental Kīlauea tholeiitic composition (see **Supplementary Table B** for chemical composition) was used as starting material for our crystallization experiments, partly because Hawaiian basalts have played a central role in our understanding of the formation and evolution of mafic magmas (Garcia, 2015). This composition also has the advantage of replicating complexities that exist in natural systems (e.g., all major, minor, and trace elements present), while avoiding the effects of crystallization of other mineral phases (e.g., Clague et al., 1995; Garcia and Hulsebosch, 1995; Herzberg, 2011). Phase equilibria of Hawaiian tholeiitic magmas show that olivine is the only crystallizing phase for >100°C below the liquidus (Wright, 1971), which is also consistent with MELTS models at 1-atm and a range of fO_2 (**Figure 1A**). Oxygen fugacity conditions are relatively well constrained for Kīlauea magmas within ∼1 order of magnitude in $\log(fO_2)$ (Rhodes and Vollinger, 2005; Helz et al., 2017). The low viscosity of tholeiitic basalts also has the benefit of reducing kinetic delays for melting and crystallization. The starting material consists in glassy, weakly olivine-phyric (<4 vol.%) pyroclasts from the 1820 CE eruption at Kīlauea with a relatively primitive bulk composition (11.4 wt.% MgO, with an equilibrium olivine composition $Fo_{85.5}$) (Garcia et al., 2003). Olivine crystals >500 μm were removed from the starting powder in order to reduce variations in starting composition induced by the presence of large phenocrysts between different experiments. One olivine phenocryst "seed" (∼0.5–1 mm) from the 1820 CE powder with typical core composition Fo_{87-89} (Lynn et al., 2017) was added to every experiment to test for the potential effect of overgrowth on calculated olivine growth rates. Each experiment consists in two duplicate ∼5 mm diameter beads of starting material glued with polyvinyl alcohol around rhenium wire loops. Using rhenium largely circumvents problems of Fe, Ni, and Co loss to precious metals (e.g., Borisov and Jones, 1999; Filiberto et al., 2010). EDS analyses of rhenium wires after experimental runs yield barely detectable (<0.1 wt.%) Fe, Ni, or Co. Having a duplicate for each experiment meant that one could be used for 3D measurements, while the other could be sectioned and (1) analyzed for glass compositions, and (2) measured for 2D growth rates (see below). The two Re wires holding the charges were attached to a hanger so as to be side-by-side, and then hung on a 0.38 mm "zap" platinum wire, within in a 1-atm CO_2 – H_2 gas-mixing furnace with fO_2 control. One-atmosphere experiments are appropriate for the study of Hawaiian tholeiite magmas, which typically crystallize at low pressure (0.05–0.2 GPa; Wright and Klein, 2014) and are H_2O-poor (∼0.1–0.5 wt.%; Wallace and Anderson, 1998). The olivine liquidus temperature (T_{liq} = 1280 ± 3°C) was defined by carrying out equilibrium experiments (see **Supplementary Material** for details), and tallies well with the value predicted by MELTS (1282°C) for this composition.

The starting material was annealed for ∼24 h at T_i = 1290°C, about 10°C above the olivine liquidus (**Figure 1B**) to ensure dissolution of any finely crushed residual olivine and formation of pure melt plus the added larger olivine seed. After annealing, samples were cooled in a 2–4 min single step to the final temperature T_f = 1270, 1255, 1240, or 1220°C (imposing $-\Delta T$ = 10, 25, 40, and 60°C respectively, **Figure 1B**) for isothermal experiments. This range in undercooling was chosen to (1) promote a range in olivine growth rates (Jambon et al., 1992; Faure et al., 2003), and (2) be applicable to common processes such as magma mixing, where a somewhat abrupt change in temperature might occur between a recharge and a resident magma (e.g., Lynn et al., 2017). In this sense, our experiments are well-suited for the quantification of growth rate and for scenarios of rapid temperature changes, but are not meant to reproduce more continuous cooling conditions occurring in natural magma. Run durations between 20 min and 4 days were selected to resolve the early stages of growth and the beginning of crystal maturation. An additional experiment (T_i = 1290°C, T_f = 1220°C) was quenched at the end of the 4 min-long rapid cooling step and lacked newly formed olivine entirely. Mg X-ray maps acquired within a sample quenched after 24 h at the initial conditions (1290°C) confirmed the absence of localized magnesium heterogeneities that could influence subsequent growth of olivine (see **Supplementary Figure S2**).

It should be noted that aside from differences in experimental volumes and techniques used to estimate growth rates, the experimental strategy employed herein differs from that of Jambon et al. (1992) in one major respect: they used closed melt inclusions as experimental vessels for olivine crystallization in order to isolate the process of growth from that of nucleation, while our olivine is allowed to grow "freely" in a much larger volume of melt. This strategy allowed them to explore growth even at high degrees of undercooling ($-\Delta T$ = 150°C), a region

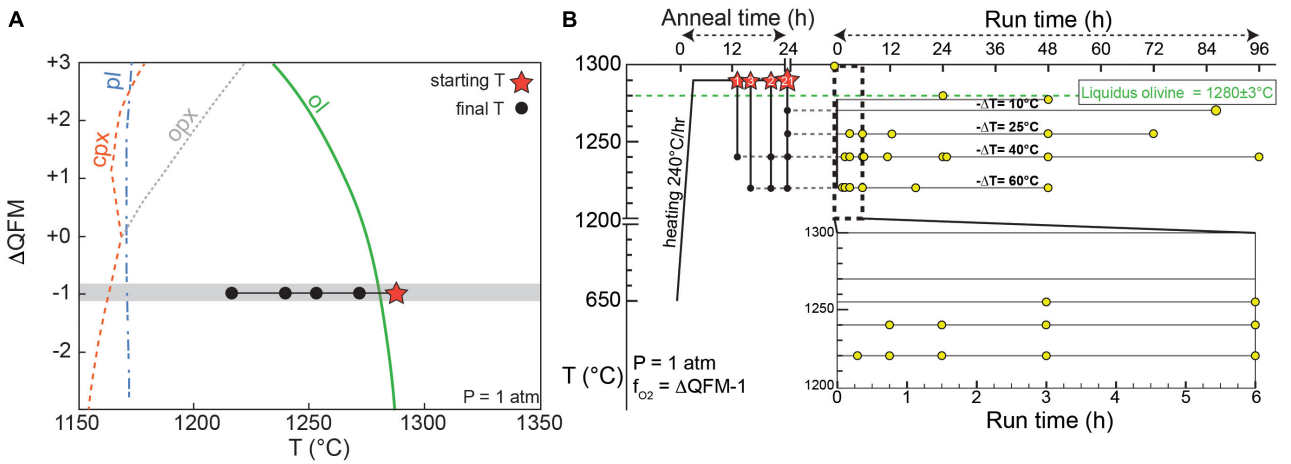

FIGURE 1 | (A) Temperature-fO_2 phase equilibria diagram calculated from MELTS using the Kīlauea 1820CE bulk composition at 1 atm (modified from Shea et al., 2019). Gray region shows the range in fO_2 imposed in the experiments. **(B)** Proposed experimental strategy, with initial superliquidus anneal periods (red stars over the olivine-in curve, numbers indicate the number of experiments for each anneal time). Anneals were followed by rapid cooling to final conditions (black circles) at T = 1220, 1240, 1255, or 1270°C, and left for dwell times 20 min – 4 days. Yellow dots are experimental quenches at given T–t conditions (27 runs total).

where nucleation rates could otherwise have an important effect in on crystal sizes (e.g., Waters and Lange, 2013). In our experiments, both nucleation and growth contribute to producing the final crystal population, with the disadvantage that separating the two becomes difficult, but with the key advantage of being directly applicable to natural crystallizing magmas where nucleation is uninhibited.

Analytical Methods

Major and minor element composition (Si, Ti, Al, Fe, Mn, Mg, Ca, Na, K, P) of the experimental glasses were determined using a JEOL JXA-8500F Hyperprobe with five wavelength-dispersive spectrometers at the University of Hawai'i. Glasses were analyzed using an accelerating voltage of 15 kV, a probe current of 10–20 nA, with a defocused 10–15 μm beam. Peak counting time was 40 s for each element. A99 basalt glass (USNM 113498/1) and VG2 was used for Si, Al, Fe, Mg, Ca, K-Orthoclase (OR-1) for K, Sphene glass for Ti, Durango F-Apatite for P, and Verma Garnet for Mn. Relative precision (2σ) based on repeat analysis of standards is better than 1% for Si, Ti, Al, Fe, Mg, Ca, 1.5% for Mn, about 4% for Na, 20% for K, and 40% for P. Accuracy is <1% for Si, Al, Mg, Ca, Na, K, about 2% for Ti, Fe, P, and 5% for Mn.

Textural Analyses

Measuring the dimensions of crystals on a 2D section is problematic due to intersection effects. Sectioning even a single crystal of a given size and morphology can cause substantial variability in section dimensions (Shea et al., 2015a). As a result, tracking the transient growth of crystals with potentially complex morphologies in 2D likely leads to significant added uncertainty. To circumvent these issues, a full, high-resolution 3D textural characterization was performed at the X-ray UTCT facility hosted at the University of Texas. For each experiment, 2D growth rates were also estimated from measured exposed crystal areas and compared with 3D measurements.

Three-dimensional analyses on seven experimental charges embedded in resin were performed using a Xradia microXCT Scanner. The samples were rotated and imaged between a standard cone-beam micro-CT (Feldkamp et al., 1984; Turbell, 2001) and a X-ray detector. The detector-sample distance was fixed at 35.5 mm for all scans, yielding a voxel size of 3.43 μm. The analytical challenge consisted in resolving the low density contrast between olivine and surrounding glass. A relatively low mean X-ray energy of 70 kV helped distinguish the glass from the crystals. Reconstruction parameters were optimized to reduce beam-hardening artifacts (see **Supplementary Table C**). The duration of one individual scan varies from 3 to 9 h depending on the resolution and the magnification. After the post-reconstruction phase, the contrast of all slices was improved using the ImageJ software. All image stacks combined were then imported in Avizo™ for manual segmentation and volume rendering. Minor smoothing was applied to minimize jagged edges. Comparison of 3D images of skeletal crystals with a 2D section from the same crystal allowed us to quickly establish and verify clear connections between crystals that appear disconnected on a 2D section. Most olivine crystals (i.e., those that appeared through at least a few slices and therefore with sizes >10–20 μm) were well resolved in the 3D renderings. Higher resolution BSE images collected using the microprobe helped confirm that the 3D renderings were not missing large populations of small crystals. Growth rates were calculated in three ways: "*2D*" and "*3D*" growth rates were obtained by dividing the dimension of the longest of the three axes (*a*, *b*, or *c*) by the experimental time. "*Chemically*"-calculated growth rates were determined from mass-balance using initial and final glass MgO contents (with the initial MgO content equal to 11.35 wt.% and the final glass composition corresponding to the composition at the end of the experiment; the fraction of olivine and the growth rates are then derived from the difference of magnesium content; see **Supplementary Material**

for details). In essence, these values provide theoretical maximum attainable growth rates.

RESULTS AND INTERPRETATIONS

Textural and Morphological Characteristics

Olivine is the only crystallizing phase in the experimental charges. The total olivine content estimated by mass-balance calculation shows that olivine crystallization occurs as a two-step process, with a high crystallization rate phase followed by a low crystallization rate "plateau" where additional crystallization is minimal (**Figure 2** and calculations available in the **Supplementary Material**). This evolution is typical of a rapid response to disequilibrium, and slower attainment of an equilibrium state (Avrami, 1939; Johnson and Mehl, 1939; Kirkpatrick, 1981). A near equilibrium crystal content is reached after ~3 h for a $-\Delta T = 60°C$, ~6 h for a $-\Delta T = 40°C$, and ~12 h for a $-\Delta T = 25°C$, consistent with an undercooling dependence of crystallization rates. Higher degrees of undercooling result in higher crystal content, reflecting a larger disequilibrium. The rapid increase in crystallization rates is well observed at $-\Delta T = 60$ and 40°C, but becomes slightly delayed at 25°C, and significantly delayed at 10°C. Run products contain phenocryst-size olivine with various two-dimensional morphologies. Single crystals are randomly oriented in all runs. Olivine from the $-\Delta T = 60°C$ and $-\Delta T = 40°C$ series generally exhibit skeletal crystals (**Figures 3C–H**) and the $-\Delta T = 25°C$ series reflects a transition between hopper/skeletal and polyhedral habits (**Figures 3A,B**). True dendritic crystals – defined here as a branch-like habit with no apparent overall faceted form – are not produced in any of the runs. Short runs at high undercooling reflecting the initiation of growth (**Figures 3C–G**) show more acicular and smaller crystals. Longer experiments (>6 h, **Figures 4A,D**) display a high density of >1 mm crystals (see variation of the crystal size in **Table 1**), with the appearance of growth sub-units or "buds" (e.g., Welsch et al., 2013) (**Figure 4A**). Short experiments with $-\Delta T = 40–60°C$ (**Figures 4B,C,E**) grow preferentially along the *a*-axis direction. The lack of preferential growth with small undercooling (e.g., $-\Delta T = 25°C$ runs, **Figures 3A,B**) suggests that growth along a preferential direction increases with the undercooling. Primary olivine branches form rapidly (<0.5 h for $-\Delta T = 40–60°C$) after reaching the final temperature (**Figure 3G**), and an outer, faceted shell forms after a few minutes to a few hours depending on the degree of undercooling (**Figures 3C–G**). After typically a few hours, skeletal olivine (**Figures 3D–H**) display secondary branches that often track the outer shell interfacial directions, and which connect the primary branches. These secondary branches progressively fill the crystals and lead to partial or complete entrapment of open and closed hour-glass inclusions (**Figures 3D,E**).

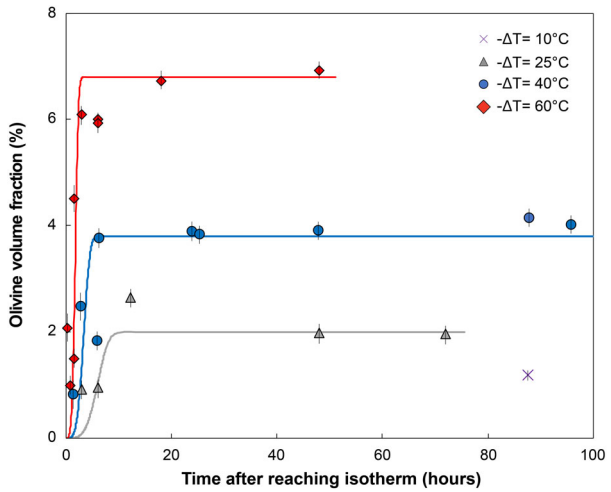

FIGURE 2 | Percentage of olivine crystallized vs. time after reaching the final isotherm (hours). Olivine volume fraction is obtained by mass-balance from the MgO content measured in the glass before and after crystallization (see **Supplementary Material** for details). Each point represents the average of three to eight electron microprobe spots per experiment, typically five to six spots. Error bars show the 2σ variation in the analysis. Global trends for each temperature were calculated from the Avrami equation $\varphi_x = 1 - \exp(-k_v I G^3 t^4)$ with φ_x the crystal volume fraction, *I* the crystal nucleation rate, *G* the crystal growth rate, *t* the time, and assuming a volumetric factor $k_v = 4\pi/3$ for spherical crystals. No attempt was made to utilize growth or nucleation rates from the experiments to calculate these curves. Instead, parameters (see **Supplementary Table E**) were chosen to best fit the data, to provide first-order predictions of the topology of crystallization rates.

Growth Rates

Growth rates are first presented by examining crystal sizes obtained from 3D μCT renderings of the $-\Delta T = 40–60°C$ runs. Measurements of the olivine were performed considering the edges of the crystals, and not with the maximum elongation of the primary branches. The error associated with this assumption reaches 10% for the fastest calculated growth rates, but is <5% for the lowest calculated growth rates. The maximum crystal size, observed systematically along the *a*-axis, increases slightly with time for all runs, although there is significant overlap between the different runs (**Figure 5B**). Values range between 120 μm for short runs (e.g., 1.5 h at $-\Delta T = 60°C$) and 1400 μm for the longest run analyzed (18 h at $-\Delta T = 60°C$). In $-\Delta T = 60°C$ runs, olivine crystals display a linear increase in the average *a*-/*b*-axis ratio during the first 6 h (**Figure 5B**) from $a/b = 4$ after 1.5 h to 7 after 6 h (**Figure 5A**). Then, the subsequent decrease of the *a*-/*b*-axis ratio can be interpreted by maturation of crystals through growth along the *b*-axis. A more gradual increase of the *a*-/*b*-axis ratio is observed for $-\Delta T = 40°C$ runs. The *a*-/*b*-axis ratio increases with time (3–6 for $t = 1.5$ h runs and between 2 and 15 for $t = 18$ h runs). This ratio is more variable for the $-\Delta T = 60°C$ runs compared to the $-\Delta T = 40°C$ runs. The same general trend is observed for the *a*-/*c*-axis ratio, with less departure from the main positive trend (c.f. **Supplementary Table D**). The highest values of the *a*-/*b*-axis ratio correspond to early skeletal crystals which are growing under high disequilibrium conditions with the melt. Smaller crystals that likely nucleated later during the run and larger, more mature crystals both have lower *a*-/*c*-axis and *a*-/*b*-axis ratios, likely reflecting a lower degree of undercooling.

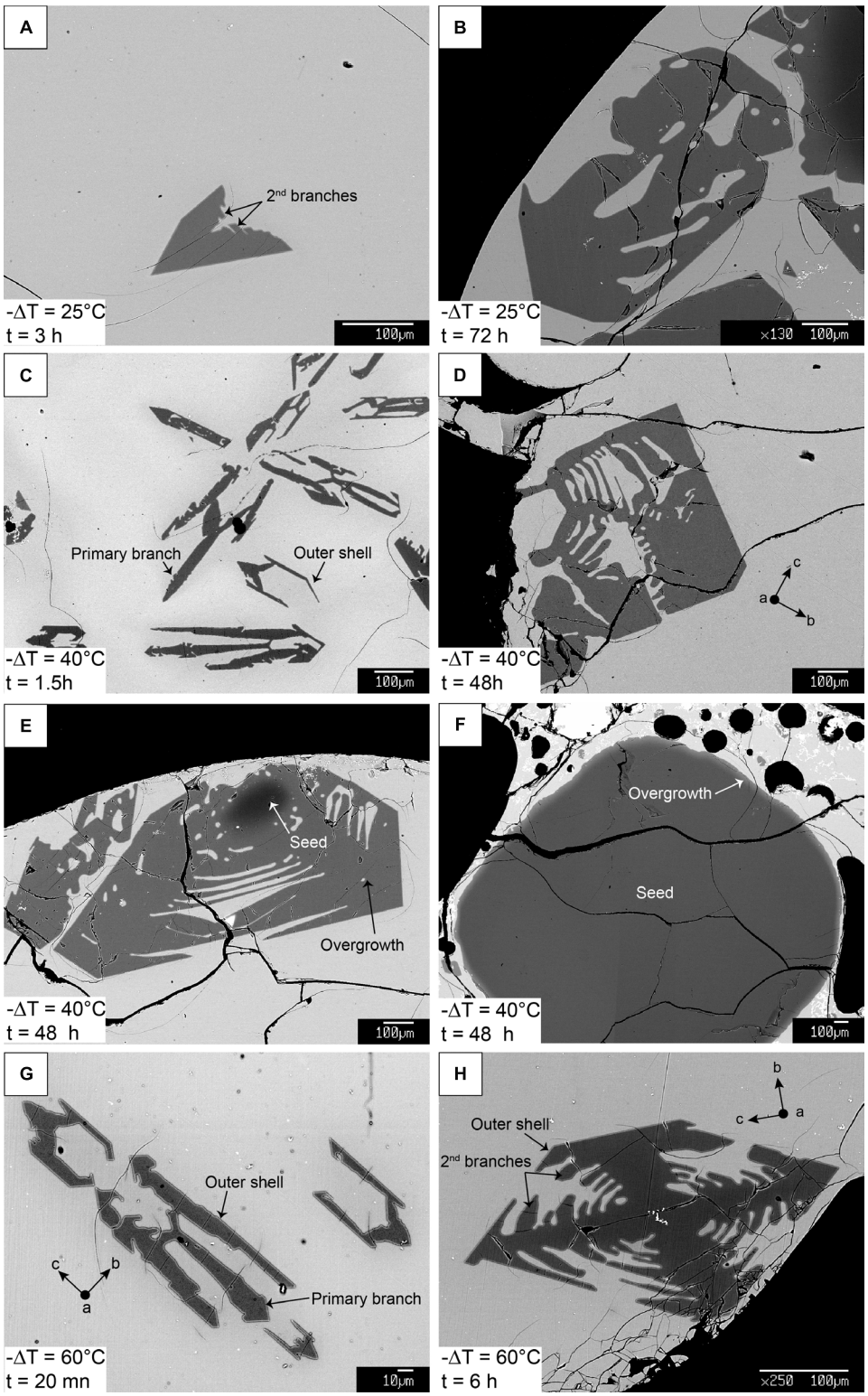

FIGURE 3 | BSE images of experimental olivine at different times and temperatures showing processes of growth and ripening. Panels **(A,C,G)** and **(B,D,H)** display shorter and longer experimental durations for each undercooling, respectively. Sections elongated along the *c*-axis in panels **(C,D,G,H)** are commonly observed in 2D. However, 3D scans reveal that true elongation is most often along the *a*-axis, illustrating how sectioning effects can influence measured growth rates. Panels **(E)** and **(F)** are examples of two overgrown seeds in the same charge at $-\Delta T = 40°C$, 48 h, showing how seed size has a strong influence on growth rate and morphology along a given direction.

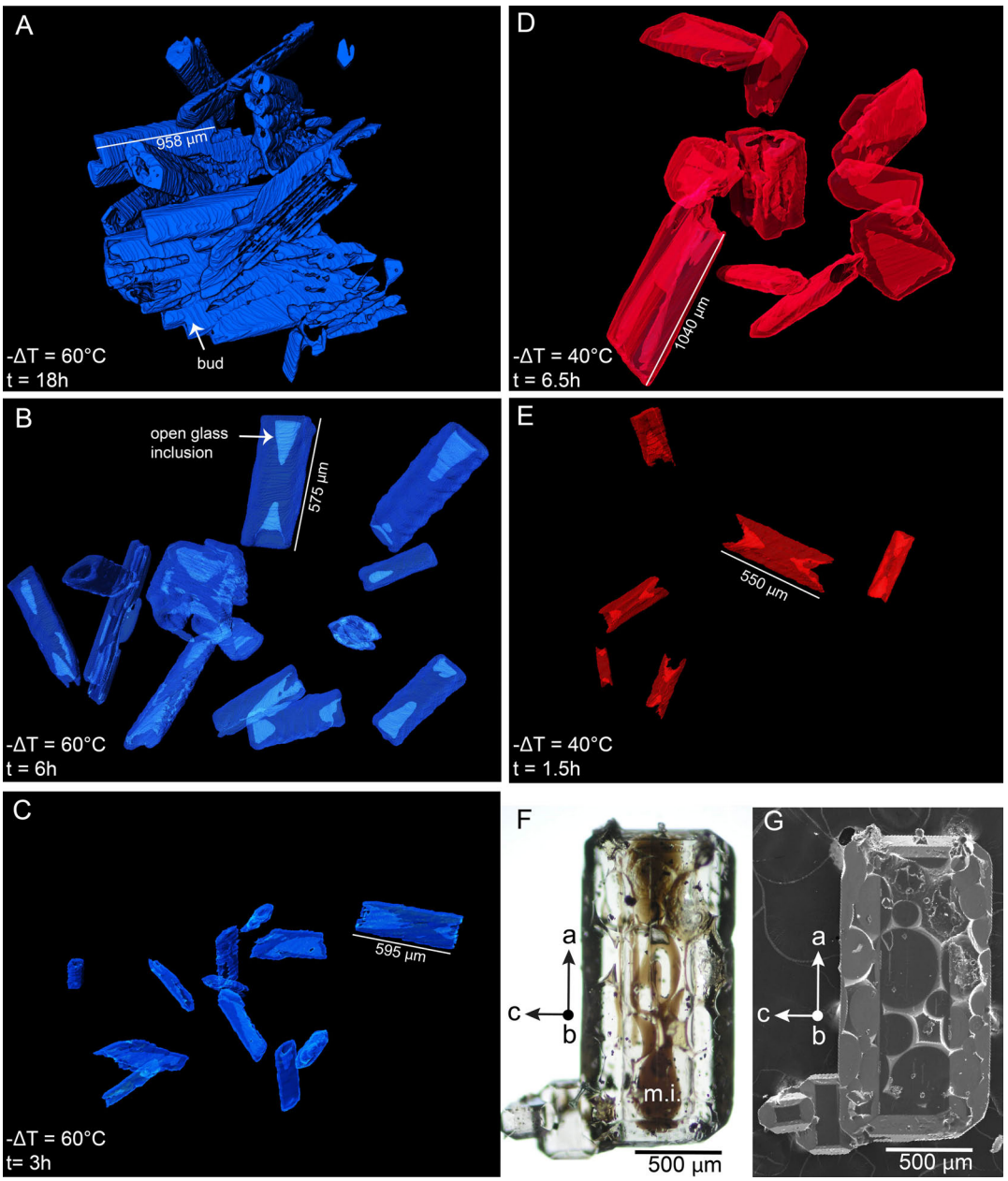

FIGURE 4 | Volume rendering of experimental olivine at different times and temperatures. **(A)** Crystals from an experiment at $-\Delta T$ = 60°C, 18 h; **(B)** Experiment at $-\Delta T$ = 60°C, 6 h; **(C)** Experiment at $-\Delta T$ = 60°C, 3 h; **(D)** Experiment at $-\Delta T$ = 40°C, 6.5 h; **(E)** Experiment at $-\Delta T$ = 40°C, 1.5 h; **(F,G)** Microscope and secondary electron image showing hourglass melt inclusions (m.i.) and the well-faceted morphology of a crystal from the 1820CE eruption of Kīlauea volcano that is also elongated along the *a*-axis.

Maturation along the *b*-axis starts after 6.5 h and 18 h for a $-\Delta T$ = 40 and 60°C, respectively (**Figure 5B**), meaning that lowering of the degree of undercooling or disequilibrium has a key role for maturation. A similar evolution is observed along the *c*-axis (c.f. **Supplementary Table D**). Maturation along the *b*-axis is faster close to the liquidus temperature. The consequence is that the volume of trapped glass inclusions globally increases with undercooling, and is also proportional to the size of the crystals (inclusions vary from 10^{-4} mm^3 for a 400-µm olivine to 5 × 10^{-3} mm^3 for a 1100-µm olivine crystal). The olivine maturation process is more obvious when the crystal size exceeds 700 µm. Compared to experimental runs at $-\Delta T$ = 40–60°C, most of the natural olivine crystals (skeletal, polyhedral, and budded crystals) from the 1820CE eruption of Kīlauea volcano have lower *a*-/*b*-axis ratios between 0.5 and 5. Extrapolation of our growth model to these natural crystals would indicate protracted maturation over timescales greater than 18 h.

TABLE 1 | Average length of experimental crystals measured in 3D (*n* = number of crystals measured) along the three crystallographic axes *a*, *b*, and *c*.

$-\Delta T$ (°C)	*t* (h)	*n*	Axis length (±10 μm)			mean *G* (m/s)	max *G* (m/s)
			a-axis	*b*-axis	*c*-axis		
60	1.5	8	127–321	39–72	87–197	$4.0 \cdot 10^{-8}$	$5.9 \cdot 10^{-8}$
60	3	12	310–674	65–108	93–244	$4.6 \cdot 10^{-8}$	$6.2 \cdot 10^{-8}$
60	6	13	381–1137	67–161	140–419	$3.1 \cdot 10^{-8}$	$5.3 \cdot 10^{-8}$
60	18	23	348–1387	64–187	112–420	$1.3 \cdot 10^{-8}$	$2.1 \cdot 10^{-8}$
40	1.5	7	277–641	100–120	137–222	$8.0 \cdot 10^{-8}$	$1.2 \cdot 10^{-7}$
40	3	5	587–817	60–144	203–276	$6.4 \cdot 10^{-8}$	$7.6 \cdot 10^{-8}$
40	6.5	10	658–1289	97–391	274–652	$3.9 \cdot 10^{-8}$	$5.5 \cdot 10^{-8}$

Growth rate values are given both as averages of all the measurement along the longest axis in 3D for each charge, as well as maxima.

The calculated volume of all experimental and natural olivine follows the same power law when considering the three axes independently (**Figure 5C**). The volume of olivine crystals increases with time, with values barely attaining the range measured for natural olivine (0.1–4 mm^3) for the longest runs (6.5 h at $-\Delta T$ = 40°C or 18 h at $-\Delta T$ = 60°C). Crystal >0.1 mm^3 are especially scattered around these main trends for the *a*-axis. The threshold at 0.1 mm^3 marked the transition from a crystallization regime during the first hours to a crystallization and maturation regime.

Growth rates, estimated from 3D renderings and MgO content of experimental charges, slowly decrease with time, with the shortest run time associated with the highest values around 10^{-7} m/s (**Figure 6**). Longest experiments thus yield the lowest values for growth rates. This temporal decrease in growth rate may be in part associated with integration of size data over longer experimental durations (e.g., Hammer, 2008; Brugger and Hammer, 2010). This integration effect may be deconvoluted by computing the growth rate as the change in crystal size between two successive experiments with different durations (i.e., rather than integrating the final size over the total duration) (see **Supplementary Table B**). Both calculation methods display a decrease in growth rate with time, though the effect of time integration becomes important after 3 h.

Two dimensional estimations of growth rates are consistent with previous values from Jambon et al. (1992). Both 3D measurements and MgO chemistry-obtained growth rates are within the same order of magnitude $\sim 10^{-8}$–10^{-7} m/s for a $-\Delta T$ = 40–60°C (**Figure 6**). The 3D values are one order of magnitude higher than those from Jambon et al. (1992) for $-\Delta T$ = 40°C runs, and within the same order of magnitude for $-\Delta$T = 60°C. The major difference in the present dataset is the decrease of growth rate with undercooling from 40 to 60°C undercooling. This decrease is likely due to the transition from growth-controlled crystallization to nucleation-controlled crystallization. This competition between nucleation and growth rates is inferred to commonly lead to fewer, larger crystals at low undercooling and numerous smaller crystals at high undercooling (e.g., Waters and Lange, 2013). The trade-off between how a crystallizing mass is distributed around fewer or more numerous crystals is well known and described by the Avrami equation (1939). Nucleation rate calculated from this equation using the 3D-measured growth rates and crystal fractions is about 10^5 olivine/m^3 at $-\Delta T$ = 40°C and 10^6 olivine/m^3 at $-\Delta T$ = 60°C, consistent with a shift toward undercooling values where nucleation becomes influential.

In some experiments it was possible to measure the 2D size of overgrown crystal seeds. Compared to 2D data from crystals that nucleated homogeneously in the charge, seed overgrowths generally yield lower growth rates. Values hover around 10^{-10}–10^{-9} m/s at $-\Delta T$ = 25°C, 10^{-10}–10^{-8} m/s at $-\Delta T$ = 40°C and 10^{-9}–10^{-8} m/s at $-\Delta T$ = 60°C, about one order of magnitude lower at $-\Delta T$ = 25°C, and comparable to newly formed crystals at $-\Delta T$ = 40–60°C.

DISCUSSION

The results presented above provide us with important constraints on growth rate of olivine as a function of time and undercooling. They highlight the relatively rapid growth kinetics of olivine in dry tholeiitic basalt, the comparatively slower process of maturing to larger phenocrysts, and importance of considering 3D morphology for growth rate calculations. The next sections examine the implications of these results in the context of (1) natural phenocryst growth, (2) growth mechanisms and element partitioning, and (3) the link between the presence of skeletal crystals in basalt magma and magma mixing processes. Subsequently, (4) a new development model for olivine is proposed, (5) the controversy surrounding the competition between growth and diffusion and its influence on compositional zoning is discussed in light of newly obtained growth rates, and (6) the applicability of the results to other basalts.

Growth of Olivine Phenocrysts in Natural Magmas

Our experiments show that phenocryst-size olivine frameworks can be formed in 1–2 h. Previous growth rate estimates (Donaldson, 1975; Armienti et al., 1991; Jambon et al., 1992; Wallace and Anderson, 1998; Ni et al., 2014) implied formation of mm-sized olivine crystals would take at least tens of days (Wallace and Anderson, 1998) or even tens of years (Mangan, 1990). The morphology of experimental crystals matches that of natural crystals (e.g., the 1820CE Kīlauea olivine), with a tendency to be

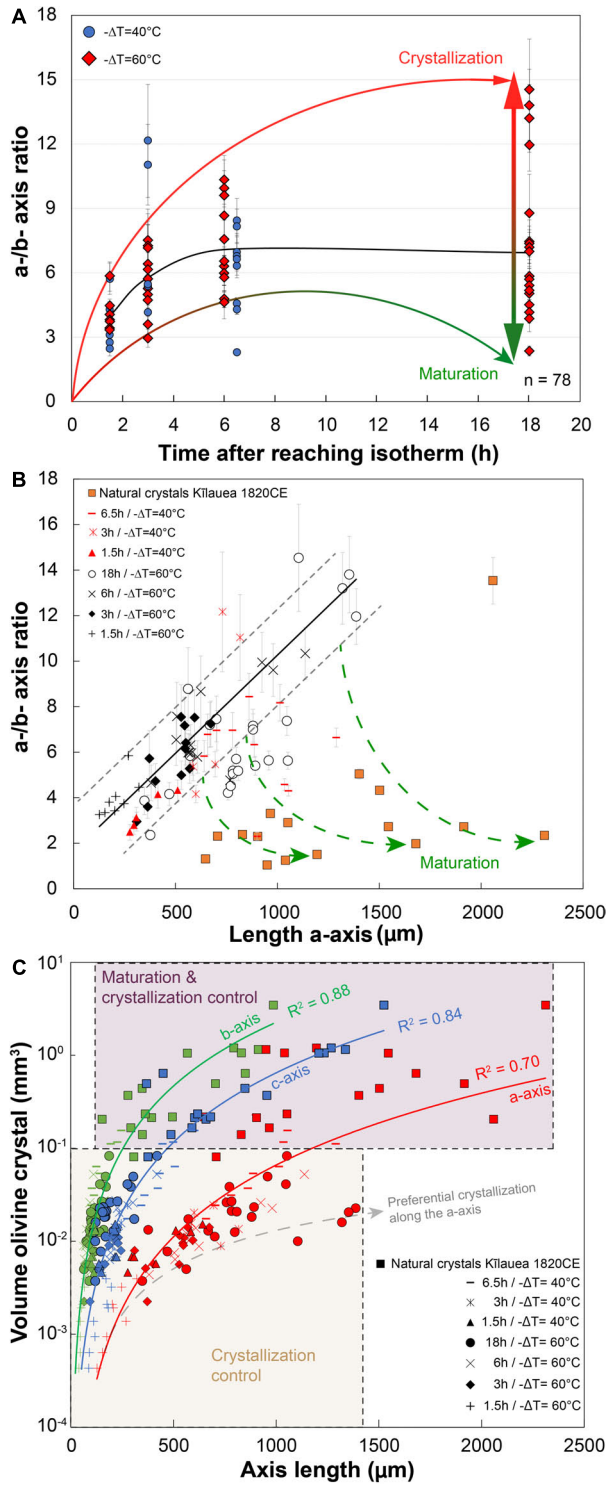

FIGURE 5 | Continued

FIGURE 5 | 3D measurements of the *a*- and *b*-axis dimensions of experimental olivine for 40 and 60°C of undercooling, illustrating processes of crystal growth and maturation. **(A)** *a*-/*b*-axis ratio vs. time after reaching isotherm; number of crystals n = 78. **(B)** *a*-/*b*-axis ratio vs. length of the *a*-axis for different run durations with 40 and 60°C undercooling. Experimental olivine is compared to natural olivine of different sizes from the 1820CE Kīlauea eruption. Natural macrocrysts were photographed with a stereomicroscope in the three directions for axis length measurements. Green arrows extrapolate this ratio that could be interpreted as an evolution of the degree of maturation along the *b*-axis, typically occurring after a few hours and for crystals longer than 700 microns. A roughly similar linear trend in **(B)** marks the main trajectory of growth before significant maturation occurs. Error bars: gray lines correspond to the standard deviation and the measurement error on each axis was estimated at 10 microns for experimental charges. **(C)** Volume of experimental and natural olivine (in log unit) vs. length of the *a*-, *b*-, and *c*-axis. The maturation along the *b*- and *c*-axis reduces the crystallization along the *a*-axis and explains the lower best fit residual for the *a*-axis (R^2 = 0.7).

elongate along the *a*-axis and contain large hourglass inclusions. Crystal buds observed in natural olivine (e.g., Welsch et al., 2013) also form in the longer experimental charges. The broad range in crystal sizes in longer experiments may be related to differences in the timing of nucleation (smaller crystals nucleate later), and/or controlled by the competition of crystals for olivine component from the melt (crystals able to grow quicker were less impeded by other crystals). The crystal size-experimental duration relationships indicate that for undercoolings between 25 and 60°C, the induction time for crystallization is <3 h (<20 min for a $-\Delta T$ = 60°C). Such small induction times imply that there is no significant barrier to crystal nucleation at the beginning of our experiments. This rapid nucleation process for moderate-to-high undercooling likely diminishes greatly after the first generation of olivine forms. Also, at equal analytical resolution, the 40 and 60°C undercooling experiments have notable differences in the number density of crystals, with the 60°C runs showing more individuals. The notable decrease in 3D-derived growth rates from $-\Delta T$ = 40–60°C is associated with an increasing influence of nucleation on how the crystallizing mass is distributed. The undercooling region around 40°C can therefore be regarded as a sweet-spot for the formation of phenocrysts: growth rates are near their maxima, while nucleation rates are still low. The limited number of undercooling values examined herein precludes a precise resolution of this region, and future experiments are needed to fully demonstrate the decreasing trend in growth rates at high ΔT.

Knowledge of the pre-eruptive history of the magma and the control over the presence or absence of nuclei at the beginning of the experiments is essential to make an analogy between experiments and natural mafic rocks (Faure et al., 2003). Natural basaltic rocks usually display large variation of olivine textures with skeletal and more mature olivine cargo (e.g., Milman-Barris et al., 2008), where both olivine dissolution and crystallization processes may be involved. Like pre-existing olivine in a magma chamber, seeds introduced in the experiments can undergo dissolution and rim growth, therefore allowing the influence of pre-existing substrate on growth rates. Growth rate values obtained for overgrowth rims are much lower compared to those of crystals that nucleated homogeneously in the charge (**Figure 6**), suggesting that the presence of a pre-existing surface is an important parameter for growth kinetics.

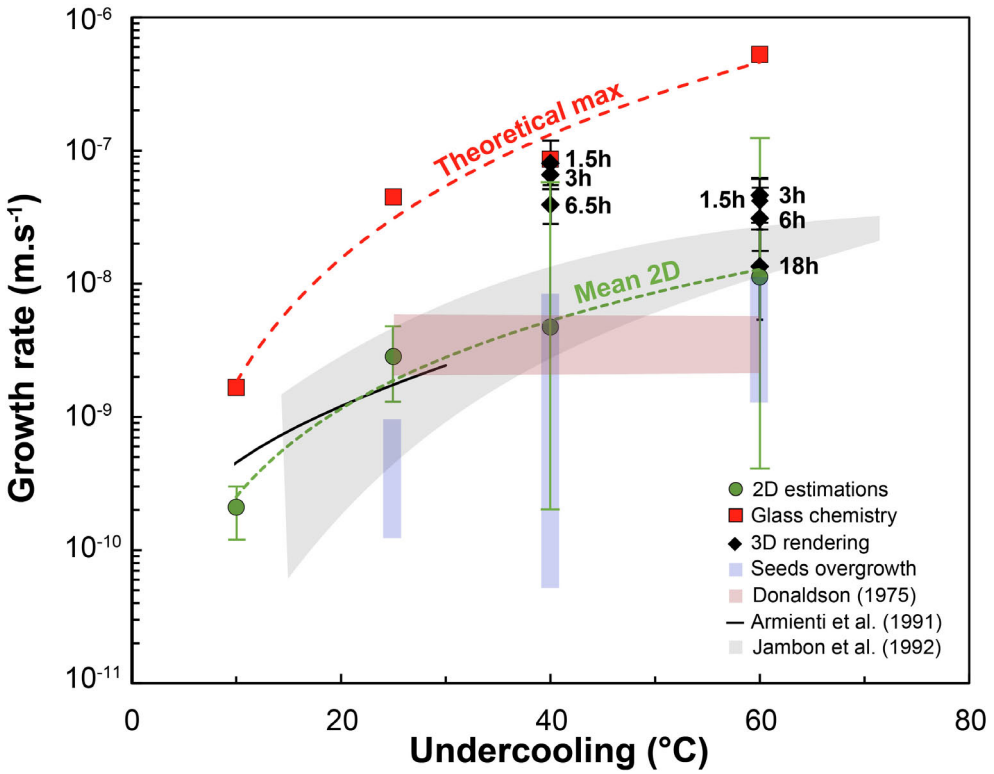

FIGURE 6 | Growth rate (m/s) vs. undercooling (°C). 2D estimates from this and other studies (e.g., Armienti et al., 1991; Jambon et al., 1992) are compared with 3D data along with values calculated from mass-balance. The latter are obtained by calculating the dimensions of a single crystal representing all the crystallized mass within an experiment, and are thus theoretical maxima. Error bars for the 3D data coincide with the minimum and maximum calculated growth rate for crystals of different sizes.

The crystallizing mass is distributed around a larger surface during rim overgrowth, resulting in lower values of growth rates. Seed overgrowth often occurs more isotropically, lacking the strong preferential growth direction observed in homogeneously nucleated crystals. Compared to newly formed crystals, rims are by definition exposed to a greater surface area of melt, meaning that olivine-forming components are more readily available and less easily locally depleted. At medium undercooling, the growth of primary branches is hence less favored for overgrown olivine than for olivine grown after homogeneous nucleation. Extrapolation of these results to natural magma reservoir systems suggests that old crystallized olivine subject to thermal and chemical disequilibrium do not grow at the same rates as new olivine crystals. The same thermal history in a magmatic chamber can thus lead to a large variation of growth rates for old and new cargo undergoing homogeneous nucleation or rim overgrowth. This variation could explain the low calculated growth rates based on bulk olivine cargo with crystal population density data (Armienti et al., 1991).

Growth Mechanisms and Consequences for Element Partitioning in Olivine

The transition from polyhedral to skeletal olivine was explained by Faure et al. (2007) as an excess of chemical supersaturation at olivine corners associated with stronger local disequilibrium (Berg, 1938), thereby promoting preferential growth along diagonal branches. Protuberances on crystal corners pierce through the regions that are least depleted in olivine-forming components (boundary layers) to create elongated crystals (Hammer, 2008). The increase in disequilibrium at moderate undercooling has been associated with the development of a layer-spreading nucleation mechanism (Faure et al., 2007). For medium undercooling values investigated in our experiments (25–60°C), spiral growth and layer-by-layer growth are often cited as dominant mechanisms for interface reaction (Ni et al., 2014). The hopper/skeletal morphologies instead suggest that the growth rate was primarily limited by chemical diffusion (Ni et al., 2014) with the formation of chemical gradients at crystal–liquid interfaces (**Figure 7** and Faure and Schiano, 2005).

Under the diffusion-controlled growth regime, the high growth rates extracted from our experiments also bear important consequences for element partitioning in olivine. Elements that are either highly compatible (Mg, Ni) or incompatible (Al, P) in olivine will be rapidly depleted or enriched in boundary layers (**Figures 7, 8**, Milman-Barris et al., 2008; Shea et al., 2015b), causing depletion or enrichment in the crystal compared to equilibrium concentrations (Lasaga, 1982; Watson and Müller, 2009). In one experiment, the presence of boundary layers in Mg during diffusion-controlled growth caused the K_d to attain fairly low values 0.27–0.28 (equilibrium K_d values range between

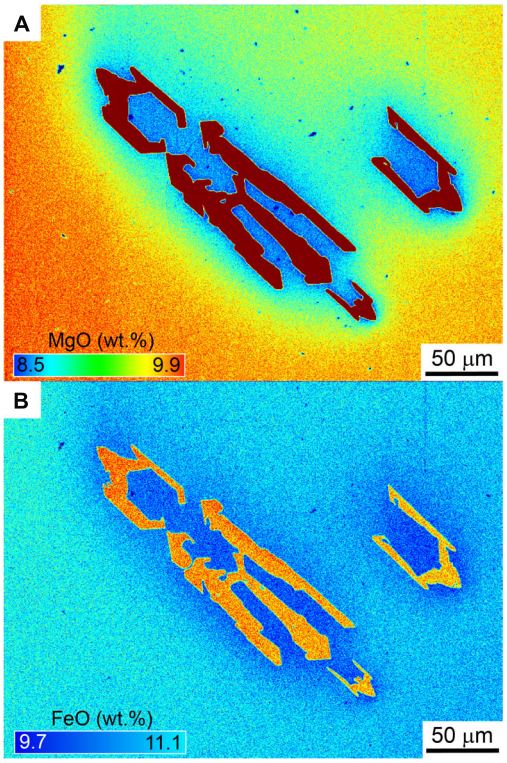

FIGURE 7 | Chemical maps of magnesium **(A)** and iron **(B)** of a skeletal olivine that crystallized in 20 min, subject to 60°C of undercooling. The presence of wide boundary layers at the crystal–liquid interface suggests that crystallization occurred under the diffusion-controlled growth regime.

0.3 and 0.345, Roeder and Emslie, 1970; Matzen et al., 2011) mostly due to lowering of the Mg partition coefficient D_{Mg} (**Figure 8**). Rapid growth may therefore impact our ability to discern equilibrium vs. disequilibrium in a basalt assemblage. Shea et al. (2015b) and Watson et al. (2015) calculated that growth rates approaching 10^{-7} m/s were needed to explain two- to threefold enrichments of trace elements like P or Al. A major issue with the boundary layer model as proposed previously was that high undercoolings that may be difficult to achieve in natural systems (e.g., $-\Delta T$ = 110°C) were needed to raise growth rates to levels that induced enough enrichment in these elements (Jambon et al., 1992). The present results show that growth rates estimated from 3D can attain these values without necessitating extreme undercooling conditions. A companion paper based on the same experiments (Shea et al., 2019) fully explores the consequences of rapid growth for P and Al, and shows that the boundary layer enrichment model works for certain elements like Al but not for P. Regardless of the peculiar behavior of P, the concentration of other elements is clearly affected by disequilibrium caused by rapid growth, which may even affect Fe–Mg contents in olivine (**Figure 7**). Our results relax the requirement for unrealistically large undercooling and may pave to way to better understanding the extent to which olivine major and trace element compositions can be controlled by disequilibrium processes.

Origin of Skeletal Crystals

Previous experimental studies focusing on the formation of spinifex and dendritic olivine have shown that preferential elongation of olivine occurs either at low cooling rate of 1–5°C/h under a thermal gradient (spinifex, Faure et al., 2006) or at high cooling rates of 1639–2182°C/h (dendritic, Faure et al., 2007). The formation of dendritic olivine has also been explained as a competition mechanism between the growth of dendrites and the growth of the parental hopper crystals (Faure et al., 2003). Skeletal olivine morphologies with "stair-like" hopper cavities and elongated open glass inclusions parallel to the (010) and (021) faces form at moderate–high cooling rates (Faure et al., 2007) but the major parameter controlling the morphology is the undercooling (Faure et al., 2003). The formation of glass inclusions in phenocryst-sized skeletal olivine is experimentally enhanced by applying several cooling–heating cycles (Faure and Schiano, 2005). These results suggested that glass inclusions in natural olivine could form during cycles of magma convection (Colin et al., 2012). However, experiments from Ni et al. (2014) produced skeletal olivine in basaltic melt under static conditions, suggesting that convection is not essential to form these crystals. Here, we propose that the transition between skeletal to hopper crystals is directly related to the decrease of the undercooling with time, which can occur isothermally. The formation of natural hopper-to-skeletal phenocrysts such as those from Kīlauea (Shea et al., 2015b and this study) does not necessitate thermal convection but can result from sudden undercooling of 25–60°C and a maturation phase exceeding 18 h. This magnitude of undercooling can result from magma recharge and mixing, where the exact degrees of thermal and chemical (i.e., constitutional) undercooling depend on the temperature and chemical differences between mixing end-members (e.g., Lynn et al., 2017). Skeletal and hopper olivine elongated along the *a*-axis are frequently found in active effusive volcanoes like Stromboli (Metrich et al., 2010), Etna (Spilliaert et al., 2006), Piton de la fournaise (Welsch et al., 2013), mid-oceanic ridge pillow basalt (Colin et al., 2012), and Kīlauea (**Figures 4F,G**), where mixing processes are inferred to be common (Viccaro et al., 2006; Corsaro et al., 2009; Vinet and Higgins, 2010; Pioli et al., 2014; Shizimu et al., 2015; Lynn et al., 2017; Petrone et al., 2018; Sundermeyer et al., 2018). These observations support that mixing between cooler degassed magma with a hotter undegassed magma can promote rapid hopper/skeletal olivine crystallization and glass inclusion entrapment (Wallace and Anderson, 1998).

Updated Model for the Development of Skeletal Crystals

Based on observations of olivine morphology in natural samples from La Reunion, Welsch et al. (2013, 2014) proposed that the development of skeletal olivine involves the rapid propagation of primary branches along the [101] direction, leading to elongation of crystal units along the *c*-axis. The dominance of olivine elongated along the *a*-axis over crystals elongated along *b* or *c*-axis in our experiments suggests that faster growth along the b and c-axis may occur under different thermal histories, where thermal and/or compositional disequilibrium are lower or

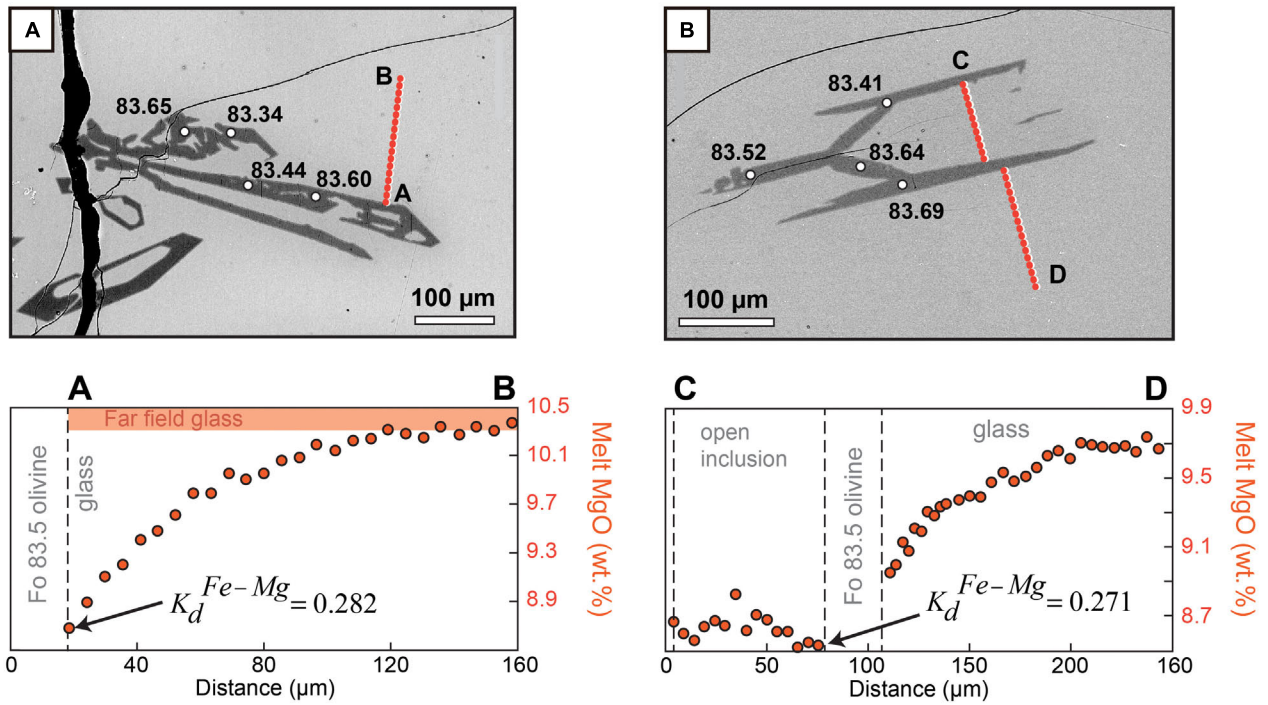

FIGURE 8 | Influence of rapid olivine growth on Fe–Mg partitioning in a run performed at $-\Delta T$ = 60°C and 1.5 h dwell time at the final conditions. Transects A–B and C–D show the presence of boundary layers in Mg during diffusion-controlled growth (change of 1–2 wt.% between far field and interface) around two different crystals from the same charge. Values on the backscatter electron images give Fo content measured at different locations. Both **(A)** and **(B)** are around $Fo_{83\cdot5}$. Equilibrium K_d values range between 0.3 and 0.345 (Roeder and Emslie, 1970; Matzen et al., 2011). Rapid growth appears to cause the K_d to decrease to 0.27–0.28 mostly due to the lower Mg partition coefficient D_{Mg} (by contrast D_{Fe} does not vary significantly since boundary layers in Fe are much more subtle).

less abrupt. The decrease in growth rate along the *a*-axis with respect to other axes (**Figure 5B**) with decreasing undercooling agrees well with this scenario. Despite important differences in the direction of the main growth axes, our experiments agree with the inferred direction of primary branches proposed by Welsch et al. (2014) along the *a*–*c* plane. The rapid formation of an outer shell (a few minutes at $-\Delta T$ = 60°C) connected to these primary branches leads to entrapment of glass inclusions (**Figure 3D**). These large glass inclusions are then variably segmented by secondary branches originating from the primary structure without necessitating thermal fluctuations. The final stage is the complete isolation, along (010) and (021) faces, of round glass inclusions. The development of the primary branches seems closely linked to the growth of the (010) and (021) faces and the hexagonal shape of the cavities with the macro-steps described inside the crystal track the different secondary branches (**Figures 9A,B**). The propensity for olivine to readily develop this outer shell compared to other phases such as feldspar or pyroxene may partly explain why glass inclusions are abundant in olivine.

Implications for Chemical Zoning in Olivine: Growth vs. Diffusion

The accuracy of timescales retrieved from diffusion modeling of chemical zoning patterns measured in natural crystals depends partly on the assumption that gradual compositional changes were not continuously acquired during crystal growth (Costa et al., 2008). Rapid growth is therefore an essential tenet of successful geospeedometry applications in the context of magmatic processes. This assumption can be tested rigorously by examining Fe–Mg isotopes in zoned olivine (e.g., Oeser et al., 2015) or by focusing on skeletal crystals that preserve multi-stage magma mixing histories (Shea et al., 2015b). In the latter study, it was proposed that if olivine crystallization commonly occurred through formation of initial diagonal branches, then any concentric zoning pattern would be the result of diffusion, not growth. The kinetic competition between growth and diffusion is therefore critical in resolving the issues of growth vs. diffusion-induced chemical zoning. Our results can be placed in this context by comparing the distances traveled during olivine growth with distances of element transport in olivine (Fe–Mg, Dohmen and Chakraborty, 2007; Li, Dohmen et al., 2010; **Figure 10**). Li is one of the fastest diffusing elements in olivine, and provides us with an upper limit for competing with growth rates. The calculations show that growth proceeds at a much faster pace than diffusion of Fe–Mg and Li on timescales of minutes to hours. Growth-induced zoning could occur during this period if the fraction of olivine crystallizing is significant enough to change the melt composition substantially. In the experiments, the low overall fractions crystallized (<10 vol.%) mean that little to no zoning in Fe–Mg occurs (e.g., **Figure 7**). Once growth rates slow down, diffusion progressively becomes an

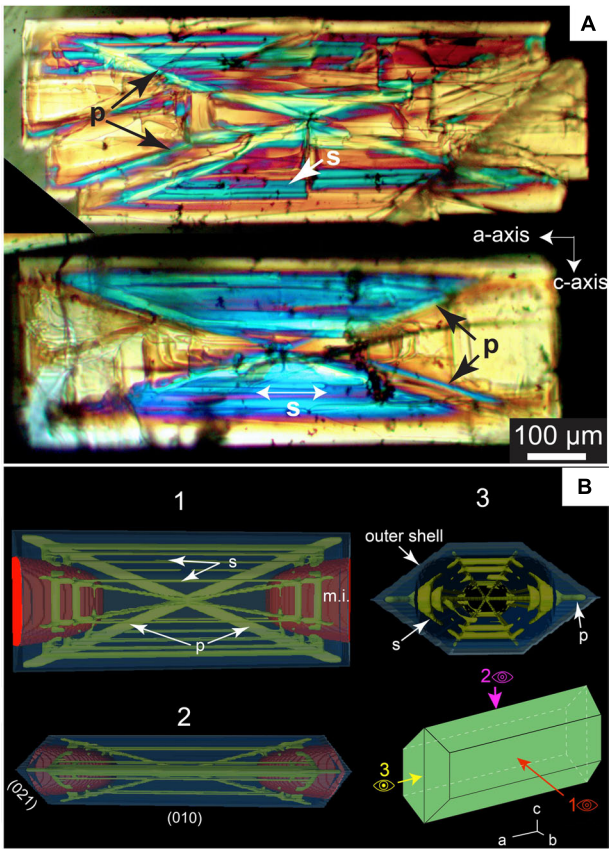

FIGURE 9 | (A) Cross-polarized photograph of two skeletal olivine crystals elongated along the *a*-axis that crystallized in 45 min with 60°C of undercooling. The variation in the birefringence is associated here with variations in thickness; Primary ("p") and secondary branches (blue regions, symbol "s" in the figure) are thicker than hourglass hopper cavities regions (in yellow, "m.i." for melt inclusion in the figure). **(B)** 3D model of a skeletal crystal elongated along the *a*-axis with hour-glass inclusions representative of experimental crystals. The primary and secondary branches are distinguished from the outer shell. In this view, the outer shell traps the glass inclusions and the primary and secondary branches segment the melt pockets. The crystal infills and grows further along the *b*-axis during the maturation process.

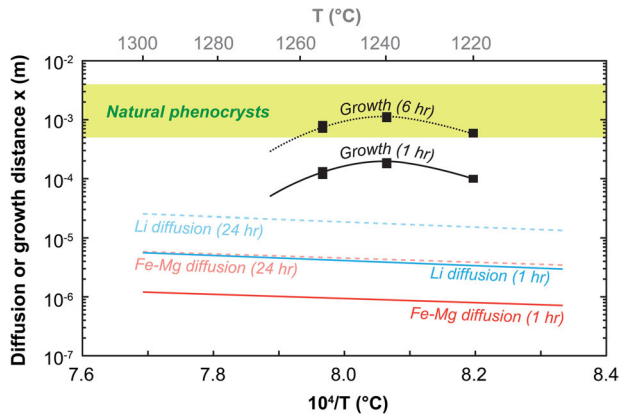

FIGURE 10 | The early competition between growth and diffusion in olivine as a function of temperature. Distances attained after 1–6 h of olivine growth and 1–24 h of diffusion of Li and Fe–Mg are calculated as $x = Gt$ with G the growth rate and $x = \sqrt{Dt}$, respectively [diffusivities from Dohmen and Chakraborty (2007) and Dohmen et al. (2010), see **Supplementary Material** for details, average and maximum growth rates are from this study and are bound by the black rectangular symbol thickness]. This comparison shows that the early history of an olivine – and therefore its chemical make-up – is dominated by growth. Diffusion is inefficient at these short timescales even for faster elements like Li. After ~3–6 h, growth slows down (cf. **Figure 6**), near final crystal sizes are reached, and diffusion gradually becomes the dominant mechanism to induce or modify compositional zoning in olivine.

efficient mechanism to transport elements from rim toward the inside of a crystal. Thus, growth is likely to occur as rapid pulses during thermal and/or compositional perturbations (e.g., magma mixing), while diffusion should be responsible for most gradual compositional changes observed in erupted mineral cargo.

Applicability of Growth-Rate Results to Other Basalts

The growth rate data derived from the present study are most directly applicable to Kīlauea tholeiitic magmas, which are H_2O-poor (<1 wt.%, e.g., Gerlach, 1986; Wallace and Anderson, 1998; Tuohy et al., 2016). This section addresses how the results may or may not be extrapolated to other basalt types (mid-ocean ridge basalt MORB, large igneous provinces LIP, wet arc basalt, komatiites).

Development of skeletal olivine morphologies likely occurs under the diffusion-controlled growth regime (e.g., Hammer, 2008; also see the section "Growth Mechanisms and Consequences for Element Partitioning in Olivine"). In this regime, diffusion of the main crystal-forming elements in the melt (Mg, Fe, and Si) toward the olivine interface controls the transition from polyhedral to skeletal growth. Since partitioning of Si and Fe between olivine and melt is not very far from unity, and they do not get depleted or enriched significantly in the boundary layer, growth rates may largely be determined by the mobility of Mg in the melt (e.g., Donaldson, 1975). Extrapolation of the present relationships between undercooling and growth regime to other basalt types will thus depend on whether Mg diffusivities are comparable. MORB, LIP, and Komatiite magmas are also H_2O-poor; hence, Mg diffusivities depend mostly on temperature. Although their temperatures differ in the mantle, MORB and LIP are on average comparable to near surface Kīlauea basalt temperatures in the shallow crust (1100–1250°C, Fisk, 1984; Ho and Cashman, 1997; Thordarson and Self, 1998; Helz et al., 2014). Our growth rate results are therefore expected to apply there as well. On the other hand, Mg diffusion is likely much faster in hotter Komatiite melts (Green et al., 1975), meaning that the formation of boundary layers may require additional undercooling than the range applied for the Kīlauea basalt. Finally, element diffusivities in the melt also depend on water content. In wet arc basalts, addition of H_2O in melts increases element diffusivity, meaning that diffusion-controlled growth and thus skeletal branching of olivine may be harder to achieve. While H_2O-rich arc basalts tend to be colder than dry tholeiites, the effect of temperature on the magnesium diffusivity

is apparently smaller than the effect of water [see Zhang et al. (2010) for a summary]. For instance, $D_{Mg} = 7.3 \times 10^{-12}$ m^2/s at 1200°C for a dry basalt while $D_{Mg} = 4.5 \times 10^{-11}$ m^2/s for the same basalt at 1050°C with 6 wt.% H_2O (Zhang et al., 2010), suggesting that the addition of H_2O is not compensated by a decrease in temperature. Nonetheless, skeletal olivine can be found in arc basalt, where additional undercooling may also incur due to decompression-induced degassing (e.g., Kuritani, 1999). Additional experiments are therefore required to test whether the degrees of undercooling required to initiate the diffusion-controlled growth regime and drive rapid growth are indeed higher in hydrous arc basalt, as would be predicted by these first order element diffusivity considerations.

CONCLUSION

Phenocryst-size olivine can form in a magma chamber a few hours after a thermal disequilibrium that can be readily induced by common magma mixing processes. Our experiments performed under low-to-moderate undercooling conditions (10–60°C) prove that it is possible to form skeletal and hopper olivine under isothermal conditions after an initial perturbation. Local thermal gradients or magma convection are not *sine qua non-conditions* for the development and maturing of phenocrystic olivine. Our results show that olivine growth is marked by the rapid development (a few hours) of an outer shell that enables the confinement of glass inclusions. Polyhedral olivine produced at lower undercooling (10 and 25°C) support the notion that relaxation of undercooling with time drives the transition between different crystal morphologies. 3D renderings of experimental charges showed that the development of olivine is a two-step process with preferential crystallization along the *a*-axis followed by maturation along the other axes. Natural olivine with low *a*-/*b*-ratios <5 presumably results from a protracted maturation period along the *b*-axis. Importantly, the order of magnitude difference between 2D and 3D growth rates illustrates the significance of considering the real complexities of olivine morphologies.

For moderate undercooling between 25 and 60°C, growth rates calculated for seed overgrowths (rims) are one order of magnitude lower than homogeneously nucleated crystals. The same thermal history in a magmatic chamber can lead to a large variation of growth rates for old and new cargo undergoing homogeneous nucleation and/or growth on existing crystals. The widespread occurrence of both olivine archetypes (elongated along *c* or *a*) in natural samples may therefore be associated with (1) their formation under a wide range of undercooling conditions and/or (2) the coexistence of both newly grown olivine (elongated along *a*) and olivine formed by multiple growth events where overgrowth rims are less prone to skeletal branching and elongation along *a*. Finally, the decrease in growth rate with undercooling at 60°C illustrates the importance of considering both nucleation and growth in yielding final crystal populations in magmas, where moderate undercooling ($-\Delta T$ = 40°C) may result in larger phenocrysts than high undercooling conditions.

DATA AVAILABILITY STATEMENT

All datasets generated for this study are included in the article/**Supplementary Material**.

AUTHOR CONTRIBUTIONS

AM and TS carried out the experiments and microprobe analyses. AM led the writing of the manuscript and performed the 3D volume processing. Both authors contributed to the interpretations.

FUNDING

This work was supported by a National Science Foundation (NSF) grant to TS (EAR 1725321).

ACKNOWLEDGMENTS

The authors thank Jessica Maisano at the NSF-supported UTCT facility for assistance with the microtomography scans, and Emily First for help in the experimental lab. They also thank the reviewers and editor for the numerous insightful and constructive comments, which helped improve the original version of the manuscript significantly. The timeliness of the editorial and review process was greatly appreciated. This is SOEST contribution number 10842.

SUPPLEMENTARY MATERIAL

The Supplementary Material for this article can be found online at: https://www.frontiersin.org/articles/10.3389/feart.2019.00300/full#supplementary-material

REFERENCES

Armienti, P., Innocenti, F., Pareschi, M. T., Pompilio, M., and Rocchi, S. (1991). Crystal population density in not stationary volcanic systems: estimate of olivine growth rate in basalts of Lanzarote (Canary Islands). *Mineral. Petrol.* 44, 181–196. doi: 10.1007/BF01166962

Armienti, P., Pareschi, M. T., Innocenti, F., and Pompilio, M. (1994). Effects of magma storage and ascent on the kinetics of crystal growth. *Contrib. Mineral. Petrol.* 115, 402–414. doi: 10.1007/BF00320974

Avrami, M. (1939). Kinetics of phase change. I general theory. *J. Chem. Phys.* 7, 1103–1112. doi: 10.1063/1.1750380

Berg, W. F. (1938). Crystal growth from solutions. *Proc. R. Soc. A* 164, 79–95. doi: 10.1098/rspa.1939.0006

Borisov, A., and Jones, J. H. (1999). An evaluation of Re, as an alternative to Pt, for the 1 bar loop technique: an experimental study at 1400°C. *Am. Mineral.* 84, 1528–1534. doi: 10.2138/am-1999-1006

Brugger, C. R., and Hammer, J. E. (2010). Crystallization kinetics in continuous decompression experiments: implications for interpreting natural magma

ascent processes. *J. Petrol.* 51, 1941–1965. doi: 10.1093/petrology/egq044

Clague, D. A., Moore, J. G., Dixon, J. E., and Friesen, W. B. (1995). Petrology of Submarine Lavas from Kilauea's Puna Ridge, Hawaii. *J. Petrol.* 36, 299–349. doi: 10.1093/petrology/36.2.299

Clark, A. H., Pearce, T. H., Roeder, P. L., and Wolfson, I. (1986). Oscillatory zoning and other microstructures in magmatic olivine and augite: Nomarski interference contrast observations on etched polished surface. *Am. Mineral.* 71, 734–741.

Colin, A., Faure, F., and Burnard, P. (2012). Timescales of convection in magma chambers below the Mid-Atlantic ridge from melt inclusions investigations. *Contrib. Mineral. Petrol.* 164, 677–691. doi: 10.1007/s00410-012-0764-2

Corsaro, R. A., Civetta, L., Di Renzo, V., and Miraglia, L. (2009). Petrology of lavas from the 2004–2005 flank eruption of Mt. Etna, Italy: inferences on the dynamics of magma in the shallow plumbing system. *Bull. Volcanol.* 71, 781–793. doi: 10.1007/s00445-009-0264-z

Costa, F., Dohmen, R., and Chakraborty, S. (2008). "Timescales of magmatic processes from modeling the zoning patterns of crystals," in *Minerals, Inclusions and Volcanic Processes. RiMG 69*, eds K. D. Putirka, and I. I. I. F. J. Tepley, (Chantilly, VA: Mineralogical Society of America), 545–594. doi: 10.2138/rmg.2008.69.14

Dohmen, R., and Chakraborty, S. (2007). Fe–Mg diffusion in olivine II: point defect chemistry, change of diffusion mechanisms and a model for calculation of diffusion coefficients in natural olivine. *Phys. Chem. Mineral.* 34, 409–430. doi: 10.1007/s00269-007-0158-6

Dohmen, R., Kasemann, S. A., Coogan, L., and Chakraborty, S. (2010). Diffusion of Li in olivine. Part I: experimental observations and a multi species diffusion model. *Geochim. Cosmochim. Acta* 74, 274–292. doi: 10.1016/j.gca.2009.10.016

Donaldson, C. H. (1975). Calculated diffusion coefficients and the growth rate of olivine in a basalt magma. *Lithos* 8, 163–174. doi: 10.1016/0024-4937(75)90023-7

Donaldson, C. H. (1976). An experimental investigation of olivine morphology. *Contrib. Mineral. Petrol.* 57, 187–213. doi: 10.1007/bf00405225

Donaldson, C. H. (1979). An experimental investigation of the delay in nucleation of olivine in mafic magmas. *Contrib. Mineral. Petrol.* 69, 21–32. doi: 10.1007/BF00375191

Faure, F., Arndt, N., and Libourel, G. (2006). Formation of spinifex texture in komatiites: an experimental study. *J. Petrol.* 47, 1591–1610. doi: 10.1093/petrology/egl021

Faure, F., and Schiano, P. (2005). Experimental investigation of equilibration conditions during forsterite growth and melt inclusion formation. *Earth Planet Sci. Lett.* 236, 882–898. doi: 10.1016/j.epsl.2005.04.050

Faure, F., Schiano, P., Trolliard, G., Nicollet, C., and Soulestin, B. (2007). Textural evolution of polyhedral olivine experiencing rapid cooling rates. *Contrib. Mineral. Petrol.* 153, 405–416. doi: 10.1007/s00410-006-0154-8

Faure, F., Trolliard, G., Nicollet, C., and Montel, J.-M. (2003). A developmental model of olivine morphology as a function of the cooling rate and the degree of undercooling. *Contrib. Mineral. Petrol.* 145, 251–263. doi: 10.1007/s00410-003-0449-y

Feldkamp, L. A., Davis, L. C., and Kress, J. W. (1984). Practical cone-beam algorithm. *J Opt. Soc. Am. A* 1, 612–619. doi: 10.1364/JOSAA.1.000612

Filiberto, J., Musselwhite, D. S., Gross, J., Burgess, K., Le, L., and Treiman, A. H. (2010). Experimental petrology, crystallization history, and parental magma characteristics of olivine-phyric shergottite NWA 1068: implications for the petrogenesis of "enriched" olivine-phyric shergottites. *Meteorit. Planet. Sci.* 45, 1258–1270. doi: 10.1111/j.1945-5100.2010.01080.x

First, E., and Hammer, J. E. (2016). Igneous cooling history of olivine-phyric shergottite Yamato 980459 constrained by dynamic crystallization experiments. *Meteorit. Planet. Sci.* 51, 1233–1255. doi: 10.1111/maps.12659

Fisk, M. R. (1984). Depths and temperatures of mid-ocean-ridge magma chambers and the composition of their source magmas. *Geol. Soc. Lond. Spec. Pub.* 13, 17–23. doi: 10.1144/gsl.sp.1984.013.01.02

Fowler, A. D., Stanley, H. E., and Daccord, G. (1989). Disequilibrium silicate mineral textures: fractal and non-fractal features. *Nature* 341, 134–138. doi: 10.1038/341134a0

Garcia, M. O. (2015). "How and why Hawaiian volcanism has become pivotal to our understanding of volcanoes from their source to the surface," in *Hawaiian Volcanoes: From Source to Surface, Geophysical Monograph*, First Edn, eds R. Carey, V. Cayol, M. Poland, and D. Weis, (Washington, DC: American Geophysical Union), 208. doi: 10.1002/9781118872079.ch1

Garcia, M. O., and Hulsebosch, T. P. (1995). "Olivine-rich submarine basalts from the southwest rift zone of Mauna Loa volcano: implications for magmatic processes and geochemical evolution," in *Mauna Loa Revealed: Structure, Composition, History, and Hazards Geophysical Monograph*, Vol. 92, eds J. M. Rhodes, and J. P. Lockwood, (Washington, DC: American Geophysical Union), 219–239. doi: 10.1029/GM092p0219

Garcia, M. O., Pietruszka, A. J., and Rhodes, J. M. (2003). A petrologic perspective of kōlauea volcano's summit magma reservoir. *J. Petrol.* 44, 2313–2339. doi: 10.1093/petrology/egg079

Gerlach, T. M. (1986). Exsolution of H2O, CO2, and S during eruptive episodes at Kilauea volcano, Hawaii. *J. Geophys. Res.* 91, 12177–12185. doi: 10.1029/JB091iB12p12177

Green, D. H., Nicholls, I. A., Viljoen, M., and Viljoen, R. (1975). Experimental demonstration of the existence of peridotitic liquids in earliest archean magmatism. *Geology* 3, 11–14. doi: 10.1130/0091-761319753<11:edoteo<2.0.co;2

Hammer, J. E. (2008). Experimental studies of the kinetics and energetics of magma crystallization. *Rev. Mineral Geochem.* 69, 9–59. doi: 10.2138/rmg.2008.69.2

Helz, R. T., Clague, D. A., Sisson, T. W., and Thornber, C. R. (2014). "Petrologic insights intobasaltic volcanism at historically active Hawaiian volcanoes," in *Characteristics of Hawaiian Volcanoes, USGS Professional Paper 1801*, Chap. 6, eds M. P. Poland, T. J. Takahashi, and C. M. Landowski, (Reston, VA: U.S. Geological Survey), 1–55. doi: 10.3133/pp1801

Helz, R. T., Cottrell, E., Brounce, M. N., and Kelley, K. A. (2017). Olivine-melt relationships and syneruptive redox variations in the 1959 eruption of Kīlauea Volcano as revealed by XANES. *J. Volcanol. Geotherm. Res.* 33, 1–14. doi: 10.1016/j.jvolgeores.2016.12.006

Herzberg, C. (2011). Basalts as temperature probes of Earth's mantle. *Geology* 39, 1179–1180. doi: 10.1130/focus122011.1

Ho, A. M., and Cashman, K. V. (1997). Temperature constraints on the Ginkgo flow of the Columbia River Basalt group. *Geology* 25, 403–406.

Isaacson, P. J., Pieters, C. M., Besse, S., Clark, R. N., Head, J. W., Klima, R. L., et al. (2011). Remote compositional analysis of lunar olivine-rich lithologies with moon mineralogy mapper (M3) spectra. *J. Geophys. Res. Atmos.* 116:E00G11. doi: 10.1029/2010JE003731

Jambon, A., Lussiez, P., Clocchiatti, R., Weisz, J., and Hernandez, J. (1992). Olivine growth rates in a tholeiitic basalt; an experimental study of melt inclusions in plagioclase. *Chem. Geol.* 96, 277–287. doi: 10.1016/0009-2541(92)90059-E

Johnson, W. A., and Mehl, R. F. (1939). Reaction kinetics in processes of nucleation and growth. *Trans. Am. Inst. Mining Metall. Petrol. Eng.* 195:416.

Kirkpatrick, R. J. (1981). Kinetics of crystallization in igneous rocks. *Mineral. Soc. Am.* 8, 321–398. doi: 10.1515/9781501508233-012

Kuritani, T. (1999). Phenocryst crystallization during ascent of alkali basalt magma at Rishiri Volcano, northern Japan. *J. Volcanol. Geotherm. Res.* 88, 77–97. doi: 10.1016/s0377-0273(98)00105-x

Lasaga, A. C. (1982). Toward a master equation in crystal growth. *Am. J. Sci.* 282, 1264–1288. doi: 10.2475/ajs.282.8.1264

Lofgren, G. E., Donaldson, C. H., Williams, R. J., Mullins, O., and Usselman, T. M. (1974). Experimentally produced textures and mineral chemistry of Apollo 15 quartz normative basalts. *Lunar Planet. Sci. Conf.* 5, 549–568.

Lynn, K. J., Shea, T., and Garcia, M. O. (2017). Nickel variability in Hawaiian olivine: evaluating the relative contributions from mantle and crustal processes. *Am. Mineral* 102, 507–518. doi: 10.2138/am-2017-5763

Mangan, M. T. (1990). Crystal size distribution systematics and the determination of magma storage times: the 1959 eruption of Kilauea volcano, Hawaii. *J. Volcanol. Geotherm. Res.* 44, 295–302. doi: 10.1016/0377-0273(90)90023-9

Matzen, A. K., Baker, M. B., Beckett, J. R., and Stolper, E. M. (2011). Fe–Mg partitioning between olivine and high-magnesian melts and the nature of Hawaiian parental liquids. *J. Petrol.* 52, 1243–1263. doi: 10.1093/petrology/egq089

Metrich, N., Bertagnini, A., and Di Muro, A. (2010). Conditions of magma storage, degassing and ascent at Stromboli: new insights into the volcano plumbing system with inferences on the eruptive dynamics. *J. Petrol.* 51, 603–626. doi: 10.1093/petrology/egp083

Milman-Barris, M. S., Beckett, J. R., Baker, M. B., Hofmann, A. E., Morgan, Z., Crowley, M. R., et al. (2008). Zoning of phosphorus in igneous

olivine. *Contrib. Mineral. Petrol.* 155, 739–765. doi: 10.1007/s00410-007-0268-7

Ni, H., Keppler, H., Walte, N., Schiavi, F., Chen, Y., Masotta, M., et al. (2014). In situ observation of crystal growth in a basalt melt and the development of crystal size distribution in igneous rocks. *Contrib. Mineral. Petrol.* 167:1003. doi: 10.1007/s00410-014-1003-9

Ody, A., Poulet, F., Bibring, J. P., Loizeau, D., Carter, J., Gondet, B., et al. (2013). Global investigation of olivine on Mars: insights into crust and mantle compositions. *J. Geophys. Res. Planets* 118, 234–262. doi: 10.1029/2012JE004149

Oeser, M., Dohmen, R., Horn, I., Schuth, S., and Weyer, S. (2015). Processes and time scales of magmatic evolution as revealed by Fe-Mg chemical and isotopic zoning in natural olivines. *Geochim. Cosmochim. Acta* 154, 130–150. doi: 10.1016/j.gca.2015.01.025

Pearce, J. A., and Cann, J. R. (1973). Tectonic setting of basic volcanic rocks determined using trace element analyses. *Earth Planet Sci. Lett.* 19, 290–300. doi: 10.1016/0012-821X(73)90129-5

Pearce, T. H. (1984). The analysis of zoning in magmatic crystals with emphasis on olivine. *Contrib. Mineral. Petrol.* 86, 149–154. doi: 10.1007/BF00381841

Petrone, C. M., Braschi, E., Francalanci, L., Casalini, M., and Tommasini, S. (2018). Rapid mixing and short storage timescale in the magma dynamics of a steady-state volcano. *Earth Planet. Sci. Lett.* 492, 206–221. doi: 10.1016/j.epsl.2018.03.055

Pioli, L., Pistolesi, M., and Rosi, M. (2014). Transient explosions at open-vent volcanoes: the case of Stromboli (Italy). *Geology* 42, 863–866. doi: 10.1130/G35844.1

Rhodes, J. M., and Vollinger, M. J. (2005). Ferric/ferrous ratios in 1984 Mauna Loa lavas: a contribution to understanding the oxidation state of Hawaiian magmas. *Contrib. Mineral. Petrol.* 149, 666–674. doi: 10.1007/s00410-005-0662-y

Roeder, P. L., and Emslie, R. F. (1970). Olivine-liquid equilibrium. *Contrib. Mineral. Petrol.* 29, 275–289. doi: 10.1007/bf00371276

Schiano, P., Provost, A., Clocchiatti, R., and Faure, F. (2006). Transcrystalline melt migration and earth's mantle. *Science* 314, 970–974. doi: 10.1126/science.1132485

Shea, T., Costa, F., Krimer, D., and Hammer, J. E. (2015a). Accuracy of timescales retrieved from diffusion modeling in olivine: a 3D perspective. *Am. Mineral.* 100, 2026–2042. doi: 10.2138/am-2015-5163

Shea, T., Hammer, J. E., Hellebrand, E., Mourey, A. J., Costa, F., First, E., et al. (2019). Phosphorus and aluminum zoning in olivine: contrasting behavior of two nominally incompatible trace elements. *Contrib. Mineral. Petrol.* 174:85. doi: 10.1007/s00410-019-1618-y

Shea, T., Lynn, K. J., and Garcia, M. O. (2015b). Cracking the olivine zoning code: distinguishing between crystal growth and diffusion. *Geology* 43, 935–938. doi: 10.1130/G37082.1

Shizimu, K., Saal, A. E., Myers, C. E., Nagel, A. N., Hauri, E. H., Forsyth, D. W., et al. (2015). Two-component mantle melting-mixing model for the generation of mid-ocean ridge basalts: implications for the volatile content of the Pacific upper mantle. *Geochim. Cosmochim. Acta* 176, 44–80. doi: 10.1016/j.gca.2015.10.033

Spilliaert, N., Allard, P., Metrich, N., and Sobolev, A. V. (2006). Melt inclusion record of the conditions of ascent, degassing, and extrusion of volatile-rich alkali basalt during the powerful 2002 flank eruption of Mount Etna (Italy). *J. Geophys. Res.* 111:B04203. doi: 10.1029/2005JB003934

Sundermeyer, C., Di Muro, A., Techmer, K., Gordeychik, B., and Wörner, G. (2018). "Heritage and residence of olivines based on Fe-Mg diffusion from the August-November 2015 eruption at Piton de la Fournaise, La Réunion," in *Proceedings of the EGU General Assembly 2018*, Vienna, 6194.

Swanson, S. E. (1977). Relation of nucleation and crystal-growth rate to the development of granitic textures. *Am. Mineral.* 62, 966–978.

Thordarson, T., and Self, S. (1998). The Roza Member, Columbia river basalt group: a gigantic pahoehoe lava flow field formed by endogenous processes? *J. Geophys. Res. Solid Earth* 103, 27411–27445. doi: 10.1029/98jb01355

Tuohy, R. M., Wallace, P. J., Loewen, M. W., Swanson, D. A., and Kent, A. J. R. (2016). Magma transport and olivine crystallization depths in Kilauea's East Rift Zone inferred from experimentally rehomogenized melt inclusions. *Geochim. Cosmochim. Acta* 185, 232–250. doi: 10.1016/j.gca.2016.04.020

Turbell, H. (2001). *Cone-beam Reconstruction Using Filtered Backprojection*, Ph.D. thesis, Linköping University, Linköping.

Viccaro, M., Ferlito, C., Cortesogno, L., Cristofolini, R., and Gaggero, L. (2006). Magma mixing during the 2001 event at Mount Etna (Italy): effects on the eruptive dynamics. *J. Volcanol. Geotherm. Res.* 149, 139–159. doi: 10.1016/j.jvolgeores.2005.06.004

Vinet, N., and Higgins, M. D. (2010). Magma solidification processes beneath Kilauea volcano, Hawaii: a quantitative textural and geochemical study of the 1969-1974 Mauna Ulu lavas. *J. Petrol.* 51, 1297–1332. doi: 10.1093/petrology/egq020

Walker, D., Kirkpatrick, R. J., Longhi, J., and Hays, J. F. (1976). Crystallization history of lunar picritic basalt Sample 12002; phase-equilibria and cooling-rate studies. *Geol. Soc. Am. Bull.* 87, 646–656.

Wallace, P. J., and Anderson, A. T. Jr. (1998). Effects of eruption and lava drainback on the H2O contents of basaltic magmas at Kilauea Volcano. *Bull. Volcanol.* 59, 327–344. doi: 10.1007/s004450050195

Waters, L. E., and Lange, R. A. (2013). Crystal-poor, multiply saturated rhyolites (obsidians) from the Cascade and Mexican arcs: evidence of degassing induced crystallization of phenocrysts. *Contrib. Mineral. Petrol.* 166, 731–754. doi: 10.1007/s00410-013-0919-9

Watson, E. B., Cherniak, D. J., and Holycross, M. E. (2015). Diffusion of phosphorus in olivine and molten basalt. *Am. Mineral.* 100, 2053–2065. doi: 10.2138/am-2015-5416

Watson, E. B., and Müller, T. (2009). Non-equilibrium isotopic and elemental fractionation during diffusion-controlled crystal growth under static and dynamic conditions. *Chem. Geol.* 267, 111–124. doi: 10.1016/j.chemgeo.2008.10.036

Welsch, B., Faure, F., Famin, V., Baronnet, A., and Bachelery, P. (2013). Dendritic crystallization: a single process for all the textures of olivine in basalts? *J. Petrol.* 54, 539–574. doi: 10.1093/petrology/egs077

Welsch, B., Hammer, J., and Hellebrand, E. (2014). Phosphorus zoning reveals dendritic architecture of olivine. *Geology* 42, 867–870. doi: 10.1130/G35691.1

Wright, T. L. (1971). *Chemistry of Kilauea and Mauna Loa lavas in space and time*. U.S. Geological Survey Professional Paper 735. Washington, DC: United States Government Printing Office, 40. doi: 10.3133/pp735

Wright, T. L., and Klein, F. W. (2014). *Two hundred years of magma transport and storage at Kīlauea Volcano, Hawai'i, 1790-2008*. USGS Professional Paper 1806. Washington, DC: United States Department of the Interior, doi: 10.3133/pp1806

Zhang, Y., Ni, H., and Chen, Y. (2010). Diffusion data in silicate melts. *Rev. Mineral. Geochem.* 72, 311–408. doi: 10.2138/rmg.2010.72.8

Conflict of Interest: The authors declare that the research was conducted in the absence of any commercial or financial relationships that could be construed as a potential conflict of interest.

frontiers in Earth Science

ORIGINAL RESEARCH
published: 07 February 2020
doi: 10.3389/feart.2020.00018

A Data Driven Approach to Investigate the Chemical Variability of Clinopyroxenes From the 2014–2015 Holuhraun–Bárdarbunga Eruption (Iceland)

Luca Caricchi[1], Maurizio Petrelli[2], Eniko Bali[3], Tom Sheldrake[1], Laura Pioli[1,4] and Guy Simpson[1]*

[1] Department of Earth Sciences, University of Geneva, Geneva, Switzerland, [2] Department of Physics and Geology, University of Perugia, Perugia, Italy, [3] Nordic Volcanological Center, Institute of Earth Sciences, University of Iceland, Reykjavík, Iceland, [4] Dipartimento di Scienze Chimiche e Geologiche, Università degli Studi di Cagliari, Cagliari, Italy

OPEN ACCESS

Edited by:
Chiara Maria Petrone, Natural History Museum, United Kingdom

Reviewed by:
Pier Paolo Giacomoni, University of Ferrara, Italy
Phil Shane, The University of Auckland, New Zealand

***Correspondence:**
Luca Caricchi
luca.caricchi@unige.ch

Specialty section:
This article was submitted to Petrology, a section of the journal Frontiers in Earth Science

Received: *28 October 2019*
Accepted: *21 January 2020*
Published: *07 February 2020*

Citation:
Caricchi L, Petrelli M, Bali E, Sheldrake T, Pioli L and Simpson G (2020) A Data Driven Approach to Investigate the Chemical Variability of Clinopyroxenes From the 2014–2015 Holuhraun–Bárdarbunga Eruption (Iceland). Front. Earth Sci. 8:18. doi: 10.3389/feart.2020.00018

The Holuhraun–Bárdarbunga (Iceland) eruption lasted approximately 6 months. Magma propagated laterally through a 40 km long dyke, while Bárdarbunga caldera was collapsing. This event was intensely monitored, providing an opportunity to investigate the relationships between eruption dynamics and erupted products. Whole rock and melt inclusion data do not show chemical variations of magma during the eruption. Nevertheless, zoning patterns in clinopyroxene suggest temporal variations of intensive parameters during crystallization. We investigated the chemical zoning of clinopyroxene using a data driven approach, on major and trace elements analyses from lava flow lobes emplaced during the eruption. We applied hierarchical clustering (HC) to identify compositional groups based on major and trace element chemistry. This analysis identifies five compositional groups, which can be associated with specific petrographic features. One cluster represents the chemistry of hourglass sectors, two constitute the oscillatory zoned mantle of the crystals, one cluster corresponds to a seldom present bright rim (in back scattered electron images) in the outer portions of the crystals, and a last one represents most of the outer rims. HC applied to trace elements also identifies five compositional clusters, which highlight progressively more evolved clinopyroxene compositions from the core to the rim of the crystals. Two of the clusters identified with trace elements corresponds to major element clusters. All together the data suggest that the chemical zoning in the inner portions of the clinopyroxene crystals was generated by crystallization in the magma reservoir and interaction between hot magma propagating through the dyke and unerupted magma cooling within the dyke. The fraction of zones produced by interaction with colder portion of the magma residing within the dyke dropped during the eruption, potentially signaling the thermal maturation of the dyke. Some of the analyses reveal that relatively close to the eruption time (i.e., the outer portions of the crystals) the dyke intercepted a lens of low temperature

magma with a chemical composition that is distinguishable from the 2014 to 2015 Bárdarbunga eruption. Our approach can provide insights on the evolution of deep processes occurring during long-lasting eruptions by combining the analysis mineral chemistry of erupted products with multiparametric monitoring signals.

Keywords: mineral chemistry, petrology, magmatic processes, magma, eruption

INTRODUCTION

The 2014–2015 Bárdarbunga–Holuhraun (Iceland) eruption lasted for approximately 6 months and the emission of lava occurred in the Holuhraun region, approximately 40 km NE of the Bárdarbunga volcano (Sigmundsson et al., 2014). Lava outflow was accompanied by progressive collapse of the Bárdarbunga caldera, with a striking correspondence between the rate of caldera volume increase and the volume of erupted magma. This suggests that a reservoir associated with the Bárdarbunga plumbing system was progressively drained during the eruption (Gudmundsson et al., 2016). Earthquake swarms tracked the propagation of a horizontally extended sub-vertical dyke through which the magma moved discontinuously first toward the SE and then to the NE from the Bárdarbunga region to the eruptive fracture (Sigmundsson et al., 2014; Gudmundsson et al., 2016; Woods et al., 2019). This eruption was intensely monitored, which makes it an excellent case study to attempt to relate monitoring signals and the chemistry of the erupted products. Petrologic investigations find that the source of magmas might be heterogeneous, but homogenization processes within the magma reservoir masked both source heterogeneity and any potential evolution of magma chemistry during the eruption (Halldórsson et al., 2018; Hartley et al., 2018).

Several previous studies suggest that magma and melt inclusion composition is broadly constant over the course of the eruption (Browning and Gudmundsson, 2015; Gauthier et al., 2016; Geiger et al., 2016; Ruch et al., 2016; Ilyinskaya et al., 2017; Bali et al., 2018; Halldórsson et al., 2018; Hartley et al., 2018; Woods et al., 2019). We focused our analysis on clinopyroxene (cpx), which are characterized by different patterns of sector and concentric oscillatory zoning. We collected samples of lava flow lobes emplaced during the eruption, except for November 2014, for which we did not manage to reach the lobe formed during this period (**Figure 1**). We present an approach that combines classic petrography and geochemistry with unsupervised learning [Hierarchical clustering (HC)] to identify how chemical zoning in minerals capture the complexity and evolution of the Bárdarbunga–Holuhraun volcanic eruption.

MATERIALS AND METHODS

Electron Probe Micro Analyzer (EPMA)

Major element analyses were collected using a JEOL JXA 8200 superprobe at the University of Geneva using 15 keV acceleration voltage, 20 nA beam current and a beam diameter of about 1 micron. Each element was measured acquiring for 30 s on the corresponding wavelength position and 30 s on each of the two background positions located on both sides of the peak. We used forsterite as a standard for Mg and fayalite for Fe, pyrophanite for Mn and Ti, wollastonite for Si and Ca, andradite for Al, Chromium oxide for Cr, and albite for Na. The uncertainty for each element was estimated by measuring the standards as unknowns and accepting only calibrations for each elements for which the ratio between the net counts per second during calibration and measurement was within of ±1%. We additionally performed the peak search for each element every 20 analyses to minimize the impact of any drift during prolonged analytical sessions.

Laser Ablation-Inductively Coupled-Mass Spectrometer (LA-ICP-MS)

Trace element analyses and high-resolution trace element mapping were performed by laser ablation–inductively coupled plasma–mass spectrometry (LA-ICP-MS) at the Department of Physics and Geology (University of Perugia), utilizing a Teledyne Photon Machine G2 laser ablation system coupled to a Thermo iCAP-Q ICP-MS (Petrelli et al., 2016a,b).

Trace elements analyses were performed on single spots of 25 μm and rasters characterized by widths of 10 μm. Data were collected for Li, Be, P, S, Cl, Sc, Ti, V, Cr, Mn, Co, Ni, Cu, Gd, Rb, Sr, Y, Zr, Nb, Cs, Ba, Hf, Ta, Pb, Th, U, plus Rare Earth Elements (REEs), with a repetition rate and fluence of 8 Hz and 4 J/cm2, respectively. The NIST 610 reference material, Si concentrations determined by EPMA, and USGS BCR2G glass were used as the calibration standard, internal standard, and quality control, respectively. Data Reduction was carried out using the Iolite v.3 software package (Paton et al., 2011). Under the reported analytical conditions, precision and accuracy are typically better than 10% (Petrelli et al., 2016a,b).

Trace elements were imaged following the line rastering technique proposed by Ubide et al. (2015). A spot size of 10 μm, a scan speed of 2 μm/s, a fluence of ∼4 J/cm^2 and a repetition rate of 10 Hz were utilized, respectively. When creating crystal maps, the number of analytes was reduced to Sc, Ti, V, Cr, Mn, and Zr to increase the efficiency of the acquisition. Crystal maps and transects were produced using the CellSpace tool (Paul et al., 2012). Finally, compositional zonation relationships were further interpreted using "Images from selections" with Monocle tool (Petrus et al., 2017).

Hierarchical Cluster Analysis

The procedure was performed using the library "cluster" within the freeware software R (R Core Team, 2017). Major element

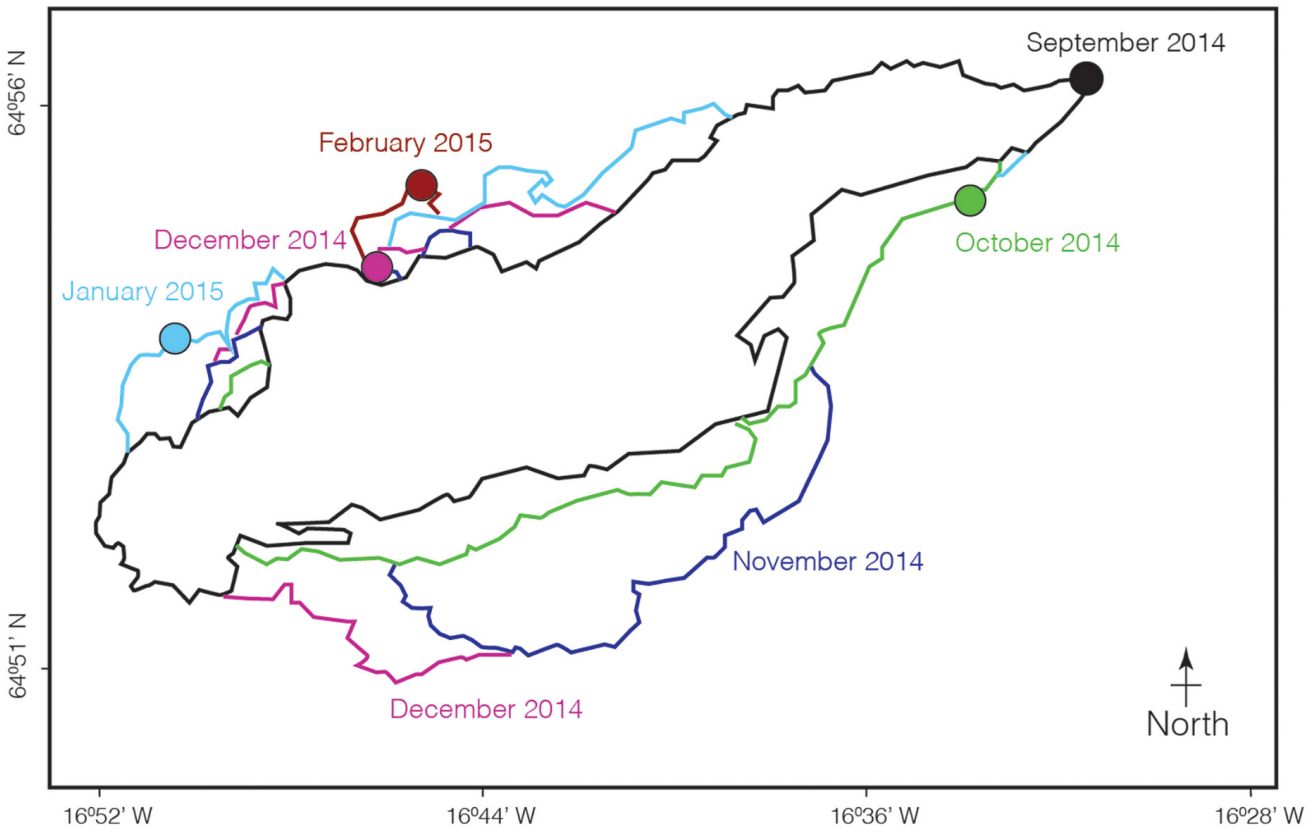

FIGURE 1 | Outlines of the Holuhraun–Bárdarbunga lava flow were drawn on the base of satellite images collected at different times. These images are available on the web-page of the Icelandic Meteorological Office. The circles indicate the sampling locations.

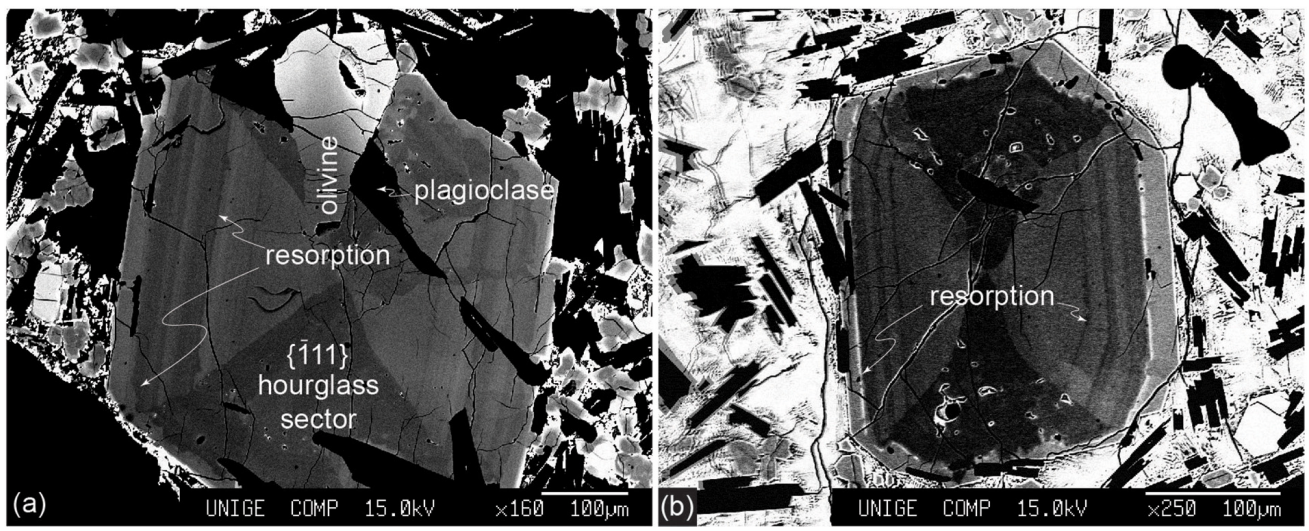

FIGURE 2 | SEM- Backscattered images of two selected clinopyroxenes. Both crystals show hourglass sector zoning, oscillatory zoning (pervasive also through the hourglass zone) and a relatively bright outer rim. **(a)** The crystals present two main regions of resorption, inclusions of plagioclase and a chemically zoned olivine crystal. **(b)** This crystal shows an example of a very bright growth region toward the outer portions of the crystal, which we observed in a small proportion of cpx. This rim invariably presents an irregular outer boundary.

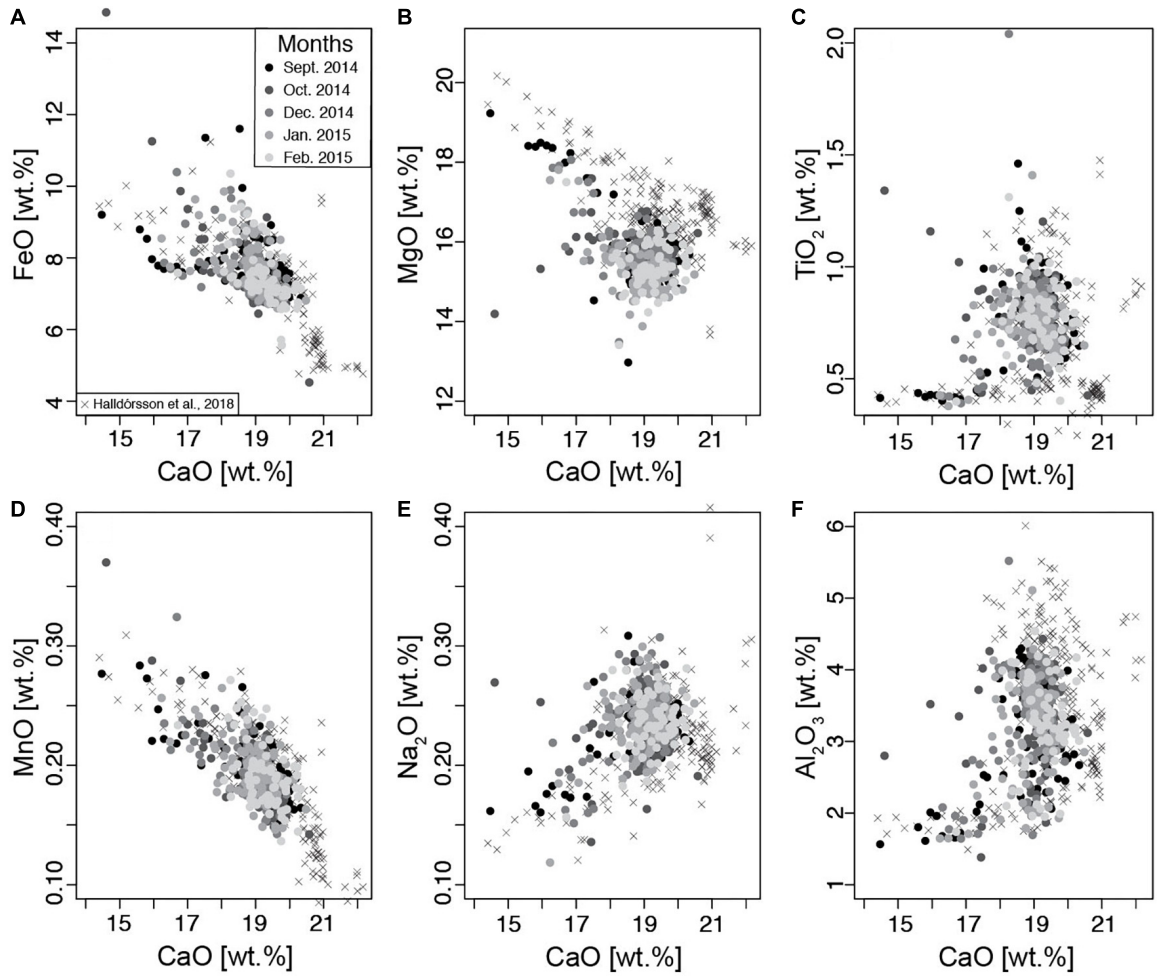

FIGURE 3 | (A–F) Major element clinopyroxene analyses. The gray-scale represents the different periods over which the samples were collected. No obvious relationship is visible between clinopyroxene chemistry and eruption time.

analyses of cpx with totals higher than 98 wt.% (n. 809; but using all 876 analyses did not change the result of the analyses) were first normalized for each element to values between 0 and 1 to give them the same weight and avoid false results. The normalized values were used to calculate the Euclidean distance (d_{ij}) between each analytical spot as:

$$d_{ij} = \sqrt{(x_i - x_j)^2 + (y_i - y_j)^2 + \ldots (z_i - z_j)^2} \qquad (1)$$

where x to z are all measured elements and i and j are the indexes of all measured points. To identify the clusters of data we use the Ward minimum variance criterion (Ward, 1963), in which pairs of clusters are first identified considering the smallest values of d_{ij} and then progressively merged minimizing the within cluster variance after merging. This procedure produces a dendrogram with decreasing number of branches upward. The length of the branches represents the difference in d_{ij} required for separated clusters to be merged into one cluster. As the number of clusters is unknown *a priori* we apply 24 different methods (R package Nbclust; Charrad et al., 2014) that evaluate the potential number of clusters in our dataset and select the number that receive the highest number of votes (five clusters in our case).

RESULTS

The crystals are oscillatory zoned, in most cases show hourglass sector zoning and are generally characterized by an outer rim, which appears relatively bright in Back Scattered Electron images (BSE; **Figure 2**). Most of the crystals show multiple (2–4) regions of resorption, commonly in either the inner portion of the crystals or immediately before the outer rim (**Figure 2a**). In a few cases, the outer resorbed rim is also very bright (**Figure 2b**). Oscillatory zoning is never conspicuous inside the inner resorption zone but, when present, it is continuous through the hourglass sector, which is, in turn, truncated by the outer resorption zone and the outer rim of the crystals. We also observed cpx that partially includes olivine that shows normal zoning and a diffused pattern toward the outer portion of the crystal (**Figure 2a**). Plagioclase is also included in cpx but is

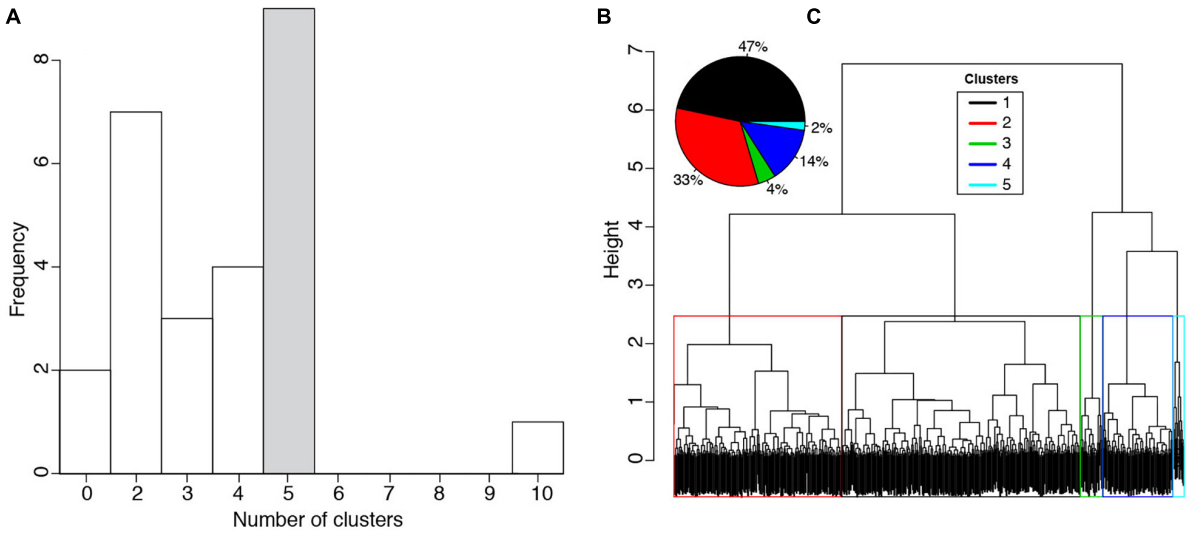

FIGURE 4 | Results of the hierarchical clustering analysis. **(A)** Frequency of clusters identified considering a total of 24 methods to estimate the number of clusters present in our cpx dataset. The majority of methods indicate that our dataset contains 5 compositional clusters. **(B)** Dendrogram obtained considering the Euclidean distance and the Ward method (Ward, 1963). The color boxes show the group of analyses associated with the respective cluster. The height represents the compositional difference required to merge clusters. The clusters are arranged horizontally so that the most different are at the two extremes of the dendrogram. **(C)** Pie chart showing the percentage of each of the five identified clusters.

not generally closer to the core than the innermost resorption zone (**Figure 2a**).

Plotting the analyses in Harker diagrams with gray-scale reflecting the month of eruption of the sample, show no chemical trends of the cpx with time (**Figure 3**), which is consistent with previous observations (Halldórsson et al., 2018). Additionally, the variation of chemistry from the core to the rim of single cpx can span the entire range of chemical variability observed throughout the eruption. A general inspection of these diagrams highlights that no two elements can be used to identify groups of cpx with distinct compositions (**Figure 3**). In these situations an unsupervised learning approach can be useful (Bergen et al., 2019) to explore more than two chemical dimensions, without any need for an *a priori* assumption on the mechanisms responsible for the presence of compositional clusters. However, we stress that while this approach always identifies compositional clusters, their validity must be cross-checked with petrography and geochemistry.

HC was applied to all cpx major element analyses (**Supplementary Table 1**), with a modal average of 5 clusters present in our dataset (**Figure 4A**). Considering all elements together, the different clusters are discernible by their chemistry (**Figure 5**). There is no combination of two elements, however, that could be used to unequivocally distinguish all five clusters, justifying our use of the clustering approach. Considering the dendrogram (**Figure 4b**), Clusters 1 and 2 are chemically similar, while Cluster 3 and 5 exhibit the largest compositional difference with respect to the other clusters, especially in Al_2O_3, TiO_2, MgO, CaO, and Na_2O (**Figure 5**). Cluster 4 differs from 1 to 2 for its lower Al_2O_3, CaO, and to a minor extent Na_2O content, with higher FeO and MnO (**Figure 5**).

While no particular temporal trends were observed in cpx chemistry (**Figure 3**), the compositional clusters occupy specific textural positions, which indicate that most pyroxenes grew following the same sequence of events. Cluster 3 corresponds to the composition of the {−111} hourglass sector of the cpx crystals, which is visible in the majority of crystals (**Figures 6a,b,g**). Analyses collected in the innermost portions of the cpx crystals belong either to Cluster 3 (dark in BSE and representing portions of the {−111} hourglass sector) or to Cluster 1. Cluster 2 is generally observed in the vicinity of a partly resorbed rim (**Figures 6a,c–f**). The oscillatory-zoned mantle of the crystals is constituted by an alternation of Cluster 1 and 2. Cluster 4 generally includes analyses of the outer rims of the cpx, although in January and February 2015 it also appears in more internal portions of the crystals (**Figure 6g**). To test if the appearance of Cluster 4 in the inner portions of crystals was associated with cluster mis-assignment we checked the composition of the analyses closest to the core assigned to Cluster 4 and find that these composition are indeed typical of Cluster 4 as they occupy the mean compositions of Cluster 4 for all elements. Cluster 5 represents only 2% of the analyses (**Figure 4c**) and corresponds exclusively to the bright and partially resorbed zone just before the outer rims of the cpx. The large chemical variance of this cluster (**Figure 5**), reflects a thickness for these zones that is at the limit or smaller than the EPMA spatial resolution. Therefore these analyses are of the lowest quality and at least some of the analyses represent mixtures of Cluster 5 composition and the chemistry of the neighboring zones.

The same approach we used for major elements was applied to analyses (no. 128) of selected trace elements present in sufficiently high concentration in cpx (Sc, Ti, V, Cr, Mn, Co, Ni). Including elements in low concentrations only adds noise to the data and

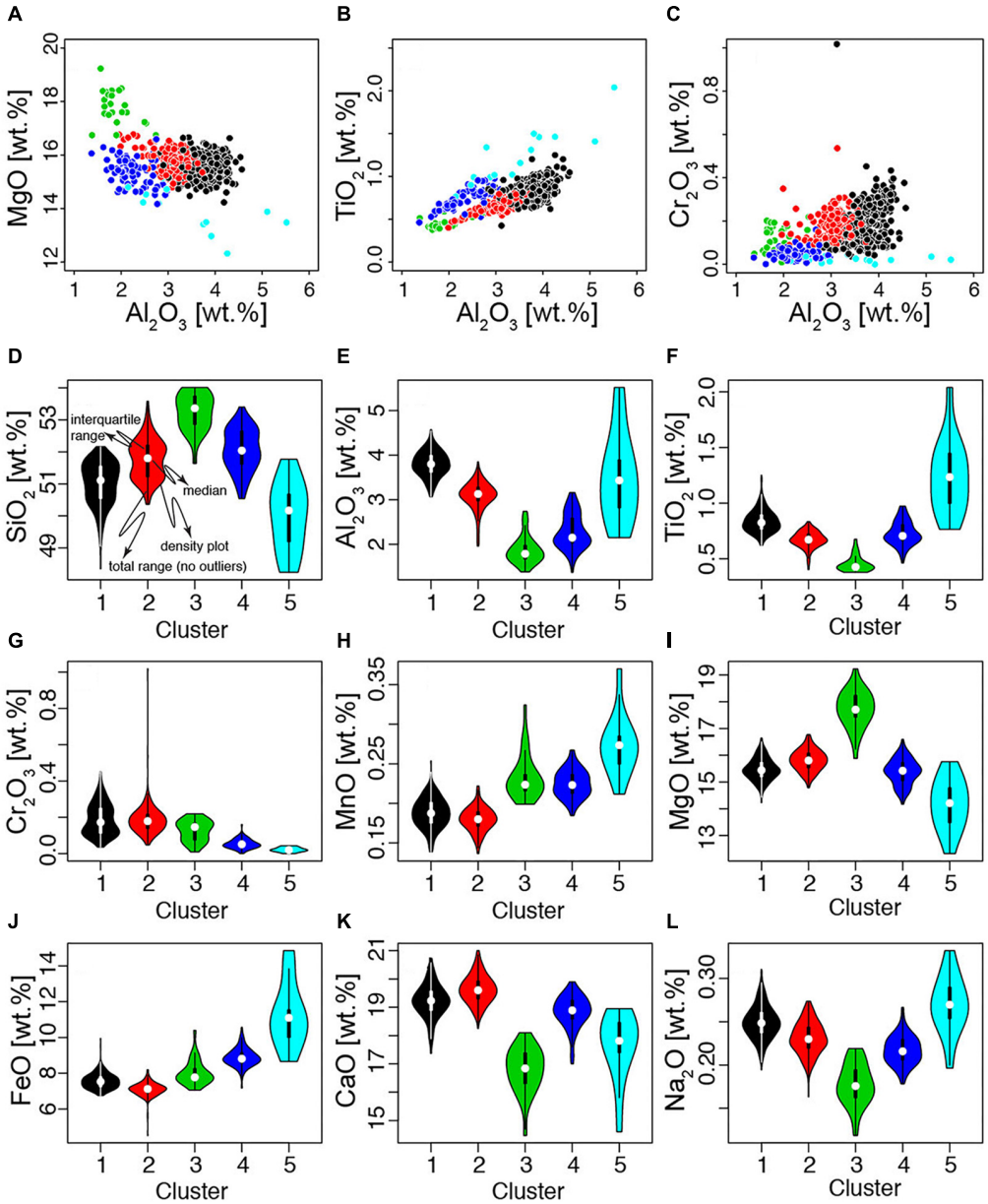

FIGURE 5 | (A–C) Harker diagrams of all analyses with color coding corresponding to the cluster assigned by HC. **(D–L)** Violin plots showing the density distribution of each oxide of each cluster of cpx chemistry. The violin plot show the density, and other descriptive characteristics of the distribution of each element for each of the compositional clusters.

complicates the clustering results (**Supplementary Table 2**). The number of clusters that received the highest amount of votes with the different tests are 2 and 5 (**Figure 7k**). Harker diagrams of the dataset suggest a better visual partitioning in five clusters with respect to two clusters (**Figures 7f–j**). The comparison between the textural positions of the clusters identified using major and trace elements (we identify the clusters identified by trace element adding "TE" after the cluster number) reveals some correspondence between the two. As Cluster 3, also Cluster 3TE corresponds to the compositions of the {−111} hourglass sector (**Figures 7b,c**). Cluster 5TE is identified in the outer portions of the crystals, which corresponds to the textural location of Cluster 4. Cluster 2TE, 4TE, and 1TE, constitute cores and mantles of the crystals and occupy progressively more external positions within the crystals (**Figures 7a–e**).

DISCUSSION

The application of HC to the major element chemical analyses of cpx of the 2014–2015 Holuhraun–Bárdarbunga eruption allowed the identification of five compositional clusters and their relative

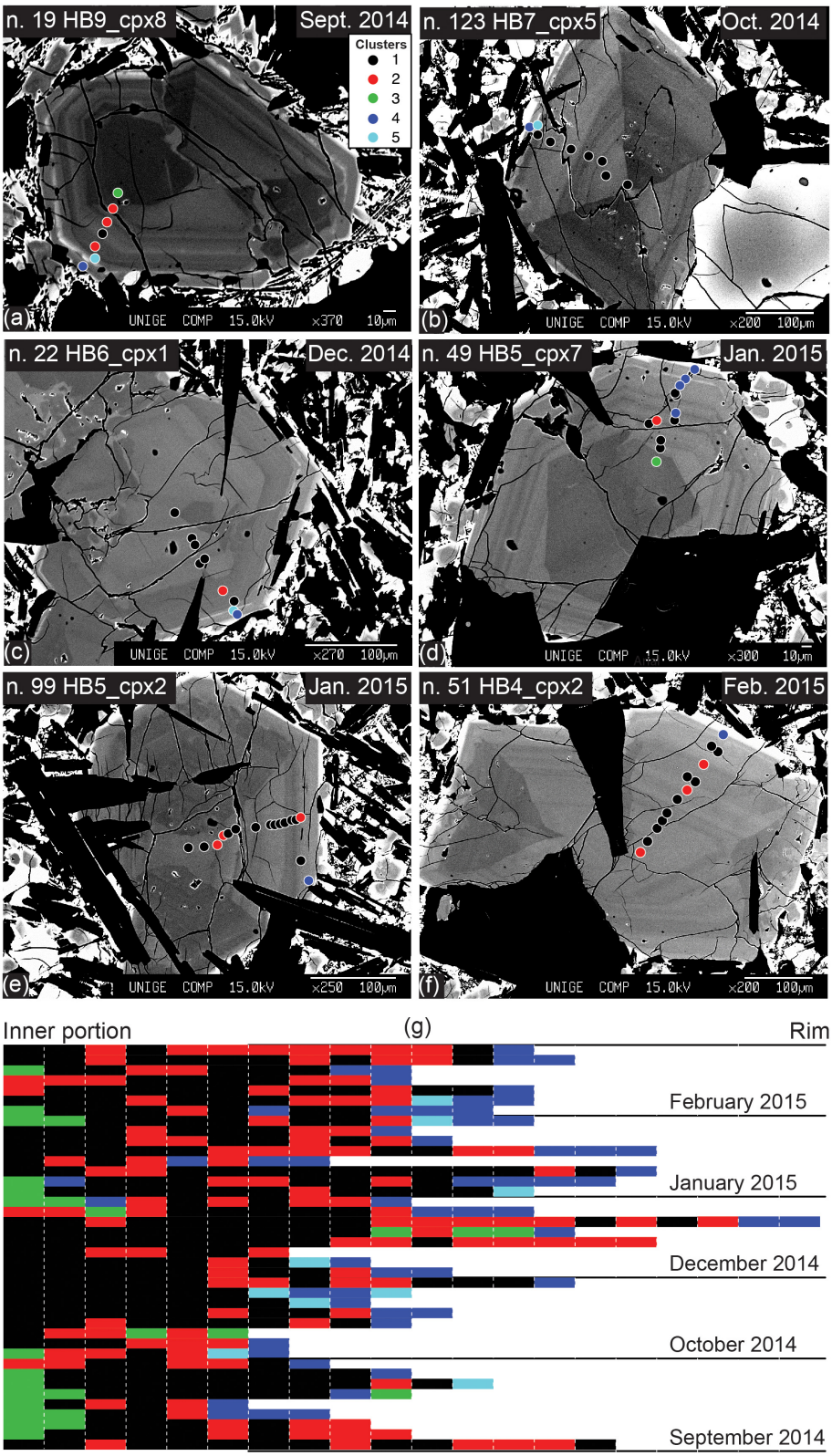

FIGURE 6 | SEM Backscattered images of selected clinopyroxene crystals with location of major and trace element analyses. **(a–f)** The circles show the location of the EPMA spots with a color corresponding to the associated cluster assignment. **(g)** Each of the horizontal segments represent a spot and the color refers to the cluster to which each spot was assigned by HC.

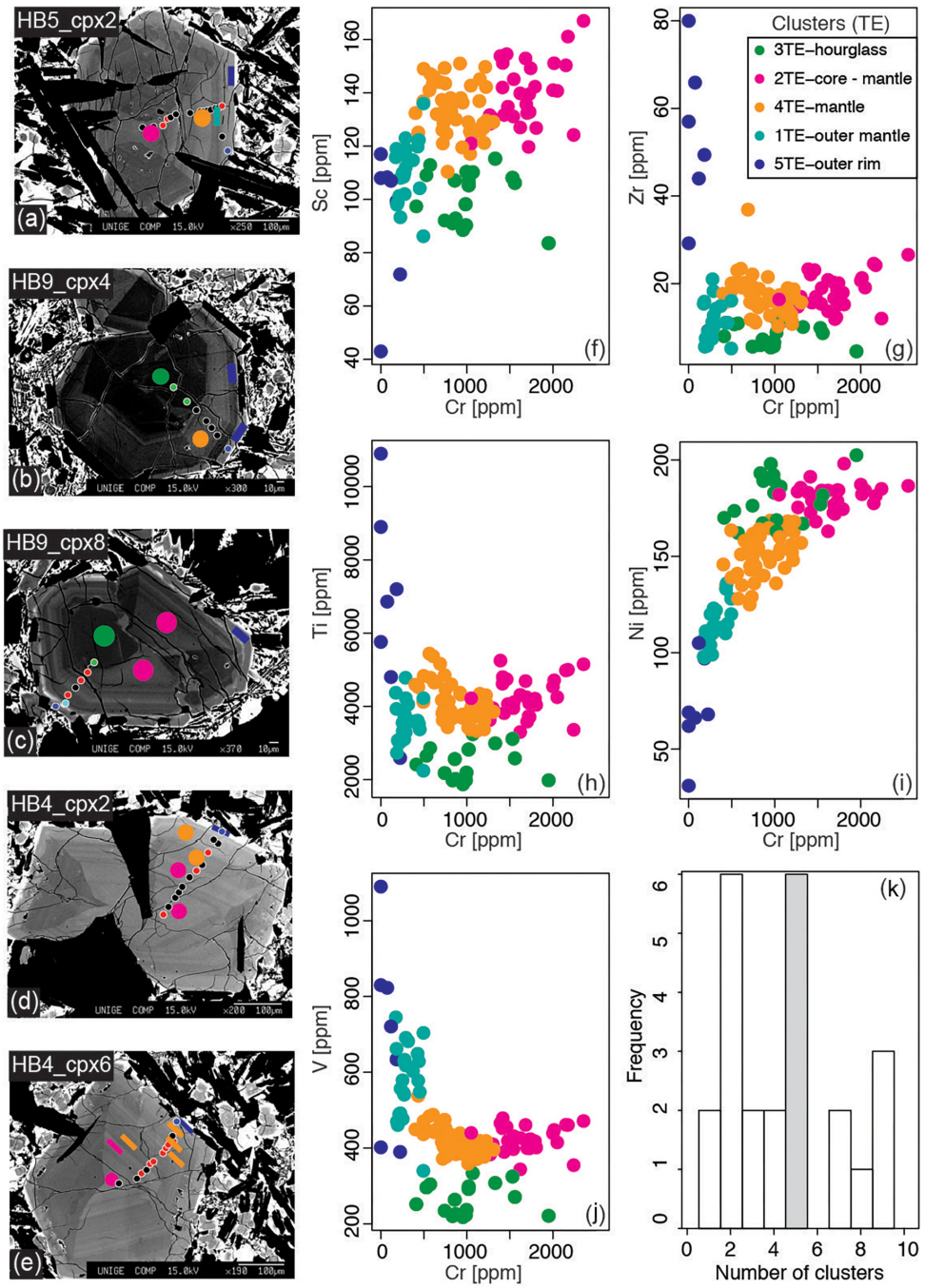

FIGURE 7 | Trace element analyses. **(a–e)** SEM Back scattered images of some of the cpx crystals selected for trace element analyses. Circles and rectangles provide the location of the spot and their color corresponds to the cluster assigned based on trace element content. Smaller circles are colored according to the cluster assigned applying HC to major elements. **(f–j)** Harker diagrams for all collected spot analyses with colors corresponding to the clusters assigned on the base of trace elements. **(k)** Histogram showing the result of the number of clusters determined using 24 different metrics. The gray shading highlights the selected number of clusters.

position within the crystals. Cluster 1 and 2 constitute most of the inner portions and mantles of the crystals, respectively; Cluster 5 represents a sparsely present bright (in BSE) outer portion of the cpx; the outer rims are part of Cluster 4, and analyses belonging to Cluster 3 are from the {−111} hourglass sectors (**Figure 6**). In the following we discuss the processes that could be responsible for the chemical variability observed in the cpx crystals and discuss potential relationships between mineral chemistry and the dynamics of magma migration during the eruption.

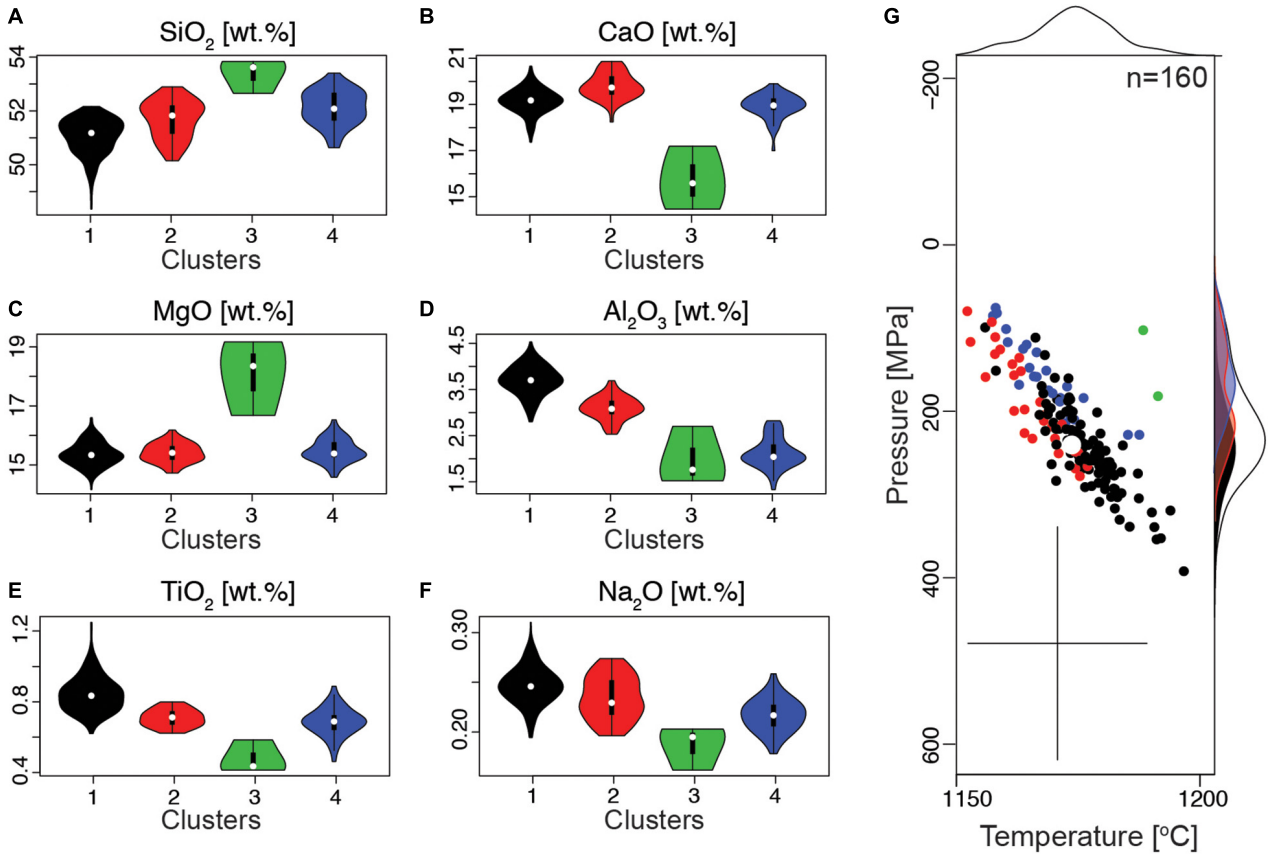

FIGURE 8 | Chemistry of cpx crystals and resulting thermo-barometry calculations. **(A–F)** Violin plots showing the density distribution of each of the oxides for all cpx analyses with color scheme as in **Figure 4**. **(G)** Pressure and temperature for each analysis were calculated using the geobarometer of Neave and Putirka (2017) together with the thermometer (Eq. 33) of Putirka (2008). The white circle provides the average value of pressure and temperature obtained with this approach. The density plots on the side of the diagram show the distribution of pressure and temperature calculations. The cross indicate the error/uncertainty of estimations.

The cpx crystals we analyzed have core to rim distances between 250 and 500 μm, which, considering experimental growth rates under kinetically controlled growth at temperature typical for basaltic magmas of 5×10^{-10} to 1.5×10^{-9} m/s (Mollo et al., 2013), imply that they grew over a period of 2–9 days. Using liquid-cpx thermobarometry (Putirka, 2008; Neave and Putirka, 2017) we calculated cpx crystallization pressures to estimate the structure of the plumbing system. We first selected only cpx crystals that were in equilibrium with the melt, following the procedure described in Neave et al. (2019). Considering the aphyric nature of the erupted magmas (Halldórsson et al., 2018) we use whole rock chemistry with H_2O content of 0.4wt.% (based on Bali et al., 2018) as an equivalent for the melt in equilibrium with the cpx crystals. Analyses in Clusters 1, 2, 4 passed the equilibrium test while no analyses from Cluster 5 were found to be in equilibrium, and only two analyses from the {−111} hourglass sector (i.e., Cluster 3) passed the equilibrium screening (**Figure 8**).

Similarly to previous determinations, the pressure estimates vary between about 100 and 400 MPa with the highest density of estimates around 200 MPa (Neave et al., 2019; **Figure 8**). The calculated storage pressure progressively decreases from Cluster 1, to 2 and 4, suggesting concurrent magma rise and crystallization. However, as these variations are within the uncertainty of the geobarometer we do not discuss further their bearing on the pre-eruptive crystallization depth (**Figure 8G**). Nevertheless, the distribution of pressures obtained with cpx-liquid barometry indicate that over the 2–9 days before eruption, magma crystallized mainly at pressures around 200 MPa (i.e., 5–6 km depth), which is close to the depth range over which magma within the dyke has been interpreted to be transported laterally to the to the eruption site (Woods et al., 2019).

Prior to using cpx chemistry to retrieve the conditions of magma storage or the dynamics of magma migration to the surface, it is important to understand whether the chemical variations we have identified are due to variations in pressure (e.g., Nimis, 1995; Nimis and Ulmer, 1998), temperature (e.g., Lindsley, 1983), melt chemistry (e.g., Neave and Putirka, 2017), or growth kinetics (Iezzi et al., 2011; Lanzafame et al., 2013; Mollo et al., 2013, 2012, 2011; Ubide et al., 2019). Additionally, experiments show that cpx zoning resulting from kinetic effects can be produced even under nominally equilibrium conditions (Neave et al., 2019), and crystal can grow rapidly generating skeletal/dendritic structures, which are subsequently filled during

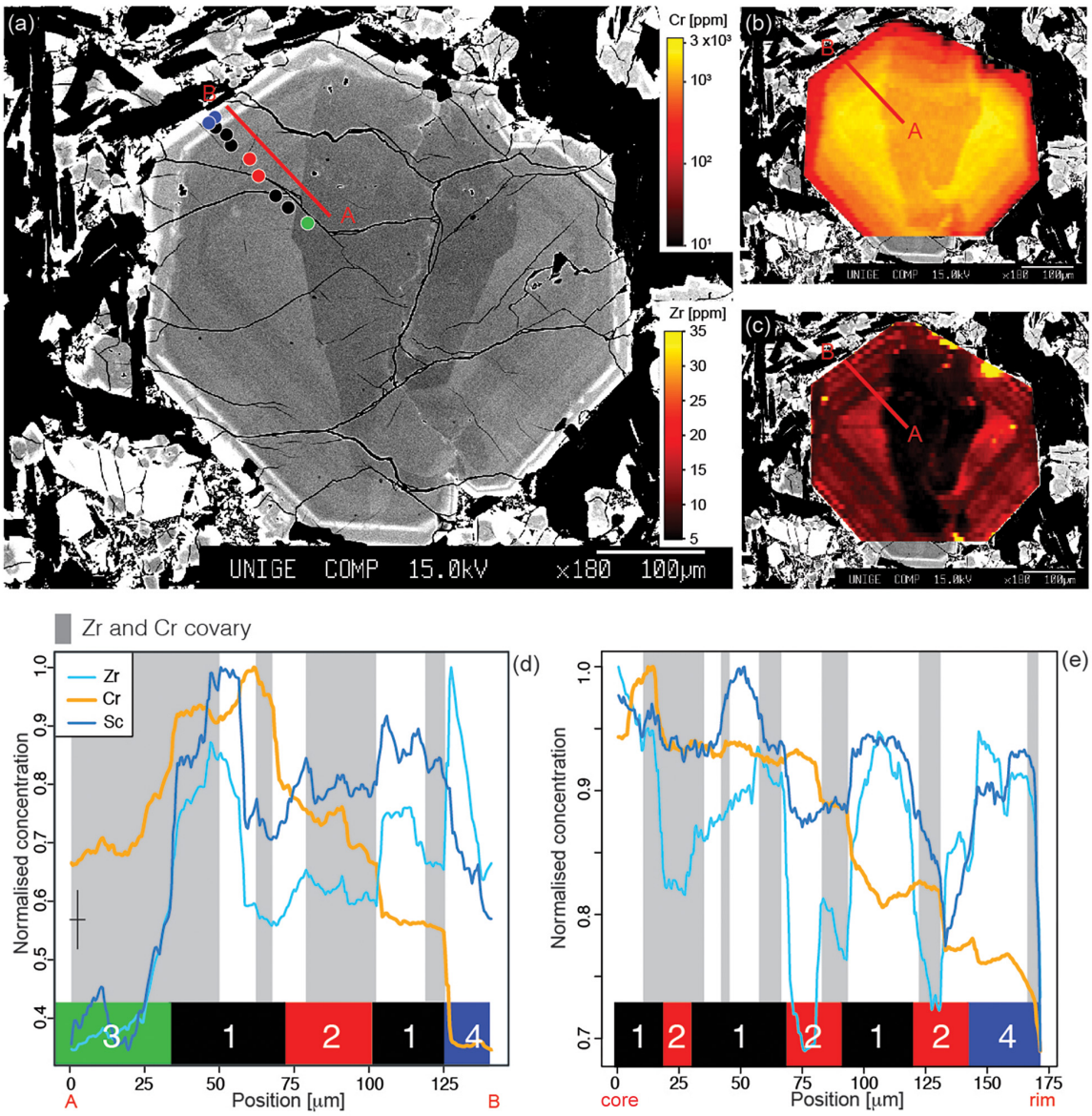

FIGURE 9 | Trace element mapping. **(a)** BSE image showing the location of the transect over which the trace element content was calculated starting from the elemental maps. The circles indicate the location of the electron microprobe analyses and the color indicates the corresponding cluster identified from major element analyses. **(b,c)** Maps of Cr and Zr for the crystal in panel **(a)**. **(d)** Concentrations of Zr, Cr, and Sc normalized to the maximum and minimum values measured in all profiles, for the crystal shown in panels **(a–c)**. The colors (and numbers) indicate the corresponding cluster identified with major elements. Panel **(e)** same as panel **(d)** but for another crystal.

growth at lower rate (Hammer et al., 2016; Welsch et al., 2016). All these effects should be taken in consideration before using cpx chemistry to identify storage conditions or processes occurring in the volcanic plumbing system.

The chemical composition of Cluster 3 is in agreement with previously measured cpx {−111} hourglass sectors (Ubide et al., 2019; **Figure 6**). Cluster 5 and 1 shows enrichment of Al, Ti and depletion of Na and lower Si, Ca, Mg (more extreme for Cluster 5) with respect to Cluster 2 (**Figure 5**). The chemistry of Cluster 1 and 5, could reflect either growth from magmas of different compositions, or as shown experimentally, be the consequence of more rapid crystal growth at relatively high undercooling with respect to Cluster 2 (Mollo et al., 2013). To test these two hypotheses, we selected cpx crystals with the highest textural complexity and with chemical composition covering all clusters identified with major elements.

Trace element profiles consistently show that Cr decreases from core to rim in a stepwise manner while Zr, Sc, V, Ti, covary (**Figures 9d,e**; we report only Cr, Zr and Sc in the figure for clarity). The profiles show that Cluster 1 is generally characterized by higher concentrations of Zr and Sc and moderate to no decrease of Cr with respect to Cluster 2 (**Figures 9d,e**). Zr

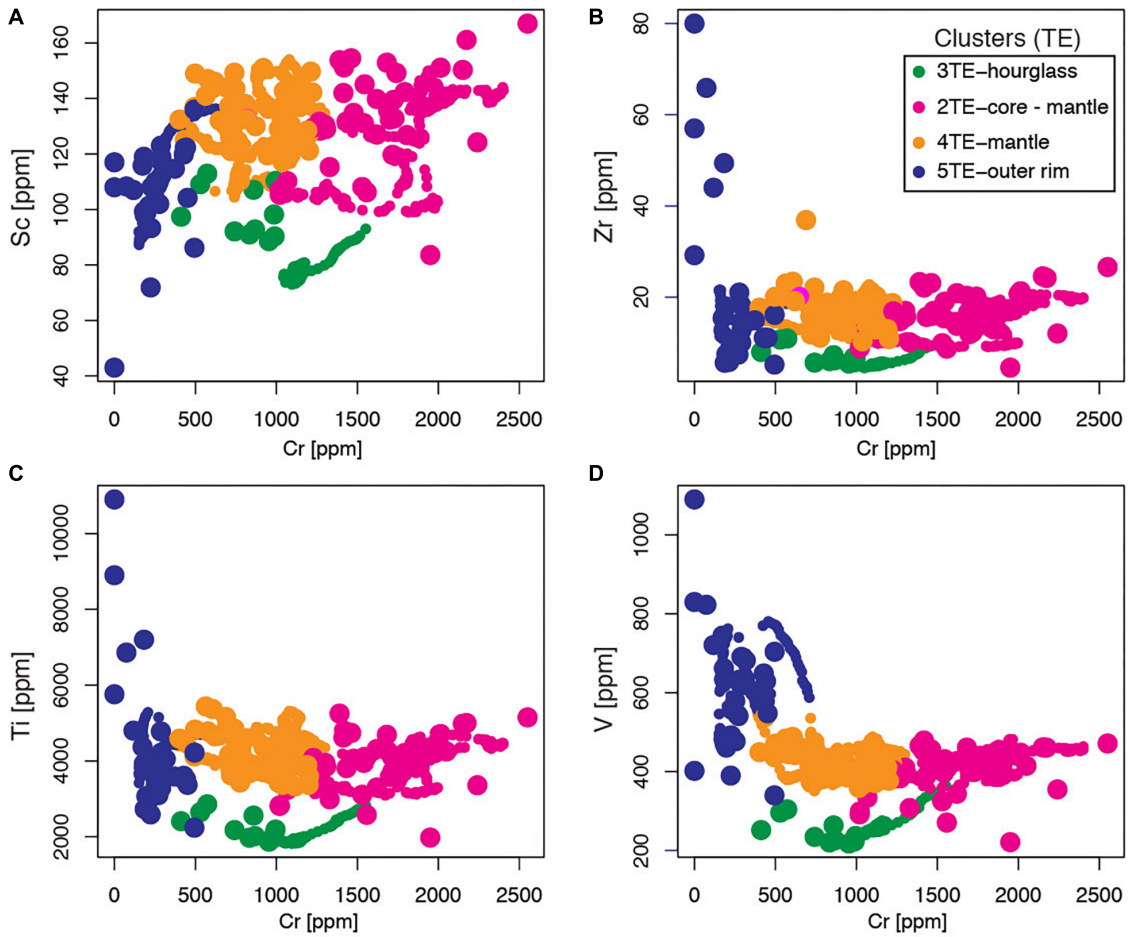

FIGURE 10 | Harker diagrams showing the variation of **(A)** Sc, **(B)** Zr, **(C)** Ti, and **(D)** V against Cr for LA-ICP-MS spot analyses (large circles) and profiles (small circles). The color coding is the same of **Figure 7**.

is incompatible in a bulk crystallizing assembly constituted by olivine, cpx and plagioclase, as is Sc, at least until the relative fraction of cpx in the crystallizing assembly does not reach about 50 wt.% and the bulk partition coefficient becomes larger than 1; partition coefficients from Earthref.org). As Cr is compatible in the crystallizing assemblage, with crystallization the concentrations of Zr and Sc in the residual melt phase (and therefore in the cpx) increases while Cr should decrease. Zr and Cr are inversely correlated in some portions of the profile, as it would be expected if the growth of the cpx zones occurred from magmas at different degrees of crystallinity, while they covary in other regions (**Figures 9d,e**), as it would be expected if the crystal growth occurred at increasing cooling rates (or undercooling; Mollo et al., 2013). No clear relationship is observable between the clusters identified by major element chemistry and the Cr-Zr variations (**Figures 9d,e**), nor between Cr-Zr and the trace element clusters (**Figure 10**). This implies that while variations of undercooling were occurring during crystal growth, they were not the only processes modulating the major element composition of the cpx. Therefore, Cluster 1 zones either (1) crystallized from a magma of similar initial composition but slightly more evolved and potentially cooler than Cluster 2, or (2) these two clusters were formed from magmas with distinct chemistry. Regarding the lack of relationships between Zr-Cr and the trace element clusters, this suggest that the ratio between these two elements is not the most significant factor controlling the trace element clusters. To test if any evidence exist of the interaction between magmas of distinct chemistry, we performed HC on the trace element profile dataset (**Supplementary Tables 3–5**) and include the LA-ICP-MS spots (**Figure 10**; clusters recognized on the base of trace element chemistry are identified by TE). Including all data, the result is similar to that obtained considering only the trace element spots data, however, the few analyses associated with Cluster 5TE are not identified as a separated cluster when including all data. Cluster 1 and 2 correspond to Cluster 4TE and Cluster 2TE, respectively and their trace element chemistry suggest that Cluster 1 cpx could crystallized at lower temperature (i.e., in a more fractionated magma) with respect to cpx from Cluster 2.

Thus, altogether major and trace element data suggest that Cluster 1 and 2 zones were formed by crystallization from the same magma at lower and higher temperature, respectively

(**Figures 5**, **9**, **10**). The higher temperature of zones belonging to Cluster 2 is also confirmed by their common growth over resorption surfaces (**Figures 6a,c,d–f**).

The trace element chemical evolution of cpx crystals from core to rim, can be plausibly explained with their crystallization from the same parental magma but at different temperatures and crystallinities (**Figure 10**). Few points located in the outer rim (Cluster 5TE), show higher content of incompatible elements such as Zr, Ti, and V and lower content of Sc (**Figure 10**). These few analyses suggest that some of the outer portions of the cpx crystals crystallize from a distinct melt. This magma does not need to be derived by a different parental magma with respect to the Bárdarbunga–Holuhraun 2014–2015 magma, but could be representing a highly crystalline lens of cold magma left over from previous eruptions. This scenario is in agreement with the major elements chemistry (**Figure 5**) of the rare bright outer zone (Cluster 5) of some cpx crystals (**Figures 7c**, **8a**), which could indicate crystal growth under rapid cooling conditions (Mollo et al., 2013).

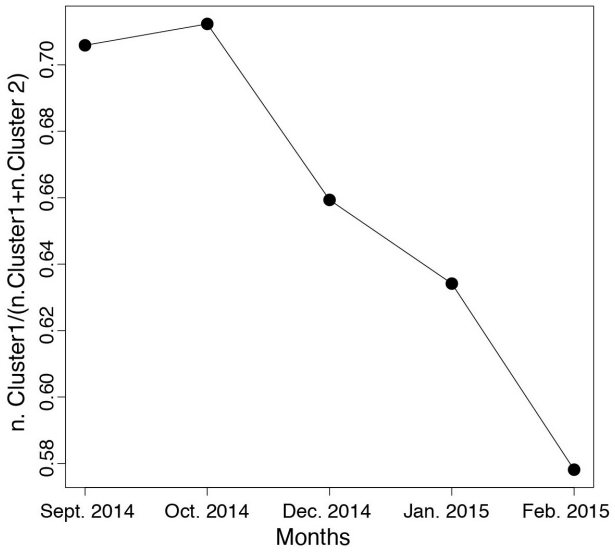

FIGURE 11 | Evolution of the fraction of Cluster 1 relative to Cluster 2. Note that we did not have samples from November 2014.

In summary, major and trace elements suggest that Cluster 1 and 2 rims grew from magmas with the same or similar composition but at lower (more chemically evolved melt) and higher temperature (lower concentration of incompatible elements; **Figure 9**), respectively. As Cluster 1 and 2 constitute the oscillatory zoned inner portions of the crystals, such temperature variations must have occurred repeatedly during the 2–9 days of cpx growth. The entrainment of cpx crystals in a higher temperature magma propagating through the dyke would lead to partial resorption of crystals followed by growth at lower degrees of undercooling and the formation of Cluster 2 growth zones. These distinct variations in temperature could be due to a number of factors, including: (1) thermal variability within the dyke due to non-uniform thermal exchange of magma with the wall rocks (e.g., complex geometry), which would result in high degrees of undercooling and crystallization of cpx marked by higher contents of Al, Ti and Na as observed for Cluster 1 and 5 compositions (**Figure 5**; Mollo et al., 2013); or (2) the temperature of the magma feeding the eruption was heterogeneous and mingling and mixing occurred within the dyke during transport resulting in the formation of Cluster 1 and 2 cpx zones. The fraction of

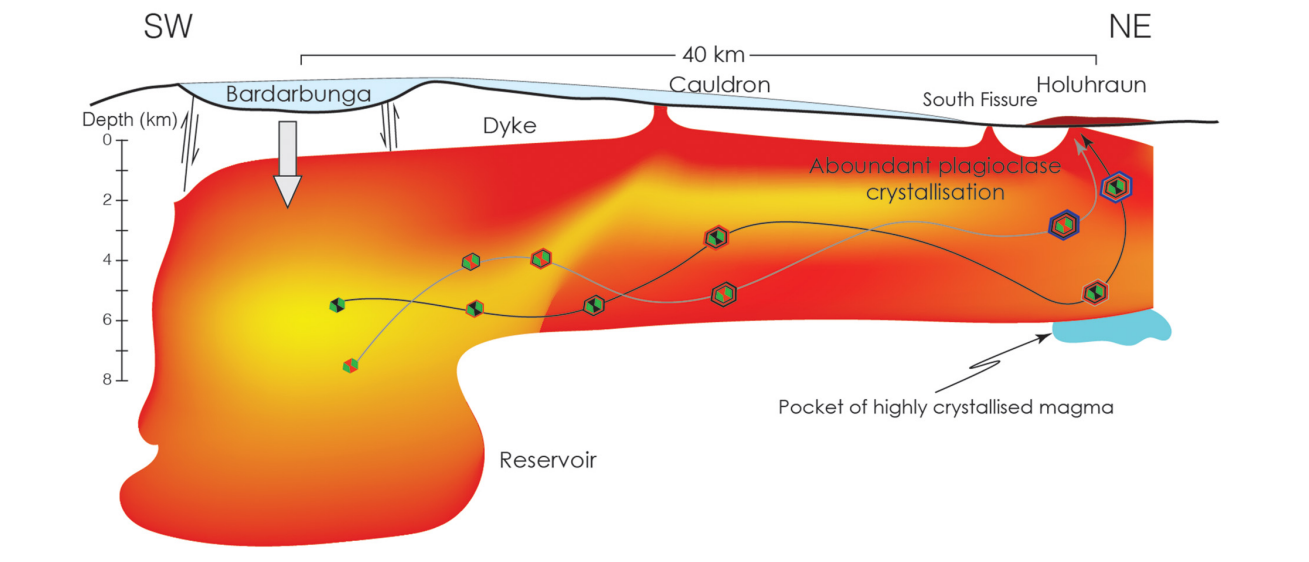

FIGURE 12 | Cartoon (not to scale) showing the potential path followed by two crystals during the 2014–2015 Bárdarbunga–Holuhraun eruption, which would best account for our measurements and calculations. The depths are approximative and based on earthquake locations and reconstruction by Woods et al. (2019). The figure is partly inspired by Gudmundsson et al. (2016), Hartley et al. (2018), Hudson et al. (2017), and Woods et al. (2019).

Cluster 1 progressively decreases with respect to Cluster 2 from October 2014 to the end of the eruption (**Figure 11**). In the first scenario, this decrease would reflect the thermal maturation of the feeder dyke leading to a decreases of cpx crystallization at high degrees of undercooling. Within the second hypothesis, such decrease of the fraction of Cluster 1 cpx crystals would result from a decrease of the fraction of lower temperature magma feeding the dyke during the eruption (**Figure 12**).

Major elements suggest that Cluster 5 was formed at the highest degrees of undercooling with respect to the other compositional clusters (**Figure 5**; Mollo et al., 2013). Because of the limited spatial resolution, the trace element composition of Cluster 5 is difficult to determine with high precision, however, trace element profiles reveal that the presence of the bright rim in the cpx crystals (**Figure 9a**) likely grew from a magma with distinct chemistry (**Figure 10**). On the basis of these data we tentatively suggest that Cluster 5 compositions were formed when the magma came into contact with chemically different pocket/s of relatively cold magma while in the proximity of the eruption site (**Figure 12**), an hypothesis proposed also by Hartley et al. (2018). Finally, the rims (Cluster 4) were formed at shallow depths, but possibly still within the dyke, as this compositional cluster can also be observed in the inner portions of the crystals from January 2015 (**Figure 5g**).

CONCLUSION

The Holuhraun–Bárdarbunga eruption lasted for approximately 6 months during which the bulk magma chemistry remained substantially the same (Halldórsson et al., 2018). However, mineral chemistry can gives more resolution on the chemical processes occurring within magmatic systems (Wallace and Bergantz, 2002; Perugini et al., 2005; Kahl et al., 2011; Cheng et al., 2017; Forni et al., 2018; Probst et al., 2018). Using HC we have identified five groups of cpx compositions in major and trace element space that constitute different zones of the crystals. This, together with the petrographic context, allow us to interpret the evolution of the crystallization conditions during the eruption and to identify the different processes responsible for the chemical variability measured in the cpx crystals. Major and trace element analyses suggest that the chemical variability in the inner portions of the cpx crystals is mainly modulated by growth at different temperatures and resulting kinetic effects (**Figures 5**, **9**, **10**; Mollo et al., 2013; Ubide et al., 2019). The chemistry of the outer portions of the crystals reflect copious crystallization at shallow depths (**Figures 5**, **6**, **8**, **9**). The chemistry of Zr-rich rims present in some of the crystals suggest the potential interaction of magma with pockets of cold and crystal-rich magma during the propagation of the magma to the eruption site (**Figure 12**). Compositional data, after removal of kinetic effects (Neave et al., 2019) suggest pre-eruptive pressure and temperature distributions in agreement with previous estimates (**Figure 8**; Halldórsson et al., 2018).

Our analysis suggests that the oscillatory zoning in the cpx mantles could be the result of either the interaction between magma propagating to the eruption site and pockets of magma that were cooling within the dyke, or by the mingling-mixing of magmas released from the reservoirs at different temperatures (**Figure 12**). The fraction of cpx rims generated at higher degrees of undercooling [Cluster 1/(Cluster1 + Cluster2)] progressively decline during the eruption (**Figure 11**), highlighting either thermal maturation of the dyke during the eruption, or the decrease of the fraction of the cooler magma entering the dyke. We propose that the approach presented here can be used to trace the evolution of long-lasting eruptions and can be useful to link monitoring parameters to magmatic processes occurring at depth.

DATA AVAILABILITY STATEMENT

All datasets generated for this study are included in the article/**Supplementary Material**.

AUTHOR CONTRIBUTIONS

LC conceived the study, led the fieldwork, and wrote the first draft of the manuscript. GS and LP assisted with the sample collection and data interpretation. MP collected the LA-ICP-MS data and contributed to their interpretation. TS assisted with the unsupervised learning approach and helped with the data interpretation. EB helped to interpreting the geochemical data and shared her expertise on the Holuhraun–Bárdarbunga 2014–2015 eruption. All authors contributed to the final version of the manuscript.

FUNDING

LC, LP, and GS appreciated the support for fieldwork of the Faculty of Science of the University of Geneva and the access provided by the Vatnajökull National Park. LC and TS received funding from the European Research Council (ERC) under the European Union's Horizon 2020 Research and Innovation Program (grant agreement no. 677493 – FEVER). LC and TS acknowledge the support of the Swiss National Science Foundation (grant no. 200021_184632). MP acknowledge the Università degli Studi di Perugia FRB2019 grant titled "ENGAGE – machinE learNinG Applications for Geological problEms."

ACKNOWLEDGMENTS

We are grateful to Jean-Marie Boccard for the preparation of excellent rock thin sections.

SUPPLEMENTARY MATERIAL

The Supplementary Material for this article can be found online at: https://www.frontiersin.org/articles/10.3389/feart.2020.00018/full#supplementary-material

REFERENCES

Bali, E., Hartley, M. E., Halldorsson, S. A., Gudfinnsson, G. H., and Jakobsson, S. (2018). Melt inclusion constraints on volatile systematics and degassing history of the 2014-2015 Holuhraun eruption, Iceland. *Contrib. Mineral. Petrol.* 173:9.

Bergen, K. J., Johnson, P. A., De Hoop, M. V., and Beroza, G. C. (2019). Machine learning for data-driven discovery in solid Earth geoscience. *Science* 36:eaau0323. doi: 10.1126/science.aau0323

Browning, J., and Gudmundsson, A. (2015). Surface displacements resulting from magma-chamber roof subsidence, with application to the 2014–2015 Bardarbunga–Holuhraun volcanotectonic episode in Iceland. *J. Volcanol. Geotherm. Res.* 308, 82–98. doi: 10.1016/j.jvolgeores.2015.10.015

Charrad, M., Ghazzali, N., Boiteau, V., and Niknafs, A. (2014). NbClust: an r package for determining the relevant number of clusters in a data set. *J. Stat. Softw.* 61:16344.

Cheng, L., Costa, F., and Roberto, C. (2017). Unraveling the presence of multiple plagioclase populations and identification of representative two-dimensional sections using a statistical and numerical approach. *Am. Mineral.* 102, 1894–1905. doi: 10.2138/am-2017-5929ccbyncnd

Forni, F., Degruyter, W., Bachmann, O., De Astis, G., and Mollo, S. (2018). Long-term magmatic evolution reveals the beginning of a new caldera cycle at Campi Flegrei. *Sci. Adv.* 4, 1–12. doi: 10.1126/sciadv.aat9401

Gauthier, P. J., Sigmarsson, O., Gouhier, M., Haddadi, B., and Moune, S. (2016). Elevated gas flux and trace metal degassing from the 2014–2015 fissure eruption at the Bárðarbunga volcanic system, Iceland. *J. Geophys. Res.* 121, 1610–1630. doi: 10.1002/2015jb012111

Geiger, H., Mattsson, T., Deegan, F. M., Troll, V. R., Burchardt, S., Gudmundsson, O., et al. (2016). Magma plumbing for the 2014-2015 Holuhraun eruption, Iceland. *Geochem. Geophys. Geosyst.* 17, 2953–2968. doi: 10.1002/2016gc006317

Gudmundsson, M. T., Jonsdottir, K., Hooper, A., Holohan, E. P., Halldorsson, S. A., Ofeigsson, B. G., et al. (2016). Gradual caldera collapse at Bardarbunga volcano, Iceland, regulated by lateral magma outflow. *Science* 353:aaf8988. doi: 10.1126/science.aaf8988

Halldórsson, S. A., Bali, E. O., Hartley, M. E., Neave, D. A., Peate, D. W., Gudhfinnsson, M., et al. (2018). Petrology and geochemistry of the 2014–2015 Holuhraun eruption, central Iceland: compositional and mineralogical characteristics, temporal variability and magma storage. *Contrib. Mineral. Petrol.* 173:64.

Hammer, J., Jacob, S., Welsch, B., Hellebrand, E., and Sinton, J. (2016). Clinopyroxene in postshield Haleakala ankaramite: 1. Efficacy of thermobarometry. *Contrib. Mineral. Petrol.* 171, 1–23. doi: 10.1007/s00410-015-1212-x

Hartley, M. E., Bali, E. O., Maclennan, J., Neave, D. A., and Halldorsson, S. A. (2018). Melt inclusion constraints on petrogenesis of the 2014-2015 Holuhraun eruption, Iceland. *Contrib. Mineral. Petrol.* 173.

Hudson, T. S., White, R. S., Greenfield, T., Ágústsdóttir, T., Brisbourne, A., and Green, R. G. (2017). Deep crustal melt plumbing of Bárðarbunga volcano, Iceland. *Geophys. Res. Lett.* 44, 8785–8794. doi: 10.1126/sciadv.aat5258

Iezzi, G., Mollo, S., Torresi, G., Ventura, G., Cavallo, A., and Scarlato, P. (2011). Experimental solidification of an andesitic melt by cooling. *Chem. Geol.* 283, 261–273. doi: 10.1016/j.chemgeo.2011.01.024

Ilyinskaya, E., Schmidt, A., Mather, T. A., Pope, F. D., Witham, C., Baxter, P., et al. (2017). Understanding the environmental impacts of large fissure eruptions: aerosol and gas emissions from the 2014–2015 Holuhraun eruption (Iceland). *Earth Planet. Sci. Lett.* 472, 309–322. doi: 10.1016/j.epsl.2017.05.025

Kahl, M., Chakraborty, S., Costa, F., and Pompilio, M. (2011). Dynamic plumbing system beneath volcanoes revealed by kinetic modeling, and the connection to monitoring data: an example from Mt. Etna. *Earth Planet. Sci. Lett.* 308, 11–22. doi: 10.1016/j.epsl.2011.05.008

Lanzafame, G., Mollo, S., Iezzi, G., Ferlito, C., and Ventura, G. (2013). Unraveling the solidification path of a pahoehoe "cicirara" lava from Mount Etna volcano. *Bull. Volcanol.* 75:703.

Lindsley, D. H. (1983). Pyroxene thermometry. *Am. Mineral.* 68, 477–493. doi: 10.1111/maps.12846

Mollo, S., Blundy, J. D., Iezzi, G., Scarlato, P., and Langone, A. (2013). The partitioning of trace elements between clinopyroxene and trachybasaltic melt during rapid cooling and crystal growth. *Contrib. Mineral. Petrol.* 166, 1633–1654. doi: 10.1007/s00410-013-0946-6

Mollo, S., Lanzafame, G., Masotta, M., Iezzi, G., Ferlito, C., and Scarlato, P. (2011). Cooling history of a dike as revealed by mineral chemistry: a case study from Mt. Etna volcano. *Chem. Geol.* 288, 39–52. doi: 10.1016/j.chemgeo.2011.06.016

Mollo, S., Putirka, K., Iezzi, G., and Scarlato, P. (2012). The control of cooling rate on titanomagnetite composition: implications for a geospeedometry model applicable to alkaline rocks from Mt. Etna volcano. *Contrib. Mineral. Petrol.* 165, 457–475. doi: 10.1007/s00410-012-0817-6

Neave, D. A., Bali, E., Guðfinnsson, G. H., Halldórsson, A., Kahl, M., Schmidt, A., et al. (2019). Clinopyroxene–liquid equilibria and geothermobarometry in natural and experimental tholeiites: the 2014–2015 Holuhraun eruption, Iceland David. *J. Petrol.* 60, 1653–1680. doi: 10.1093/petrology/egz042

Neave, D. A., and Putirka, K. D. (2017). A new clinopyroxene-liquid barometer, and implications for magma storage pressures under Icelandic rift zones. *Am. Mineral.* 102, 777–794. doi: 10.2138/am-2017-5968

Nimis, P. (1995). A clinopyroxene geobarometer for basaltic systems based on crystal-structure modeling. *Contrib. Mineral. Petrol.* 121, 115–125. doi: 10.1007/s004100050093

Nimis, P., and Ulmer, P. (1998). Clinopyroxene geobarometry of magmatic rocks part 1: an expanded structural geobarometer for anhydrous and hydrous, basic and ultrabasic systems. *Contrib. Mineral. Petrol.* 133, 122–135. doi: 10.1007/s004100050442

Paton, C., Hellstrom, J., Paul, B., Woodhead, J., and Hergt, J. (2011). Iolite: freeware for the visualisation and processing of mass spectrometric data. *J. Anal. At. Spectrom.* 26, 2508–2518. doi: 10.1039/C1JA10172B

Paul, B., Paton, C., Norris, A., Woodhead, J., Hellstrom, J., Hergt J., et al. (2012). CellSpace: a module for creating spatially registered laser ablation images within the Iolite freeware environment. *J. Anal. At. Spectrom.* 27, 700–706. doi: 10.1039/C2JA10383D

Perugini, D., Poli, G., and Valentini, L. (2005). Strange attractors in plagioclase oscillatory zoning: petrological implications. *Contrib. Mineral. Petrol.* 149, 482–497. doi: 10.1007/s00410-005-0667-6

Petrelli, M., Laeger, K., and Perugini, D. (2016a). High spatial resolution trace element determination of geological samples by laser ablation quadrupole plasma mass spectrometry: implications for glass analysis in volcanic products. *Geosci. J.* 20, 851–863. doi: 10.1007/s12303-016-0007-z

Petrelli, M., Morgavi, D., Vetere, F., and Perugini, D. (2016b). Elemental imaging and petro-volcanological applications of an improved laser ablation inductively coupled quadrupole plasma mass spectrometry. *Period. Mineral.* 85, 25–39. doi: 10.2451/2015PM0465

Petrus, J. A., Chew, D. M., Leybourne, M. I., and Kamber, B. S. (2017). A new approach to laser-ablation inductively-coupled-plasma mass-spectrometry (LA-ICP-MS) using the flexible map interrogation tool 'Monocle'. *Chem. Geol.* 463, 76–93. doi: 10.1016/j.chemgeo.2017.04.027

Probst, L. C., Sheldrake, T. E., Gander, M. J., Wallace, G., Simpson, G., and Caricchi, L. (2018). A cross correlation method for chemical profiles in minerals, with an application to zircons of the Kilgore Tuff (USA). *Contrib. Mineral. Petrol.* 173:23.

Putirka, K. D. (2008). Thermometers and barometers for volcanic systems. *Rev. Mineral. Geochem.* 69, 61–120. doi: 10.1515/9781501508486-004

R Core Team (2017). *R: A Language and Environment for Statistical Computing*. Vienna: R Foundation for Statistical Computing. Available at: https://www.R-project.org/

Ruch, J., Wang, T., Xu, W., Hensch, M., and Jónsson, S. (2016). Oblique rift opening revealed by reoccurring magma injection in central Iceland. *Nat. Commun.* 7:12352. doi: 10.1038/ncomms12352

Sigmundsson, F., Hooper, A., Hreinsdóttir, S., Vogfjörd, K. S., Ófeigsson, B. G., Heimisson, E. R., et al. (2014). Segmented lateral dyke growth in a rifting event at Bárðarbunga volcanic system, Iceland. *Nature* 517, 191–195. doi: 10.1038/nature14111

Ubide, T., McKenna, C. A., Chew, D. M., and Kamber, B. S. (2015). High-resolution LA-ICP-MS trace element mapping of igneous minerals: in search of magma histories. *Chem. Geol.* 409, 157–168. doi: 10.1016/j.chemgeo.2015.05.020

Ubide, T., Mollo, S., Zhao, J., Nazzari, M., and Scarlato, P. (2019). Sector-zoned clinopyroxene as a recorder of magma history, eruption triggers, and

ascent rates. *Geochim. Cosmochim. Acta* 251, 265–283. doi: 10.1016/j.gca.2019.02.021

Wallace, G. S., and Bergantz, G. W. (2002). Wavelet-based correlation (WBC) of zoned crystal populations and magma mixing. *Earth Planet. Sci. Lett.* 202, 133–145. doi: 10.1016/s0012-821x(02)00762-8

Ward, J. H. Jr. (1963). Hierarchical grouping to optimize an objective function. *J. Am. Stat. Assoc.* 58, 236–244. doi: 10.1080/01621459.1963.10500845

Welsch, B., Hammer, J., Baronnet, A., Jacob, S., Hellebrand, E., and Sinton, J. (2016). Clinopyroxene in postshield haleakala ankaramite: 2. texture, compositional zoning and supersaturation in the magma. *Contrib. Mineral. Petrol.* 171, 1–19. doi: 10.1007/s00410-015-1213-9

Wood, B. J., and Banno, S. (1973). Garnet-orthopyroxene and orthopyroxene-clinopyroxene relationships in simple and complex systems. *Contrib. Mineral. Petrol.* 42, 109–124. doi: 10.1007/BF00371501

Woods, J., Winder, T., White, R. S., and Brandsdóttir, B. (2019). Evolution of a lateral dike intrusion revealed by relatively-relocated dike-induced earthquakes: the 2014–15 Bárðarbunga–Holuhraun rifting event, Iceland. *Earth Planet. Sci. Lett.* 506, 53–63. doi: 10.1016/j.epsl.2018.10.032

Conflict of Interest: The authors declare that the research was conducted in the absence of any commercial or financial relationships that could be construed as a potential conflict of interest.

frontiers in Earth Science

ORIGINAL RESEARCH
published: 06 May 2020
doi: 10.3389/feart.2020.00132

Pyroxenites and Megacrysts From Alkaline Melts of the Calatrava Volcanic Field (Central Spain): Inferences From Trace Element Geochemistry and Sr-Nd Isotope Composition

Carlos Villaseca[1,2], Javier García Serrano[1] and David Orejana[1]*

[1] Dpt. Mineralogía y Petrología, Facultad CC Geológicas, UCM, Madrid, Spain, [2] Instituto de Geociencias IGEO (UCM, CSIC), Madrid, Spain

OPEN ACCESS

Edited by:
Teresa Ubide,
The University of Queensland,
Australia

Reviewed by:
Phil Shane,
The University of Auckland,
New Zealand
Michel Grégoire,
Centre National de la Recherche Scientifique (CNRS), France

****Correspondence:***
Carlos Villaseca
granito@ucm.es

Specialty section:
This article was submitted to Petrology, a section of the journal Frontiers in Earth Science

Received: *28 January 2020*
Accepted: *07 April 2020*
Published: *06 May 2020*

Citation:
Villaseca C, García Serrano J and Orejana D (2020) Pyroxenites and Megacrysts From Alkaline Melts of the Calatrava Volcanic Field (Central Spain): Inferences From Trace Element Geochemistry and Sr-Nd Isotope Composition. Front. Earth Sci. 8:132. doi: 10.3389/feart.2020.00132

Alkaline volcanic rocks from explosive monogenetic centers often carry an unusual cargo of crystals and rock fragments, which may provide valuable constraints on magma source, ascent and eruption. One of such examples is the Cenozoic Calatrava Volcanic Field in central Spain, a still poorly explored area to address these issues. Clinopyroxene, amphibole and phlogopite appear either as megacryst/phenocrysts or forming fine-grained cumulates (pyroxenite enclaves s.l.) in some eruptive centers of this volcanic field. They have previously been interpreted as cogenetic high-P minerals formed within the upper lithospheric mantle. The presence of Fe-Na-rich green and Mg-Cr-rich colorless clinopyroxene types as phenocryst cores or as oscillatory zoned crystals in pyroxenite enclaves points to a complex evolution of mineral fractionates from petrogenetically related magmas. In trace element chemistry all studied clinopyroxene types show parallel rare earth element patterns irrespective of whether they are megacrysts, colorless or green core phenocrysts, or zoned crystals within pyroxenite cumulates. This similarity indicates a genetic relationship between all the fractionated minerals. This is in agreement with the overlapping of initial $^{143}Nd/^{144}Nd$ and $^{87}Sr/^{86}Sr$ ratios of pyroxenite enclaves (0.512793–0.512885 and 0.703268–0.703778) that is within the chemical field of the host magmas and the Calatrava volcanics. The initial $^{143}Nd/^{144}Nd$ and $^{87}Sr/^{86}Sr$ ratios of megacrystic clinopyroxene, amphibole and phlogopite show a more restricted range (0.512832–0.512890 and 0.703217–0.703466), also falling within the isotopic composition of the Calatrava volcanic rocks. Deep magmatic systems beneath monogenetic volcanic fields involve several stages of melt accumulation, fractionation and contamination at variable depths. Trace element and isotope mineral chemistry are powerful tools to understand the history of ascent and stagnation of alkaline basaltic magmas and discriminate between magma mixing, wall-rock contamination and closed magmatic system evolution. In our study, we establish

a cogenetic origin for green and colorless clinopyroxene as high-pressure precipitates from liquids of different fractionation degrees (up to 80%, for the highly evolved melts equilibrated with the green clinopyroxene), originated from a highly solidified front of silica-undersaturated alkaline magmas at mantle reservoirs.

Keywords: trace element composition, mafic megacrysts, clinopyroxenite enclaves, melilitite and nephelinite melts, monogenetic volcanoes, Calatrava volcanic field, alkaline circum-Mediterranean province

INTRODUCTION

The study of monogenetic volcanic fields provide important information regarding primary magma genesis, deep-seated differentiation processes and the architecture of the sub-volcanic plumbing systems (e.g. Mattsson et al., 2013; Re et al., 2017). These magmas commonly carry a heterogeneous crystal cargo with complex compositional and textural features, relevant to interpreting the depths and rates of magma storage, transport, fractionation and mixing (e.g. Jankovics et al., 2016). Such data are also useful to understand the mechanisms which trigger volcanic eruption and control its characteristics (Mattsson et al., 2013).

Many monogenetic volcanoes are formed by alkaline rocks which transport mafic megacrysts and ultramafic xenoliths (e.g. Irving and Frey, 1984; Praegel, 1981; Jankovics et al., 2016), whereas pyroxenite enclaves are not so common (Downes, 2007). These enclaves have been interpreted as recycled subducted lithosphere (Allègre and Turcotte, 1986), metasomatic products (Garrido and Bodinier, 1999) or high pressure cumulates (e.g. Bodinier et al., 1987; Wilkinson and Stolz, 1997). When formed by deep-seated fractionation, clinopyroxenite enclaves contain volatile-rich minerals, such as amphibole and phlogopite, and are accompanied by equivalent megacrysts (Orejana et al., 2006 and references therein). Green and colorless anhedral to subhedral phenocryst/megacryst cores can also be found in alkaline volcanic rocks and have been studied in order to unravel their enigmatic origin (e.g. Duda and Schmincke, 1985; Ubide et al., 2014; Jankovics et al., 2016). *In situ* trace element data from such a variety of relic clinopyroxene cores are still sparse and completely lacking in most of the Cenozoic volcanic fields of the Iberian Peninsula, where mafic megacrysts and phenocrysts are common within the pyroclastic deposits of these mafic volcanic centers.

Mafic minerals are important petrogenetic indicators of the evolution of basic-ultrabasic magmas (e.g. Green and Ringwood, 1964; Irving and Frey, 1984; Liotard et al., 1988). Their geochemical composition helps to constrain whether they derive from a common parental melt or from diverse melt batches, and if any genetic affinity is possible between the host volcanic magma and any other melt formed in the context of an active magma plumbing system. A study on the major element geochemistry of mafic megacrysts (clinopyroxene, amphibole and phlogopite) and associated pyroxenite enclaves from two volcanoes of the Calatrava volcanic field was recently published by our research team (Villaseca et al., 2019a). The two host magmas are highly porphyritic, showing a complex crystal population of mafic megacrysts (>5 mm), macrocrysts (5–0.5 mm) and phenocrysts with significant geochemical similarities. Moreover, their major element composition resembles that of equivalent phases in clinopyroxenite enclaves, suggesting that all of them constitute a cogenetic suite of igneous origin. These fractionates were interpreted as high-P cumulates from mantle magma reservoirs whose rigid chilled margins (solid crusts) were fragmented by subsequent deep CO_2 boiling of the fractionated host magmas. The variable crystal cargo dragged by the volcanic magmas (crystals and pyroxenite cumulates) added to variable amounts of peridotite xenoliths entrained from the mantle wall-rocks (Villaseca et al., 2019a).

This work adds new trace element compositional data of minerals (megacrysts, phenocrysts and clinopyroxenite enclaves) within the host alkaline magmas of previously sampled Calatrava volcanoes. We have also determined the whole-rock composition of host rocks and selected clinopyroxenite enclaves along with the Sr-Nd isotope composition of host magmas, pyroxenites and megacrysts. The main objective of this study is to constrain the degree of consanguinity between megacrysts, enclaves and their host magmas and check the previously established cumulate origin. With this objective, our work aims to deepen the understanding of the origin of pyroxenitic and related (mica- and amphibole-rich) cumulates, as well as the generation of diverse types of colored (green to colorless) clinopyroxene pheno-to-megacrysts, in silica-undersaturated alkaline magmas. This work also contributes to a better characterisation of the mantle beneath Central Iberia and to the understanding of differentiation processes operating beneath monogenetic volcanic fields.

GEOLOGICAL SETTING

The Cenozoic Calatrava Volcanic Field comprises more than 200 monogenetic volcanic centers in an area of around 5500 km^2 (Ancochea, 1982). Volcanism in the Calatrava Field took place in two different stages (Ancochea, 1982): (1) a minor ultrapotassic event around 8.7–6.4 Ma and (2) alkaline basalts, basanites and olivine nephelinites and melilitites from 3.7 to 0.7 Ma. The two studied volcanic centers have been recently dated by Ar-Ar on mafic megacrysts yielding ages of 2.2 $\pm$ 0.04 Ma (phlogopite from the Cerro Pelado) and 2.8 $\pm$ 0.1 Ma (amphibole from the El Aprisco) (Villaseca et al., 2019b). The Pliocene ages of mafic megacrysts from both volcanoes are in agreement with their derivation from the host magmatic systems and represent ages much younger than mantle metasomatic events dated in peridotite xenoliths from the El Aprisco volcano (Villaseca et al., 2019b).

Two volcanoes were sampled due to the common presence of mafic megacrysts and pyroxenite enclaves in their pyroclastic

deposits: the Cerro Pelado scoria cone (olivine nephelinite) and the El Aprisco maar (olivine melilitite) (**Supplementary Figure S1**). The variety and size of these mafic megacrysts are higher in the Cerro Pelado pyroclastic fall deposits than in other Calatrava centers (Villaseca et al., 2019a). Moreover, mantle xenoliths are also present in both volcanoes and they have been described and interpreted as peridotites that have undergone small-to-moderate degrees of partial melting (≤10%) (Villaseca et al., 2010). These peridotite xenoliths have been overprinted by different metasomatic agents, mostly alkaline silica-undersaturated melts (Villaseca et al., 2010; Lierenfeld and Mattsson, 2015) but also carbonatite fluids (e.g. González-Jiménez et al., 2014; Villaseca et al., 2019b).

The trace element composition and Sr-Nd isotopic data of primary alkaline magmas suggest that most of the Calatrava volcanics are derived from enriched asthenospheric sources, similar to those defined for the European asthenospheric mantle (Cebriá and López Ruiz, 1995; Granet et al., 1995). Clinopyroxene, amphibole and phlogopite megacrysts are found in different Calatrava volcanoes, but the hydrous mafic megacrysts (amphibole, phlogopite) recorded in the pyroclastic fall deposits of the Cerro Pelado scoria cone outstand by their large size (up to 8.5 cm; Villaseca et al., 2019a). Marginal pyroclastic surge layers of olivine melilitites from the El Aprisco maar also show fragments of clinopyroxene and amphibole megacrysts with a heterogeneous size. Ultramafic clinopyroxene-rich enclaves with variable amounts of hydrous minerals (amphibole and phlogopite), and scarce olivine, can be found associated with these megacrysts in both volcanoes. A rare variety of phlogopite-rich clinopyroxenite (glimmerite, mica > 90 vol%) occurs in the El Aprisco maar (e.g. Villaseca et al., 2019a).

SAMPLES AND ANALYTICAL METHODS

Four samples were collected from the host mafic rocks. It is important to note that, due to their pyroclastic nature, the bulk of these samples may include contributions from xenoliths (peridotites of mantle derivation and shallow crustal fragments), crystal cargo and hydrothermal alteration. Accordingly, it has been difficult to obtain geochemical data representative of the erupting melts (see also Lierenfeld and Mattsson, 2015). Only one sample from the Cerro Pelado volcanic center (CAL-73) plotted within the main Calatrava volcanic rock data of Cebriá and López Ruiz (1995), whereas the other three (one from El Aprisco and other two from Cerro Pelado) must be considered crystal-contaminated samples. On the other hand, three clinopyroxenite enclaves were also sampled, and there are five additional samples from the Calatrava volcanoes (eruptive centers in **Table 1**).

Whole-rock samples were fused using a lithium metaborate-tetraborate mixture. The melt produced by this process was completely dissolved with 5% HNO_3. Major oxide analyses were carried out using a Variant Vista 735 ICP while trace elements were diluted and analyzed by a Perkin Elmer Sciex ELAN 6000 mass spectrometer (ICP-MS) following code 4 Lithoresearch at Activation Laboratories (ACTLABS, Canada). Relative uncertainties for major elements are bracketed between 1 and 3%, except for MnO (5–10%). The precision for Rb, Sr, Zr, Y, V, Hf and most of the rare earth elements (REE) range from 1 to 5%, and between 5 and 10% for the rest of trace elements. Some samples have concentrations in Pb below detection limits (5 ppm). The precision was evaluated from repeated analyses of the international standards NIST 694, DNC-1, GBW071113, W-2, SY-4, JR-1 and BIR-1a (**Supplementary Table S1**). More information on the procedure, precision and accuracy of ACTLABS ICP-MS analyses can be found at www.actlabs.com. Whole-rock chemical compositions are shown in **Table 1**.

Sr-Nd isotopic ratios were measured on four volcanic rocks (including samples from the Cerro Pelado and El Aprisco host rocks, together with volcanics from other eruptive centers of the Calatrava Volcanic Field), three clinopyroxenites and four mafic megacrysts (**Table 2**) at the Centro de Asistencia a la Investigación (CAI) of Geochronology and Isotope Geochemistry (Complutense University of Madrid, Spain). Whole-rock and megacryst samples were dissolved in ultra-pure reagents and the isotopes were subsequently isolated by exchange chromatography. Isotope analyses were carried out using a Phoenix-IsotopX Multicollector Thermal Ionization Mass Spectrometer with data acquired in multidynamic mode. The analytical procedures used in this laboratory have been described elsewhere (Reyes et al., 1997). Repeated analyses on the NBS-987 standard gave $^{87}Sr/^{86}Sr = 0.710240 \pm 0.00005$ (2σ, $n = 8$) and for the La Jolla JNdi-1 standard, values of $^{143}Nd/^{144}Nd = 0.512109 \pm 0.000005$ (2σ, $n = 16$) were obtained (**Supplementary Table S1**). The BHVO-2 standard was also used as internal reference for precision. The 2σ analytical errors are 0.01% for $^{87}Sr/^{86}Sr$ and 0.006% for $^{143}Nd/^{144}Nd$.

Trace element analysis of mafic minerals (clinopyroxene, amphibole, phlogopite) was performed on the mineral grains previously analyzed by EMP (Villaseca et al., 2019a). Two clinopyroxene and amphibole megacrysts (from each volcanic center) and one phlogopite megacryst (from the Cerro Pelado scoria cone), along with two phenocryst-rich samples (one from each volcano), were selected for trace element analyses (**Supplementary Tables S2, S3**). Two phlogopite-amphibole pyroxenites, one amphibole pyroxenite and a phlogopite-rich (glimmerite) pyroxenite were also used for trace element studies. Trace element mineral compositions were obtained by laser ablation inductively coupled plasma mass spectrometry (LA-ICP-MS) at the Instituto Andaluz de Ciencias de la Tierra (CSIC, UGR, Granada) using a CETAC-Photon Machines 193 nm laser attached to an Agilent 8800 ICP-MS. The diameter of the laser beam was 40 to 60 μm associated to repetition rates of 10 Hz and laser fluence at the target of ca. 8 J/cm^2. A 30 s gas blank was analyzed first to establish the background, followed by 60 s measurements for the remainder of the analysis. Relative element sensitivities were calibrated with a NIST SRM 611 glass standard. Then, each analysis was normalized to Si or Ca using concentrations determined by electron microprobe. Precision and accuracy were assessed from repeated analyses of the USGS-BIR 1G standard and were estimated to be between 2 and 10% for most of the analyzed trace elements.

TABLE 1 | Whole-rock major (wt%) and trace element (ppm) composition of the Calatrava Volcanic Field (CVF) rocks.

Sample	**115605**	**111643**	**111646**	**CAL-73**	**114406**	**115271**	**116613**	**117459**	**117460**	**46273***	**115591**	**115601**	**116598**
Volcano	**Aprisco**	**C. Pelado**			**Yezosa**	**C. Gordo**	**Tormos**	**Encomienda**		**Bienvenida**	**Aprisco**	**Aprisco**	**C. Pelado**
Rock-type	**Melilitite**	**Nephelinite**			**Nephelinite**	**Nephelinite**	**Nephelinite**	**Melilitite**	**Melilitite**	**Melilitite**	**Clinopiroxenites**		
	Crystal-rich	**Crystal-rich**	**Crystal-rich**									**Phl-rich**	**Phl-rich**
SiO_2	42.30	39.21	46.81	41.07	40.51	41.23	39.36	34.47	35.51	37.37	38.53	40.79	42.52
Al_2O_3	12.31	10.33	5.73	10.61	11.22	12.82	10.60	9.15	9.90	9.31	8.84	13.05	12.40
Fe_2O_3	11.14	12.09	8.70	12.12	12.15	13.13	12.50	11.99	13.37	12.19	18.34	11.18	9.11
MnO	0.10	0.18	0.12	0.18	0.19	0.21	0.18	0.21	0.19	0.19	0.17	0.09	0.10
MgO	14.20	13.85	20.61	11.72	10.22	8.41	12.75	10.06	11.33	13.57	9.73	12.74	13.19
CaO	10.75	11.45	15.51	13.36	15.03	12.36	13.32	17.31	16.13	15.78	13.90	11.63	13.40
Na_2O	2.71	1.42	0.76	2.84	3.24	4.25	1.72	2.45	2.95	2.66	1.40	1.31	0.92
K_2O	1.69	1.05	0.21	0.65	1.63	2.22	0.97	1.74	2.01	1.00	0.69	2.82	2.30
TiO_2	3.44	3.22	1.34	2.85	2.89	3.36	3.05	2.98	3.52	2.98	5.99	4.04	3.84
P_2O_5	0.08	1.40	0.23	1.10	1.46	1.29	1.39	1.64	2.04	1.52	0.37	0.16	0.10
LOI	1.73	4.91	0.35	2.83	1.78	1.14	4.62	8.60	3.59	1.30	2.77	2.79	2.66
Total	100.40	99.12	100.40	99.32	100.30	100.40	100.50	100.60	100.60	97.87	100.70	100.60	100.60
Sc	35	22	44	23	21	21	21	19	20	23	26	33	47
V	302	290	205	250	249	266	269	229	255	266	395	387	314
Cr	120	30	1470	460	360	180	410	470	460	380	30	320	440
Co	55	56	65	56	50	51	57	45	55	52	52	65	57
Ni	160	90	350	250	180	120	290	190	200	250	30	110	180
Ga	20	19	9	18	20	21	17	17	20	18	18	21	15
Rb	12	6	6	57	38	67	23	33	45	22	5	119	72
Sr	388	882	203	2422	1383	1248	1001	1082	1056	1458	389	348	238
Y	12.1	17.7	12.1	29.5	35.8	34.5	32.9	36.7	35	29.4	16.5	10.1	10.5
Zr	174	240	73	252	345	431	311	328	301	292	244	113	103
Nb	24	52.5	10.9	67	104	118	105	113	98.3	96.6	44.1	18	11.1

(Continued)

TABLE 1 | Continued

Sample	115605	111643	111646	CAL-73	114406	115271	116613	117459	117460	46273*	115591	115601	116598
Volcano	Aprisco	C. Pelado			Yezosa	C. Gordo	Tormos	Encomienda		Bienvenida	Aprisco	Aprisco	C. Pelado
Rock-type	Melilitite	Nephelinite			Nephelinite	Nephelinite	Nephelinite	Melilitite	Melilitite	Melilitite	Clinopiroxenites		
	Crystal-rich	Crystal-rich	Crystal-rich									Phl-rich	Phl-rich
Ba	726	870	152	620	736	954	972	855	534	804	235	915	1487
La	8.45	17.2	12.2	75.3	95.7	83.6	97.6	105	95.4	89.1	18	12	9.22
Ce	25.1	49.2	25.8	145	187	165	193	209	200	172	50.3	25.8	22.5
Pr	3.98	7.07	3.5	16.7	21.9	18.9	21.4	25.2	24.6	20.3	7.09	3.51	3.26
Nd	19.9	33.4	15.7	65.6	85.8	74.5	82	92.3	93.6	76.7	31.8	16.4	15.4
Sm	5.16	7.66	3.91	12.4	15.5	13.8	14.6	16.4	17.2	13.6	7.6	4.17	4.03
Eu	1.7	2.56	1.32	3.76	4.79	4.25	4.41	5.03	5.19	4.15	2.52	1.29	1.38
Gd	4.8	6.7	3.66	9.99	12.1	11.3	11.4	13.3	13.5	10.3	6.41	3.61	3.47
Tb	0.65	0.91	0.53	1.3	1.62	1.49	1.49	1.74	1.71	1.39	0.84	0.53	0.51
Dy	3.08	4.69	2.72	6.71	7.82	7.49	7.42	8.48	8.59	6.98	4.23	2.65	2.56
Ho	0.49	0.71	0.47	1.16	1.34	1.27	1.25	1.41	1.46	1.13	0.69	0.4	0.4
Er	1.11	1.61	1.16	2.77	3.24	3.14	3.06	3.59	3.52	2.65	1.48	0.95	0.95
Tm	0.131	0.184	0.14	0.349	0.403	0.39	0.378	0.426	0.42	0.341	0.185	0.121	0.115
Yb	0.71	1	0.76	2.04	2.18	2.31	2.2	2.45	2.33	1.99	1.02	0.7	0.66
Lu	0.098	0.137	0.1	0.294	0.319	0.337	0.31	0.36	0.33	0.309	0.135	0.1	0.097
Hf	5.5	6.6	2.0	5.0	5.9	7.8	5.9	5.5	5.4	5.8	6.5	2.7	3.5
Ta	2.67	4.9	0.75	5.11	6.54	7.26	6.34	7.48	7.18	6.09	4.27	1.59	0.92
Pb	24	<5	<5	<5	<5	6	7	<5	<5	<5	9	<5	<5
Th	0.47	1.33	1.15	9.16	9.75	9.49	13.2	9.75	8.86	9.55	1.29	0.64	0.56
U	0.15	2.66	0.36	2.08	3.04	3.03	2.35	3.57	2.76	3.4	2.46	1.9	2.38
P (GPa)**	3.20	2.90		2.55	2.87	2.60	2.90	4.63	5.70	4.74			
T (°C)**	1402	1305		1309	1335	1294	1328	1410	1499	1460			

**Analysis from Keenan et al. (2019) **Pressure (P) and temperature (T) estimates of magma segregation from a lherzolitic mantle source (Lee et al., 2009).*

TABLE 2 | Isotopic (Sr, Nd) composition of the Calatrava Volcanic Field (CVF) rocks and associated megacrysts.

Sample	Volcano	$(^{87}Sr/^{86}Sr)m$	1 SE	$(^{143}Nd/^{144}Nd)m$	1 SE
CVF rocks					
CAL-73	C. Pelado	0.703891	0.000003	0.512881	0.000002
115271	C. Gordo	0.703271	0.000002	0.512887	0.000001
116613	Tormos	0.703477	0.000003	0.512857	0.000001
117460	Encomienda	0.703460	0.000002	0.512889	0.000002
Clinopyroxenite enclaves					
115591	El Aprisco	0.703778	0.000004	0.512793	0.000001
115601	El Aprisco	0.703268	0.000003	0.512883	0.000001
116598	C. Pelado	0.703555	0.000004	0.512885	0.000001
Megacrysts					
114403 Phlogopite	C. Pelado	0.703466	0.000003	0.512874	0.000012
111653 Amphibole	C. Pelado	0.703217	0.000003	0.512855	0.000002
111639 Clinopyroxene	C. Pelado	0.703243	0.000002	0.512890	0.000002
114404 Amphibole	El Aprisco	0.703480	0.000002	0.512832	0.000002

PETROGRAPHY

Below we summarize the textural features of the studied mafic crystals and clinopyroxe-rich enclaves that appear as crystal cargo in alkaline basaltic rocks of the Calatrava Volcanic Field. A detailed petrographic description of the studied samples can be found in Villaseca et al. (2019a).

Clinopyroxene, amphibole and phlogopite megacrysts are single pyroclasts (lapillus) or small fragments in the Cerro Pelado and El Aprisco pyroclastic rocks. Clinopyroxene megacrysts are colorless and mostly unzoned, except for a thin reaction rim with the host magma. In contrast, the Cerro Pelado volcanic rocks show two types of relic clinopyroxene phenocryst cores: (1) anhedral green and (2) anhedral to euhedral colorless. In the El Aprisco maar only the second type of relic clinopyroxene core (colorless) was observed. Both phenocryst cores develop pale purple rims petrographically similar to melilitite/nephelinite groundmass clinopyroxene (**Figures 1A,C**). Amphibole makes up the largest megacrysts (up to 8.5 cm in the Cerro Pelado volcano), and phlogopite is usually unzoned and no larger than 4.5 cm. Most megacrysts display reaction rims or corrosion gulfs.

The studied pyroclastic rocks also include small black and elongated enclaves that can be classified as amphibole clinopyroxenite, amphibole-phlogopite clinopyroxenite, phlogopite clinopyroxenite and glimmerite (>90% phlogopite) (Villaseca et al., 2019a). Their size ranges from 1 to 7 cm. They show mostly medium- to fined-grained equigranular texture (**Figure 1B**). Pyroxenites lack typical metamorphic textures, which is indicative of a recent magmatic origin before volcanic entrainment. Clinopyroxene can be colorless or pale green and appear mutually intergrowing as complex oscillatory zoned crystals (**Figure 1D**), mantled by an external discordant thin purple rim, suggesting a genetic link with the two types of phenocryst cores described in the nephelinite from the Cerro Pelado cone. Amphibole shows slight zoning in the form of irregular patches. Occasionally, phlogopite may show kinked textures in the glimmeritic enclaves, likely associated to flowage and collisions with the conduit walls during ascent (Peterson and LeCheminant, 1993). The studied volcanic rocks also include a varied xenocryst population from the fragmentation of mantle xenoliths (e.g. Fo-rich olivine, orthopyroxene and Al-Mg-rich spinel).

WHOLE-ROCK GEOCHEMISTRY OF VOLCANIC HOST ROCKS AND PYROXENITE ENCLAVES

Although studied volcanic rocks have been classified as melilitites (El Aprisco) or nephelinites (Cerro Pelado) by petrographic means (Ancochea, 1982), their variable silica and alkali contents causes them to plot in the foidite, basanite and basalt fields when using the TAS diagram (**Figure 2A**). The complexity of sampling pyroclastic rocks representative of the transporting melt is evident, as they appear as mingled rocks comprising a mixture of crystal cargo (phenocrysts, fragmented antecrysts, xenoliths), juvenile material and accidental crustal lithics (see also Lierenfeld and Mattsson, 2015). Previous attempts to record the original composition of host magma that transported such a great quantity of solid cargo failed to reproduce the melilitic or nephelinitic original character of the volcanic host (Lierenfeld and Mattsson, 2015). In this work, only sample CAL-73 from the Cerro Pelado nephelinite volcano (sample provided by J.M. Cebriá) yields a consistent composition when compared to other nephelinites from the Calatrava Field (**Figure 2**; **Table 1**). Most crystal-rich samples from these volcanoes have low alkali contents and plot outside the typical compositional field of Calatrava volcanic rocks (**Figure 2A**). On the basis of the silica-undersaturated diagram of Le Bas (1989), studied rocks of the two volcanoes (including pyroxenites) plot in the nephelinite field (**Figure 2B**). The higher MgO contents (>13.8 wt%, **Table 1**) of phenocryst-rich rocks of these two volcanic centers, with respect to other Calatrava volcanic rocks (mostly in the range of 8.4 to 12.8 wt%) are likely related to the relative abundance of mafic crystal cargo (clinopyroxene, olivine, amphibole and phlogopite). When using binary major

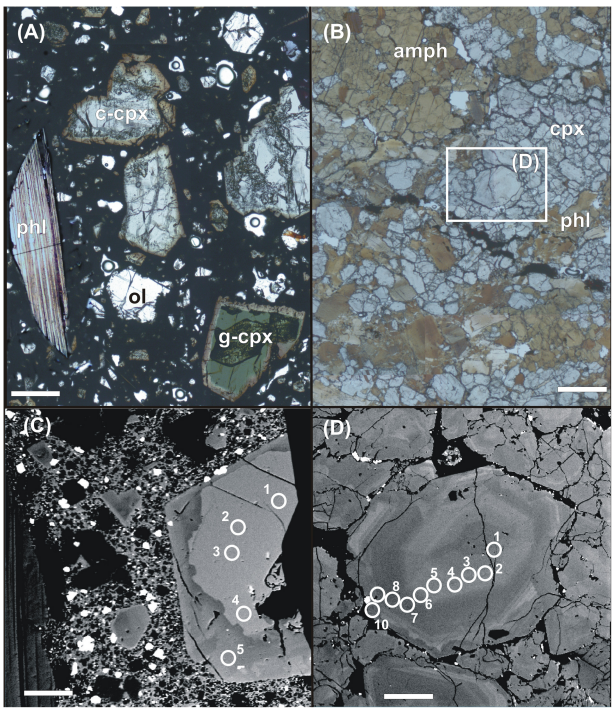

FIGURE 1 | Petrographic characteristics of El Aprisco and Cerro Pelado volcanic rocks (Calatrava Volcanic Field, central Spain). **(A)** Photomicrograph of an olivine nephelinite from the Cerro Pelado volcano (sample 116596) showing clinopyroxene phenocrysts with relic cores (c-cpx: colorless core, g-cpx: green core) close to phlogopite(phl) and olivine (ol) phenocrysts. **(B)** Photomicrograph of an amphibole- and phlogopite-rich clinopyroxenite enclave from the El Aprisco volcano (sample 115601). The white bar at the bottom of photomicrographs represents 500 mm. **(C)** Back-scattered electron (BSE) image of green core (light) clinopyroxene phenocryst with a brownish rim (dark). **(D)** BSE image of zoned clinopyroxene crystal from clinopyroxenite enclave 115601 of picture B (see marked grain). Circles in BSE images represent laser ablation spots of 116596 CPXV2 and 115601 CPX1 grains, respectively, from **Supplementary Table S2**. The white bar at the bottom of each BSE picture **(C,D)** represents 100 mm.

element diagrams, most of the Calatrava volcanic rocks define a broad trend that might be induced by operation of minor fractional crystallization processes (Cebriá, 1992; **Figure 2**). In these diagrams, pyroxenites usually plot defining contrasted evolution lines or they are clearly outside of the main Calatrava compositional field (**Figures 2C,D**, respectively). Pyroxenite composition seems to be mainly controlled by mafic phases, especially by clinopyroxene or amphibole chemistry.

Major and trace element variation diagrams for pyroxenites and host-rocks display a marked data scatter, but in some diagrams, a clear distinction is drawn between pyroxenites and host magma compositional fields (**Figures 2**, **3**). Pyroxenites have markedly low contents of Na, P, Nb, Ta, Th, U, Zr, Hf, LILE (except for K, Rb and Ba in phogopite-bearing types: 115601, 116598), Cr, Ni, and REE-Y (**Figure 3**). On the contrary, phlogopite-bearing pyroxenites are markedly rich in Al, K, Ti, Rb, Ba and Sc-V. Phlogopite-rich pyroxenites also display higher SiO_2, Al_2O_3 contents than the variety without mica (**Table 1** and **Figure 2C**). Most of the chemical features of pyroxenites seem to be controlled by the combination of their mafic phases and Fe-Ti-rich minerals (Ti-magnetite, ilmenite, titanite). Pyroxenites in most trace element diagrams plot outside the compositional field of Calatrava volcanic rocks (**Figure 3**).

In chondrite normalized REE patterns all the pyroxenites show a similar pattern, with a mostly flat LREE pattern and a steeper shape from Eu to Lu (**Figure 4**). On the contrary, melilitites/nephelinites of the Calatrava Field (including sample CAL-73 from El Aprisco) exhibit a significant homogeneity in composition, displaying a strongly fractionated REE pattern (**Figure 4**). The analyzed pyroxenites show marked negative anomalies in Th, Nb (Ta) and P (and positive in Ti), contrasting with the patterns of the Calatrava volcanic rocks. Phlogopite-bearing pyroxenites show slightly positive Rb, Ba and K anomalies (**Figure 4**). The CAL-73 sample and other Calatrava rocks show a similar pattern when compared to the Late-rift volcanic rocks of the Neogene Bohemian Massif, with characteristic negative anomalies in K and Zr and positive anomalies in P (Ulrych et al., 2011).

The Sr and Nd isotopic composition of pyroxenites and the Calatrava volcanic rocks fall in the same range of 0.703270–0.703890 and 0.512790–0.512890, plotting close to the HIMU and FOZO components, and overlapping the EAR, common asthenospheric mantle reservoir of the circum-Mediterranean area (**Figure 5** and **Table 2**). This good fitting in isotopic composition suggests that the pyroxenite cumulates likely crystallized directly from magmas cogenetic with the host volcanic melts.

TRACE ELEMENT AND Sr-Nd ISOTOPE GEOCHEMISTRY OF MEGACRYSTS-PHENOCRYSTS

Clinopyroxene

Clinopyroxene megacrysts show Mg# values [(MgO/(MgO+FeOt) on a molecular basis] that are indicative of a primitive composition, with only a minor variation between volcanoes (0.81–0.83 in El Aprisco and 0.83–0.84 in Cerro Pelado) (Villaseca et al., 2019a). Two types of phenocryst cores appear in the Cerro Pelado volcanics: colorless and green clinopyroxenes. They show a contrasted composition, with the green cores exhibiting lower Mg#, TiO_2 and Al_2O_3, and higher FeO and Na_2O contents than the colorless clinopyroxene (Villaseca et al., 2019a).

The trace element composition of clinopyroxene megacrysts, plotted on chondrite- and primitive mantle-normalized diagrams, displays a relatively uniform pattern in both volcanic centers, although slightly higher contents can be found in megacrysts from the El Aprisco melilitite (**Figure 6**). They all present characteristic convex-upward LREE patterns, with strong depletion in the HREEs and negative anomalies in Rb-Ba, K, Pb and P (**Figures 6A,B**). The colorless cores of clinopyroxene phenocrysts exhibit an overlapping composition with respect to megacrysts (**Supplementary Table S2** and **Figure 6C**). This feature suggests a genetic connection between

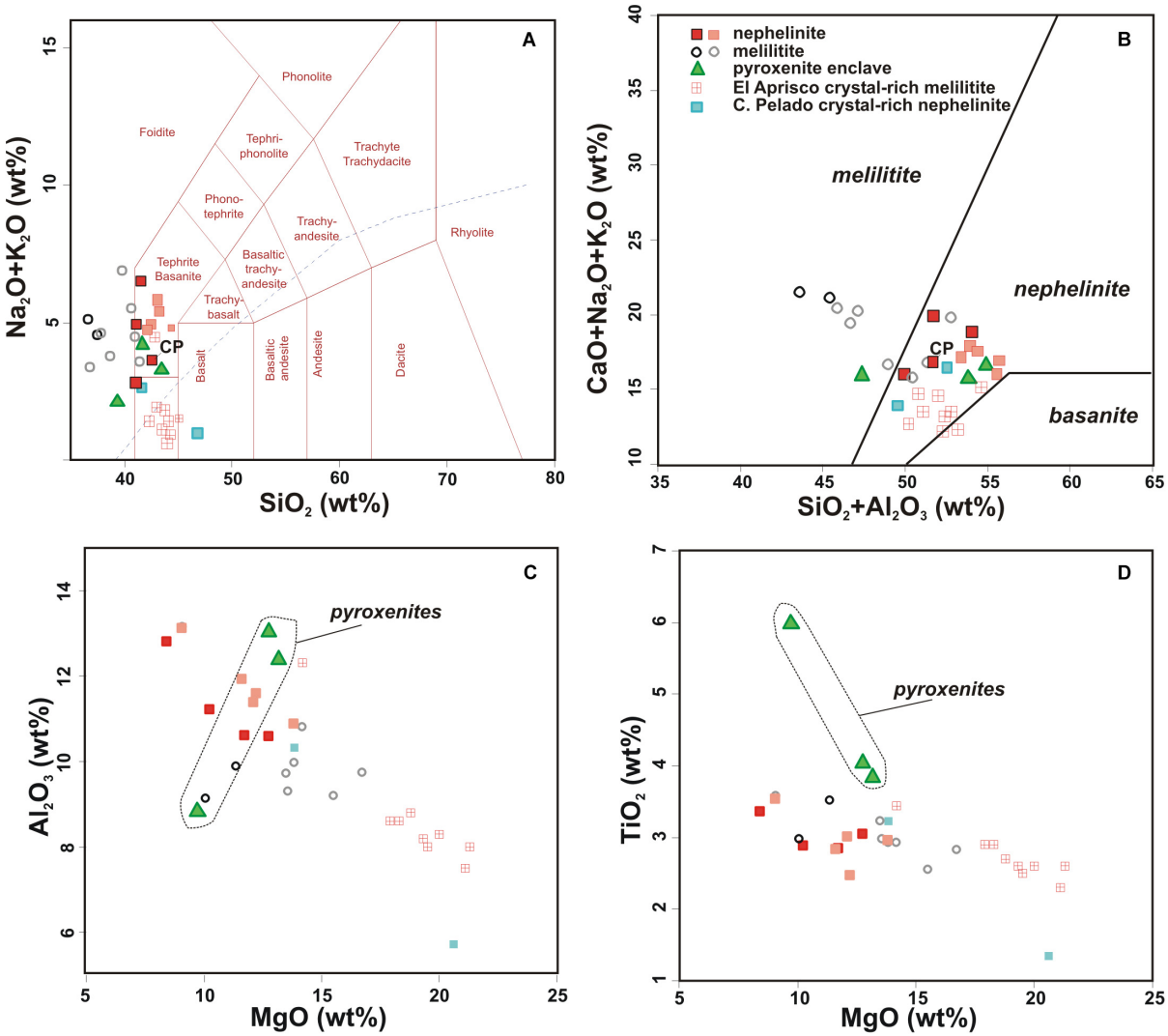

FIGURE 2 | Calatrava volcanic rocks in the TAS diagram (Le Maitre, 2002) **(A)** and in the nephelinite-melilitite-basanite classification of Le Bas (1989) **(B)**, showing a clear predominance of nephelinitic magma compositions in the studied volcanic rocks. Melilitite and nephelinite samples in gray color are from the literature (Cebriá and López Ruiz, 1995; Keenan et al., 2019). Al_2O_3 **(C)** and TiO_2 **(D)** vs MgO diagrams for Calatrava rocks and pyroxenite enclaves. CP in plots **(A,B)** is the nephelinite sample CAL-73 from the Cerro Pelado centre.

both types of crystals. The trace element chemistry of these Calatrava clinopyroxene megacrysts-phenocrysts is very similar to that described in types II and III of megacrysts from the Eifel (Shaw and Eyzaguirre, 2000) but is clearly different to the xenocrystic cores of phenocrysts in alkaline basalts from the Carpathian-Pannonian region (Jankovics et al., 2016).

The green core phenocrysts show REE patterns parallel to those from colorless megacrysts and phenocrysts (**Figure 6C**), reinforcing the cogenetic character of all studied clinopyroxene types. Nevertheless, the green cores have higher REE, Zr-Hf and Nb-Ta and lower Ti-Cr-Ni contents than colorless clinopyroxenes (**Figures 6C,D**, **7**). The chemistry of purple rims around green and colorless phenocryst cores, showing intermediate values in Mg# and Ni (Cr) (**Figure 7**), suggests that the host magma that transported the crystal cargo might have an intermediate chemical composition between those deep magmas that originated both phenocryst core types. Nevertheless, the wide REE and other incompatible trace element contents shown by purple clinopyroxene rims (**Figures 6G,H**) suggests a complex melt evolution of the host magma during volcanic emplacement.

Amphibole

The amphibole megacrysts found in the Cerro Pelado and El Aprisco volcanoes constitute a homogeneous group displaying a moderate chemical variation (Villaseca et al., 2019a). Amphibole Mg# may reach high values (up to 0.83), which is indicative of a fairly primitive composition and is positively correlated with Al_2O_3 and K_2O (Villaseca et al., 2019a). Patchy zoning and smaller amphibole crystals can be observed occasionally within

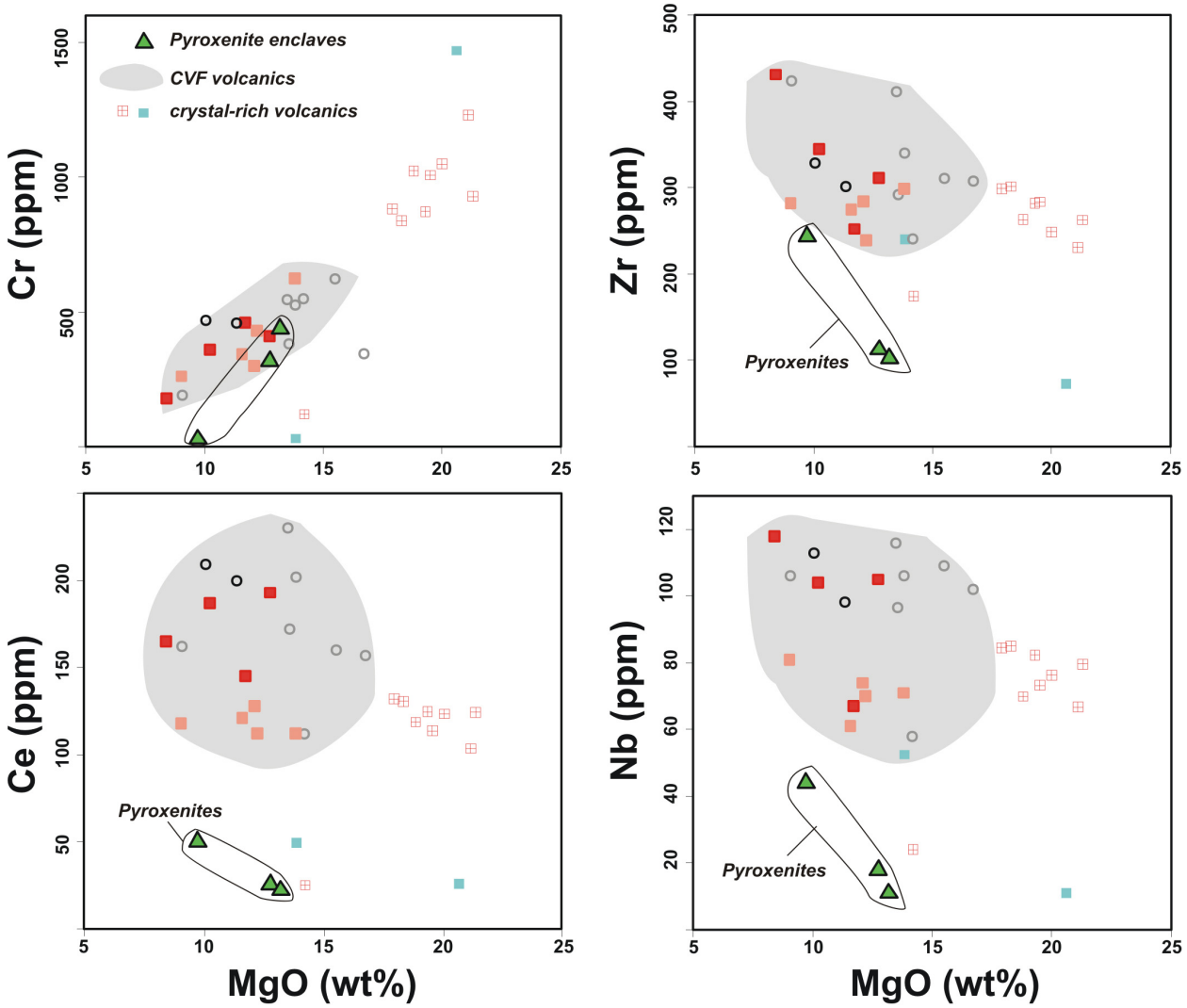

FIGURE 3 | Trace element variation diagrams for the Calatrava Volcanic Field (CVF) rocks and associated pyroxenite enclaves. Same symbols as in **Figure 2**. The Calatrava compositional field does not overlap with most of the crystal- and xenolith-rich (contaminated) magmatic rocks from the El Aprisco and the Cerro Pelado volcanic centers.

megacrysts. Amphibole phenocrysts have never been found in the studied pyroclastic rocks of these two volcanoes.

The amphibole megacrysts exhibit a REE pattern similar to that of clinopyroxene megacrysts, characterized by a convex-upward shape for the LREE and depleted HREE (**Figure 8A**). Nevertheless, amphibole primitive mantle-normalized patterns are very different to those of clinopyroxene due to its higher LILE (K, Rb, Ba > Sr), Nb-Ta and Pb contents (**Figure 8B**). The trace element chemistry of the Calatrava amphibole megacrysts (**Supplementary Table S3**) is very similar to that described in megacrysts from the Eifel (Shaw and Eyzaguirre, 2000) or from the Bohemian Massif (Mayer et al., 2014; Ulrych et al., 2018), as was the case of clinopyroxenes. Moreover, the $D^{amp/cpx}$ (REE,Th,U, Zr and Hf) estimated for both mineral megacrysts are in the range of 0.6–2, which is very similar to the values obtained from natural rocks and experimental data (Chazot et al., 1996; Grégoire et al., 2000; Raffone et al., 2009; Ubide et al., 2014), indicating the approach of chemical equilibrium between them.

Phlogopite

The major element composition of phlogopite megacrysts, phenocrysts and microinclusions in other mafic megacrysts of the Cerro Pelado volcano defines a narrow chemical variation (Figure 9 of Villaseca et al., 2019a). These phlogopites exhibit a fairly primitive composition, with Mg# ranging mostly from 0.85 to 0.78 and high Al_2O_3 (15.6–17.4 wt%), TiO_2 (4.4–6.5 wt%) and K_2O (7.5–10 wt%) concentrations. Cr_2O_3 contents are lower than 0.2 wt% in all cases. The close resemblance in major element composition between microinclusions and larger crystals (megacrysts and macrocrysts) was interpreted as their derivation from a common magma batch (Villaseca et al., 2019a).

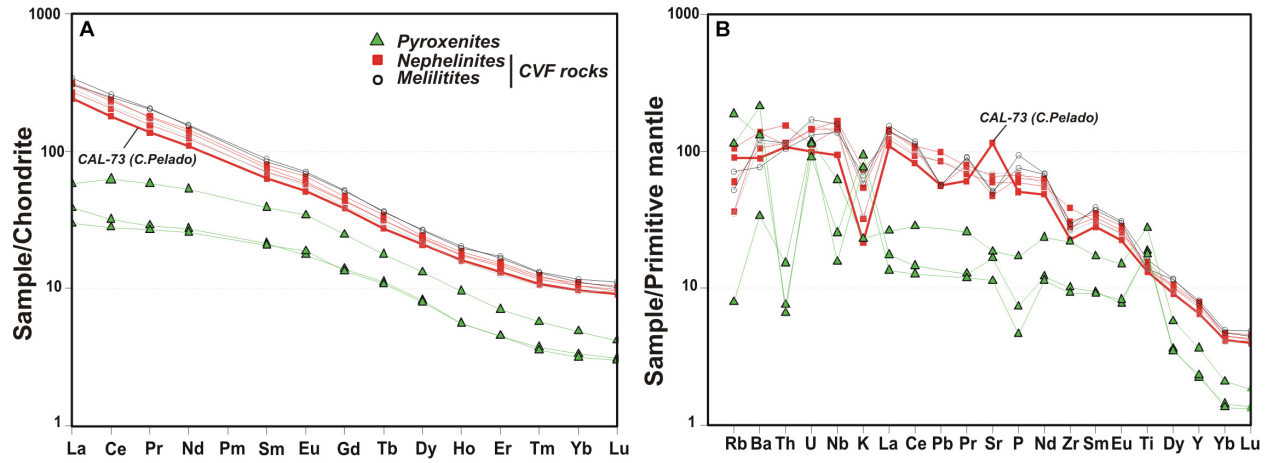

FIGURE 4 | Rare earth elements (REE) **(A)** and trace element **(B)** abundances of rocks and clinopyroxenite enclaves from the Calatrava Volcanic Field (CVF) normalized to chondrite (Boynton, 1985) and primitive mantle (Sun and McDonough, 1989), respectively.

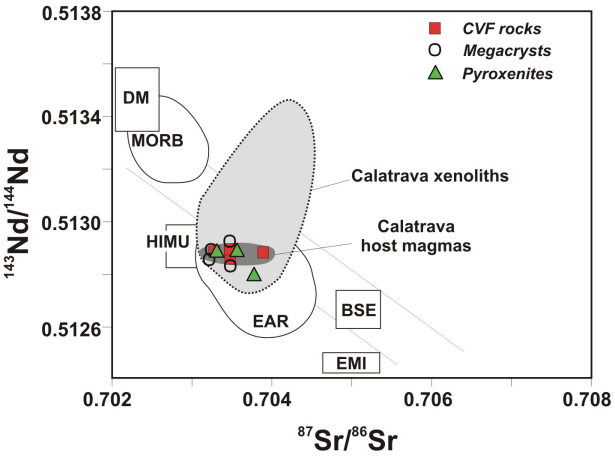

FIGURE 5 | $^{143}Nd/^{144}Nd$ vs $^{87}Sr/^{86}Sr$ ratios of volcanic rocks, megacrysts and associated pyroxenite enclaves from the Cerro Pelado and El Aprisco volcanoes (Calatrava Volcanic Field, CVF). Mantle-end members (DM, MORB, HIMU, BSE and EMI) are from Zindler and Hart (1986). EAR (European Asthenospheric Reservoir) after Downes et al. (2003). Calatrava peridotite xenoliths from Villaseca et al. (2010) and authors' unpublished data.

The phlogopite megacryst has very low (subchondritic) REE-Y contents (**Figure 8C**). Its LILE (K, Rb, Ba) and Cr-Ni-(Ti) contents are higher than those of amphibole, as can be seen in multitrace primitive mantle-normalized diagrams (**Figure 8D**). To our knowledge, there are no published trace element contents of phlogopite megacrysts from any Cenozoic volcano of the European Western circum-Mediterranean area, although this hydrous mafic mineral is an occasional megacryst in some of these volcanic centers (Hegner et al., 1995; Shaw and Eyzaguirre, 2000; Mayer et al., 2014). Only phlogopite megacryst of Cenozoic melilitites from the Ahaggar Swell (Algeria) has similar trace element patterns with slightly higher contents than the studied crystals (Kaczmarek et al., 2016). It is interesting to note that $D^{Phl/Amp}$ for Nb-Ta (0.5–0.6), Zr-Hf (0.06–0.12), Rb (16–20), Ba (8–9) and Sr (0.3–0.4) are broadly similar to those reported in other studies (Grégoire et al., 2000; Kaczmarek et al., 2016).

Regarding the isotopic composition, the four analyzed megacrysts (two amphiboles from both volcanic centers and the phlogopite and clinopyroxene from the Cerro Pelado volcano) (**Table 2**) yield similar $^{87}Sr/^{86}Sr$ (0.703217–0.703480) and $^{143}Nd/^{144}Nd$ ratios (0.512832–0.512890) and plot within the wider isotopic field of the Calatrava volcanic rocks (**Figure 5**). These isotopic signatures suggest that the studied mafic megacrysts crystallized from melilititic-nephelinitic melts are similar in composition to their host magmas.

TRACE ELEMENT GEOCHEMISTRY OF PYROXENITE MINERALS

The composition of clinopyroxene from the pyroxenite enclaves overlaps the field of megacrysts, although defining a wider range for the REE contents, plotting toward either more enriched but also less differentiated compositions (**Figures 6E–F**). The two clinopyroxenites included in pyroclasts from the El Aprisco maar, which show colorless-greenish zoned crystals, have the lowest (sample 115591) and highest (sample 115601) REE contents of all the studied high-P clinopyroxenes (**Figure 6E**).

Zoning profiles in these clinopyroxenes were previously characterized by the alternation of Si–Mg- and Fe–Al–Ti-Na-rich bands (Villaseca et al., 2019a). With respect to trace element contents, the green bands (**Figure 1D**) have slightly higher P, REE, Y, Th, U, Nb and Ta contents than the colorless ones (**Figure 9**). This chemical contrast is smaller than that shown by green and colorless phenocryst cores, at least for some elements (e.g. Zr, Sc, Cr and Ni) (**Figures 6**, **7**). In any case, the similarity in composition of the colorless phenocryst cores, megacrysts and most clinopyroxenes from the pyroxenite enclaves is remarkable. Similarly, some greenish clinopyroxene

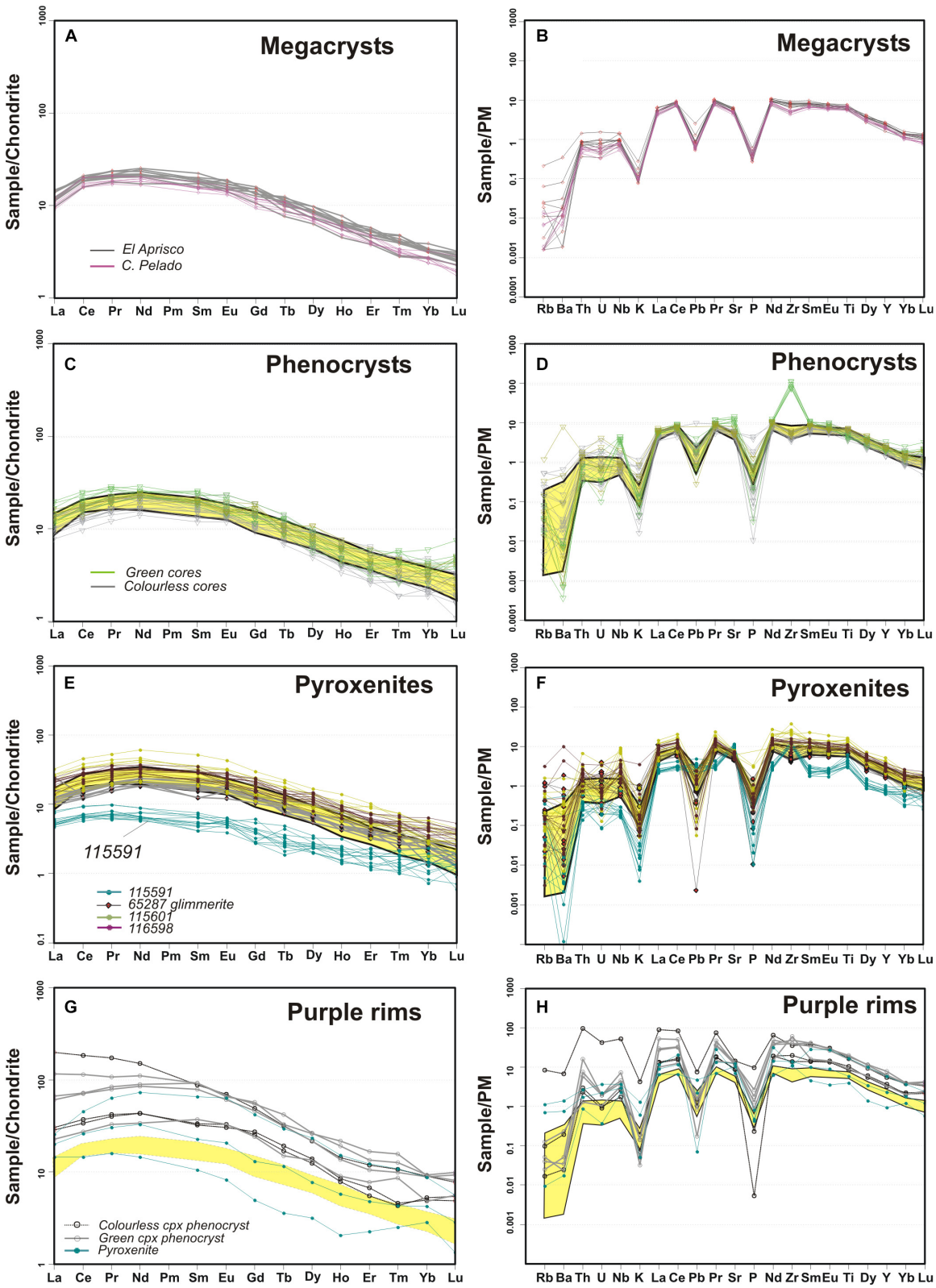

FIGURE 6 | REE and trace element composition of clinopyroxene: **(A)** and **(B)** megacrysts, **(C)** and **(D)** green and colorless phenocryst cores, **(E)** and **(F)** clinopyroxenite enclaves and **(G)** and **(H)** purple rims on colorless and green phenocryst cores and on clinopyroxene grains from pyroxenite enclaves. Chondrite-normalizing values are from Boynton (1985), whereas primitive mantle (PM) normalizing values are from Sun and McDonough (1989). The compositional field of clinopyroxene megacrysts (yellow field) is plotted in diagrams **(C–H)**.

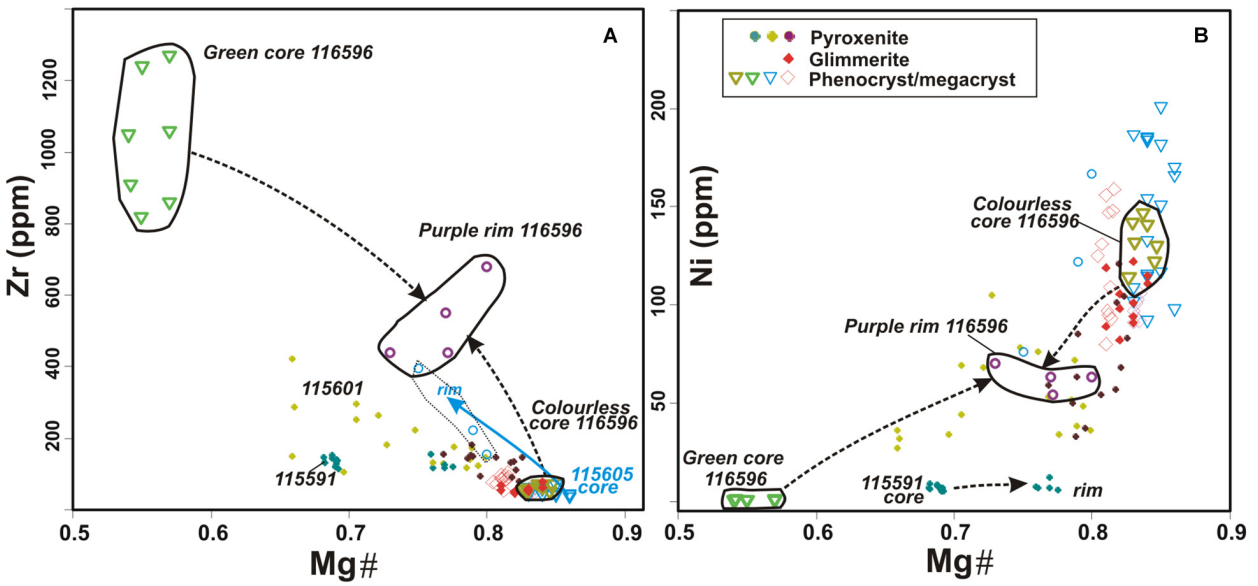

FIGURE 7 | Variation diagrams (Zr and Ni vs. Mg#) (Mg# = molecular MgO/(MgO+FeOt)) of the studied clinopyroxene populations. The arrows represent the zoning evolution from green and colorless cores toward purple rims of phenocrysts of the Cerro Pelado nephelinite 116596. A narrower core-to-rim chemical zoning of colorless phenocryst from the El Aprisco melilitite 115605 is also shown with a blue arrow **(A)**. Low-Mg greenish clinopyroxenes from El Aprisco 115591 [with core-to-rim zoning in panel **(B)** plot] and 115601 pyroxenites are also marked.

from pyroxenite cumulates shows positive Zr (Hf) and Nb (Ta) anomalies in multi-trace element patterns (**Figure 6F**), although less marked than green phenocryst cores of sample 116596.

Amphiboles from the pyroxenite enclaves yield a more heterogeneous composition than megacrysts, although certain overlapping between both fields exists (**Figure 8**). Amphiboles from pyroxenite 115591 (El Aprisco) display the lowest Mg# values (up to 0.59), and something similar can be observed for REE, Y, Th, P and Ti (**Figures 8A,B**). On the contrary, amphiboles from this sample exhibit higher Pb and Zr (Hf) contents, similar to the accompanying greenish clinopyroxene, and consequently yield positive Pb and Zr (Hf) peaks in the multi-trace element pattern (**Figure 8B**).

The trace element composition of phlogopite is highly variable (**Supplementary Table S3**) reaching extreme values in the clinopyroxenite and glimmerite enclaves, whereas phlogopite megacrysts and phenocrysts show an intermediate composition within that broader range but display similar normalized trace element patterns (**Figures 8C,D**). The mica from the glimmerite enclave has Mg# values similar to megacrysts and phenocrysts (averaging 0.83) and the highest REE contents, in contrast to phlogopite from pyroxenite enclave 115601, which shows the lowest REE and Th-U contents and the lowest Mg# (averaging 0.71) of all the studied micas (**Figures 8C,D**).

DISCUSSION

Origin of Megacrysts and Phenocrysts

It is not unusual that large mafic minerals (clinopyroxene, amphibole, phlogopite) were found within alkaline mafic to ultramafic rocks. The origin of these megacrysts is controversial and could be either xenocrystic (i.e. mantle-derived) or phenocrystic/antecrystic (i.e. melt-derived). In the former case, megacrysts could be considered fragments of mantle wall-rocks, whereas melt-derived megacrysts could be either (i) pieces of mantellic cumulates unrelated to the host melt or (ii) minerals crystallized at high pressure conditions from their host volcanic magma or a cogenetic melt fraction (e.g. Shaw and Eyzaguirre, 2000; Gernon et al., 2016). The textural features and major element chemistry of the studied mafic megacryst-phenocrysts strongly support that the most primitive minerals were close to equilibrium and crystallized from primitive melts with a composition similar to that of the El Aprisco and Cerro Pelado volcanic rocks (Villaseca et al., 2019a). Nevertheless, the existence of different types of phenocryst cores with a variable composition, and the presence of reaction textures and mineral zoning indicates a more complex scenario.

A xenocrystic origin of the megacrysts is not favored on the basis of several petrological and geochemical features. The crystal size (a few millimeters) and the interstitial character of the metasomatic hydrous phases in peridotites (amphibole and phlogopite) do not support the possibility of the large mafic crystals being fragments from these mantle rocks. The major element mineral composition is also different in the peridotites and the megacrysts and phenocryst cores: mainly, the lower Mg# and Cr and higher Ti values shown by the latter minerals (Villaseca et al., 2019a). Mineral trace element data reinforces this conclusion, since a clear disagreement exists between the geochemistry of the lherzolite minerals and that of megacrysts. These discrepancies are apparent for most elements in the El Aprisco volcano (clinopyroxene and amphibole composition;

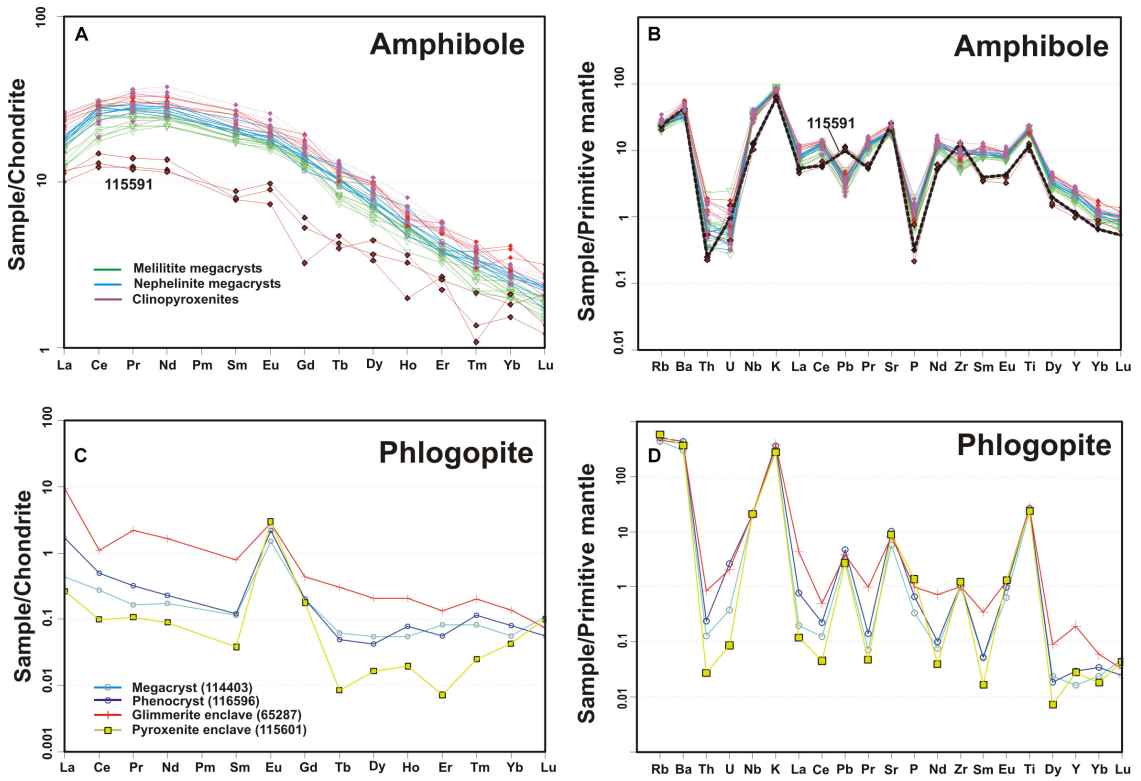

FIGURE 8 | REE and multi-element patterns of amphibole **(A,B)** and phlogopite **(C,D)**. Amphibole megacrysts are from El Aprisco melilitite (115603, 114404) and from the Cerro Pelado nephelinite (111653); amphibole from clinopyroxenite enclaves comes from samples 115601 and 116598. Amphibole from pyroxenite 115591 has low REE contents **(A)**, and its average is highlighted in panel **(B)**, showing marked Pb and Zr positive anomalies. Phlogopite patterns in panel **(C,D)** are averaged values. Mineral chemical data from **Supplementary Table S3**. Chondrite and primitive mantle normalizing values are from Boynton (1985) and Sun and McDonough (1989), respectively.

Figures 10C,D, **11E,F**) and also for REE, Th, U, Nb and Ti of lherzolite clinopyroxene from the Cerro Pelado scoria cone (**Figures 10A,B**). Nevertheless, some similarities can be found for both major and trace elements only when comparing with the heterogeneous composition of clinopyroxene from wehrlite xenoliths from the Cerro Pelado volcano. However, this similitude is likely associated with the metasomatic origin of these wehrlites, since its metasomatic signature is genetically related to reaction with the host nephelinitic magma (Villaseca et al., 2010). Accordingly, the metasomatic amphibole and phlogopite of the Cerro Pelado wehrlite xenoliths display similar trace element patterns to those shown by the associated megacrysts, which are high-pressure fractionates derived from similar melts (**Figures 11A–D**). Nevertheless, this geochemical resemblance does not necessarily imply that megacrysts represent wehrlite fragments, which is not supported by petrographic features. Moreover, green clinopyroxene phenocryst cores have chemical features clearly different to wehrlitic clinopyroxene, including their notorious Zr positive peak in multitrace element patterns (**Figure 6**), also indicating a non-xenocrystic (mantle fragmentation) origin for these deep-seated crystals.

It has been long recognized that convex-upward REE patterns, such as those depicted by the Calatrava clinopyroxene and amphibole megacrysts, are typical of minerals crystallized from alkaline mafic magmas at high-pressure (Irving and Frey, 1984). Colorless clinopyroxene phenocryst cores display a chemical composition overlapping that of the equivalent megacrysts. This feature, which has also been observed for the major elements (Villaseca et al., 2019a), is apparent for the trace elements (**Figures 6C,D**) and implies that they all must share a common origin as deep mineral fractionates. Studied clinopyroxene and amphibole megacrysts are in chemical equilibrium, as their intermineral partition coefficients (see comments above) are close to those previously published for basic-ultrabasic lithotypes (Vannucci et al., 1995; Raffone et al., 2009). This suggests that they are cogenetic phases derived from the same magma. This is confirmed by the similar composition of the liquids in equilibrium with studied clinopyroxene and amphibole calculated using mineral/melt distribution coefficients of high-*T* and high-*P* basaltic systems (Hart and Dunn, 1993; La Tourrette et al., 1995; Ionov et al., 1997; **Figure 12**). The results compare well with the whole-rock data of the Calatrava host magmas, with REE patterns of similar slope and equivalent positive and negative trace element anomalies (**Figure 12**). Nevertheless, the higher chemical heterogeneity shown by the calculated melts with megacryst/phenocryst clinopyroxene, mainly for the LIL

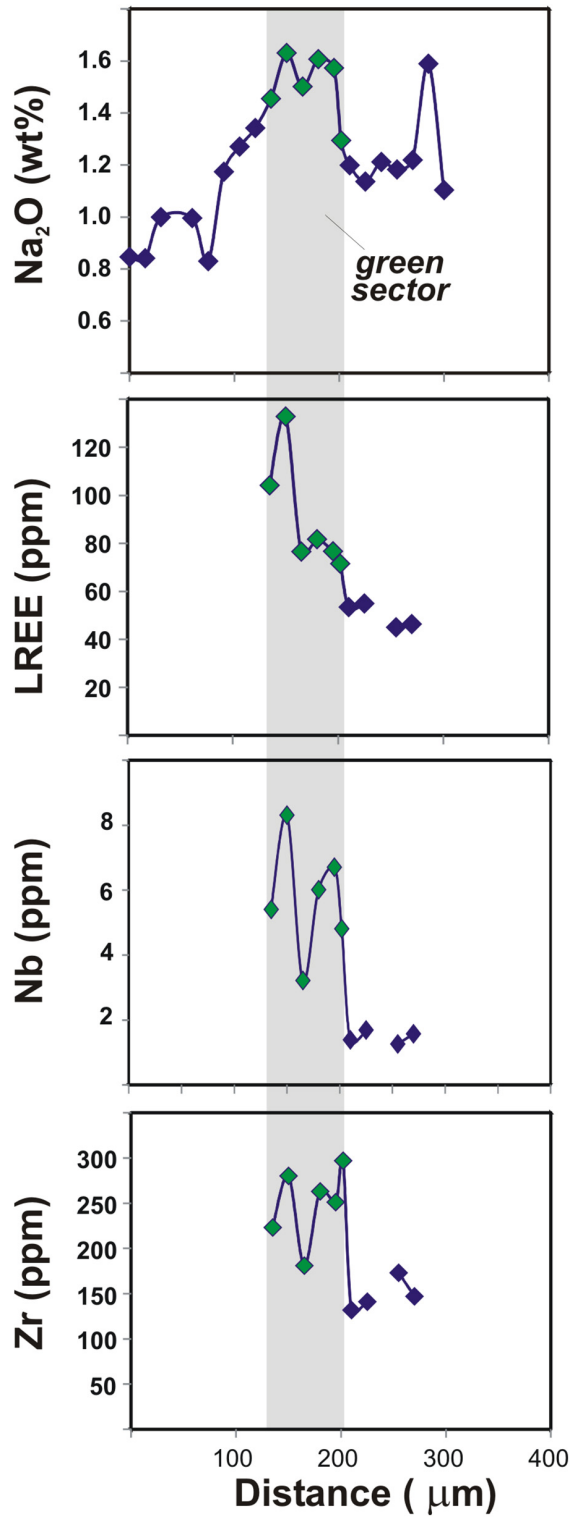

FIGURE 9 | Chemical profiles showing compositional variations in a greenish-to-colorless zoned clinopyroxene crystal of pyroxenite 115601. The Na_2O vs. distance plot is taken from Villaseca et al. (2019a). Green clinopyroxene area is marked, and laser spots are depicted in **Figure 1D** of this work. Note the high Na_2O, REE and HFSE contents in the green bands relative to the surrounding (colorless) clinopyroxene.

elements (Rb, Ba, Th, U), is likely associated with the variable composition of these mafic minerals and the evolution of magma at deep stagnation levels. Even so, the broad similarity between the calculated melts and the Calatrava volcanics indicates that mafic megacrysts derive from high-pressure fractional crystallization of melts with a composition similar to that of the host alkaline magmas.

On the other hand, the Fe-rich green clinopyroxene phenocryst cores are slightly trace element-enriched (remarkably for Zr), and some purple clinopyroxene rims are clearly different from other clinopyroxenes due to their elevated trace element concentrations (**Figures 6G,H**). The calculated geochemical heterogeneity of equilibrated melts with these clinopyroxene types (**Figures 12A–D**) supports the involvement of magmas with a variable degree of evolution for their origin, within a complex scenario of crystallization at different levels in the upper lithosphere (see discussion below).

Origin of Pyroxenite and Glimmerite Enclaves

The Calatrava clinopyroxenite and glimmerite enclaves do not have characteristics of xenolithic mantle rocks. While minerals in peridotites and metasomatic veins are usually unzoned and very homogeneous in major element composition (Villaseca et al., 2010; Lustrino et al., 2016), clinopyroxene and amphibole of the studied pyroxenites display oscillatory or patchy zoning, (respectively), commonly interpreted as igneous textures. The absence of exsolution lamellae in clinopyroxene from these enclaves also contradicts their origin as wall-rock mantle fragments entrapped by the ascending basic magma (Villaseca et al., 2019a).

The mineral geochemistry also favors the magmatic origin of the Calatrava pyroxenite and glimmerite enclaves, due to their low Mg# values when compared to those of the mantle minerals (<0.85; Villaseca et al., 2019a). The trace element composition of the main mafic minerals of these enclaves (colorless clinopyroxene, amphibole and phlogopite) is coincident with that of the megacrysts and colorless phenocryst cores dispersed within the host volcanic magma (**Figures 6**, **8**), which implies that they crystallized from similar cogenetic basic melts. Nevertheless, liquids in equilibrium with greenish clinopyroxene from these enclaves show REE patterns parallel to those from the Calatrava volcanics but showing different REE contents (**Figure 12C**) or having spikier trace element patterns with a marked Zr positive anomaly that is absent in Calatrava volcanic rocks (**Figure 12D**), as was the case with the data from green clinopyroxene phenocryst cores.

Relationships Between Magmatism and Metasomatism Within Peridotite Wall-Rocks

As shown above, we have observed similarities among the trace element compositions of clinopyroxene, amphibole and phlogopite megacrysts in the Cerro Pelado center and the equivalent metasomatic phases in associated peridotite xenoliths, mostly in the case of the "Fe-Ti metasomatised" wehrlites. These

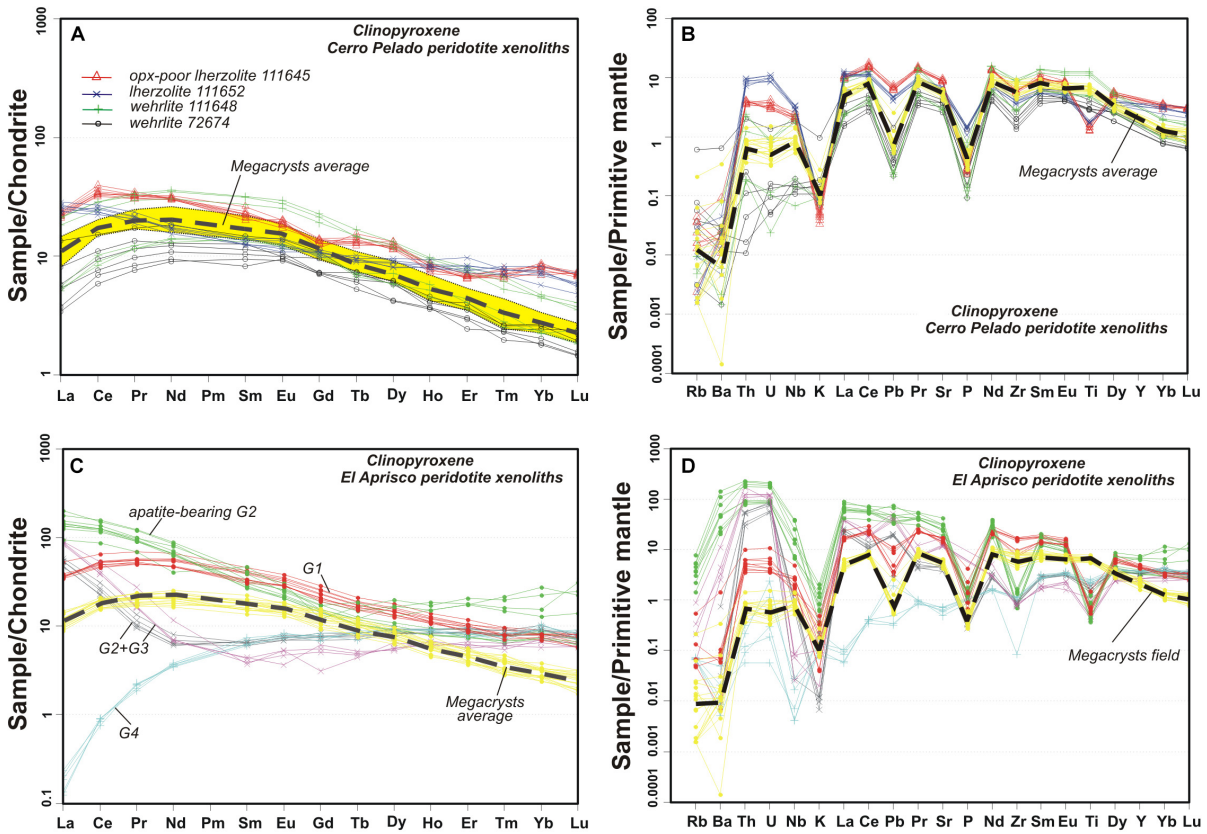

FIGURE 10 | Chondrite-normalized REE and primitive mantle-normalized trace element patterns of clinopyroxene of peridotite xenoliths from studied volcanic centers. Clinopyroxene trace element compositions of mantle xenoliths from the Cerro Pelado scoria cone are authors' unpublished data **(A,B)**. Those (G1 to G4 groups) from the El Aprisco maar **(C,D)** are taken from Villaseca et al. (2010, 2019b) and González-Jiménez et al. (2014). The clinopyroxene megacryst average composition (discontinuous line within yellow field) from **Figure 6** is shown for comparison. Chondrite and primitive mantle values are from Boynton (1985) and Sun and McDonough (1989), respectively.

latter enclaves have neoblastic spongy clinopyroxene (samples 72674 and 116648) and interstitial phlogopite, amphibole and alkaline glass. Taking into account that the studied megacrysts-phenocrysts crystallized from magmas similar in composition to their present host melts, the compositional similarities might indicate that the metasomatic agents which reacted with the Cerro Pelado peridotites and the host alkaline mafic magmas were genetically related. In fact, previous studies in those mantle xenoliths already established that they had undergone mafic silicate metasomatism, and that the most metasomatised wehrlites were probably connected with reactive infiltration of alkaline melts similar to their host magmas (Villaseca et al., 2010). Thus, although some interstitial amphibole and phlogopite in lherzolites record reaction with the Calatrava alkaline magma, these hydrous minerals would rarely give rise to euhedral cm-sized megacrysts, and their much higher Mg and Cr contents make it easy to discriminate magmatic megacrysts of melt-mantle metasomatic minerals from strongly transformed mantle xenoliths (Yu et al., 2019). Neither amphibole- (or phlogopite-) rich pegmatite-like veins nor large idiomorphic crystals (megacrysts) have been recorded in the studied peridotite suites.

Mantle xenoliths from the El Aprisco maar have metasomatic phases remarkably different in composition to the studied megacrysts and phenocrysts. The study of these mantle xenoliths has enabled the identification of at least three old metasomatic events occurring during the Cretaceous (∼118 Ma), the Oligocene (∼29 Ma) and the Miocene (∼16–4 Ma) (Villaseca et al., 2019b). As in the case of the Cerro Pelado peridotites, the high Cr, Ni and Sc contents of metasomatic amphiboles from the El Aprisco peridotite suites also agree with a longer time of equilibration within the mantle in comparison to the much younger age of mafic minerals formed during the Calatrava volcanic event (2.8 to 2.2 Ma ages for megacrysts formed in both volcanic centers, after Villaseca et al., 2019b), even if their formation occurred at similar *P-T* conditions at mantle depths.

Melting, Storage and Melt Evolution Within a Magmatic Plumbing System

The main alkaline silica-undersaturated magmas of the Calatrava Volcanic Field have been interpreted as being generated from a mantle asthenosphere source with trace element and isotopic ratios similar to the HIMU (or EAR) OIB-reservoir

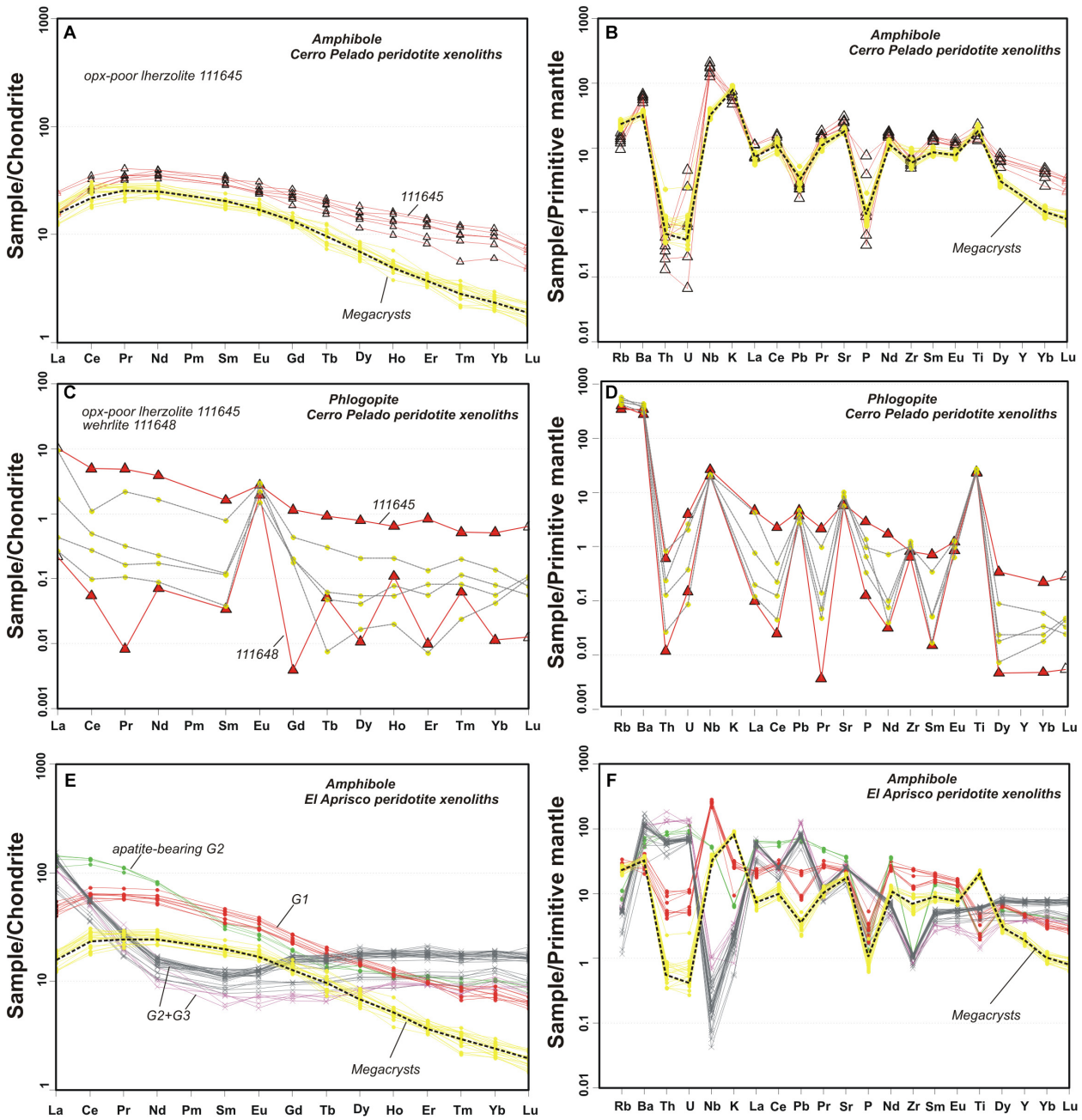

FIGURE 11 | Chondrite-normalized REE and primitive mantle-normalized trace element patterns of amphibole **(A,B,E,F)** and phlogopite **(C,D)** of peridotite xenoliths from studied volcanic centers. Amphibole trace element composition of mantle xenoliths (G1 to G3 groups) from the El Aprisco maar is taken from Villaseca et al. (2010, 2019b) and González-Jiménez et al. (2014). Those from the Cerro Pelado scoria cone are unpublished data. Amphibole megacryst field (in yellow) and the average (black line) is taken from **Figure 8**. Chondrite values are from Boynton (1985) whereas primitive mantle normalizing values are from Sun and McDonough (1989).

(Cebriá and López Ruiz, 1995). Phlogopite and garnet are considered residual phases in the mantle sources, consistent with the fractionated HREE patterns and negative K anomalies shown by Calatrava volcanic rocks (**Figure 4**). The determination of accurate *P-T* conditions of mantle melting is challenging. We have considered the geothermobarometry approach of Lee et al. (2009), which estimates the *P-T* condition of basaltic melt extraction in equilibrium with an averaged lherzolitic peridotite source. The high MgO content (>10 wt%) of most of the Calatrava magmas (**Table 1**) renders them suitable for this calculation. Nevertheless, some studied rocks have no features of primary melts. Thus, samples with MgO > 18 wt% and

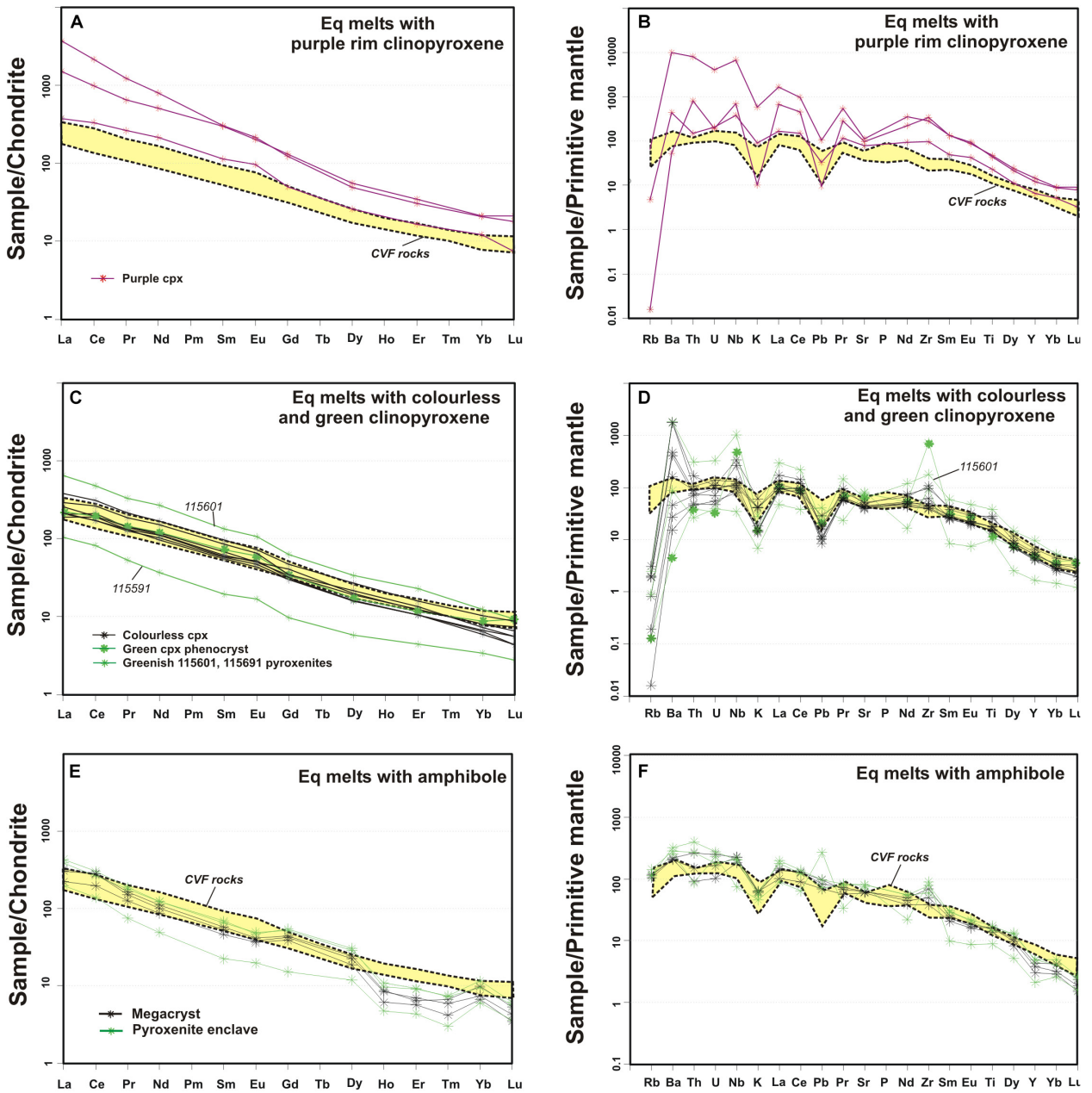

FIGURE 12 | Chondrite- and primitive mantle- normalized patterns of calculated melt compositions in equilibrium with clinopyroxene **(A–D)** and amphibole **(E,F)**, compared to the Calatrava Volcanic Field (CVF) compositional field. Chondrite and primitive mantle values are from Boynton (1985) and Sun and McDonough (1989), respectively.

pyroxenite enclaves have been excluded due to their high crystal cargo or cumulate origin, respectively. The resulting pressure and temperature of melt segregation from the mantle source are in the range of 2.3 to 5.6 GPa and 1,300 to 1,540°C, respectively (**Table 1**). These values have to be considered as rough estimates of partial melting conditions for Calatrava magmas from a lherzolite protolith. It is interesting to note that these estimations imply melt extraction within the stability field of garnet, in agreement with the chemical features of these alkaline magmas.

During their ascent, some of the Calatrava magmas were arrested in shallow lithospheric mantle reservoirs, where fractional crystallization was triggered. This is illustrated by the formation of a suite of mafic megacryst-phenocrysts and pyroxenitic cumulates, such as those described in this study. The conditions of crystallization indicate pressures of 1.2–1.6 GPa and temperatures in the range 1,275–1,350°C, corresponding to the uppermost mantle (Villaseca et al., 2019a). The relative wide depth range for magma stagnation derived from the pressure

data could imply either a polybaric crystallization during melt ascent or uncertainties in the *P-T* calculations. In any case, the much lower pressure provided by clinopyroxene phenocryst purple rims (~0.3–0.8 GPa, Villaseca et al., 2019a) points to the formation of these overgrowths during the magma transport through the crust.

The presence of clinopyroxene phenocrysts of contrasted composition (colorless and green cores), sharing similar purple rims, reveals a complex magmatic story. The green cores are enriched in Fe and incompatible trace elements when compared to the colorless cores, and the corresponding melts in equilibrium must represent a more evolved composition (**Figure 13**). This feature is indicative of a magma differentiation process occurring at depth and responsible for the formation of a heterogeneous suite of mafic minerals with a variable degree of evolution. Clinopyroxene and amphibole might be the main liquidus minerals during magma crystallization at depth due to their modal abundance as megacrysts and mineral phases in pyroxenite enclaves. Phlogopite and olivine (and accessory Fe-Ti-rich minerals) were also involved in minor proportions. As an approximation of this process, we have applied a model of fractional crystallization starting from a melt C_0 representing a primitive host basaltic composition (see caption to **Figure 13**) and assuming clinopyroxene + amphibole + minor olivine fractionation. The distribution coefficients used are those of La Tourrette et al. (1995) (Zr-Hf) and Irving and Frey (1984) (REE) for amphibole; Hart and Dunn (1993) for clinopyroxene and Adam and Green (2006) for olivine. The results indicate that a high degree of fractionation is needed (up to 80%) in order to obtain the high Zr/Hf and the slightly low Gd/Yb ratios of the evolved melts equilibrated with green clinopyroxene (**Figure 13**). The presence of mica-rich (glimmerite) enclaves is an evidence in favor of phlogopite crystallization during differentiation, but its participation does not change significantly the above estimated evolution pattern.

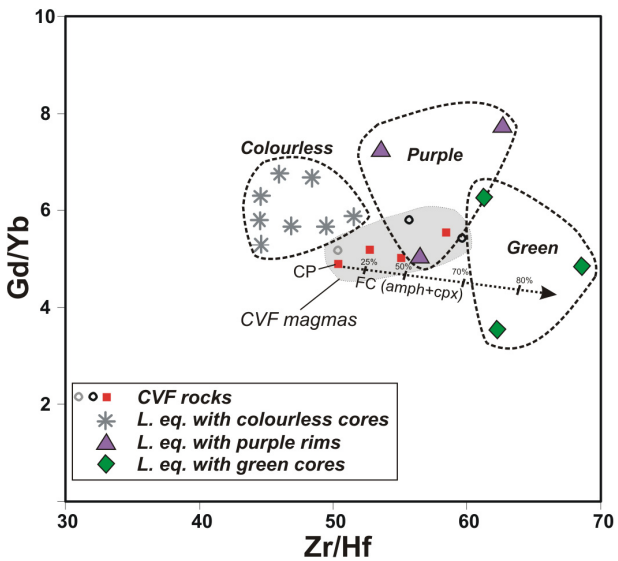

FIGURE 13 | Gd/Yb vs Zr/Hf ratios of melts equilibrated with clinopyroxenes. The compositional field of Calatrava Volcanic Field (CVF) magmas is also shown for comparison. The clinopyroxene compositions used for calculations are averaged values for selected colorless megacrysts (115603, 114404, 111639) and phenocryst cores (115605, 116596), together with green phenocryst cores (116596) and pyroxenites (115601, 115591). Purple rims overgrow phenocrysts (115605, 116596) and pyroxenite crystals (115591) (see **Supplementary Table S2** for averaged clinopyroxene values). The C_0 for the fractional crystallization model is the CAL-73 nephelinite (from the Cerro Pelado volcano, CP in figure). The arrow represents the trend of chemical evolution of melts based on the fractionation model (up to 80% of fractional crystallization) considering extraction of 45% clinopyroxene + 45% amphibole + 10% olivine.

A fractional crystallization process also explains the clinopyroxene zoning in pyroxenite enclaves, with variable Mg# (around 0.65 in the green bands and 0.82 in the colorless core) and trace element contents within the same crystal (**Figure 9**). The fact that this zoning is frequently oscillatory requires a connection with a more primitive magma batch acting as a recharge source. The geochemical similarities shared by the evolved green phenocrysts cores and the pale green clinopyroxenes in pyroxenites supports their formation in a similar context: magma pools stagnated within the mantle. We think that magmas slightly more primitive than the volcanic host melts evolved by fractional crystallization within mantle reservoirs, generating a wide range of liquid compositions (either more primitive or significantly more fractionated) at local scale. This large chemical heterogeneity contrasts with the coincident isotopic composition of megacrysts, pyroxenite enclaves and host rocks (**Figure 5**), which is indicative of the cogenetic nature of the involved magmas. This model contrast with previous works studying clinopyroxene green phenocryst cores in alkaline volcanoes of the European circum-Mediterranean region, where their origin from significantly more evolved melts than host lavas was interpreted as xenocrystic fragments from non-cogenetic rocks (Aulinas et al., 2013; Jankovics et al., 2013; Matusiak-Malek et al., 2018).

A typical feature of chilled margins in cooling magmatic bodies is the presence of interstitial highly fractionated liquids within crystal mush carapaces (e.g. Marsh, 1996). The pyroxenitic cumulates found in the Calatrava volcanic rocks can be considered pieces of this crystalline margin, and the complex zoned crystals they include serve as evidence of the involvement of highly evolved melts. These latter liquids could give rise to single microcrysts (green phenocryst cores), subsequently incorporated as crystal cargo in ascending and less fractionated magmas from the same magmatic system. Nevertheless, there are several differences between the trace element composition of melts in equilibrium with green clinopyroxene and the most evolved Calatrava volcanic rocks, such as the marked Zr content of green phenocryst cores (**Figures 12**, **13**). The highly evolved liquids which gave rise to the low-Mg green clinopyroxene have not been erupted in Calatrava volcanoes, and were probably trapped within the cumulate chilled margins of deep mantle reservoirs. The small volume of highly fractionated liquids generated hinders to collect them to be transported toward the Earth's surface; they are relatively immobile.

The major and trace element composition of the clinopyroxene purple rims is broadly intermediate between primitive colorless and evolved green cores (**Figures 8**, **13**; see also Villaseca et al., 2019a). Purple rims can be found overgrowing both types of phenocryst cores and also forming the most external margin of clinopyroxene in some marginal areas of pyroxenite enclaves. It is thus likely that rims were formed from the magma that entrapped megacrysts, phenocrysts and enclaves, and erupted at the Earth's surface. This conclusion is supported by the broadly similar composition of calculated melts in equilibrium with thin purple rims and the host melts (**Figure 13**). Other rims provide equilibrated melts with trace element contents significantly higher than the Calatrava magmas (**Figures 12**, **13**). This feature is in accordance with an increase in the cooling and decompression rates, during the rise of magma toward the surface, which favors the enrichment in incompatible trace elements as a consequence of modification of the partitioning of elements and crystallization being governed by kinetic effects (e.g. Re et al., 2017 and references therein).

The crystal fractionation process described in this study adds novel information regarding the magmatic differentiation associated with deep plumbing systems beneath monogenetic volcanos. Mafic mineral crystallization is one of the main factors controlling magma differentiation inducing changes in magma buoyancy, volatile composition and, eventually, the onset of volcanic eruption (Mattsson et al., 2013; Re et al., 2017). The cumulate origin of clinopyroxene, amphibole and phlogopite, assessed via trace element modeling, implies that the primary magmas were volatile-rich and that a significant proportion of minerals was removed from the melt due to crystal fractionation at mantle reservoirs. It is commonly accepted that volcanic eruptions of carbonate-rich nephelinitic and melilititic magmas generating large maar-diatreme volcanoes can be triggered by pressure oversaturation associated with deep exsolution of CO_2 due to silicate crystallization (e.g. Mattsson et al., 2013). This process is favored by decompression during magma ascent or due to recharge of deep juvenile volatile-rich melts into the magma reservoirs (Ubide et al., 2019 and references therein). Although such discussion is beyond the scope of this work, our data leaves open the possibility of the CO_2 increase being related with deep-seated crystal fractionation (Villaseca et al., 2019a). The combination of CO_2 increase in the environs of the solidification front and upward movement of magma within the upper mantle could explain magma boiling, fragmentation and a rapid ascent to the surface, carrying a heterogeneous suite of crystals, pyroxenitic enclaves and mantle xenoliths.

CONCLUSION

This is the first study focused on the characterisation and interpretation of the trace element mineral chemistry of phenocrysts, megacrysts, and clinopyroxenite and glimmerite enclaves carried by alkaline rocks of the Calatrava volcanic field (El Aprisco and Cerro Pelado volcanoes), central Spain. Mineral data were complemented with whole-rock and isotopic (Sr-Nd) data of megacrysts, enclaves and volcanic rocks. Mineral analyses focused on clinopyroxene, amphibole and phlogopite, which appear as megacrysts and phenocrysts, and as main constituents of the pyroxenite enclaves. The mafic megacrysts display a chemical composition more akin to an origin as deep segregates rather than fragments of a peridotitic mantle. They show clear differences in composition when compared to minerals from the mantle xenoliths carried by the Calatrava volcanics but are similar to the same phases in clinopyroxenite and glimmerite enclaves.

The presence of disequilibrium textures, complex zoning and contrasting compositions in clinopyroxene crystals indicates that they did not crystallize from a single melt. Clinopyroxene is the most common and widespread phase, occurring as megacrysts, macrocrysts and phenocrysts in these volcanic rocks. Two types of high-P crystals of different colors have been observed: green and colorless phenocryst cores. The former are less abundant and have low Mg# (Cr, Ni, Sc) and high Zr-Sr contents, which is indicative of their derivation from melts much more fractionated than those related to the primitive high Mg# colorless cores. The contrasting compositions also coexists in complexly zoned crystals of clinopyroxenites, suggesting that the colorless and green types might be cognate and derive from mixing of primitive and evolved fractionated liquids within the same magmatic system. The geochemistry of clinopyroxene supports a fractionation process mainly controlled by clinopyroxene and amphibole crystallization.

The similarity in mineral chemistry and the homogeneous whole-rock Sr-Nd ratios of all the analyzed minerals and rocks suggest that the deep fractionating magma batches and the melts transporting this complex crystal cargo were likely generated from similar sources. The possibility that this suite of fractionated magmas derive from a single magma batch is supported by the overlapping composition of the melts in equilibrium with the mafic megacrysts/phenocrysts and the volcanic host magmas and also may explain the presence of oscillatory zoning at micron-scale in some cumulates, linked to crystallization fronts in deep magma chambers, where repeated infiltration of recharging external liquids is probably limited. This model contrasts with previous studies that suggested that clinopyroxene green phenocryst cores in alkaline melts are xenocrystic fragments from non-cogenetic rocks.

DATA AVAILABILITY STATEMENT

All datasets generated for this study are included in the article/**Supplementary Material**.

AUTHOR CONTRIBUTIONS

All authors collaborated in the sampling, petrographic study and the performing of analytical data and contributed to the final version of the manuscript, figures, and tables. CV conceived the study and wrote an original draft later improved with inputs from JG and DO.

FUNDING

This work is included in the objectives of, and supported by, the CGL2016-78796 project of the Ministerio de Economía y Competitividad de España, and the 910492 UCM project.

ACKNOWLEDGMENTS

We acknowledge Alfredo Fernández Larios for his assistance with the electron microprobe in the Centro Nacional de Microscopía Electrónica Luis Bru (UCM). Manuel Alpiste is thanked for his assistance with the LA-ICP-MS of the Instituto Andaluz de Ciencias de la Tierra (Granada). We also greatly appreciate the comments made by PS, MG, and the associated editor Teresa Ubide on a previous version of the manuscript.

SUPPLEMENTARY MATERIAL

The Supplementary Material for this article can be found online at: https://www.frontiersin.org/articles/10.3389/feart.2020.00132/full#supplementary-material

FIGURE S1 | (A) The Calatrava Volcanic Field and location of the two studied volcanoes: El Aprisco and Cerro Pelado (Ancochea, 1982; Cebriá et al., 2011). **(B)** Sketch map of the Iberian Peninsula showing the location of the main Cenozoic volcanic fields (in black; Lustrino and Wilson, 2007).

TABLE S1 | Compositional data on certified standards analyzed with the samples in this study.

TABLE S2 | Clinopyroxene trace element contents (in ppm) in megacrysts, phenocrysts and pyroxenite enclaves.

TABLE S3 | Amphibole and phlogopite trace element contents (in ppm) in megacrysts, phenocrysts and pyroxenite enclaves.

REFERENCES

Adam, J., and Green, T. (2006). Trace element between mica- and amphibole-bearing garnet lherzolite and hydrous basanitic melt: 1. Experimental results and the investigation of controls on partitioning behavior. *Contrib. Mineral. Petrol.* 152, 1–17.

Allègre, C. J., and Turcotte, D. L. (1986). Implications of a two-component marble-cake mantle. *Nature* 323, 123–127.

Ancochea, E. (1982). *Evolución Espacial y Temporal del Volcanismo Reciente de España Central.* Ph.D. thesis., Universidad Complutense de Madrid, Madrid.

Aulinas, M., Gisbert, G., Gimeno, D., and Gasperini, D. (2013). Cannibalization of previous Na-rich clinopyroxenes by ascending magmas of the Garrotxa Volcanic Field (NE, Spain). *Mineral. Mag.* 77:631.

Bodinier, J. L., Guiraud, M., Fabries, J., Dostal, J., and Dupuy, C. (1987). Petrogenesis of layered pyroxenites from the Lherz, Freychinede and Prades ultramafic bodies (Ariege, French Pyrenees). *Geochim. Cosmochim. Acta* 51, 279–290.

Boynton, W. V. (1985). "Geochemistry of the rare earth elements: meteorite studies," in *Rare Earth Element Geochemistry*, ed. P. Henderson (New York, NY: Elsevier), 63–114. doi: 10.1186/s12932-015-0022-4

Cebriá, J. M. (1992). *Geoquímica de las Rocas Basálticas y Leucititas de la Región Volcánica de Campo de Calatrava, España*. Ph.D. thesis., Universidad Complutense de Madrid, Madrid.

Cebriá, J. M., and López Ruiz, J. (1995). Alkali basalts and leucitites in an extensional intracontinental plate setting: the late Cenozoic Calatrava volcanic province (central Spain). *Lithos* 35, 27–46.

Cebriá, J. M., Martín-Escorza, C., López-Ruiz, J., Morán-Zenteno, D. J., and Martiny, B. M. (2011). Numerical recognition of alignments in monogenetic volcanic areas: examples from the Michoacán-Guanajato Volcanic Field in Mexico and Calatrava in Spain. *J. Volcan. Geotherm. Research* 201, 73–82. doi: 10.1016/j.jvolgeores.2010.07.016

Chazot, G., Menzies, M. A., and Harte, B. (1996). Determination of partition coefficients between apatite, clinopyroxene, amphibole, and melt in natural spinel lherzolites from Yemen: implications for wet melting of the lithospheric mantle. *Geochim. Cosmochim. Acta* 60, 423–437.

Downes, H. (2007). Origin and significance of spinel and garnet pyroxenites in the shallow lithospheric mantle: ultramafic massifs in orogenic belts in Western Europe and NW Africa. *Lithos* 99, 1–24.

Downes, H., Reichow, M. K., Mason, P. R. D., Beard, A. D., and Thirlwall, M. F. (2003). Mantle domains in the lithosphere beneath the French Massif Central: trace element and isotopic evidence from mantle clinopyroxenes. *Chem. Geol.* 200, 71–87.

Duda, A., and Schmincke, H.-S. (1985). Polybaric differentiation of alkali basaltic magmas: evidences from green-core clinopyroxenes (Eifel, FRG). *Contrib. Mineral. Petrol.* 91, 340–353.

Garrido, C. J., and Bodinier, J. L. (1999). Diversity of mafic rocks in the Ronda Peridotite; evidence for pervasive melt–rock reaction during heating subcontinental lithosphere by upwelling asthenosphere. *J. Petrol.* 40, 729–754.

Gernon, T. M., Upton, B. G. J., Ugra, R., Yücel, C., Taylor, R. N., and Elliott, H. (2016). Complex subvolcanic magma plumbing system of an alkali basaltic maar-diatreme volcano (Elie Ness, Fife, Scotland). *Lithos* 264, 70–85.

González-Jiménez, J. M., Villaseca, C., Griffin, W. I., O'Reilly, S. Y., Belousova, E., Ancochea, et al. (2014). Significance of ancient sulfide PGE and Re-Os signatures in the mantle beneath Calatrava, Central Spain. *Contrib. Mineral. Petrol.* 168:1047.

Granet, M., Wilson, M., and Achauer, U. (1995). Imaging a mantle plume beneath the French Massif Central. *Earth Planet. Sci. Lett.* 136, 281–296.

Green, D. H., and Ringwood, A. E. (1964). Fractionation of basalt magmas at high pressures. *Nature* 201, 1276–1279.

Grégoire, M., Moine, B. N., O'Reilly, S. Y., Cottin, J. Y., and Giret, A. (2000). Trace element residence and partitioning in mantle xenoliths metasomatized by high alkaline silicate and carbonate-rich melts (Kerguelen Islands, Indian Ocean). *J. Petrol.* 41, 477–509.

Hart, S. R., and Dunn, T. (1993). Experimental cpx/melt partitioning of 24 trace element. *Contrib. Mineral. Petrol.* 113, 1–8.

Hegner, E., Walter, H. J., and Satir, M. (1995). Pb-Sr-Nd isotopic composition and trace element geochemistry of megacrysts and melilitites from the Tertiary Urach volcanic field: source composition of small volume melts under SW Germany. *Contrib. Mineral. Petrol.* 122, 322–335.

Ionov, D. A., Griffin, W. L., and O'Reilly, S. Y. (1997). Volatile-bearing minerals and lithophile trace elements in the upper mantle. *Chem. Geol.* 141, 153–184.

Irving, A. J., and Frey, F. A. (1984). Trace element abundances in megacrysts and their host basalts; constraints on partition coefficients and megacryst genesis. *Geochim. Cosmochim. Acta* 48, 1201–1221.

Jankovics, M. E., Dobosi, G., Embey-Isztin, A., Kiss, B., Sági, B., Harangi, S., et al. (2013). Origin and ascent history of unusually crystal-rich alkaline basaltic magmas from the western Pannonian Basin. *Bull. Volcanol.* 75:23.

Jankovics, M. E., Taracsák, Z., Dobosi, G., Embey-Isztin, A., Batki, A., Harangi, S., et al. (2016). Clinopyroxene with diverse origins in alkaline basalts from the western Pannonian Basin: implications from trace element characteristics. *Lithos* 262, 120–134.

Kaczmarek, M. A., Bodinier, J. L., Bosch, D., Tommasi, A., Dautria, J. M., and Kechid, S. A. (2016). Metasomatized mantle xenoliths as a record of the lithospheric mantle evolution of the northern edge of the Ahaggar Swell, In Teria (Algeria). *J. Petrol.* 57, 345–382.

Keenan, B., Huertas, M. J., and Ancochea, E. (2019). Edad y composición del volcán Bienvenida (Campos de Calatrava). *Geogaceta* 65, 23–26.

La Tourrette, T., Hervig, R. L., and Holloway, J. R. (1995). Trace element partitioning between amphibole, phlogopite, and basanite melt. *Earth Planet. Sci. Lett.* 135, 13–30.

Le Bas, M. J. (1989). Nephelinitic and basanitic rocks. *J. Petrol.* 30, 1299–1312.

Le Maitre, R. W. (ed.) (2002). *Igneous Rocks: A Classification and Glossary of Terms*. Cambridge: Cambridge University Press.

Lee, C. T. A., Luffi, P., Plank, T., Dalton, H., and Leeman, W. P. (2009). Constraints on the depths and temperatures of basaltic magma generation on Earth and other terrestrial planets using new thermobarometers for mafic magmas. *Earth Planet. Sci. Lett.* 279, 20–33.

Lierenfeld, M. B., and Mattsson, H. B. (2015). Geochemistry and eruptive behaviour of the Finca la Nava maar volcano (Campo de Calatrava, south-central Spain). *Int. J. Earth Sci.* 104, 1795–1817.

Liotard, J. M., Briot, D., and Boivin, P. (1988). Petrological and geochemical relationships between pyroxene megacrysts and associated alkali-basalts from Massif Central (France). *Contrib. Mineral. Petrol.* 98, 81–90.

Lustrino, M., Prelevic, D., Agostini, S., Gaeta, M., Di Rocco, T., Stagno, V., et al. (2016). Ca-rich carbonates associated with ultrabasic-ultramafic melts: carbonatite or limestone xenoliths? A case study from the late Miocene Morron de Villamayor volcano (Calatrava Volcanic Field, central Spain). *Geochim. Cosmochim. Acta* 185, 477–497.

Lustrino, M., and Wilson, M. (2007). The circum-Mediterranean anorogenic Cenozoic igneous province. *Earth Sci. Rev.* 81, 1–65.

Marsh, B. D. (1996). Solidification fronts and magmatic evolution. *Mineral. Mag.* 60, 5–40.

Mattsson, H. B., Nandedkar, R. H., and Ulmer, P. (2013). Petrogenesis of the melilitic and nephelinitic rock suites in the lake Natron-Engaruka monogenetic volcanic field, northern Tanzania. *Lithos* 179, 175–192.

Matusiak-Malek, M., Ntaflos, T., Puziewicz, J., Woodland, A., Uenver-Thiele, L., and Lipa, D. (2018). From mantle to crust: variable origin of clinopyroxene from eastern limb of Central European Volcanic Province. *Geophys. Res. Abstracts* 20, EGU2018–EGU17407.

Mayer, B., Jung, S., Romer, R. L., Pfänder, J. A., Llügel, A., Pack, A., et al. (2014). Amphibole inalkaline basalts from intraplate settings: implications for the petrogenesis of alkaline lavas from the metasomatised lithospheric mantle. *Contrib. Mineral. Petrol.* 167:989.

Orejana, D., Villaseca, C., and Paterson, B. A. (2006). Geochemistry of pyroxenitic and hornblenditic xenoliths in alkaline lamprophyres from the Spanish Central System. *Lithos* 86, 167–196.

Peterson, T. D., and LeCheminant, A. N. (1993). Glimmerite xenoliths in early proterozoic ultrapotassic rocks from the Churchill province. *Canad. Mineral.* 31, 801–819.

Praegel, N. O. (1981). Origin of ultramafic inclusions and megacrysts in a monchiquite dyke at Streap, Inverness-shire, Scotland. *Lithos* 14, 305–322.

Raffone, N., Chazot, G., Pin, C., Vannucci, R., and Zanetti, A. (2009). Metasomatism in the lithospheric mantle beneath Middle Atlas (Morocco) and the origin of Fe- and Mg-rich wehrlites. *J. Petrol.* 50, 197–249.

Re, G., Palin, J. M., White, J. D. L., and Parolari, M. (2017). Unravelling the magmatic system beneath a monogenetic volcanic complex (Jagged Rocks Complex, Hopi Buttes, AZ, USA). *Contrib. Mineral. Petrol.* 172:94.

Reyes, J., Villaseca, C., Barbero, L., Quejido, A. J., and Santos Zalduegui, J. F. (1997). *Description of a Rb, Sr, Sm and Nd Separation Method for Silicate Rocks in Isotopic Studies*. Soria: I Congreso Ibérico de Geoquímica, 46–55.

Shaw, C. S. J., and Eyzaguirre, J. (2000). Origin of megacrysts in the mafic alkaline lavas of the West Eiffel volcanic field, Germany. *Lithos* 50, 75–95.

Sun, S. S., and McDonough, W. F. (1989). "Chemical and isotopic systematics of oceanic basalts: implications for mantle composition and processes", in Magmatism in ocean basins, eds A.D. Saunders, and M.J. Norry. *Geol. Soc. Spec. Publ.* 42, 313–345.

Ubide, T., Caulfield, J., Brandt, C., Bussweiler, Y., Mollo, S., Di Stefano, F., et al. (2019). Deep magma storage revealed by multi-method elemental mapping of clinopyroxene megacrysts at Stromboli volcano. *Front. Earth Sci.* 7:239.

Ubide, T., Galé, C., Larrea, P., Arranz, E., and Lago, M. (2014). Antecrysts and their effect on rock compositions: the Cretaceous lamprophyre suite in the Catalonian Coastal ranges (NE Spain). *Lithos* 20, 214–233.

Ulrych, J., Dostal, J., Adamovic, J., Jelínek, E., Spacek, P., Hegner, E., et al. (2011). Recurrent Cenozoic activity in the Bohemian Massif (Czech Republic). *Lithos* 123, 133–144.

Ulrych, J., Krmícek, L., Teschner, C., Skála, R., Adamovic, J., Durisová, J., et al. (2018). Chemistry and Sr-Nd isotope signature if aamphibole of the magnesio-hastingsite-pargasite-kaersutite series in Cenozoic volcanic rocks: insights into lithospheric mantle beneath the Bohemian Massif. *Lithos* 31, 308–321.

Vannucci, R., Piccardo, G. B., Rivalenti, G., Zanetti, A., Rampone, E., Ottolini, L., et al. (1995). Origin of LREE-depleted amphiboles in the subcontinental mantle. *Geochim. Cosmochim. Acta* 59, 1763–1771.

Villaseca, C., Ancochea, E., Orejana, D., and Jeffries, T. E. (2010). "Composition and evolution of the lithospheric mantle in central Spain: inferences from peridotite xenoliths from the Cenozoic Calatrava volcanic field", in Petrological evolution of the European Lithospheric Mantle, eds M. Coltorti, H., Downes, M., Grégoire, and S.Y. O'Reilly. *Geol. Soc. Spec. Publ. Lon.* 337, 125–151.

Villaseca, C., Dorado, O., and Orejana, D. (2019a). Mineral chemistry of megacryts and associated clinopyroxenite enclaves in the Calatrava Volcanic Field: crystallization processes in mantle magma chambers. *J. Iberian Geol.* 45, 401–426.

Villaseca, C., Belousova, E., Barfod, D., and González-Jiménez, J. M. (2019b). Dating metasomatic events in the lithospheric mantle beneath the Calatrava volcanic field (central Spain). *Lithosphere* 11, 192–208.

Wilkinson, J. F. G., and Stolz, A. J. (1997). Subcalcic clinopyroxenites and associated ultramafic xenoliths in alkali basalt near Glen Innes, northeastern New South Wales, Australia. *Contrib. Mineral. Petrol.* 127, 272–291.

Yu, X., Zeng, G., Chen, L. H., Hu, S. L., and Yu, Z. Q. (2019). Magma-magma interaction in the mantle recorded by megacrysts from cenozoic basalts in eastern China. *Int. Geol. Rev.* 61, 675–691.

Zindler, A., and Hart, S. R. (1986). Chemical geodynamics. *Annu. Rev. Earth Planet. Sci.* 14, 493–571.

Conflict of Interest: The authors declare that the research was conducted in the absence of any commercial or financial relationships that could be construed as a potential conflict of interest.

frontiers in Earth Science

ORIGINAL RESEARCH
published: 22 May 2020
doi: 10.3389/feart.2020.00135

Phosphorus Coupling Obfuscates Lithium Geospeedometry in Olivine

Kendra J. Lynn[1], Michael O. Garcia[2] and Thomas Shea[2]*

[1] Department of Earth Sciences, University of Delaware, Newark, DE, United States, [2] Department of Earth Sciences, University of Hawai'i at Mānoa, Honolulu, HI, United States

Lithium zoning in zircon and olivine provides a powerful record of crystal histories and magmatic processes in volcanic systems. Characterizing Li behavior in olivine is important because it is one of the few elements in basaltic systems that track short-duration magmatic processes (e.g., less than a few days). However, the potential for trace element coupling and the competing effects of crystal growth and subsequent diffusion obfuscate interpretations of Li zoning patterns and their use for geospeedometry. Here, we use diverse analytical techniques (EPMA, LA-ICPMS, nanoSIMS) to untangle records of growth and diffusion in carefully oriented olivine crystals from Kīlauea (Hawai'i). Li, P, and Al are targeted because they show correlations despite contrasting behaviors during growth and diffusion. Lithium zoning exhibits two styles: (1) non-coupled, wherein Li (1–3 ppm) shows diffuse zoning over 10s–100s of μm between the crystal core and rim with low (10s of ppm) and homogeneous P, and (2) coupled, wherein sub-ppm Li enrichments <40 μm wide are correlated with P-rich zones (100s of ppm) that preserve a blueprint of crystal growth. Non-coupled Li zoning modeled for diffusive re-equilibration yields hours–days timescales, reflecting magma-mixing events that primed the system for eruption. Coupled Li peaks consistently occur where analyses traverse the dendritic framework of P zoning that reflects rapid crystal growth. This correlation results from Li^{+} ions partially satisfying charge balancing requirements of P^{5+} ions in the olivine lattice. Aluminum balances most of the P budget in olivine but has non-systematic correlations with Li peaks. Transects can exhibit both non-coupled and coupled Li behaviors, preserving histories of both crystal growth and diffusive re-equilibration. Modeling a near-rim Li enrichment peak with the Li diffusion coefficient yields a timescale of <3 min, too short to represent the time elapsed following crystallization. If the near-rim Li and P peaks are modeled using the diffusion coefficient for P, congruent timescales of 5–11 days suggest that they have the potential to record magmatic processes. Several caveats such as poorly constrained initial conditions and analytical challenges limit the practicality of enrichment peak geospeedometry. Only broad zoning of non-coupled Li should be modeled for timescales of magmatic processes.

Keywords: olivine, diffusion, trace element zoning, crystal growth, Kīlauea, Hawai'i

OPEN ACCESS

Edited by:
David A. Neave, University of Manchester, United Kingdom

Reviewed by:
Peter Tollan, ETH Zürich, Switzerland
Euan James Forsyth Mutch, University of Maryland, United States

****Correspondence:***
Kendra J. Lynn
kjlynn@udel.edu

Specialty section:
This article was submitted to Petrology, a section of the journal Frontiers in Earth Science

Received: *10 January 2020*
Accepted: *14 April 2020*
Published: *22 May 2020*

Citation:
Lynn KJ, Garcia MO and Shea T (2020) Phosphorus Coupling Obfuscates Lithium Geospeedometry in Olivine. Front. Earth Sci. 8:135. doi: 10.3389/feart.2020.00135

INTRODUCTION

Lithium is an increasingly popular element for investigating diverse processes in volcanic systems, including volatile partitioning and degassing (e.g., Vlastélic et al., 2011; Edmonds, 2015), magmatic differentiation (Weyer and Seitz, 2012), and diffusive re-equilibration (e.g., Beck et al., 2006; Parkinson et al., 2007; Gallagher and Elliott, 2009; Ellis et al., 2018). As a fast-diffusing cation, Li re-equilibrates faster than all major and minor elements in olivine and is a potentially powerful geospeedometer for characterizing the sub-solidus histories of magma storage (Rubin et al., 2017), rapidly occurring volcanic processes (Charlier et al., 2012; Lynn et al., 2018), and the post-eruptive cooling of volcanic deposits (Ellis et al., 2018). However, trace element crystal chemical effects such as charge balancing requirements and element coupling may obfuscate Li geospeedometry. Coupling with other elements leads to multi-component diffusion, where the mobility of an element is also dependent on the concentration and mobility of other elements (e.g., Zhang, 2010).

Lithium diffusion in zircon exemplifies these complexities despite its usage to infer the timescales of magmatic processes in silicic magmas (e.g., Ushikubo et al., 2008; Cooper et al., 2017; Tang et al., 2017; Wilson et al., 2017). Retention of Li in zircon despite crystal ages spanning 10s of thousands of years (Rubin et al., 2017) sparked debate over apparently "slow" diffusion when Li is coupled with rare earth elements (REE) vs. "fast" when it is not coupled (Ushikubo et al., 2008; Cooper et al., 2017; Tang et al., 2017; Wilson et al., 2017). Trace element zoning in zircon is also strongly dependent on the 3D crystal structure during growth (Trail et al., 2016), making clear distinctions between non-coupled vs. coupled Li diffusion challenging. As a result, timescales and magmatic process interpretations drawn from Li zoning in zircon are currently vigorously debated (Cooper et al., 2017; Rubin et al., 2017; Wilson et al., 2017; Sliwinski et al., 2018).

Trace element zoning in olivine, the dominant phenocryst phase in most basaltic systems, is also complicated by charge coupling effects. Numerous studies have proposed that Li in olivine is subject to charge balancing requirements of other trace elements that are incorporated during rapid crystal growth (e.g., P, Al, Cr; Woodland et al., 2004; Milman-Barris et al., 2008; Mallmann et al., 2009; Grant and Wood, 2010; Spandler and O'Neill, 2010; Tomascak et al., 2016). Monovalent cations (e.g., Li^+, Na^+, H^+) are thought to occupy octahedrally coordinated sites to charge balance P^{5+} substitution in tetrahedrally coordinated sites (Woodland et al., 2004; Milman-Barris et al., 2008; Mallmann et al., 2009) based on the following reaction:

$$^{IV}Si^{4+} + {}^{VI}Mg^{2+} = {}^{IV}P^{5+} + {}^{VI}\left(Li^+, Na^+, H^+\right) \quad (1)$$

where *IV* denotes coordination in a tetrahedral site and *VI* denotes that for the octahedral site. Phosphorus, a normally highly incompatible element, is enriched in a skeletal olivine framework during early rapid growth (Milman-Barris et al., 2008; Welsch et al., 2013, 2014; Shea et al., 2019). The above mechanism (Eq. 1) would allow rapidly growing olivine to incorporate monovalent cations like Li^+. Phosphorus is also one of the slowest diffusing elements in olivine (Watson et al., 2015), meaning that the mobility of faster diffusing Li (Dohmen et al., 2010) may be subsequently hindered by the charge coupling conditions in Eq. 1. Alternatively, Li may exhibit "inter-site reaction" diffusion behavior analogous to H^+ decorating pre-existing defects associated with trace elements like Ti (Jollands et al., 2016). In this case, Li would diffuse through P-rich regions by hopping between site vacancies or interstitial sites and vacancies associated with trace element charge balancing.

Phosphorus enrichments are probably also balanced by a combination of other substitution reactions, including vacancies and/or 3 + ions in octahedral sites (Agrell et al., 1998; Boesenberg et al., 2004; Milman-Barris et al., 2008; Mallmann et al., 2009; Boesenberg and Hewins, 2010):

$$5^{IV}Si^{4+} = 4^{IV}P^{5+} + {}^{IV}[] \quad (2)$$

$$^{IV}Si^{4+} + 2^{VI}M^{2+} = {}^{IV}P^{5+} + {}^{VI}R^{3+} + {}^{VI}[] \quad (3)$$

$$2^{IV}Si^{4+} = {}^{IV}P^{5+} + {}^{IV}Al^{3+} \quad (4)$$

where $^{VI}M^{2+}$ refers to a divalent cation in an octahedral site (e.g., Fe^{2+}, Mg^{2+}), $^{VI}R^{3+}$ refers to a trivalent cation in an octahedral site (e.g., Al^{3+}, Cr^{3+}, Fe^{3+}), and $^{VI}[]$ represents an octahedral site vacancy. Aluminum also frequently shows fine-scale zoning inferred to preserve rapid crystal growth and may partially charge balance P^{5+} via tetrahedral or octahedral substitutions outlined in Eqs 3 and/or 4 (Evans et al., 2008; Milman-Barris et al., 2008; Welsch et al., 2013, 2014; Zhukova et al., 2017; Shea et al., 2019).

Here, we document the distribution of Li, P, and Al in magmatic olivine to distinguish the signatures of growth- and diffusion-induced zoning for these trace elements in natural basalts. Pumice from explosive Keanakāko'i Tephra (KT, 1500–1820 C.E.; Swanson et al., 2012) eruptions at Kīlauea Volcano are ideal for this study because of the following reasons: (a) the tephra contains euhedral olivine that was easily extracted and oriented perpendicular to a crystallographic axis for sectioning; (b) samples were quenched very rapidly, avoiding complications of post-eruptive Li diffusion (e.g., Ellis et al., 2018); and (c) the magmatic histories of many of the tephra units are well characterized based on previous studies of glass and olivine compositions (Lynn et al., 2017, 2018; Garcia et al., 2018). We combine backscattered images and X-ray element maps of P and Al by EPMA; laser ablation ICPMS measurements of Li, P, and Al; and nanoscale secondary ion mass spectrometry (nanoSIMS) measurements of Li and P in linear core-to-rim transects and ion element maps and to document the distribution and correlation of Li and P. These data are used to identify coupled vs. non-coupled Li zoning and provide recommendations on selecting Li profiles for geospeedometry.

MATERIALS AND METHODS

Sample Preparation and Previous Work

Samples used in this study were previously examined for major and minor elements in olivine (see Lynn et al., 2017,

2018) and major, minor, and trace element geochemistry in glasses (Garcia et al., 2018). The euhedral olivine phenocrysts (>0.5 mm) examined in this study had core forsterite [Fo mol%; (Mg/(Mg + Fe) × 100)] contents of 83.9–88.5, with one crystal at 79.2 (**Supplementary Material**). Each crystal was oriented perpendicular to a crystallographic axis, confirmed via electron backscatter diffraction (EBSD) analyses (see below) and/or recognizable euhedral crystal faces (Lynn et al., 2017). Well-oriented crystals allow analytical profiles to be made parallel to principal crystallographic axes and minimize oblique sectioning through complex 3D distributions of elements like P (Welsch et al., 2014).

Electron Probe Micro Analysis (EPMA)

X-ray maps of Al and P in olivine were obtained using the JEOL JXA-8500F Hyperprobe at the University of Hawai'i. Maps were collected using a 15-kV accelerating voltage and a 300- to 500-nA beam current, with dwell times between 100 and 200 ms/pixel.

Electron Backscatter Diffraction

Crystal orientations were confirmed using the HKL Nordlys EBSD detector on the JEOL JSM-5900LV scanning electron microscope at the University of Hawai'i (UH). Final polishing with a 50- to 70-nm colloidal silica suspension for 4 h on a vibratory polisher improved the quality of electron backscatter patterns (EBSPs). Measurements were made using a 70° sample tilt, 25-kV accelerating voltage, and a working distance of 16–17 mm. Grids of 10 × 10 individual analysis spaced at least 10 μm apart achieved average mean angular deviation values of <1°. The EBSPs were processed using the HKL Technology *Channel 5* software package, and axis locations were output into lower hemisphere stereographic projections.

Laser Ablation Inductively Coupled Plasma Mass Spectrometry

Trace element analyses for 10 transects in 7 olivine crystals were acquired by laser ablation inductively coupled plasma mass spectrometry (LA-ICPMS) using the same methodology of Lynn et al. (2018). Only seven elements were analyzed in our routine (^{7}Li, ^{23}Na, ^{27}Al, ^{29}Si, ^{31}P, ^{52}Cr, and ^{60}Ni), which allowed significantly longer dwell times on Li (65 ms) than typical for multi-element (e.g., 20+) routines (<10 ms per element). The Ni abundances were measured here to compare with previous EPMA analyses (Lynn et al., 2017) and are not discussed further. Both Na and Cr showed inconsistent relationships with Li and P zoning and are not discussed here. Measurements were made with a Photon Machines Analyte G2 excimer laser connected to an iCAP Q ICPMS in an Ar–He atmosphere at the Earth Observatory of Singapore (Nanyang Technological University). Machine settings were optimized to reduce oxide production and interferences by achieving a ThO^{+} signal intensity of <0.6% of the Th^{+} signal. The laser was run at 70% output, 5.9 J cm^{-2} fluence, and frequency of 8 Hz with constant voltage. Twenty seconds of background signal (laser off) was acquired followed by 40 s sample ablation.

Measurements utilized 10 × 50-μm spots oriented with the 50-μm length parallel to the crystal-melt boundary (**Supplementary Figure S1**). An 11-μm spacing was used to avoid overlap and to create a 1-μm separation between individual spot analyses. Data reduction in Iolite© (Paton et al., 2011) removed the first and last 3 s of counts for each analysis before converting counts to concentrations. Analyses with fluctuations or spikes in the counts that might represent ablation of Cr-spinel, glass, or fluid inclusions were removed from the dataset before processing. The internal reference isotope ^{29}Si was used to convert raw counts to concentrations based on the EPMA measurements of SiO_2 in olivine (data from Lynn et al., 2017). The NIST 612 silicate glass was used to calibrate relative sensitivities for Li (40.2 ppm), P (46.6 ppm), and Al (10746 ppm). NIST 610 and USGS BCR-2G were run as unknowns (see **Supplementary Material**). The three reference materials were analyzed in between each olivine transect to monitor instrumental drift. Analytical precision (2σ) values for repeated measurements of NIST 612 glass are 0.83 ppm for Li (compared with 1.3 ppm given error on preferred GeoReM value), 206 ppm for Al (GeoReM error 212 ppm), and 6.3 ppm for P (GeoReM error 6.9 ppm; **Supplementary Material**). Measured values were compared with the GeoReM database preferred values (Jochum et al., 2011, 2016) to assess data quality. Average 2σ errors for Li measurements of KT olivine crystals were calculated by Iolite© (Paton et al., 2011) and are typically ±0.08 ppm for Li abundances of 1–3, ±6 ppm for Al abundances of 100s of ppm, and ±10 ppm for P abundances of 10s to 100s of ppm.

Nanoscale Secondary Ion Mass Spectrometry

High-resolution nanoSIMS analyses of Li and P zoning were collected for two crystals based on coupled increases of Li and P concentrations observed in LA-ICPMS profiles. The isotopes of ^{31}P and ^{7}Li were measured using different beam sources on the Cameca Ametek nanoSIMS 50L at Arizona State University. Samples were sputtered with a $^{133}Cs^{+}$ primary beam of 100 pA to measure P and a $^{16}O^{-}$ primary beam of 100 pA to measure Li. An electron gun was used to compensate sample charge. Both trace elements were normalized to ^{30}Si, measured in each routine, in order to monitor possible instrumental drift. Point analyses were collected to identify zones of interest before high-resolution line scans were made. Areas 50 × 50 μm (256 × 256 px) were pre-sputtered to acquire ion images that were used to precisely orient line scans perpendicular to bands of P and Li enrichment. Line scans were collected using a 0.5-μm beam (3 × 3 px) for 500 cycles with a dwell time of 10–20 ms/px and are reported as accumulated counts. Line scans were run past the crystal-melt boundary into regions of adhering glass to isolate mixed signals and remove possible edge effects. The San Carlos olivine standard (NMNH 111312-42; a split specifically characterized for its trace element composition; E. Hauri, personal communication, 2017) was measured with a 5 × 5-μm raster (128 × 128 px) with a dwell time of 1 ms/px for 10 blocks and 10 cycles/block. Phosphorus (23.4 ± 1.2 ppm) and Li concentrations (1.63 ± 0.08 ppm; E. Hauri, unpublished) were used to convert count ratios of $^{31}P/^{30}Si$

and $^{7}Li/^{30}Si$ to concentrations. There is excellent correlation between the $^{31}P/^{30}Si$ ratio and ^{31}P counts (R^2 = 0.9762) and the $^{7}Li/^{30}Si$ ratio and ^{7}Li counts (R^2 = 0.9998), demonstrating that the ratios depend primarily on their trace element concentrations and were not strongly affected by ^{30}Si variations or instrument drift (**Supplementary Figure S2**).

RESULTS

Lithium and P zoning in the Kīlauea olivine crystals follow two systematic and distinct behaviors: non-coupled and coupled. Non-coupled behavior usually shows a smooth gradient in Li with 1–2 ppm variation over 10s to 100s of μm between the crystal core and rim (**Figure 1A**), which is amenable to diffusion modeling. Diffuse, non-coupled Li zoning always occurs in transects where P concentrations are low (a few 10s of ppm) and homogeneous within LA-ICPMS error (typically ∼10 ppm; **Figure 1A**). We chose to use the term "non-coupled" because it indicates simply that the P and Li concentrations are not correlated. The term "uncoupled" (used by Tang et al., 2017) or "decoupled" implies that the trace elements may have been coupled originally. Non-coupled profiles occur in olivine crystals with both normal ($Li_{core} > Li_{rim}$; **Figure 1**) and reverse zoning ($Li_{core} < Li_{rim}$). These profiles from Kīlauea olivine were previously interpreted to represent diffusive re-equilibration initiated by late-stage magmatic intrusions and were modeled to extract the timing and duration of magma mixing and transport (Lynn et al., 2018).

In "coupled" Li and P zoning profiles, abrupt changes in Li concentration are positively correlated with variations in P (**Figure 1B**). Zoning of Li typically increases on the order of 15–80% (0.3–1.6 ppm), compared with P variations that can be up to 2,800% (10s to 100s of ppm) across an entire profile. Six of the analytical profiles (4 of 7 crystals) have coupled Li + P zoning. Coupled Li does not systematically correlate with Al.

Both non-coupled and coupled behaviors of Li + P are observed in some olivine crystals (**Figure 2**). The core-to-rim transects in these crystals have broad regions of diffuse Li zoning (occurring at P concentrations of only a few 10s of ppm) and

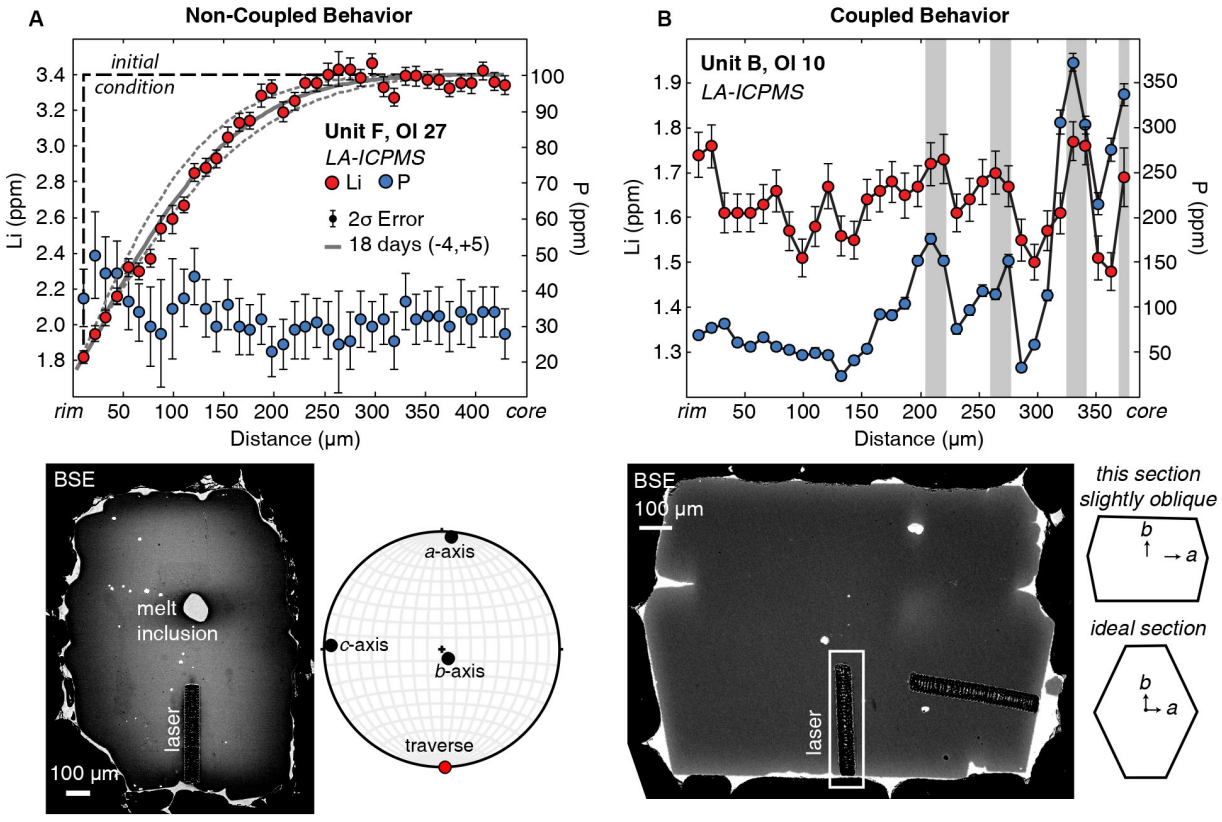

FIGURE 1 | Examples of non-coupled and coupled Li behaviors in Kīlauea olivine. **(A)** Non-coupled behavior of Li. Diffuse Li is strongly zoned, whereas P concentrations are low and essentially non-zoned outside the error bars. The gray line through the Li data is the 1D diffusion model best fit of 18 days, and the dashed lines represent model uncertainties of –4 and +5 days (Lynn et al., 2018) that reflect the 2σ analytical error and spacing of analyses (1 spot per 11 μm) Additional timescale uncertainties related to temperature calculations (±10°C; Helz and Thornber, 1987) are on average 10% of the timescales calculated for a given profile. The BSE image (lower left) and EBSD lower hemisphere stereonet projection show that the traverse was done parallel to the *a*-axis. **(B)** Coupled behavior of Li. Regions of high P marked by gray bars also correspond to regions of high Li, produced by elemental charge balancing requirements imposed during crystal growth. The orientation of this crystal was estimated by comparing the 2D section with an ideal olivine section taken perpendicular to the *c*-axis (e.g., Shea et al., 2015a). The traverse was collected roughly parallel to the *b*-axis.

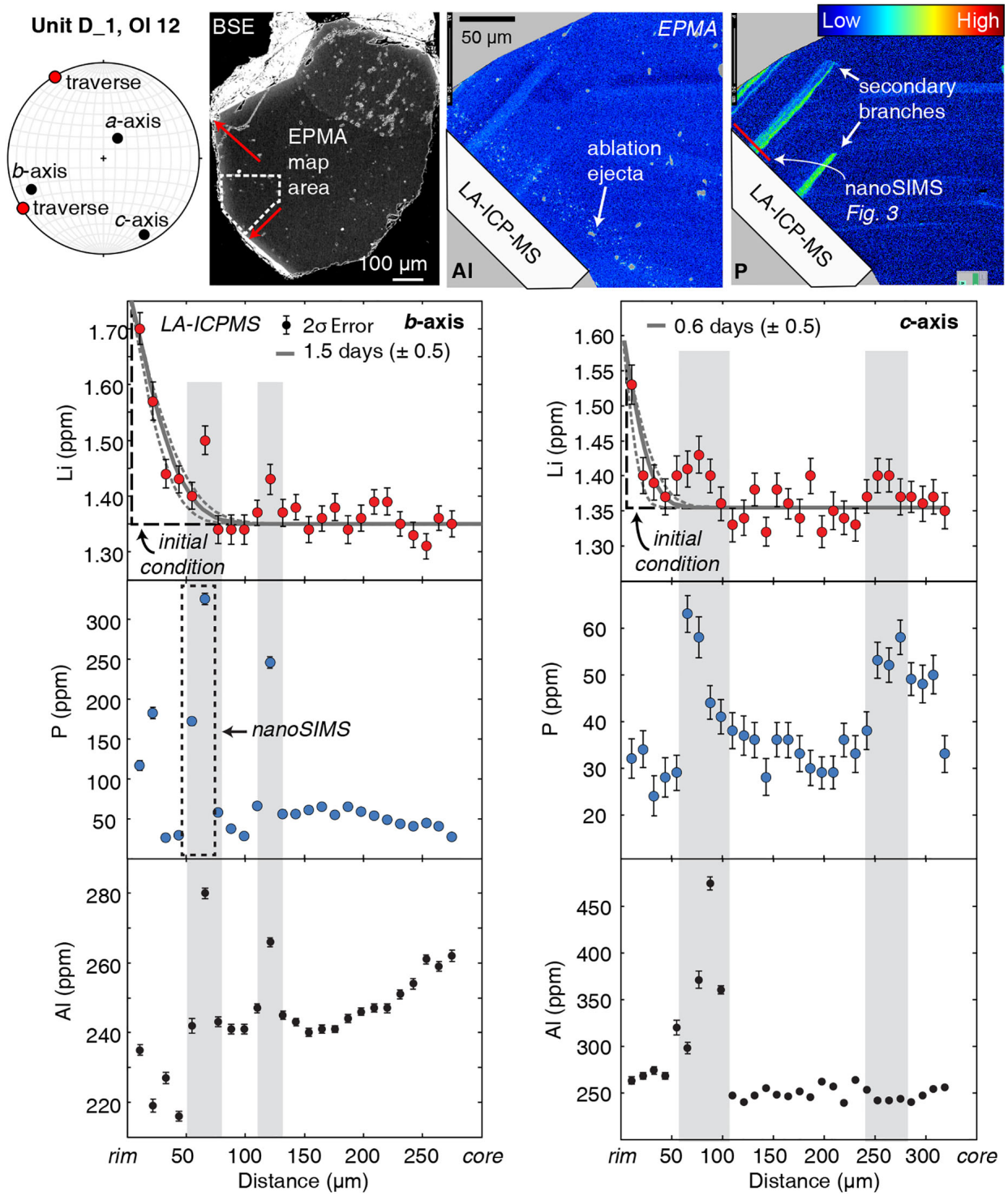

FIGURE 2 | Two transects that show both non-coupled and coupled behaviors of Li and P. The two profiles (marked by red arrows on BSE image) from the same olivine crystal parallel to the *b*- and *c*-axes have diffuse zoning of lithium that can be fit with 1D diffusion models. The gray line through the Li data is the model best fit, and the dashed lines represent model uncertainties that reflect the 2σ analytical error and spacing of analyses (1 spot per 11 µm; Lynn et al., 2018). Additional timescale uncertainties related to temperature calculations (±10°C; Helz and Thornber, 1987) are on average 10% of the timescales calculated for a given profile. These profiles also contain enrichment peaks (marked by gray bars) that have correlated Li and P enrichments. In this example, Al is also positively correlated with Li and P. The EPMA X-ray maps for Al and P show correlations in enrichment peak regions. The red line on the P X-ray map indicates the location of the nanoSIMS profile shown in **Figure 3**, which measured the enrichment peak outlined in the dashed black box.

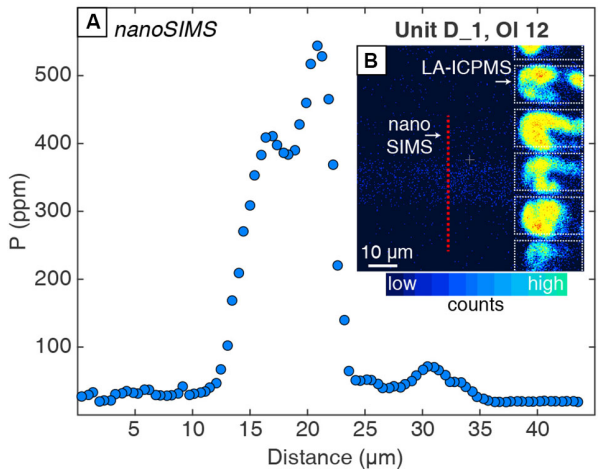

FIGURE 3 | (A) NanoSIMS profile across an enrichment peak in Unit D_1 Ol 12 (dashed black box from **Figure 2**). **(B)** The nanoSIMS ion image shows that the enrichment peak (~15 µm wide in blue on nanoSIMS image) is straddled by two laser ablation pits, demonstrating how small enrichment features can be distorted or homogenized by coarser beam size analytical routines. LA-ICPMS pits (dotted white boxes) appear to have high counts because the ablated crystal in those regions is poorly polished (e.g., not a true reflection of counts or concentration). Analytical error is smaller than the symbol size.

10- to 30-µm-wide regions of elevated Li + P. In such complex profiles, coupled Li + P usually occurs as abrupt increases in concentration relative to adjacent portions of the crystal. These locally coupled regions are herein referred to as "enrichment peaks." LA-ICPMS profiles reveal peaks with a 10–20% (0.1–0.6 ppm) increase of Li and a 300–900% (10s to 100s of ppm) increase of P compared with adjacent analyses (**Figure 2**). Where present, Li enrichment peaks are always correlated with P enrichments. Aluminum, another trace element in olivine that is commonly but not always positively correlated with P, is not systematically correlated with Li enrichment peaks.

Measurements by nanoSIMS show that enrichment peaks have much higher concentrations (e.g., 550 vs. 340 ppm; *b*-axis profile in **Figure 2** vs. **Figure 3**) than measured by LA-ICPMS because of the much smaller analytical spot size (e.g., <1 µm vs. 10 µm, respectively). The shape of this peak is better defined in the nanoSIMS profile, which shows a doublet in P zoning (**Figure 3**) that is not resolved by LA-ICPMS (**Figure 2**). Another enrichment peak that is 15 µm wide in a Unit K1 olivine has 700 ppm P measured by nanoSIMS, but the peak is absent in the LA-ICPMS profile from the same crystal (**Figure 4**).

The coupled vs. non-coupled behaviors can be distinguished by distinct trends in P vs. Li expressed as cations per four oxygens (atoms per formula unit; **Figure 5**). Non-coupled behavior shows a near-vertical trend with variable Li at relatively constant P. Coupled Li and P covary positively with a shallow slope and relatively high R^2 values (**Figure 5**). Analytical profiles that exhibit both behaviors can be divided into two groups of data with either a near-vertical trend or a shallow positive trend (**Figure 5C**).

DISCUSSION

Coupled and non-coupled behaviors of Li with P zoning in olivine clearly distinguish signatures of crystal growth and diffusive re-equilibration. These features provide a framework for applying Li geospeedometry in olivine. The abundances, zoning styles, and spatial variations in Li and P correlations are used in the following sections to (a) examine the value of high-resolution analytical methods for discerning and interpreting small-scale zoning features to understand trace element behavior in minerals; (b) provide insights into the mechanisms controlling non-coupled and coupled Li zoning; (c) illustrate the complex, 3D distribution of these elements; (d) test diffusion models on coupled Li and P enrichment peaks; and (e) provide guidelines for applying and interpreting Li geospeedometry in olivine.

High-Resolution Is Needed to Characterize Enrichment Peak Features

The spatial resolution of trace element analyses affects the magnitude of apparent enrichment relative to non-zoned portions of crystals (e.g., Bouvet de Maisonneuve et al., 2016; Shea et al., 2019). Trace element enrichment peaks in olivine that reflect rapid crystal growth are typically less than a few 10s of µm wide (e.g., Welsch et al., 2013, 2014; Shea et al., 2015b, 2019; Manzini et al., 2017). Analytical methods with large beam sizes (e.g., this LA-ICPMS method with 10-µm-wide spots) or continuous scanning (e.g., raster method; Bouvet de Maisonneuve et al., 2016) smear fine-scale trace element zoning and yield reduced concentrations in these peaks. Finer beam size methods such as nanoSIMS (<1 µm beam size) allow details of the enrichment peaks to be revealed (**Figures 2**, **3**; see also Manzini et al., 2017). Two olivine crystals were analyzed with LA-ICPMS and nanoSIMS methods to assess the loss of information that occurs when using coarse analytical methods such as laser ablation. The LA-ICPMS profile shows a 20-µm-wide Li + P enrichment peak near the crystal rim with P concentrations of 340 ppm (**Figure 2**), enriched by about a factor of ~7 compared with the nearby non-zoned regions characterized by ~50 ppm P. The nanoSIMS analyses of the same peak revealed a P doublet ~10 µm wide with up to 550 ppm (**Figure 3**). The 60% higher concentration of P and presence of a doublet in the nanoSIMS profile illustrate the superiority of this method for resolving fine-scale details about trace element zoning in olivine as well as other minerals (e.g., Manzini et al., 2017; Tang et al., 2017; Seitz et al., 2018). Thus, coarse-resolution methods such as laser ablation are not suitable for characterizing and subsequently modeling the enrichment peak features.

Mechanisms Controlling Non-coupled and Coupled Li Zoning

Diffusion Generates Broad Non-coupled Lithium Zoning

The majority of Li profiles are dominantly non-coupled and amenable to diffusion modeling. In these profiles, P concentrations are low, a few 10s of ppm, and there is no correlation of P with Li content (**Figure 5**). Thus, we propose here that Li is not charge balancing P or other elements at such

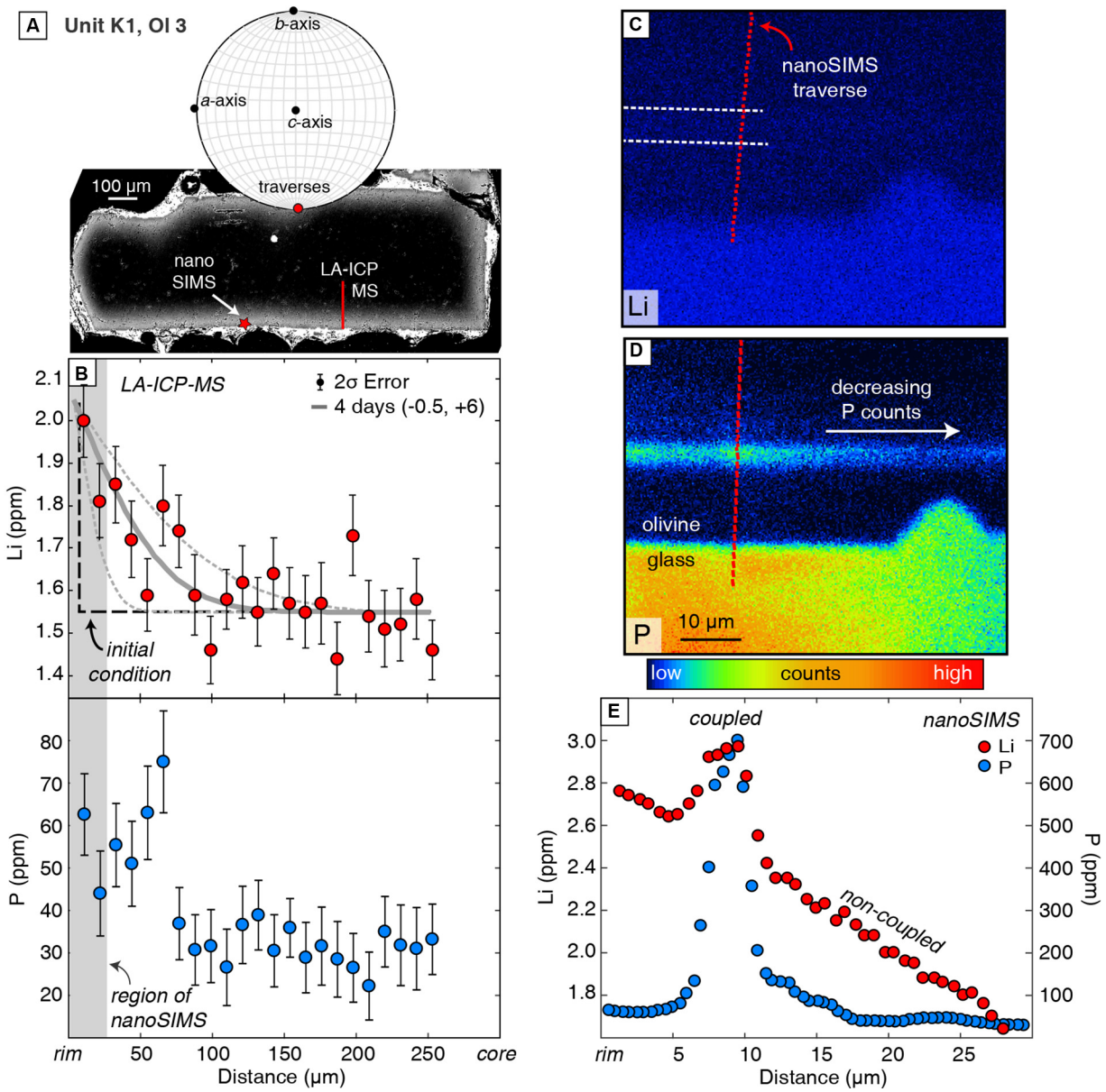

FIGURE 4 | LA-ICPMS and nanoSIMS data for traverses parallel to the *b*-axis in Unit K1, Ol 3. **(A)** The BSE image (upper left) and EBSD lower hemisphere stereonet projection show that this crystal is elongated along the *a*-axis and was sectioned perpendicular to the *c*-axis. **(B)** Overall diffuse zoning of Li and low P concentrations, as measured by LA-ICPMS with modeled timescale and uncertainties associated with analytical error and spatial resolution (described above). **(C,D)** NanoSIMS ion images show that proximal to the olivine–melt boundary, there is a <10-µm enrichment peak with coupled Li and P. **(E)** NanoSIMS measurements across the enrichment peak, showing coupled P and Li in the peak region and steadily increasing, non-coupled Li surrounding it. Analytical error on all nanoSIMS data is smaller than the symbol size.

low concentrations (typically <50 ppm) and is able to diffuse readily. Charge balancing for P substitution in the tetrahedral site is balanced by other ionic species (Al, Cr, Fe^{3+}) and/or vacancies (Eqs 2–4). Aluminum charge balances most or all of the P budget in low-P regions of both natural and experimental olivine (Shea et al., 2019). Regions of both low P and Al (e.g., <100 molar ppm) have an approximately 1:1 correlation (region "3" on Figure 10b in Shea et al., 2019). Thus, P is balanced by Al in low-P regions, and Li is unaffected by charge balance requirements.

In the absence of charge balancing requirements, we propose that Li atoms diffuse within the olivine lattice via the slower vacancy diffusion mechanism of ^{7}Li inferred for low-Li basaltic systems (Dohmen et al., 2010; Lynn et al., 2018). This interpretation is supported by our previous documentation of both normally and reversely zoned Li profiles in diverse olivine populations within these samples (Lynn et al., 2018). This indicates a common origin for the non-coupled Li profiles via re-equilibration after magma mixing, yielding timescales that range

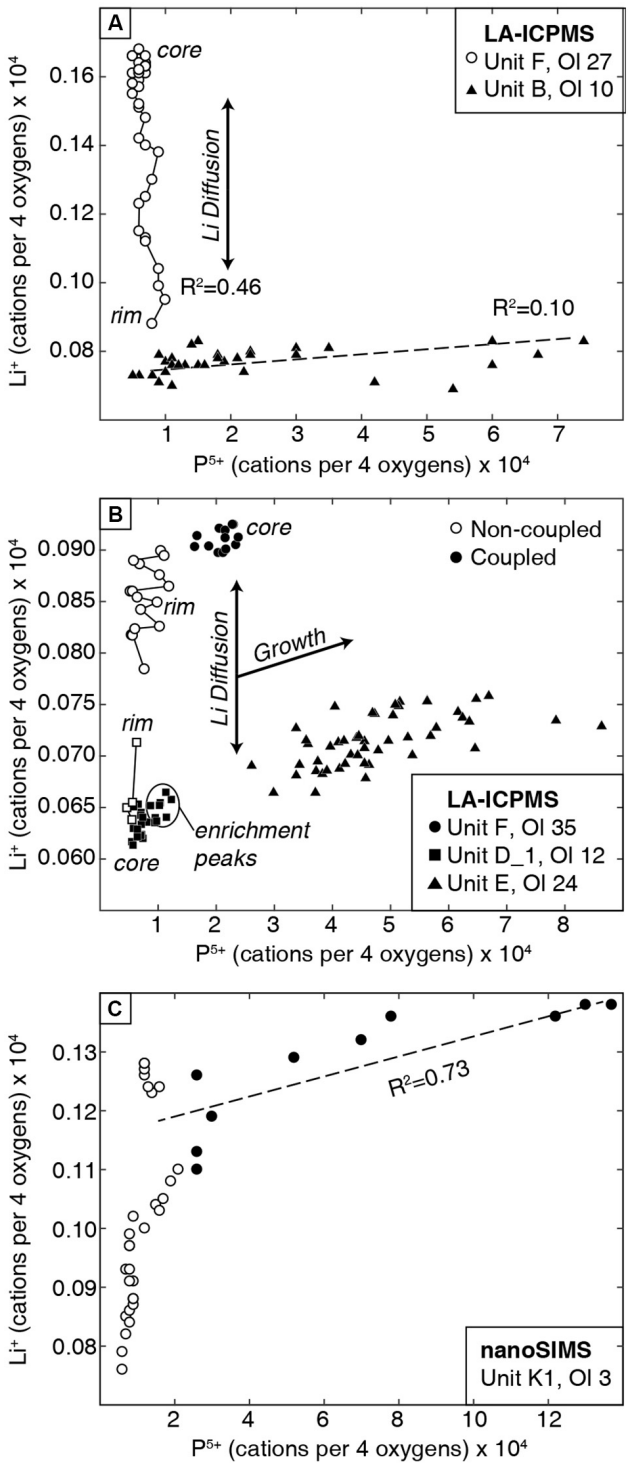

FIGURE 5 | P^{5+} vs. Li^{+} for olivine transects, as cations per formula unit of four oxygens, measured by **(A,B)** LA-ICPMS and **(C)** nanoSIMS. Non-coupled (open symbols) and coupled (filled symbols) data have different slopes that represent either diffusive re-equilibration or crystal growth. Solid lines connect non-coupled Li profiles that are generated via diffusive re-equilibration. Non-coupled data have variable Li content with minimal variation in P. These trends are clearer in the nanoSIMS data (bottom panel), which show distinct differences in slope for coupled vs. non-coupled Li and P.

from hours to days that were interpreted to reflect late-stage magma mixing and ascent.

Charge Coupling of Li and P in Enrichment Peaks Record Crystal Growth

Lithium enrichment peaks are always positively correlated with P enrichments that are 10s to 100s of ppm higher than in regions of low P (e.g., **Figures 2**, **4**). This coupled behavior is consistent with the charge balancing substitution reaction in Eq. 1 and therefore reflects growth, not diffusion. The high-resolution nanoSIMS measurements show systematic and positive correlation between P and Li within an enrichment peak (**Figure 5C**), indicating that Li in these regions is likely utilized for charge balancing. The similar widths of the Li and P peaks support this interpretation (**Figure 4E**). Lithium is also two orders of magnitude less abundant than P measured in the enrichment peaks (1–3 ppm vs. 100s of ppm; **Figure 5**), indicating that charge coupling will dominate the behavior of Li in these regions. This is consistent with interpretations of ppb level Li contents charge coupling with 10^2–10^4 ppm concentrations of Y + REE in zircon (Rubin et al., 2017; Tang et al., 2017; Wilson et al., 2017). Thus, we interpret that Li enrichment peaks are generated during crystal growth as Li^{+} ions in octahedrally coordinated Mg sites in olivine charge balance P^{5+} ions occupying tetrahedral sites (Woodland et al., 2004; Mallmann et al., 2009).

Lithium enrichments are inconsistently correlated with Al, another trace element that is commonly but not always associated with P zoning (Evans et al., 2008; Milman-Barris et al., 2008; Welsch et al., 2013, 2014; Zhukova et al., 2017; Shea et al., 2019). Uncommon correlations of Li and Al are likely a consequence of multiple charge balancing relationships that share P as a common element (e.g., Eqs 1, 3, and 4). Aluminum charge balances most of the P budget, the behavior of Al during crystal growth is different from P, and Al is frequently a marker for sector zoning in olivine, contrary to P zoning (Pack and Palme, 2003; Milman-Barris et al., 2008; Shea et al., 2019). Thus, the non-systematic correlation of Li with Al in enrichment peaks probably results from several charge balancing equations accommodating most of the budget of P-rich zones.

A Model of Coexisting Growth and Diffusion Signatures

Interpreting non-coupled vs. coupled Li signatures in olivine—and subsequently extracting timescales of magmatic processes from Li zoning—requires careful consideration of zoning variations in individual transects and distributions across 2D olivine sections. Current models of P zoning in olivine (e.g., Welsch et al., 2014) demonstrate how coupled and non-coupled (i.e., growth and diffusion) Li zoning patterns may occur within individual transects and single olivine crystals (**Figure 6**).

The initial dendritic or hopper morphology of rapidly growing olivine (Donaldson, 1976) is recorded by P-rich (and by extension, Li-rich) zones (**Figure 6A**). Phosphorus zoning is concentrated during rapid crystal growth in both primary and secondary branches that are usually <10 μm wide; they represent a minor fraction of the olivine volume (**Figure 6B**, following Welsch et al., 2014). Most of the olivine volume has low P, as

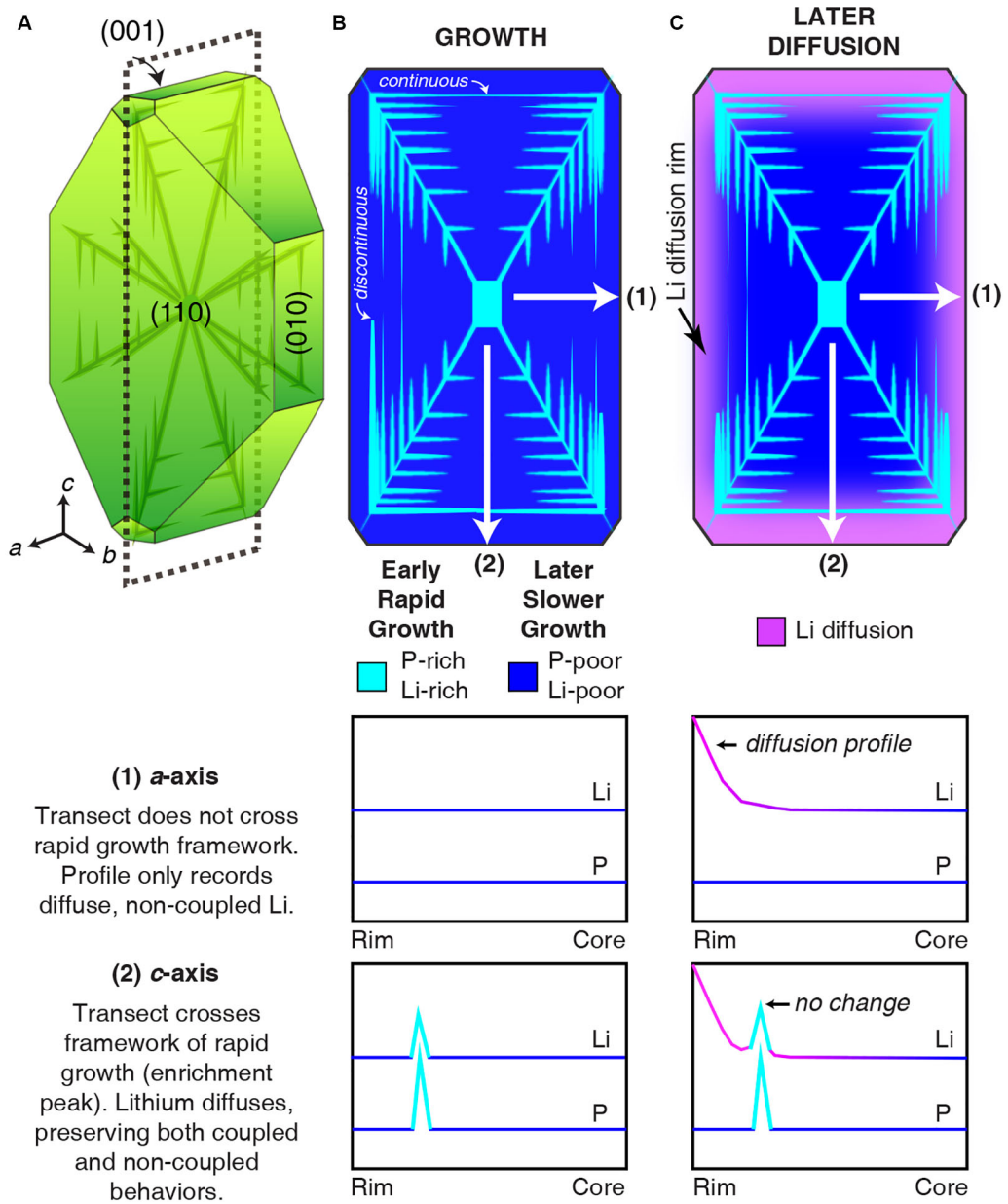

FIGURE 6 | Illustration of Li and P zoning resulting from growth and diffusion. **(A)** Euhedral olivine crystal with volumetrically small P-rich skeletal structure (e.g., Welsch et al., 2014). Dashed line marks the plane of the section perpendicular to the *b*-axis. **(B)** Zoning of Li + P rich skeleton (light blue) from rapid growth surrounded by Li- and P-poor compositions from later slow growth during crystal maturation (dark blue). Li- and P-rich zones in secondary branches may be discontinuous or continuous. White lines mark the locations of compositional profiles presented below the section. **(C)** Zoning generated by subsequent diffusion of Li (pink rim). Transect 1 has a diffusive rim with no change to the Li enrichment peak. Transect 2 shows Li diffusion in the absence of growth-related enrichment peak zoning. P is unchanged throughout the diffusion process due to its slow diffusivity (Watson et al., 2015) and short time elapsed (hours to days) in this scenario.

maturation of an initially skeletal crystal leads to in-filling under slower growth conditions. Thus, most of the area in 2D sections will have low P concentrations (a few 10s of ppm; **Figure 6B**). Because Li is interpreted to not charge balance low-P regions, non-coupled Li throughout most of the olivine volume permits diffusive re-equilibration as a dominant signature for zoning (**Figure 6C**, *a*-axis profile). Due to the complex distribution of P zoning in 3D, analytical traverses within a single 2D section may sample both fine-scale P-rich zones and low-P regions (**Figure 6C**, *c*-axis profile). Thus, individual profiles that exhibit both non-coupled and coupled Li behaviors record both crystal growth and subsequent diffusion processes.

Multiple transects collected within a single olivine crystal in this study record different Li and P zoning patterns as a result of this complex 3D distribution of trace elements. Within the olivine crystal in **Figure 4**, LA-ICPMS and

nanoSIMS profiles located 100s of μm apart from each other record different trace element zoning patterns. Lithium exhibits dominantly non-coupled behavior in the LA-ICPMS profile where maximum P concentrations are up to ∼80 ppm. In contrast, the nanoSIMS profile reveals a clear enrichment peak of 700 ppm P and 3 ppm Li about 8 μm away from the crystal rim (**Figure 4E**). Differences in zoning between these profiles may be due to the loss of information from the 10-μm-wide LA-ICPMS analyses traverse (as discussed above). However, 2D sectioning through complex 3D distributions of trace elements likely also plays a role. The nanoSIMS ion image of P zoning in **Figure 4E** shows clearly decreasing counts along the length of the secondary branch toward the direction of the LA-ICPMS profile (**Figure 4A**). Thus, the Li- and P-rich zone sampled by the nanoSIMS traverse in **Figure 4** is likely not continuous along the crystal face and was not sampled by the LA-ICPMS traverse. This example underscores the complexities of interpreting 1D transects that sample complex 3D distributions of trace elements in olivine. Collecting multiple traverses from well-oriented crystals is essential for using trace element zoning for robust interpretations of geologic processes.

Lithium Enrichment Peak Chronometry

Diffusion Models of Enrichment Peaks

Transects exhibiting both coupled and non-coupled Li behaviors (**Figure 2**) contradict the notion that rapid diffusion of Li in olivine should homogenize zoning over hours to days within basaltic systems. Here we apply diffusion models to the highly resolved nanoSIMS enrichment peaks of Li and P, as has been done for Li in zircon (e.g., Rubin et al., 2017), to assess the potential impacts of coupled diffusion on Li timescales. The results are used to determine whether these fine-scale features can be used to extract meaningful information about magmatic processes.

Coupled Li in enrichment peaks is likely controlled by the slower diffusion of P (Watson et al., 2015) because charge balanced elements within the olivine lattice are susceptible to sharing coupled fluxes during diffusive re-equilibration (Lasaga, 1979; Ganguly, 2002). Several diffusion models for the nanoSIMS Li profiles were run assuming either non-coupled or coupled behavior to test whether coupled fluxes influence Li diffusion in enrichment peaks. Non-coupled Li diffusion proceeds at the expected "slow" rate for Li in basaltic systems following the vacancy mechanism of Dohmen et al. (2010). Coupled Li diffusion is assumed to be slowed to the rate of phosphorus diffusion (D_P; Watson et al., 2015) due to charge coupling. These assumptions yield radically different diffusion timescales because the diffusion coefficient for phosphorus at 1,200°C is 3.5 orders of magnitude slower than Li ($D_P = 10^{-18.1}$ m^2/s vs. $D_{7Li} = 10^{-14.6}$ m^2; Watson et al., 2015; Dohmen et al., 2010).

Finite difference diffusion models were applied to the coupled nanoSIMS peaks in **Figure 4** to evaluate whether one or both of these diffusion coefficients are viable for applying Li geospeedometry in enrichment peaks. We used the non-concentration dependent one-dimensional form of Fick's second law (Crank, 1975):

$$\frac{\partial C}{\partial t} = D\frac{\partial^2 C}{\partial x^2} \tag{5}$$

where C is concentration (ppm), t is time (s), D is the diffusion coefficient (m^2/s), and x is distance (m). The diffusion coefficient of Li (D_{7Li}) parallel to the c-axis can be calculated using the Arrhenius relation (Dohmen et al., 2010):

$$\log\left(D_{7Li}\right) = -5.92\,(\pm 1.0) - 1.2847 \times \frac{10^4}{T(K)} \tag{6}$$

where T is temperature. This expression is appropriate for diffusion in olivine containing 1–10 ppm Li and temperatures 800–1,200°C (Dohmen et al., 2010). The diffusion coefficient of P in olivine can be calculated using the Arrhenius relation (Watson et al., 2015):

$$D_P = 10^{-10.06\pm 0.08}\exp\left(\frac{-229 \pm 16}{RT(K)}\right) \tag{7}$$

where R is the ideal gas constant (8.314 J/mol K). The Li enrichment peak was modeled using both D_{7Li} and D_P to assess potential timescales of non-coupled and coupled diffusion, respectively.

The model temperature was assumed to be constant at 1,237°C (taken from Li diffusion models in Lynn et al., 2018) and was calculated using the Kīlauea glass MgO thermometer (uncertainty of ±10°C; Helz and Thornber, 1987) and the inferred melt Mg# in equilibrium with olivine rim Fo contents ($Kd^{ol/melt}_{Fe-Mg}$=0.343 ± 0.018; Matzen et al., 2011). This value is akin to the magma temperature for mixing and diffusion recorded in the near-rim olivine composition (Lynn et al., 2017, 2018). This approach is suitable for our modeling here because the nanoSIMS enrichment peak is located very near to the crystal-melt boundary (**Figure 4**).

Initial conditions (C_0; the composition of the enrichment peak prior to diffusion) have a high degree of uncertainty, and several were estimated due to the absence of a compositional plateau in the enrichment peak. We assessed this effect on retrieved timescales by testing four assumptions: (1) the initial peak had a flat plateau near the maximum measured concentration, (2) the initial peak had a "dipping plateau" akin to sectioning the enrichment peak off-center from its maximum value, (3) the initial peak plateau was higher than maximum measured value, and (4) the initial peak was tapered with a maximum value higher than that measured in the profile (**Table 1**). An additional model was run to fit the non-coupled region of the profile assuming that Li ions diffused through the enrichment peak without significantly modifying it. This follows the hypothesis of inter-site reaction diffusion, where Li ions may diffuse quickly through P-rich regions by hopping between site vacancies and/or interstitial sites and vacancies associated with P. This is analogous to previous studies of H^+ diffusion in olivine, where H^+ was decorating pre-existing defects associated with trace elements like Ti (Jollands et al., 2016). Boundary conditions were set to P and Li concentrations in the far field around the enrichment peaks, and Li values were constrained by the core composition measured by LA-ICPMS in **Figure 4** and **Table 1**.

TABLE 1 | Timescales of diffusive re-equilibration for diffusion models using the Unit K1 olivine 3 coupled enrichment peak in **Figure 4**.

Initial condition	$Li_{initial}$ (ppm)	$Li_{far\ field}$ (ppm)	t_{Li} (D_{Li}) (min)	t_{Li} (D_P) (days)	$P_{initial}$ (ppm)	$P_{far\ field}$ (ppm)	t_P (D_P) (days)
C_0 1	3.0	1.5	2.8	6.0	720	67	5.5
C_0 2	Sloping	1.5	2.7	5.0	Sloping	67	5.5
C_0 3	3.1	1.5	10.5	11.6	800	67	11.2
C_0 4	Tapered	1.5	17.0	28.0	Tapered	67	13.0
C_0 5	Enrichment peak	1.5 (core) 2.8 (rim)	576 (9.6 h)	–	–	–	–

*C_0 are the assumed initial and far field conditions prior to the onset of diffusion, where 1, 2, and 3 represent the different assumptions shown on **Figure 7**. D_{Li} is the diffusion coefficient from Dohmen et al., 2010 (slower mechanism of ^{7}Li diffusion) and D_P from Watson et al. (2015).*

Interpreting Enrichment Peak Timescales

Modeling the Li enrichment peak in **Figure 4** using D_{Li} (Dohmen et al., 2010) yields a diffusion timescale of 2.8–17 min depending on the initial condition assumptions (**Table 1** and **Figure 7**). These timescales are far too short to reflect a magma mixing event prior to eruption, and they do not agree with timescales from non-coupled Li profiles (hours to days; Lynn et al., 2018). It is also unlikely that they represent the time elapsed between crystal growth and eruption. The short Li timescales are also inconsistent with diffusion timescales recorded by the P peak (using D_P; Watson et al., 2015), which are much longer and range from 5.5 to 13 days (**Table 1**). Inconsistent Li and P timescales modeled here support the interpretation that Li + P are likely coupled in enrichment peak regions. Thus, Li enrichment peaks should not be modeled using D_{Li}.

If instead the Li peak is fit using the diffusion coefficient for P (Watson et al., 2015), the resulting Li timescales are broadly congruent with P and range from 5.0 to 28 days (**Table 1**). Regardless of the assumed initial conditions, congruent timescales derived from using D_P to model both profiles suggest that Li in enrichment peaks is subject to coupled diffusive fluxes with P. These durations are also generally consistent with the late-stage magma mixing timescales of hours to days obtained from non-coupled Li zoning in other Kīlauea olivine crystals (generally hours to days, but up to a few weeks; Lynn et al., 2018). Thus, diffusion chronometry of enrichment peak features in olivine might need to account for coupled diffusive fluxes by using D_P to model coupled Li behavior.

An additional model was run to fit the non-coupled portion of the nanoSIMS profile assuming that Li ions diffuse through the enrichment peak without significantly modifying it. Following this inter-site reaction hypothesis, the enrichment peak does not hinder the movement of Li ions, and the timescale retrieved reflects the non-coupled diffusion of Li from the olivine core to its rim. The retrieved timescale is 9.6 h, but we note that the 25-μm nanoSIMS profile lacks a clear core plateau and only samples a small part of the olivine rim. The 9.6-h duration is shorter than the timescale of several days modeled for the full crystal's LA-ICP-MS profile in **Figure 5**, which is likely a symptom of incompletely measuring the full diffusion profile from core to rim.

Caveats and Challenges With Modeling Enrichment Peaks

Several caveats and challenges limit the application of enrichment peak chronometry despite the congruency between Li and P timescales derived from our nanoSIMS profiles. Interpreting timescales from enrichment peaks is made difficult by their 3D distribution within the olivine volume during initial rapid growth (e.g., Welsch et al., 2014). The enrichment peak from **Figure 4** is located within 15 μm of the crystal-melt boundary and could plausibly be related to a late-stage process occurring shortly before eruption. However, there is increasing consensus that mineral chemistry from core to rim (following the canonical "tree-ring" approach) does not provide chronological records of the magmatic histories (e.g., Welsch et al., 2014; Shea et al., 2015b, 2019). Phosphorus-rich zones located near crystal rims can be products of early stages of crystal growth, invalidating the geologic interpretation of the timescales retrieved here.

Model temperatures are also uncertain, as the thermal history associated with the early crystal growth is not well recorded and the entire crystal history is likely not isothermal. Temperatures calculated for Kīlauea magmas using the glass MgO thermometer (Helz and Thornber, 1987) and the inferred melt MgO in equilibrium with the olivine forsterite content (using the Fe–Mg partition coefficient K_D = 0.343 ± 0.008 of Matzen et al., 2011) likely record a more recent temperature history for the olivine crystals than the early P-rich zones experienced. Thus, a more detailed examination of P zoning in high resolution, the timescales derived from enrichment peaks, and their distribution across 2D sections is needed before using these features to characterize magmatic histories.

The enrichment peak diffusion timescales are also highly uncertain due to the absence of initial plateaus in our nanoSIMS data. Our retrieved timescales are largely insensitive to the shape of our initial conditions (flat vs. dipping plateau) but are strongly affected by the concentration chosen for the plateau (**Figure 7**). At present, few studies have measured P zoning profiles in high resolution (Bouvet de Maisonneuve et al., 2016; Manzini et al., 2017), and those profiles generally lack clear compositional plateaus. Fewer P profiles have been modeled for diffusive re-equilibration (e.g., Manzini et al., 2017), and uncertainty related to unknown initial conditions was not addressed. Because the P-rich zones introduce an extremely steep compositional contrast with nearby low-P regions (100s vs. 10s of ppm), P may never preserve an initial plateau, and constraining an appropriate initial condition would be impractical. The assumption of a step function across branch may also be inappropriate—growth models of fine-scale P-rich zones show they are subject to micrometer-scale P zoning at their edges instead of sharp boundaries with adjacent low-P regions (Shea et al., 2019). In this

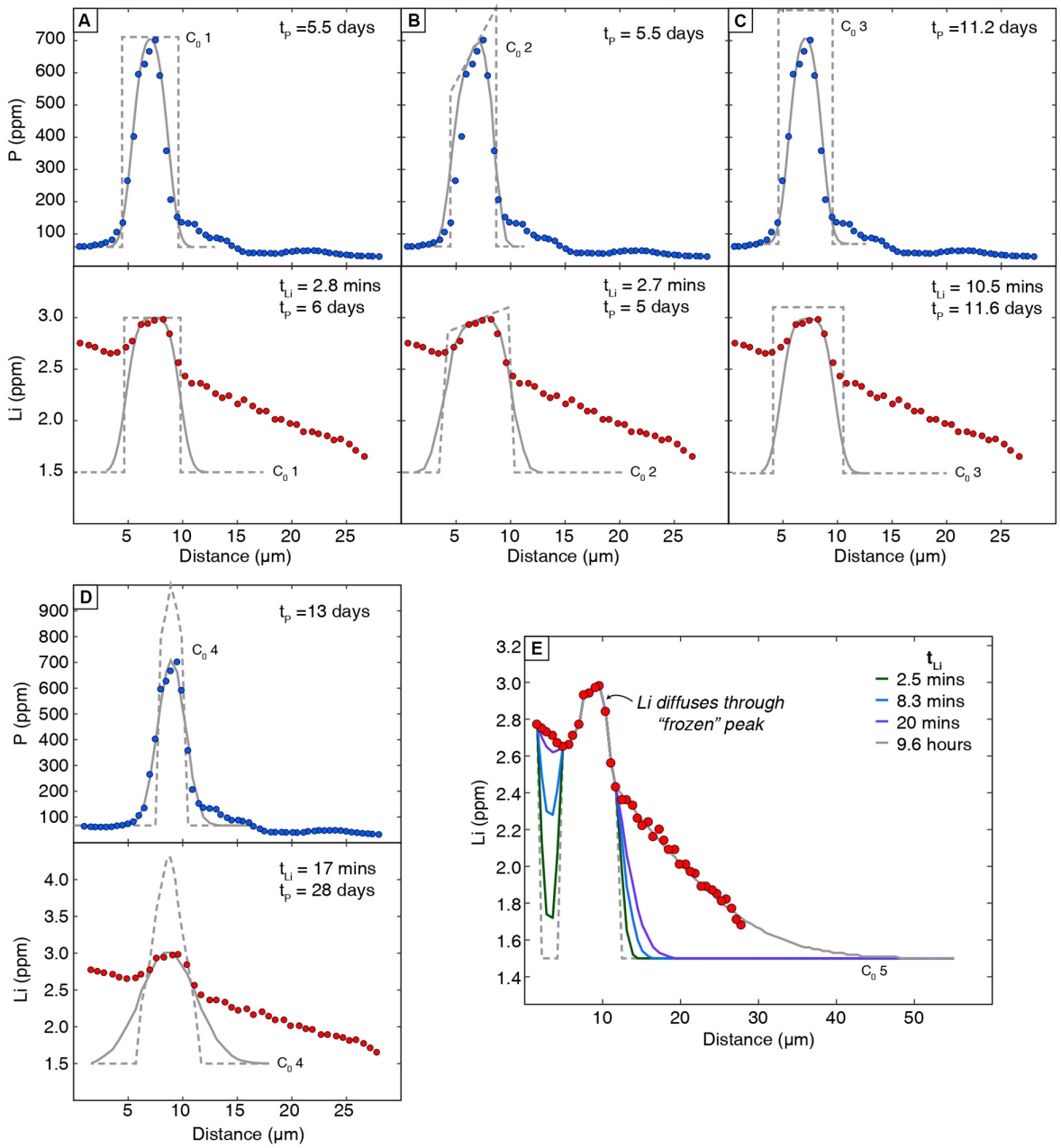

FIGURE 7 | Diffusion models of Li and P enrichment peaks with different assumed initial conditions (C_0; dashed lines). Analytical error on all nanoSIMS data is smaller than the symbol size. Model fits are shown in solid gray lines. Lithium peaks were modeled assuming that the sloped region surrounding the enrichment peak was generated by non-coupled Li diffusion and is not fit here. Initial conditions were constrained by the Li content at the core of the olivine crystal (1.5 ppm far field; from LA-ICPMS data in **Figure 5**) and different assumptions about peak compositions: **(A)** a flat plateau near the maximum value measured in the profile (C_0 1), **(B)** a "sloping" plateau from a non-ideal section through the enrichment peak (C_0 2), **(C)** a higher plateau than measured (actual value unknown; C_0 3), and **(D)** a tapered initial condition with a maximum value greater than was measured (actual value unknown; C_0 4). Li timescales represent models that utilized the diffusion coefficient for Li (t_{Li}; Dohmen et al., 2010) and for P (t_P; Watson et al., 2015). **(E)** Additional model to fit the non-coupled portion of the profile assuming inter-site reactions allows Li ions to diffuse through the enrichment peak without modifying it significantly (after models for H diffusion; Jollands et al., 2019).

case, the measured enrichment peaks may dominantly reflect crystal growth and minimal diffusive re-equilibration.

A remaining challenge with enrichment peaks is understanding how Li ions diffuse within peaks and/or the regions surrounding them. The assumptions of coupled diffusion for the models above follow recent studies on zircon in assuming that Li mobility is dependent on P in these regions and diffusion through the peaks is slowed relative to adjacent regions. However, Li may hop between sites and vacancies in the olivine lattice via an inter-defect site reaction behavior, as has been shown for H^+

(e.g., Jollands et al., 2016, 2019). If Li diffusion occurs via site reactions, then the assumption of Li and P diffusive coupling ($D_{Li} = D_P$) is invalid. Inter-defect site reactions would allow Li to diffuse through the peak regions, rather than being slowed within them. Regardless of how Li behaves in/around peak regions, we maintain that enrichment peak features should not be modeled for timescales.

Finally, collecting enough Li and P enrichment peak profiles for accurate timescales modeling is both analytically challenging and potentially expensive. At least 20 profiles are needed to accurately constrain diffusion timescales in a given olivine population, and complex zoning or magmatic histories warrant more (Shea et al., 2015a). Measurements of Li and P by nanoSIMS require different primary beams ($^{16}O^-$ and $^{133}Cs^+$, respectively), so the minimum number of timescales suggested by Shea et al. (2015a) requires at least 40 profiles measured by nanoSIMS to characterize 20 enrichment peaks. Given the caveats, challenges, and analytical difficulty of measuring and modeling nanoSIMS profiles of Li and P, fine-scale enrichment peaks in olivine are unlikely to be viable chronometers for most studies.

Guidelines for Applying Lithium Geospeedometry in Olivine

The dual behavior of both coupled and non-coupled Li zoning within individual olivine crystals provides a framework on how to apply Li geospeedometry in basaltic systems. Diffuse, non-coupled profiles of Li should be modeled using D_{Li} (vacancy mechanism from Dohmen et al., 2010; Lynn et al., 2018). This approach is applicable to both normally and reversely zoned lithium profiles to provide timescales for magma mixing events shortly (hours to days) before eruption in basaltic systems. Lithium enrichment peaks in olivine should only be modeled if high-resolution analyses resolve many peaks well (e.g., with nanoSIMS), an initial plateau can be identified, and better constraints on the diffusion mechanism controlling Li in peak regions (e.g., coupled, inter-defect site reactions) can be defined. Ideally, these coupled Li timescales should also be interpreted in context with other diffusion chronometers.

The complexities arising from coupled Li behavior may be avoided by modeling only non-coupled Li profiles that are greater than a few 10s of μm wide, minimizing the risk of increasing Li at the rim caused by coupled enrichments of P and Li. Coupled Li and P can also be avoided by preferentially selecting and measuring well-oriented olivine crystals. Crystals with obvious skeletal morphologies (**Figure 6**) should be avoided because they represent the blueprint of crystal growth with pervasive P-rich zones. In the case of thin sections, crystals should be screened for those closest to perpendicular to the *a*- or *b*-axis, and 1D traverses should be taken in the center of well-defined crystal faces to take advantage of incomplete secondary branching (e.g., **Figure 4**).

Ideally, euhedral olivine crystals should be sectioned through crystal cores, perpendicular to a crystallographic axis. Preferential sectioning of olivine crystals perpendicular to the *a*-axis and traverses parallel to the *b*-axis would be most likely to yield non-coupled Li profiles for modeling. Olivine crystals are commonly initially elongated along the *a*-axis, and branches rich in Li and P are concentrated in the *a*–*c* plane during rapid growth (Mourey and Shea, 2019). Subsequent maturation and slower olivine growth occur along the *b*-axis, resulting in low-P regions that allow diffusive re-equilibration of non-coupled Li. Sectioning perpendicular to the *b*-axis and measuring parallel to the *c*- or *a*-axis may reduce the chances of crossing P-rich zones (Welsch et al., 2014; cf. our **Figure 1A**).

CONCLUSION

Carefully oriented and sectioned olivine crystals provide a unique opportunity to document trace element zoning and the timescales of processes in basaltic magmas. Profiles using Li zoning are especially important for characterizing magma mixing events just prior to eruption (hours to days). Combining profiles of Li and P zoning using EMPA, LA-ICPMS, and nanoSIMS methods in rapidly quenched olivine from explosive Kīlauea eruptions reveals systematic differences between records of crystal growth and subsequent diffusive re-equilibration.

(1) Lithium and phosphorus have two distinct relationships in olivine: (a) non-coupled, wherein Li diffuses over 10–300 μm of low P concentrations (a few 10s of ppm) and is amenable to diffusion modeling, and (b) coupled, in which Li and P covary positively and reflect a framework of rapid crystal growth.
(2) Both non-coupled and coupled behaviors can be preserved in a single crystal because the dendritic nature of early rapid growth results in trace element enrichments that are volumetrically limited within the olivine. The preservation of Li and P enrichment peaks within diffusion profiles is a consequence of Li maintaining local (e.g., few μm scale) growth-induced charge balancing with P.
(3) Li is always systematically coupled to P enrichments, although P zoning may also be correlated with other trace elements (e.g., Al). We interpret this to reflect crystal growth processes and the role of P in driving the charge balancing requirements in the olivine lattice.
(4) Robust interpretations of trace element zoning documented by 1D analytical transects require knowledge of the 2D and 3D spatial distribution given the complexity of zoning generated during crystal growth.

These observations provide a framework for identifying Li profiles suitable for diffusion modeling. The following practical guidelines are recommended:

- Avoid crystals with skeletal or dendritic morphologies. They probably contain pervasive P-rich zones with coupled Li.
- Euhedral crystals should be preferentially sectioned perpendicular to the *a*- or *b*-axis. For randomly sectioned olivine (i.e., thin sections), crystals should be screened to avoid sections highly oblique to the *a*- or *b*-axis.
- Analytical traverses should be taken parallel to crystallographic axes and in the center of well-formed faces to maximize potential of sampling between incomplete secondary branches. Two optimal orientations for measuring non-coupled Li are (1) perpendicular to the

a-axis with a traverse measured parallel to the *b*-axis and (2) perpendicular to the *b*-axis with traverses measured parallel to either the *a*- or *c*-axis.
- Collect Li and P data concurrently to discern if profiles are significantly affected by charge coupling. If P data are unavailable, modeling diffuse non-coupled Li that is both normally and reversely zoned within a single eruption (e.g., as a result of magma mixing) is suitable.
- Model only wider non-coupled profiles (many 10s of μm) with a well-defined core plateau delineating the initial conditions.

The complexities documented here for olivine highlight the need for careful geochemical studies using well-oriented crystals to resolve the disparate interpretations drawn from trace element zoning in other silicate minerals such as zircon.

DATA AVAILABILITY STATEMENT

All datasets generated for this study are included in the article/**Supplementary Material**.

AUTHOR CONTRIBUTIONS

KL conducted LA-ICPMS, EPMA, and EBSD analyses. KL and MG collected nanoSIMS data. All authors assisted in sample collection, contributed to the interpretations. KL led the writing of the manuscript.

FUNDING

This work was supported by the Fred M. Bullard Graduate Fellowship at the University of Hawai'i and the National Science Foundation (NSF) East Asia and Pacific Summer Institutes grant OISE1513668 to KL. Additional support was provided by NSF grants EAR1347915 and EAR1449744 to MG, and EAR1725321 to TS. This is SOEST contribution number 10977.

ACKNOWLEDGMENTS

We thank the Smithsonian Institution National Museum of Natural History for San Carlos standard NMNH 111312-42 and Erik Hauri for unpublished trace element values for this specific split of the standard. We thank Eileen Chen for support with sample preparations, and for assistance with analytical techniques, we also thank Eric Hellebrand (EPMA), Gareth Fabbro and Fidel Costa (LA-ICPMS), and Zan Peeters and Maitrayee Bose (nanoSIMS). We appreciate editorial handling by DN and constructive reviews from PT and EM, which helped to improve this manuscript.

SUPPLEMENTARY MATERIAL

The Supplementary Material for this article can be found online at: https://www.frontiersin.org/articles/10.3389/feart.2020.00135/full#supplementary-material

REFERENCES

Agrell, S. O., Charnley, N. R., and Ghinner, G. A. (1998). Phosphoran olivine from Pine Canyon, Piute Co., Utah. *Miner. Mag.* 62, 265–269. doi: 10.1180/002646198547620

Beck, P., Chaussidon, M., Barrat, J. A., Gillet, P. H., and Bohn, M. (2006). Diffusion induced Li isotopic fractionation during the cooling of mafic rocks: the case of pyroxene phenocrysts from nakhlite meteorites. *Geochim. Cosmochim. Acta* 70, 4813–4825.

Boesenberg, J. S., Ebel, D. S., and Hewins, R. H. (2004). *An Experimental Study of Phosphoran Olivine and its Significance in Main Group Pallasites*. Houston, TX: Lunar Planet Sci Conf, 1366.

Boesenberg, J. S., and Hewins, R. H. (2010). An experimental investigation into the metastable formation of phosphoran olivine and pyroxene. *Geochim. Cosmochim. Acta* 74, 1923–1941. doi: 10.1016/j.gca.2009.12.008

Bouvet de Maisonneuve, C., Costa, F., Huber, C., Vonlanthen, P., Bachmann, O., and Dungan, M. A. (2016). How do olivines record magmatic events? Insights from major and trace element zoning. *Cont. Min. Petrol.* 171:56. doi: 10.1007/s00410-016-1264-6

Charlier, B. L. A., Morgan, D. J., Wilson, C. J. N., Wooden, J. L., Allan, A. S. R., and Baker, J. A. (2012). Lithium concentration gradients in feldspar and quartz record the final minutes of magma ascent in an explosive supereruption. *Earth Planet. Sci. Lett.* 319-320, 218–227. doi: 10.1016/j.epsl.2011.12.016

Cooper, K. M., Till, C. B., Kent, A. J. R., Costa, F., Rubin, A. E., Gravley, D., et al. (2017). Response to comment on "Rapid cooling and cold storage in a silicic magma reservoir recorded in individual crystals. *Science* 358, 1–2. doi: 10.1126/science.aam8720

Crank, J. (1975). *The Mathematics of Diffusion*, 2nd Edn. Oxford: Oxford Science Publications.

Dohmen, R., Kasemann, S. A., Coogan, L., and Chakraborty, S. (2010). Diffusion of Li in olivine. Part I: experimental observations and a multi species diffusion model. *Geochim. Cosmochim. Acta* 74, 274–292. doi: 10.1016/j/gca.2009.10.1016

Donaldson, C. H. (1976). An experimental investigation of olivine morphology. *Contrib. Miner. Petrol.* 57, 187–213. doi: 10.1007/BF00405225

Edmonds, M. (2015). Partitioning of light lithophile elements during basalt eruptions on Earth and application to Martial shergottites. *Earth Planet. Sci. Lett.* 411, 142–150. doi: 10.1016/j.epsl.2014.11.034

Ellis, B. S., Szymanowski, D., Magna, T., Neukampf, J., Dohmen, R., Bachmann, O., et al. (2018). Post-eruptive mobility of lithium in volcanic rocks. *Nat. Commun.* 9:3228. doi: 10.1038/s41467-018-05688-2

Evans, T. M., O'Neill, H. S. C., and Tuff, J. (2008). The influence of melt composition on the partitioning of REEs, Y, Sc, Zr, and Al between forsterite and melt in the system CMAS. *Geochim. Cosmochim. Acta* 72, 5708–5721.

Gallagher, K., and Elliott, T. (2009). Fractionation of lithium isotopes in magmatic systems as a natural consequence of cooling. *Earth Planet. Sci. Lett.* 278, 286–296. doi: 10.1016/j.epsl.2008.12.009

Ganguly, J. (2002). Diffusion kinetics in minerals: principles and applications to tectono-metamorphic processes. *EMU Notes Miner.* 4, 271–309.

Garcia, M. O., Mucek, A. E., Lynn, K. J., Swanson, D. A., and Norman, M. D. (2018). "Geochemical evolution of Keanakako'i Tephra, Kilauea Volcano, Hawai'i," in *Field Volcanology: A Tribute to the Distinguished Career of Don Swanson*, eds M. Poland, M. Garcia, V. Camp, and A. Grunder (London: Geol Soc Am Sp Pap), 538.

Grant, K. J., and Wood, B. J. (2010). Experimental study of the incorporation of Li, Sc, Al, and other trace elements into olivine. *Geochim. Cosmochim. Acta* 74, 2412–2428. doi: 10.1016/j.gca.2010.01.015

Helz, R. T., and Thornber, C. R. (1987). Geothermometry of Kilauea Iki lava lake Hawaii. *Bull. Volc.* 49, 651–688.

Jochum, K. P., Weis, U., Schwager, B., Stoll, B., Wilson, S. A., Haug, G. H., et al. (2016). Reference values following ISO guidelines for frequently requested rock

reference materials. *Geostand. Geoanal. Res.* 40, 333–350. doi: 10.1111/j.1751-908X.2015.00392.x

Jochum, K. P., Weis, U., Stoll, B., Kuzmin, D., Qichao, Y., Raczek, I., et al. (2011). Determination of reference values for NIST SRM 610-617 glasses following ISO guidelines. *Geostand. Geoanal. Res.* 35, 397–429. doi: 10.1111/j.1751-908X.2011.00120.x

Jollands, M. C., Hermann, J., O'Neill, H. St. C., Spandler, C., and Padrón-Navarta, J. A. (2016). Diffusion of Ti and some divalent cations in olivine as a function of temperature, oxygen fugacity, chemical potentials and crystal orientation. *J. Petrol.* 57, 1983–2010. doi: 10.1093/petrology/egw067

Jollands, M. C., Kempf, E., Hermann, J., and Müntener, O. (2019). Coupled inter-site reaction and diffusion: rapid dehydrogenation of silicon vacancies in natural olivine. *Geochim. Cosmichim. Acta* 262, 220–242. doi: 10.1016/j.gca.2019.07.025

Lasaga, A. C. (1979). Multicomponent exchange and diffusion in silicates. *Geochim. Cosmochim. Acta* 43, 455–469. doi: 10.1016/0016-7037(79)90158-3

Lynn, K. J., Garcia, M. O., Shea, T., and Costa, F. (2017). Timescales of mixing and storage for Keanakāko'i Tephra magmas (1500-1823 C.E.), Kīlauea Volcano, Hawai'i. *Contrib. Miner. Petrol.* 172:76. doi: 10.1007/s00410-017-1395-4

Lynn, K. J., Shea, T., Garcia, M. O., Costa, F., and Norman, M. D. (2018). Lithium diffusion in olivine records magmatic priming of explosive basaltic eruptions. *Earth Planet. Sci. Lett.* 500, 127–135. doi: 10.1016/j.epsl.2018.08.002

Mallmann, G., O'Neill, H. S. C., and Klemme, S. (2009). Heterogeneous distribution of phosphorus in olivine from otherwise well-equilibrated spinel peridotite xenoliths and its implications for the mantle geochemistry of lithium. *Contrib. Miner. Pet.* 158, 485–504. doi: 10.1007/s00410-009-0393-6

Manzini, M., Bouvier, A.-S., Baumgartner, L. P., Müntener, O., Rose-Koga, E. F., Schiano, P., et al. (2017). Weekly to monthly time scale of melt inclusion entrapment prior to eruption recorded by phosphorus distribution in olivine from mid-ocean ridges. *Geology* 45, 1059–1062. doi: 10.1130/G39463.1

Matzen, A. K., Baker, M. B., Beckett, J. R., and Stolper, E. M. (2011). Fe–Mg partitioning between olivine and high-magnesian melts and the nature of Hawaiian parental liquids. *J. Petrol.* 52, 1243–1263. doi: 10.1093/petrology/egq089

Milman-Barris, M. S., Beckett, J. R., Backer, M. B., Hofmann, A. E., Morgan, Z., Crowley, M. R., et al. (2008). Zoning of phosphorus in igneous olivine. *Contrib. Miner. Pet.* 155, 739–765. doi: 10.1007/s00410-007-0268-7

Mourey, A. J., and Shea, T. (2019). Forming olivine phenocrysts in basalt: a 3D characterization of growth rates in laboratory experiments. *Front. Earth Sci.* 7:300. doi: 10.3389/feart.2019.00300

Pack, A., and Palme, H. (2003). Partitioning of Ca and Al between forsterite and silicate melt in dynamic systems with implications for the origin of Ca, Al-rich forsterites in primitive meteorites. *Meteorl. Planet. Sci.* 38, 1263–1281.

Parkinson, I. J., Hammond, S. J., James, R. H., and Rogers, N. W. (2007). High-temperature lithium isotope fractionation: insights from lithium isotope fractionation in magmatic systems. *Earth Planet. Sci. Lett.* 257, 609–621. doi: 10.1016/j.epsl.2007.03.023

Paton, C., Hellstrom, J., Paul, B., Woodhead, J., and Hergt, J. (2011). Iolite: freeware for the visualization and processing of mass spectrometric data. *J. Anal. At Spectrom.* 26:2508. doi: 10.1039/c1ja10172b

Rubin, A. E., Cooper, K. M., Till, C. B., Kent, A. J. R., Costa, F., Bose, M., et al. (2017). Rapid cooling and cold storage in a silicic magma reservoir recorded in individual crystals. *Science* 356, 1154–1156.

Seitz, S., Putlitz, B., Baumgartner, L., Meibom, A., Escrig, S., and Bouvier, A.-S. (2018). A nanoSIMS investigation on timescales recorded in volcanic quartz from the silicic Chon Aike Province (Patagonia). *Front. Earth Sci.* 6:95. doi: 10.3389/feart.2018.00095

Shea, T., Hammer, J., Hellebrand, E., Mourey, A., Costa, F., First, E., et al. (2019). Phosphorus and aluminum zoning in olivine: contrasting behavior of two nominally incompatible trace elements. *Contrib. Miner. Petrol.* 174:85. doi: 10.1007/s00410-019-1618-7

Shea, T., Costa, F., Krimer, D., and Hammer, J. E. (2015a). Accuracy of timescales retrieved from diffusion modeling in olivine: a 3D perspective. *Am. Miner.* 100, 2026–2042. doi: 10.2138/am-2015-5163

Shea, T., Lynn, K. J., and Garcia, M. O. (2015b). Cracking the olivine zoning code: distinguishing between crystal growth and diffusion. *Geology* 43, 935–938. doi: 10.1130/G37082.1

Sliwinski, J. T., Keuter, N., Marxer, F., Ulmer, P., Guillong, M., and Bachmann, O. (2018). Controls on lithium concentration and diffusion in zircon. *Chem. Geol.* 501, 1–11. doi: 10.1016/jchemgeo.2018.09.038

Spandler, C., and O'Neill, H. S. (2010). Diffusion and partition coefficients of minor and trace elements in San Carlos olivine at 1,300°C with some geochemical implications. *Contrib. Miner. Pet.* 159, 791–818. doi: 10.1007/s00410-009-0456-8

Swanson, D. A., Rose, T. R., Fiske, R. S., and McGeehin, J. P. (2012). Keanakāko'i Tephra produced by 300 years of explosive eruptions following collapse of Kīlauea's caldera in about 1500 C.E. *J. Volcanol. Geotherm. Res.* 21, 8–25. doi: 10.1016/j.jvolgeores.2011.11.009

Tang, M., Rudnick, R., McDonough, W. F., Bose, M., and Goreva, Y. (2017). Multi-mode Li diffusion in natural zircons: evidence for diffusion in the presence of step-function concentration boundaries. *Earth Planet. Sci. Lett.* 474, 110–119. doi: 10.1016/j.epsl.2017.06.034

Tomascak, P. B., Magna, T., and Dohmen, R. (2016). *Advances in Lithium Isotope Geochemistry*. Switzerland: Springer International Publishing.

Trail, D., Cherniak, D. J., Watson, E. B., Harrison, T. M., Weiss, B. P., and Szumila, I. (2016). Li zoning in zircon as a potential geospeedometer and peak temperature indicator. *Contrib. Miner. Petrol.* 171:25. doi: 10.1007/s00410-016-1238-8

Ushikubo, T., Kita, N. T., Cavosie, A. J., Wilde, S. A., Rudnick, R. L., and Valley, J. W. (2008). Lithium in Jack Hills zircons: evidence for extensive weathering of Earth's earliest crust. *Earth Planet. Sci. Lett.* 272, 666–676. doi: 10.1016/j.epsl.2008.05/032

Vlastélic, I., Staudacher, T., Bachélery, P., Télouk, P., Neuville, D., and Benbakkar, M. (2011). Lithium isotope fractionation during magma degassing: constraints from silicic differentiates and natural gas condensates from Piton de la Fournaise volcano (Réunion Island). *Chem. Geol.* 284, 26–34. doi: 10.1016/j.chemgeo.2011.02.002

Watson, E. B., Cherniak, D. J., and Holycross, M. E. (2015). Diffusion of phosphorus in olivine and molten basalt. *Am. Miner.* 100, 2053–2065. doi: 10.2138/am-2015-5416

Welsch, B., Faure, F., Famin, V., Baronnet, A., and Bachèlery, P. (2013). Dendritic crystallization: a single process for all textures of olivine in basalts? *J. Petrol.* 54, 539–574. doi: 10.1093/petrology/egs077

Welsch, B., Hammer, J. E., and Hellebrand, E. (2014). Phosphorus reveals dendritic architecture of olivine. *Geology* 42, 867–870. doi: 10.1130/G35691.1

Weyer, S., and Seitz, H.-M. (2012). Coupled lithium- and iron isotope fractionation during magmatic differentiation. *Chem. Geol.* 294-295, 42–50. doi: 10.1016/j.chemgeo.2011.11.020

Wilson, C. J. N., Morgan, D. J., Charlier, B. L. A., and Barker, S. J. (2017). Comment on "Rapid cooling and cold storage in a silicic magma reservoir recorded in individual crystals. *Science* 8429, 1–2. doi: 10.1126/science.aap8429

Woodland, A. B., Seitz, H. M., and Yaxley, G. M. (2004). Varying behavior of Li in metasomatised spinel peridotite xenoliths from western Victoria, Australia. *Lithos* 75, 55–66. doi: 10.1016/j.lithos.2003.12.014

Zhang, Y. (2010). Diffusion in minerals and melts: theoretical background. *RIMG* 72, 5–59. doi: 10.2138/rmg.2010.72.2

Zhukova, I., O'Neill, H., and Campbell, I. H. (2017). A subsidiary fast-diffusing substitution mechanism of Al in forsterite investigated using diffusion experiments under controlled thermodynamic conditions. *Contrib. Miner. Petrol.* 172:53. doi: 10.1007/s00410-017-1365-x

Conflict of Interest: The authors declare that the research was conducted in the absence of any commercial or financial relationships that could be construed as a potential conflict of interest.

frontiers in Earth Science

ORIGINAL RESEARCH
published: 05 June 2020
doi: 10.3389/feart.2020.00157

Magma Plumbing During the 2014–2015 Eruption of Fogo (Cape Verde Islands)

Andreas Klügel[1], Simon Day[2], Markus Schmid[3] and Bruno Faria[4]*

[1] Fachbereich Geowissenschaften, Universität Bremen, Bremen, Germany, [2] Institute for Risk and Disaster Reduction, University College London, London, United Kingdom, [3] Department für Geo- und Umweltwissenschaften, Ludwig-Maximilians-Universität München, Munich, Germany, [4] Instituto Nacional de Meteorologia e Geofisica, Mindelo, Cape Verde

Phenocrysts in volcanic rocks are recorders of magmatic processes that have occurred at depth before and during a volcanic eruption. Our petrological investigations of stratigraphically controlled tephrite and phonotephrite samples from the latest eruption of Fogo (Cape Verde Islands) aimed to reconstructing magma storage and transport. The dates of sample emplacement have been determined using satellite instrument – derived high resolution thermal infrared maps. All samples are strongly phyric and commonly contain complexly zoned clinopyroxene crystals and cumulate fragments. Clinopyroxenes from all samples exhibit 10–50 μm wide rim zones, inferred to have grown in a few days to weeks during the ongoing eruption as a consequence of H_2O loss from the melt. Clinopyroxene-melt thermobarometry using tephrite groundmass compositions suggests that the rims formed at upper mantle pressures of around 600 MPa (21 km depth). This level is interpreted to reflect temporary reduction in magma ascent velocity by near-isobaric movement through a complex storage system. Previously, the tephrite magma had accumulated at a deeper level, possibly between 700 and 900 MPa as indicated by clinopyroxene cores (Mata et al., 2017). The cause for H_2O loss initiating rim growth could be degassing after rise of the magma from the deeper level, or CO_2 flushing by a carbonic fluid phase released at depth. Corresponding data from phonotephrites indicate last equilibration at around 440 MPa (16 km); the phonotephrite magma is inferred to be a residuum from an earlier magmatic event that was entrained by advancing tephrite. Microthermometry of CO_2-dominated fluid inclusions in tephrite clinopyroxenes results in pressures of around 330 MPa (12 km), indicating another short pause in magma ascent in the lowermost crust. Rim zonations of olivine phenocrysts indicate that after leaving this final stalling zone, the magma ascended to the surface in less than half a day. In strong contrast to these petrological equilibration depths, seismic events precursory to the eruption were located at < 5 km below sea level, with only two exceptions at 17 and 21 km depth consistent with our barometry. Our results enhance the understanding of this potentially dangerous volcano, which helps to interpret future pre-eruptive unrest.

Keywords: magma storage, magma ascent, thermobarometry, intraplate volcanism, petrology

OPEN ACCESS

Edited by:
Teresa Ubide,
University of Queensland, Australia

Reviewed by:
Silvio Mollo,
Sapienza University of Rome, Italy
Takeshi Kuritani,
Hokkaido University, Japan

****Correspondence:***
Andreas Klügel
akluegel@uni-bremen.de

Specialty section:
This article was submitted to Petrology, a section of the journal Frontiers in Earth Science

Received: *28 February 2020*
Accepted: *27 April 2020*
Published: *05 June 2020*

Citation:
Klügel A, Day S, Schmid M and Faria B (2020) Magma Plumbing During the 2014–2015 Eruption of Fogo (Cape Verde Islands). Front. Earth Sci. 8:157. doi: 10.3389/feart.2020.00157

INTRODUCTION

The eruptive behavior of a volcano is intrinsically related to the composition of its magmas and therefore to a variety of magmatic processes modifying them at depth. Whereas some processes produce detectable surface manifestations such as seismicity, deformation and degassing, others cannot be observed directly but can be reconstructed from their record in magmatic crystals and xenoliths. Information retrieved from minerals and their inclusions include depths and temperatures of magma storage, nature and rates of magmatic processes, degassing behavior, and rates of magma ascent (reviewed in Putirka and Tepley, 2008). During the last decades, our understanding of volcanoes and the underlying processes has improved through many detailed investigations of volcanic rock samples and application of modern microanalytical techniques (e.g., Davidson et al., 2007; Costa and Morgan, 2011; Cashman et al., 2017; Ubide et al., 2019). One major aim of petrological investigations is to reconstruct the depths of pre- and syn-eruptive igneous processes. A number of suitable and well-tested geobarometers exist, but obtaining accurate and precise data requires some analytical effort and careful consideration of equilibrium tests (Putirka, 2008, Putirka, 2016a; Mollo et al., 2013; Neave and Putirka, 2017; Neave et al., 2019; Ubide et al., 2019). For mineral-melt barometers, which are more precise than mineral-only barometers (Putirka, 2008), it is not always possible to obtain appropriate melt analyses if the matrix is not glassy. This problem can be circumvented by using whole-rock data for approximation (e.g., Mata et al., 2017) or phenocryst-corrected whole-rock data (Hildner et al., 2011), or by selecting a putative equilibrium melt composition from a data base (Barker et al., 2015; Neave and Putirka, 2017).

The petrological investigations only enable *post hoc* reconstructions of the magmatic processes that have affected any one sample before and during its eruption. It is therefore particularly rewarding if these reconstructions can be integrated with independent surveillance data (e.g., Kahl et al., 2011, 2013; Longpré et al., 2014). This requires that the timing of emplacement of the chosen samples, within the eruption, can be constrained by that surveillance data.

This study investigates a suite of chronologically-controlled samples from the 2014 to 2015 eruption of Fogo in the Cape Verde Islands. The samples were chosen on the basis of eyewitness accounts of the eruption, satellite monitoring data, and field observations of within-eruption stratigraphy that were made during sampling. They provide a sequence that covers most of the eruption and provide a base for detailed petrological investigation of its products. The focus of the study is on mineral-melt thermobarometry, fluid inclusion barometry, and investigation of mineral rim zonations. The aim of our study is to better understand the magma supply system to this eruption. As we show, the availability of a chronologically-controlled sample set can be very useful for the interpretation of petrological data.

GEOLOGICAL SETTING

The Cape Verde Islands, located in the Northern Atlantic ∼500–800 km west of the African coast between 15° and 17° N, consist of nine inhabited islands and several islets, all of volcanic origin (**Figure 1A**) and with a broadly decreasing age progression from east to west (Holm et al., 2008). They are on the Cape Verde Rise, the largest geoid and bathymetric seafloor anomaly on earth and the surface expression of the Cape Verde hotspot (Crough, 1978, 1982). Magmatism is dominated by silica-undersaturated alkaline melts of basanitic through phonolitic composition; carbonatites also occur.

Geological Overview of Fogo

Fogo is at present the most active volcano of the Cape Verde Islands with 28 eruptions since 1500 AD (Ribeiro, 1954; Torres et al., 1997) and a number of large explosive eruptions in prehistoric times (Eisele et al., 2015). The island has a diameter of ∼25 km and features an up-to 1 km high horseshoe-shaped depression open to the east, interpreted as the product of one (Day et al., 1999; Masson et al., 2008) or more (Marques et al., 2019) flank collapses, or a combination of vertical caldera collapses and flank collapse (Torres et al., 1997; Madeira et al., 2008; Martínez-Moreno et al., 2018; **Figure 1B**). The geological evolution of Fogo can be subdivided into four distinct phases according to Day et al. (1999) and Foeken et al. (2009): (1) The uplifted seamount series (∼4.5 Ma) is composed of carbonatites and alkalic basalts. (2) The Monte Barro Group includes the first subaerial lavas that unconformably overlie the seamount series. So far there are no absolute age determinations for this group. (3) The Monte Amarelo Group unconformably overlies the Monte Barro Group and formed after a period of cliff incision. Its deposits reach a total thickness of 2–3 km and consist mainly of highly alkalic, basic to intermediate lavas and scoria cones, probably entirely of Quaternary age. This volcanic phase ended with the giant lateral Monte Amarelo flank collapse(s), the age estimates of which range between 43 and 123 ka (Foeken et al., 2009; Ramalho et al., 2015; Madeira et al., 2019; Marques et al., 2019). (4) The post-collapse Cha das Caldeiras Group is primarily represented by an up to 2 km thick sequence (Day et al., 1999) infilling the collapse scar (Cha das Caldeiras plain and the 2829 m high Pico do Fogo), and by lava sequences on the outer flanks of the island that are mainly of basanitic to tephritic composition.

Petrological studies of Fogo provided detailed data for the magma plumbing systems of the 1951, 1995, and 2014–2015 eruptions (Munhá et al., 1997; Hildner et al., 2011, 2012; Mata et al., 2017), thermobarometric data for earlier eruptions (Hildner et al., 2012), and analyses of some melt inclusions (Moussallam et al., 2019). These studies showed that the erupted magmas were stored before eruption within the uppermost mantle between 15 and 30 km depth, and stalled during ascent within the lower crust at 8–13 km depth. There is no evidence for a shallow crustal magma reservoir to have existed during the eruptions studied. It is not uncommon that an eruption of mostly tephritic to basanitic magma was accompanied by small volumes of more

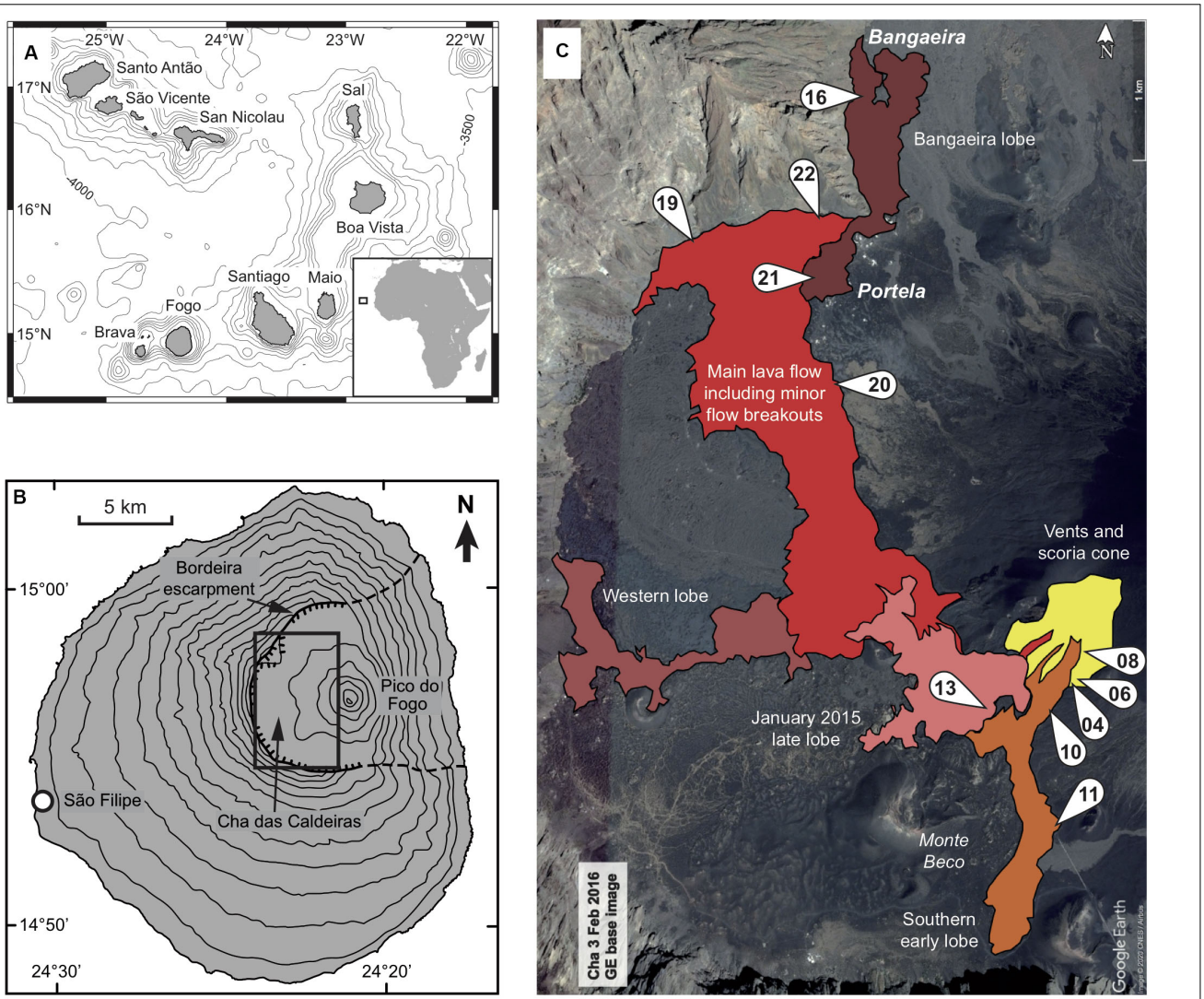

FIGURE 1 | (A) Map of the Cape Verde Islands with 500 m isobaths, and **(B)** overview map of Fogo with 200 m contours. **(C)** Detail map of the area outlined in **(B)** showing the extent of the lava flows emplaced during the 2014–2015 eruption. Numbers indicate the sample localities (e.g., 04 refers to sample SD04). Base map by Google, using data from CNES/Airbus.

differentiated (phonotephritic) magma. So far, no study has addressed possible variations in magma storage depth and plumbing dynamics during the course of a single eruption, because the temporal succession of samples was not known. Seismic monitoring data exist for only the two most recent eruptions, those of 1995 (Heleno da Silva et al., 1999) and 2014–15 (INMG network operated by one of us (BF) and discussed in Faria and Fonseca (2014).

Summary of the 2014–2015 Eruption

The following account is based partly on data from González et al. (2015), Worsley (2015), Cappello et al. (2016), Richter et al. (2016), Jenkins et al. (2017), and Mata et al. (2017), and on seismic data from the INMG network. Remarkably, the 2014–2015 eruption was not preceded by significant island-wide surface deformation (González et al., 2015). Seismic activity precursory to the eruption began on 4 October 2014 with a single magnitude (M) 2.5 seismic event around 17 km depth below sea level (b.s.l.), after which the rate of very weak background seismicity increased. The main seismic precursor of the eruption was a swarm beneath Pico do Fogo from 17 to 23 November, which involved almost 300 small events ($M < 2.5$) mostly at < 4 km b.s.l., except for one event on 21 November at 21 km b.s.l. Local surface deformation near Pico was recorded during 7 h prior to the start of the eruption. A fissure array opened on the morning of 23 November on the southwest flank of Pico, just near the site of the 1995 eruption (**Figures 1B,C**), and produced vigorous eruptive activity.

During the first days, hawaiian and strombolian activity prevailed whilst effusion of lava focused on one major vent at the southwest end of the initial fissure. Lava flows were produced

from the beginning of the eruption, in two major lobes to the northwest and to the south (**Figure 1C**). The southern lobe ceased to grow on 24 November as the effusive activity focused on the southwest end of the vent array, whilst the northwest lobe continued to grow into December. A'a lava dominated, with occasional breakouts of more fluid pa'hoe'hoe and a'a lava expanding the lava fields, especially to the north where new lobes destroyed large parts of the villages of Portela and Bangaeira. In mid-December activity temporarily decreased, but soon increased again and produced a new lava lobe to the west. In early January 2015, lava emission rates decreased and strombolian activity intensified, whilst in mid to late January vents at the southwest end of the vent array produced a new lava lobe that expanded to the southwest. In February explosive activity was at a low level, but intensified on 7 February for a short period, until cessation of volcanic tremor at 20h00 UTC marked the sudden end of the eruption.

MATERIALS AND METHODS

Sampling

The samples were collected in March 2015 during the dry season. The aim was to collect a set of samples covering the whole period of the eruption, from lava outcrops and pyroclastic units whose dates of emplacement were known or could at least be bracketed. The principal method for determining the age of emplacement of lavas was to sample at sites that were last incandescent on known dates, on the basis of infrared emission maps produced by B. Hirn and F. Ferrucci, using short-wave infrared and near-infrared bands monitored at 30 m pixel resolution by the Landsat 8 Operational Land Imager (OLI) and Earth Observing-1 Advanced Land Imager (ALI) instruments. The date of last incandescence for a lava surface would be later than the date of eruption of a sample collected from that surface, because of the finite travel time of the lava from its eruption site to its emplacement site. The dates were cross-checked with eyewitness reports, and with field observations that allowed determination of stratigraphic relationships of our samples to units of known age. Tephras and fragments of juvenile spatter were also collected near the eruptive vents and from an observation point on Monte Beco, where recognizable stratigraphies were present.

A key limitation of this approach was that cloud cover disrupted the time series of incandescence data, particularly between 24 November and 6 December 2014 when the northwestern flow lobe forming the main lava field south of Portela village was largely emplaced. Our sampling of this main phase was thus limited. In contrast, the southern lava flow early in the eruption and the later breakout lava flows were emplaced in periods of clear weather, and so the OLI and ALI data were extremely useful in sampling these parts of the lava field. However, the end of acquisition of high-resolution OLI and ALI data on 1 January 2015 meant that the sampling of near-vent lavas and pyroclastic deposits formed in early 2015 had to be based upon detailed field observations and the few eyewitness observations from that period. Finally, examination of ∼0.5 m pixel post-eruption panchromatic imagery from Pleiades and WorldView satellites in conjunction with those field observations also allowed the determination of age relationships between different lava flow lobes, and thus cross-checking the relative ages of samples.

A total of 23 samples of 2014–15 lavas and pyroclasts were collected, of which 11 were selected for this study. Sample locations and age constraints for these samples are provided in **Table 1**, and the locations are shown in **Figure 1C**. Petrographic investigations of the samples were carried out on a petrological microscope. Mineral contents were determined by point counting or visual estimate, and are given on a vesicle-free basis.

Electron Microprobe Analyses

Electron microprobe (EMP) analyses of phenocrysts were carried out on a Cameca SX-100 at the Faculty of Geosciences, Bremen University. Quantitative analyses used a focussed beam with an acceleration voltage/beam current of 15 kV/15 nA for clinopyroxene, 15 kV/20 nA for Fe-Ti oxides, and 20 kV/30 nA for olivine; peak counting times were 20 or 30 s. Calibrations used reference standards from the Smithsonian Institution (Jarosewich et al., 1980, 1987), and the built-in PAP correction was applied for data reduction. Analytical precision and accuracy were controlled by regular analyses of reference standards from the Smithsonian Institution along with the samples (**Supplementary Table S1**). In addition, qualitative measurements of element intensities along traverses were carried out with a focussed beam of 50 nA and a dwell time of 200 ms per point.

Laser-Ablation Inductively Coupled Plasma Mass Spectrometry (LA-ICP-MS)

The major element composition of microcrystalline to glassy groundmass was determined on thin sections by LA-ICP-MS, using a NewWave UP193 solid-state laser coupled to a ThermoFinnigan Element2 at the Faculty of Geosciences, Bremen University. Helium (∼0.8 l/min) was used as sample gas and argon (∼0.8 l/min) was subsequently added as make-up gas; plasma power was 1200 W. For each sample six to ten line scans (0.6 mm length, 5 μm/s scan speed, 100 μm spot size, 5 Hz laser pulse rate, irradiance of ∼1 GW/cm^2) were carried out. Positions of these scans were selected to cover representative areas of the groundmass. The isotopes ^{23}Na, ^{24}Mg, ^{27}Al, ^{28}Si, ^{31}P, ^{39}K, ^{44}Ca, ^{48}Ti, ^{55}Mn, and ^{56}Fe were analyzed at high resolution with a 150% mass window and a total dwell time of 0.15 s per isotope. Blanks were measured during 25 s prior to ablation. The basalt glass standard BCR2G was analyzed as external calibration standard using the values of Jochum et al. (2005). For data quantification the Cetac GeoPro^{TM} software was used with Ca as internal standard, and all concentrations were subsequently normalized to a volatile-free sum of 100 wt% oxides. Analytical precision and accuracy were monitored by regular analyses of basalt glasses BHVO2G and BIR and are mostly better than 3% for

TABLE 1 | List of investigated samples, their localities and their order in eruptive sequence.

Sample	Easting	Northing	Sample type	Date of emplacement	Seq.#
SD04	784657	1653400	Well sorted glassy lapilli, highly vesicular	Mid-January 2015	8
SD06	784680	1653441	Fragments of volcanic bomb cratering tephra sequence	Mid-January 2015 to end of eruption	9
SD08	784711	1653660	Fragments of mingled volcanic bomb	Mid-January 2015 to end of eruption	9
SD10	784559	1653182	Blocky fragments from rubbly flow front ~2 m high	23 or 24 November 2014 (early)	1
SD11	784646	1652341	From low-vesicularity lava in a'a flow front ~ 5 m high	23 or 24 November 2014 (later)	2
SD13	784140	1653197	Pieces from slabby pahoehoe lava flow	mid-January 2015	8
SD16	783110	1657295	Low-vesicularity pieces from a'a flow	16 December 2014	7
SD19	781947	1656265	Pieces from low-vesicularity layer in slabby pahoehoe flow	8 or 9 December 2014	5
SD20	783035	1655328	Moderately vesicular pieces from disrupted slabby pahoehoe	14 December 2014	6
SD21	782824	1656045	Vesicular pieces from pahoehoe	7 December 2014	4
SD22	782836	1656503	Lava from a'a flow, some brownish or greenish surfaces	30 November to 7 December 2014	3

Sample localities refer to UTM Zone 26P/WGS84. Seq.# is the order in the eruptive sequence.

concentration > 1 wt%, which is comparable to EMP analyses (**Supplementary Table S2**).

Microthermometry

Fluid inclusions used for barometry were examined in 100 μm thick doubly polished sections. Microthermometric measurements were carried out on small chips using a Linkam THMSG 600 heating-cooling stage at the Faculty of Geosciences, Bremen University. The stage was calibrated with SYNFLINC^{TM} synthetic CO_2 and H_2O fluid inclusion standards at −56.6, 0.0, and 374.1°C. Accuracy of CO_2 triple-point measurements, and reproducibility of melting and homogenization temperatures, were within ± 0.2°C. Densities of CO_2-dominated inclusions were calculated from measured homogenization temperatures using the auxiliary equations 3.14 and 3.15 of Span and Wagner (1996), and isochores were computed with the Sterner and Pitzer (1994) equation of state for the CO_2-H_2O system; see also Hansteen and Klügel (2008).

RESULTS

Petrography and Rock Compositions

The 2014–2015 eruption produced lavas and tephra of dominantly tephritic and subordinate phonotephritic composition (cf. Mata et al., 2017). The vesicularity of the tephrites is highly variable and ranges up to 90 vol% for some pyroclastic lapilli. The investigated samples are strongly porphyritic with euhedral to subhedral phenocrysts of clinopyroxene (8–18 vol%, up to 5 mm in size), olivine (0–2 vol%), titanomagnetite (1–3 vol%), and few plagioclase microphenocrysts. Some early erupted tephrites also contain apatite microphenocrysts, and/or rare amphibole that is either rounded or partly to completely opacitized (cf. Mata et al., 2017). Clinopyroxene commonly contains titanomagnetite and melt inclusions, and rarely sulfide blebs along the rims. The crystals are variably zoned including simple core-rim, multiple concentric, patchy, and/or sector zonations (**Figures 2A–D**), indicating complex growth histories. Most clinopyroxene phenocrysts exhibit a rim zone that is typically 10–50 μm wide and sharply bounded against the core region. Cumulus microxenoliths of clinopyroxene ± titanomagnetite ± olivine are common, and some phenocrysts appear to resemble aggregates from crystal mush zones (**Figures 2C,D**). The microcrystalline groundmass consists of plagioclase + titanomagnetite + clinopyroxene ± olivine ± glass.

Phonotephritic lava and pyroclasts were erupted at the beginning as well as near the end of the eruption. Their vesicles have ragged shapes due to shearing, suggesting a comparatively high viscosity of the melt. Phonotephrites are far less porphyritic than tephrites and contain phenocrysts of clinopyroxene, amphibole and titanomagnetite (up to 2 vol% each). In contrast to the samples investigated by Mata et al. (2017), amphiboles in our phonotephrites show little opacitization. One particular sample (SD08) is a phonotephrite bomb with a sharply bounded rim of tephrite, and abundant dark patches and streaks in the groundmass (**Figure 2E**).

Whole-rock compositions of 2014–2015 eruptive products are presented by Mata et al. (2017); they are similar to those from the 1995 eruption (**Figure 3**). However, because our samples are highly porphyritic and the rims form only a small fraction of the crystals, we consider that for the purposes of mineral-melt equilibrium studies our groundmass analyses provide a close approximation to pre-eruptive melt compositions at depth. Groundmass of tephrite samples has compositions more evolved than whole-rock, with 43.1–45.6 wt% SiO_2, 4.6–5.2 wt% Na_2O, 2.8–3.6 wt% K_2O, 4.2–5.2 wt% MgO, 3.0–3.9 wt% TiO_2, and a Mg# of 43.2–48.1 (Mg# = molar $X_{MgO}/(X_{MgO}+X_{FeO,tot})*100$) (**Table 2**, details in **Supplementary Table S3**). The data indicate some variability in tephrite melt composition during the eruption, but no gradual or systematic

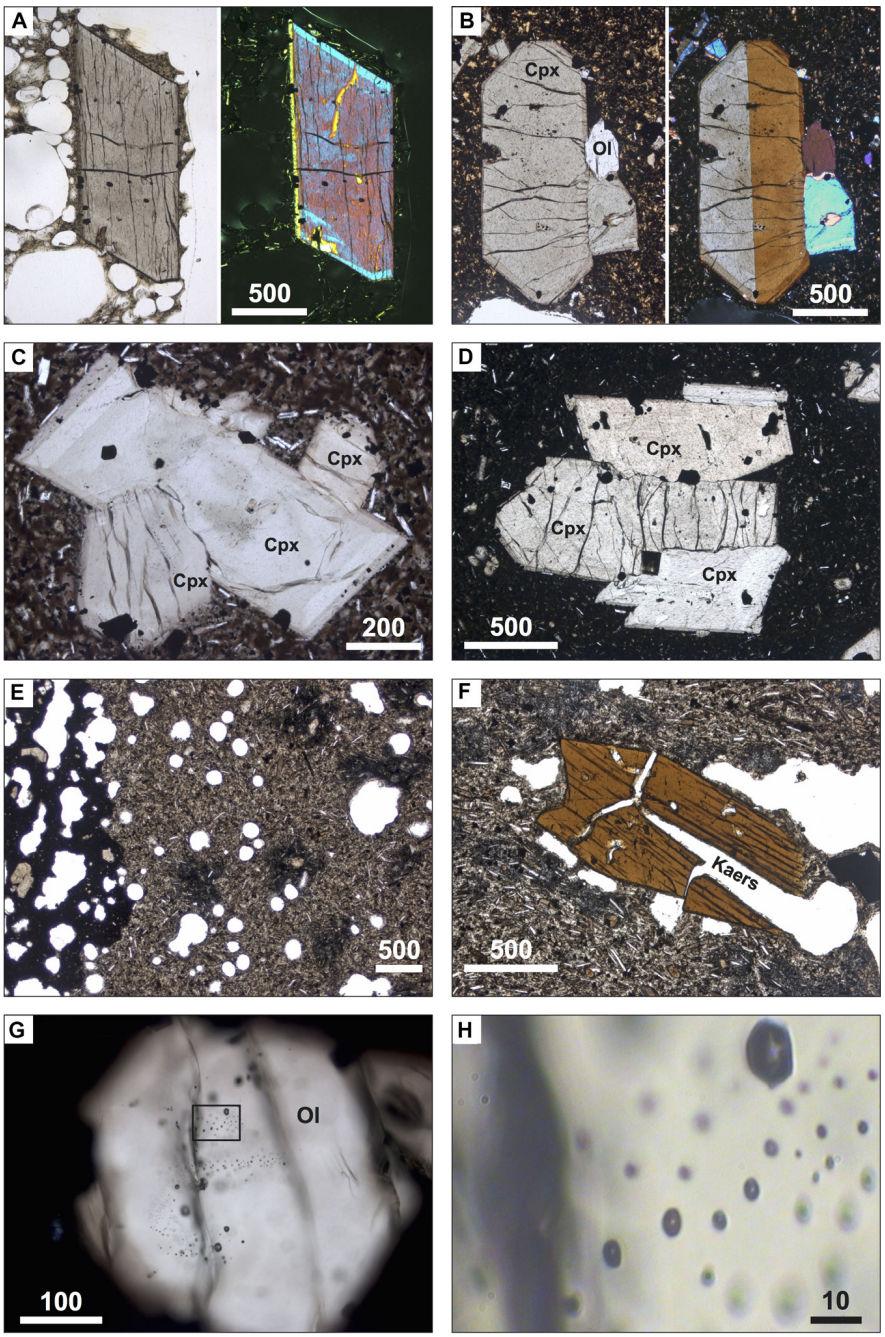

FIGURE 2 | Microphotographs from selected samples taken at plane polarized light [right parts of panels **(A,B)**] with crossed polarizers). Scale bars are in micrometers. **(A)** Euhedral clinopyroxene phenocryst with patchy core zonation and distinct rim zone (sample SD04 Cpx6). **(B)** Crystal aggregate with euhedral clinopyroxene and olivine (sample SD19 Cpx9). **(C)** Crystal aggregate of intergrown euhedral clinopyroxenes with complex zonations, interpreted as fragment from crystal mush (sample SD16 Cpx15). **(D)** Clinopyroxene aggregate interpreted as fragment from crystal mush (sample SD16). **(E)** Vesicular phonotephrite with basanite rind (left) and dark patches of "K-rich foidite" (sample SD08). **(F)** Kaersutite phenocryst with thin opacite rim in phonotephrite (sample SD08). **(G)** Trails of secondary CO_2-dominated fluid inclusions in clinopyroxene (sample SD13). **(H)** Detail of area outlined in panel **(G)**.

changes. Sample SD04 is lower in SiO_2 and alkalies, and higher in MgO, FeO, and TiO_2, than all other samples. One tephrite from the late phase of the eruption (sample SD06) is transitional having a melt composition between tephrites and phonotephrites (**Figure 3**), possibly due to mixing of melts. Groundmass of phonotephrites is chemically similar to phonotephrite whole-rock from earlier eruptions. The dark patches and streaks in the groundmass of sample SD08 are chemically distinct. Their

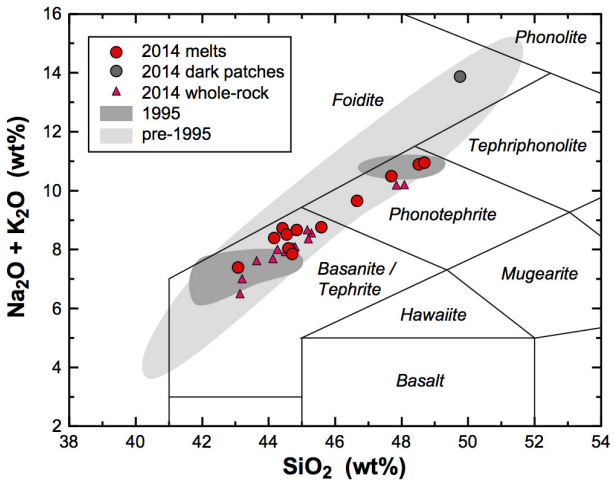

FIGURE 3 | Total alkalis versus silica (TAS) diagram with boundaries after LeMaitre et al. (1989), showing the groundmass compositions of the investigated samples. Whole-rock compositions from the 2014–2015 eruption are from Mata et al. (2017). The fields for whole-rock compositions from previous eruptions are based on data from Munhá et al. (1997), Kokfelt (1998), Doucelance et al. (2003), Escrig et al. (2005), and Hildner et al. (2011, 2012). All data are normalized to 100 wt.% volatile-free.

composition deviates from the liquid line of descent of Fogo magmas in being highly enriched in K_2O (>10 wt%), and depleted in Na_2O and Al_2O_3 (**Table 2**). The origin of these "potassic foidite" domains is unknown, but textures (**Figure 2E**) and composition suggest mingling of the phonotephrite with an exotic evolved melt or assimilation of a K-rich mineral phase. However, the analyzed compositions cannot be produced by simple binary mixing between known Fogo melts and any known mineral phase.

Mineral Compositions

All mineral compositions are provided in **Supplementary Tables S4–S7**. Clinopyroxene phenocrysts in tephrites and phonotephrites are Ti-rich aluminian diopsides showing a wide compositional range (2.1–6.6 wt% TiO_2, 3.7–13.0 wt% Al_2O_3, 0.3–1.1 wt% Na_2O, up to 0.09 wt% Cr_2O_3). The Mg# ranges from 64 to 81 for tephrites and from 56 to 80 for phonotephrites. With decreasing Mg# or Mg content, Si decreases, and Na, Ti, and Al increase; Ca shows little variation (**Figure 4A**). Compositions of the outermost crystal rims overlap with those of the core regions but extend to lower Mg# and Si, and higher Ti, Al, and Na. Overall, the rims are compositionally more variable than the cores. Also, rim compositions of phonotephrite-hosted clinopyroxenes define a distinct trend that is distinguished from tephrite-hosted ones by higher Si, and lower Ti and Al^{total}, at given Mg# (**Figure 4A**). Core compositions, in contrast, are very similar for phonotephrite- and tephrite-hosted clinopyroxenes. Most core analyses are within the upper part of the Mg# and Cr_2O_3 range.

TABLE 2 | Groundmass composition of the investigated samples as analyzed by LA-ICP-MS.

Sample	SiO_2	TiO_2	Al_2O_3	FeO^{tot}	MnO	MgO	CaO	Na_2O	K_2O	P_2O_5	Sum	Mg#	Comment
SD04	43.1 (0.5)	3.86 (0.2)	16.1 (0.2)	10.8 (0.6)	0.21 (0.01)	5.21 (0.2)	12.2 (0.3)	4.56 (0.1)	2.83 (0.1)	1.14 (0.06)	100.0	46.1 (1.4)	Tephrite
SD06	46.7 (0.7)	2.72 (0.3)	18.5 (0.9)	8.26 (0.6)	0.19 (0.01)	3.68 (0.2)	9.02 (0.5)	5.75 (0.2)	3.90 (0.1)	1.32 (0.12)	100.0	44.3 (1.3)	Tephrite
SD08	48.5 (0.7)	2.39 (0.1)	19.0 (0.6)	7.17 (0.5)	0.20 (0.01)	2.97 (0.3)	8.00 (0.9)	7.26 (0.4)	3.62 (0.2)	0.91 (0.09)	100.0	42.5 (3.2)	Pale part of mingled bomb (phonotephrite)
SD08-dark	44.2 (0.4)	3.38 (0.1)	17.0 (0.4)	9.83 (0.5)	0.21 (0.01)	4.66 (0.4)	10.9 (0.2)	4.94 (0.2)	3.46 (0.1)	1.41 (0.03)	100.0	45.8 (1.0)	Dark part of mingled bomb (tephrite)
SD08-patch	49.8 (0.6)	2.17 (0.1)	17.5 (0.4)	6.95 (0.4)	0.18 (0.02)	2.44 (0.1)	6.19 (0.3)	2.72 (0.6)	11.2 (0.8)	0.89 (0.04)	100.0	38.5 (2.1)	Dark patches in mingled bomb
SD10	44.6 (0.8)	3.35 (0.1)	16.5 (0.4)	9.89 (0.3)	0.20 (0.00)	4.86 (0.4)	11.2 (0.5)	4.78 (0.1)	3.26 (0.1)	1.35 (0.10)	100.0	46.7 (2.5)	Tephrite
SD11	48.7 (0.8)	2.24 (0.2)	19.3 (0.4)	7.34 (0.5)	0.21 (0.01)	2.92 (0.3)	7.57 (0.6)	6.54 (0.2)	4.41 (0.2)	0.81 (0.05)	100.0	41.5 (3.0)	Phonotephrite
SD13	44.4 (0.5)	3.36 (0.2)	16.7 (0.4)	10.1 (0.3)	0.21 (0.01)	4.76 (0.4)	10.5 (0.6)	5.18 (0.2)	3.54 (0.2)	1.32 (0.05)	100.0	45.7 (2.2)	Tephrite
SD16	44.8 (0.5)	3.07 (0.1)	17.0 (0.7)	9.26 (0.3)	0.20 (0.01)	4.81 (0.5)	10.8 (0.7)	5.02 (0.2)	3.64 (0.2)	1.33 (0.10)	100.0	48.1 (2.4)	Tephrite
SD19	44.7 (0.8)	3.35 (0.1)	16.5 (0.7)	10.0 (0.4)	0.20 (0.01)	4.87 (0.4)	11.2 (0.8)	4.77 (0.3)	3.07 (0.2)	1.26 (0.08)	100.0	46.4 (2.4)	Tephrite
SD20	45.6 (1.1)	3.04 (0.2)	17.2 (0.6)	9.80 (0.5)	0.20 (0.01)	4.18 (0.4)	10.0 (0.6)	5.24 (0.3)	3.52 (0.2)	1.19 (0.08)	100.0	43.2 (2.4)	Tephrite
SD21	44.5 (0.4)	3.30 (0.2)	16.6 (0.5)	10.2 (0.3)	0.21 (0.01)	4.75 (0.3)	10.5 (0.7)	5.11 (0.3)	3.40 (0.2)	1.34 (0.07)	100.0	45.4 (1.4)	Tephrite
SD22	45.1 (1.1)	3.22 (0.4)	16.5 (0.7)	10.1 (1.4)	0.22 (0.01)	4.72 (0.3)	10.1 (0.4)	5.16 (0.2)	3.45 (0.2)	1.33 (0.11)	100.0	45.4 (3.2)	Tephrite

Compositions are given in wt%. Mg# = 100 x molar MgO/(MgO+FeO^{tot}).
Data are the mean of 6 to 10 single analyses; parentheses indicate one standard deviation.

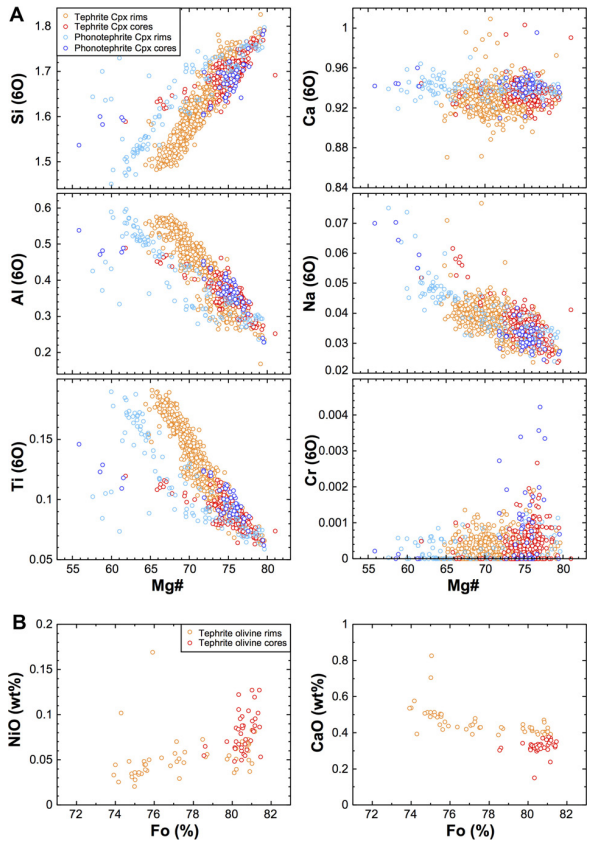

FIGURE 4 | (A) Compositional variations of clinopyroxene phenocrysts in tephrites and phonotephrites, plotted as Mg# versus cation fractions normalized to six oxygens. Rim compositions were analyzed at 3–8 μm distance to planar crystal faces, all other analyses are denoted as cores. Note the different trends of phonotephrite- and tephrite-hosted clinopyroxene rims in the diagrams of Mg# versus Si, Ti and Al. **(B)** Compositional variations of olivine phenocrysts in tephrites. Note the small range of rim compositions (Fo_{74-81}) as compared to clinopyroxene rims (Mg# of 64–79).

Olivine phenocrysts show little compositional variation. Most cores have nearly constant composition of $Fo_{80.0-81.5}$ with 0.05–0.13 wt% NiO and 0.30–0.38 wt% CaO (**Figure 4B**). All investigated crystals exhibit a steep normal zonation with rim compositions of Fo_{74-81}, 0.03–0.07 wt% NiO and 0.40–0.60 wt% CaO. Notably, the zoning profiles are shorter in lava flow samples collected near the vents (SD10, SD13: ∼4–14 μm) than in those collected far from the vents (SD16, SD21: ∼9–30 μm); in quenched glassy lapilli from sample SD04 the zonations are hardly detectable by electron microprobe and show only mildly decreasing forsterite content (**Supplementary Figure S1** and **Supplementary Table S8**).

Amphibole phenocrysts in phonotephrites are kaersutites showing little zonation and little compositional variation with 5.7–6.1 wt% TiO_2, 12.3–12.7 wt% CaO, 2.0–2.4 wt% Na_2O, 1.6–1.8 wt% K_2O, and Mg# between 64 and 71. Spinel phenocrysts in tephrites and phonotephrites are titaniferous magnetites with 12.6–19.8 wt% TiO_2, 5.7–10.1 wt% MgO, 6.2–9.2 wt% Al_2O_3, and 0.42–0.69 wt% MnO. The proportion of the ulvöspinel component is comparatively high, ranging between 0.32 and 0.52. The compositional ranges for rims and cores overlap strongly, but rims tend to higher TiO_2 and lower FeO^{tot}.

Clinopyroxene-Melt Thermobarometry

Rationale

In this study we focused on thermobarometers based on clinopyroxene-melt equilibria. For hydrous samples Putirka (2008) recommends combination of models A and B of Putirka et al. (2003) if melt H_2O content is unknown, or the combination of his Equations (30) and (33) if H_2O is known. The standard errors of estimate (SEE) for test data are 500 MPa/60°C for models A and B, and 360 MPa/42°C for Equations (30) and (33), respectively; SEE for the calibration data are significantly lower. Errors can be significantly reduced by averaging estimates for a number of phenocrysts to perhaps < 150 MPa (Putirka et al., 2003). Here we consistently apply the Putirka et al. (2003) models in which P_2O_5 is not used for the calculation of molar proportions in the melt, similar to earlier thermobarometric data from Fogo (Hildner et al., 2011, 2012). In contrast, the supplementary spreadsheet of Putirka (2008) includes P_2O_5 in the calculations, which for our data set would increase calculated pressures by 30–50 MPa.

In order to constrain pre-eruptive pressures and temperatures, we applied the thermobarometer to compositions of clinopyroxene phenocryst rims and the sample groundmass. This has the advantage that mineral-melt pairs have a well-defined petrographic relationship and are near equilibrium texturally, albeit not necessarily chemically due to e.g., sector zonations (Neave et al., 2019). Clinopyroxene rim compositions were determined by analyzing a number of points along the periphery of euhedral phenocrysts close to their surfaces, similar to prior studies of Fogo lavas (Hildner et al., 2011, 2012). The distance to crystal faces was around 5 μm to avoid excitation of adjacent groundmass phases by the electron beam. Every single analysis was then tested for equilibrium with the respective host groundmass composition by applying and comparing three different filters:

Filter 1: the Fe-Mg partition coefficient $K_D(\text{Fe-Mg})^{cpx-liq}$ between clinopyroxene and melt has to be within the mean equilibrium value of 0.28 ± 0.08 for global experimental data, where Fe^{tot} is used for Fe (Putirka, 2008). In addition, the measured clinopyroxene components Jd, DiHd, EnFs and CaTs (Putirka et al., 2003) have to agree with those predicted from the groundmass composition within 2 SEE of the prediction equations (Putirka, 1999). This is our main filter used, consistent with earlier barometric studies of Fogo lavas (Hildner et al., 2011, 2012).

Filter 2: the difference between the predicted DiHd component after Equation (7) of Mollo et al. (2013) and the observed value for DiHd, denoted ΔDiHd, has to be within 1 SEE of the prediction equation (±0.06). This criterion was specifically chosen to be stricter than the DiHd criterion in filter 1. The value of ΔDiHd is a particularly sensitive indicator for

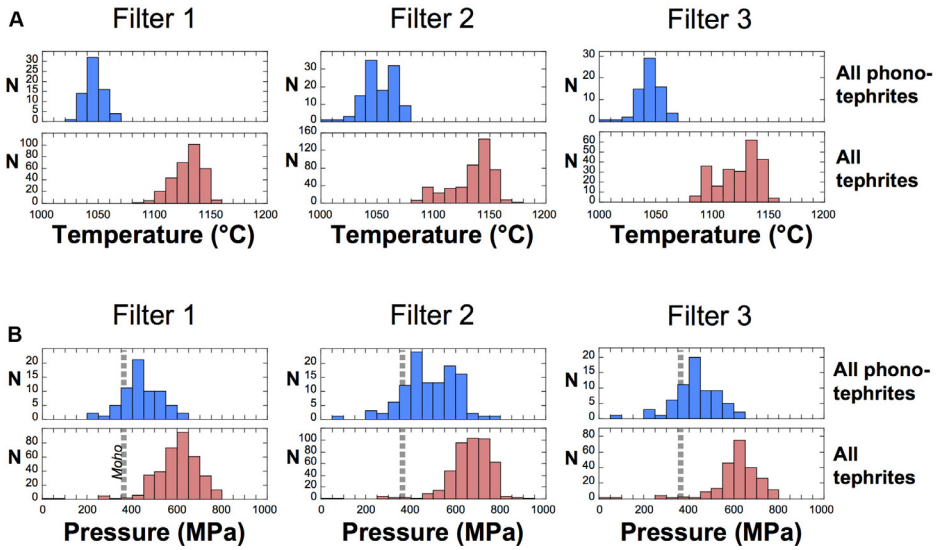

FIGURE 5 | Summarized results of clinopyroxene-melt thermobarometry using the Putirka et al. (2003) calibration. Shown are the data for all clinopyroxenes in phonotephrites (blue) and in tephrites (red); N is the number of values. Data were filtered as described in the text and show little dependency of the filter used. **(A)** Temperature histograms with 10°C bins. **(B)** Pressure histograms with 50 MPa bins; dashed lines mark the approximate pressure at Moho depth after the crustal model of Pim et al. (2008).

disequilibrium conditions during crystal growth (Mollo et al., 2013; Mollo and Masotta, 2014) and is independent of Fe-Mg partitioning.

Filter 3: both the $K_D(\text{Fe-Mg})^{cpx-liq}$ criterion of filter 1 and the ΔDiHd criterion have to be satisfied.

Thermobarometry of Clinopyroxene Rims

Overall, we analyzed the rims of 100 phenocrysts in nine tephrite and 20 phenocrysts in two phonotephrite samples (**Figures 5**, **6** and **Supplementary Table S4**). A large number of crystal-melt pairs do not pass the chemical equilibrium tests despite textural equilibrium. Filter 1 removes around 40% of all analyzed points, which is almost entirely due to the $K_D(\text{Fe-Mg})^{cpx-liq}$ criterion, because the Mg# of many rim analyses is below the equilibrium range indicated by the host groundmass composition. Observed clinopyroxene components, in contrast, are within the predicted values for almost all analyses. We note that the values for the EnFs component predicted after Mollo et al. (2013) closely resemble those after Putirka (1999), and closely agree with observed values. Filter 2 discriminates far less whereas filter 3 is particularly strict, removing around 60% of all points in tephrites and 45% in phonotephrites (**Table 3**).

Temperatures obtained after applying the different filters are remarkably similar, with averages of 1123–1134°C for tephrites and 1045–1052°C for phonotephrites; standard deviations (σ) are around 18 and 10°C, respectively. For average pressures there is little difference between filters 1 and 3, with values around 600–620 MPa for tephrites and 420–440 MPa for phonotephrites, and respective standard deviations around 100 MPa (**Table 3**). Filter 2 results in average pressures that are around 50 MPa higher. Overall the frequency distributions for the different filters are very similar, and differences are within the prediction errors of the thermobarometer (**Figure 5**). Our calculated pressures are around 150–200 MPa lower than those from Mata et al. (2017), who applied the same thermobarometer to cores of clinopyroxene phenocrysts paired with whole-rock compositions.

For comparison, we applied Equations (33) and (30) of Putirka (2008) to the same data assuming a H_2O content of 2.5 wt% based on results for olivine-hosted melt inclusions (Moussallam et al., 2019). By using filter 1, average temperatures are 1135 ± 15°C for tephrites and 1079 ± 13°C for phonotephrites; corresponding pressures are 825 ± 115 and 701 ± 145 MPa, respectively (±1 σ indicated). The leverage of melt H_2O on calculated temperatures and pressures is around −12°C and +35 MPa per wt% increase, hence variations by a few wt% of H_2O would affect P-T estimates within the calibration errors of the thermobarometers. The data show that the alternative calibration yields higher pressures than the Putirka et al. (2003) model, a greater variance, and smaller pressure differences between tephrites and phonotephrites. Nevertheless, the data for both models still overlap within their prediction errors. The discrepancies illustrate that the possible error of our data may be larger than the standard deviation for a single data set might suggest. We also assessed the effect of analytical uncertainty of the groundmass data on calculated pressures. For this we generated a test data set by randomly imposing up to ±3 standard deviations for each element on a mean melt analysis (cf. Klügel et al., 2005). By using uncertainties reported in **Supplementary Table S3** we obtained pressure uncertainties of around ±70 MPa, which is well below the calibration error of the barometers but may cause a significant part of the observed data spread.

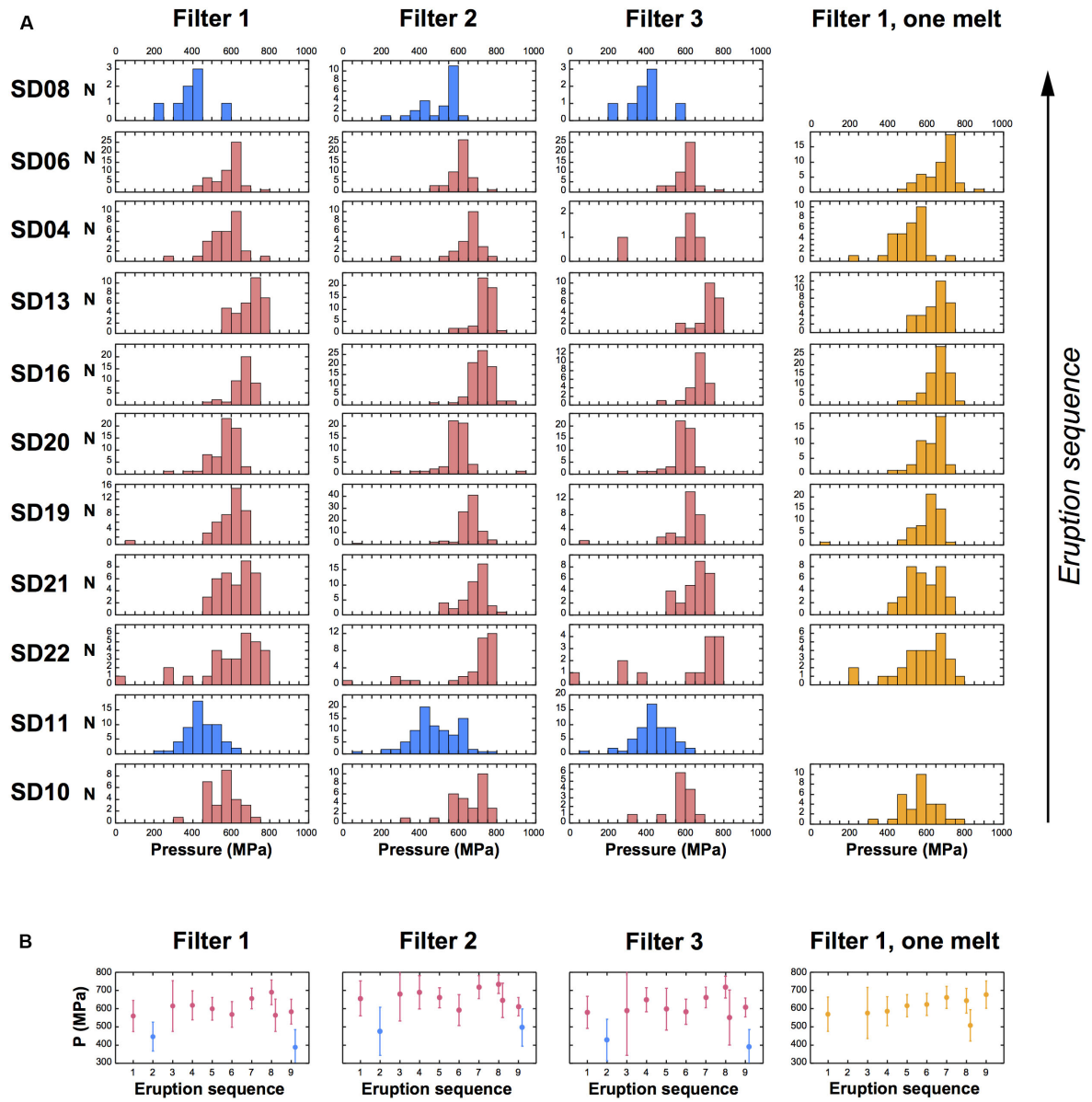

FIGURE 6 | Single-sample results of clinopyroxene-melt barometry using the Putirka et al. (2003) calibration; data were filtered as described in the text. First three columns use each sample's groundmass composition, fourth column uses the average tephrite groundmass composition for all tephrite samples. **(A)** Pressures for every sample sorted by eruption sequence from bottom (oldest) to top (youngest). Note that samples SD13 and SD04 have the same sequential order based on field relations, as do samples SD06 and SD08. **(B)** Average pressure for every sample plotted against eruption sequence number; error bars indicate ± 1 standard deviation. The data display some inter-sample variability that is only weakly dependent of the filter used.

Looking at thermobarometric data for individual samples, calculated pressures indicate some inter-sample variability among the tephrites (**Figure 6A**). This is best seen in diagrams of average pressure for each sample versus eruption sequence, where variations are similar for each filter, although most pressures overlap within one standard deviation (**Figure 6B**). However, this is uncertain for filter 3, which removes all but a few points for some samples. Likewise, calculated temperatures also show considerable variability (**Supplementary Figure S2**). Samples SD04 and SD06, the most and least MgO-rich of our tephrite samples (**Table 2**), yield the highest and lowest temperatures, respectively. Remarkably, pressure and temperature variabilities are strongly reduced if the average tephrite melt composition is used for all tephrite samples. In this case all samples except SD04 show strongly overlapping pressure and temperature ranges (**Figure 6** and **Supplementary Figure S3**).

To sum up, the different filters and calibrations yield mean pressures between about 600 and 800 MPa for the tephrites and slightly lower values for the phonotephrites, with 600 and

TABLE 3 | Overview of P-T data for clinopyroxene rims and host melt.

	Filter 1	Filter 2	Filter 3
TEPHRITE Cpx (592 ANALYSES)			
% of data removed by filter	39	23	61
Average P (MPa)	601	665	616
Standard deviation (MPa)	97	99	102
Average T (°C)	1124	1134	1123
Standard deviation (°C)	18	19	18
PHONOTEPHRITE Cpx (125 ANALYSES)			
% of data removed by filter	46	9	46
Average P (MPa)	440	479	421
Standard deviation (MPa)	83	126	113
Average T (°C)	1046	1052	1045
Standard deviation (°C)	7	13	9

Pressures and temperatures were calculated using the Putirka et al. (2003) calibration; see text for description of filters applied.

440 MPa being our preferred values, respectively. As the Moho near Fogo is located at 12–13 km depth, or around 350 MPa (Pim et al., 2008), this consistently indicates pre-eruptive storage of the 2014–2015 tephrites and phonotephrites in the uppermost mantle, in agreement with the findings by Mata et al. (2017) obtained for clinopyroxene cores.

Thermobarometry Along Clinopyroxene Rim Traverses

In order to assess the effect of clinopyroxene rim zonations on the thermobarometric data, we analyzed some compositional profiles perpendicular to planar crystal surfaces across the 10–50 μm wide rim zones (**Figure 7** and **Supplementary Table S4**). Overall the rim zones are complex and chemically highly variable. In most but not all cases they are characterized by steeply decreasing Mg# and Si toward the crystal surface, accompanied by increasing Ti and Al; variations in Na show little systematics. In BSE images many crystals also show an outermost zone < 2 μm wide, which could not be analyzed reliably. The compositions within the rim zones can vary considerably between phenocrysts of a single sample, and also between different faces of a single crystal. For the traverses shown in **Figure 7**, pressures calculated along the rim zones range between 430 and 880 MPa, and temperatures between 1127 and 1164°C. When applying filter 3, these ranges are reduced to 500–670 MPa and 1131–1153°C, respectively, within the range for single clinopyroxene rim analyses (**Figure 5**).

Olivine-Melt Thermometry and Melt Redox

In order to assess olivine-melt equilibria, to predict the Fe-Mg partition coefficient $K_D(\text{Fe-Mg})^{ol-liq}$ and to calculate melt temperature and redox, we used measured groundmass compositions as our preferred approximation to pre-eruptive melt compositions (**Table 2**). The predicted $K_D(\text{Fe-Mg})^{ol-liq}$ after Equation (8c) of Putirka (2016b) for five olivine-phyric samples are within a narrow range of 0.305–0.310. These values combined with measured olivine compositions yield molar Fe^{2+}/Mg ratios of the groundmass between 0.76 and 0.86, implying Fe^{3+}/Fe^{tot} between 0.26 and 0.36 (average 0.31). These results exclude olivine compositions that would yield groundmass Fe^{3+} below or close to zero, as these obviously indicate disequilibrium. For the average Fe^{3+}/Fe^{tot} ratio of 0.31 the analyzed groundmass compositions would be in equilibrium with olivine $Fo_{79.7-81.4}$, which agrees well with the observed range for phenocryst cores ($Fo_{80.0-81.5}$) and some rims. Most observed rim compositions, however, are too low in forsterite content to be in equilibrium with the groundmass (**Figure 4B**).

Oxygen fugacity was calculated using the recent calibration of Putirka (2016b). For a Fe^{3+}/Fe^{tot} ratio of 0.31 we obtained $\log(f_{O2})$ between −7.7 and −7.6, or 0.2–0.3 log units above the NNO buffer, for the 2014–2015 tephrite melt. This is 0.6–2.0 log units below the estimates of Mata et al. (2017), which were based on kaersutite phenocryst compositions (see below). For comparison, calculation of $K_D(\text{Fe-Mg})^{ol-liq}$ using the model of Toplis (2005) would yield an average value of 0.27, resulting in a mean Fe^{3+}/Fe^{tot} ratio of 0.21 and an oxygen fugacity of 0.5–0.6 log units below NNO.

For olivine-melt thermometry we used a melt H_2O content of 2.5 wt% as above and a pressure of 600 MPa derived from clinopyroxene-melt barometry, considering that olivine and clinopyroxene are coexisting phenocryst phases in these rocks. According to Putirka (2008) the most precise olivine thermometer for hydrous systems is Equation (4) of Putirka et al. (2007), with a SEE of 29°C for hydrous systems and 43°C overall. Its application to groundmass and mean olivine core compositions yields 1113–1122°C (**Supplementary Table S5**), in good agreement with clinopyroxene-melt thermometry (**Figure 5**). The dependency of calculated temperatures on melt H_2O and pressure is about −18°C per wt% and +5°C per 100 MPa increase, respectively. Thus, variations by 2 wt% H_2O or 700 MPa would affect temperature estimates within the calibration uncertainty. Olivine rims have lower forsterite contents but give higher temperatures than cores (1122–1138°C), which is not plausible and reaffirms the inferred disequilibrium between rim and groundmass compositions.

Amphibole Thermobarometry and Hygrometry

The empirical thermobarometric and chemometric equations of Ridolfi et al. (2012) allow calculation of melt temperature, pressure, H_2O content, and oxygen fugacity based on the composition of amphibole crystals alone. The reported SEE for the calibration data are T ± 24°C, P ± 12%, H_2O_{melt} ± 0.8 wt% and f_{O2} ± 0.4 log units. Recent tests by Putirka (2016a) show that the thermometer is comparatively precise, whereas the performance of the barometer is intrinsically limited by the lack of P-sensitive amphibole components, as is expressed by a precision of ± 400 MPa for a test data set. Pressures obtained from the amphibole barometer should thus be compared to independent barometers. Likewise, the precision of the hygrometer is limited because amphibole saturation

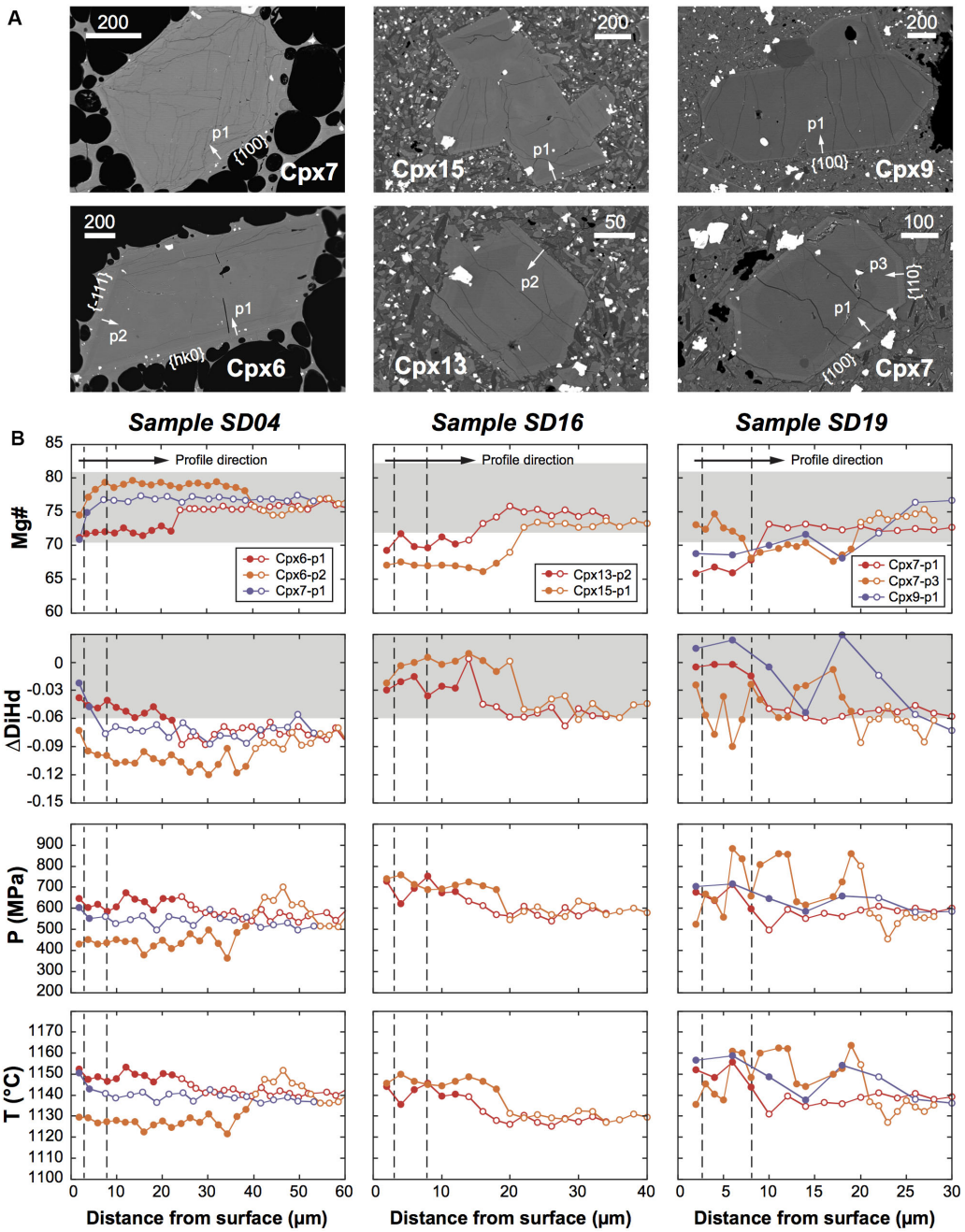

FIGURE 7 | (A) BSE images of zoned clinopyroxene phenocrysts from three samples, indicating the locations of compositional traverses. The outer rim zones are well recognized. See **Figure 2** for microphotographs of some of the crystals. **(B)** Profiles across the clinopyroxene rims indicated above. Shown are clinopyroxene Mg#, ΔDiHd calculated after Mollo et al. (2013), and pressures and temperatures after Putirka et al. (2003); all calculated values use the host groundmass composition. Filled symbols mark points located within the rim zones. Dashed lines delimit the range of 3–8 µm distance to the crystal surface, where most rim analyses for thermobarometry were carried out. Gray shading marks the equilibrium range used for the $K_D(Fe\text{-}Mg)^{cpx-liq}$ and ΔDiHd filter criteria.

and composition show little dependency on melt H_2O (Putirka, 2016a).

Application of the Ridolfi et al. (2012) equations on average compositions of seven amphibole phenocrysts from an early and a late erupted phonotephrite yield temperatures of 1040–1056°C, pressures of 610–660 MPa, melt H_2O contents of 3.9–4.3 wt%, and oxygen fugacities of 1.1–1.6 log units above the NNO buffer (**Supplementary Table S6**), comparable to data from Mata et al. (2017). The amphibole-derived temperatures show excellent agreement with clinopyroxene-melt thermobarometry on the host phonotephrites, whereas the pressures are slightly higher, although they overlap with

those obtained using the alternative calibration (Equation 30 of Putirka, 2008). Calculated oxygen fugacities are higher than those for the tephrites (NNO+0.3), which is plausible because Fe^{3+}/Fe^{tot} ratios typically increases during crystal fractionation. The values imply a melt Fe^{3+}/Fe^{tot} ratio of 0.40–0.46 (after Putirka, 2016b), as compared to 0.26–0.36 found for the tephrites. Considering that Fe^{3+}/Fe^{tot} of 0.46 seems rather oxidized, we suggest that an oxygen fugacity of NNO+1.1 provides an upper bound for the phonotephrites. The calculated melt H_2O contents are above those found in olivine-hosted melt inclusions from Fogo (up to 2.6 wt%; Moussallam et al., 2019), but appear plausible considering the differentiated nature of the phonotephrites compared to the mafic tephras investigated by these authors.

Fluid Inclusion Barometry

Fluid inclusions are comparatively rare in phenocrysts from the 2014–2015 eruptive products, in contrast to melt inclusions. We analyzed 216 primary and secondary fluid inclusions in 12 clinopyroxene phenocrysts from samples SD04 (pyroclasts) and SD10, SD13, and SD16 (lava flows). Primary inclusions occur either singly or randomly orientated in clusters, whereas secondary inclusions form trails that extend to grain boundaries (**Figures 2G,H**). Secondary inclusions are more abundant and tend to be smaller than primary ones. Inclusions are oval to spherical or are negatively crystal-shaped. The largest measured inclusion was 25 μm in size, but most were < 5 μm. Inclusions indicating partial decrepitation, such as small cracks or radiating trails of micro-inclusions (cf. Roedder, 1984), were not investigated.

The investigated inclusions froze to solid CO_2 and vapor during cooling to between −90 and −100°C; further cooling to −190°C did not generate additional phase transitions. During reheating, few inclusions showed a melting interval with initial melting temperatures (T_i) between −59.7 and −57.5°C, but for most inclusions initial and final melting (T_m) coincided. Overall T_m ranged between −59.3 and −56.6°C, the triple point of pure CO_2 (**Supplementary Table S9**). Melting temperatures below −56.6°C indicate the presence of components such as N_2 or CH_4 in the inclusions (Andersen and Neumann, 2001; Frezzotti et al., 2002). Inclusions with T_m between −57.5 and −56.6°C contain less than 5 mole% of these components (van den Kerkhof, 1990), which should not significantly affect the interpretation of the P-T conditions during fluid trapping if pure CO_2 inclusions are assumed. Inclusions with T_m below −57.5°C (18 inclusions from sample SD13) were discarded. We found no evidence for H_2O or OH-bearing secondary phases in any observed inclusion (cf. Andersen and Neumann, 2001; Frezzotti et al., 2002; Frezzotti and Touret, 2014). Our data thus suggest that the fluid inclusions consist of almost pure CO_2, similar to inclusions observed in lavas from other Fogo eruptions (Hildner et al., 2011, 2012).

Most measured inclusions homogenized into the liquid phase between 27.9 and 31.1°C, close to the critical point of pure CO_2 (**Figure 8A**). No systematic difference between primary and secondary inclusions was found. For eleven inclusions no phase transition above the CO_2 triple point could be observed; these probably homogenized into the vapor phase. Calculated densities range from 0.47 to 0.66 g/cm^3 and show a bimodal distribution (**Figure 8B**), however, the upper frequency maximum is due to a single inclusion-rich crystal. Importantly, fluid inclusions in the quenched sample SD04 yield higher densities than those in lava flow samples. For a model temperature of 1140°, CO_2 isochores calculated after Sterner and Pitzer (1994) indicate a pressure range of 190–340 MPa (average 297 ± 31 MPa) (**Figure 8B**). The dependency on temperature is weak; a variation of ± 20°C would result in a pressure variation of ± 3 to ± 6 MPa for the density range observed. The calculated pressures are less than those indicated by clinopyroxene-melt barometry, and are equivalent to the depth of the lower oceanic crust and Moho boundary near Fogo (Pim et al., 2008).

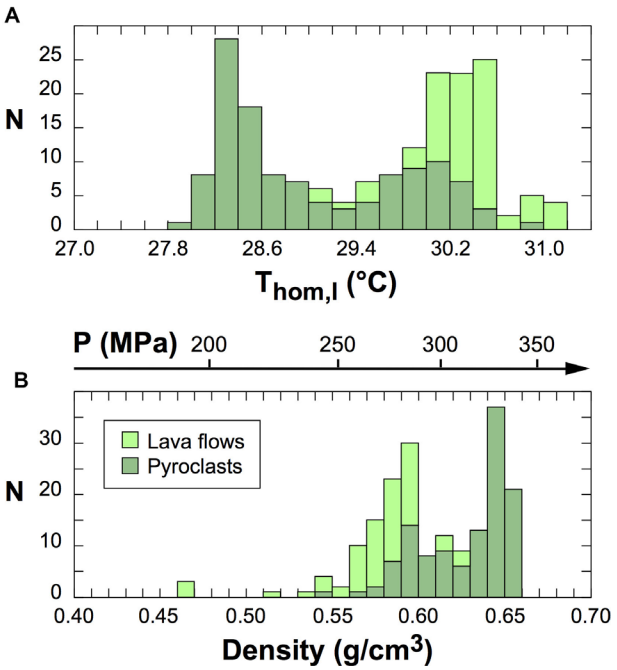

FIGURE 8 | Frequency distribution of **(A)** homogenization temperatures and **(B)** densities of clinopyroxene-hosted fluid inclusions as determined by microthermometry. Inclusions from quenched glassy lapilli (sample SD04) have higher densities than those from lava flow samples, indicating continuing re-equilibration during the time the samples resided in the flowing lava.

DISCUSSION

In this study, we have obtained petrological data to shed light on magmatic processes before and during the 2014–2015 Fogo eruption. We begin the discussion with a critical appraisal of the thermobarometric data obtained for clinopyroxene rims, with emphasis on equilibrium tests and the role of sector zonations. We then discuss the origin and implications for rim zonations of clinopyroxene and olivine phenocrysts, and evaluate the fluid inclusion data. After summarizing the data in a model of magma

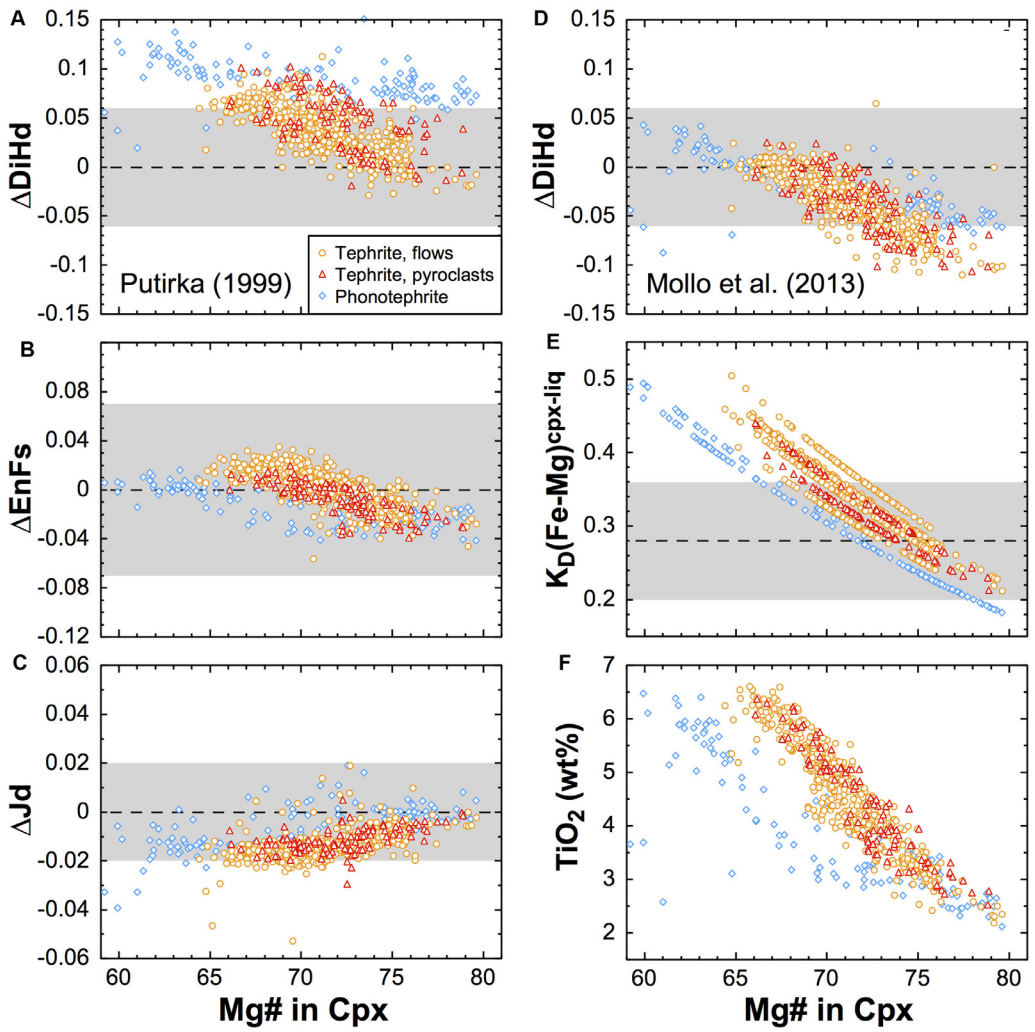

FIGURE 9 | Compositional range and equilibrium criteria for the rims of clinopyroxene phenocrysts in tephrites (590 analyses) and phonotephrites (diamonds; 125 analyses) from the 2014–2015 eruption. The diagrams present clinopyroxene Mg# versus **(A)** ΔDiHd; **(B)** ΔEnFs; **(C)** ΔJd; **(D)** ΔDiHd after Mollo et al. (2013); **(E)** measured K_D(Fe-Mg)$^{cpx-liq}$ using groundmass compositions; and **(F)** TiO_2 in clinopyroxene. In **(A–C)** the delta notations indicate the difference between predicted and measured clinopyroxene components after Putirka (1999). For ΔEnFs, the more recent calibration of Mollo et al. (2013) yields a similar distribution but is shifted by +0.010 to +0.015. Dashed lines show the equilibrium values for clinopyroxene components and the global mean for K_D(Fe-Mg)$^{cpx-liq}$; gray fields encompass ± 1 SEE of the model error for clinopyroxene components, and ± 1 standard deviation for the mean K_D(Fe-Mg)$^{cpx-liq}$ (Putirka, 2008). For tephrites the diagrams discriminate between crystals in rapidly cooled pyroclasts (samples SD04 and SD06; triangles) and slowly cooled lava flows (circles), showing that there is no significant difference between both groups.

storage and ascent during the 2014–2015 eruption, a synopsis of the magmatic plumbing system beneath Fogo is given.

Clinopyroxene-Melt Equilibrium Tests

The coefficient K_D(Fe-Mg)$^{cpx-liq}$ is an often-used but insufficient test for chemical equilibrium between clinopyroxene and melt. As the equilibrium range of 0.04–0.68 for global experimental data is rather large, with a mean of 0.28 ± 0.08 (Putirka, 2008), the test provides a minimum requirement rather than a tight filter. It is also not reliable, because K_D(Fe-Mg)$^{cpx-liq}$ still can be around 0.28 in the case of disequilibrium crystallization (Putirka, 2008; Mollo et al., 2013; Mollo and Masotta, 2014). Conversely, the coefficient can be beyond the equilibrium range if sector zonations occur, because Mg is strongly susceptible to sector partitioning (Ubide et al., 2019). Despite these weaknesses, K_D(Fe-Mg)$^{cpx-liq}$ provides information on equilibrium and crystal growth conditions when used together with other partition coefficients and/or tests comparing predicted and measured clinopyroxene components DiHd, EnFs, Jd, and CaTs (Putirka, 2008; Ubide et al., 2019; Neave et al., 2019). The ΔDiHd test is particularly useful in this respect, because the DiHd component is a robust disequilibrium indicator and strongly depends on cooling rates (Mollo et al., 2010, 2013).

The usefulness of ΔDiHd for equilibrium tests has been demonstrated by phase equilibrium experiments and by investigations on natural samples (e.g., Mollo et al., 2013; Ubide

et al., 2019), yet interpretations are not always straightforward as is shown by our data for clinopyroxene rims. For tephrite-hosted clinopyroxenes, ΔDiHd values calculated after the prediction equations of Putirka (1999) and of Mollo et al. (2013) show good negative correlations with clinopyroxene Mg# and dominantly have positive and negative values, respectively (**Figures 9A,D**). As the Mg# decreases, ΔDiHd after Mollo et al. (2013) approaches zero, whereas ΔDiHd after Putirka (1999) departs from zero. These relations reflect the dependency of both models on uncertainties in our P-T estimates used as input parameters. The Putirka (1999) model for DiHd is T-dependent, whereas the more recent Mollo et al. (2013) model is P-T-dependent and calibrated over a much broader experimental data set. Indeed, if temperatures for the Putirka (1999) model were increased by 40°C, the values for ΔDiHd shown in **Figure 9A** would be almost identical to **Figure 9D**. Nonetheless, both prediction models indicate equilibrium (ΔDiHd = 0) within 2 SEE for most values of our data set. By comparison with the compositions of co-existing olivine phenocrysts, clinopyroxenes in equilibrium with the host melt should have high Mg# around 75–80; for these compositions the observed $K_D(\text{Fe-Mg})^{cpx-liq}$ is close to 0.28 (**Figure 9E**).

Our results confirm the suitability of sector-zoned phenocryst rims for clinopyroxene-melt thermobarometry (Ubide et al., 2019). By using appropriate melt compositions and applying robust filters, useful pressure and temperature estimates can be obtained, as is corroborated by the low standard deviations of our P-T estimates (**Table 3**), and by the good agreement between predicted and measured EnFs and Jd components (**Figures 9B,C**). The advantage of our approach is that the known melt composition for each sample permits removal of rim analyses that are not in equilibrium with the melt. Another useful approach is iterative selection of putative equilibrium melts from a data base of glass and whole-rock analyses until a composition that best meets given equilibrium criteria is found (Barker et al., 2015; Neave and Putirka, 2017). This is the only way to go if the former host melt of the crystals cannot be analyzed, but has the disadvantage that analyses representing a period of disequilibrium growth may also be included and paired with "equilibrium" liquids. The present study uses one fixed (melt composition) and one variable (rim compositions) quantity, whereas the alternative approach uses two variable quantities. This may bias the results and yield a larger spread of pressure and temperature estimates.

We also tested our filtering approach by tentatively using tephrite whole-rock rather than groundmass compositions for thermobarometry on clinopyroxene rims, even though this violates textural evidence. This increases the number of crystal-melt pairs removed from 39 to 61% for filter 1 mostly due to the $K_D(\text{Fe-Mg})^{cpx-liq}$ criterion, and from 23 to 60% for filter 2; filter 3 removes almost all data. Calculated mean temperatures and pressures increase considerably to 1171°C/830 MPa for filter 1 and 1188°C/940 MPa for filter 2 (cf. **Table 3**); the standard deviations of pressure estimates also increase. These pressures overlap with the data reported for clinopyroxene phenocryst cores paired with whole-rock compositions (Mata et al., 2017), which is not unexpected because core and rim compositions overlap (**Figure 4**). The test thus shows that filters 1 and 2 have limited capability in removing clinopyroxene-melt pairs that are not in textural equilibrium, and that a wide range of P-T estimates can be obtained when testing for compositional equilibrium alone. Whereas we do not know which of these P-T estimates are closer to true values, we favor our data shown in **Table 3** as these are backed by the petrographic relationships.

Zonations in Clinopyroxene Rims and Implications for Thermobarometry

An intriguing aspect of our data set is the large variability of rim compositions of clinopyroxene phenocrysts (**Figure 4A**). Even though all clinopyroxene rims were analyzed close to planar crystal faces, they encompass a larger compositional range than the cores. This is remarkable because the rims represent similar pressures and temperatures during growth, at least within a single sample. The most plausible explanation for this observation is sector zonation of clinopyroxene rim zones, as is also apparent in many BSE images (**Figure 7A**).

It has long been recognized that sector zonations are very common in clinopyroxene phenocrysts in alkalic as well as in sub-alkalic melts, even if they are euhedral (e.g., Strong, 1969; Ferguson, 1973; Nakamura and Coombs, 1973; Wass, 1973; Downes, 1974; Leung, 1974; Brophy et al., 1999). The zonations are attributed to kinetic effects when crystals grow at conditions beyond equilibrium, at considerable degrees of undercooling (Kouchi et al., 1983; Schwandt and McKay, 2006). As a consequence, cations of major and trace elements are partitioned among different sectors that grow at different rates. The partitioning depends on the degree of undercooling and cation charge/radius in a complex way. Commonly, fast-growing {−111} hourglass sectors are Si-Mg enriched, whereas slow-growing {hk0} prism sectors are Al-Ti enriched; other elements show a more variable behavior (Leung, 1974; Kouchi et al., 1983; Welsch et al., 2016; Ubide et al., 2019). Indeed, our data for clinopyroxene rims show good positive correlation of Mg# with Si, and good negative correlations with Al, Ti and Na (**Figure 4A**). This can be expressed in terms of a coupled substitution reaction between {−111} hourglass and {hk0} prism sectors: $[Si^{4+} + Mg^{2+}]_{\{-111\}} \Longleftrightarrow [Al^{3+} + Ti^{4+} + Na^{+}]_{\{hk0\}}$ (Welsch et al., 2016; Ubide et al., 2019; Neave et al., 2019). In consequence, different sectors have strongly differing compositions even if they grew concomitantly, which results in highly variable pressure and temperature estimates when thermobarometry is applied (Mollo et al., 2013; Mollo and Masotta, 2014; Hammer et al., 2016; Neave et al., 2019; Ubide et al., 2019).

The complex influence of sector zonations on thermobarometric results is exemplified by our compositional traverses across clinopyroxene rim zones (**Figure 7**). Crystal Cpx6 from sample SD04 (**Figure 2A**) exhibits a concentrical but heterogeneous rim zone. At profile Cpx6-p1 it is 22 μm wide and has higher Fe, Al, and Ti, and lower Mg and Si, than at profile Cpx6-p2 where it is 40 μm wide. This clearly reflects sector zonation, with profile Cpx6-p1 crossing a prism sector {hk0} and Cpx6-p2 crossing the hourglass or basal sector

{−111} (cf. Downes, 1974; Leung, 1974; Welsch et al., 2016; Ubide et al., 2019). Clinopyroxene components, Mg# and ΔDiHd thus differ strongly between both profiles but tend to converge near the crystal surface. Consequently, pressures and temperatures calculated for both profiles differ by ca. 200 MPa and 20°C, respectively, almost independent of the distance to the crystal surface. Indeed, pressures calculated along Cpx6-p2 are below the values for most tephrite-hosted clinopyroxenes of the eruption (cf. **Figure 5**). Profile Cpx6-p1, in contrast, yields reasonable P-T estimates at the outer rim zone; the values also agree with those at the outer rim of profile Cpx7-p1 from another phenocryst.

Considering sample SD16, the rim zones of profiles Cpx13-p2 and Cpx15-p1 are both around 20 μm wide and have slightly different compositions (**Figure 7**). The values for ΔDiHd after Mollo et al. (2013) are all within the equilibrium range, as are the differences between predicted and measured clinopyroxene components after Putirka (1999), suggesting that both rim zones grew at conditions not far from equilibrium. Both profiles also indicate similar pressures and temperatures. The Mg# of the rim zones, however, are well below the equilibrium range considered, probably because the profiles are located in Mg-poor sectors. In sample SD19, crystal Cpx7 exhibits a rim zone of about 10–20 μm thickness that is well recognized in a BSE image (**Figure 7**). Profile Cpx7-p3 at prism form {110} reveals irregular variability of ΔDiHd and Mg# with little correlation between both, and large variability of P-T estimates. In contrast, profile Cpx7-p1 at prism form {100} reveals consistently low values for ΔDiHd, strongly decreased Mg#, and less variable P-T estimates in the rim zone, similar to the profiles from sample SD16.

In summary, our clinopyroxene rim traverses show that P-T estimates can be critically affected by the choice of the crystal facet or sector analyzed, but show little dependence on the distance to the crystal surface. This is surprising because the analyzed host groundmass composition is in equilibrium strictly with the clinopyroxene surface only. Nevertheless, the distance of analytical spots to the crystal surface should be as small as possible, although the outermost few μm cannot be analyzed reliably by electron microprobe due to excitation of the adjacent groundmass by the electron beam.

Origin of Clinopyroxene Rim Zonations

The presence of sector zonations in clinopyroxene rim zones, but lack of hopper or dendritic morphologies, suggest that the rims formed by rapid but near-equilibrium crystal growth at low degrees of undercooling, likely < 25°C (Kouchi et al., 1983). Clinopyroxene crystal cores, in contrast, are commonly anhedral and/or complexly zoned, and are inferred to have formed in diverse conditions. Many appear to represent cumulate fragments or entrained crystal mush. Sector zonations in the cores are common (**Figure 7A**), but their limited compositional range compared to rim zones suggests that they formed at lower growth rates. This situation is comparable to clinopyroxene phenocrysts at Etna volcano (Ubide et al., 2019), but is in contrast to the results from a detailed clinopyroxene study from Haleakala volcano, Hawaii, which record initial rapid disequilibrium growth followed by a period of slower crystallization before eruption (Hammer et al., 2016; Welsch et al., 2016). The rims of phonotephrite-hosted clinopyroxenes show similar correlations of Mg# with Si, Al, and Ti as tephrite-hosted ones, but shifted to lower Mg# (**Figure 4A**). This is consistent with rapid but near-equilibrium growth of the rims in a more evolved melt, resulting in sector zonation as expressed by the covariations of Mg, Si, Al, and Ti observed.

The sector-zoned clinopyroxene rim zones raise the question whether they formed in magma reservoirs at depth, or at shallow levels or surface during eruption. For the second scenario, one would expect differences in rim thickness and composition between quickly cooled pyroclasts with glassy matrix (samples SD04 and SD06) and samples that cooled slowly during lava flow emplacement and cooling. **Figure 9** shows that this is not the case, as compositional range and equilibrium criteria of clinopyroxene rims do not differ between pyroclasts and lava flow samples. This similarity implies similar growth conditions for all clinopyroxene rim zones, no matter how fast the magma had cooled after eruption. It follows that the rims must have grown at depth, which is consistent with the barometric results giving overlapping mantle pressures for all tephrite-hosted clinopyroxenes, irrespective of the sample type (**Figure 6**). An exception are the < 2 μm thin outermost rim zones recognized in BSE images of many crystals from lava flows. These likely formed during cooling of the lava, but are too thin to be analyzed reliably with the electron microprobe.

The time scale to form the rim zones may be approximated by a simple one-dimensional diffusion model for the boundary between rim zone and crystal core. We assume that the rim zone formed instantaneously at time $t = 0$ with a stepwise change in Mg# (**Figure 7**), that will subsequently be leveled by Fe-Mg interdiffusion to form an s-shaped gradient. The time for a compositional step to develop an s-shaped profile of length L by diffusion is then approximated as:

$$t = (L/2)^2/(16D^{Fe-Mg})$$

(e.g., Klügel et al., 2000), where D^{Fe-Mg} is the Fe-Mg interdiffusion coefficient. The time t thus represents the period between rim zone formation and the end of diffusion across the rim-crystal core boundary. By using a constant D^{Fe-Mg} of 4×10^{-19} m^2s^{-1} calculated after Müller et al. (2013) for diopside at 1140°C, we obtain diffusion times ranging from 4 days for a < 3 μm long gradient (sample SD04 profile Cpx6-p1), to max. 30 days for up to 8 μm long s-shaped gradients in other profiles (**Figure 7**). These values provide an upper limit for the actual duration of the period in which the rim zones formed, because crystal growth during diffusion (the moving boundary problem) as well as 3-D cutting effects of the investigated crystals are neglected (cf. Costa et al., 2008). Being well aware of these limitations, we suggest that the rim zones of clinopyroxene phenocrysts formed during a few days to weeks. Remarkably, this range of time scales holds for the entire eruption, because neither the width of the rim zones nor

their transition to the core region vary systematically between our samples, whose emplacement dates cover a period of about 2 months (**Table 1**). Indeed, the sharpest rim zone boundary and therefore the shortest diffusion time scale is for profile Cpx6-p1 in sample SD04 from the late stage of the eruption. These observations have the important implication that the rim zones do not reflect an event precursory to the 2014–2015 eruption, but formed sequentially during the course of the eruption within the uppermost mantle, at pressures indicated by our barometric data.

We envisage two plausible scenarios for undercooling and rapid growth of clinopyroxene rim zones at depth: cooling of the host melt due to mixing with a cooler and more evolved magma, or rapid undercooling due to H_2O loss and consequent rise in liquidus temperature (Sparks and Pinkerton, 1978). Magma mixing is a common process for many basaltic volcanoes and may trigger eruptions, as is indicated by petrological studies (e.g., Klügel and Klein, 2006; Kahl et al., 2011). However, the rim zonations of tephrite-hosted clinopyroxenes are not consistent with growth in a more evolved melt. Such a melt would be higher in SiO_2, Al_2O_3 and alkalies, and lower in Mg# and CaO, as is indicated by the liquid line of descent (cf. Hildner et al., 2012). This is at odds with the observed compositional changes in most rim zones, and with the contrasting changes in Mg# at the rims of the same crystal (Cpx6 in sample SD04; **Figure 7**), which are better explained by sector zonations. We conclude, instead, that the rim zones reflect an episode of significant H_2O loss from the melt driving increased crystallization. This could be caused by rapid rise of the magma to another storage level in the mantle or within a convecting reservoir, followed by closed-system degassing, which more effectively removes H_2O from a melt than open-system degassing (Métrich and Wallace, 2008). Alternatively, rapid H_2O loss could occur by CO_2 flushing of the magma reservoir, when the melt re-equilibrates with large amounts of a CO_2-rich fluid phase released from another melt at deeper levels (Métrich and Wallace, 2008; Caricchi et al., 2018). This scenario is not unlikely because highly alkalic Si-undersaturated melts as at Fogo can dissolve >1 wt% of CO_2 at upper mantle conditions (Shishkina et al., 2014; Longpré et al., 2017), and begin to exsolve a carbonic fluid at pressures in excess of 1 GPa as is indicated by fluid inclusion data (Hansteen et al., 1991). The assumption of high CO_2 contents in primary Fogo melts is also consistent with the occurrence of carbonatites on Fogo and adjacent Cape Verde islands (e.g., Hoernle et al., 2002).

A distinction between closed-system degassing and CO_2 flushing as major cause for the inferred H_2O loss would require H_2O-CO_2 data from melt inclusions (Métrich and Wallace, 2008), which are not available. But our data for clinopyroxene rim zones require either process to occur during the ongoing eruption, at a stage where the continuous flux of magma involved movement within a limited pressure range, around 600 MPa, for a few days to weeks. Such near-isobaric magma movement during eruption can occur within a complex storage system (Klügel et al., 2015). This suggests the presence of a deeper storage level from where the eruption was fed, as is probably reflected by the higher pressures obtained for tephrite clinopyroxene cores than for the rims (Mata et al., 2017; **Figure 10**).

Implications of Olivine Rim Zonations

Our data for olivine phenocrysts in lava flow samples reveal that forsterite contents at the rims are too low as to be in equilibrium with the groundmass, and that the rim zoning profiles are shorter in lava flow samples collected near the vents than in those collected far from the vents. These observations imply formation of the olivine rim zonations mainly during lava flow emplacement and cooling after eruption. As the Mg# of the melt decreased due to growth of ferromagnesian crystals, normal zonations developed by a combination of Fe-Mg interdiffusion within the olivine crystals and their growth. The disequilibrium between olivine rims and groundmass likely reflects the preservation of compositional heterogeneities within the advancing lava. As melt transport in the lava flow was not sufficiently turbulent for homogenization to occur, Fe-Mg equilibrium was maintained only locally at the olivine-melt interface, but not at some millimeters distance where our groundmass analyses were carried out. For the quenched lapilli sample SD04, in contrast, there was no time for post-eruptive crystal growth, and olivine rims are close to Fe-Mg equilibrium with the glassy matrix.

The length of zoning profiles at olivine rims from samples SD10 and SD13 (∼4–14 μm) are remarkably similar to those from lava flow samples from the 1995 Fogo eruption that were also collected near the vent (Hildner et al., 2011). These authors analyzed the zonations using a simple semi-infinite slab model for one-dimensional Fe-Mg diffusion, assuming constant olivine composition for time $t < 0$ and instantaneous change to different but constant composition at the olivine-melt interface at $t = 0$; olivine growth or dissolution were neglected. We applied the same diffusion model to olivines from the 2014–2015 lavas and obtained good agreement between analyzed and modeled rim zonations (**Supplementary Figure S1** and **Supplementary Table S8**). Hildner et al. (2011) concluded that the zonations had developed in less than half a day if temperature was fixed at 1100°C. In a slowly cooling lava flow, however, diffusion rates gradually decrease and inferred time scales increase. If we assume a constant D^{Fe-Mg} for a putative mean temperature of 1000 °C as crude approximation, we obtain a value of 2.2×10^{-17} m^2s^{-1} for diffusion along [001] (Dohmen and Chakraborty, 2007). This would increase the time scale of Hildner et al. (2011), who used a value of 1.1×10^{-16} m^2s^{-1}, by a factor of 5. We suggest, therefore, that the zoning profiles from samples SD10 and SD13 developed within 2–3 days during lava flow emplacement and cooling. For samples SD16 and SD21 collected from breakout lobes far from the vents (**Figure 1C**), zoning profiles in olivines are broadly twice as long, resulting in a time scale on the order of 1–2 weeks. This is consistent with the time interval between the rapid advance of the main flow lobe in the last week of November and its inflation in the first few days of December, and the subsequent formation of the Bangaeira breakout lobe, mainly in the period between 7 and 16 December (**Figure 1C** and **Table 1**).

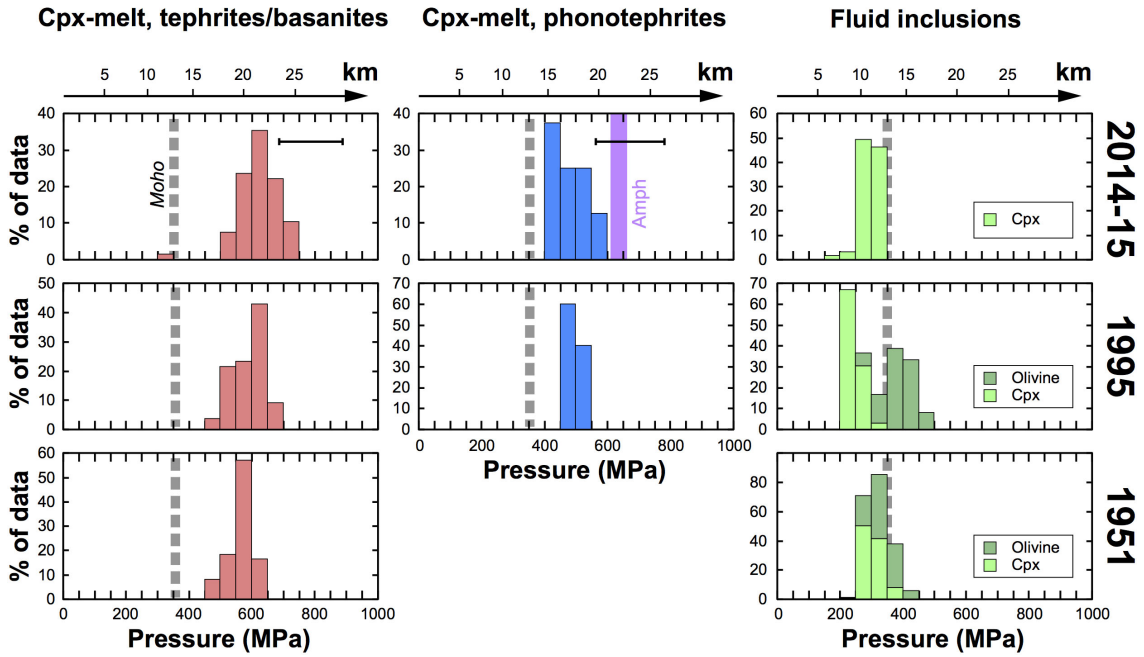

FIGURE 10 | Overview of barometric data for the 2014–2015 eruption (first row), and comparison to data for the preceding 1995 and 1951 eruptions (second and third row; after Hildner et al., 2011, 2012). The diagrams for clinopyroxene-melt barometry display data for phenocryst rims, using the Putirka et al. (2003) calibration and filter 1 as equilibrium test. Shown are the average pressures calculated for each crystal, rather than single analyzed points as in **Figure 5**. Horizontal bars mark the data range for clinopyroxene cores from Mata et al. (2017), and vertical bar labeled "Amph" indicates the pressure range obtained for amphiboles in phonotephrites after Ridolfi et al. (2012). During the 1951 eruption no phonotephrite was erupted. The depth of the Moho (dashed thick lines) and the conversion of pressure to depth are based on the crustal model of Pim et al. (2008).

The very short zoning profiles in sample SD04 (<3 μm) have implications for the speed of magma ascent during the phase of intense strombolian activity in January 2015. When applying the same diffusion model using a temperature of 1140°C as derived from our thermometry, the zonations yield a time scale of <3 h for concomitant growth and diffusive Fe-Mg exchange at olivine rims; for profile directions other than [001] the time scale increases to < 12 h owing to diffusion anisotropy (cf. Dohmen and Chakraborty, 2007). Growth and diffusion are both a consequence of intense H_2O degassing of the ascending magma at shallow levels, because this results in increasing liquidus temperature, increasing degree of undercooling, increasing crystal nucleation and growth, and decreasing melt Mg# (Sparks and Pinkerton, 1978). Our data thus suggest a magma transit time of less than 3–12 h from the final storage level to the surface for the period of intense strombolian activity represented by this sample.

Pressures Derived From Fluid Inclusion Barometry

The clustering of pressures obtained by fluid inclusion barometry is commonly attributed to storage or temporary residence of magma at a discrete level, where formation and/or re-equilibration of inclusions occur (e.g., Roedder, 1983; Hansteen et al., 1998; Zanon et al., 2003; Frezzotti and Peccerillo, 2004; Hansteen and Klügel, 2008; Zanon, 2015). Most pressures derived from CO_2-dominated fluid inclusions in the 2014–2015 tephrites are in the range 240–340 MPa (**Figure 8B**), well below the range indicated by clinopyroxene-melt barometry. This difference is partly due to post-entrapment processes, in particular diffusive H_2O loss and volumetric re-equilibration, which reduce inclusion densities (Roedder, 1984; Bodnar, 2003). The CO_2-dominated fluid inclusions from Fogo should have contained significant H_2O upon trapping, a part of which may have become lost by rapid hydrogen diffusion when the host crystal re-equilibrated with the degassing host melt (Mackwell and Kohlstedt, 1990; Bakker and Jansen, 1991; Lloyd et al., 2016). We assess the impact of this effect by assuming complete loss of 10 mol% of H_2O in the trapped fluid, an amount estimated from a degassing model for basanite melt at about 500 MPa (Dixon et al., 1997). Adding this amount back to the inclusions increases densities by a factor of 1.045 (Hansteen and Klügel, 2008) and changes the main pressure range of our data to 280–410 MPa, calculated using the Kerrick and Jacobs (1981) equation of state for the H_2O-CO_2 system. It is, however, possible that the trapped fluid had contained far less H_2O if CO_2 flushing of the magma had occurred from a deep source. In this case H_2O loss during magma ascent would be less significant, and fluid inclusion compositions would closely reflect trapping conditions.

Volumetric re-equilibration of fluid inclusions can occur by plastic deformation (stretching) of the host crystal, in response to increasing inclusion overpressure during magma ascent (Bodnar, 2003). Stretching is fast at magmatic temperatures; for example,

decompression by 1000 MPa within two days can lower the densities of olivine-hosted CO_2 inclusions by around 10% (Wanamaker and Evans, 1989). To our knowledge, no such data exist for clinopyroxene, but fluid inclusion data suggest similar or larger degrees of re-equilibration than for olivine (Klügel et al., 2000). The effect of stretching is not optically evident but can be recognized by density distributions (Hansteen and Klügel, 2008), as is exemplified by our data. The highest CO_2 inclusion densities were obtained for quickly quenched lapilli (sample SD04), with a maximum at around 0.65 g/cm^3 and a tailing toward lower values, whereas inclusions from lava flow samples have lower densities with a maximum around 0.56–0.60 g/cm^3 (**Figure 8**). This difference suggests that considerable re-equilibration occurred during the residence time of a sample in the flowing lava, and underlines the advantage of using glassy tephra for fluid inclusion studies. The best pressure estimate for fluid inclusion trapping or re-equilibration is thus based on the highest densities for sample SD04, indicating minimum pressures of 320–340 MPa, i.e., within the lowermost crust (**Figure 10**).

The pressures indicated by fluid inclusions likely reflect temporary residence of magma near the Moho boundary, as it moves from a mantle reservoir to the surface during eruption. For short residence times on the order of hours to days, this pending level will not necessarily be reflected by the more sluggish mineral-based barometers. The result is a bimodal pressure distribution (**Figure 10**), as is commonly observed (Klügel et al., 2015). This explanation was corroborated by combined seismic and petrological observations from the 2011–2012 eruption at El Hierro, Canary Islands (Longpré et al., 2014). The El Hierro eruption also demonstrated that a section of lateral magma flow is a possible explanation for temporary magma residence at a limited pressure range during an eruption (López et al., 2012; Martí et al., 2013). We suggest that the fluid inclusion data for the 2014–2015 Fogo eruption reflect short-term "stalling" (i.e., near-isobaric magma movement) of the ascending magma within a complex accumulation zone in the lowermost crust, following previous movement within the uppermost mantle as discussed above.

Model for Magma Plumbing During the 2014–2015 Eruption

Based on the combined data we propose a model for magma storage and transport during the 2014–2015 eruption of Fogo (**Figure 11**). The main storage level where the tephrite magma had accumulated before eruption is probably reflected by barometric data for the cores of normally zoned or unzoned clinopyroxene phenocrysts, indicating 700–900 MPa (24–30 km depth b.s.l.), within the uppermost mantle (Mata et al., 2017). During the course of the eruption the ascending magma picked up crystal mush and cumulate fragments from the walls of the reservoir system, as is indicated by abundant crystal aggregates (microxenoliths) and complex and/or patchy zonations of many clinopyroxene phenocryst cores. At pressures around 600 MPa (21 km depth), the flowing magma passed through a complex storage region, possibly an interconnected network of magma pockets and dikes/sills, where it moved or stayed at nearly isobaric conditions for a few days to weeks (**Figure 11**). Here the observed rim zones grew around clinopyroxene crystals at increased growth rates, expressed by pronounced sector zonations. The reason for undercooling was probably significant H_2O loss of the magma, either by closed-system degassing following decompression, or by flushing with a CO_2-rich fluid phase released from a melt at deeper levels.

During its passage through the storage system in the uppermost mantle, the magma encountered a small pocket of phonotephritic magma, probably a remnant from an earlier eruption or intrusive event. Small volumes of the phonotephrite ascended and were erupted alongside with the tephrite during some phases of the eruption (**Figure 6**). This was accompanied by mingling and limited mixing, as is exemplified by samples SD08 (mingled bomb) and SD06 (transitional composition). The rims of phonotephrite-hosted clinopyroxenes have a similar compositional variability as tephrite-hosted ones, which suggests formation at similar conditions. This coincidence may lend some support to the idea of CO_2 flushing to cause H_2O loss in different magma pockets. The time between H_2O loss and phonotephrite eruption was too short to form thick opacite reaction rims around amphiboles (**Figure 2F**). In contrast, amphiboles in the phonotephrite samples investigated by Mata et al. (2017) show thick reaction rims that were inferred to have grown in $>$ 1 month.

Complex near-isobaric magma movement in the mantle storage system at around 600 MPa, combined with varying flow rates and local mixing with earlier remnant magmas, may explain the mild irregular variations in melt composition during the course of eruption (**Table 2**). It may also explain the variations of barometric results between different samples (**Figure 6B**), as these depend not only on pressure but also on melt composition and on crystal growth rates as discussed above. The magma flow rate might have had an influence on the barometric results, but deciphering causal relationship would require barometric data for more samples as well as data for the magma flux over time.

As the magma continued to rise, it entered another "stalling" level around the Moho to lowermost crust. This horizon has been denoted as magma accumulation zone (Klügel et al., 2015) and is reflected by density distributions of fluid inclusions, but not by clinopyroxene barometry. The magma thus remained at this level for not very long, probably no more than a day. After leaving this zone, final ascent to the surface was fast and occurred in less than 3–12 h in the case of sample SD04 from the late phase of the eruption, as was deduced from olivine rim zonations. There is no petrological indication for another horizon between the lower crust and the surface that would slow down the ascending magma.

Implications for Magma Plumbing at Fogo

A comparison of the barometric data for the 2014–2015, 1995, and 1951 Fogo eruptions reveals a consistent picture of magma storage and transport (**Figure 10**). Clinopyroxene-melt barometry on phenocryst rims and groundmass in tephrites yields very similar pressure distributions for all three eruptions

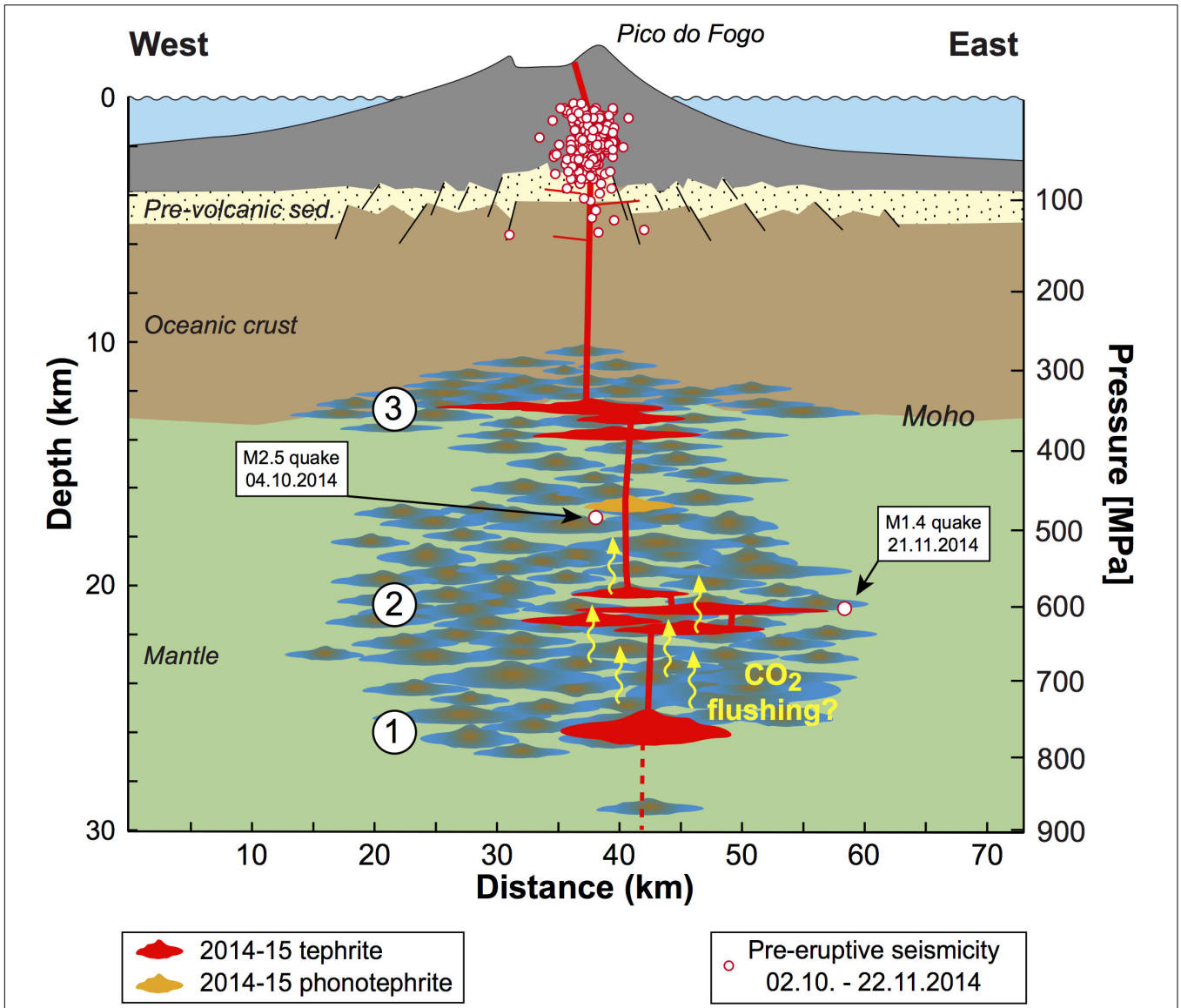

FIGURE 11 | Cross-section of Fogo (2x vertical exaggeration) with lithological boundaries after the crustal model of Pim et al. (2008), showing the inferred magma plumbing and seismic precursors of the 2014–2015 eruption. Magma storage in the uppermost mantle is envisaged as a complex system with interconnected small pockets or compartments, in which batches of melt can evolve separately. This allows compositionally diverse magmas to be discharged in a single eruption (Klügel et al., 2005; Gudmundsson, 2012; Hildner et al., 2012). Major magma storage levels for the 2014–2015 magmas are indicated: (1) storage and crystal fractionation before eruption as indicated by clinopyroxene cores; (2) temporary stalling (near-isobaric magma flow) in a complex storage zone as indicated by clinopyroxene rims; (3) temporary stalling in a magma accumulation zone near the Moho as indicated by fluid inclusions.

with maxima around 550–700 MPa. The small differences between eruptions may reflect different methods to determine melt compositions: the present study applied in-situ groundmass analyses by LA-ICP-MS, whereas data for the 1995 and 1951 eruptions used glass analyses and whole-rock compositions corrected for phenocryst content (Hildner et al., 2011, 2012). The pressures document last equilibration between clinopyroxene phenocrysts and host melt at about 19–24 km depth, in a complex storage system in the uppermost mantle. This is not necessarily the depth at which the bulk of the magma accumulates before eruption, because data for the 2014–2015 eruption suggest prior storage at deeper levels (Mata et al., 2017). Magma movement into or from deeper reservoirs was probably the cause for an isolated cluster of >20 earthquakes with focal depths between approximately 38 and 44 km, that were recorded on 15 August 2016 (Leva et al., 2019). The presence of magma reservoirs at such great depths is, however, not reflected by existing mineral barometry data from Fogo.

Phonotephrites appear to form at similar or slightly shallower levels than tephrites and basanites, as is suggested by clinopyroxene-melt barometry data for the 1995 and 2014–2015 eruptions (**Figure 10**). It appears common that small amounts

of phonotephrite are discharged at the beginning and/or end of an eruption (Munhá et al., 1997; Hildner et al., 2011). The phonotephrites are probably derived by crystal fractionation from magmas left in the mantle storage system after an eruption, and are pushed ahead by the newly arriving magma. Mixing between the different magmas is limited, however, as only few samples have intermediate compositions.

Another complex magma accumulation zone common to recent Fogo eruptions appears to exist at about 10–14 km depth, around the Moho. This is inferred from fluid inclusion barometry on phenocrysts from the 2014–2015 and 1951 tephrites, yielding overlapping pressures around 250–400 MPa (**Figure 10**). Inclusions in phenocrysts from the 1995 eruption indicate a more widespread pressure distribution, which can be explained by two distinct host lava types (tephrites/basanites and phonotephrites) for the investigated phenocrysts. Magmas are believed to remain at this depth range for a short time, on the order of a day, before rapid final ascent to the surface continues. Such behavior could be explained by lateral magma movement around Moho depths, as was the case for the 2011–2012 El Hierro eruption (López et al., 2012; Martí et al., 2013; Longpré et al., 2014), but for Fogo no such evidence exists.

The available petrological and geodetic data demonstrate that crustal magma storage is subordinate at Fogo. This does not rule out that sills and dikes in addition to the main conduit intrude the crust and volcanic edifice at various levels before and during an eruption. But the volume of individual intrusions is limited, because no island-wide deformation was recorded during the pre-eruptive and co-eruptive phases of the 1995 and 2014–2015 eruptions (Amelung and Day, 2002; González et al., 2015). Neither is there a crustal magma reservoir, nor has there been one in the recent past of the island (Hildner et al., 2012).

Comparison With Seismic Monitoring Data

Remarkably, the seismic precursors of the 2014–2015 eruption were much shallower than the depths inferred for magma storage (**Figure 11**). The only exceptions are a single M2.5 event at ca. 17 km depth, which was considered to be the first precursor heralding the ascent of new magma, and a M1.4 event at ca. 21 km depth. These depths coincide very well with our clinopyroxene-melt barometry data. Further movement of the magma through newly formed dikes occurred almost aseismically, until it reached the sediment layer beneath Fogo and the volcanic edifice itself. Dike emplacement resulted in a seismic swarm of <300 small events during 6 days before eruption. The situation at Fogo in 2014 was thus very different from the 2011–2012 eruption at El Hierro, where precursory unrest involved >10,000 seismic events located within the lower crust to Moho, as well as island-wide surface deformation and increased CO_2, H_2S and radon emissions, over 3 months (López et al., 2012; Pérez et al., 2012; Martí et al., 2013; González et al., 2015). This difference in precursory unrest is likely related to the much longer recurrence intervals at El Hierro (1–2 kyrs; Carracedo et al., 2001) compared to Fogo (around 20 years; Day et al., 2000), resulting in a different thermal state of the crust beneath both islands. In addition, the volume erupted in 2011–2012 at El Hierro (330×10^6 m^3; Rivera et al., 2013) was considerably larger than at Fogo (44×10^6 m^3; Richter et al., 2016), implying a much greater deformation of the host rocks around the magma reservoirs.

CONCLUSION

Our petrological study of samples from the Fogo 2014–2015 eruption yields the following conclusions:

- The strategy of sampling a stratigraphically controlled sequence was beneficial and revealed some variation in melt composition during the course of the eruption.
- Clinopyroxene-melt thermobarometry was successfully applied to phenocryst rim and host groundmass pairs, even though the rims are sector-zoned due to rapid growth. Mineral-melt pairs had to be filtered using appropriate equilibrium criteria.
- Rim zones around clinopyroxene phenocrysts formed during the ongoing eruption, within a few days to weeks, as a consequence of H_2O loss from the melt. This could have been caused by either degassing following a rise of the magma, or CO_2 flushing by a carbonic fluid phase released at deeper levels. The rim zones do not reflect an event precursory to the 2014–2015 eruption.
- Our barometric data suggest that most clinopyroxene rim zones formed at around 600 MPa pressure, during a phase of near-isobaric magma movement through a complex storage system within the uppermost mantle. The magma entered this system after having accumulated at deeper levels before eruption.
- CO_2-dominated fluid inclusions in clinopyroxene phenocrysts document short stalling (on the order of a day) of the ascending magma within the lowermost crust to Moho.
- Normal rim zonations of olivine phenocrysts formed mainly during lava flow emplacement and cooling after eruption. Olivine zonations are very short in quenched samples, suggesting a magma transit time of less than 3–12 h from the last storage level to the surface.

DATA AVAILABILITY STATEMENT

All datasets generated for this study are included in the article/**Supplementary Material**.

AUTHOR CONTRIBUTIONS

SD developed the sampling strategy, selected sampling sites, and collected the samples. BF collected and processed the seismic data. AK and MS analyzed the samples with electron microprobe and LA-ICP-MS. MS carried out microthermometry. AK led the petrological modeling and the writing of the manuscript. All authors were actively involved in the discussion, interpretation of the data, and participated in the preparation of the manuscript.

FUNDING

The analyses at Bremen University were carried out during the M.Sc. thesis of MS and were supported by department funds and by the German Research Foundation (DFG Grant KL1313/9-2, Programmpauschale).

ACKNOWLEDGMENTS

We thank B. Hirn and F. Ferrucci (Open University, United Kingdom) for processing the Operational Land Imager (OLI) and Earth Observing-1 Advanced Land Imager (ALI) data, and S. Sopke and P. Monien (Universität Bremen) for support during the analytical work. We appreciate the thoughtful and constructive reviews by SM and TK, and the comments by the associate editor, TU, which clarified some aspects and improved the manuscript.

SUPPLEMENTARY MATERIAL

The Supplementary Material for this article can be found online at: https://www.frontiersin.org/articles/10.3389/feart.2020.00157/full#supplementary-material

Downloadable Excel versions of **Tables 1–3** are available as **Supplementary Material S10–S12**.

REFERENCES

Amelung, F., and Day, S. (2002). InSAR observations of the 1995 Fogo, Cape Verde, eruption: implications for the effects of collapse events upon island volcanoes. *Geophys. Res. Lett.* 29, 41–47. doi: 10.1029/2001GL013760

Andersen, T., and Neumann, E. R. (2001). Fluid inclusions in mantle xenoliths. *Lithos* 55, 301–320. doi: 10.1016/s0024-4937(00)00049-9

Bakker, R. J., and Jansen, J. B. H. (1991). Experimental post-entrapment water loss from synthetic CO2-H2O inclusions in natural quartz. *Geochim. Cosmochim. Acta* 55, 2215–2230. doi: 10.1016/0016-7037(91)90098-p

Barker, A., Troll, V., Carracedo, J., and Nicholls, P. (2015). The magma plumbing system for the 1971 Teneguía eruption on La Palma, Canary Islands. *Contribut. Mineral. Petrol.* 170, 1–21. doi: 10.1007/s00410-015-1207-7

Bodnar, R. J. (2003). "Reequilibration of fluid inclusions," in *Fluid Inclusions: Analysis and Interpretation, Short Course Series*, eds I. Samson, A. Anderson, and D. Marshall (Vancouver: Mineralogical Association of Canada), 213–231.

Brophy, J. G., Whittington, C. S., and Park, Y. R. (1999). Sector-zoned augite megacrysts in Aleutian high alumina basalts: implications for the conditions of basalt crystallization and the generation of calc-alkaline series magmas. *Contribut. Mineral. Petrol.* 135, 277–290. doi: 10.1007/s004100050512

Cappello, A., Ganci, G., Calvari, S., Pérez, N. M., Hernández, P. A., Silva, S. V., et al. (2016). Lava flow hazard modeling during the 2014-2015 Fogo eruption, Cape Verde. *J. Geophys. Res. Solid Earth* 121, 2290–2303. doi: 10.1002/2015jb012666

Caricchi, L., Sheldrake, T. E., and Blundy, J. (2018). Modulation of magmatic processes by CO2 flushing. *Earth Planet. Sci. Lett.* 491, 160–171. doi: 10.1016/j.epsl.2018.03.042

Carracedo, J. C., Badiola, E. R., Guillou, H., de La Nuez, J., and Pérez Torrado, F. J. (2001). Geology and volcanology of la palma and el hierro, western Canaries. *Estud. Geol.* 57, 175–273.

Cashman, K. V., Sparks, R. S. J., and Blundy, J. D. (2017). Vertically extensive and unstable magmatic systems: a unified view of igneous processes. *Science* 355:eaag3055. doi: 10.1126/science.aag3055

Costa, F., Dohmen, R., and Chakraborty, S. (2008). Time scales of magmatic processes from modeling the zoning patterns of crystals. *Rev. Mineral. Geochem.* 69, 545–594. doi: 10.1515/9781501508486-015

Costa, F., and Morgan, D. (2011). "Time constraints from chemical equilibration in magmatic crystals," in *Timescales of Magmatic Processes: From Core to Atmosphere*, eds A. Dosseto, S. P. Turner, and J. A. Van Orman (Hoboken, NJ: Blackwell Publishing Ltd), 125–159. doi: 10.1002/9781444328509.ch7

Crough, S. T. (1978). Thermal origin of mid-plate hot-spot swells. *Geophys. J. R. Astron. Soc.* 55, 451–469. doi: 10.1111/j.1365-246x.1978.tb04282.x

Crough, S. T. (1982). Geoid anomalies over the Cape Verde Rise. *Mar. Geophys. Res.* 5, 263–271. doi: 10.1007/BF00305564

Davidson, J. P., Morgan, D. J., Charlier, B. L. A., Harlou, R., and Hora, J. M. (2007). Microsampling and isotopic analysis of igneous rocks: implications for the study of magmatic systems. *Ann. Rev. Earth Planet. Sci.* 35, 273–311. doi: 10.1146/annurev.earth.35.031306.140211

Day, S. J., Carracedo, J. C., Guillou, H., Pais Pais, F. J., Badiola, E. R., Fonseca, J. F. B. D., et al. (2000). Comparison and cross-checking of historical, archaeological and geological evidence for the location and type of historical and sub-historical eruptions of multiple-vent oceanic island volcanoes. *Geol. Soc. Lond. Spec. Public.* 171:281. doi: 10.1144/GSL.SP.2000.171.01.21

Day, S. J., Heleno da Silva, S. I. N., and Fonseca, J. F. B. D. (1999). A past giant lateral collapse and present-day flank instability of Fogo, Cape Verde Islands. *J. Volcanol. Geotherm. Res.* 94, 191–218. doi: 10.1038/s41467-017-01256-2

Dixon, J. E., Clague, D. A., Wallace, P., and Poreda, R. (1997). Volatiles in alkalic basalts from the North Arch volcanic field, Hawaii: extensive degassing of deep submarine-erupted alkalic series lavas. *J. Petrol.* 38, 911–939. doi: 10.1093/petroj/38.7.911

Dohmen, R., and Chakraborty, S. (2007). Fe-Mg diffusion in olivine II: point defect chemistry, change of diffusion mechanisms and a model for calculation of diffusion coefficients in natural olivine. *Phys. Chem. Miner.* 34, 409–430. doi: 10.1007/s00269-007-0158-6

Doucelance, R., Escrig, S., Moreira, M., Gariépy, C., and Kurz, M. (2003). Pb-Sr-He isotope and trace element geochemistry of the Cape Verde Archipelago. *Geochim. Cosmochim. Acta* 67, 3717–3733. doi: 10.1016/s0016-7037(03)00161-3

Downes, M. J. (1974). Sector and oscillatory zoning in calcic augites from M. Etna, Sicily. *Contribut. Mineral. Petrol.* 47, 187–196. doi: 10.1007/BF00371538

Eisele, S., Reißig, S., Freundt, A., Kutterolf, S., Nürnberg, D., Wang, K. L., et al. (2015). Pleistocene to Holocene offshore tephrostratigraphy of highly explosive eruptions from the southwestern Cape Verde Archipelago. *Mar. Geol.* 369, 233–250. doi: 10.1016/j.margeo.2015.09.006

Escrig, S., Doucelance, R., Moreira, M., and Allégre, C. J. (2005). Os isotope systematics in Fogo Island: evidence for lower continental crust fragments under the Cape Verde Southern Islands. *Chem. Geol.* 219, 93–113. doi: 10.1016/j.chemgeo.2005.02.011

Faria, B., and Fonseca, J. F. B. D. (2014). Investigating volcanic hazard in Cape Verde Islands through geophysical monitoring: network description and first results. *Nat. Hazards Earth Syst. Sci.* 14, 485–499. doi: 10.5194/nhess-14-485-2014

Ferguson, A. K. (1973). On hour-glass sector zoning in clinopyroxene. *Mineral. Magaz.* 39, 321–325. doi: 10.1180/minmag.1973.039.303.08

Foeken, J. P. T., Day, S., and Stuart, F. M. (2009). Cosmogenic 3He exposure dating of the Quaternary basalts from Fogo, Cape Verdes: Implications for rift zone and magmatic reorganisation. *Q. Geochronol.* 4, 37–49. doi: 10.1016/j.quageo.2008.07.002

Frezzotti, M. L., Andersen, T., Neumann, E. R., and Simonsen, S. L. (2002). Carbonatite melt–CO2 fluid inclusions in mantle xenoliths from Tenerife, Canary Islands: a story of trapping, immiscibility and fluid–rock interaction in the upper mantle. *Lithos* 64, 77–96. doi: 10.1016/s0024-4937(02)00178-0

Frezzotti, M. L., and Peccerillo, A. (2004). Fluid inclusion and petrological studies elucidate reconstruction of magma conduits. *EOS Trans. Am. Geophys. Union* 85, 157–163. doi: 10.1029/2004eo160001

Frezzotti, M.-L., and Touret, J. L. R. (2014). CO2, carbonate-rich melts, and brines in the mantle. *Geosci. Front.* 5, 697–710. doi: 10.1016/j.gsf.2014.03.014

González, P. J., Bagnardi, M., Hooper, A. J., Larsen, Y., Marinkovic, P., Samsonov, S. V., et al. (2015). The 2014–2015 eruption of Fogo volcano: geodetic modeling of Sentinel-1 TOPS interferometry. *Geophys. Res. Lett.* 42, 9239–9246. doi: 10.1002/2015GL066003

Gudmundsson, A. (2012). Magma chambers: formation, local stresses, excess pressures, and compartments. *J. Volcanol. Geotherm. Res.* 23, 19–41. doi: 10.1016/j.jvolgeores.2012.05.015

Hammer, J., Jacob, S., Welsch, B., Hellebrand, E., and Sinton, J. (2016). Clinopyroxene in postshield *Haleakala ankaramite*: 1. efficacy of thermobarometry. *Contribut. Mineral. Petrol.* 171, 1–23. doi: 10.1007/s00410-015-1212-x

Hansteen, T. H., Andersen, T., Neumann, E. R., and Jelsma, H. (1991). Fluid and silicate glass inclusions in ultramafic and mafic xenoliths from Hierro, Canary Islands: implications for mantle metasomatism. *Contribut. Mineral. Petrol.* 107, 242–254. doi: 10.1007/bf00310710

Hansteen, T. H., and Klügel, A. (2008). "Fluid inclusion thermobarometry as a tracer for magmatic processes," in *Reviews in Mineralogy Vol. 69: Minerals, Inclusions And Volcanic Processes*, eds K. D. Putirka and F. J. Tepley (Chantilly: Mineralogical Society of America), 143–177. doi: 10.2138/rmg.2008.69.5

Hansteen, T. H., Klügel, A., and Schmincke, H. U. (1998). Multi-stage magma ascent beneath the Canary Islands: evidence from fluid inclusions. *Contribut. Mineral. Petrol.* 132, 48–64. doi: 10.1007/s004100050404

Heleno da Silva, S., Day, S., and Fonseca, J. (1999). Fogo volcano, Cape Verde Islands: seismicity-derived constraints on the mechanism of the 1995 eruption. *J. Volcanol. Geotherm. Res.* 94, 219–231. doi: 10.1016/s0377-0273(99)00104-3

Hildner, E., Klügel, A., and Hansteen, T. H. (2012). Barometry of lavas from the 1951 eruption of Fogo, Cape Verde Islands: implications for historic and prehistoric magma plumbing systems. *J. Volcanol. Geotherm. Res.* 21, 73–90. doi: 10.1016/j.jvolgeores.2011.12.014

Hildner, E., Klügel, A., and Hauff, F. (2011). Magma storage and ascent during the 1995 eruption of Fogo, Cape Verde Archipelago. *Contribut. Mineral. Petrol.* 162, 751–772. doi: 10.1007/s00410-011-0623-6

Hoernle, K., Tilton, G., Le Bas, M. J., Duggen, S., and Garbe-Schönberg, D. (2002). Geochemistry of oceanic carbonatites compared with continental carbonatites: mantle recycling of oceanic crustal carbonatite. *Contribut. Mineral. Petrol.* 142, 520–542. doi: 10.1007/s004100100308

Holm, P. M., Grandvuinet, T., Friis, J., Wilson, R., Barker, A. K., and Plesner, S. (2008). An 40Ar-39Ar study of the Cape Verde hot spot: temporal evolution in a semistationary plate environment. *J. Geophys. Res.* 113:B08201.

Jarosewich, E., Gooley, R., and Husler, J. (1987). Chromium augite - a new microprobe reference sample. *Geostand. Newslett.* 11, 197–198. doi: 10.1111/j.1751-908x.1987.tb00027.x

Jarosewich, E. J., Nelen, J. A., and Norberg, J. A. (1980). Reference samples for electron microprobe analysis. *Geostand. Newslett.* 44, 257–258.

Jenkins, S. F., Day, S. J., Faria, B. V. E., and Fonseca, J. F. B. D. (2017). Damage from lava flows: insights from the 2014-2015 eruption of Fogo, Cape Verde. *J. Appl. Volcanol.* 6:6. doi: 10.1186/s13617-017-0057-6

Jochum, K. P., Willbold, M., Raczek, I., Stoll, B., and Herwig, K. (2005). Chemical Characterisation of the USGS Reference Glasses GSA-1G, GSC-1G, GSD-1G, GSE-1G, BCR-2G, BHVO-2G and BIR-1G Using EPMA, ID-TIMS, ID-ICP-MS and LA-ICP-MS. *Geostand. Geoanalyt. Res.* 29, 285–302. doi: 10.1111/j.1751-908x.2005.tb00901.x

Kahl, M., Chakraborty, S., Costa, F., and Pompilio, M. (2011). Dynamic plumbing system beneath volcanoes revealed by kinetic modeling, and the connection to monitoring data: an example from Mt. Etna. *Earth Planet. Sci. Lett.* 308, 11–22. doi: 10.1016/j.epsl.2011.05.008

Kahl, M., Chakraborty, S., Costa, F., Pompilio, M., Liuzzo, M., and Viccaro, M. (2013). Compositionally zoned crystals and real-time degassing data reveal changes in magma transfer dynamics during the 2006 summit eruptive episodes of Mt. Etna. *Bull. Volcanol.* 75:692. doi: 10.1007/s00445-013-0692-7

Kerrick, D. M., and Jacobs, G. K. (1981). A modified Redlich-Kwong equation for H2O, CO2 and H2O-CO2 mixtures at elevated temperatures and pressures. *Am. J. Sci.* 281, 735–767.

Klügel, A., Hoernle, K. A., Schmincke, H. U., and White, J. D. L. (2000). The chemically zoned 1949 eruption on La Palma (Canary Islands): petrologic evolution and magma supply dynamics of a rift-zone eruption. *J. Geophys. Res.* 105, 5997–6016. doi: 10.1029/1999jb900334

Klügel, A., Hansteen, T. H., and Galipp, K. (2005). Magma storage and underplating beneath Cumbre Vieja volcano, La Palma (Canary Islands). *Earth Planet. Sci. Lett.* 236, 211–226. doi: 10.1016/j.epsl.2005.04.006

Klügel, A., and Klein, F. (2006). Complex magma storage and ascent at embryonic submarine volcanoes from Madeira Archipelago. *Geology* 34, 337–340.

Klügel, A., Longpré, M.-A., García-Cañada, L., and Stix, J. (2015). Deep intrusions, lateral magma transport and related uplift at ocean island volcanoes. *Earth Planet. Sci. Lett.* 431, 140–149. doi: 10.1016/j.epsl.2015.09.031

Kokfelt, T. F. (1998). *A Geochemical And Isotopic Study Of The Island Of Fogo, The Cape Verde Islands*. Ph.D. thesis, University of Copenhagen, Copenhagen.

Kouchi, A., Sugawara, Y., Kashima, K., and Sunagawa, I. (1983). Laboratory growth of sector zoned clinopyroxenes in the system CaMgSi2O6-CaTiAl2O6. *Contribut. Mineral. Petrol.* 83, 177–184. doi: 10.1007/BF00373091

LeMaitre, R. W., Bateman, P., Dudek, A., Keller, J., Lameyre, J., Le Bas, M. J., et al. (1989). *A Classification of Igneous Rocks and Glossary of Terms - Recommendations of the International Union of Geological Sciences Subcommission on the Systematics of Igneous Rocks*. Oxford: Blackwell Scientific Publications.

Leung, I. S. (1974). Sector-zoned titanaugites: morphology, crystal chemistry, and growth. *Am. Mineral.* 59, 127–138.

Leva, C., Rümpker, G., Link, F., and Wölbern, I. (2019). Mantle earthquakes beneath Fogo volcano, Cape Verde: evidence for subcrustal fracturing induced by magmatic injection. *J. Volcanol. Geotherm. Res.* 386:106672. doi: 10.1016/j.jvolgeores.2019.106672

Lloyd, A. S., Ferriss, E., Ruprecht, P., Hauri, E. H., Jicha, B. R, and Plank, T. (2016). An assessment of clinopyroxene as a recorder of magmatic water and magma ascent rate. *J. Petrol.* 57, 1865–1886. doi: 10.1093/petrology/egw058

Longpré, M. A., Klügel, A., Diehl, A., and Stix, J. (2014). Mixing in mantle magma reservoirs prior to and during the 2011–2012 eruption at El Hierro, Canary Islands. *Geology* 42, 315–318. doi: 10.1130/G35165.1

Longpré, M.-A., Stix, J., Klügel, A., and Shimizu, N. (2017). Mantle to surface degassing of carbon- and sulphur-rich alkaline magma at El Hierro, Canary Islands. *Earth Planet. Sci. Lett.* 460, 268–280. doi: 10.1016/j.epsl.2016.11.043

López, C., Blanco, M. J., Abella, R., Brenes, B., Cabrera Rodríguez, V. M., Casas, B., et al. (2012). Monitoring the volcanic unrest of El Hierro (Canary Islands) before the onset of the 2011–2012 submarine eruption. *Geophys. Res. Lett.* 39, 1–7. doi: 10.1029/2012GL051846

Mackwell, S. J., and Kohlstedt, D. L. (1990). Diffusion of hydrogen in olivine: implications for water in the mantle. *J. Geophys. Res.* 95, 5079–5088.

Madeira, J., Brum da Silveira, A., Mata, J., Mourao, C., and Martins, S. (2008). The role of mass movements on the geomorphologic evolution of ocean islands: examples from Fogo and Brava in the Cape Verde archipelago. *Comunões Geol.* 95, 99–112.

Madeira, J., Ramalho, R. S., Hoffmann, D. L., Mata, J., and Moreira, M. (2019). A geological record of multiple Pleistocene tsunami inundations in an oceanic island: the case of Maio, Cape Verde. *Sedimentology* 67, 1529–1552. doi: 10.1111/sed.12612

Marques, F. O., Hildenbrand, A., Victória, S. S., Cunha, C., and Dias, P. (2019). Caldera or flank collapse in the Fogo volcano? What age? Consequences for risk assessment in volcanic islands. *J. Volcanol. Geotherm. Res.* 388:106686. doi: 10.1016/j.jvolgeores.2019.106686

Martí, J., Pinel, V., López, C., Geyer, A., Abella, R., Tárraga, M., et al. (2013). Causes and mechanisms of the 2011–2012 El Hierro (Canary Islands) submarine eruption. *J. Geophys. Res.* 118, 1–17. doi: 10.1002/jgrb.50087

Martínez-Moreno, F. J., Monteiro Santos, F. A., Madeira, J., Pous, J., Bernardo, I., Soares, A., et al. (2018). Investigating collapse structures in oceanic islands using magnetotelluric surveys: the case of Fogo Island in Cape Verde. *J. Volcanol. Geotherm. Res.* 357, 152–162. doi: 10.1016/j.jvolgeores.2018.04.028

Masson, D. G., Le Bas, T. P., Grevemeyer, I., and Weinrebe, W. (2008). Flank collapse and large-scale landsliding in the Cape Verde Islands, off West Africa. *Geochem. Geophys. Geosyst.* 9:Q07015.

Mata, J., Martins, S., Mattielli, N., Madeira, J., Faria, B., Ramalho, R. S., et al. (2017). The 2014–15 eruption and the short-term geochemical evolution of the Fogo

volcano (Cape Verde): evidence for small-scale mantle heterogeneity. *Lithos* 288-289, 91–107. doi: 10.1016/j.lithos.2017.07.001

Métrich, N., and Wallace, P. J. (2008). "Volatile abundances in basaltic magmas and their degassing paths tracked by melt inclusions," in *Reviews in Mineralogy and Geochemistry Vol. 69: Minerals, Inclusions And Volcanic Processes*, eds K. D. Putirka and F. J. Tepley (Chantilly: Mineralogical Society of America), 363–402. doi: 10.1515/9781501508486-011

Mollo, S., Del Gaudio, P., Ventura, G., Iezzi, G., and Scarlato, P. (2010). Dependence of clinopyroxene composition on cooling rate in basaltic magmas: implications for thermobarometry. *Lithos* 118, 302–312. doi: 10.1016/j.lithos.2010.05.006

Mollo, S., and Masotta, M. (2014). Optimizing pre-eruptive temperature estimates in thermally and chemically zoned magma chambers. *Chem. Geol.* 368, 97–103. doi: 10.1016/j.chemgeo.2014.01.007

Mollo, S., Putirka, K., Misiti, V., Soligo, M., and Scarlato, P. (2013). A new test for equilibrium based on clinopyroxene-melt pairs: clues on the solidification temperatures of Etnean alkaline melts at post-eruptive conditions. *Chem. Geol.* 352, 92–100. doi: 10.1016/j.chemgeo.2013.05.026

Moussallam, Y., Longpré, M.-A., McCammon, C., Gomez-Ulla, A., Rose-Koga, E. F., Scaillet, B., et al. (2019). Mantle plumes are oxidised. *Earth Planet. Sci. Lett.* 527:115798. doi: 10.1016/j.epsl.2019.115798

Müller, T., Dohmen, R., Becker, H. W., Heege, J., and Chakraborty, S. (2013). Fe-Mg interdiffusion rates in clinopyroxene: experimental data and implications for Fe-Mg exchange geothermometers. *Contribut. Mineral. Petrol.* 166, 1563–1576. doi: 10.1007/s00410-013-0941-y

Munhá, J. M., Mendes, M. H., Palácios, T., Silva, L. C., and Torres, P. C. (1997). "Petrologia e geoquímica da erupção de 1995 e de outras lavas históricas na Ilha do Fogo, Cabo Verde," in *A Erupção Vulcanica de 1995 Na Ilha Do Fogo, Cabo Verde*, ed. A. Réffega (Lisbon: Instituto de Investigação Científica e Tropical), 171–186.

Nakamura, Y., and Coombs, D. S. (1973). Clinopyroxenes in the tawhiroko tholeiitic dolerite at Moeraki, north-eastern Otago, New Zealand. *Contribut. Mineral. Petrol.* 42, 213–228. doi: 10.1007/BF00371586

Neave, D. A., Namur, O., Shorttle, O., and Holtz, F. (2019). Magmatic evolution biases basaltic records of mantle chemistry towards melts from recycled sources. *Earth Planet. Sci. Lett.* 520, 199–211. doi: 10.1016/j.epsl.2019.06.003

Neave, D. A., and Putirka, K. (2017). A new clinopyroxene-liquid barometer, and implications for magma storage pressures under Icelandic rift zones. *Am. Mineral.* 102, 777–794. doi: 10.2138/am-2017-5968

Pérez, N. M., Padilla, G. D., Padrón, E., Hernández, P. A., Melián, G. V., Barrancos, J., et al. (2012). Precursory diffuse CO2 and H2S emission signatures of the 2011–2012 El Hierro submarine eruption, Canary Islands. *Geophys. Res. Lett.* 39:L16311. doi: 10.1029/2012gl052410

Pim, J., Peirce, C., Watts, A. B., Grevemeyer, I., and Krabbenhoeft, A. (2008). Crustal structure and origin of the Cape Verde Rise. *Earth Planet. Sci. Lett.* 272, 422–428. doi: 10.1016/j.epsl.2008.05.012

Putirka, K. (1999). Clinopyroxene + liquid equilibria to 100 kbar and 2450 K. *Contribut. Mineral. Petrol.* 135, 151–163. doi: 10.1007/s004100050503

Putirka, K. (2016a). Amphibole thermometers and barometers for igneous systems and some implications for eruption mechanisms of felsic magmas at arc volcanoes. *Am. Mineral.* 101, 841–858. doi: 10.2138/am-2016-5506

Putirka, K. (2016b). Rates and styles of planetary cooling on Earth, Moon, Mars, and Vesta, using new models for oxygen fugacity, ferric-ferrous ratios, olivine-liquid Fe-Mg exchange, and mantle potential temperature. *Am. Mineral.* 101, 819–840. doi: 10.2138/am-2016-5402

Putirka, K. D. (2008). "Thermometers and barometers for volcanic systems," in *Reviews in Mineralogy and Geochemistry Vol. 69: Minerals, Inclusions And Volcanic Processes*, eds K. D. Putirka and F. J. Tepley (Chantilly: Mineralogical Society of America), 61–120. doi: 10.1515/9781501508486-004

Putirka, K. D., Mikaelian, H., Ryerson, F., and Shaw, H. (2003). New clinopyroxene-liquid thermobarometers for mafic, evolved, and volatile-bearing lava compositions, with applications to lavas from Tibet and the Snake River Plain, Idaho. *Am. Mineral.* 88, 1542–1554. doi: 10.2138/am-2003-1017

Putirka, K. D., Perfit, M., Ryerson, F. J, and Jackson, M. G. (2007). Ambient and excess mantle temperatures, olivine thermometry, and active vs. passive upwelling. *Chem. Geol.* 241, 177–206. doi: 10.1016/j.chemgeo.2007.01.014

Putirka, K. D., and Tepley, F. J. (eds) (2008). *Reviews in Mineralogy and Geochemistry Vol. 69: Minerals, Inclusions And Volcanic Processes*. Chantilly: Mineralogical Society of America.

Ramalho, R. S., Winckler, G., Madeira, J., Helffrich, G. R., Hipólito, A., Quartau, R., et al. (2015). Hazard potential of volcanic flank collapses raised by new megatsunami evidence. *Sci. Adv.* 1:e1500456. doi: 10.1126/sciadv.1500456

Ribeiro, O. (1954). *A Ilha Do Fogo E As Suas Erupções*. Lisbon: Junta de Investigações do Ultramar.

Richter, N., Favalli, M., De Zeeuw-van Dalfsen, E., Fornaciai, A., Fernandes, R., Pérez, N., et al. (2016). Lava flow hazard at Fogo Volcano, Cabo Verde, before and after the 2014–2015 eruption. *Nat. Hazards Earth Syst. Sci.* 16, 1925–1951. doi: 10.5194/nhess-16-1925-2016

Ridolfi, F., Renzulli, A., and Puerini, M. (2012). Calcic amphiboles in calc-alkaline and alkaline magmas: thermobarometric and chemometric empirical equations valid up to 1,130 °C and 2.2 GPa. *Contribut. Mineral. Petrol.* 163, 877–895. doi: 10.1007/s00410-011-0704-6

Rivera, J., Lastras, G., Canals, M., Acosta, J., Arrese, B., Hermida, N., et al. (2013). Construction of an oceanic island: insights from the El Hierro (Canary Islands) 2011-2012 submarine volcanic eruption. *Geology* 41, 355–358. doi: 10.1130/G33863.1

Roedder, E. (1983). Geobarometry of ultramafic xenoliths from Loihi Seamount, Hawaii, on the basis of CO2 inclusions in olivine. *Earth Planet. Sci. Lett.* 66, 369–379. doi: 10.1016/0012-821x(83)90152-8

Roedder, E. (1984). *Fluid inclusions*. Washington, DC: Mineralogical Society of America.

Schwandt, C. S., and McKay, G. A. (2006). Minor- and trace-element sector zoning in synthetic enstatite. *Am. Mineral.* 91, 1607–1615. doi: 10.2138/am.2006.2093

Shishkina, T. A., Botcharnikov, R. E., Holtz, F., Almeev, R. R., Jazwa, A. M., and Jakubiak, A. A. (2014). Compositional and pressure effects on the solubility of H2O and CO2 in mafic melts. *Chem. Geol.* 388, 112–129. doi: 10.1016/j.chemgeo.2014.09.001

Span, R., and Wagner, W. (1996). A new equation of state for carbon dioxide covering the fluid region from the triple point temperature to 1100 K at pressures up to 800 MPa. *J. Phys. Chem. Ref. Data* 25, 1509–1596. doi: 10.1063/1.555991

Sparks, R. S. J., and Pinkerton, H. (1978). Effect of degassing on rheology of basaltic lava. *Nature* 276, 385–386. doi: 10.1038/276385a0

Sterner, S. M., and Pitzer, K. S. (1994). An equation of state for carbon dioxide valid from zero to extreme pressures. *Contribut. Mineral. Petrol.* 117, 362–374. doi: 10.1007/bf00307271

Strong, D. F. (1969). Formation of hour glass structure in augite. *Mineral. Magaz.* 37, 472–479. doi: 10.1180/minmag.1969.037.288.07

Toplis, M. J. (2005). The thermodynamics of iron and magnesium partitioning between olivine and liquid: criteria for assessing and predicting equilibrium in natural and experimental systems. *Contribut. Mineral. Petrol.* 149, 22–39. doi: 10.1007/s00410-004-0629-4

Torres, P., Madeira, J., Silva, L., Brum da Silveira, A., Serralheiro, A., and Mota Gomes, A. (1997). Carta Geológica das Erupções Históricas da Ilha do Fogo (Cabo Verde): revisão e actualização. *Comun. Instit. Geol. Mine.* 84, A193–A196.

Ubide, T., Mollo, S., Zhao, J.-X., Nazzari, M., and Scarlato, P. (2019). Sector-zoned clinopyroxene as a recorder of magma history, eruption triggers, and ascent rates. *Geochim. Cosmochim. Acta* 251, 265–283. doi: 10.1016/j.gca.2019.02.021

van den Kerkhof, A. M. (1990). Isochoric phase diagrams in the systems CO2-CH4 and CO2-N2: application to fluid inclusions. *Geochim. Cosmochim. Acta* 54, 621–629. doi: 10.1016/0016-7037(90)90358-r

Wanamaker, B. J., and Evans, B. (1989). Mechanical re-equilibration of fluid inclusions in San Carlos olivine by power-law creep. *Contribut. Mineral. Petrol.* 102, 102–111. doi: 10.1007/bf01160194

Wass, S. Y. (1973). The origin and petrogenetic significance of hour-glass zoning in titaniferous clinopyroxenes. *Mineral. Magaz.* 39, 133–144. doi: 10.1180/minmag.1973.039.302.01

Welsch, B., Hammer, J., Baronnet, A., Jacob, S., Hellebrand, E., and Sinton, J. (2016). Clinopyroxene in postshield *Haleakala ankaramite*: 2. Texture, compositional zoning and supersaturation in the magma. *Contribut. Mineral. Petrol.* 171, 1–19. doi: 10.1007/s00410-015-1213-9

Worsley, P. (2015). Physical geology of the Fogo volcano (Cape Verde Islands) and its 2014–2015 eruption. *Geol. Today* 31, 153–159. doi: 10.1111/gto.12102

Zanon, V. (2015). "Conditions for mafic magma storage beneath fissure zones at oceanic islands. The case of São Miguel Island (Azores archipelago)," in *Chemical, Physical and Temporal Evolution of Magmatic Systems*, eds L. Caricchi and J. D. Blundy (London: Geological Society of London Special Publications), 85–104. doi: 10.1144/sp422.4

Zanon, V., Frezzotti, M. L., and Peccerillo, A. (2003). Magmatic feeding system and crustal magma accumulation beneath Vulcano Island (Italy): evidence from CO2 fluid inclusions in quartz xenoliths. *J. Geophys. Res.* 108:2298. doi: 10.1029/2002JB002140

Conflict of Interest: The authors declare that the research was conducted in the absence of any commercial or financial relationships that could be construed as a potential conflict of interest.

frontiers in Earth Science

ORIGINAL RESEARCH
published: 10 June 2020
doi: 10.3389/feart.2020.00188

Clinopyroxene Dissolution Records Rapid Magma Ascent

David A. Neave[1]* *and John Maclennan*[2]

[1] Department of Earth and Environmental Sciences, The University of Manchester, Manchester, United Kingdom,
[2] Department of Earth Sciences, University of Cambridge, Cambridge, United Kingdom

Magma ascent rates control volcanic eruption styles. However, the rates at which basaltic magmas ascend through the crust remain highly uncertain. Although recent studies have successfully exploited records of decompression driven degassing to estimate the rates at which H_2O-rich basalts ascend, such approaches cannot readily be applied to primitive and H_2O-poor basalts that erupt in ocean island and mid-ocean ridge settings. Here we present magma ascent rates obtained by modeling the dissolution of clinopyroxene crystals in a wehrlitic nodule from the primitive Borgarhraun lava flow in North Iceland. High-Al_2O_3 clinopyroxene core compositions are consistent with crystallization near the Moho (~800 MPa), whereas low-Al_2O_3 clinopyroxene rims and inclusion compositions are consistent with crystallization at or near the surface. We interpret low-Al_2O_3 rims and inclusions as the crystallized remnants of boundary layers formed by the dissolution of high-Al_2O_3 clinopyroxene during magma ascent. By combining characteristic rim dissolution lengths of 50–100 μm with published experimental calibrations of clinopyroxene dissolution behavior, we estimate that the Borgarhraun magma most likely decompressed and ascended at rates of 3.0–15 kPa.s^{-1} and 0.11–0.53 m.s^{-1}, respectively. These rates are slightly faster than published estimates obtained by modeling the diffusive re-equilibration of olivine crystals, suggesting that the Borgarhraun magma either accelerated upwards or that it stalled briefly at depth prior to final ascent. Comparisons with other basaltic eruptions indicate that the H_2O-poor magma that fed the dominantly effusive Borgarhraun eruption ascended at a similar rate to some H_2O-rich magmas that have fed explosive eruptions in arc settings. Thus, magma ascent rates do not appear to correlate simply with magma H_2O contents. Overall, our findings confirm that primitive and H_2O-poor basalts can traverse the crust within days, and may erupt with little precursory warning of magma ascent.

Keywords: magma ascent rate, plumbing system, clinopyroxene dissolution, basalt, disequilibrium, Iceland

OPEN ACCESS

Edited by:
Mattia Pistone,
University of Georgia, United States

Reviewed by:
Silvio Mollo,
Sapienza University of Rome, Italy
Chiara Maria Petrone,
Natural History Museum,
United Kingdom

***Correspondence:**
David A. Neave
david.neave@manchester.ac.uk

Specialty section:
This article was submitted to Petrology, a section of the journal Frontiers in Earth Science

Received: *09 March 2020*
Accepted: *11 May 2020*
Published: *10 June 2020*

Citation:
Neave DA and Maclennan J (2020) Clinopyroxene Dissolution Records Rapid Magma Ascent. Front. Earth Sci. 8:188. doi: 10.3389/feart.2020.00188

1. INTRODUCTION

Volcanoes are underlain by vertically extensive and geometrically complex magmatic plumbing systems that are capable of dynamically reorganizing themselves over the timescales of individual eruptions (Marsh, 2004; Cashman et al., 2017; Sparks and Cashman, 2017; Magee et al., 2018; Maclennan, 2019; Sparks et al., 2019). It is therefore essential to quantify magma storage and transport timescales if we are to develop accurate models of volcanic behavior. Magma ascent rates

are of particular importance in this respect because they play a central role in determining the style of volcanic eruptions, with eruptions fed by rapidly ascending magmas typically being more explosive than those fed by slowly ascending magmas (Gonnermann and Manga, 2007; Rutherford, 2008). Changes in magma ascent rate can also drive potentially hazardous transitions in eruption style (Woods and Koyaguchi, 1994). Importantly, global systematics in the eruptive behavior of volcanoes can now be resolved through the local complexity of individual events (Cassidy et al., 2018). However, most published estimates of magma ascent rate are from silicic systems despite the fact that basaltic systems are geographically widespread and dominate global magma budgets (Cassidy et al., 2018, and references therin). Although a number of studies have gone some way toward redressing this imbalance (e.g., Ruprecht and Plank, 2013; Lloyd et al., 2014; Peslier et al., 2015; Newcombe et al., 2020), estimates of magma ascent rate from basaltic systems remain few in number and somewhat uncertain in nature.

Magma ascent rates are commonly estimated using numerical modeling approaches of varying complexity (Wilson and Head, 1981; Mastin, 2002; La Spina et al., 2015, 2019). Analog modeling approaches have also been used to constrain magma ascent rates and inform the application of numerical models to natural systems (Namiki and Manga, 2006, 2008; Wright et al., 2012). However, ascent rates determined using modeling approaches are often subject to large uncertainties because conduit dimensions and eruptive mass fluxes are often very poorly constrained. Direct estimates of magma ascent rate have been obtained by modeling the diffusive re-equilibration of crystals entrained shortly before eruption (e.g., Ruprecht and Plank, 2013; Mollo et al., 2015; Mutch et al., 2019b; Newcombe et al., 2020), and the diffusive loss of volatiles from melt inclusions and melt embayments as a result of decompression-driven degassing (e.g., Humphreys et al., 2008; Lloyd et al., 2014; Hartley et al., 2018; Barth et al., 2019). Crystal textures have also been used to determine ascent rates in cases where crystallization kinetics are sufficiently well-understood (Armienti et al., 2013). However, ascent rates estimated from the re-equilibration of crystals, whether chemical or textural, convolve isobaric intervals of crystal entrainment with polybaric intervals of magma ascent, and are thus likely to underestimate true values. Although techniques that exploit decompression-driven volatile exsolution circumvent this particular problem, they can only be applied to magmas that degas significantly en route to the surface. Given that primitive basalts from ocean island and mid-ocean ridge settings often degas little during ascent because of their low volatile (i.e., H_2O) contents (<0.2 wt.% H_2O; Michael, 1988; Saal et al., 2002; Miller et al., 2019), the rates at which they ascend must be derived using different and volatile-independent approaches.

Basalts frequently carry crystals and nodules formed at depth to the surface, and exploiting the pressure-dependent stability of these crystalline cargoes provides a means of directly estimating the rates at which H_2O-poor primitive basalts ascend (e.g., Brearley and Scarfe, 1986). Clinopyroxene is especially important in this regard because it commonly crystallizes from primitive basalts and its stability correlates strongly with pressure (**Figure 1**; Bender et al., 1978; Presnall et al., 1978; Fujii and Bougault, 1983; Chen and Zhang, 2009; Holland et al., 2018). Clinopyroxene crystals formed at depth may therefore dissolve during ascent, as evidenced by the resorbed nature of phenocrystic and xenocrystic clinopyroxenes erupted from some basaltic volcanoes (e.g., Tsuchiyama, 1986; Gurenko and Sobolev, 2006; Eason and Sinton, 2009). Indeed, the dissolution of clinopyroxene crystals during magma ascent may be responsible for the pyroxene paradox whereby many mid-ocean ridge basalts preserve geochemical signals of clinopyroxene crystallization but contain no clinopyroxene crystals (O'Donnell and Presnall, 1980; Thompson et al., 1980; Grove et al., 1992).

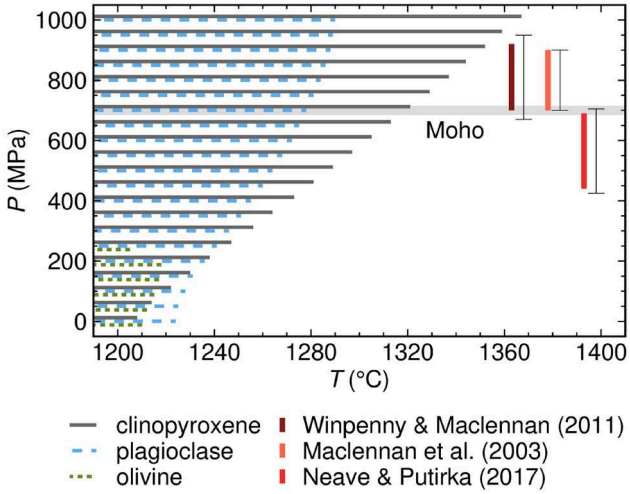

FIGURE 1 | Mineral stabilities in the Borgarhraun lava flow from North Iceland calculated with the MELTS algorithm (Ghiorso and Sack, 1995; Smith and Asimow, 2005). Calculations were performed using the matrix glass composition reported by Sigurdsson et al. (2000), and highlight the strong pressure dependence of clinopyroxene stability. Horizontal lines indicate the temperature ranges over which clinopyroxene, plagioclase and olivine are stable during isobaric fractional crystallization at different pressures. The depth of the seismic Moho from Staples et al. (1997) is shown alongside petrological estimates of pre-eruptive magma storage pressures (Maclennan et al., 2003b; Winpenny and Maclennan, 2011; Neave and Putirka, 2017). Vertical colored bars show 1σ uncertainties in pressure estimates; vertical error bars show model uncertainties expressed as standard errors of estimate (SEEs).

Here we exploit a quantitative but little used description of clinopyroxene stability in basaltic magmas to estimate the rates at which primitive Icelandic basalts ascend through the crust. We do this by modeling the dissolution of clinopyroxene crystals in a wehrlitic nodule from the Borgarhraun lava flow in North Iceland. Our findings suggest that H_2O-poor basalts from ocean island and mid-ocean ridge systems can ascend as fast as many of their H_2O-rich counterparts from arc systems. This has important implications for evaluating risks posed by basaltic volcanoes as primitive magmas appear capable of traversing the whole crust within a few days.

2. NODULES IN ICELANDIC BASALTS

Basaltic magmas often carry nodules of crystalline material to the surface. These nodules provide crucial insights into

the chemical structure of Earth's interior and the dynamics of magmatic plumbing systems (e.g., Rudnick, 1992; Pearson et al., 2003; Holness et al., 2007; Cooper et al., 2016). Magmatic nodules occur in the products of numerous Icelandic eruptions and are variably wehrlitic, gabbroic, troctolitic and feldspathic in composition (Trønnes, 1990; Hansen and Grönvold, 2000; Maclennan et al., 2003a; Gurenko and Sobolev, 2006; Holness et al., 2007). Gabbroic, troctolitic and feldspathic nodules in lavas and tephras from the Eastern Rift Zone of Iceland are thought to constitute the disaggregated remnants of plagioclase-rich crystal mushes from the mid-crust (Hansen and Grönvold, 2000; Holness et al., 2007); macrocrysts and glomerocrysts of anorthitic plagioclase from the same samples are likewise considered to reflect more efficiently disaggregated portions of the same mushes (Halldórsson et al., 2008; Neave et al., 2014). In contrast, wehrlitic, gabbroic and troctolitic nodules from the Miðfell and Borgarhraun lava flows in the Western and Northern Volcanic Zones of Iceland, respectively, are thought to reflect the crystallization, mixing and reaction of primitive magmas in the lower crust and uppermost mantle (Trønnes, 1990; Maclennan et al., 2003a; Gurenko and Sobolev, 2006). Nodules from the Borgarhraun lava flow are of particular interest because of their extremely primitive compositions [olivine X_{Fo} up to 0.92, where X_{Fo} = molar Mg/(Mg+Fe); plagioclase X_{An} up to 0.92, where X_{An} = molar Ca/(Ca+Na); and clinopyroxene $Mg\#_{cpx}$ up to 0.90, where $Mg\#_{cpx}$ = Mg/(Mg+Fe)]. These crystals therefore preserve information about the earliest evolution of mantle-derived melts that would have otherwise been obscured by mixing and sampling bias (Maclennan, 2008; Winpenny and Maclennan, 2011; Neave et al., 2019b).

Nodules from the Borgarhraun lava flow are well-suited for estimating primitive basalt ascent rates because there are excellent geobarometric constraints on the pressure (i.e., depth) at which they were stored prior to eruption (**Figure 1**); the depth from which magma ascended is well-known. Clinopyroxene-liquid geobarometry using the model of Putirka et al. (1996) indicates that the Borgarhraun magma was stored at 810 ± 110(1σ) MPa in the uppermost mantle prior to eruption (Winpenny and Maclennan, 2011). The model uncertainty (standard error of estimate, SEE) associated with the geobarometer of Putirka et al. (1996) is 140 MPa. This pre-eruptive storage pressure is corroborated by experimental petrology and geobarometry exploiting the pressure dependence of olivine-plagioclase-augite-melt cotectic positions (Yang et al., 1996; Maclennan et al., 2003b, 2012). In contrast, clinopyroxene-liquid geobarometry using the model of Neave and Putirka (2017) suggests that the Borgarhraun magma was stored within the lower crust at a slightly lower pressure of 570 ± 120(1σ) MPa. This model is also associated with an SEE of 140 MPa. Despite this discrepancy in storage pressure estimates, which probably reflects the model of Neave and Putirka (2017) being optimized for lower pressures and more evolved compositions than those considered here, it is nevertheless clear that the Borgarhraun magma was stored near, and quite probably below, the Moho immediately before eruption.

A further advantage of investigating the Borgarhraun lava flow is that two recent studies into magma storage and ascent timescales provide an excellent framework within which we can interpret our new observations (Mutch et al., 2019a,b). Specifically, Mutch et al. (2019a) exploited the diffusive re-equilibration of spinel chadacrysts within clinopyroxene oikocrysts from wehrlitic nodules to estimate deep magma residence times on the order of 1,000 years. Exploiting the diffusive re-equilibration of olivine macrocrysts in the rims of wehrlitic nodules then allowed Mutch et al. (2019b) to estimate transcrustal magma transport times on the order of 10 days that correspond to minimum magma ascent rates of 0.02–0.1 $m.s^{-1}$.

Here we investigate a wehrlitic nodule in sample JM27 collected in July 1999 from the eastern edge of the Borgarhraun lava flow (65°51.05′N, 16°59.93′W). Although nodules with variably dunitic, wehrlitic, gabbroic and troctolitic compositions have been described from the same location by Maclennan et al. (2003a), we focus on wehrlitic sample JM27 for three reasons: firstly, the abundance of clinopyroxene makes it possible to robustly constrain the minimum apparent dissolution lengths required to avoid dissolution time estimates being compromised by 3-D cutting effects; secondly, the presence of variably orientated crystals allows the effects of anisotropy on apparent dissolution lengths to be evaluated; and thirdly, the nodule's internal porosity likely prevented the dissipation of dissolution textures by convection or turbulent mingling. Nevertheless, we note that other nodules described by Maclennan et al. (2003a) show similar features to those we describe in sample JM27 (**Supplementary Material**), indicating that our findings are applicable to the Borgarhraun eruption as a whole.

3. METHODS

QEMSCAN imaging of sample JM27 was performed on a FEI Quanta-650F instrument in the Department of Earth Sciences at the University of Cambridge, UK. Images were collected with a 4-μm pixel spacing, and 2000-count EDX spectra were used to produce phase and Al concentration maps following the principles discussed by Pirrie et al. (2004) and Neave et al. (2017a). Additional backscattered electron (BSE) imaging was performed on a FEI Quanta-650F instrument in the Department of Earth and Environmental Sciences at the University of Manchester, UK.

Mineral compositions were determined by electron probe microanalysis (EPMA) on a Cameca SX100 instrument in the Department of Earth Sciences at the University of Cambridge, UK. Silicon, Ti, Al, Cr, Fe, Mn, Mg, Ca, Na, K, and Ni were measured in minerals with an accelerating voltage of 15 kV. Olivine, clinopyroxene and spinel were measured with a current of 20 nA and a spot size of 1 μm. Plagioclase was measured with a current of 10 nA and a spot size of 5 μm. The following standards were used for calibration: diopside (Si and Ca), rutile (Ti), corundum (Al), Cr metal (Cr), fayalite (Fe), Mn metal (Mn), St. Johns olivine (Mg), jadeite (Na), orthoclase (K), and NiO (Ni). Peak and background counting times were typically 20 and 10 s, respectively for major elements and 40 and 20 s, respectively for minor elements, with the exception of Na that was counted on-peak for 10 s. Data quality was monitored by measuring

the following secondary standards (representative analyses are provided in the **Supplementary Material**): San Carlos olivine (NMNH 111312-44), Lake County plagioclase (NMNH 115900), Kakanui augite (NMNH 122142), and Ney County Cr-augite (NMNH 164905) (Jarosewich et al., 1980, 1987). Accuracy and precision are both estimated as ≤1% relative for major elements (present at >1 wt.%) and ≤5% relative for minor elements (present at <1 wt.%).

4. RESULTS

4.1. Petrography and QEMSCAN Imaging

The wehrlitic nodule in sample JM27 is composed of clinopyroxene with subordinate olivine and rare plagioclase (**Figures 2A**, **3A**; **Supplementary Material**). Equant clinopyroxene crystals in the nodule are typically 500 μm to 1 mm in diameter, while equant olivine crystals are typically 200–500 μm in diameter. Rare tabular plagioclase crystals up to 250 μm in length also occur. The nodule hosts a network of microcrystalline pockets and embayments of groundmass that are contiguous with the host lava groundmass (**Figure 3B**). These pockets and channels are sometimes vesiculated, indicating that the nodule was porous to its host lava prior to lava flow emplacement. Both lava and nodule groundmasses are composed of high-aspect-ratio plagioclase crystals intergrown with small crystals of olivine, clinopyroxene and ilmenite (**Figure 3B**). The boundary between the wehrlitic nodule and the groundmass—defined by the limit of connected clinopyroxene crystals—is highly sinuous (**Figure 2A**). Crystals of olivine, plagioclase and clinopyroxene occur outside the nodule both as individual macrocrysts and as macrocrysts within monomineralic and polymineralic glomerocrysts (**Figures 2A**, **3D**). Typical macrocrystic and glomerocrystic crystal diameters span the following ranges: 200 μm to 2 mm for olivine; 200–800 μm for plagioclase; and 200–800 μm for clinopyroxene. Glomerocrystic plagioclase and clinopyroxene crystals often occur in ophitic arrangements (**Figure 3D**).

QEMSCAN phase maps highlight abundant plagioclase inclusions within the cores of nodule clinopyroxene crystals that have not been described in previous studies (**Figure 2B**). These plagioclase inclusions are typically 20–100 μm in length and irregular to vermicular in form (**Figure 3A**). Many plagioclase inclusions are associated with small (10–50 μm) and irregular pockets of mesostasis that are texturally distinct from spheroidal melt inclusions (**Figure 3C**). Numerous small crystals of plagioclase also occur within the rims of nodule clinopyroxene crystals. Some of these crystals are separated from the groundmass by their host crystals and represent true inclusions. Others form continuous chains of crystals that extend from clinopyroxene rims deep into the interior of clinopyroxene cores. Within the limited compositional resolution of QEMSCAN phase identification, plagioclase inclusions have similar compositions to groundmass plagioclase crystals (bytownitic to labradoritic), while plagioclase macrocrysts and nodule plagioclase crystals are more primitive (anorthitic to bytownitic).

Semi-quantitative Al concentration maps indicate that plagioclase inclusions are located within domains of low-Al_2O_3 clinopyroxene that also appear to form inclusions within high-Al_2O_3 clinopyroxene cores (**Figure 2C**). Note that we refer to these low-Al_2O_3 clinopyroxene domains as inclusions without implying any genetic connotations. In other words, low-Al_2O_3 clinopyroxene inclusions are simply considered as domains of low-Al_2O_3 clinopyroxene that appear to be enclosed by high-Al_2O_3 clinopyroxene. Importantly, the presence and nature of these low-Al_2O_3 clinopyroxene inclusions was only revealed through Al concentration mapping; variations in clinopyroxene Al_2O_3 content were not apparent during optical microscopy or phase mapping. Nodule clinopyroxene rims have similarly low Al_2O_3 contents to clinopyroxene inclusions. Indeed, the chains of plagioclase crystals described in the preceding paragraph lie within low-Al_2O_3 channels that extend from clinopyroxene rims deep into their cores. Low-Al_2O_3 clinopyroxene inclusions are on the order of 50–250 μm in diameter, while the thinnest nodule clinopyroxene rims—those least affected by sectioning effects—are 50–100 μm wide.

High-Al_2O_3 clinopyroxene cores have relatively low BSE intensities while low-Al_2O_3 clinopyroxene rims and inclusions have relatively high BSE intensities (**Figures 3A,B**). Boundaries between nodule clinopyroxene cores and rims are often rounded (**Figure 3B**). As previously documented by Winpenny and Maclennan (2011), subtle variations in BSE intensity within nodule clinopyroxene cores delimit sector zones. Patchy variations in BSE intensity also occur at the edges of some clinopyroxene inclusions (**Figure 3A**), but appear to represent complex interfaces between inclusions and their host crystals rather than zoning intrinsic to low-Al_2O_3 clinopyroxene inclusions (**Figures 3B,C**). Importantly, we see no crystallographically controlled variations in BSE intensity that would reveal the presence of exsolution lamellae within nodule clinopyroxene cores (e.g., Holness et al., 2011).

Although BSE intensity is broadly constant within low-Al_2O_3 clinopyroxene inclusions, some inclusions contain films and pockets of very high BSE intensity (**Figure 3C**). These films and pockets typically occur next to plagioclase inclusions and along the inclusions' boundaries with high-Al_2O_3 clinopyroxene hosts, suggesting that they represent domains of late-stage crystallization. Further evidence for late-stage crystallization is provided by the small oxide crystals (5–20 μm in diameter, and subsequently identified as titanomagnetite) that occur along some interfaces between plagioclase inclusions and portions of clinopyroxene inclusions with very high BSE intensities (**Figure 3C**).

4.2. Electron Probe Microanalysis

Plagioclase and olivine compositions from sample JM27 are summarized in **Figure 4**. Plagioclase compositions range from $X_{An} = 0.70$ to $X_{An} = 0.91$ (**Figure 4A**), and different compositions are found in different textural associations. High X_{An} contents (>0.85) are only found in rare nodule plagioclase cores and the cores of some macrocrysts and glomerocrysts. Moderate X_{An} contents (0.78–0.85) are found in nodule plagioclase rims, some plagioclase inclusions and in the cores and rims of some macrocrysts and glomerocrysts. Low X_{An} contents (<0.78) are found in some plagioclase inclusions

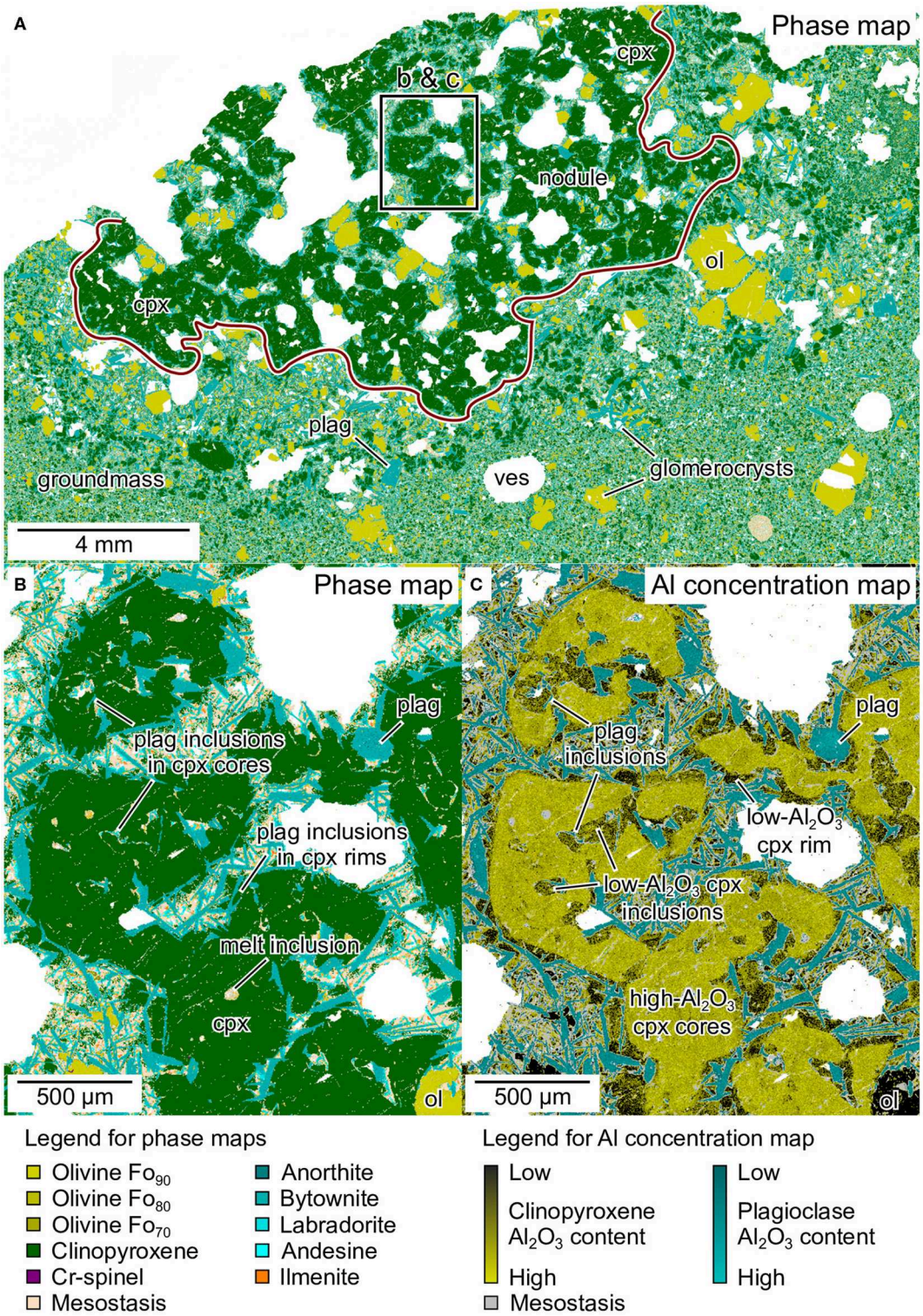

FIGURE 2 | Phase and Al concentration maps of a wehrlitic nodule in sample JM27 from the Borgarhraun lava flow in North Iceland obtained by QEMSCAN. **(A)** The wehrlitic nodule is composed of clinopyroxne with subordinate olivine and rare plagioclase. It also contains pockets and channels of crystalline groundmass that are contiguous with the lava groundmass, indicating that the nodule was porous at the point of lava flow emplacement. Macrocrystic and glomerocrystic olivine, plagioclase and clinopyroxene also occur in the lava groundmass. **(B)** Plagioclase inclusions are present in the cores and rims of clinopyroxenes in the wehrlitic nodule. **(C)** Clinopyroxene cores in the wehrlitic nodule have relatively high Al_2O_3 contents, whereas clinopyroxene rims have relatively low Al_2O_3 contents. Plagioclase inclusions in clinopyroxene cores are associated with inclusions of low-Al_2O_3 clinopyroxene that are not evident in phase maps.

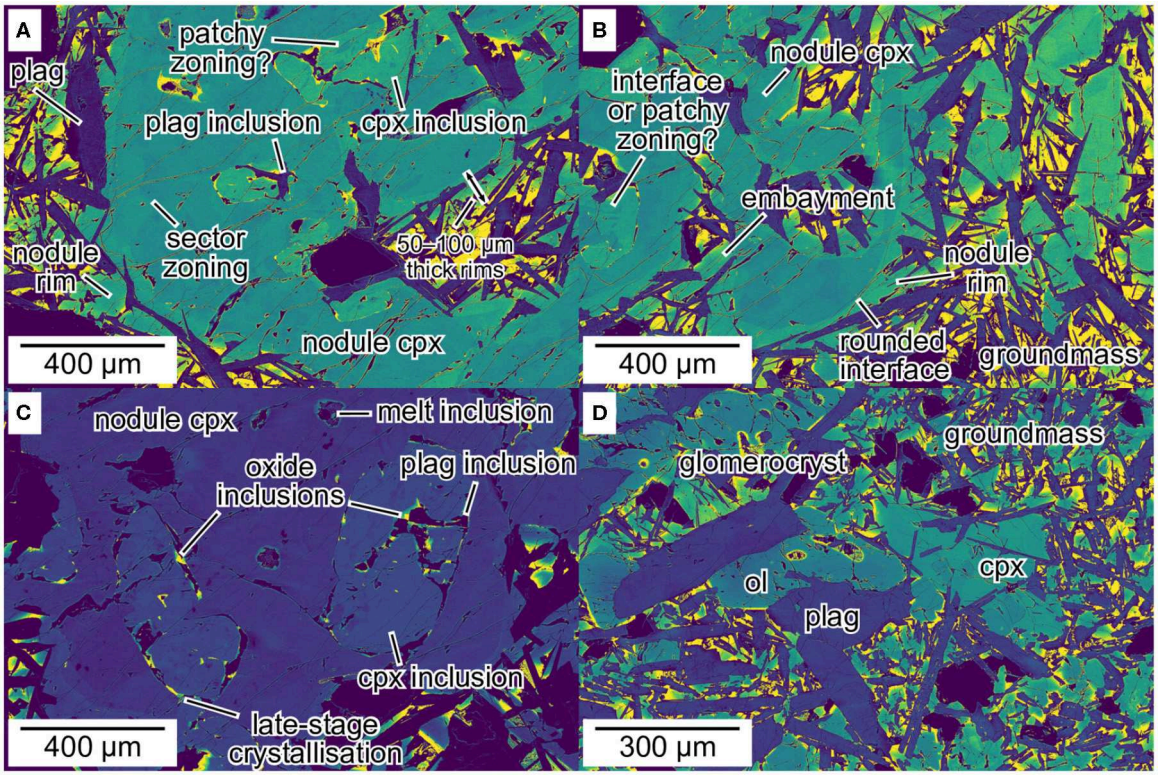

FIGURE 3 | Backscattered electron (BSE) images of mineral textures in sample JM27 from the Borgarhraun lava flow in North Iceland. Raw and additional representative images are provided in the **Supplementary Material**. **(A,B)** Nodule clinopyroxene cores have low but variable BSE intensities consistent with the presence of sector zoning. Nodule clinopyroxene rims and inclusions have slightly higher BSE intensities that increase greatly toward the groundmass and pockets of late-stage crystallization respectively. Nodule clinopyroxene rims and inclusions both contain irregular plagioclase inclusions. **(C)** Pockets of late-stage crystallization within clinopyroxene inclusions have very high BSE intensities and are associated with both plagioclase and oxide (titanomagnetite) inclusions. **(D)** Macrocrystic and glomerocrystic olivine, plagioclase and clinopyroxene occur in the crystalline lava groundmass. Plagioclase macrocrysts and glomerocrysts are typically larger than plagioclase crystals in the wehrlitic nodule. Clinopyroxene macrocrysts and glomerocrysts are often arranged in ophitic arrangements with plagioclase.

and the outermost rims of macrocrysts, glomerocrysts and nodule plagioclase crystals. These low X_{An} contents are typically located close to films and pockets of late-stage crystallization (**Figure 3C**). Olivine compositions range from $X_{Fo} = 0.81$ to $X_{Fo} = 0.90$ (**Figure 4B**). Relationships between composition and texture are less clear for olivine than plagioclase, though nodule, macrocryst, and glomerocryst olivine cores typically contain the highest X_{Fo} contents (>0.85). Lower X_{Fo} contents (0.82–0.85) are found in the cores and rims of some macrocrysts and glomerocrysts, and the lowest X_{Fo} content measured (0.81) is from a nodule olivine rim in contact with the groundmass.

Clinopyroxene compositions are summarized in **Figures 5**, **6**, and range from $Mg\#_{cpx} = 0.35$ to $Mg\#_{cpx} = 0.91$, with the majority of compositions lying between $Mg\#_{cpx} = 0.85$ and $Mg\#_{cpx} = 0.90$. Different clinopyroxene compositions are closely linked with different textural associations. Nodule clinopyroxene cores are primitive ($Mg\#_{cpx} = 0.88–0.91$; **Figures 5**, **6**) and rich in octahedral Al ($Al_{vi} = 0.08–0.11$, where Al_{vi} is calculated on a six-oxygen basis; **Figure 6A**). They are also somewhat enriched in jadeite component [$X_{Jd} = 0.012–0.018$, where X_{Jd} is calculated following Putirka (2008); **Figure 6B**]. Variability in TiO_2 (0.11–0.20 wt.%; **Figure 5B**), Al_2O_3 (4.0–5.5 wt.%; **Figure 5D**) and wollastonite component [$X_{Wo} = 0.41–0.44$, where $X_{Wo} = Ca/(Ca+Mg+Fe)$ on a molar basis; **Figure 5F**] over the range of $Mg\#_{cpx}$ contents present in nodule clinopyroxene cores reflects sector zoning (**Figure 3A**). Some macrocryst and glomerocryst cores have similar compositions to nodule clinopyroxene cores (i.e., $Mg\#_{cpx} = 0.88–0.90$ and $Al_{vi} = 0.09–0.11$), while others are slightly more evolved. Nodule clinopyroxene rims are consistently more evolved than nodule clinopyroxene cores ($Mg\#_{cpx} = 0.72–0.88$), a feature highlighted by the positive correlation between $Mg\#_{cpx}$ and TiO_2 defined by analyses from nodule clinopyroxene rims (**Figure 5B**). Rims are also considerably poorer in Al_{vi} (<0.08; **Figure 6A**) and slightly poorer in X_{Jd} (<0.014; **Figure 6B**) than nodule clinopyroxene cores. Some macrocryst and glomerocryst compositions overlap with nodule clinopyroxene compositions, though a few analyses extend to much more evolved compositions ($Mg\#_{cpx}$ reaches as low as 0.55 and TiO_2 reaches as high as 1.0 wt.%), probably reflecting late-stage crystallization during lava flow emplacement.

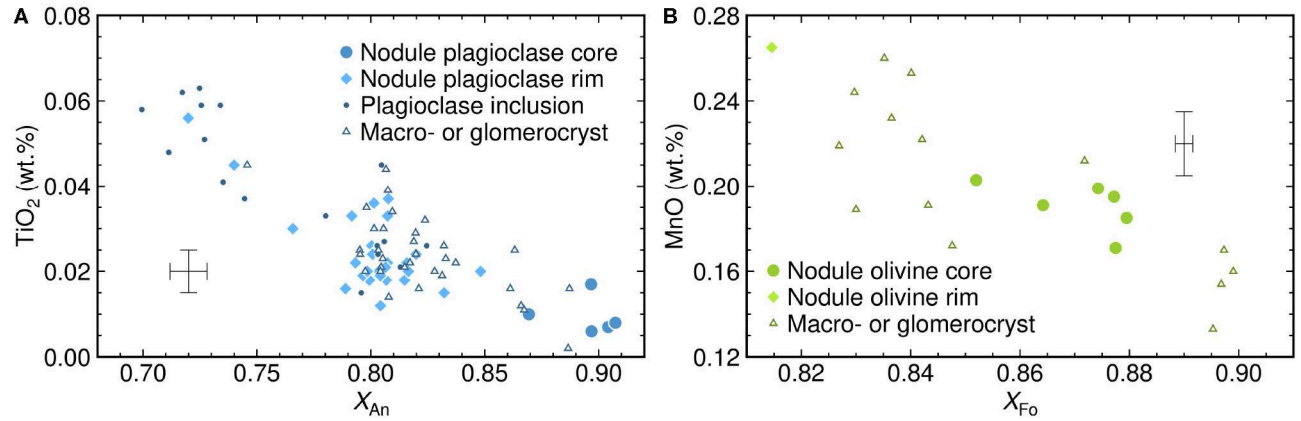

FIGURE 4 | Plagioclase and olivine compositions in sample JM27 from the Borgarhraun lava flow in North Iceland. **(A)** Plagioclase compositions summarized in terms of X_{An} [where X_{An} = molar Ca/(Ca+Na)] and TiO_2. Analyses are divided into four textural associations: nodule cores, nodule rims, inclusions, and macrocrysts or glomerocrysts. 2σ analytical uncertainties based on repeat measurements of the Lake County plagioclase (NMNH 115900) are shown (Jarosewich et al., 1980). **(B)** Olivine compositions summarized in terms of X_{Fo} [where X_{Fo} = molar Mg/(Mg+Fe)] and MnO. Analyses are divided into three textural associations: nodule cores, nodule rims, and macrocrysts or glomerocrysts. 2σ analytical uncertainties based on repeat measurements of the San Carlos olivine (NMNH 111312-44) are shown (Jarosewich et al., 1980).

Clinopyroxene inclusions are the most compositionally variable of all clinopyroxene textural types ($Mg\#_{cpx}$ = 0.35–0.90). The majority of inclusion analyses fall within a compositional range shared with some macrocryst and glomerocryst analyses, as well as with analyses from nodule clinopyroxene rims ($Mg\#_{cpx}$ = 0.85–0.87, Al_2O_3 = 2.0–3.0 wt.% and Al_{vi} = 0.03–0.06; **Figures 5B,D**, **6A**). These analyses are located within constant-BSE-intensity domains of clinopyroxene inclusions (**Figure 3A**). A primitive subpopulation of analyses from patchy zones at inclusion edges overlaps with analyses from nodule clinopyroxene core compositions ($Mg\#_{cpx}$ = 0.88–0.90, Al_2O_3 = 4.5–5.0 wt.% and Al_{vi} = 0.08–0.09), and probably constitutes analyses of complex, folded interfaces between inclusions and nodule clinopyroxene cores (**Figure 3B**). An evolved subpopulation of inclusion analyses overlaps partly with analyses from nodule clinopyroxene rims. These analyses are located within domains of very high BSE intensity that we have interpreted as pockets of late-stage crystallization (**Figure 3C**). The inflection of TiO_2 content with decreasing $Mg\#_{cpx}$ within this subpopulation reflects the onset of titanomagnetite crystallization.

5. IDENTIFYING CLINOPYROXENE DISSOLUTION

High-Mg# clinopyroxene crystals in the Borgarhraun lava flow record high pre-eruptive magma storage pressures of 570–810 MPa (Winpenny and Maclennan, 2011; Neave and Putirka, 2017). These pressures are consistent with the high Al_2O_3, Al_{vi}, and X_{Jd} contents of macrocryst, glomerocryst, and nodule clinopyroxene cores investigated here, confirming the ultimately deep origin of sample JM27 (**Figures 3**, **5B,C**, **6**; Aoki and Kushiro, 1968; Thompson, 1974; Blundy et al., 1995; Putirka et al., 1996). Given that the liquidus temperature of clinopyroxene is significantly higher at 570–810 MPa than 1 atm in Borgarhraun-like magmas [90–140°C higher according to calculations with the MELTS algorithm (**Figure 1**; Ghiorso and Sack, 1995; Smith and Asimow, 2005), and 70–120°C higher according to calculations on a compositionally analogous basalt from the Reykjanes Peninsula with THERMOCALC (RE46; Yang et al., 1996; Holland et al., 2018)], clinopyroxene crystals formed near the Moho are thus unlikely to have been in equilibrium with their carrier liquids upon eruption. Assuming that the ascending Borgarhraun magma cooled along an adiabatic gradient of $<1°C.km^{-1}$ (Katz et al., 2003), it thus seems probable that deep-formed high-Al_2O_3 clinopyroxene crystals would have at least partly dissolved en route to the surface.

The rounded nature of high-Al_2O_3, high-Al_{vi}, and high-X_{Jd} nodule clinopyroxene cores indicates that they underwent dissolution prior to their encapsulation within low-Al_2O_3, low-Al_{vi}, and low-X_{Jd} rims at or near the surface (**Figures 3B**, **5B,C**, **6**; Aoki and Kushiro, 1968; Thompson, 1974; Blundy et al., 1995; Putirka et al., 1996). A low-pressure origin for clinopyroxene rims is indicated by comparisons with the products of 1-atm experiments performed by Yang et al. (1996), as well as by clinopyroxene-liquid geobarometry performed on nodule clinopyroxene rims using the model of Neave and Putirka (2017). Geobarometry was undertaken on clinopyroxene rims using the matrix glass composition of Sigurdsson et al. (2000), and returned a pressure of 210 ± 35(1σ) MPa with an associated model SEE of 140 MPa. All clinopyroxene-liquid pairs were checked for multicomponent equilibrium following the approach of Neave et al. (2019a). Although 210 MPa is appreciably greater than 1 atm, it is, model uncertainties notwithstanding, considerably lower than the 570–810 MPa range obtained from high-Al_2O_3 cores (**Figure 1**; Winpenny and Maclennan, 2011; Neave and Putirka, 2017). Moreover, that only

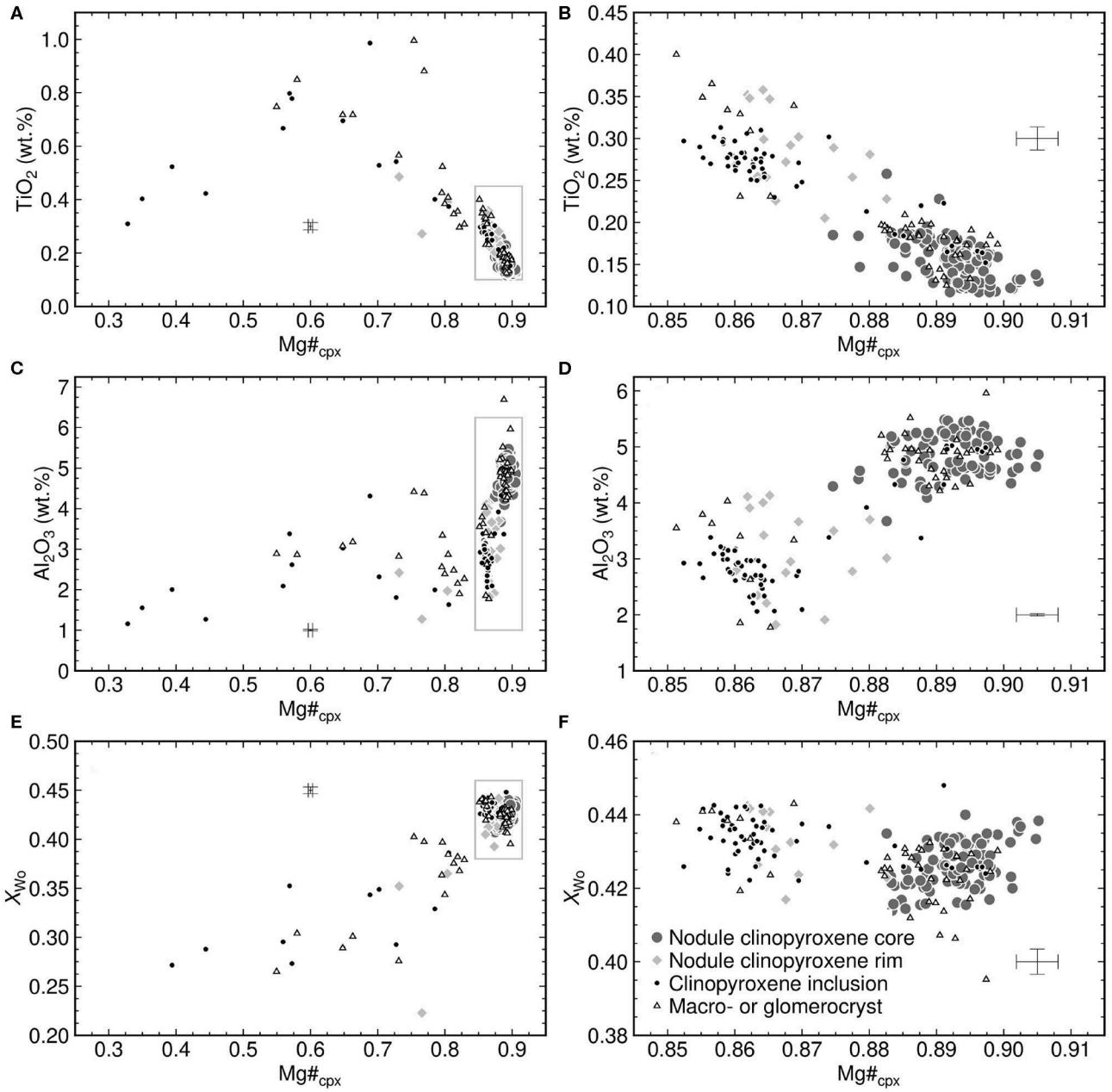

FIGURE 5 | Clinopyroxene compositions in sample JM27 from the Borgarhraun lava flow in North Iceland. Analyses are divided into four textural associations: nodule cores, nodule rims, inclusions, and macrocrysts or glomerocrysts. 2σ analytical uncertainties based on repeat measurements of the Ney County Cr-Augite (NMNH 164905) are shown (Jarosewich et al., 1987). **(A,B)** Plots of $Mg\#_{cpx}$ [where $Mg\#_{cpx}$ = molar Mg/(Mg+Fe)] vs. TiO_2. **(C,D)** Plots of $Mg\#_{cpx}$ vs. Al_2O_3. **(E,F)** Plots of $Mg\#_{cpx}$ vs. wollastonite component [X_{Wo}, where X_{Wo} = Ca/(Ca+Mg+Fe) on a molar basis]. **(B,D,E)** Show the regions outlined with gray box in **(A,C,E)**.

a few analyses passed equilibrium filters ($n = 3$) suggests that clinopyroxene rims crystallized under disequilibrium conditions, feasibly resulting in an overestimation of crystallization pressures (Mollo et al., 2010).

The presence of abundant low-Al_2O_3 clinopyroxene inclusions within high-Al_2O_3 nodule clinopyroxene cores implies that dissolution was not only restricted to crystal faces, but also permeated crystal cores (**Figure 3A**). Similar textures have been described in clinopyroxene macrocrysts from Haleakala volcano in Hawaii by Welsch et al. (2016), but were attributed to rapid, kinetically controlled crystal growth rather than dissolution. These authors came to this interpretation because both low-Al_2O_3 and high-Al_2O_3 domains of clinopyroxene macrocrysts are in contact the groundmass in their samples, indicating that low- and high-Al_2O_3 clinopyroxene grew concurrently. However, only

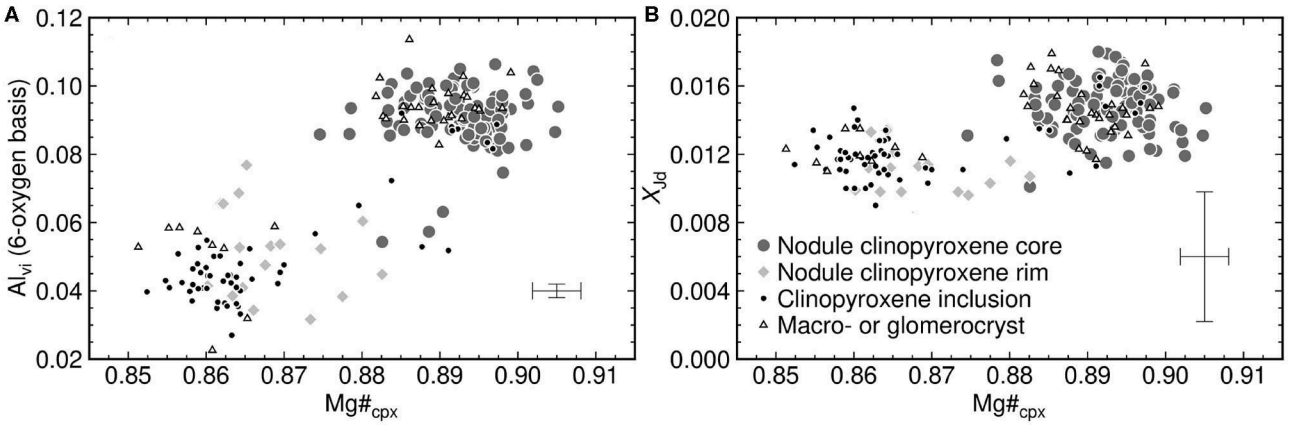

FIGURE 6 | Variations in pressure-sensitive clinopyroxene components in sample JM27 from the Borgarhraun lava flow in North Iceland. Analyses are divided into four textural associations: nodule cores, nodule rims, inclusions and macrocrysts or glomerocrysts. 2σ analytical uncertainties based on repeat measurements of the Ney County Cr-Augite (NMNH 164905) are shown (Jarosewich et al., 1987). **(A)** Plot of Mg#$_{cpx}$ [where Mg#$_{cpx}$ = molar Mg/(Mg+Fe)] vs. octahedral Al (Al_{vi}) calculated on a six-oxygen basis. **(B)** Plot of Mg#$_{cpx}$ vs. jadeite component (X_{Jd}) content calculated following Putirka (2008).

low-Al_2O_3 rims are in contact the groundmass in sample JM27, ruling out concurrent growth in our case. Low-Al_2O_3 clinopyroxene inclusions in the Borgarhraun lava flow also cut across boundaries between sector zones within high-Al_2O_3 nodule clinopyroxene cores, demonstrating that the inclusions formed by the resorption of pre-existing crystal cores. The occurrence of low-Al_2O_3 clinopyroxene embayments within high-Al_2O_3 cores also suggests that clinopyroxene inclusions may represent ramifying networks of low-Al_2O_3 clinopyroxene channels in 3-D rather than isolated inclusions of the kind visible in 2-D. Indeed, the compositional similarity between clinopyroxene inclusions and nodule clinopyroxene rims suggests that they share a common dissolution-reprecipitation origin that we discuss in detail below (**Figure 5**). Finally, domains of patchy zoning associated with complex interface geometries between inclusions and their host crystals are similar to cellular dissolution textures in other systems (**Figure 3B**; Streck, 2008), highlighting dissolution's central role in clinopyroxene inclusion genesis.

Our observations from the Borgarhraun lava flow are not unique; similar observations from lavas erupted elsewhere in Iceland validate our identification of substantial clinopyroxene dissolution. For example, Trønnes (1990) and Hansteen (1991) described resorbed "Al- and Cr-rich endiopside" crystals equivalent to our nodule clinopyroxene cores in primitive basalts from the Hengill volcanic system in the Western Rift Zone. Gurenko and Sobolev (2006) also describe spongy and embayed high-Al_2O_3 clinopyroxene crystals in glass-hosted nodules from the primitive Miðfell lava flow, also from the Hengill volcanic system, though these authors account for dissolution by melt-rock reaction rather than decompression during ascent. Clinopyroxene dissolution has also been proposed as an explanation for the chemical systematics of lavas from both the Eastern and Western Rift Zones (Halldórsson et al., 2008; Eason and Sinton, 2009), illustrating its potentially widespread role in basalt petrogenesis.

In contrast with the glassy nodules from the Miðfell lava flow described by Gurenko and Sobolev (2006), the wehrlitic nodule we describe here is fully crystalline; gabbroic and troctolitic nodules collected from the same location are similarly crystalline (**Supplementary Material**). Thus, while previously studied clinopyroxenes from the Miðfell lava flow are surrounded by glass, those we have studied from the Borgarhraun lava flow are surrounded by low-Al_2O_3 clinopyroxene rims. They are also permeated by low-Al_2O_3 clinopyroxene inclusions that host inclusions of relatively low-X_{An} plagioclase. This important textural difference—the presence or absence of low-Al_2O_3 clinopyroxene around and within high-Al_2O_3 clinopyroxene cores—reflects the contrasting emplacement histories of the Miðfell and Borgarhraun lava flows. Specifically, the Miðfell lava flow was erupted subglacially, making it possible for Gurenko and Sobolev (2006) to collect glassy material from rapidly quenched pillow basalt rims. In contrast, the Borgarhraun lava flow erupted subaerially, meaning that sample JM27 cooled slowly and crystallized *in situ*. The relatively slow cooling of the Borgarhraun lava flow did however allow important information about the extent of pre-eruptive high-Al_2O_3 dissolution to be captured. Namely, low-Al_2O_3 clinopyroxene rims and inclusions record the approximate dimensions of boundary layers formed by the dissolution of high-Al_2O_3 clinopyroxene during magma ascent which were then preserved during cooling by the high closure temperature of major element diffusion within clinopyroxene (Freer et al., 1982).

Fractional crystallization calculations performed on the mean composition of high-Al_2O_3 nodule clinopyroxene cores with the MELTS algorithm at 1 atm reproduce the phase assemblage and phase proportions observed in clinopyroxene rims and inclusions (Ghiorso and Sack, 1995; Smith and Asimow, 2005). Crystallization was assumed to be fractional because lava flow cooling rates probably outpaced mineral-mineral equilibration rates. Olivine crystallization was also suppressed in favor of epitactic clinopyroxene growth. Calculations were performed without imposing oxygen fugacity constraints; oxygen fugacity was imposed from the starting clinopyroxene Fe^{2+}/Fe^{3+} estimated by charge balance following Lindsley and Andersen (1983). Once the calculated mass fraction of melt (F) reached

0.05, calculated mass fractions of clinopyroxene, plagioclase and spinel-structured oxide were 0.89, 0.05, and 0.01, respectively, broadly in line with BSE observations from clinopyroxene inclusions (**Figures 3A,C**). Melts with the mean composition of high-Al_2O_3 nodule clinopyroxene cores thus crystallize clinopyroxene and plagioclase in a ratio of ∼18:1, a ratio much closer to that observed in clinopyroxene inclusions than the ∼1:1 ratio calculated to result from matrix glass crystallization at 1 atm (**Figures 3A,B**). Moreover, pigeonite was predicted to crystallize at $F < 0.12$, consistent with the low X_{Wo} content of low-$Mg\#_{cpx}$ analyses from rims and inclusions associated with pockets of late-stage crystallization (**Figures 3C**, **5E**).

Despite calculations with the MELTS algorithm reproducing the phase assemblage and phase proportions observed in clinopyroxene inclusions, they nevertheless return consistently higher $Mg\#_{cpx}$ and X_{An} than observed in sample JM27 ($Mg\#_{cpx} > 0.9$ until $F < 0.25$ and $X_{An} > 0.8$ until $F < 0.15$). Although discrepancies between calculations with the MELTS algorithm and observations from both natural and experimental systems are well-documented (e.g., Neave et al., 2019b), they are probably exacerbated in this case by differences between the mean composition of high-Al_2O_3 nodule clinopyroxene cores and the compositions for which the MELTS algorithm has been calibrated (Ghiorso and Sack, 1995). However, a more fundamental explanation for these discrepancies stems from assuming that the boundary layers created by clinopyroxene dissolution were closed and compositionally homogeneous systems for their entire lifespans. Although these assumptions make performing illustrative calculations with the MELTS algorithm tractable, they are incorrect in detail. This is because our observations suggest Mg-rich and Na-poor high-Al_2O_3 clinopyroxene cannot be mass balanced against a Mg-poor and Na-rich assemblage containing low-Al_2O_3 clinopyroxene, plagioclase and titanomagnetite.

The dissolution rate of crystals is strongly controlled by the diffusivity of their constituent components in their surrounding melts, which results in the creation of concentration gradients around dissolving crystals (e.g., Zhang et al., 1989). Mean boundary layer compositions will therefore lie between those of dissolving crystals and their host melts. This may account for the slightly lower Mg# of most clinopyroxene inclusion and nodule clinopyroxene rim analyses (i.e., those not associated with pockets of late-stage crystallization) with respect to nodule clinopyroxene core analyses (**Figure 5**). Boundary layer compositions will also depend on the relative diffusivities of different elements, meaning that some exchange with the surrounding melt is highly likely to occur; even convectively stable boundary layers are unlikely to be fully isolated from the surrounding melt. Complex multicomponent effects notwithstanding (e.g., Liang et al., 1996), Na typically diffuses more quickly than other major species in silicate melts (Zhang et al., 2010b), providing a mechanism by which initially Na-poor boundary layers could have acquired sufficient Na to crystallize $X_{An} \leq 0.82$ plagioclase. In contrast, Al diffuses more slowly than most other major species in silicate melts (Chen and Zhang, 2008; Yu et al., 2016), providing a mechanism by which Al-poor boundary layers formed by dissolution could have been preserved during magma ascent (cf. Neave et al., 2017b). However, evaluating the exact composition of boundary layers in sample JM27 would be challenging, and we suggest that such information would be best recovered from glassy nodules with feasibly intact boundary layers (e.g., Gurenko and Sobolev, 2006).

The narrowest nodule clinopyroxene rims we observed are typically 50–100 μm wide (**Figures 3A,B**). These minimum rim widths provide our best estimates of the distances that nodule clinopyroxene cores dissolved during ascent. This is because they are probably associated with crystal faces oriented normal to the plane of the thin section that are hence are minimally affected by 3-D cutting effects (e.g., Shea et al., 2015). Moreover, rim widths do not appear to vary substantially between different crystal faces, indicating that mineral anisotropy does not significantly affect clinopyroxene dissolution lengthscales in sample JM27. Clinopyroxene inclusions and embayments probably resulted from dissolution over greater distances than 100 μm, but may also reflect the exploitation of pre-existing fractures and cleavage planes (Chen and Zhang, 2009). It is also possible that the development of dissolution channels in 3-D may have affected the apparent dissolution lengths visible in 2-D. Importantly, the geometry of the wehrlitic nodule investigated here means that nodule clinopyroxene rims were largely protected from turbulence in the external magma during ascent. That is, we expect that nodule clinopyroxene rims record dissolution that was primarily diffusive rather than convective in nature (Kerr, 1995; Zhang and Xu, 2003). As a consequence, the thickness of nodule clinopyroxene rims encodes robust information about clinopyroxene dissolution times that can be used to estimate magma decompression and ascent rates.

6. MODELING CLINOPYROXENE DISSOLUTION

Experimental investigations of clinopyroxene dissolution by Chen and Zhang (2009) provide a framework for modeling clinopyroxene dissolution recorded in the Borgarhraun lava flow. Specifically, Chen and Zhang (2009) characterized rates of diffusive diopside dissolution into a tholeiitic basalt by experimentally dissolving diopside crystals at a range of pressures and temperatures. They then used their experimental results to calibrate a model from which dissolution time could be predicted as a function of pressure, temperature, melt composition, clinopyroxene composition and dissolution length. We do however note the important limitation that Chen and Zhang (2009) did not incorporate any effects of mineral anisotropy into their simplified model. Nevertheless, coherence in their experimental results suggests that anisotropy exerts only second order effects over crystal dissolution rates. Importantly, dissolution experiments were carefully designed to avoid convection, making the resulting model well-suited for estimating dissolution times from the nodule clinopyroxene rims we describe here. Furthermore, the high-$Mg\#_{cpx}$ compositions from the Borgarhraun lava flow are amongst the closest to pure diopside of any known compositions from Iceland (Maclennan et al., 2003a; Winpenny and Maclennan, 2011), making the

Borgarhraun eruption an ideal candidate for estimating magma decompression and ascent rates using a model based on diopside dissolution. Moreover, clinopyroxene crystals in JM27 are free from exsolution lamellae that may complicate the interpretation of features created by diffusion and dissolution processes (e.g., Dohmen and Milke, 2010).

Chen and Zhang (2009) provided a series of five equations (their Equations 4, 5a–5d) that, in theory, can be solved iteratively to obtain the parameters required to quantitatively relate dissolution length and dissolution time in diopside-liquid systems. However, our attempts to iteratively solve these equations with the optim() function in the stats package of R often failed to converge (R Development Core Team, 2016), making it difficult to explore clinopyroxene stability across diverse pressure and temperature conditions. We therefore rearranged the equations of Chen and Zhang (2009) to reduce the number of unknown parameters from five to one, allowing the single remaining unknown parameter (the fitting parameter α) to be obtained through a more stable root-finding approach implemented with the uniroot() function in the stats package of R. These rearrangements are documented below.

As described by Chen and Zhang (2009) in their Equation (2a), chemical profiles in melts adjacent to dissolving crystals can be described by the 1-D diffusive dissolution equation (Crank, 1975):

$$C = C_\infty + (C_0 - C_\infty)\frac{\operatorname{erfc}\left(\frac{x}{2\sqrt{Dt}} - \alpha\right)}{\operatorname{erfc}(-\alpha)}, \quad (1)$$

where C is the concentration of a component in the melt, C_0 is concentration in the melt at the crystal-melt interface and C_∞ is the far-field concentration. x is the distance from the crystal-melt interface, D is the effective binary diffusivity of the element or oxide in question and t is duration of experiment. α is a fitting parameter related to the dissolution rate that, as per Equation (2b) of Chen and Zhang (2009), satisfies:

$$\exp(\alpha^2)\operatorname{erfc}(-\alpha)\sqrt{\pi}\alpha = \frac{C_0 - C_\infty}{C_c - C_0}, \quad (2)$$

where C_c is the concentration of the element or oxide in question in the crystal.

As per Equation (2c) of Chen and Zhang (2009), the crystal diffusive dissolution distance can be expressed as:

$$L = 2\alpha\frac{\rho_m}{\rho_c}\sqrt{Dt}, \quad (3)$$

where ρ_m and ρ_c are the densities of melt and crystal, respectively.

The stability of clinopyroxene crystals in basaltic melts is mediated, in part, by the diffusion of Mg and Ca cations within their host liquids (Chen and Zhang, 2009); the diffusion of Mg and Ca within clinopyroxene crystals is many orders of magnitude slower than within basaltic melts (Zhang et al., 2010a), and thus does not affect clinopyroxene stability over the timescales of interest here. As per Equations (3a) and (3b) of Chen and Zhang (2009), Mg and Ca diffusion within basaltic melts can be described by:

$$\ln D_{\mathrm{Mg}} = -6.664(\pm 0.745) - \frac{28897 \pm 1221(2\sigma)}{T}, \quad (4)$$

and:

$$\ln D_{\mathrm{Ca}} = -10.517(\pm 0.901) - \frac{21205 \pm 1476(2\sigma)}{T}, \quad (5)$$

where T is in K and D is in $\mathrm{m}^2.\mathrm{s}^{-1}$.

As per Equation (4) of Chen and Zhang (2009), the saturation condition at the clinopyroxene-melt interface can be expressed when:

$$\ln\left(C_0^{\mathrm{Mg}} \times C_0^{\mathrm{Ca}}\right) = a + bP + \frac{e}{T} + g\frac{P^2}{T^2}, \quad (6)$$

where C_0 values are expressed in oxide wt.%, P is pressure in GPa and a, b, e and g are fitting parameters with values of $22.85 \pm 1.82(2\sigma)$, $2.10 \pm 0.44(2\sigma)$, $26360 \pm 2565(2\sigma)$, and $1.22 \pm 0.43(2\sigma) \times 10^6$, respectively.

Rearranging Equation (6) and gathering the terms then allows us to define a function in which $C_0^{\mathrm{Mg}} \times C_0^{\mathrm{Ca}}$ depends upon P and T alone:

$$H(P,T) = a + bP + \frac{e}{T} + g\frac{P^2}{T^2}, \quad (7)$$

and thus:

$$C_0^{\mathrm{Mg}} \times C_0^{\mathrm{Ca}} = \exp(H(P,T)) = h(P,T). \quad (8)$$

Given that L is equal for both MgO and CaO, Equation (3) leads to the expression:

$$\alpha_{\mathrm{Mg}} = \alpha_{\mathrm{Ca}}\sqrt{\frac{D_{\mathrm{Ca}}}{D_{\mathrm{Mg}}}}. \quad (9)$$

If we define:

$$f(\alpha) = \exp(\alpha^2)\operatorname{erfc}(-\alpha)\sqrt{\pi}\alpha, \quad (10)$$

then rearranging Equation (2) provides:

$$f(\alpha) = \frac{C_0 - C_\infty}{C_c - C_0}. \quad (11)$$

Given that, as per Equation (8), $C_0^{\mathrm{Mg}} = h/C_0^{\mathrm{Ca}}$, then:

$$f(\alpha_{\mathrm{Mg}}) = \frac{(h/C_0^{\mathrm{Ca}}) - C_\infty^{\mathrm{Mg}}}{C_c^{\mathrm{Mg}} - (h/C_0^{\mathrm{Ca}})}, \quad (12)$$

and:

$$f(\alpha_{Ca}) = \frac{C_0^{Ca} - C_\infty^{Ca}}{C_c^{Ca} - C_0^{Ca}}. \quad (13)$$

Rearranging these equations then gives:

$$C_0^{Ca} = \frac{h[1 + f(\alpha_{mg})]}{f(\alpha_{Mg})C_c^{Mg} + C_\infty^{Mg}} = \frac{f(\alpha_{Ca})C_c^{Ca} + C_\infty^{Ca}}{1 + f(\alpha_{Ca})}, \quad (14)$$

and therefore:

$$h[1 + f(\alpha_{Mg})][1 + f(\alpha_{Ca})] = [f(\alpha_{Ca})C_c^{Ca} + C_\infty^{Ca}] [f(\alpha_{Mg})C_c^{Mg} + C_\infty^{Mg}] \quad (15)$$

A root finding approach can then be used to find values of α_{Mg} where the following expression is zero and substitutions are made using Equation (9):

$$Q = h[1 + f(\alpha_{Mg})][1 + f(\alpha_{Ca})] - [f(\alpha_{Ca})C_c^{Ca} + C_\infty^{Ca}] [f(\alpha_{Mg})C_c^{Mg} + C_\infty^{Mg}], \quad (16)$$

and Equation (3) can then be used to calculate t.

The results of dissolution calculations performed assuming a fixed dissolution time of 1 s are presented in **Figure 7** and demonstrate the strong effects of pressure and temperature on the stability of clinopyroxene with the mean composition of nodule clinopyroxene cores in the Borgarhraun matrix glass composition reported by Sigurdsson et al. (2000). Calculated clinopyroxene liquidus temperatures vary from ∼1,190°C at 1 atm to ∼1,320°C at 800 MPa and are encouragingly consistent with the results of calculations with the MELTS algorithm (**Figure 1**). These calculations also illustrate the strong dependence of dissolution rate on temperature and hence the vital importance of estimating magma eruption temperatures accurately when determining magma decompression and ascent rates from clinopyroxene dissolution lengths.

Indicative clinopyroxene dissolution times for the Borgarhraun lava flow were estimated by assuming that all dissolution took place at the surface following instantaneous magma ascent from near-Moho depths (**Figure 8**). A magma temperature of 1,230°C was taken from Mutch et al. (2019b) who performed calculations with the geothermometer of Sugawara (2000) that has an associated model SEE of 30°C. The temperature decrease associated with adiabatic cooling of the ascending magma over the pressure interval of relevance is well within the SEE of the geothermometer used (<8°C over 215 MPa; see below; Katz et al., 2003), and is thus not considered further. Uncertainties in dissolution time estimates were evaluated by resampling (n = 1,000) temperature and fitting parameters in Equation (6) for each dissolution length increment according to their respective uncertainties (Sugawara, 2000; Chen and Zhang, 2009). Resulting median dissolution times range from 30 min for a dissolution length of 50 μm to 150 min for a dissolution length of 100 μm—the range of minimum observed dissolution lengths (**Figure 3**). Lower 1σ bounds on dissolution times (i.e., 17th percentiles) are typically a factor of ten shorter than the median times and 1σ bounds (83rd percentiles) are typically a factor of 18 longer. Dissolution times are thus associated with 1σ uncertainties on the order of one order of magnitude which primarily reflect uncertainties in magma eruption temperatures that are challenging to overcome with currently available approaches (Putirka, 2008).

Mean magma decompression rates were estimated from clinopyroxene dissolution times by assuming that dissolution started as soon the ascending magma reached a pressure of 215 MPa, the pressure at which Equations (3) and (6) predict a change from clinopyroxene crystallization to clinopyroxene dissolution (**Figure 7**). Estimated mean decompression rates vary from 110 kPa.s^{-1} for a dissolution length of 50 μm to 24 kPa.s^{-1} for a dissolution length of 100 μm (**Figure 9A**). Estimated rates increase substantially to 210 MPa.s^{-1} for a dissolution length of 5 μm, and decrease modestly to 3.3 kPa.s^{-1} for a dissolution length of 300 μm. Mean magma ascent rates were estimated by converting the clinopyroxene saturation pressure of 215 MPa into a depth of 7.6 km by assuming a mean crustal density of 2.88 Mg.m^{-3} (Maclennan et al., 2001). Resulting mean ascent rate estimates vary from 3.9 m.s^{-1} for a dissolution length of 50 μm to 0.85 m.s^{-1} for a dissolution length of 100 μm (**Figure 9B**), and are subject to propagated uncertainties on order of one order of magnitude. However, assuming that all dissolution occurred at the surface following instantaneous ascent is likely to overestimate true magma decompression and ascent rates because it unrealistically implies that all dissolution occurred under the highest possible degrees of disequilibrium. In line with other studies (e.g., Lloyd et al., 2014; Mutch et al., 2019b; Newcombe et al., 2020), we therefore performed additional calculations with the more naturalistic assumption that magma ascended at a constant rate.

Assuming that clinopyroxene dissolution took place in response to decompression at a constant rate, dissolution lengths of 50 and 100 μm imply decompression rates of 15 and 3.0 kPa.s^{-1} respectively (**Figure 9A**). These values are approximately one order of magnitude lower than the mean decompression rates estimated by assuming that all dissolution took place following instantaneous ascent. Estimated magma ascent rates are also correspondingly lower: 0.53 and 0.11 m.s^{-1} for dissolution lengths of 50 and 100 μm respectively (**Figure 9B**). The difference between rates estimated with instantaneous and constant-rate assumptions primarily reflects the dependence of clinopyroxene dissolution rate on pressure (**Figure 7**). That is, clinopyroxene dissolution rates are much lower at high pressures where disequilibrium is negligible than at the surface where disequilibrium is greatest, meaning that very little clinopyroxene dissolves during the initial stages of clinopyroxene-undersaturated magma decompression.

Magma decompression rates estimated from clinopyroxene dissolution are compared with those estimated from the diffusive re-equilibration of primitive olivine crystals carried by the Borgarhraun magma in **Figure 9C** (Mutch et al., 2019b).

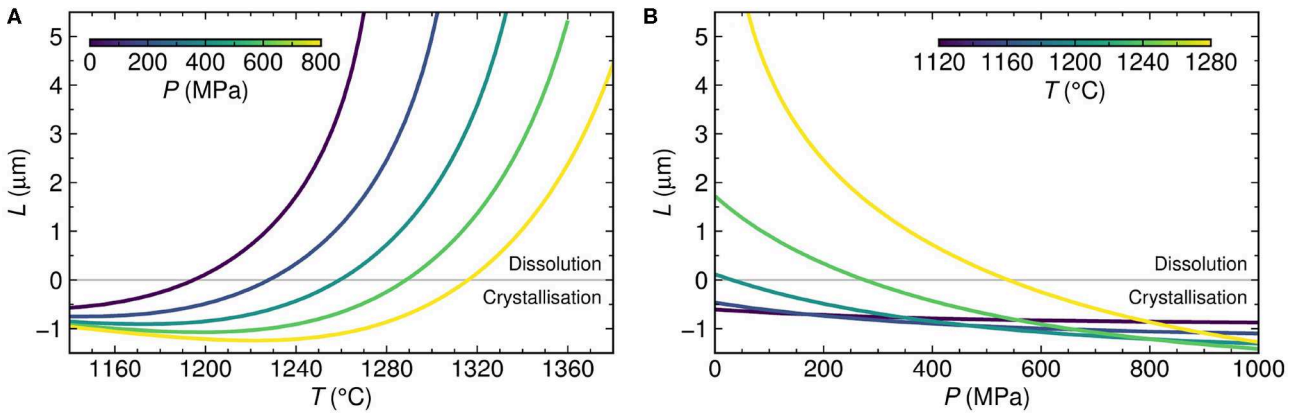

FIGURE 7 | The stability of nodule clinopyroxene cores in the Borgarhraun lava flow as functions of pressure and temperature. Colored lines show the length that the mean nodule clinopyroxene core composition is predicted to dissolve or crystallize in 1 s under different pressure and temperature conditions according to the model of Chen and Zhang (2009). Calculations were performed assuming dissolution into or crystallization from the Borgarhraun matrix glass composition reported by Sigurdsson et al. (2000). **(A)** Isobaric calculations performed at a range of temperatures. **(B)** Isothermal calculations performed at a range of pressures.

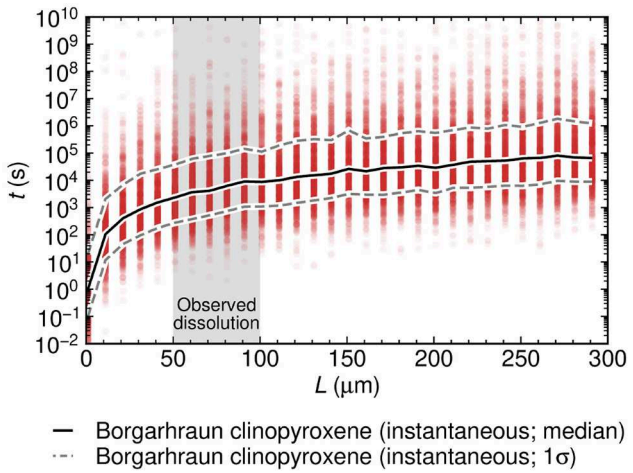

FIGURE 8 | Dissolution time as a function of dissolution length for nodule clinopyroxene cores dissolving into the Borgarhraun matrix glass upon instantaneous ascent to the surface. Red points show the result of simulations performed to evaluate the effect of uncertainties in temperature and dissolution model fitting parameters (Sugawara, 2000; Chen and Zhang, 2009; Mutch et al., 2019b). The black line shows the median dissolution time at each dissolution length; dashed gray lines represent 1σ confidence intervals (i.e., 66% of simulations lie between the gray dashed lines). The vertical gray bar represents the range of clinopyroxene rim dissolution lengths identified from QEMSCAN and BSE images (**Figures 2**, **3**) that constrain our best estimates of minimum dissolution times.

Encouragingly, our best estimates (3.0–15 kPa.s^{-1}) are broadly comparable with those obtained from a wholly independent diffusion chronometry approach for the same eruption (0.7–3.3 kPa.s^{-1}). Our findings thus corroborate those of Mutch et al. (2019b) who estimated a mean magma ascent rate of 0.02–0.1 m.s^{-1}, and confirm that transcrustal magma transport in Iceland may be considerably more rapid than reported in arc settings (0.5–1 mm.s^{-1}; Ruprecht and Plank, 2013). On the basis of comparisons with transcrustal transport estimates from Mutch et al. (2019b), our best estimates also suggest that the Borgarhraun magma ascended more rapidly near the surface than it did at depth, consistent with either the upward acceleration of rising magma or the convolution of isobaric intervals of magma mixing with polybaric intervals of magma ascent by diffusion-based methods.

Magma decompression rates estimated for the Borgarhraun eruption are compared with published estimates from other basaltic systems in **Figure 9C**. Note that we compare decompression rather than ascent rates in order to avoid introducing additional uncertainties from converting pressures to depths across a range of different settings with different crustal density structures. Perhaps unsurprisingly, our best decompression rate estimates for the Borgarhraun eruption (3.0–15 kPa.s^{-1}) are about two orders of magnitude lower than those reported for the sub-plinian 1974 eruption of Volcán de Fuego, Guatemala, based on the loss of volatiles from melt embayments and the loss of H_2O from olivine crystals (240–600 and 380–450 kPa.s^{-1}, respectively; Lloyd et al., 2014; Newcombe et al., 2020). Decompression rates estimated from the loss of volatiles from melt embayments for a series of Hawaiian to sub-plinian eruptions of Kīlauea, Hawaii, are also greater than those estimated for the Borgarhraun eruption (50–450 kPa.s^{-1}), with the greatest Kīlauean rates being associated with the most explosive, sub-plinian eruptions (Ferguson et al., 2016). Indeed, decompression rates estimated for episode 1 of the Hawaiian 1959 Kīlauea Iki eruption from both the loss of volatiles from melt embayments and the loss of H_2O from olivine crystals are only about one order of magnitude greater than our estimates for the Borgarhraun eruption (~50 kPa.s^{-1}; Ferguson et al., 2016; Newcombe et al., 2020). Similar rates also been estimated for the Hawaiian 1977 eruption of Seguam, Alaska, using the same techniques (20–130 kPa.s^{-1} from embayments and 40–230 kPa.s^{-1} from olivine; Newcombe et al., 2020). Thus, magmas

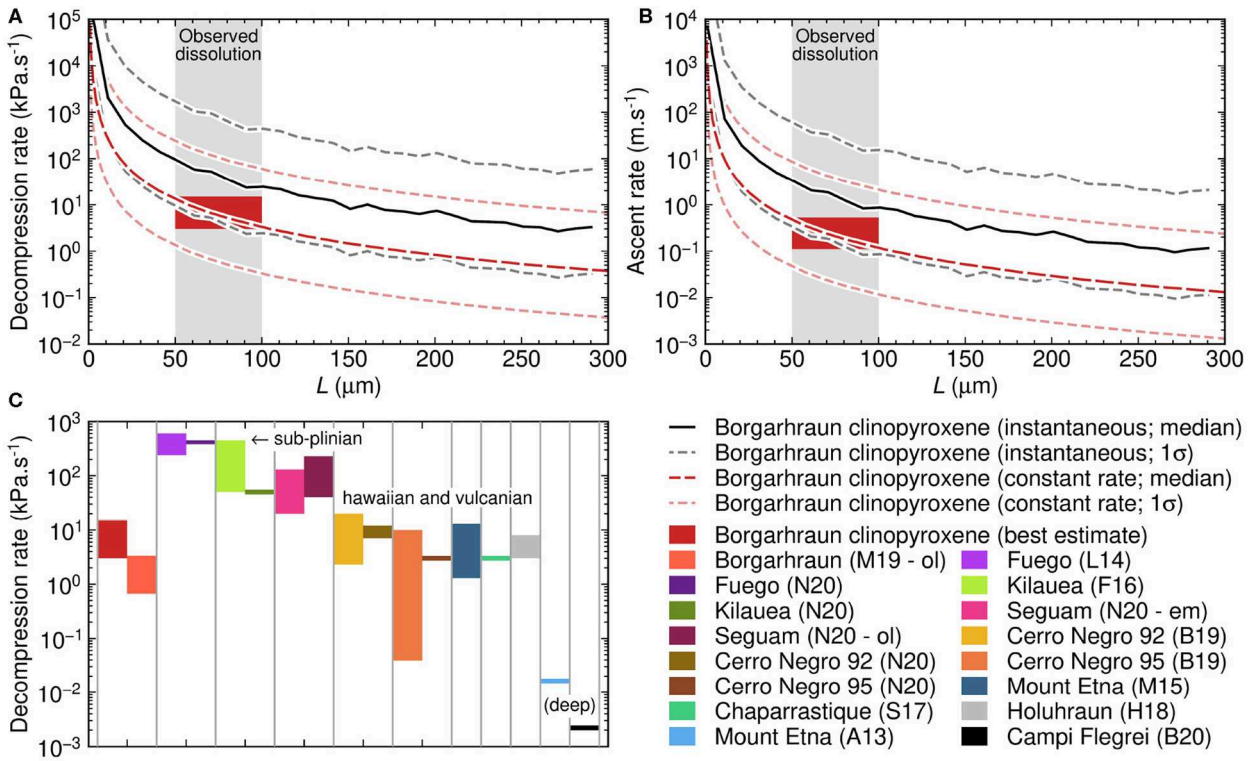

FIGURE 9 | Magma decompression and ascent rates in basaltic systems. **(A,B)** Magma decompression and ascent rates are shown as functions of dissolution length for nodule clinopyroxene cores dissolving into the Borgarhraun matrix glass in **(A,B)**, respectively. Solid black lines show decompression and ascent rates calculated using the dissolution times shown in **Figure 8**. These decompression and ascent rates represent mean values calculated with the simplifying assumption that all dissolution took place at the surface following instantaneous ascent. Dashed red lines show decompression and ascent rates calculated assuming that magma decompression and ascent took place at a constant rate from onset of clinopyroxene dissolution. The vertical gray bar represents the range of dissolution lengths identified from QEMSCAN and BSE images (**Figures 2**, **3**) that constrain our best estimates of magma decompression and ascent rates. **(C)** Literature estimates of magma decompression rate from basaltic systems compared with our best estimate for the Borgarhraun eruption. Methods and sources of decompression rate estimates are as follows: M19, olivine diffusion for the Borgarhraun eruption by Mutch et al. (2019b); L14, diffusive volatile loss from embayments for the 1974 eruption of Fuego by Lloyd et al. (2014); F16, diffusive volatile loss from embayments for various eruptions of Kīlauea by Ferguson et al. (2016); N20, diffusive volatile loss from embayments for the 1977 eruption of Seguam (em), and diffusive H_2O loss from olivine for episode 1 of the 1959 eruption of Kīlauea Iki, the 1974 eruption of Fuego, the 1992 and 1995 eruptions of Cerro Negro, and the 1977 eruption of Seguam (ol) by Newcombe et al. (2020); B19, diffusive volatile loss from olivine-hosted melt inclusions for the 1992 and 1995 eruptions of Cerro Negro by Barth et al. (2019); M15, clinopyroxene-ilmenite re-equilibration for the 2011 eruption of Mount Etna by Mollo et al. (2015); S17, plagioclase disequilibrium for the 2013 eruption of Chaparrastique by Scarlato et al. (2017); H18, diffusive volatile loss from olivine-hosted melt inclusions for the 2014–2015 Holuhraun eruption by Hartley et al. (2018); A13, clinopyroxene textures for deep magma ascent at Mount Etna by Armienti et al. (2013); and B20, clinopyroxene textures for deep magma ascent at Campi Flegrei by Bonechi et al. (2020).

that have fed explosive basaltic eruptions ranging from Hawaiian to sub-plinian in style have typically decompressed more rapidly than the magma that fed the Borgarhraun eruption. However, this does not appear to have been the case for all explosively erupted basaltic magmas.

Decompression rates estimated for two moderately explosive eruptions of Cerro Negro, Nicaragua, in 1992 (VEI3, likely vulcanian) and 1995 (VEI2, likely Hawaiian) are broadly similar to those estimated for the Borgarhraun eruption, especially in the case of less explosive 1995 eruption (Barth et al., 2019; Newcombe et al., 2020). Specifically, rates estimated for the 1992 and 1995 eruptions from the loss of volatiles from melt embayments are 2.3–20 and 0.039–10 kPa.s^{-1} respectively (Barth et al., 2019), and those from the loss of H_2O from olivine crystals are 7–12 and 3 kPa.s^{-1} respectively (Newcombe et al., 2020). Decompression rates comparable to those from the Borgarhraun eruption have also been reported for the vulcanian 2013 eruption of Chaparrastique, El Salvador, based on plagioclase dissolution textures (∼3 kPa.s^{-1}; Scarlato et al., 2017). Although deep magma decompression rates of ∼16 and ∼2.2 Pa.s^{-1} beneath Mount Etna and Campi Flegrei, Italy, estimated from clinopyroxene textures by Armienti et al. (2013) and Bonechi et al. (2020) respectively are about three orders of magnitude lower than our best estimates for the Borgarhraun eruption, shallow decompression rates estimated for Hawaiian eruptions of Mount Etna in 2011 on the basis of clinopyroxene-ilmenite re-equilibration are very similar to those we report here (1.3–13 kPa.s^{-1}; Mollo et al., 2015). Finally, we note that our estimated decompression rates overlap with those obtained by modeling the diffusive loss of H_2O from moderately evolved olivine-hosted melt inclusions in magmatic tephra collected during weakly Hawaiian phases of the 2014–2015 Holuhraun

eruption, Iceland (3–8 kPa.s^{-1}; Hartley et al., 2018). During its final ascent, the Borgarhraun magma therefore appears to have decompressed as rapidly as magmas that have fed various explosive basaltic eruptions ranging from Hawaiian to vulcanian in style.

The magma decompression rates that both we and Mutch et al. (2019b) estimate for the dominantly effusive and at most transiently explosive Borgarhraun eruption are broadly consistent with recently established relationships between explosivity and magma decompression rate (e.g., Barth et al., 2019). Namely, we find that the effusively erupted Borgarhraun magma decompressed more slowly than the magmas that fed basaltic sub-plinian eruptions at Fuego and Kīlauea. However, differences in magma decompression rate are modest or even absent when comparing the Borgarhraun eruption with Hawaiian and vulcanian eruptions at Cerro Negro, Chaparrastique and Mount Etna. Our calculations thus suggest that effusively erupted H_2O-poor basalts from ocean island and mid-ocean ridge settings can decompress and ascend through the shallow crust just as rapidly as some explosively erupted H_2O-rich basalts from arc settings. Moreover, it seems unlikely that the ascent rates of basaltic magmas are simply related to their H_2O contents. Although H_2O exsolution certainly plays a major role in driving the ascent of myriad magma types, other factors, such as melt buoyancy and CO_2 exsolution must therefore drive the rapid ascent of primitive and H_2O-poor basalts like the Borgarhraun magma.

Comparing rates of shallow, syn-eruptive magma decompression (including our estimate for the Borgarhraun eruption) with those for deep decompression associated with inter-eruptive magma assembly beneath Mount Etna and Campi Flegrei (**Figure 9C**; Armienti et al., 2013; Bonechi et al., 2020), suggests that magmas ascend much more rapidly during eruptions than during pre-eruptive magma recharge at depth. Magma transport leading to eruption may therefore operate in a fundamentally different way from magma transport out of the mantle and between magma reservoirs. It thus remains unclear how well seismic signals of inter-eruptive magma transport reflect likely rates of pre-eruptive magma ascent (White et al., 2011; Tarasewicz et al., 2012; Mutch et al., 2019b). Indeed, our results suggest that primitive and H_2O-poor basalts may erupt with no more than a few days' precursory warning, making it challenging to evaluate the risks posed by some basaltic volcanoes.

7. CONCLUSIONS

Mineral textures and compositions in a wehrlitic nodule from the primitive Borgarhraun lava flow erupted in North Iceland record clinopyroxene dissolution during magma ascent from near-Moho depths. Mapping the distribution of Al distinguishes high-Al_2O_3 clinopyroxene cores from low-Al_2O_3 clinopyroxene rims and inclusions. The high Al_2O_3 content of clinopyroxene cores is consistent with crystallization at ∼800 MPa, in line with published estimates of pre-eruptive magma storage pressures. In contrast, the low Al_2O_3 of clinopyroxene rims and inclusions is consistent with crystallization at or near the surface. Given that clinopyroxene rim and inclusion boundaries cut across sector zone boundaries within resorbed clinopyroxene cores, we infer that high-Al_2O_3 clinopyroxene cores dissolved during ascent as a consequence of the strong dependence of clinopyroxene stability on pressure. We thus interpret clinopyroxene rims and inclusions as recrystallized boundary layers protected from convective or turbulent dissipation by their host nodule. Corroborating evidence for clinopyroxene dissolution is provided by plagioclase and titanomagnetite crystals within clinopyroxene rims and inclusions that occur in proportions consistent with low-pressure crystallization of molten high-Al_2O_3 clinopyroxene cores during lava flow emplacement. Our findings are supported by textural and geochemical observations from across Iceland that indicate a potentially widespread role for clinopyroxene dissolution in basalt petrogenesis. It thus seems feasible that clinopyroxene dissolution could occur within any vertically extensive basaltic plumbing system and could hence offer a compelling explanation for the pyroxene paradox reported from mid-ocean ridge basalts.

Experimental calibrations of clinopyroxene stability suggest clinopyroxene began to dissolve once the Borgarhraun magma decompressed below the pressure of clinopyroxene saturation at 215 MPa. Our best decompression rate estimates of 3.0–15 kPa.s^{-1} were obtained from calculations assuming that decompression took place at a constant rate. These estimates could nonetheless be improved in future by quantifying the effects of mineral anisotropy on clinopyroxene dissolution kinetics with further experiments. Converting magma decompression rates into magma ascent rates results in values of 0.11–0.53 m.s^{-1} that are similar published estimates obtained from the diffusive re-equilibration of olivine (Mutch et al., 2019b). Nevertheless, our ascent rates are slightly faster than these published values, consistent with magma acceleration during ascent or the temporary stalling of magma after mush disaggregation. Although the Borgarhraun eruption broadly conforms to global correlations between eruption explosivities and magma decompression rates, the decompression rates we estimate are comparable to those obtained from some moderately explosive basaltic eruptions in arc settings, implying that there is no simple relationship between magma decompression rate and magma H_2O content. Indeed, comparing magma ascent rates from Iceland with those from arc settings suggests that primitive and H_2O-poor basalts can traverse the crust considerably faster than some H_2O-rich basalts, though further work is required to evaluate how ascent rates are affected by the differing structures of mid-ocean ridge, ocean island and arc plumbing systems. It is, however, clear that magmas tapped from reservoirs near the Moho in ocean island and mid-ocean ridge settings may reach the surface within days. This represents a major challenge when evaluating the risks posed by infrequent but nonetheless potentially hazardous eruptions of primitive basalt.

DATA AVAILABILITY STATEMENT

All datasets generated for this study are included in the article/**Supplementary Material**.

AUTHOR CONTRIBUTIONS

DN and JM co-designed the project. DN performed the BSE imaging and EPMA, implemented the clinopyroxene dissolution model, and wrote the manuscript. JM collected the sample, facilitated the QEMSCAN imaging, rearranged the equations of Chen and Zhang (2009), and contributed to writing the manuscript.

FUNDING

DN and this work were supported by a Presidential Fellowship from the University of Manchester.

ACKNOWLEDGMENTS

We thank Lewis Hughes for assisting with BSE imaging at the University of Manchester and Iris Buisman for performing QEMSCAN imaging and assisting with EPMA at the University of Cambridge. We also thank CP and SM for their insightful and constructive reviews, and MP for his efficient editorial handling.

SUPPLEMENTARY MATERIAL

The Supplementary Material for this article can be found online at: https://www.frontiersin.org/articles/10.3389/feart.2020.00188/full#supplementary-material

Supplementary Data Sheet 1 | Raw BSE images.

Supplementary Table 1 | EMPA data.

Supplementary Figure 1 | JM21 4 μm QEMSCAN Al Map.

Supplementary Figure 2 | JM21 4 μm QEMSCAN Phase Map.

Supplementary Figure 3 | JM24 4 μm QEMSCAN Al Map.

Supplementary Figure 4 | JM24 4 μm QEMSCAN Phase Map.

Supplementary Figure 5 | JM27 4 μm QEMSCAN Al Map.

Supplementary Figure 6 | JM27 4 μm QEMSCAN Phase Map.

Supplementary Figure 7 | QEMSCAN legend.

REFERENCES

Aoki, K., and Kushiro, I. (1968). Some clinopyroxenes from ultramafic inclusions in Dreiser Weiher, Eifel. *Contrib. Mineral. Petrol.* 18, 326–337. doi: 10.1007/BF00399694

Armienti, P., Perinelli, C., and Putirka, K. D. (2013). A new model to estimate deep-level magma ascent rates, with applications to Mt. Etna (Sicily, Italy). *J. Petrol.* 54, 795–813. doi: 10.1093/petrology/egs085

Barth, A., Newcombe, M., Plank, T., Gonnermann, H., Hajimirza, S., Soto, G. J., et al. (2019). Magma decompression rate correlates with explosivity at basaltic volcanoes–constraints from water diffusion in olivine. *J. Volcanol. Geotherm. Res.* 387:106664. doi: 10.1016/j.jvolgeores.2019.106664

Bender, J. F., Hodges, F. N., and Bence, A. E. (1978). Petrogenesis of basalts from the project FAMOUS area: experimental study from 0 to 15 kbars. *Earth Planet. Sci. Lett.* 41, 277–302. doi: 10.1016/0012-821X(78)90184-X

Blundy, J. D., Falloon, T. J., Wood, B. J., and Dalton, J. A. (1995). Sodium partitioning between clinopyroxene and silicate melts. *J. Geophys. Res. Solid Earth* 100, 15501–15515. doi: 10.1029/95JB00954

Bonechi, B., Perinelli, C., and Gaeta, M. (2020). Clinopyroxene growth rates at high pressure: constraints on magma recharge of the deep reservoir of the Campi Flegrei Volcanic District (south Italy). *Bull. Volcanol.* 82:5. doi: 10.1007/s00445-019-1342-5

Brearley, M., and Scarfe, C. M. (1986). Dissolution rates of upper mantle minerals in an alkali basalt melt at high pressure: an experimental study and implications for ultramafic xenolith survival. *J. Petrol.* 27, 1157–1182. doi: 10.1093/petrology/27.5.1157

Cashman, K. V., Sparks, R. S. J., and Blundy, J. D. (2017). Vertically extensive and unstable magmatic systems: a unified view of igneous processes. *Science* 355:eaag3055. doi: 10.1126/science.aag3055

Cassidy, M., Manga, M., Cashman, K. V., and Bachmann, O. (2018). Controls on explosive-effusive volcanic eruption styles. *Nat. Commun.* 9:2839. doi: 10.1038/s41467-018-05293-3

Chen, Y., and Zhang, Y. (2008). Olivine dissolution in basaltic melt. *Geochim. Cosmochim. Acta* 72, 4756–4777. doi: 10.1016/j.gca.2008.07.014

Chen, Y., and Zhang, Y. (2009). Clinopyroxene dissolution in basaltic melt. *Geochim. Cosmochim. Acta* 73, 5730–5747. doi: 10.1016/j.gca.2009.06.016

Cooper, G. F., Davidson, J. P., and Blundy, J. D. (2016). Plutonic xenoliths from Martinique, Lesser Antilles: evidence for open system processes and reactive melt flow in island arc crust. *Contrib. Mineral. Petrol.* 171:87. doi: 10.1007/s00410-016-1299-8

Crank, J. (1975). *The Mathematics of Diffusion. 2nd Edn.* Oxford: Clarendon Press.

Dohmen, R., and Milke, R. (2010). Diffusion in polycrystalline materials: grain boundaries, mathematical models, and experimental data. *Rev. Mineral. Geochem.* 72, 921–970. doi: 10.2138/rmg.2010.72.21

Eason, D. E., and Sinton, J. M. (2009). Lava shields and fissure eruptions of the Western Volcanic Zone, Iceland: evidence for magma chambers and crustal interaction. *J. Volcanol. Geotherm. Res.* 186, 331–348. doi: 10.1016/j.jvolgeores.2009.06.009

Ferguson, D. J., Gonnermann, H. M., Ruprecht, P., Plank, T. A., Hauri, E. H., Houghton, B. F., et al. (2016). Magma decompression rates during explosive eruptions of Klauea volcano, Hawaii, recorded by melt embayments. *Bull. Volcanol.* 78:71. doi: 10.1007/s00445-016-1064-x

Freer, R., Carpenter, M. A., Long, J. V. P., and Reed, S. J. B. (1982). "Null result" diffusion experiments with diopside: implications for pyroxene equilibria. *Earth Planet. Sci. Lett.* 58, 285–292. doi: 10.1016/0012-821X(82)90201-1

Fujii, T., and Bougault, H. (1983). Melting relations of a magnesian abyssal tholeiite and the origin of MORBs. *Earth Planet. Sci. Lett.* 62, 283–295. doi: 10.1016/0012-821X(83)90091-2

Ghiorso, M. S., and Sack, R. O. (1995). Chemical mass transfer in magmatic processes IV. A revised and internally consistent thermodynamic model for the interpolation and extrapolation of liquid-solid equilibria in magmatic systems at elevated temperatures and pressures. *Contrib. Mineral. Petrol.* 119, 197–212. doi: 10.1007/s004100050036

Gonnermann, H. M., and Manga, M. (2007). The fluid mechanics inside a volcano. *Annu. Rev. Fluid Mech.* 39, 321–356. doi: 10.1146/annurev.fluid.39.050905.110207

Grove, T. L., Kinzler, R. J., and Bryan, W. B. (1992). "Fractionation of mid-ocean ridge basalt (MORB)," in *Mantle Flow and Melt Generation at Mid-Ocean Ridges, Geophysical Monograph, Vol. 71*, eds J. P. Morgan, D. K. Blackman, and J. M. Sinton (Washington DC: American Geophysical Union), 281–310. doi: 10.1029/GM071p0281

Gurenko, A. A., and Sobolev, A. V. (2006). Crust-primitive magma interaction beneath neovolcanic rift zone of Iceland recorded in gabbro xenoliths from Midfell, SW Iceland. *Contrib. Mineral. Petrol.* 151, 495–520. doi: 10.1007/s00410-006-0079-2

Halldórsson, S. A., Óskarsson, N., Grönvold, K., Sigurdsson, G., Sverrisdottir, G., and Steinthórsson, S. (2008). Isotopic-heterogeneity of the Thjorsa lava-Implications for mantle sources and crustal processes within the Eastern Rift Zone, Iceland. *Chem. Geol.* 255, 305–316. doi: 10.1016/j.chemgeo.2008.06.050

Hansen, H., and Grönvold, K. (2000). Plagioclase ultraphyric basalts in Iceland: the mush of the rift. *J. Volcanol. Geotherm. Res.* 98, 1–32. doi: 10.1016/S0377-0273(99)00189-4

Hansteen, T. H. (1991). Multi-stage evolution of the picritic Mælifell rocks, SW Iceland: constraints from mineralogy and inclusions of glass and fluid in olivine. *Contrib. Mineral. Petrol.* 109, 225–239. doi: 10.1007/BF00306481

Hartley, M. E., Bali, E., Maclennan, J., Neave, D. A., and Halldórsson, S. A. (2018). Melt inclusion constraints on petrogenesis of the 2014–2015 Holuhraun eruption, Iceland. *Contrib. Mineral. Petrol.* 173:10. doi: 10.1007/s00410-017-1435-0

Holland, T. J. B., Green, E. C. R., and Powell, R. (2018). Melting of peridotites through to granites: a simple thermodynamic model in the system KNCFMASHTOCr. *J. Petrol.* 59, 881–900. doi: 10.1093/petrology/egy048

Holness, M. B., Anderson, A. T., Martin, V. M., Maclennan, J., Passmore, E., and Schwindinger, K. R. (2007). Textures in partially solidified crystalline nodules: a window into the pore structure of slowly cooled mafic intrusions. *J. Petrol.* 48, 1243–1264. doi: 10.1093/petrology/egm016

Holness, M. B., Stripp, G., Humphreys, M. C. S., Veksler, I. V., Nielsen, T. F. D., and Tegner, C. (2011). Silicate liquid immiscibility within the crystal mush: late-stage magmatic microstructures in the Skaergaard intrusion, East Greenland. *J. Petrol.* 52, 175–222. doi: 10.1093/petrology/egq077

Humphreys, M. C. S., Menand, T., Blundy, J. D., and Klimm, K. (2008). Magma ascent rates in explosive eruptions: constraints from H_2O diffusion in melt inclusions. *Earth Planet. Sci. Lett.* 270, 25–40. doi: 10.1016/j.epsl.2008.02.041

Jarosewich, E., Gooley, R., and Husler, J. (1987). Chromium augite–a new microprobe reference sample. *Geostand. Geoanal. Res.* 11, 197–198. doi: 10.1111/j.1751-908X.1987.tb00027.x

Jarosewich, E., Nelen, J. A., and Norberg, J. A. (1980). Reference samples for electron microprobe analysis. *Geostand. Newslett.* 4, 43–47. doi: 10.1111/j.1751-908X.1980.tb00273.x

Katz, R. F., Spiegelman, M., and Langmuir, C. H. (2003). A new parameterization of hydrous mantle melting. *Geochem. Geophys. Geosyst.* 4, 1–19. doi: 10.1029/2002GC000433

Kerr, R. C. (1995). Convective crystal dissolution. *Contrib. Mineral. Petrol.* 121, 237–246. doi: 10.1007/BF02688239

La Spina, G., Burton, M., and de' Michieli Vitturi, M. (2015). Temperature evolution during magma ascent in basaltic effusive eruptions: a numerical application to Stromboli volcano. *Earth Planet. Sci. Lett.* 426, 89–100. doi: 10.1016/j.epsl.2015.06.015

La Spina, G., Clarke, A. B., de' Michieli Vitturi, M., Burton, M., Allison, C. M., Roggensack, K., et al. (2019). Conduit dynamics of highly explosive basaltic eruptions: the 1085 CE sunset crater sub-Plinian events. *J. Volcanol. Geotherm. Res.* 387:106658. doi: 10.1016/j.jvolgeores.2019.08.001

Liang, Y., Richter, F. M., and Watson, E. B. (1996). Diffusion in silicate melts: II. multicomponent diffusion in CaO-Al_2O_3-SiO_2 at 1500°C and 1 GPa. *Geochim. Cosmochim. Acta* 60, 5021–5035. doi: 10.1016/S0016-7037(96)00352-3

Lindsley, D. H., and Andersen, D. J. (1983). A two-pyroxene thermometer. *J. Geophys. Res.* 88, A887–A906. doi: 10.1029/JB088iS02p0A887

Lloyd, A. S., Ruprecht, P., Hauri, E. H., Rose, W., Gonnermann, H. M., and Plank, T. A. (2014). NanoSIMS results from olivine-hosted melt embayments: magma ascent rate during explosive basaltic eruptions. *J. Volcanol. Geotherm. Res.* 283, 1–18. doi: 10.1016/j.jvolgeores.2014.06.002

Maclennan, J. (2008). Concurrent mixing and cooling of melts under Iceland. *J. Petrol.* 49, 1931–1953. doi: 10.1093/petrology/egn052

Maclennan, J. (2019). Mafic tiers and transient mushes: evidence from Iceland. *Philos. Trans. R. Soc. A* 377:20180021. doi: 10.1098/rsta.2018.0021

Maclennan, J., Gaetani, G. A., Hartley, M. E., Neave, D. A., and Winpenny, B. (2012). "Petrological constraints on the crustal structure under rift zones," in *AGU Fall Meeting Abstracts* (San Francisco, CA), T41G.

Maclennan, J., McKenzie, D., Grönvold, K., Shimizu, N., Eiler, J. M., and Kitchen, N. (2003a). Melt mixing and crystallization under Theistareykir, northeast Iceland. *Geochem. Geophys. Geosyst.* 4, 1–40. doi: 10.1029/2003GC000558

Maclennan, J., McKenzie, D., Grönvold, K., and Slater, L. (2001). Crustal accretion under Northern Iceland. *Earth Planet. Sci. Lett.* 191, 295–310. doi: 10.1016/S0012-821X(01)00420-4

Maclennan, J., McKenzie, D., Hilton, F., Grönvold, K., and Shimizu, N. (2003b). Geochemical variability in a single flow from northern Iceland. *J. Geophys. Res.* 108, 1–21. doi: 10.1029/2000JB000142

Magee, C., Stevenson, C. T. E., Ebmeier, S. K., Keir, D., Hammond, J. O. S., Gottsmann, J. H., et al. (2018). Magma plumbing systems: a geophysical perspective. *J. Petrol.* 59, 1217–1251. doi: 10.1093/petrology/egy064

Marsh, B. D. (2004). A magmatic mush column Rosetta stone: the McMurdo dry valleys of Antarctica. *EOS Trans. Am. Geophys. Union* 85, 497–508. doi: 10.1029/2004EO470001

Mastin, L. G. (2002). Insights into volcanic conduit flow from an open-source numerical model. *Geochem. Geophys. Geosyst.* 3, 1–18. doi: 10.1029/2001GC000192

Michael, P. J. (1988). The concentration, behavior and storage of H_2O in the suboceanic upper mantle: implications for mantle metasomatism. *Geochim. Cosmochim. Acta* 52, 555–566. doi: 10.1016/0016-7037(88)90110-X

Miller, W. G. R., Maclennan, J., Shorttle, O., Gaetani, G. A., Le Roux, V., and Klein, F. (2019). Estimating the carbon content of the deep mantle with Icelandic melt inclusions. *Earth Planet. Sci. Lett.* 523:115699. doi: 10.1016/j.epsl.2019.07.002

Mollo, S., Del Gaudio, P., Ventura, G., Iezzi, G., and Scarlato, P. (2010). Dependence of clinopyroxene composition on cooling rate in basaltic magmas: implications for thermobarometry. *Lithos* 118, 302–312. doi: 10.1016/j.lithos.2010.05.006

Mollo, S., Giacomoni, P. P., Andronico, D., and Scarlato, P. (2015). Clinopyroxene and titanomagnetite cation redistributions at Mt. Etna volcano (Sicily, Italy): footprints of the final solidification history of lava fountains and lava flows. *Chem. Geol.* 406, 45–54. doi: 10.1016/j.chemgeo.2015.04.017

Mutch, E. J. F., Maclennan, J., Holland, T. J. B., and Buisman, I. (2019a). Millennial storage of near-Moho magma. *Science* 264, 260–264. doi: 10.1126/science.aax4092

Mutch, E. J. F., Maclennan, J., Shorttle, O., Edmonds, M., and Rudge, J. F. (2019b). Rapid transcrustal magma movement under Iceland. *Nat. Geosci.* 12, 569–574. doi: 10.1038/s41561-019-0376-9

Namiki, A., and Manga, M. (2006). Influence of decompression rate on the expansion velocity and expansion style of bubbly fluids. *J. Geophys. Res. Solid Earth* 111, 1–17. doi: 10.1029/2005JB004132

Namiki, A., and Manga, M. (2008). Transition between fragmentation and permeable outgassing of low viscosity magmas. *J. Volcanol. Geotherm. Res.* 169, 48–60. doi: 10.1016/j.jvolgeores.2007.07.020

Neave, D. A., Bali, E., Gufinnsson, G. H., Halldórsson, S. A., Kahl, M., Schmidt, A.-S., et al. (2019a). Clinopyroxene-liquid equilibria and geothermobarometry in natural and experimental tholeiites: the 2014–2015 Holuhraun eruption, Iceland. *J. Petrol.* 60, 1653–1680. doi: 10.1093/petrology/egz042

Neave, D. A., Buisman, I., and Maclennan, J. (2017a). Continuous mush disaggregation during the long-lasting Laki fissure eruption, Iceland. *Am. Mineral.* 102, 2007–2021. doi: 10.2138/am-2017-6015CCBY

Neave, D. A., Hartley, M. E., Maclennan, J., Edmonds, M., and Thordarson, T. (2017b). Volatile and light lithophile elements in high-anorthite plagioclase-hosted melt inclusions from Iceland. *Geochim. Cosmochim. Acta* 205, 100–118. doi: 10.1016/j.gca.2017.02.009

Neave, D. A., Maclennan, J., Hartley, M. E., Edmonds, M., and Thordarson, T. (2014). Crystal storage and transfer in basaltic systems: the Skuggafjöll eruption, Iceland. *J. Petrol.* 55, 2311–2346. doi: 10.1093/petrology/egu058

Neave, D. A., Namur, O., Shorttle, O., and Holtz, F. (2019b). Magmatic evolution biases basaltic records of mantle chemistry towards melts from recycled sources. *Earth Planet. Sci. Lett.* 520, 199–211. doi: 10.1016/j.epsl.2019.06.003

Neave, D. A., and Putirka, K. D. (2017). A new clinopyroxene-liquid barometer, and implications for magma storage pressures under Icelandic rift zones. *Am. Mineral.* 102, 777–794. doi: 10.2138/am-2017-5968

Newcombe, M. E., Plank, T., Barth, A., Asimow, P., and Hauri, E. (2020). Water-in-olivine magma ascent chronometry: every crystal is a clock. *J. Volcanol. Geotherm. Res.* 398:106872. doi: 10.1016/j.jvolgeores.2020.106872

O'Donnell, T., and Presnall, D. C. (1980). Chemical variations of the glass and mineral phases in basalts dredged from 25–30 N along the Mid-Atlantic Ridge. *Am. J. Sci.* 280, 845–868.

Pearson, D. G., Canil, D., and Shirey, S. B. (2003). Mantle samples included in volcanic rocks: xenoliths and diamonds. *Treat. Geochem.* 2–9, 171–275. doi: 10.1016/B0-08-043751-6/02005-3

Peslier, A. H., Bizimis, M., and Matney, M. (2015). Water disequilibrium in olivines from Hawaiian peridotites: recent metasomatism, H diffusion and magma ascent rates. *Geochim. Cosmochim. Acta* 154, 98–117. doi: 10.1016/j.gca.2015.01.030

Pirrie, D., Butcher, A. R., Power, M. R., Gottlieb, P., and Miller, G. L. (2004). Rapid quantitative mineral and phase analysis using automated scanning electron

microscopy (QemSCAN); potential applications in forensic geoscience. *Geol. Soc. Lond. Spec. Publ.* 232, 123–136. doi: 10.1144/GSL.SP.2004.232.01.12

Presnall, D. C., Dixon, S. A., Dixon, J. R., O'Donnell, T. H., Brenner, N. L., Schrock, R. L., et al. (1978). Liquidus phase relations on the join diopside-forsterite-anorthite from 1 atm to 20 kbar: their bearing on the generation and crystallization of basaltic magma. *Contrib. Mineral. Petrol.* 66, 203–220. doi: 10.1007/BF00372159

Putirka, K. D. (2008). Thermometers and barometers for volcanic systems. *Rev. Mineral. Geochem.* 69, 61–120. doi: 10.2138/rmg.2008.69.3

Putirka, K. D., Johnson, M., Kinzler, R. J., Longhi, J., and Walker, D. (1996). Thermobarometry of mafic igneous rocks based on clinopyroxene-liquid equilibria, 0–30 kbar. *Contrib. Mineral. Petrol.* 123, 92–108. doi: 10.1007/s004100050145

R Development Core Team (2016). *R: A Language and Environment for Statistical Computing*. Vienna: R Foundation for Statistical Computing.

Rudnick, R. L. (1992). Xenoliths–samples of the lower continental crust. *Contin. Lower Crust* 23, 269–316.

Ruprecht, P., and Plank, T. A. (2013). Feeding andesitic eruptions with a high-speed connection from the mantle. *Nature* 500, 68–72. doi: 10.1038/nature12342

Rutherford, M. J. (2008). Magma ascent rates. *Rev. Mineral. Geochem.* 69, 241–271. doi: 10.2138/rmg.2008.69.7

Saal, A. E., Hauri, E. H., Langmuir, C. H., and Perfit, M. R. (2002). Vapour undersaturation in primitive mid-ocean-ridge basalt and the volatile content of earth's upper mantle. *Nature* 419, 451–455. doi: 10.1038/nature01073

Scarlato, P., Mollo, S., Del Bello, E., von Quadt, A., Brown, R. J., Gutierrez, E., et al. (2017). The 2013 eruption of Chaparrastique volcano (El Salvador): effects of magma storage, mixing, and decompression. *Chem. Geol.* 448, 110–122. doi: 10.1016/j.chemgeo.2016.11.015

Shea, T., Lynn, K. J., and Garcia, M. O. (2015). Cracking the olivine zoning code: distinguishing between crystal growth and diffusion. *Geology* 43, 935–938. doi: 10.1130/G37082.1

Sigurdsson, I. A., Steinthórsson, S., and Grönvold, K. (2000). Calcium-rich melt inclusions in Cr-spinels from Borgarhraun, northern Iceland. *Earth Planet. Sci. Lett.* 183, 15–26. doi: 10.1016/S0012-821X(00)00269-7

Smith, P. M., and Asimow, P. D. (2005). Adiabat-1ph: a new public front-end to the MELTS, pMELTS, and pHMELTS models. *Geochem. Geophys. Geosyst.* 6, 1–8. doi: 10.1029/2004GC000816

Sparks, R. S. J., Annen, C., Blundy, J. D., Cashman, K. V., Rust, A. C., and Jackson, M. D. (2019). Formation and dynamics of magma reservoirs. *Philos. Trans. R. Soc. A* 377:20180019. doi: 10.1098/rsta.2018.0019

Sparks, R. S. J., and Cashman, K. V. (2017). Dynamic magma systems: implications for forecasting volcanic activity. *Elements* 13, 35–40. doi: 10.2113/gselements.13.1.35

Staples, R. K., White, R. S., Brandsdóttir, B., Menke, W., Maguire, P. K. H., and McBride, J. H. (1997). Färoe-Iceland ridge experiment 1. Crustal structure of northeastern Iceland. *J. Geophys. Res. Solid Earth* 102, 7849–7866. doi: 10.1029/96JB03911

Streck, M. J. (2008). Mineral textures and zoning as evidence for open system processes. *Rev. Mineral. Geochem.* 69, 595–622. doi: 10.2138/rmg.2008.69.15

Sugawara, T. (2000). Empirical relationships between temperature, pressure, and MgO content in olivine and pyroxene saturated liquid. *J. Geophys. Res.* 105, 8457–8472. doi: 10.1029/2000JB900010

Tarasewicz, J., Brandsdóttir, B., White, R. S., Hensch, M., and Thorbjarnardóttir, B. (2012). Using microearthquakes to track repeated magma intrusions beneath the Eyjafjallajkull stratovolcano, Iceland. *J. Geophys. Res. Solid Earth* 117, 1–13. doi: 10.1029/2011JB008751

Thompson, G., Bryan, W. B., and Melson, W. G. (1980). Geological and geophysical investigation of the mid-Cayman rise spreading center: geochemical variation and petrogenesis of basalt glasses. *J. Geol.* 88, 41–55. doi: 10.1086/628472

Thompson, R. N. (1974). Some high-pressure pyroxenes. *Mineral. Mag.* 39, 768–787. doi: 10.1180/minmag.1974.039.307.04

Trønnes, R. G. (1990). Basaltic melt evolution of the Hengill volcanic system, SW Iceland, and evidence for clinopyroxene assimilation in primitive tholeiitic magmas. *J. Geophys. Res. Solid Earth* 95, 15893–15910. doi: 10.1029/JB095iB10p15893

Tsuchiyama, A. (1986). Melting and dissolution kinetics: application to partial melting and dissolution of xenoliths. *J. Geophys. Res.* 91:9395. doi: 10.1029/JB091iB09p09395

Welsch, B., Hammer, J. E., Baronnet, A., Jacob, S., Hellebrand, E., and Sinton, J. M. (2016). Clinopyroxene in postshield Haleakala ankaramite 2. Texture, compositional zoning, and supersaturation in the magma. *Contrib. Mineral. Petrol.* 171:6. doi: 10.1007/s00410-015-1213-9

White, R. S., Drew, J., Martens, H. R., Key, J., Soosalu, H., and Jakobsdóttir, S. S. (2011). Dynamics of dyke intrusion in the mid-crust of Iceland. *Earth Planet. Sci. Lett.* 304, 300–312. doi: 10.1016/j.epsl.2011.02.038

Wilson, L., and Head, J. W. (1981). Ascent and eruption of basaltic magma on the earth and moon. *J. Geophys. Res. Solid Earth* 86, 2971–3001. doi: 10.1029/JB086iB04p02971

Winpenny, B., and Maclennan, J. (2011). A partial record of mixing of mantle melts preserved in Icelandic phenocrysts. *J. Petrol.* 52, 1791–1812. doi: 10.1093/petrology/egr031

Woods, A. W., and Koyaguchi, T. (1994). Transitions between explosive and effusive eruptions of silicic magmas. *Nature* 370, 641–644. doi: 10.1038/370641a0

Wright, H. M. N., Cashman, K. V., Mothes, P. A., Hall, M. L., Ruiz, A. G., and Le Pennec, J. L. (2012). Estimating rates of decompression from textures of erupted ash particles produced by 1999–2006 eruptions of Tungurahua volcano, Ecuador. *Geology* 40, 619–622. doi: 10.1130/G32948.1

Yang, H.-J., Kinzler, R. J., and Grove, T. L. (1996). Experiments and models of anhydrous, basaltic olivine-plagioclase-augite saturated melts from 0.001 to 10 kbar. *Contrib. Mineral. Petrol.* 124, 1–18. doi: 10.1007/s0041000 50169

Yu, Y., Zhang, Y., Chen, Y., and Xu, Z. (2016). Kinetics of anorthite dissolution in basaltic melt. *Geochim. Cosmochim. Acta* 179, 257–274. doi: 10.1016/j.gca.2016.02.002

Zhang, X., Ganguly, J., and Ito, M. (2010a). Ca-Mg diffusion in diopside: tracer and chemical inter-diffusion coefficients. *Contrib. Mineral. Petrol.* 159, 175–186. doi: 10.1007/s00410-009-0422-5

Zhang, Y., Ni, H., and Chen, Y. (2010b). Diffusion data in silicate melts. *Rev. Mineral. Geochem.* 72, 311–408. doi: 10.2138/rmg.2010.72.8

Zhang, Y., Walker, D., and Lesher, C. E. (1989). Diffusive crystal dissolution. *Contrib. Mineral. Petrol.* 102, 492–513. doi: 10.1007/BF00371090

Zhang, Y., and Xu, Z. (2003). Kinetics of convective crystal dissolution and melting, with applications to methane hydrate dissolution and dissociation in seawater. *Earth Planet. Sci. Lett.* 213, 133–148. doi: 10.1016/S0012-821X(03)00297-8

Conflict of Interest: The authors declare that the research was conducted in the absence of any commercial or financial relationships that could be construed as a potential conflict of interest.

frontiers in Earth Science

ORIGINAL RESEARCH
published: 18 June 2020
doi: 10.3389/feart.2020.00201

Multi-Stage Magma Evolution in Intra-Plate Volcanoes: Insights From Combined *in situ* Li and Mg–Fe Chemical and Isotopic Diffusion Profiles in Olivine

Lena K. Steinmann, Martin Oeser, Ingo Horn and Stefan Weyer*

Institute of Mineralogy, Leibniz University Hannover, Hanover, Germany

Understanding the timescales of magma evolution and ascent is essential for interpreting geophysical monitoring signals from active volcanoes. In this study, we explore the potential of diffusion-driven Li concentration and isotope zoning profiles recorded by magmatic olivine crystals to unravel time scales of magma evolution processes. Lithium is a fast-diffusing element and may provide the opportunity to investigate changes in magma composition during magma ascent, shortly before eruption. Lithium chemical and isotopic profiles were determined in olivines from two localities in the Massif Central volcanic region (France) that have previously been investigated for their Fe–Mg isotope systematics. The combined investigation of isotopic and chemical profiles makes it possible to distinguish between crystal growth and diffusion events. Extremely low δ^7Li-values down to −30.7‰ (relative to the commonly used Li isotope standard IRMM-16) in the crystal core regions and elevated values at crystal rims (δ^7Li ∼8 to 10‰), along with increasing concentrations from cores (∼3 to 1 μg/g) toward rims (12 to 6 μg/g) were found. The shape and orientation of both the chemical and isotopic profiles indicate that they were dominantly generated by Li diffusion into and within the olivine grains during magmatic differentiation. While Mg–Fe isotope and major element profiles have been modeled by a single diffusion event (Oeser et al., 2015), concentration and isotope profiles of Li indicate that a second diffusion event took place, that was not recorded by the Mg–Fe exchange diffusion couple. The first diffusion event was interpreted as reflecting the residence of the olivine crystals in a magma chamber. As diffusion coefficients for Fe–Mg exchange diffusion are very well determined, the time scales of this event are likely best quantified by Mg–Fe isotopic exchange diffusion modeling (Oeser et al., 2015). This event probably also generated the low δ^7Li observed in olivine cores. Comparing the length of the Mg–Fe and Li profiles could thus be used to determine the less well-known diffusion coefficients of Li in the studied olivine crystals. The findings of this study indicate that Li diffusion at low Li concentration levels, as typically observed in natural olivine, may be not as fast as previously thought. The second diffusion event might represent a short-lived event, such as degassing, related to the ascent of the magma and/or magma cooling after emplacement of the lava. Such

OPEN ACCESS

Edited by:
David A. Neave, University of Manchester, United Kingdom

Reviewed by:
Ian Parkinson, University of Bristol, United Kingdom
Takeshi Kuritani, Hokkaido University, Japan

***Correspondence:**
Lena K. Steinmann
s.weyer@mineralogie.uni-hannover.de

Specialty section:
This article was submitted to Petrology, a section of the journal Frontiers in Earth Science

Received: *20 December 2019*
Accepted: *18 May 2020*
Published: *18 June 2020*

Citation:
Steinmann LK, Oeser M, Horn I and Weyer S (2020) Multi-Stage Magma Evolution in Intra-Plate Volcanoes: Insights From Combined in situ Li and Mg–Fe Chemical and Isotopic Diffusion Profiles in Olivine. Front. Earth Sci. 8:201. doi: 10.3389/feart.2020.00201

a process would only affect Li, which, in contrast to the refractory elements Fe and Mg, is volatile during degassing. The findings of this study show that, according to their different diffusion rates and physiochemical properties, the combined use of spatially resolved Li and Mg–Fe chemical and isotopic diffusion profiles, is a powerful tool to model even multi-stage evolution processes in magmatic systems.

Keywords: multi-stage magma evolution, two-step diffusion modeling, femtosecond-laser ablation-MC-ICP-MS, Massif Central (France), lithium isotopes, lithium diffusion in olivine

INTRODUCTION

In principle, chemically zoned crystals can be the result of crystal growth in an evolving melt (growth zoning) or of chemical diffusion, as the result of disequilibrium, between minerals and the surrounding melt (diffusion zoning) (Costa et al., 2008). In the case of Li, this can be caused either by an increase in Li concentration in the magma, typically either due to magma mixing or crystal fractionation, or, due to a decrease in Li concentration in the melt, e.g., during degassing (Vlastélic et al., 2011; Lynn et al., 2018). The resulting zoning can be used to reconstruct the migration of crystals through dynamic plumbing systems with several reservoirs of compositionally different melts (Kahl et al., 2013, 2015). Olivine and clinopyroxene, as early forming crystals, are the most likely minerals to accept Li in their structure due to similar ionic radii of Mg and Fe in the octahedrally coordinated sites (Shannon, 1976). Nevertheless, Li behaves incompatibly during magma differentiation, with typical concentration levels of 3 to 8 μg/g in basalts and of ∼20 μg/g in rhyolites (Ryan and Langmuir, 1987; Ryan and Kyle, 2004) and with olivine/melt distribution coefficients of 0.2–0.35 (Ryan and Langmuir, 1987; Brenan et al., 1998). As olivine is a very abundant mineral in primitive basalts and chemical diffusion in olivine is well characterized, e.g., for Fe–Mg exchange (Dohmen and Chakraborty, 2007; Dohmen et al., 2007) or for Li (Dohmen et al., 2010; Richter et al., 2017), it frequently serves for diffusion studies (e.g., Lynn et al., 2018; Oeser et al., 2018). However, growth and diffusive origins of zoning cannot easily be distinguished by the investigation of chemical zoning alone and, notably, only the latter bears timescale information.

At magmatic temperatures, diffusion results in large isotope fractionation, e.g., of Li, Fe, and Mg, which may be recorded as isotopic zoning (e.g., Richter et al., 2003). Isotopic zoning coupled with chemical zoning is a strong indicator for a diffusive origin of the zoning because high-temperature equilibrium isotope fractionation is very limited, e.g., for Li (Tomascak et al., 1999b; Jeffcoate et al., 2007; Parkinson et al., 2007), Fe (Weyer and Ionov, 2007), and Mg (Teng et al., 2007; Liu et al., 2011). The combined information of chemical and isotopic zoning of Fe and Mg were successfully used in a number of recent studies to investigate complex magmatic evolution processes, such as magmatic differentiation and magma mixing, in a variety of different settings and to evaluate the effects of the end member processes of crystal growth and pure diffusion on the development of compositional zoning (Teng et al., 2011; Sio et al., 2013; Oeser et al., 2015, 2018; Collinet et al., 2017). Lithium is the lightest alkali metal and has two stable isotopes with a relative mass difference of ∼17%. Accordingly, large isotopic fractionations are observed between different geochemical reservoirs (see compilation in Penniston-Dorland et al., 2017 and references therein). Large Li isotope fractionations have also been observed on the mineral scale, e.g., up to 29‰ in a clinopyroxene from the Solomon Islands volcanic rocks (Parkinson et al., 2007), 29‰ in San Carlos olivine and 38‰ for an orthopyroxene crystal (Jeffcoate et al., 2007), which is thought to be mainly caused by chemical diffusion. However, the origin of the low δ^7Li-values in olivines remain debated. They may be directly caused by subduction-derived metasomatized material, such as isotopically light lower crust (Hamelin et al., 2009) or the ingress of light subduction-derived fluids in the mantle (Gu et al., 2016). On the other hand, they are assumed to be the result of Li diffusion in the mantle or during magmatic processes such as subduction or magma differentiation (Marschall et al., 2007a,b; Magna et al., 2008).

Here, we explore the suitability of using Li and Li isotope profiles recorded by chemically and isotopically zoned magmatic olivine to unravel magmatic processes and timescales of magmatic events. As Li is thought to diffuse faster than the Fe–Mg diffusion couple and also has specific physiochemical properties in melts such as volatility, it may record short magmatic processes which occur just before (or even after) eruption, and which are not otherwise recorded. The aim of this study is to investigate if the fast-diffusing Li isotope system is coupled with or decoupled from Mg–Fe exchange diffusion (Weyer and Seitz, 2012). We focus on chemically zoned magmatic olivine crystals from the Massif Central continental intra-plate volcanic system, which were previously investigated for Fe–Mg inter-diffusion processes and diffusion-driven Fe–Mg isotopic zoning of olivine (Oeser et al., 2015), thus providing a framework for investigating Li in this study. Li concentrations and isotope ratios of olivine are analyzed by a newly developed matrix independent measurement method by femtosecond-laser ablation-MC-ICP-MS (Steinmann et al., 2019). By combining diffusion profiles of Fe–Mg and Li, we intend to decipher complex magma evolution scenarios, including cooling, magma mixing and degassing.

MATERIALS AND METHODS

Samples and Geological Setting

Samples from two locations [Roche Sauterre (N45°54.858′, E02°55.674′) and Banne D'Ordanche (N45°36.671′, E02°46.355′)] in the continental intra-plate volcanic setting

Massif Central (France) were investigated in this study. Olivine-phyric basanites from Roche Sauterre may originate from a large lava flow that merged into a small lava lake in a paleo-topographic low during the late Miocene to early Pliocene (Nehlig et al., 2001; Lorand et al., 2003; Richet, 2003). At the summit of the Banne D'Ordanche, an olivine- and clinopyroxene-bearing ∼710,000-year-old basanite from the north-west slope of a former strato-volcano was sampled (Richet, 2003). The samples were characterized regarding their major and trace element composition by Oeser et al. (2015). All investigated olivines are normally zoned with respect to Mg# (Mg# = [Mg]/([Mg] + [Fe])) with high Mg# (0.86 to 0.90) in their cores and low Mg# (0.74 to 0.8) in their rims. Nickel concentrations follow this trend. The width of Mg# zoning reaches up to 400 μm into the up-to-2 mm in diameter olivine crystals. Mg# zoning is accompanied by inversely correlated Mg and Fe isotopic signatures underlining a diffusive origin of the zoning. The inter-correlation indicates an inter-diffusion process with Mg diffusing out of the olivine and Fe diffusing into the olivine (Oeser et al., 2015). Lithium concentrations and Mg# are summarized in **Supplementary Table S1** and backscattered electron images of the investigated crystals are displayed in **Supplementary Figure S1**.

Methods

Bulk Li Isotope Analyses With Solution Nebulization MC-ICP-MS

Two rock samples from Roche Sauterre (St6 and St3) were ground to a fine powder in order to perform whole rock δ^7Li analyses. Sample dissolution and chromatographic Li purification was conducted as described in detail in Tomascak et al. (1999a), Bouman et al. (2004), and Seitz et al. (2004). Analyses of the purified Li fraction were conducted on a Thermo-Scientific Neptune Plus MC-ICP-MS for the simultaneous measurement of ^{6}Li and ^{7}Li. Following Seitz et al. (2004), a Cetac Aridus II desolvation unit equipped with a pneumatic nebulizer with an uptake rate of ca. 50 μl/min fitted into a PFA spray chamber was used. Sample analysis was performed sequentially, applying sample-standard-bracketing with the IRMM-16 Li reference solution. The reference material JB-2 (basalt powder, Geological survey of Japan) was measured relative to IRMM-16 with 3.2 ± 1.2‰ (2 SD) which agrees within uncertainties to the compiled literature values of 3.5–4.9‰ (Brant et al., 2012; Dellinger et al., 2014; Coogan et al., 2017).

Lithium Isotope Analyses With fs-LA-MC-ICP-MS

For *in situ* Li isotope analyses, a femtosecond laser ablation system (Spectra-Physics Solstice) was coupled to a multi collector inductively coupled plasma mass spectrometer (MC-ICP-MS, Thermo-Scientific Neptune Plus). The ablation beam has a pulse duration of ∼100 fs and a wavelength of 194 nm which is generated via frequency conversion from an infrared beam with 775 nm wavelength in a mirror and lens system and focused on the sample surface via a modified in-house built New Wave (ESI) stage combined with an optical microscope (Horn et al., 2006; Horn and von Blanckenburg, 2007). The laser spot size of ∼26 μm on the bracketing standard GOR132-G (Gorgona Island komatiite) allows for sufficient spatial resolution to resolve diffusion profiles. The protocol for Li isotope measurement was applied as described in detail by Steinmann et al. (2019). In brief, measurements were performed at relatively cool plasma conditions (900 W) in order to avoid matrix ionization in the plasma. *In situ* Li isotope ratio measurements were performed in static mode at low mass resolution which is sufficient to resolve atomic interferences. In order to keep background Li signals low, the measurements were performed under dry plasma conditions. The sample was mixed in a homogenization device to increase signal stability (Steinmann et al., 2019). For the detection of ^{7}Li a 10^{13} Ω amplifier coupled to a faraday cup was deployed, while a secondary ion multiplier was used for the detection of the less abundant ^{6}Li. Due to the slower signal response of the 10^{13} Ω amplifiers (as compared to 10^{11} Ω amplifiers) a *tau* correction (Kimura et al., 2016) was applied during data reduction. All measurements were performed using standard-sample-bracketing with the komatiitic MPI DING reference glass GOR132-G as bracketing standard according to Eq. (1):

$$\delta^7 Li = \left[\frac{\left(\frac{^7Li}{^6Li}\right)_{sample}}{\left(\frac{^7Li}{^6Li}\right)_{GOR132-G}} - 1 \right] \times 1000 \quad (1)$$

Subsequently, all data were converted relative to the internationally used Li isotope standard IRMM-16 (with $\delta^7Li_{IRMM-16} = \delta^7Li_{GOR132-G} + 8.6$; Jochum et al., 2006; Steinmann et al., 2019). Measurements of the bracketing standard GOR132-G were performed in raster ablation mode with a scan speed of 20 μm/s; the olivine profiles were measured in line ablation mode with lines arranged parallel to the crystal rim so that each line accounts for one measured δ^7Li-value. Individual measurements consist of 180 cycles, each with an integration time of 1.049 s. The first ∼35 cycles were used for background correction, measuring only the gas blank without a laser ablation signal. This was followed by ∼130 cycles of sample ablation. As internal control for the accuracy of the method, the MPI DING reference glass T1-G [δ^7Li = 1.6–2.4‰, (Jochum et al., 2006; Le Roux, 2010; Xu et al., 2013)] was measured and yielded a long term value of 2.1‰ (δ^7Li = 0.4‰, 2 SD for n = 64 in 16 sessions throughout 22 months) in agreement with Steinmann et al. (2019). All individual data points along the profiles were conducted as ∼100 μm long line scans parallel to the crystal rim [similar to trace element and Fe- and Mg isotope analyses (Oeser et al., 2015) (**Figure 1**)]. This was necessary to detect a sufficient number of Li ions in order to satisfy counting statistics due to the low concentration of Li in the samples, and in order to achieve a stable signal over the duration of the measurement. One crystal (St6-2b_ol4b, displayed in **Figure 1**) was analyzed across the whole crystal; all other crystals were analyzed from rim to core.

Diffusion Models

Diffusion has been modeled in several studies by applying an analytical or numerical approach to solve Fick's second law of diffusion with the aim of equilibrating an initially homogeneous olivine with new boundary conditions, e.g., by changing the conditions and concentration in the surrounding

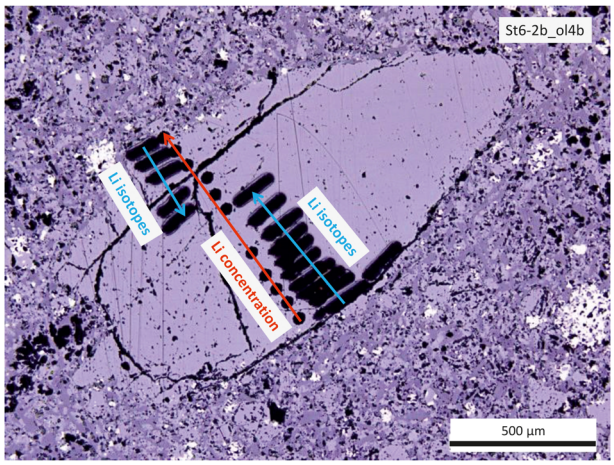

FIGURE 1 | Photomicrograph (reflected light) of sample St6-2b_ol4b showing the positions for major and trace element and isotope analyses. Black dots are from laser ablation for trace element analyses (indicated by the red arrow), which were conducted exactly along the profile previously analyzed for major elements with EMPA (not visible). Short black lines are from laser ablation for isotope analyses, which was conducted from both rims toward the core of the olivine grain (indicated by blue arrows).

melt (Costa et al., 2008). Most of the investigated olivine crystals have an elongated shape and we always analyzed the short distance to the core of those crystals (i.e., vertically to the long side, see **Figure 1**). For this purpose, a one-dimensional expression for the diffusion equation in a plane sheet (rather than a spherical) geometry in Eq. (2) has been solved for diffusion modeling with analytical and numerical calculations (see **Supplementary Material** for equations).

$$\frac{\partial C(x,t)}{\partial t} = \mathrm{D}\frac{\partial^2 C(x,t)}{\partial x^2} \tag{2}$$

This equation is valid for diffusive processes, which are not dependent on concentration, which was used for modeling Li diffusion in this study. The diffusivity of Li in olivine has been investigated in several studies following different approaches, either based on laboratory experiments at defined conditions or based on the analyses of natural samples.

(1) An experimental study performed by Dohmen et al. (2010) found two diffusion mechanisms for Li in olivine: one "fast" diffusion mechanism, operating at interstitial sites in the olivine structure and one "slow," metal vacancy-controlled diffusion mechanism, operating at octahedral sites. The existence of these mechanisms was later confirmed by Richter et al. (2017). In natural systems, the slower mechanism, Li diffusion via octahedral sites, is assumed to dominate (Dohmen et al., 2010). From their experiments, conducted at 800 to 1200°C and at controlled fO_2 (≈ WM buffer), Dohmen et al. (2010) have developed an equation from an approximated Arrhenius relation to determine the diffusivity of the "slow" diffusion mechanism in olivine as a function of temperature:

$$\log(D_{Li}) = -5.92\,(\pm 1.0) - 1.2847 \times 10^4/T(K) \tag{3}$$

The resulting diffusion coefficients are still about an order of magnitude faster than those of most divalent cations, such as Mg, Fe, or Ni.

(2) Several other studies investigated the diffusivity of Li relative to that of other cations and observed an interdependence of the diffusivities of e.g., Fe, Mg, Ni, Mn, Li, and other trace elements (Qian et al., 2010; Spandler and O'Neill, 2010; Oeser-Rabe, 2015). The diffusivity of Li was determined relative to that of Mg–Fe exchange diffusion as given in Eq. (4). The factor Γ denotes the product of diffusion coefficient and duration which equals the diffusive flux ($\Gamma = D{\cdot}t$; e.g., Ganguly, 2002). For this purpose the concentration profiles of Li and Mg# (recalculated from MgO and FeO concentrations) are analyzed and Mg# is fitted with Eqs. (S.1) and (S.2). The concentration profile of Li is fitted by adjusting Γ, which gives the relative diffusivity of Li depending on Mg–Fe. Eq. (4) is valid under the assumption that the diffusion time t is the same or very similar for all elements.

$$\frac{\Gamma_{Li}}{\Gamma_{Mg-Fe}} \cong \frac{\mathrm{D}_{Li}}{\mathrm{D}_{Mg-Fe}} \tag{4}$$

(3) We applied an approach similar to approach (2) for the olivine investigated in this study. As all olivine crystals, analyzed for their Li isotope composition in this study, were previously analyzed for their major and trace element compositions, including Fe, Mg, and Li, as well as for their Fe–Mg isotope compositions, we were able to determine Li diffusivity data relative to those of the well-determined Fe–Mg exchange diffusion. In detail, we used the timescales, as determined by Oeser et al. (2015), by modeling chemical and isotopic Mg and Fe inter-diffusion, which were interpreted to represent the residence of the olivine crystals in a magma between crystal formation for phenocrysts and the entrainment of xenocrysts in the host magma and eruption of the magma. Based on these time scales (fixed parameter t), the Li concentration and isotope profiles were fitted by adjusting D_{Li} in order to determine the diffusivity of Li. Thus, the resulting Li diffusivity is based on modeling of two Li profiles, i.e., the concentration and isotope profiles. To be consistent with modeling by Oeser et al. (2015) for the same samples we applied constant temperature conditions for the system. We decided to assume a temperature of 1250°C, as this was shown to be best suited for the investigated samples (Oeser et al., 2015). We are aware that a rim Mg# of 0.8 indicates lower temperatures around 1200°C (Roeder and Emslie, 1970). However, Costa et al. (2008) demonstrated that modeling with an integrated cooling rate does not affect the modeled time scales significantly as most of the diffusive flux occurs in the highest temperature regime of the system. In contrast to Fe–Mg diffusion, Li diffusion was generally modeled from both sides of the crystal, even if the profile was not measured as a complete transect. This was necessary because, due to the relatively fast diffusive character of Li, the crystal core composition was affected by diffusion from both of the opposite crystal rims, in several cases. For all crystals measured as half transects, boundary conditions for the unknown crystal rim are assumed to be in accordance with those of the measured rim. For St6-2b_ol4b, a complete transect was measured, and hence the measured values were applied in the model.

From the samples described above, olivine crystals with high Li concentrations and with the largest variations in Li concentrations from rim to core were selected for Li isotope analysis and modeling of profiles. For approach (1) the diffusivity is calculated according to Eq. (3), as the diffusivity depends on the temperature T. For approach (2) an analytical solution [Eq. (S.1) and Eq. (S.2) in **Supplementary Table S1**] of Eq. (2) is applied and for approach (3) a numerical solution by the method of finite differences of the diffusion equation in Eq. (2) (Eq. (S.3) in **Supplementary Table S1** is applied.

The relation between the diffusion coefficients of the two isotopes of Li can be described by the empirical formula of Richter et al. (1999):

$$\frac{D_{6Li}}{D_{7Li}} = \left(\frac{m_{7Li}}{m_{6Li}}\right)^{\beta} \quad (5)$$

Where D values are the diffusion coefficients of ^{6}Li and ^{7}Li, m values are the atomic masses of ^{6}Li and ^{7}Li in Dalton and the β-value describes the diffusion-driven isotope fractionation. β is an empirical constant which depends on the diffusion medium and is smaller than 0.5 (Richter et al., 1999). A β-value of 0.5 is the factor for a non-uniform gas (Chapman and Cowling, 1953), and the maximum value achievable. The β-value for Li has been determined experimentally and can be fitted by values of $\beta = 0.4 \pm 0.1$ for the crystallographic *a*- and *c*-axis whereas the fractionation along the *b*-axis appears to be slightly lower (Richter et al., 2017). Transferring the relative difference in the diffusivities of the two Li isotopes, determined by Dohmen et al. (2010) to a β-value, a β_{Li} of 0.19 may be assumed for the slow diffusion mechanism (^{6}Li diffuses 3% faster than ^{7}Li) and of 0.32 for the fast diffusion mechanism (^{6}Li is 5% faster than ^{7}Li). Compared to Richter et al. (2017), these values are slightly lower but comparable to Li diffusivity in molten oxides (Richter et al., 2003).

RESULTS

Four olivines from Banne D'Ordanche (BdOr-1_ol1, BdOr-1_ol2, BdOr-1_olxen1, and BdOr-1_olxen2) were analyzed regarding their Li isotope composition. Major- and trace element concentration data were taken from Oeser-Rabe (2015). The investigated olivine grains display Li concentrations varying from ~8 to 9 μg/g at their rims to 1–2 μg/g in their core regions. The lava lake of Roche Sauterre was been sampled at two positions. Two olivines from one sample (St6-2b_ol4b and St6-2b_ol5) display concentrations varying from 7 μg/g at their rims to 3 μg/g in their cores. Two olivines in the other sample (St3-3a_ol1 and St3_3a_ol2) have somewhat lower Li concentrations ranging from 4 μg/g at their rims to 1 μg/g in their cores. All investigated grains display the lowest Li concentrations in their cores. Nevertheless, Li concentration profiles show different shapes (**Figures 2A–C**), i.e., some of them show a slight decrease of Li toward the very rim. Lithium concentrations and isotope compositions for all investigated samples are compiled in **Table 1**.

Lithium isotope profiles of all measured olivines display elevated δ^7Li-values at the crystal rims and significantly

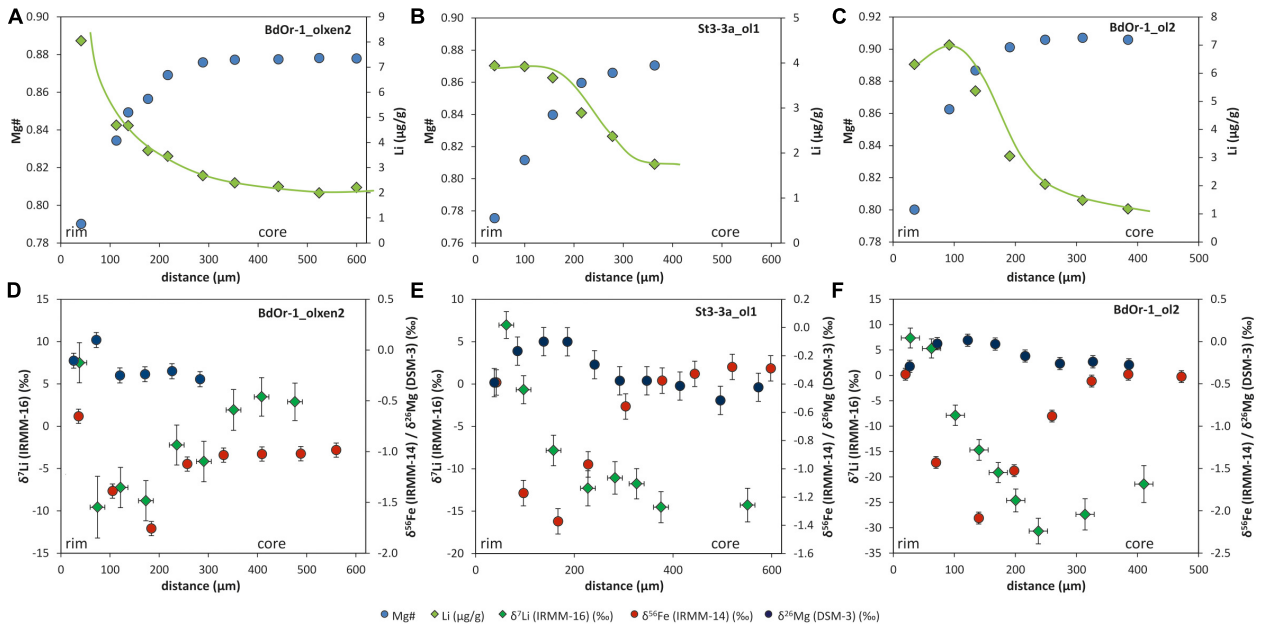

FIGURE 2 | Mg–Fe and Li concentration zoning for **(A)** BdOr1_olxen2, **(B)** St3-3a_ol1, and **(C)** BdOr-1_ol2. Li concentration zoning with best-fit shape of the concentration profile (green lines) and Mg# are reversely correlated Mg, Fe, and Li isotope profiles for **(D)** BdOr1_olxen2, **(E)** St3-3a_ol1, and **(F)** BdOr-1_ol2. The isotope profiles show a coupling between Li and Mg–Fe diffusion, however, with an offset toward a wider zoning for Li for most olivines. Horizontal error bars display the spot size for laser ablation (~30 μm) and vertical error bars represent the analytical uncertainty (2σ) during one sample-standard-bracketing for Li and 2SD during one analytical session for Mg and Fe [values for Mg and Fe isotopes are taken from Oeser et al. (2015)].

TABLE 1 | Lithium rim and core compositions of investigated olivines.

	Li_{rim} (μg/g)*	Li_{core} (μg/g)*	$Li_{bulkrock}$ (μg/g)*	$\Delta^7Li^{max-min}$ (‰)	δ^7Li_{max} (‰)	δ^7Li_{min} (‰)	δ^7Li_{bulk} (‰)
BdOr-1_ol1	8.5	1.7	6.14	13.5	2.3	−11.3	–
BdOr-1_ol2	6.3	1.2	6.14	38.0	7.4	−30.7	–
BdOr-1_olxen1	12.5	8.7	6.14	18.2	5.1	−13.1	–
BdOr-1_olxen2	8.1	2.0	6.14	17.1	7.5	−9.6	–
St3-3a_ol1	3.9	1.8	5.70	21.5	7.0	−14.5	2.3 ± 2.0
St3-3a_ol2	2.3	1.1	5.70	23.1	9.0	−14.1	2.3 ± 2.0
St6-2b_ol4b	5.5	3.9	5.78	22.2	11.4	−10.7	3.3 ± 1.2
St6-2b_ol5	5.9	3.1	5.78	22.9	13.2	−14.2	3.3 ± 1.2

**Published in Oeser et al. (2015) and Oeser-Rabe (2015).*

lower values in the core regions (**Figure 2**) with a Li isotope fractionation between rim and core ranging from $\Delta^7Li^{rim-core}$ = 21.5‰ to 27.3‰ for Roche Sauterre and $\Delta^7Li^{rim-core}$ = 13.5‰ to 38‰ for Banne D'Ordanche. In most cases $\Delta^7Li^{rim-core}$ is equal- or close to the largest Li isotope fractionation $\Delta^7Li^{min-max}$ observed for each grain, which indicates that the cores are strongly affected by diffusion and have not preserved their original Li isotopic composition. The δ^7Li-values in the cores (−9.6 to −14.5‰ and −30.7‰ for one crystal) are clearly lower than δ^7Li-values of ∼4‰ of volcanic bulk rock (Seitz et al., 2004; Magna et al., 2006; Jeffcoate et al., 2007). Similar low δ^7Li–δ^7Li values in natural olivines were observed for other olivines from the Massif Central (Gu et al., 2016) and for San Carlos olivine xenoliths (Jeffcoate et al., 2007). Lithium concentration and isotope profiles are broadly correlated, with high Li concentration and high δ^7Li-values at the rim and decreasing Li concentrations and low δ^7Li-values toward the core (**Figure 2**). The shape of the Li isotope profiles is consistent with the shape that would be expected from diffusion-driven isotope fractionation (Parkinson et al., 2007). Iron and magnesium isotope profiles, displaying diffusion-driven zoning of δ^{56}Fe and δ^{26}Mg are shown for comparison in **Figures 2D–F** (taken from Oeser et al., 2015). The width of Li isotopic zoning slightly exceeds that of Fe and Mg isotopic zoning, in most cases. All measured Li concentration and isotope ratios (this study) are listed in **Supplementary Tables S2, S3** together with the Mg and Fe isotope compositions determined by Oeser et al. (2015).

DISCUSSION AND MODELING OF DIFFUSION EVENTS

Boundary Conditions of the System

Coupled Li concentration and isotope profiles from the rims of the crystals toward their cores, and the extremely light isotopic composition of the olivine cores (δ^7Li_{min}-values down to −30.7‰, **Table 1**) strongly indicate a diffusive origin of the zoning caused by faster diffusion of ^{6}Li into the crystal compared to ^{7}Li. The coupled zoning profiles for Li concentrations and isotope compositions are similar, though not identical in scale and magnitude, to previously investigated Fe concentration and isotope profiles (and anti-correlated Mg concentration and isotope profiles), which were generated by Fe–Mg exchange diffusion (Oeser et al., 2015; **Figure 2**). The Li concentration profile shapes observed for olivine from the Massif Central can be distinguished into three types (indicated by the green lines in **Figures 2A–C**, which represent best fits through the data), with always higher Li concentrations in the rims and lower concentrations in the cores. Type I (**Figure 2A**) shows decreasing Li concentrations toward the cores which is a typical profile for diffusion into the crystals. Type II (**Figure 2B**) consists of two compositional plateaux with constant Li concentrations at outermost rims and cores and gradually decreasing Li concentrations in transition zones. Type III (**Figure 2C**) exhibits maximum Li concentrations at some distance from rims (∼100 μm) and then decreases of Li concentrations toward cores. These latter profiles may indicate two diffusion events with a first event of Li diffusion into the crystals and a second event causing Li diffusion out of the crystals. While the differences between the three types of Li concentration profiles are striking, the corresponding isotope profiles cannot be distinguished as clearly.

Before diffusion models can be established, the boundary conditions of the system at the start of diffusion have to be evaluated (Costa et al., 2008). These include the Li concentration (profile) before diffusion started and here also the initial isotope composition (or isotope profile). Here, we assume that the crystals were initially homogeneous and grew in equilibrium with the melt. Assuming that the melt initially had a similar Li concentration to that analyzed for whole rock samples [BdOr1 = 6.14 μg/g, St3-3a = 5.7 μg/g, and St6-2b = 5.78 μg/g (Oeser et al., 2015)] and applying the Li olivine/melt partition coefficient determined by Brenan et al. (1998) for olivine with high Mg# (of ∼0.2), this results in equilibrium concentrations for olivine of 1.16 to 1.47 μg/g (see also **Supplementary Figure S2**). Lithium concentrations in the olivine cores range from 1 to 2 μg/g for the two olivine crystals from sample St3a from Roche Sauterre, as well as for three out of four Banne D'Ordanche olivines. The other two Roche Sauterre crystals (from St6) exhibit higher Li concentrations of 3.1 μg/g and 3.9 μg/g (**Table 1**). Only one crystal from Banne D'Ordanche displays a Li_{core} concentration of 8.7 μg/g, likely indicating significant Li diffusion into this core. Two of the crystals are found in a glomerocryst and hence are described as xenocrysts by Oeser et al. (2015). The initial concentration of such crystals is difficult to constrain. Notably, the rim Li concentration of most olivine grains is on the order of 4 to 8 μg/g and difficult to explain with olivine/melt

partition coefficient on the order of 0.2 (Brenan et al., 1998), as this would indicate extremely high Li concentrations (on the order of 20 to 40 μg/g) in the melt at the time when diffusion ceased, i.e., at the end of fractional crystallization. Such high Li concentrations were not observed for any of the investigated basalts (Oeser et al., 2015). However, although Brenan et al. (1998) suggested low olivine/melt partition coefficient on the order of ∼0.2, those were essentially determined for extremely forsterite-rich olivine (Mg# = 99 to 100), while a higher olivine/melt partition coefficient (of ∼0.35) was observed for an olivine with a slightly lower Mg# (of 92). Other authors have observed higher partition coefficients, between 0.21 and 0.56 (Taura et al., 1998; McDade et al., 2003; Ottolini et al., 2009), which are always in combination with lower Mg# than the forsterite-rich olivines form Brenan et al. (1998). Ottolini et al. (2009) have interpreted, that there might be an influence of the melt composition on the partition coefficient, and Taura et al. (1998) supposed a pressure dependence. Thus, Li partitioning into olivine potentially increases with decreasing Mg#. If so, the high Li contents, observed in the olivine rims, may primarily be driven by increasing Li partitioning into olivine during fractional crystallization, rather than by increasing Li contents in the melt, though Li concentrations in the melt at the end of fractional crystallization may also have been slightly higher than those observed in the sampled basalts.

Similar to the Li concentrations, the measured δ^7Li_{bulk} of the basalts may be assumed as the initial Li isotope composition of the olivine crystals before diffusion started. The isotopic composition of fresh basalts varies from +2‰ to +5‰ and does not appear to change significantly during fractional crystallization (Chan et al., 1992; Elliott et al., 2006; Tomascak et al., 2008). The degassing of a melt causes a transition of Li from the melt or crystal to a vapor phase and a decrease in δ^7Li to lower values (Vlastélic et al., 2011). For Roche Sauterre St6 and St3 a δ^7Li_{bulk} of 3.3 ± 1.3‰ and 2.3 ± 2.0‰ were determined, respectively. For Banne D'Ordanche, no δ^7Li_{bulk} is available and a mean basaltic δ^7Li value of 3.5‰ was assumed as the initial value for the modeling. Furthermore, the initial isotopic composition of the crystals is assumed to be homogeneous and the isotopic composition of the melt to be constant during fractional crystallization (e.g., Tomascak et al., 1999b). The initial Li isotope composition of the potential xenocrysts is uncertain and may as well be different from that of basalts. Mantle olivine may have heterogeneous δ^7Li, which is ascribed to metasomatic overprinting (e.g., Nishio et al., 2004; Tang et al., 2012; Ackerman et al., 2013; Su et al., 2016) or diffusion in the mantle (e.g., Marschall et al., 2007a,b; Magna et al., 2008).

The First Diffusion Event: Constraints on Li Diffusion Coefficients and β Values

For the model applied here, an open system is assumed due to the quasi-infinite supply of Li from the surrounding melt. This quasi-infinite supply of Li also justifies the use of a fixed boundary concentration. As outlined above, a variety of Li diffusion coefficients, determined with different approaches, are available in the literature for modeling the observed chemical and isotopic zoning of Li. As will be shown below, the choice of Li diffusion coefficients is critical for the determination of diffusion timescales. We considered the Mg–Fe diffusion time determined by Oeser et al. (2015) as a fixed diffusion event to determine Li diffusivity. For this purpose we applied a combined approach of chemical and isotopic modeling of Mg–Fe exchange diffusion, because the diffusivity of Li in olivine is less well constrained than that of Mg–Fe (Dohmen et al., 2007). This event was interpreted as the residence time of the olivine crystals in a magma reservoir. Iron–Mg exchange diffusion was driven by the chemical evolution of the magma, as a result of fractional crystallization, which generated a chemical gradient between the melt and previously formed olivine crystals (Oeser et al., 2015). This chemical evolution would have also generated a chemical gradient in Li between olivine and surrounding melt (and as described above, likely also a change in Li partitioning), forcing Li diffusion. This scenario is consistent with increasing Li concentrations toward olivine rims and decreasing δ^7Li values toward the olivine cores, indicating diffusion of Li (and preferentially of isotopically light Li) into olivine, as would be expected during magma differentiation. We therefore assume that the light Li and Fe isotope- (and heavy Mg isotope) signatures were generated by the same event.

Based on this assumption, Li diffusion into olivine was modeled using the timescales given by Oeser et al. (2015) for the same samples (for BdOr1_ol2 = 239 days, for BdOr1_olxen2 = 252 days and for St3-3a_ol1 = 3.26 years) and fitting the measured Li concentration and isotope profiles. The initial concentration calculated above was assumed as the Li core concentration (C_{core}) and in some cases it was adapted to fit the measured profile. In the first modeled event a Li rim concentration (C_{rim1}) of 3.5 to 21 μg/g was applied in order to match the slope of the measured profiles (**Table 2**). Notably, all crystals were modeled assuming equivalent diffusion and C_{rim} from both crystal rims toward the core. The only exception was St6-2b_ol 4b, because the crystal was measured as a whole transect, and hence both measured rim concentrations were modeled. As mentioned above, the investigated olivines display three different types of Li zoning (**Figure 2**) and the shapes with constant or decreasing Li concentrations at the very rim (type II and III, **Figures 2B,C**) cannot have formed during a single diffusion event, but rather indicate a second diffusion event (with Li diffusion in opposite direction). For those olivines, including BdOr1_ol2, BdOr1_olxen1, St3-3a_ol1, and St6-2b_ol4b, the Li concentration and isotope composition measured at the very rim was excluded when modeling the olivine core composition and the slope of the core-rim transition during the first diffusion event. As will be shown below, the very rim composition of such olivines can be modeled with a second diffusion event.

Our results show that the initial concentration in crystal cores (C_{core}) changed during the course of diffusion for several grains, as a result of the faster diffusion of Li, as compared to that of Fe and Mg. Assuming a fixed diffusion timescale from Fe–Mg diffusion, the diffusion coefficient D_{Li} was fitted to obtain congruent modeled and measured zoning profiles, for both, the Li concentration and Li isotope profiles, with a particular focus on Li core compositions. Another important variable for modeling

TABLE 2 | Modeling parameters of the first and second diffusion event.

	t_{step1} (days)$^{+}$	D_{fit} (m^2/s)	δ^7Li_{start} (‰)	C_{core} (μg/g)	C_{rim1} (μg/g)	β_{step1}	C_{rim2}(μg/g)	β_{step2}	t_{step2} (days)
BdOr1-ol1*	∼239	$2*10^{-16}$	3.5	1.2	11	0.15	6	0.15	20–40
BdOr1-ol2	∼239	$5*10^{-16}$	3.5	1.1	12	0.23	6	0.25	20–60
BdOr1-olxen1	∼252	$4.5*10^{-16}$	3.5	7	21	0.2	8	0.2	40–80
BdOr1-olxen2	∼252	$3.5*10^{-16}$	3.5	2	10	0.13	8	0.2	20–60
St3-3a_ol1	∼1190	$2.5*10^{-16}$	2.3	1.1	4.5	0.15	3.8	0.25	100–200
St3-3a_ol2	∼1190	$3.0*10^{-16}$	2.3	0.7	3.5	0.19	2.5	0.25	100–200
St6-2b_ol4b	∼1190	$2.0*10^{-16}$	3.3	2.8	9/7.5$^{\#}$	0.22	5/3$^{\#}$	0.2	60–120
St6-2b_ol5	∼1190	$5.0*10^{-16}$	3.3	2.2	6.5	0.2	5.5	0.25	30–90

*Note that the duration of the first diffusion event was fix (taken from Oeser et al., 2015) and D_{Li} was fitted, whereas for the second diffusion event, the duration, t_{step2} was a model outcome, β_{step1} is the modeled value from the first diffusion event and β_{step2} is the value determined from the second diffusion event. For comparison the experimentally determined β values of the slow diffusion process from Dohmen et al. (2010) and Richter et al. (2017) are 0.19 and 0.4 ± 0.1, respectively. *BdOr1-ol1 was modeled in a 3-step model with an additional step 0 before step 1 with C_{rim0} = 5 μg/g, β_{step0} = 0.25 and t_{step0} = 2760 days. $^{+}t_{step1}$ durations were taken from Oeser et al. (2015). $^{\#}$St6-2b_ol4b was measured from rim to rim, for modeling C_{rim} was adjusted relative to $C_{measured}$.*

the isotopic profiles of Li is the β-value, which describes isotope fractionation during diffusion. It also has to be fitted in order to match the amplitude of the measured isotope profiles. β-values were determined in this study by fitting the modeled isotope profiles to the measured ones (as done for Fe and Mg in previous studies, e.g., Sio et al., 2013; Oeser et al., 2015 and others). With this approach, β-values determined in this study do not exceed 0.25 which is lower than the β-values of 0.4 ± 0.1 determined by Richter et al. (2017) for the crystallographic a- and c-axes, (for the *b*-axis somewhat lower β-values were determined), and also lower than that those that have been modeled by the same authors for a natural olivine (β = 0.30–0.36). The β-values obtained here indicate a 1.6% (β = 0.1) to 3.9% (β = 0.25) higher relative diffusivity of ^{6}Li as compared to ^{7}Li. This is similar to the results of Dohmen et al. (2010), who determined a ∼3% faster diffusivity of ^{6}Li relative to ^{7}Li in their experiments, which corresponds to β = 0.19. These findings imply, that β-values for Li may depend on intensive thermodynamic variables which have not yet been explored in detail. As the zoning profiles of several of the investigated olivines indicate a second diffusion event (see below), a slightly lower β value (than required for a perfect match of the core composition in only one diffusion step) was generally assumed for modeling of the first event, in order to match the measured isotopic zoning with a combined model of both diffusion events. Thus, the final β-value for the first diffusion event could only be determined after modeling both diffusion events. This is described in more detail below. Notably, assuming that some of the olivine grains (type I, **Figure 2A**) were unaffected by the second diffusion event would result in a slight underestimation of the β value for those samples. For example, olivine grain BdOr1-olxen2 was modeled with both one and two diffusion events. This revealed β-values of 0.16 for one diffusion event (**Figure 3**) and 0.13 for the first of two diffusion events (**Supplementary Figure S3F**), respectively. However, the assumption of a second diffusion event had no effect on the modeled values for D_{fit}. All modeled D_{Li} and β-values are listed in **Table 2**.

Diffusivities of Li relative to the diffusion couple Mg–Fe were obtained from the equations for the analytical solution in **Supplementary Table S1** and yield D_{Li}/D_{Mg-Fe} ratios of ∼2 for BdOr1, which means the diffusivity of Li is twice as fast as the diffusivity of Mg–Fe in BdOr1. For St3-3a and St6-2b the diffusivity of Li is ∼1.5 times faster than the diffusivity of Mg–Fe (**Figure 4**). These results are similar to previous findings by Qian et al. (2010) and Spandler and O'Neill (2010). The parametrization for the determination of the diffusion coefficient of Mg–Fe diffusion in olivine by Dohmen and Chakraborty (2007) depends on temperature (T), pressure (P), oxygen fugacity (fO_2), the mole fraction of the fayalite component (X_{Fe}), and the crystallographic orientation of the measured profile. With Eq. (4) and the relative diffusivities of Mg–Fe and Li and the absolute calculated diffusion coefficients for Mg–Fe (D_{Mg-Fe}) the diffusion coefficient for Li (D_{Li}) is obtained (Table 3).

The effect of using different Li diffusion coefficients was evaluated, by comparatively modeling Li diffusion with the experimentally determined diffusion coefficient (D_{exp}) (for this comparison, we used the slower diffusion mechanism of Dohmen et al., 2010) and the fitted diffusion coefficient from this study (D_{fit}). In **Figure 3** the effect of both models on the shape of the chemical and isotopic diffusion profiles is compared (for sample BdOr1_olxen2). For the comparison in **Figure 3**, a crystal was selected, for which the effect of a potential second diffusion event was negligible. The experimentally determined diffusion coefficient for Li from Dohmen et al. (2010) was adjusted to a temperature of 1250°C (Oeser et al., 2015), according to Eq. (3), although, experimental diffusion coefficients were only determined in the temperature range between 800°C and 1200°C. This comparison reveals that applying the experimentally determined diffusivity of Li, the modeled Li concentrations and isotope compositions do not match the observed profiles when assuming a diffusion time from Oeser et al. (2015) (**Figures 4A,B**). In turn, applying D_{exp} and fitting the modeled Li and δ^7Li to the measured profile would indicate a significantly shorter diffusion time scale than that determined by modeling Mg–Fe exchange diffusion (**Figures 3C,D**). This would imply, however, that the development of Li concentration gradients was entirely decoupled from the development of Fe–Mg concentration gradients for all investigated samples, i.e., was generated by a much later event. Exchange diffusion between Fe and Mg was likely driven by the chemical differentiation of the

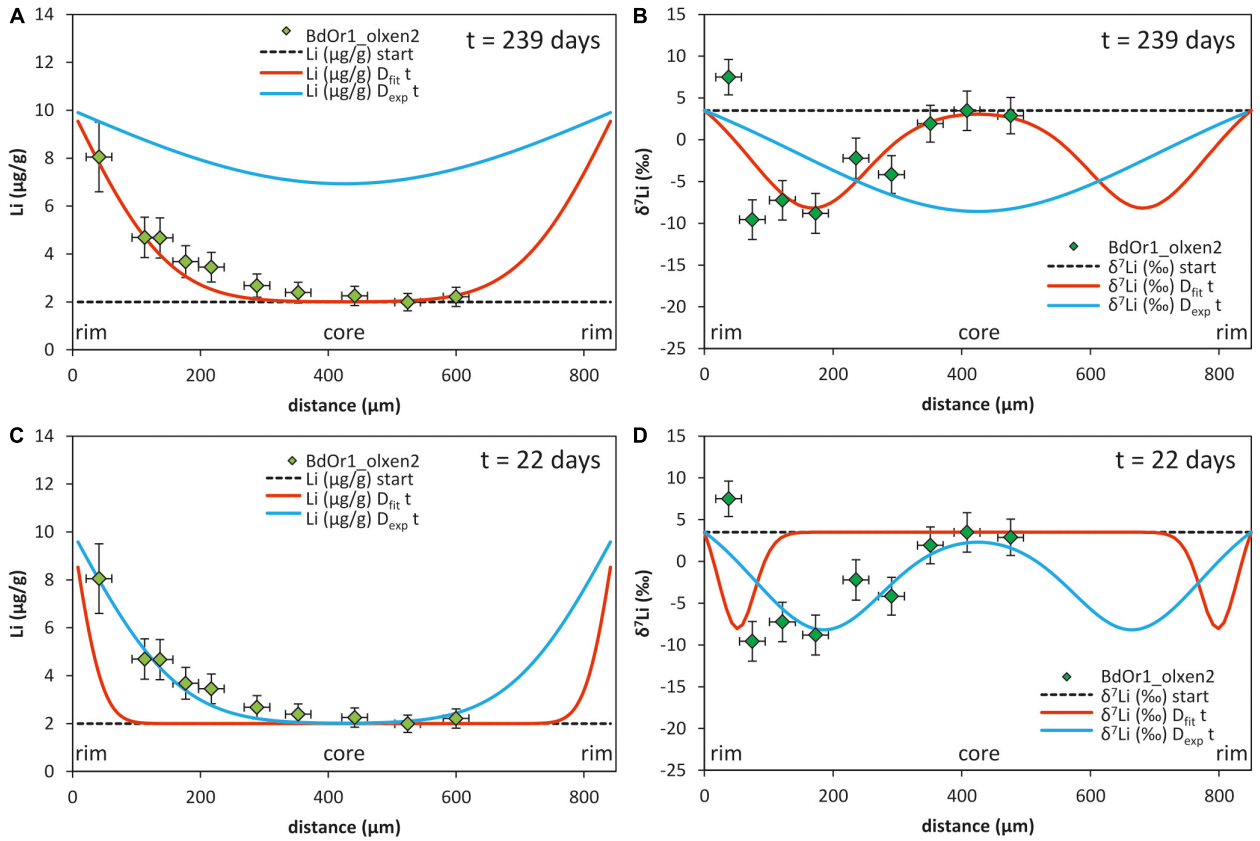

FIGURE 3 | Modeling of the observed Li concentration and isotope composition profiles of olivine grain BdOr1 olxen2 with a 1-step diffusion model; **A,B**) by using the times scale as determined by Fe–Mg modeling (t = 239 days, taken from Oeser et al., 2015) and fitting the Li diffusivity (D_{fit}) to the measured profiles (red line); for comparison the same model (with t = 239 days) is shown using D_{exp} of Dohmen et al. (2010) which does not match the observed Li concentration and isotope profiles (blue lines). **(C,D)** the same model is shown using the diffusivity D_{exp} (Dohmen et al., 2010) and fitting the time scale to match the Li concentration and isotope profiles yields a diffusion time of t = 22 days (blue line); for comparison the profile is also modeled with the same time applying the fitted diffusivity from **(A,B)** (red line). All fits were modeled assuming a diffusivity $D_{exp} = 4.42*10^{-15}$ m^2/s according to a temperature of 1250°C and $D_{fit} = 3.5*10^{-16}$ m^2/s.

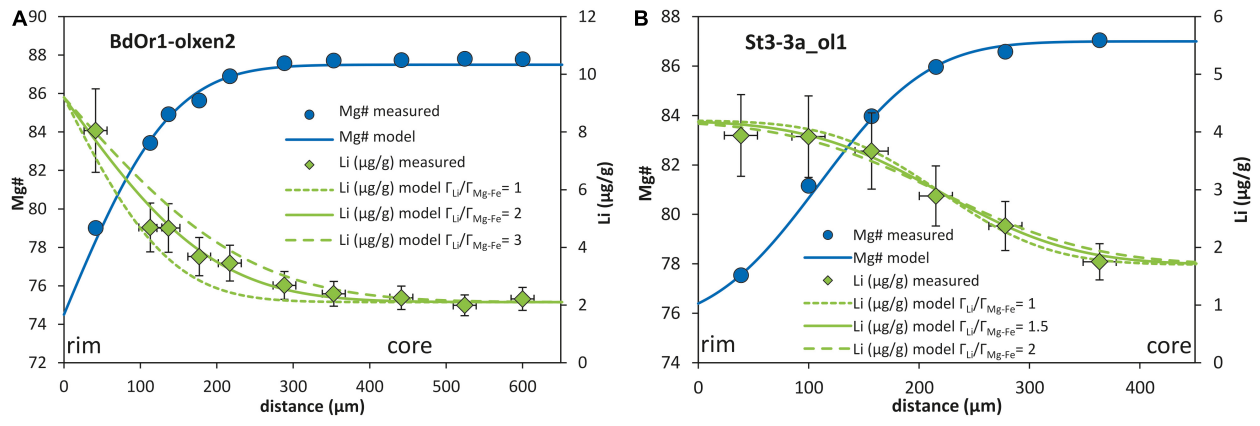

FIGURE 4 | Relative modeling of Mg# and Li (µg/g). The Mg# and Li profiles are fitted by adjusting $\tilde{A}_{Mg\text{-}Fe}$, and $\tilde{A}_{Li}$, respectively. The ratio of the Ã-values is calculated giving the relative diffusivity of Li relative to Mg–Fe, various curves for the Li profile show the variability and uncertainty in the modeled factor for relative diffusities. **(A)** BdOr1-olxen2 is modeled with an infinite analytical approach assuming a fixed rim concentration. The modeled profile for Li yields a factor for the Li diffusivity relative to that of the Fe–Mg exchange (indicated by Mg#) $\tilde{A}_{Li}/\tilde{A}_{Mg\text{-}Fe}$ from 1 to 3, which may be considered as the uncertainty of this approach. **(B)** St3-3a_ol1 is modeled with a semi-infinite analytical approach assuming the equilibration of two chemically distinct layers of the crystal over time, yielding a relative diffusivity factor within an uncertainty of $\tilde{A}_{Li}/\tilde{A}_{Mg\text{-}Fe}$ from 1 to 2.

melt in the magma chamber. Thus, this scenario would imply that both Li concentration in the melt, as well as Li partitioning between olivine and melt, which itself is dependent on Mg# of the olivine, remained about constant for most of the time and then only changed at the end of magma differentiation. In contrast, assuming the time scales for the individual samples, given by modeling of Fe–Mg diffusion (Oeser et al., 2015) and fitting the Li diffusivity to the measured profiles, a narrow range of D_{fit} does acceptably fit to all analyzed Li concentration- and Li isotope profiles. We therefore conclude that diffusion timescales for Li were likely similar to those for Fe–Mg and that Li diffusivities in the investigated olivines are likely more similar to those suggested by Qian et al. (2010); Spandler and O'Neill (2010) and Oeser-Rabe (2015), rather than to those determined by Dohmen et al. (2010) (here labeled as D_{exp}). These findings demonstrate that additional experimental investigations on Li diffusivity at lower concentration levels are urgently demanded.

Differences between experimentally determined and fitted diffusion coefficients may arise from differences in the initial and boundary conditions between those imposed in experiments and those assumed for the investigated natural samples, e.g., Li concentration in the melt (or in the powder of the experiments) surrounding the olivine crystals. In the investigated samples, the melt Li concentrations were estimated (from bulk rocks and model fits), between 5.7 and 6.14 μg/g. In contrast, the powder mixture of 90% San Carlos olivine and Li_2SiO_3, used in the experimental setup of Dohmen et al. (2010), had significantly higher Li concentrations. Notably, it was observed by Dohmen et al. (2010) that Li diffusivity in olivine depends on the Li concentration and appears to decrease with decreasing Li concentrations.

Furthermore, other intensive thermodynamic variables of the system, including the chemical composition of the crystals and melt and fO_2, which may not have yet been investigated in sufficient detail, may affect Li diffusion in olivine. In a recent experimental study, Richter et al. (2014) demonstrated a strong sensitivity of Li diffusion in clinopyroxene to fO_2. Also the experiments of Dohmen et al. (2010) imply that the diffusion mechanism of Li in olivine depends on environmental variables, such as fO_2 and $aSiO_2$ (amongst other factors). These parameters affect the vacancy concentrations in olivine which control the diffusion mechanism (Dohmen et al., 2010). For a series of trace elements in olivine, including Al, Cr and Be, several studies observed a dependence of the diffusivity on factors, such as silica activity ($aSiO_2$) and oxygen fugacity (fO_2) (Jollands et al., 2016a,b; Zhukova et al., 2017). The diffusivity of Al in forsterite at low $aSiO_2$ for example is up to three orders of magnitude slower than at high $aSiO_2$ (Zhukova et al., 2017). These studies show that diffusion in olivine may depends on parameters involving the activity of SiO_2 and fO_2.

The Second Diffusion Event

While our models broadly reproduce the low Li isotope compositions observed in olivine cores, modeled Li concentrations do not match the rim areas of several of the olivine grains investigated (e.g., BdOr1_ol2; BdOr1_olxen1; St3-3a_ol1). Similarly, the Li isotope composition does not match the observed δ^7Li profiles for these olivine grains. Rather, the change in slope of the Li concentration profile in **Figure 2C** indicates that the flux of Li into the crystal (assumed in the first diffusion event) changed to a flux of Li out of the crystal during a second diffusion event at a later stage (**Figure 5**). The latter is not visible in all Li concentration profiles and potentially has not affected all olivine crystals to the same extent.

Such a second diffusion step was modeled using the Li diffusivity that was determined by modeling the first diffusion event, but assuming a different Li rim concentration (C_{rim2}; **Figure 5**). C_{rim2} was estimated based on the bulk rock Li concentration of the samples [5.78 μg/g for St6-2b, 5.7 μg/g for St3-3a and 6.14 μg/g for BdOr-1; Oeser et al. (2015)] and slightly adapted to better fit the observed Li concentrations (**Table 2**). This second diffusion event was modeled by fitting the Li isotope and concentration profiles to those observed at the crystal rims. As the diffusivity of Li was assumed to be given by the results of the first diffusion step, the modeled profiles were fitted by adjusting the duration of diffusion, which was unknown for this second event. Applying such a model, yields durations of 20 to 80 days for Banne D'Ordanche, 100 to 200 days for St3-3a from Roche Sauterre and 30 to 120 days for St6-2b from Roche Sauterre for this event (**Figure 6**). For the second modeling step the β-value was readjusted in order to fit the amplitude of the Li isotope diffusion profile. As described above, modeling of the second diffusion event also has an effect on the amplitude of the isotope profiles modeled in the first diffusion event. Best fit modeling of the olivine core- (first diffusion event) and rim (second diffusion event) isotope compositions furthermore, resulted in different β-values for the first and second diffusion event (**Table 2**).

The second diffusion event of Li diffusion out of the olivine crystals indicates a decrease of the Li concentration in the melt, which may be associated to the ascent of the melt, or even have occurred after the emplacement of the lava. During the exsolution of H_2O-rich vapor in the course of decompression Li is largely mobilized in magmatic systems (Sakuyama and Kushiro, 1979). For example, Neukampf et al. (2019) observed a significant decrease in Li concentrations in plagioclase, which they interpreted to be driven by a Li loss in the melt during degassing of the magma. The low Li concentrations in the melt caused Li diffusion out of the crystals. Similarly (though to a lower extent than observed by Neukampf et al., 2019), decreasing or constant Li concentrations at the olivine rims, observed in this study, may be related to degassing-driven Li loss in the melt during magma ascent or emplacement, resulting in Li diffusion out of the olivine crystals. Notably, the second event, which operated in an opposite direction to the first diffusion event, is not visible in the Mg–Fe chemical or isotopic zoning. This finding may support degassing as the driving force for diffusion during the final melt evolution, which would have affected fluid mobile elements, such as Li, but not refractory elements, such as Fe and Mg. Hence, though Li and Fe–Mg diffusion were likely coupled during the first diffusion event, they were apparently decoupled during the

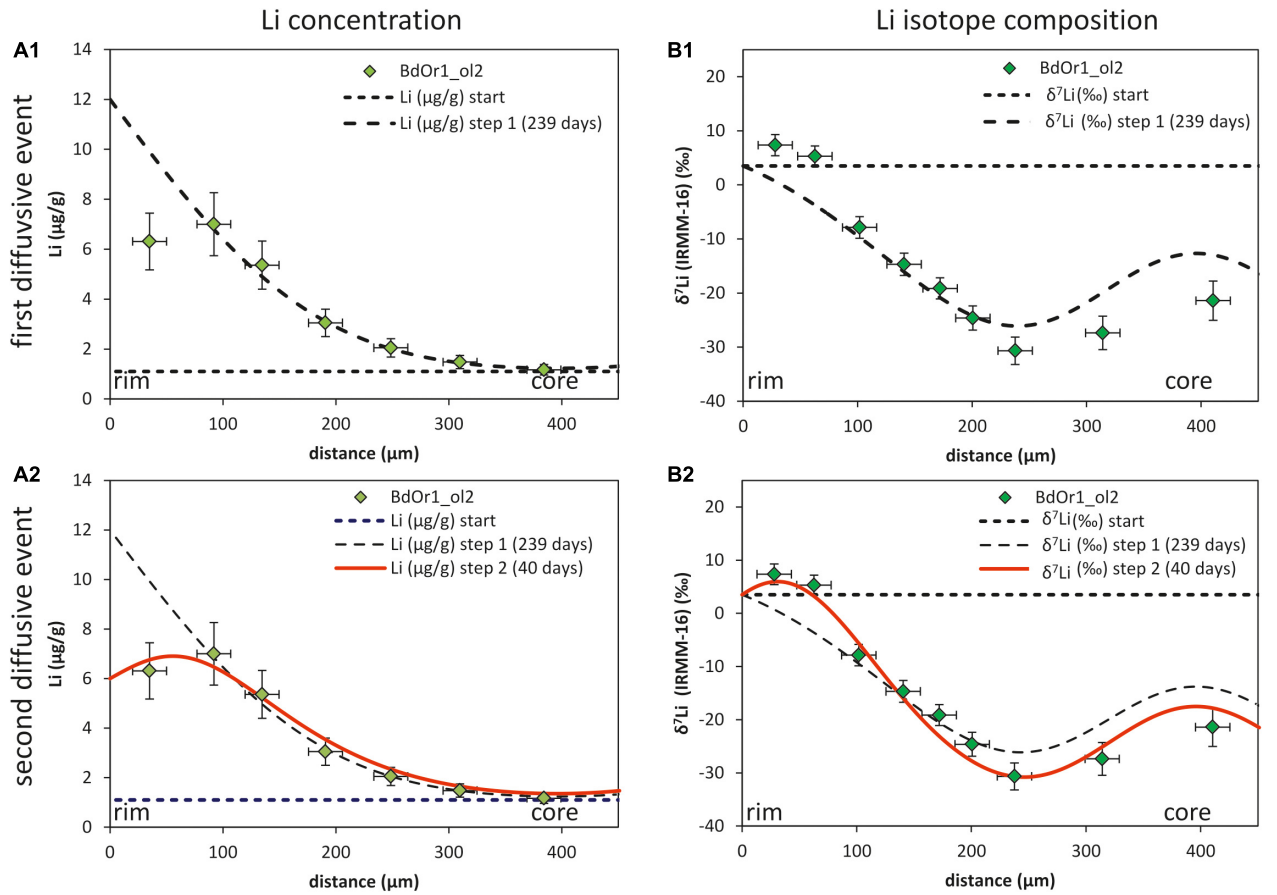

FIGURE 5 | (A1) and **(B1)** show the Li concentration and isotopic composition of the first diffusion event for BdOr1_ol2 with a duration of t = 239 days, C_{core} = 1.1 µg/g, C_{rim1} = 12 µg/g and β = 0.25. **(A2)** and **(B2)** show the model for the second diffusion event (which is based on the first diffusion event) with t = 40 days, C_{rim2} = 6 µg/g and β = 0.2, the Li diffusion coefficient was determined by fitting the observed Li concentrations and isotope compositions to $5.5*10^{-16}$ m^2/s. Core Li concentrations and isotope compositions are marked by a dashed line.

second event. This final decoupling was likely the result of the different physiochemical properties and diffusivity of Li, as compared to Fe–Mg. Accordingly, Li concentrations and isotopes may unravel processes which cannot be seen with Mg–Fe isotopes alone.

Some profiles are not matched perfectly by modeled curves (e.g., **Figure 6D** and **Supplementary Figure S3B**) which may be the result of cutting effects during the preparation of the sections. That is some sections probably do not sample the core of the crystals, which would result in an underestimation of the diffusive mass flux and isotope fractionation (Weyrauch et al., 2019). Furthermore, some sections were probably not cut perpendicularly to crystal rims, which may be indicated by asymmetric zoning (e.g., crystal St6-2b1_ol4) in the case of rim-to-rim profiles. This effect would result in artificially elongated Li diffusion profiles. For Mg and Fe diffusion modeling, the orientation of the crystallographic axes was determined by Oeser et al. (2015) by electron backscatter diffraction analyses. This is necessary due to the difference in diffusivities along the crystallographic axes (Dohmen et al., 2007). However, crystallographic orientation does not seem to have a large effect on Li diffusivity in olivine (Dohmen et al., 2010) and thus was not considered.

The time scales of the second diffusion event determined by Li diffusion modeling are 20–80 days for Banne D'Ordanche and 30–200 days for Roche Sauterre which is longer than the time scales obtained by Lynn et al. (2018) for the Keanakâko'i Tephra (Kîlauea Volcano, Hawai'i), also using Li diffusion modeling (only Li concentrations). The authors conclude a similar process of syn-eruptive degassing in their study with time scales of only hours to days which is 1–2 orders of magnitude faster than that estimated with the fitted D_{Li} values of this study. The difference in the determined time scales of the degassing process is essentially the result of the different diffusion coefficients used in the studies. In this study, the same diffusion coefficient, as determined from the first diffusion event (**Table 3**, derived from the comparison of Li- with Fe–Mg diffusion profiles) has been assumed for both diffusion events. However, as the diffusion coefficient may depend on temperature, fO_2 and the fluid content of the melt (Coogan et al., 2005; Dohmen et al., 2007) it may have changed during the second diffusion event, at which the melt may have become water saturated

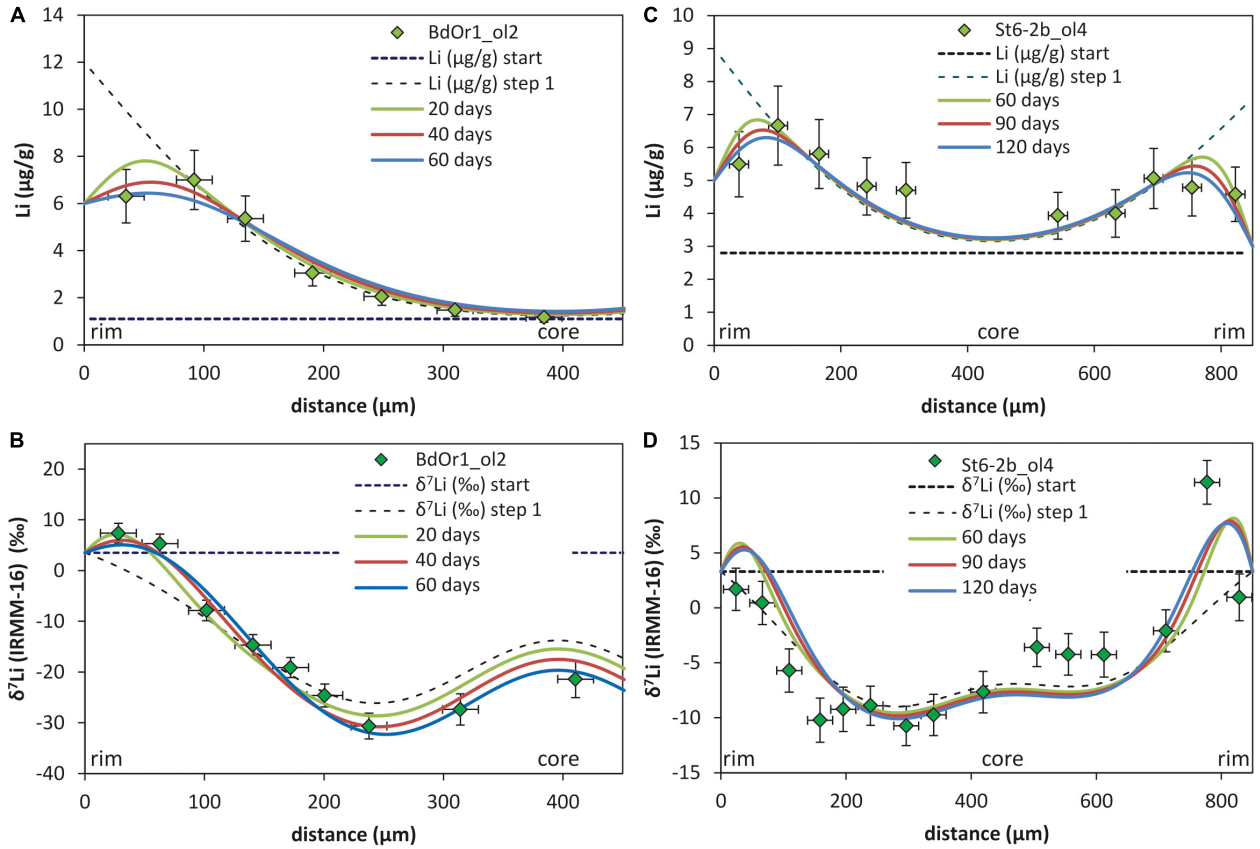

FIGURE 6 | Two step model of Li concentration **(A,C)** and Li isotope profiles **(B,D)** fitted with t = 239–252 days for Banne D'Ordanche (BdOr1_ol2) and t = 3.26 years for Roche Sauterre (St6-2b_ol4b) for the first diffusion event (dashed lines, time scales are taken from Oeser et al., 2015). The time scales for the second diffusion event are modeled be fitting the observed Li concentrations and isotope compositions at the rims of the olivines are indicated by the solid lines. The models of all other investigated samples can be found in **Supplementary Figure S.3**.

during degassing. Accordingly, it cannot be excluded that Li diffusion was faster during the second diffusion event and the modeled time scales overestimate the duration of a potential degassing process.

Notably, however, the basalts investigated in this study, originate from massive flows, or in the case of Roche Sauterre, even from a small lava lake (Nehlig et al., 2001; Lorand et al., 2003; Richet, 2003). Thus degassing, as recorded by Li diffusion,

TABLE 3 | Comparison of the Li diffusion coefficients, as determined (1) relative to the diffusivity of Mg–Fe exchange diffusion ($D_{Lirelative}$), (2) by fitting D_{Li} to the observed Li concentration and isotope profiles assuming the time scales from Fe–Mg exchange diffusion modeling (Oeser et al., 2015), and (3) the experimentally determined D_{Li} and D_{Mg-Fe} (Dohmen et al., 2007, 2010) calculated for 1250°C.

	D_{Mg-Fe} (m²/s)*	(D_{Li}/D_{Mg-Fe}) relative$^{\Delta}$	$D_{Li\_relative}$ (m²/s)	D_{Li_fit} (m²/s)	(D_{Li}/D_{Mg-Fe}) fit	D_{Li_exp} (m²/s)$^{\#}$	(D_{Li}/D_{Mg-Fe}) experimental
BdOr1-ol1	$5.65*10^{-17}$	2.0	$1.13*10^{-16}$	$2*10^{-16}$	3.5	$4.42*10^{-15}$	78.2
BdOr1-ol2	$2.62*10^{-16}$	2.0	$5.24*10^{-16}$	$5*10^{-16}$	2.1	$4.42*10^{-15}$	16.9
BdOr1-olxen1	$3.01*10^{-16}$	2.0	$6.02*10^{-16}$	$4.5*10^{-16}$	1.5	$4.42*10^{-15}$	14.7
BdOr1-olxen2	$7.44*10^{-17}$	2.0	$1.49*10^{-16}$	$3.5*10^{-16}$	4.7	$4.42*10^{-15}$	59.4
St3-3a_ol1	$1.01*10^{-16}$	1.5	$1.51*10^{-16}$	$2.5*10^{-16}$	2.5	$4.42*10^{-15}$	43.9
St3-3a_ol2	$7.53*10^{-17}$	1.5	$1.13*10^{-16}$	$3.0*10^{-16}$	4.0	$4.42*10^{-15}$	58.7
St6-2b_ol4b	$9.52*10^{-17}$	1.5	$1.43*10^{-16}$	$2.0*10^{-16}$	2.1	$4.42*10^{-15}$	46.4
St6-2b_ol5	$3.89*10^{-16}$	1.5	$5.84*10^{-16}$	$5.0*10^{-16}$	1.3	$4.42*10^{-15}$	11.4

**Calculated at P = 500 Pa, T = 1250°C, fO_2 = NNO-2, crystallographic orientation, X_{Fe} and concentration profiles from Oeser et al. (2015).* $^{\Delta}$ *(D_{Li}/D_{Mg-Fe}) relative is calculated by multiplying the actual diffusivity of Mg–Fe at 1250°C and recalculated to the crystallographic orientation of the profile, with $\tilde{A}_L i/\tilde{A}_{Mg-Fe}$ dcalculated with approach (2) according to Eq. (4).* $^{\#}$*Experimentally determined D_{Li} calculated at 1250°C according to Eq (3) from Dohmen et al. (2010).*

may have occurred mostly during cooling of the magma after lava emplacement and thus lasted much longer than timescales typically expected for magma ascent. Assuming the outcrop of Roche Sauterre samples represents a small lava lake, this scenario would explain the longer degassing timescales for samples from this locality as compared to those from Banne D'Ordanche. It may also explain that some samples appear to be more affected by degassing than others, as degassing rates would depend on the position of the samples in the lava flow/lake.

CONCLUSION

Combined *in situ* Li concentration and isotope analyses were performed on zoned olivines from the Massif Central volcanic region. A diffusive origin for Li concentration and isotope profiles was deducted from correlations with Mg–Fe isotopic inter-diffusion. However, in contrast to Fe and Mg, Li indicates two diffusion episodes. The first likely represents the residence time of olivine in a (deeper) part of the plumbing system, as implied by Mg–Fe isotope diffusion modeling (Oeser et al., 2015). This diffusion event is likely driven by an increase in Li concentration in the melt and, likely also, by an increased partitioning of Li into olivine, driven by decreasing Mg# in olivine during fractional crystallization. Lithium diffusion into the olivines generated low δ^7Li-values in the cores of the crystals. A second and shorter diffusion event, recorded by several of the investigated olivine grains resulted in Li diffusion out of olivine crystals, indicating a Li decrease in the melt. This second event is likely related to degassing of the melt during its ascent and after lava emplacement, resulting in the mobilization of Li into a vapor phase. Such a diffusion event can be deduced by modeling Li concentration and Li isotope profiles simultaneously. The second diffusion episode is not recorded in Mg–Fe profiles, which highlights that Li profiles can preserve information about magmatic evolution that is not recorded by Mg–Fe zoning, potentially due to the volatile character of Li in magmatic fluids. These findings demonstrate that combining information from chemical and isotopic zoning of Li with those from Fe–Mg is a very powerful tool for unraveling the timing of complex magma evolution scenarios, such as commonly observed in magma plumbing systems.

DATA AVAILABILITY STATEMENT

All datasets generated for this study are included in the article/**Supplementary Material**.

AUTHOR CONTRIBUTIONS

LS contributed to the analyses of Li isotope profiles with femtosecond-laser ablation-MC-ICP-MS, solution nebulization isotope analyses with MC-ICP-MS and proceeding Li column chromatography, and data processing and interpretation, diffusion modeling, and writing the manuscript. MO contributed to the project design, analytical support with fs-LA-MC-ICP-MS, support with diffusion modeling, and data interpretation, support with manuscript writing. IH contributed to the analytical support with fs-LA-MC-ICP-MS and support with manuscript writing. SW contributed to the project design, support with data interpretation, and support with manuscript writing.

ACKNOWLEDGMENTS

This study was supported by the Deutsche Forschungsgemeinschaft (grant # OE 653/1-1) which is gratefully acknowledged. We are grateful for the reviews of TK and IP and editorial handling by DN, whose constructive comments significantly helped to improve this paper.

SUPPLEMENTARY MATERIAL

The Supplementary Material for this article can be found online at: https://www.frontiersin.org/articles/10.3389/feart.2020.00201/full#supplementary-material

REFERENCES

Ackerman, L., Špaček, P., Magna, T., Ulrych, J., Svojtka, M., Hegner, E., et al. (2013). Alkaline and carbonate-rich melt metasomatism and melting of subcontinental lithospheric mantle: evidence from mantle xenoliths, NE Bavaria, Bohemian Massif. *J. Petrol.* 54, 2597–2633. doi: 10.1093/petrology/egt059

Bouman, C., Elliott, T., and Vroon, P. Z. (2004). Lithium inputs to subduction zones. *Chem. Geol.* 212, 59–79. doi: 10.1016/j.chemgeo.2004.08.004

Brant, C., Coogan, L. A., Gillis, K. M., Seyfried, W. E., Pester, N. J., and Spence, J. (2012). Lithium and Li-isotopes in young altered upper oceanic crust from the East Pacific Rise. *Geochim. Cosmochim. Acta* 96, 272–293. doi: 10.1016/j.gca.2012.08.025

Brenan, J. M., Neroda, E., Lundstrom, C. C., Shaw, H. F., Rverson, F. J., and Phinney, D. L. (1998). Behaviour of boron, beryllium, and lithium during melting and crystallization: constraints from mineral-melt partitioning experiments. *Geochim. Cosmochim. Acta* 62, 2129–2141. doi: 10.1016/S0016-7037(98)00131-8

Chan, L. H., Edmond, J. M., Thompson, G., and Gillis, K. (1992). Lithium isotopic composition of submarine basalts: implications for the lithium cycle in the oceans. *Earth Planet. Sci. Lett.* 108, 151–160. doi: 10.1016/0012-821X(92)90067-6

Chapman, S., and Cowling, T. G. (1953). *Mathematical Theory of Non-uniform Gases - An account of the Kinetic Theory of Viscosity, Thermal Conduction and Diffusion in GASES*, 3rd Edn. Cambridge: Cambridge Mathematical Library.

Collinet, M., Charlier, B., Namur, O., Oeser, M., Médard, E., Vander Auwera, J., et al. (2014). *Fe and Mg Isotope Fractionation in Olivine from the NWA 1068 Shergottite*. Sacramento, CA: Goldschmidt california.

Collinet, M., Charlier, B., Namur, O., Oeser, M., Médard, E., and Weyer, S. (2017). Crystallization history of enriched shergottites from Fe and Mg isotope fractionation in olivine megacrysts. *Geochim. Cosmochim. Acta* 207, 277–297. doi: 10.1016/j.gca.2017.03.029

Coogan, L. A., Gillis, K. M., Pope, M., and Spence, J. (2017). The role of low-temperature (off-axis) alteration of the oceanic crust in the global Li-cycle: insights from the Troodos ophiolite. *Geochim. Cosmochim. Acta* 203, 201–215. doi: 10.1016/j.gca.2017/01.002

Coogan, L. A., Kasemann, S. A., and Chakraborty, S. (2005). Rates of hydrothermal cooling of new oceanic upper crust derived from lithium-geospeedometry. *Earth Planet. Sci. Lett.* 240, 415–424. doi: 10.1016/j.epsl.2005.09.020

Costa, F., Dohmen, R., and Chakraborty, S. (2008). Time scales of magmatic processes from modeling the zoning patterns of crystals. *Rev. Mineral. Geochemistry* 69, 545–594. doi: 10.2138/rmg.2008.69.14

Dellinger, M., Gaillardet, J. Ô, Bouchez, J., Calmels, D., Galy, V., Hilton, R. G., et al. (2014). Lithium isotopes in large rivers reveal the cannibalistic nature of modern continental weathering and erosion. *Earth Planet. Sci. Lett.* 401, 359–372. doi: 10.1016/j.epsl.2014.05.061

Dohmen, R., Becker, H. W., and Chakraborty, S. (2007). Fe-Mg diffusion in olivine I: experimental determination between 700 and 1,200°C as a function of composition, crystal orientation and oxygen fugacity. *Phys. Chem. Miner.* 34, 389–407. doi: 10.1007/s00269-007-0157-7

Dohmen, R., and Chakraborty, S. (2007). Fe-Mg diffusion in olivine II: point defect chemistry, change of diffusion mechanisms and a model for calculation of diffusion coefficients in natural olivine. *Phys. Chem. Miner.* 34, 409–430. doi: 10.1007/s00269-007-0158-6

Dohmen, R., Kasemann, S. A., Coogan, L., and Chakraborty, S. (2010). Diffusion of Li in olivine. Part I: experimental observations and a multi species diffusion model. *Geochim. Cosmochim. Acta* 74, 274–292.

Elliott, T., Thomas, A., Jeffcoate, A., and Niu, Y. (2006). Lithium isotope evidence for subduction-enriched mantle in the source of mid-ocean-ridge basalts. *Nature* 443, 565–568. doi: 10.1038/nature05144

Ganguly, J. (2002). Diffusion kinetics in minerals: principles and applications to tectono-metamorphic processes. *EMU Notes Mineral. Energy Model. Miner.* 4, 271–309.

Gu, X., Deloule, E., France, L., and Ingrin, J. (2016). Multi-stage metasomatism revealed by trace element and Li isotope distributions in minerals of peridotite xenoliths from Allègre volcano (French Massif Central). *Lithos* 264, 158–174. doi: 10.1016/j.lithos.2016.07.019

Hamelin, C., Seitz, H. M., Barrat, J. A., Dosso, L., Maury, R. C., and Chaussidon, M. (2009). A low δ7Li lower crustal component: evidence from an alkalic intraplate volcanic series (Chaîne des Puys, French Massif Central). *Chem. Geol.* 266, 205–217.

Horn, I., and von Blanckenburg, F. (2007). Investigation on elemental and isotopic fractionation during 196 nm femtosecond laser ablation multiple collector inductively coupled plasma mass spectrometry. *Spectrochim. Acta B At. Spectrosc.* 62, 410–422. doi: 10.1016/j.sab.2007.03.034

Horn, I., von Blanckenburg, F., Schoenberg, R., Steinhoefel, G., and Markl, G. (2006). In situ iron isotope ratio determination using UV-femtosecond laser ablation with application to hydrothermal ore formation processes. *Geochim. Cosmochim. Acta* 70, 3677–3688. doi: 10.1016/j.gca.2006.05.002

Jeffcoate, A. B., Elliott, T., Kasemann, S. A., Ionov, D., Cooper, K., and Brooker, R. (2007). Li isotope fractionation in peridotites and mafic melts. *Geochim. Cosmochim. Acta* 71, 202–218. doi: 10.1016/j.gca.2006.06.1611

Jochum, K. P., Stoll, B., Herwig, K., Willbold, M., Hofmann, A. W., Amini, M., et al. (2006). MPI-DING reference glasses for in situ microanalysis: new reference values for element concentrations and isotope ratios. *Geochem. Geophys. Geosyst.* 7, 1–44. doi: 10.1029/2005GC001060

Jollands, M. C., Burnham, A. D., O'Neill, H. S. C., Hermann, J., and Qian, Q. (2016a). Beryllium diffusion in olivine: a new tool to investigate timescales of magmatic processes. *Earth Planet. Sci. Lett.* 450, 71–82. doi: 10.1016/j.epsl.2016.06.028

Jollands, M. C., Hermann, J., St. O'Neill, H. C., Spandler, C., and Padrón-Navarta, J. A. (2016b). Diffusion of Ti and some divalent cations in olivine as a function of temperature, oxygen fugacity, chemical potentials and crystal orientation. *J. Petrol.* 57, 1983–2010. doi: 10.1093/petrology/egw067

Kahl, M., Chakraborty, S., Costa, F., Pompilio, M., Liuzzo, M., and Viccaro, M. (2013). Compositionally zoned crystals and real-time degassing data reveal changes in magma transfer dynamics during the 2006 summit eruptive episodes of Mt. Etna. *Bull. Volcanol.* 75, 1–14. doi: 10.1007/s00445-013-0692-7

Kahl, M., Chakraborty, S., Pompilio, M., and Costa, F. (2015). Constraints on the nature and evolution of the magma plumbing system of Mt. Etna volcano (1991-2008) from a combined thermodynamic and kinetic modelling of the compositional record of minerals. *J. Petrol.* 56, 2025–2068. doi: 10.1093/petrology/egv063

Kimura, J.-I., Chang, Q., Kanazawa, N., Sasaki, S., and Vaglarov, B. S. (2016). High-precision in situ analysis of Pb isotopes in glasses using 1013 Ω resistor high gain amplifiers with ultraviolet femtosecond laser ablation multiple Faraday collector inductively coupled plasma mass spectrometry. *J. Anal. At. Spectrom.* 31, 790–800. doi: 10.1039/C5JA00374A

Le Roux, P. J. (2010). Lithium isotope analysis of natural and synthetic glass by laser ablation MC-ICP-MS. *J. Anal. At. Spectrom.* 25, 1033–1038. doi: 10.1039/b920341a

Liu, S. A., Teng, F. Z., Yang, W., and Wu, F. Y. (2011). High-temperature inter-mineral magnesium isotope fractionation in mantle xenoliths from the North China craton. *Earth Planet. Sci. Lett.* 308, 131–140. doi: 10.1016/j.epsl.2011.05.047

Lorand, J. P., Alard, O., Luguet, A., and Keays, R. R. (2003). Sulfur and selenium systematics of the subcontinental lithospheric mantle: inferences from the Massif Central xenolith suite (France). *Geochim. Cosmochim. Acta* 67, 4137–4151. doi: 10.1016/S0016-7037(03)00305-3

Lynn, K. J., Shea, T., Garcia, M. O., Costa, F., and Norman, M. D. (2018). Lithium diffusion in olivine records magmatic priming of explosive basaltic eruptions. *Earth Planet. Sci. Lett.* 500, 127–135. doi: 10.1016/j.epsl.2018.08.002

Magna, T., Ionov, D. A., Oberli, F., and Wiechert, U. (2008). Links between mantle metasomatism and lithium isotopes: evidence from glass-bearing and cryptically metasomatized xenoliths from Mongolia. *Earth Planet. Sci. Lett.* 276, 214–222. doi: 10.1016/j.epsl.2008.09.027

Magna, T., Wiechert, U., and Halliday, A. N. (2006). New constraints on the lithium isotope compositions of the Moon and terrestrial planets. *Earth Planet. Sci. Lett.* 243, 336–353. doi: 10.1016/j.epsl.2006.01.005

Marschall, H. R., Altherr, R., and Rüpke, L. (2007a). Squeezing out the slab - modelling the release of Li, Be and B during progressive high-pressure metamorphism. *Chem. Geol.* 239, 323–335. doi: 10.1016/j.chemgeo.2006.08.008

Marschall, H. R., Pogge von Strandmann, P. A. E., Seitz, H. M., Elliott, T., and Niu, Y. (2007b). The lithium isotopic composition of orogenic eclogites and deep subducted slabs. *Earth Planet. Sci. Lett.* 262, 563–580. doi: 10.1016/j.epsl.2007.08.005

McDade, P., Blundy, J. D., and Wood, B. J. (2003). Trace element partitioning on the Tinaquillo solidus at 1.5 *GPa. Phys. Earth Planet. Inter.* 139, 129–147. doi: 10.1016/S0031-9201(03)00149-3

Nehlig, P., Boivin, P., de Goër, A., Mergoil, J., Poutrau, G., Sustrac, G., et al. (2001). Les volcans du Massif Central. *Géologues* 130/131, 66–91.

Neukampf, J., Ellis, B. S., Laurent, O., Steinmann, L. K., Dohmen, R., Ubide, T., et al. (2019). *Timescales of Degassing in Rhyolitic Magmas Tracked by Li in Plagioclase*. Italy: University of Palermo.

Nishio, Y., Nakai, S., Yamamoto, J., Sumino, H., Matsumoto, T., Prikhod'ko, V. S., et al. (2004). Lithium isotopic systematics of the mantle-derived ultramafic xenoliths: implications for EM1 origin. *Earth Planet. Sci. Lett.* 217, 245–261. doi: 10.1016/S0012-821X(03)00606-X

Oeser, M., Dohmen, R., Horn, I., Schuth, S., and Weyer, S. (2015). Processes and time scales of magmatic evolution as revealed by Fe–Mg chemical and isotopic zoning in natural olivines. *Geochim. Cosmochim. Acta* 154, 130–150. doi: 10.1016/j.gca.2015.01.025

Oeser, M., Ruprecht, P., and Weyer, S. (2018). Combined Fe-Mg chemical and isotopic zoning in olivine constraining magma mixing-to-eruption timescales for the continental arc volcano Irazú (Costa Rica) and Cr diffusion in olivine. *Am. Mineral.* 103, 582–599. doi: 10.2138/am-2018-6258

Oeser-Rabe, M. (2015). *Constraints on the Evolution of Magmas from Diffusion-driven Chemical and Fe-Mg Isotopic Zoning in Natural Olivines analyzed by Femtosecond-LA-ICP-MS*. Ph.D. thesis, Universitätsbibliothek Hannover, Hannover.

Ottolini, L., Laporte, D., Raffone, N., Devidal, J.-L., and Le Fèvre, B. (2009). New experimental determination of Li and B partition coefficients during upper mantle partial melting. *Contrib. Mineral. Petrol.* 157, 313–325. doi: 10.1007/s00410-008-0336-7

Parkinson, I. J., Hammond, S. J., James, R. H., and Rogers, N. W. (2007). High-temperature lithium i fractionation: insights from lithium isotope diffusion in magmatic systems. *Earth Planet. Sci. Lett.* 257, 609–621. doi: 10.1016/j.epsl.2007.03.023

Penniston-Dorland, S., Liu, X.-M., and Rudnick, R. L. (2017). Lithium isotope geochemistry. *Rev. Mineral. Geochemistry* 82, 165–217. doi: 10.2138/rmg.2017.82.6

Qian, Q., O'Neill, H. S. C., and Hermann, J. (2010). Comparative diffusion coefficients of major and trace elements in olivine at ˜950 °C from a xenocryst included in dioritic magma. *Geology* 38, 331–334. doi: 10.1130/G30788.1

Richet, P. (2003). *Guide des volcans de France. 1st ed., BRGM*. Paris: Belin.

Richter, F., Chaussidon, M., Bruce Watson, E., Mendybaev, R., and Homolova, V. (2017). Lithium isotope fractionation by diffusion in minerals Part 2: olivine. *Geochim. Cosmochim. Acta* 219, 124–142. doi: 10.1016/j.gca.2017.09.001

Richter, F., Watson, B., Chaussidon, M., Mendybaev, R., and Ruscitto, D. (2014). Lithium isotope fractionation by diffusion in minerals. Part 1: pyroxenes. *Geochim. Cosmochim. Acta* 126, 352–370. doi: 10.1016/j.gca.2013.11.008

Richter, F. M., Davis, A. M., DePaolo, D. J., and Watson, E. B. (2003). Isotope fractionation by chemical diffusion between molten basalt and rhyolite. *Geochim. Cosmochim. Acta* 67, 3905–3923. doi: 10.1016/S0016-7037(03)00174-1

Richter, F. M., Liang, Y., and Davis, A. M. (1999). Isotope fractionation by diffusion in molten oxides. *Geochim. Cosmochim. Acta* 63, 2853–2861. doi: 10.1016/S0016-7037(99)00164-7

Roeder, P. L., and Emslie, R. F. (1970). Olivine-liquid equilibrium. *Contr. Mineral. Petrol.* 29, 275-289. doi: 10.1007/BF00371276

Ryan, J. G., and Kyle, P. R. (2004). Lithium abundance and lithium isotope variations in mantle sources: insights from intraplate volcanic rocks from Ross Island and Marie Byrd Land (Antarctica) and other oceanic islands. *Chem. Geol.* 212, 125–142. doi: 10.1016/j.chemgeo.2004.08.006

Ryan, J. G., and Langmuir, C. H. (1987). The systematics of lithium abundances in young volcanic rocks. *Geochim. Cosmochim. Acta* 51, 1727–1741. doi: 10.1016/0016-7037(87)90351-6

Sakuyama, M., and Kushiro, I. (1979). Vesiculation of hydrous andesitic melt and transport of alkalies by separated vapor phase. *Contrib. Mineral. Petrol.* 71, 61–66. doi: 10.1007/BF00371881

Seitz, H.-M., Brey, G. P., Lahaye, Y., Durali, S., and Weyer, S. (2004). Lithium isotopic signatures of peridotite xenoliths and isotopic fractionation at high temperature between olivine and pyroxenes. *Chem. Geol.* 212, 163–177. doi: 10.1016/j.chemgeo.2004.08.009

Shannon, R. D. (1976). Revised effective ionic radii in halides and chalcogenides. *Acta Crystallogr. A* 32, 751–767. doi: 10.1107/S0567739476001551

Sio, C. K. I., Dauphas, N., Teng, F. Z., Chaussidon, M., Helz, R. T., and Roskosz, M. (2013). Discerning crystal growth from diffusion profiles in zoned olivine by in situ Mg-Fe isotopic analyses. *Geochim. Cosmochim. Acta* 123, 302–321. doi: 10.1016/j.gca.2013.06.008

Spandler, C., and O'Neill, H. S. C. (2010). Diffusion and partition coefficients of minor and trace elements in San Carlos olivine at 1,300°C with some geochemical implications. *Contrib. Mineral. Petrol.* 159, 1–28. doi: 10.1007/s00410-009-0456-8

Steinmann, L. K., Oeser, M., Horn, I., Seitz, H.-M., and Weyer, S. (2019). In situ high-precision lithium isotope analyses at low concentration levels with femtosecond-LA-MC-ICP-MS. *J. Anal. At. Spectrom.* 34, 1447–1458. doi: 10.1039/C9JA00088G

Su, B. X., Zhou, M. F., and Robinson, P. T. (2016). Extremely large fractionation of Li isotopes in a chromitite-bearing mantle sequence. *Sci. Rep.* 6, 1–9. doi: 10.1038/srep22370

Tang, Y. J., Zhang, H. F., Deloule, E., Su, B. X., Ying, J. F., Xiao, Y., et al. (2012). Slab-derived lithium isotopic signatures in mantle xenoliths from northeastern North China Craton. *Lithos* 149, 79–90. doi: 10.1016/j.lithos.2011.12.001

Taura, H., Yurimoto, H., Kurita, K., and Sueno, S. (1998). Pressure dependence on partition coefficients for trace elements between olivine and the coexisting melts. *Phys. Chem. Miner.* 25, 469–484. doi: 10.1007/s002690050138

Teng, F. Z., Dauphas, N., Helz, R. T., Gao, S., and Huang, S. (2011). Diffusion-driven magnesium and iron isotope fractionation in Hawaiian olivine. *Earth Planet. Sci. Lett.* 308, 317–324. doi: 10.1016/j.epsl.2011.06.003

Teng, F. Z., Wadhwa, M., and Helz, R. T. (2007). Investigation of magnesium isotope fractionation during basalt differentiation: implications for a chondritic composition of the terrestrial mantle. *Earth Planet. Sci. Lett.* 261, 84–92. doi: 10.1016/j.epsl.2007.06.004

Teng, F. Z., Yang, W., Rudnick, R. L., and Hu, Y. (2013). Heterogeneous magnesium isotopic composition of the lower continental crust: a xenolith perspective. *Geochem. Geophys. Geosyst.* 14, 3844–3856. doi: 10.1002/ggge.20238

Tomascak, P. B., Carlson, R. W., and Shirey, S. B. (1999a). Accurate and precise determination of Li isotopic compositions by multi-collector sector ICP-MS. *Chem. Geol.* 158, 145–154. doi: 10.1016/S0009-2541(99)00022-4

Tomascak, P. B., Langmuir, C. H., Le Roux, P. J., and Shirey, S. B. (2008). Lithium isotopes in global mid-ocean ridge basalts. *Geochim. Cosmochim. Acta* 72, 1626–1637. doi: 10.1016/j.gca.2007.12.021

Tomascak, P. B., Tera, F., Helz, R. T., and Walker, R. J. (1999b). The absence of lithium isotope fractionation during basalt differentiation: new measurements by multicollector sector ICP-MS. *Geochim. Cosmochim. Acta* 63, 907–910.

Vlastélic, I., Staudacher, T., Bachèlery, P., Télouk, P., Neuville, D., and Benbakkar, M. (2011). Lithium isotope fractionation during magma degassing: constraints from silicic differentiates and natural gas condensates from Piton de la Fournaise volcano (Réunion Island). *Chem. Geol.* 284, 26–34. doi: 10.1016/j.chemgeo.2011.02.002

Weyer, S., and Ionov, D. A. (2007). Partial melting and melt percolation in the mantle: the message from Fe isotopes. *Earth Planet. Sci. Lett.* 259, 119–133. doi: 10.1016/j.epsl.2007.04.033

Weyer, S., and Seitz, H.-M. (2012). Coupled lithium- and iron isotope fractionation during magmatic differentiation. *Chem. Geol.* 29, 42–50. doi: 10.1016/j.chemgeo.2011.11.020

Weyrauch, M., Zipfel, J., and Weyer, S. (2019). Origin of metal from CB chondrites in an impact plume – A combined study of Fe and Ni isotope composition and trace element abundances. *Geochim. Cosmochim. Acta* 246, 123–137. doi: 10.1016/j.gca.2018.11.022

Xu, R., Liu, Y., Tong, X., Hu, Z., Zong, K., and Gao, S. (2013). In-situ trace elements and Li and Sr isotopes in peridotite xenoliths from Kuandian, North China Craton: insights into Pacific slab subduction-related mantle modification. *Chem. Geol.* 354, 107–123. doi: 10.1016/j.chemgeo.2013.06.022

Zhukova, I., O'Neill, H., and Campbell, I. H. (2017). A subsidiary fast-diffusing substitution mechanism of Al in forsterite investigated using diffusion experiments under controlled thermodynamic conditions. *Contrib. Mineral. Petrol.* 172, 1–12. doi: 10.1007/s00410-017-1365-x

Conflict of Interest: The authors declare that the research was conducted in the absence of any commercial or financial relationships that could be construed as a potential conflict of interest.

The handling Editor declared a past co-authorship with the authors MO, SW.

frontiers in Earth Science

ORIGINAL RESEARCH
published: 19 June 2020
doi: 10.3389/feart.2020.00223

Insights Into the Eruptive Dynamics of Small Caldera-Forming Eruptions: The Case Study of the Welded Scoriae of Vulcano (Aeolian Islands, Italy)

Eugenio Nicotra, Marta Minniti, Paola Donato and Rosanna De Rosa*

Dipartimento di Biologia, Ecologia e Scienze della Terra, University of Calabria, Cosenza, Italy

A multi-disciplinary study, integrating volcanological field observations, petrography, whole rock geochemistry and textural and compositional analyses on plagioclase crystals has been carried out on the products of Monte Luccia, Spiaggia Lunga, and Quadrara eruptions, occurred between 48 and 21 kyrs on the island of Vulcano. These products are all characterized by welded scoria blankets, and their eruptions have been generally related to the formation and/or re-activation of ring faults bordering the "Il Piano" caldera. The aim of the work is to reconstruct the pre- and syn-eruptive dynamics acting within their magma plumbing systems and the related link with the phases of caldera collapse. At the bottom of the stratigraphic sequences, the presence of base surge deposits suggests that all the eruptions started with a phreatomagmatic phase fed by a shallow reservoir. Textural and microanalytical study of plagioclase crystals of Spiaggia Lunga eruption revealed that the phreatomagmatic event activated the ascent of a volatile-rich, basaltic magma residing at 5–11 km of depth. This basaltic magma mixed with the resident shallow one, and was poured out during the course of the eruption producing a sustained lava-fountaining phase. The subsequent caldera collapse, identified by a layer of chaotic breccia interbedded in the scoriae deposit, has been linked to the partial emptying of the shallow magma reservoir. In contrast to what observed for recent eruptive events at Vulcano, the onset of the magmatic phase would be attributed to a self-activation due to volcano-tectonic events, and not to a pressurization of the plumbing system related to the ascent of deep magma batches. As concerns the Mt. Luccia deposits, bordering the eastern rim of the "Il Piano" caldera, the absence of plagioclase in the mineralogical assemblage suggests the eruption of a deeper magma (>11 km b.s.l.), rapidly ascending through the re-activated ring faults of "Il Piano" caldera. At Quadrara eruption, the occurrence of a layer of white biotite-bearing latitic pumices overlying the basal phreatomagmatic deposits suggests the involvement a shallow, isolated reservoir where the increase of volatile pressure allowed the crystallization of hydrous phases. A deeper shoshonitic magma was involved later in the eruption, forming the welded scoria level at the top of the sequence.

Keywords: caldera, plagioclase, magma plumbing system, eruptive scenario, pre-eruptive conditions, welded scoriae, volcanology, eruptive conditions

OPEN ACCESS

Edited by:
Marc-Antoine Longpré, Queens College (CUNY), United States

Reviewed by:
Andrea Di Muro, UMR 7154 Institut de Physique du Globe de Paris (IPGP), France
Jason Peter Coumans, Durham University, United Kingdom

****Correspondence:***
Eugenio Nicotra
eugenio.nicotra@unical.it

Specialty section:
This article was submitted to Petrology, a section of the journal Frontiers in Earth Science

Received: *28 February 2020*
Accepted: *27 May 2020*
Published: *19 June 2020*

Citation:
Nicotra E, Minniti M, Donato P and De Rosa R (2020) Insights Into the Eruptive Dynamics of Small Caldera-Forming Eruptions: The Case Study of the Welded Scoriae of Vulcano (Aeolian Islands, Italy). Front. Earth Sci. 8:223. doi: 10.3389/feart.2020.00223

INTRODUCTION

Calderas are one of the most evident morphological elements of a volcanic edifice. They differentiate from sector/flank-collapses or explosion craters, which could have similar aspect, chiefly for their direct link with the dynamics acting into the magmatic plumbing systems prior and during an eruptive event (e.g., Ventura et al., 1999; Peccerillo et al., 2007; Davì et al., 2009; Nicotra and Viccaro, 2012b; Fabbro et al., 2013; Fontaine et al., 2014; Kennedy et al., 2018; Albert et al., 2019). The processes promoting a caldera collapse are necessarily related to the presence of a magma reservoir, regardless of its shape, depth and composition. Collapses are chiefly related to magma displacement, which can produce a lateral intrusion or give rise to an eruption. The decrease of pressure within the reservoir can then lead to the collapse of its roof (Cashman and Giordano, 2014 for a review). Depending on the strength and thickness of the overlying country rock and on the width and depth of the magma chamber, caldera collapse can occur during syn- or post-eruptive phases of a single (or a sequence of) eruptive event(s). Usually this happens throughout some steps associated with seismic activity and/or minor aseismic creep subsidence events. Indeed, not all the caldera-forming processes are related to high-volume and catastrophic eruptive events, as the magnitude of the collapse is related to the ratio between the volume of the outpoured magmas and that of the magma chamber, and it is also function of the depth of the reservoir.

In most of geodynamic settings where magmatic processes develop through hundreds of thousands of years (e.g., continental rifting, collisional settings, back-arc extensional basin, complex geodynamic settings), magmas can pond and crystallize also at shallow depth, evolving toward silicic compositions (e.g., Davì et al., 2010; Peccerillo and Frezzotti, 2015; Andersen et al., 2017). The extreme evolution of such magmatic systems toward rhyolitic *s.l.* compositions, often leads to large-volume and high-energy caldera-forming eruptions (e.g., Jellinek and de Paolo, 2003; Cashman and Giordano, 2014). Despite the very low aspect ratio of mafic magma reservoirs, also the associated volcanic edifices can be affected by calderas. One of the best examples is represented by Etna volcano, which underwent repeated caldera-forming episodes at the ends of periods of huge magma withdrawal from its shallow reservoirs ["Il Piano" (15 kyrs), 122 b.C. eruption and 1669 eruption calderas; Coltelli et al., 1998; Nicotra and Viccaro, 2012b]. Other famous, and in some cases similar, examples are the Kilauea, Piton de la Fournaise and some volcanoes of Galapagos and Canary archipelagos (e.g., Fontaine et al., 2014; Harpp and Geist, 2018; Kennedy et al., 2018; Albert et al., 2019; Sainz-Maza Aparicio et al., 2019). Nonetheless, the mechanisms controlling the caldera formation at mafic systems, usually drawn as a sequence of melt lenses or stacked sills at different depths of the magmatic plumbing system (e.g., Marsh, 1996; Annen and Sparks, 2006; Gudmundsson, 2012; Nicotra et al., 2018), are still poorly understood.

Within the last 130 kyrs of its volcanic activity, the morphology of the island of Vulcano deeply changed due to several caldera-forming stages, finally leading to the formation of the two calderas of "Il Piano" and "La Fossa" (**Figure 1**). In particular, the re-activation of the "Il Piano" caldera is usually associated to some small-volume, but highly energetic, eruptions developed between 48 and 21 kyrs on its caldera rims (i.e., Monte Luccia, Spiaggia Lunga, Quadrara Formations; **Figure 1**). The most voluminous (ca. 0.1 km^3) and best preserved of them is certainly that of Spiaggia Lunga (**Figures 1**, **2**; ca. 24 kyrs; Soligo et al., 2000). One of the most intriguing features of these eruptions is the similarity of their products, having all erupted massive reddish and strongly welded scoriae with a shoshonitic affinity. Similar volcanic deposits have been also successively erupted later on at Monte Saraceno, on the southern border of the caldera of "La Fossa" (ca. 8 kyrs; De Astis et al., 2013). The welded scoriae of Vulcano, especially those of Spiaggia Lunga, have been subject to different interpretations of their eruptive mechanisms, being considered as trachybasaltic ignimbrites (Keller, 1980; Gioncada and Sbrana, 1991) or, alternatively, as the products of a strong Strombolian activity, forming a clastogenic lava flow on the western slope of the island (**Figure 1**; De Rosa et al., 1988; De Astis et al., 2013). According to both interpretations, the strong welding of the deposits gives them a "lava-like" aspect. However, despite the great similarity of the Monte Luccia, Spiaggia Lunga, and Quadrara deposits and the similar topographic position along the ring faults of the caldera of "Il Piano," the possible relationship between these eruptive events and the episode of caldera formation has not been analyzed in detail.

The present study is focused on the reconstruction of the pre- and syn-eruptive magma dynamics acting into the plumbing systems of these eruptions, their eruptive scenarios and possible role in triggering episodes of caldera collapse. These purposes have been pursued by means of multi-disciplinary studies joining the volcanological field survey with petrographic observations, textural and compositional (EMPA) studies on plagioclase crystals and whole rock compositions (XRF).

VOLCANOLOGICAL BACKGROUND

The Island of Vulcano

Vulcano is the southernmost island of the Aeolian archipelago, a volcanic arc located between the back-arc oceanic basin of Marsili and the continental foreland Calabrian arc. Aeolian islands are the result of the subduction of the Mesozoic Ionian slab beneath the Calabrian arc, as testified by the presence of a NW-dipping Benioff zone under the arc (e.g., Barberi et al., 1974; Gasparini et al., 1982; Ellam et al., 1989). Seismicity observed in this area is attributed to the passive subduction and de-hydration of a detached slab, which would be also the cause of the Aeolian volcanism in a context of post-subduction extensional tectonic regime (Wang et al., 1989; Crisci et al., 1991; Esperança et al., 1992; Gvirtzman and Nur, 1999). The islands of Vulcano, Lipari and Salina, in the central portion of the archipelago, are affected by NNW–SSE-striking faults (Tindari–Letojanni Fault System; cf. Barberi et al., 1994; Ventura, 2013) and are located above a 15–20 km thick continental crust (De Ritis et al., 2013) consisting of the Hercynian metamorphic and granitic rocks and Mesozoic sediments of the Calabrian basement (Keller, 1980; Del Moro et al., 1998; Frezzotti et al., 2004).

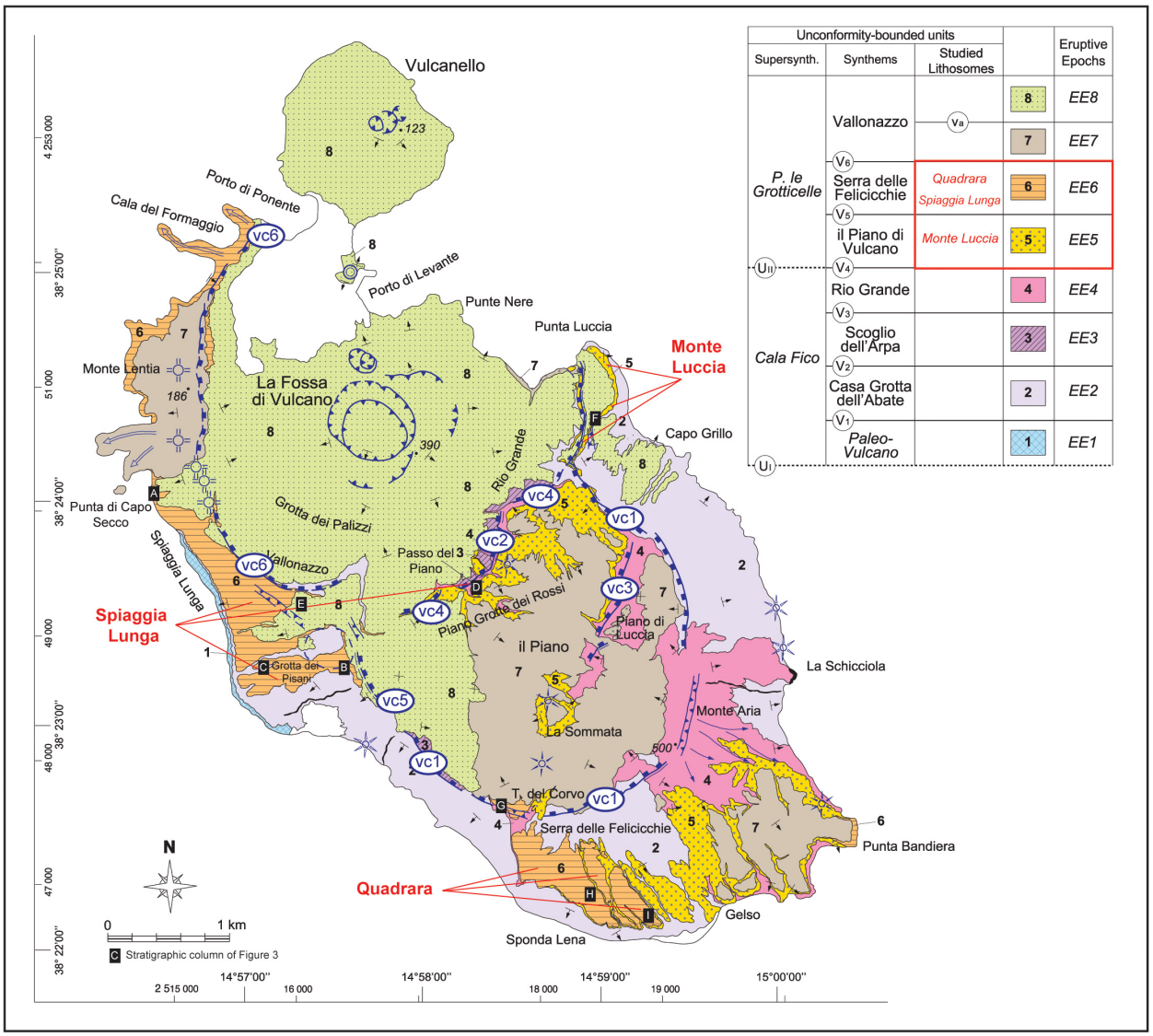

FIGURE 1 | Geological sketch map of the island of Vulcano (from De Astis et al., 2013). The studied areas of Monte Luccia, Spiaggia Lunga and Quadrara are indicated. vc = volcano-tectonic collapse. White letters in black box are referred to the stratigraphic columns of **Figure 5**.

The subaerial portion of the island of Vulcano is part of a wider complex including the islands of Lipari and Salina, developed along a graben-like structure controlled by the NNW-SSE strike-slip Tindari-Letojanni fault system (e.g., Ventura, 2013; Ruch et al., 2016). The subaerial activity at Vulcano covers the last 127 kyrs, and spatially shifted with time from south toward north. In the eruptive history of Vulcano De Astis et al. (2013) distinguished 8 Eruptive Epochs (EEs; cf. **Figure 1**) separated by 6 different volcano-tectonic (vc) collapses, which produced the multi-stage calderas of "Il Piano" and "La Fossa."

The first vc1 collapse occurred at about 100 kyrs during the EE3 and produced the main depression of the "Il Piano" caldera (**Figure 1**). It was followed by the vc2 collapse, which formed the southern border of the younger "La Fossa" caldera. The vc3 collapse was internal to the "Il Piano" caldera, in the area of Piano di Luccia (**Figure 1**), and it is supposed to have formed between 70 and 42 kyrs. While vc4 and vc6 collapses were related to the "La Fossa" caldera, the vc5 collapse is a tardive volcano-tectonic vertical movement occurred (probably) between 24 and 21 kyrs and reactivating the western rim of "Il Piano" caldera (**Figure 1**; De Astis et al., 2013).

The Welded-Scoriae Enigma

The present work focuses on blankets of mafic-intermediate welded scoriae outcropping in different areas of the island of Vulcano dated between 48 and 21 kyrs (**Figures 1–4**), whose relationships and stratigraphic position has been a matter of debate during the last 40 years, mainly due to the lack of certainty in absolute dating. Following De Astis et al. (2013) we will adopt the "classical" names of these deposits, related to the locus of

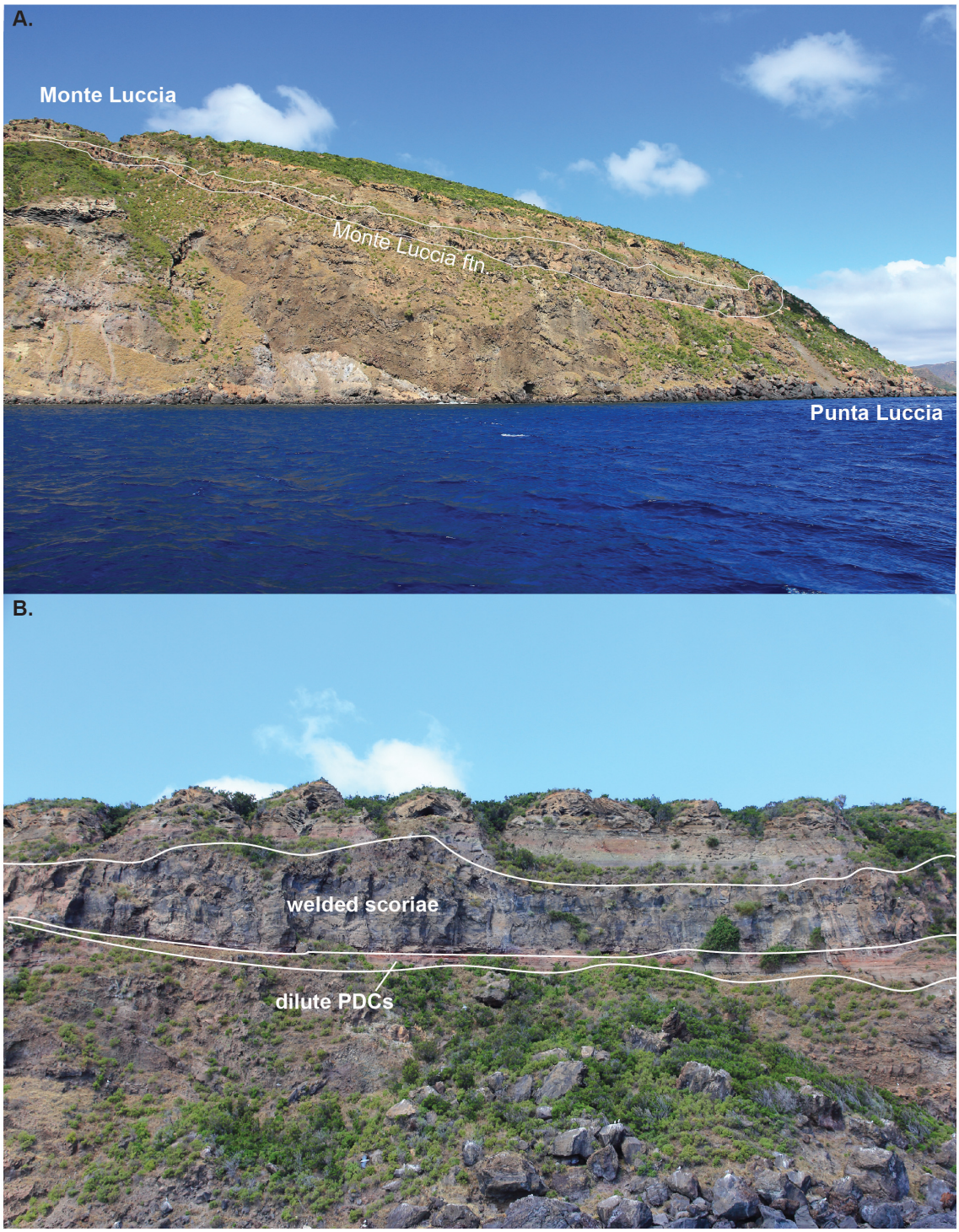

FIGURE 2 | Photos of Punta Luccia area, along the northern coasts of Vulcano island. **(A)** Panorama of the Monte Luccia formation; here the welded scoriae reach 25 m of thickness. **(B)** Detail photo of the Monte Luccia Formation, with indication of the dilute PDCs deposits at its base.

the best-preserved stratigraphy, i.e., Monte Luccia (ML), Spiaggia Lunga (SL), and Quadrara (Qu) formations. Before and after these eruptive periods, other welded scoriae have been erupted at Vulcano island (e.g., Monte Aria, Passo del Piano, La Sommata, Monte Saraceno; cf. De Astis et al., 2013); however, each of these eruptive events presents different and peculiar features and compositions with respect to the more homogeneous ML-SL-Qu sequences.

FIGURE 3 | Photos of various areas of Spiaggia Lunga deposits. **(A)** Panoramic photos of the southern cliffs of Vulcano island; at its top the SL blanket, whose thickness increases from Capo Secco (south) to Punta di Capo Secco (north). **(B)** Particular of SL deposits. **(C)** "Lava-like" portion of the SL deposits. **(D)** Proximal area of SL deposits in a 10 m thick succession: it is possible to see the variation of welding from distal (left) to more proximal (right) portions of the deposit. **(E)** Particular of the base of the succession of SL deposits at Punta di Capo Secco. A metric block produced a bomb sag on the soft cross-laminated underlying deposits of dilute PDCs. **(F)** Proximal area of SL Formation, at the top of Monte Saraceno: the two different portions of the outcrops, with different degree of welding, are very evident. At the top, Saraceno ftn. Is overlying with angular unconformity. **(G)** Lower portion of the deposits of SL in the same location of **(F)**. It is still possible to recognize an agglutinated spatter block.

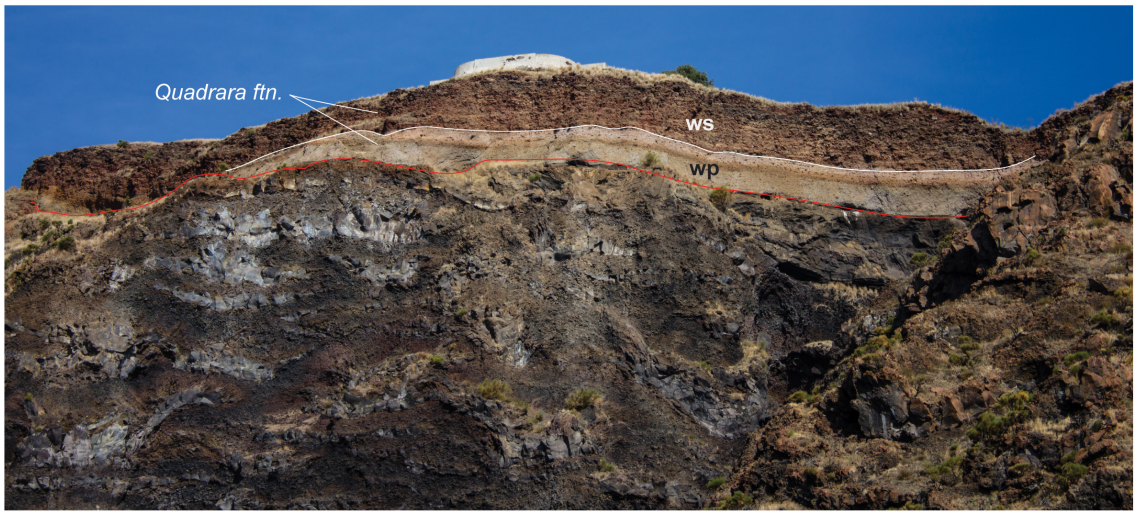

FIGURE 4 | Panoramic view of the Quadrara Formation, in the southernmost area of Vulcano island. Deposit can be divided into the wp (white pumices) and WS (welded scoriae) portions.

Keller (1980) defined blankets of welded scoriae the pyroclastic deposits outcropping at Monte Luccia, Spiaggia Lunga, and Quadrara areas, and considered all of them in the same stratigraphic position. He described these products as "lava-like banks" covering a pre-existing morphology which, toward their marginal and top portions, turn in deposits with coarse eutaxitic "fiamme" structures and then in less agglutinated scoriae and bombs. Keller (1980) interpreted these features as related to the deposition of trachybasaltic ignimbrites, with gas-rich magma erupted as hot pyroclastic flow during the collapse of segments of the "Il Piano" caldera. Such interpretation has been also embraced later by Gioncada and Sbrana (1991).

De Rosa et al. (1988), studying the SL welded scoriae (**Figure 2**), related these deposits to a low-energy fissure eruption along a segment of the "Il Piano" caldera. During the initial stages of the eruption magma interacted with external water, whereas at the climax a purely magmatic eruption led to the craterization of the fissure and very rapid drainage of the uprising magma.

The stratigraphic position of these formations has been discussed by De Astis et al. (1989), which gave an age of 48.5 ± 6.5 kyrs for ML deposits. The authors hypothesized also a stratigraphic continuity between the top of SL deposits and the base of Lentia dome (ca. 15 kyrs), linking them with two phases of collapse of the "La Fossa" caldera. According to De Astis et al. (1989) and in contrast with the Keller (1980) hypothesis, the ML-SL-Qu deposits would belong to three different eruptions and, therefore, occupy three different stratigraphic positions. Further U/Th absolute dating of Soligo et al. (2000) did not allow to definitively assess the different stratigraphic position for the Spiaggia Lunga (24.0 ± 5.0 kyrs) and Quadrara (21.3 ± 3.4 kyrs) Formations, due to the overlapping ages.

Recently, the ML welded deposits (**Figure 3**) have been attributed by De Astis et al. (2013) to Strombolian-Hawaiian explosive activity, coupled with a density-stratified scoria flow. This would be consistent with the lentiform geometry of the unit, its valley-ponding thickness variations, a well-developed foliation and the homogeneous SW-NE magnetic fabric found by Zanella et al. (2001). Furthermore, these authors recognized a lithic-rich horizon in the medial portion of the outcrop, and a cross-laminated tuff layer at the base of the unit, related to a short-lived phreatomagmatic phase that produced a sequence of discontinuous dilute PDCs. A similar deposit has been recognized also at the base of SL (**Figure 2E**; De Astis et al., 2013). Here, the activity continued with open-conduit-related, lithic-rich deposits and evolved into intense Strombolian explosive activity. Also in this case, a slight valley-ponding thickness variation, together with the homogeneous magnetic fabric and SE-NW magnetic lineation recognized by Zanella et al. (2001), led to the interpretation of SL deposits as due to a fountain-fed fallout coupled with scoria flow movements. De Astis et al. (2013) recognized for the first time an epiclastic breccia layer within the SL sequence. The same depositional mechanism has been also hypothesized for the Qu sequence (**Figure 4**), which at its base shows inversely graded biotite-bearing light pumices, gradually passing into a scoria blanket (De Astis et al., 2013), suggesting the progressive tapping of a zoned magma reservoir during the Quadrara eruption.

SAMPLING AND ANALYTICAL METHODS

A volcanological survey and a sampling campaign were carried out on all the deposits of welded scoriae belonging to the ML-SL-Qu Formations (**Figures 1–4**). As a whole, 43 representative rock samples were collected from 9 volcano-statigraphic columns (**Figure 5**).

Whole rock data for all the collected samples are reported in **Table 1**. Whole rock compositions in terms of major and some trace elements were obtained at the Dipartimento di Biologia, Ecologia e Scienze della Terra of the University

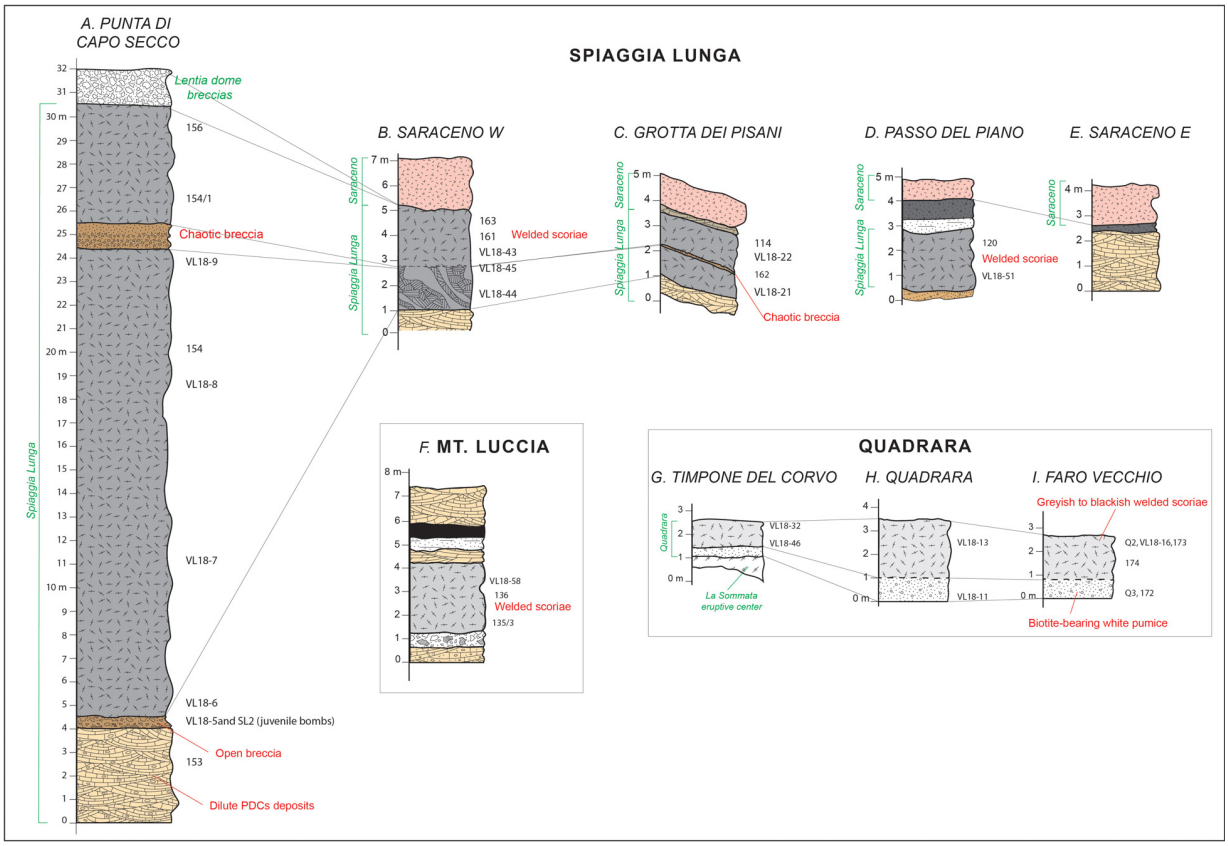

FIGURE 5 | Stratigraphic successions of the studied eruptive events. The location of each column is indicated by the capital white letter in the black box of **Figure 1**.

of Calabria (Italy) by means of a Bruker S8 Tiger XRF spectrometer on powder pellets with matrix effect corrections. The precision, measured as percentage difference between certified and measured composition of standards analyzed as unknown samples, was always <5% for major elements and 10% for trace elements. FeO was determined by titration. Loss on ignition was determined by gravimetric methods and corrected for Fe^{2+} oxidation. The sum of oxides was always higher than 98%. All the analyses were re-calculated for a sum of 100%.

On 25 selected rock samples, polished thin sections were obtained. Mineralogical and petrographic observations were performed by means of optical and polarized microscope. Compositional core-to-rim profiles were executed on 23 plagioclase crystals on polished, graphite-coated thin sections by means of Electron MicroProbe Analyzer (EMPA). Plagioclase crystals were selected on the basis of the representativeness of their texture within each sample. Only phenocrysts were considered for this type of analysis; in this regard, the plagioclase xenocrysts of Monte Luccia and the xenocrystic cores occurring in Spiaggia Lunga welded scoriae were not taken into account for textural and compositional analysis. All compositional data on plagioclase are reported in **Supplementary Material**. We used the JEOL JXA-8230 of SILA-CM2 lab at the University of Calabria, equipped with 5 WDS and one EDS spectrometers. WDS analyses were carried out with an accelerating voltage of 15 kV and probe current of 10 nA. Count times were of 15 s for Na and 30 s for other elements.

FIELD DATA

Monte Luccia Formation (ML)

Monte Luccia formation (48.5 ± 6.5 kyrs; De Astis et al., 1989) crops out on the northern and central portion of the island, where the rim of the "Il Piano" caldera is cut by that of the "La Fossa" (**Figure 1**). It consists of a pyroclastic succession with variable thickness from 3 m at the top of Monte Luccia up to 25 m at its base (**Figure 3**). Welded scoriae overlie a 0.5–1 m thick cross-laminated tuff layer (**Figure 3B**), generated by dilute PDCs, and by a level of altered breccia, whose thickness increases in the morphological depressions. The main portion of ML is made up by a blanket of reddish scoriaceous bombs, from very (at the base) to poorly welded (at its top). At the very top of the layer it is possible to distinguish each single lava spatter shred. The deposits are covered by the Grotta dei Palizzi Formation belonging to the "La Fossa" hystorical activity (cf. De Astis et al., 2013).

Spiaggia Lunga Formation (SL)

Among all the outcrops of welded scoriae at Vulcano island, those of the Spiaggia Lunga Formation (24.0 ± 5.0 kyrs;

TABLE 1 | Whole rock composition for the considered eruptive events.

Formation	Mt. Luccia	Mt. Luccia	Mt. Luccia	Spiaggia Lunga	Spiaggia Lunga	Spiaggia Lunga	Spiaggia Lunga	Spiaggia Lunga	Spiaggia Lunga	Spiaggia Lunga	Spiaggia Lunga	Spiaggia Lunga	Spiaggia Lunga	Spiaggia Lunga	Spiaggia Lunga
Type	**wd**	**wd**	**pdc**	**wd**	**wd**	**wd**	**wd**	**wd**	**scoriae**	**wd**	**wd**	**wd**	**wd**	**wd**	**wd**
Sample	**VL18_58**	**136**	**135/3**	**120**	**VL18_51**	**114**	**VL18_22**	**VL18_21**	**163**	**161**	**VL18_43**	**VL18_45**	**VL18_44**	**156**	**154/1**
SiO_2	52.8	52.0	50.5	49.8	50.3	50.9	51.2	52.0	48.6	51.3	52.4	53.2	54.0	48.3	48.3
TiO_2	0.68	0.72	0.84	0.84	0.78	0.69	0.77	0.80	0.86	0.67	0.65	0.69	0.71	0.68	0.70
Al_2O_3	17.0	19.0	16.4	19.8	18.4	18.7	19.3	16.6	18.6	20.3	21.6	18.5	17.9	22.1	19.6
Fe_2O_3	5.71	5.63	10.42	6.39	6.02	3.79	8.75	7.00	8.49	5.40	7.14	7.85	6.34	7.64	6.24
FeO	3.02	2.69	2.40	3.57	3.75	3.84	1.20	3.00	1.90	1.55	0.48	0.49	1.75	0.17	1.96
MnO	0.16	0.13	0.13	0.21	0.17	0.22	0.16	0.17	0.28	0.43	0.13	0.14	0.17	0.16	0.17
MgO	3.66	3.00	2.58	3.36	3.71	3.01	3.00	4.32	3.96	1.96	1.77	2.81	3.33	2.02	3.01
CaO	7.02	5.48	4.79	7.48	7.55	6.08	7.60	8.84	8.77	5.99	5.43	6.72	6.93	6.60	7.06
Na_2O	2.78	2.75	1.76	2.12	2.69	2.78	2.69	2.94	2.60	2.46	2.53	2.99	2.92	2.17	4.11
K_2O	3.51	3.65	2.59	2.76	2.74	2.87	2.78	2.93	2.44	3.07	3.45	3.33	3.21	3.22	2.67
P_2O_5	0.32	0.31	0.56	0.26	0.29	0.33	0.30	0.29	0.29	0.36	0.35	0.37	0.33	0.34	0.32
Ba	763	770	n.a.	785	776	851	801	831	786	997	887	892	903	740	722
Ce	122	85	n.a.	84	77	73	98	72	100	110	90	102	102	100	102
Co	42	n.a.	n.a.	n.a.	32	n.a.	36	37	n.a.	n.a.	16	23	26	n.a.	n.a.
Cr	67	51	n.a.	20	23	16	21	25	15	13	14	14	13	11	10
La	61	43	n.a.	47	48	44	45	37	43	49	52	59	67	42	43
Nb	15	12	n.a.	7	9	7	9	7	6	10	13	12	13	6	6
Ni	31	24	n.a.	20	22	41	14	22	22	37	17	22	18	16	22
Pb	20	n.a.	n.a.	n.a.	16	n.a.	12	19	n.a.	n.a.	9	15	15	n.a.	n.a.
Rb	104	111	n.a.	62	68	55	41	62	52	91	110	100	71	70	56
Sr	936	735	n.a.	1075	1131	1526	1134	1322	1282	958	943	1280	1153	969	1137
V	240	245	n.a.	277	280	297	231	292	292	117	113	163	214	209	223
Y	31	33	n.a.	56	36	29	40	19	29	45	46	24	28	69	31
Zr	123	122	n.a.	109	101	109	102	99	105	126	132	134	137	98	100

(Continued)

TABLE 1 | Continued

Formation	Spiaggia Lunga	Spiaggia Lunga	Spiaggia Lunga	Spiaggia Lunga	Spiaggia Lunga	Spiaggia Lunga	Spiaggia Lunga	Quadrara	Quadrara	Quadrara	Quadrara	Quadrara	Quadrara	Quadrara
Type	**wd**	**wd**	**wd**	**wd**	**wd**	**scoriae**	**Bomb**	**wd**	**wd**	**wd**	**wd**	**pumice**	**pumice**	**pumice**
Sample	**154**	**VL18_9**	**VL18_8**	**VL18_7**	**VL18_6**	**SL2**	**VL18_5**	**VL18_32**	**VL18_16**	**173**	**174**	**VL18_13**	**VL18_11**	**172**
SiO_2	50.2	50.3	51.6	51.4	51.7	50.9	50.3	53.4	54.5	55.5	55.8	59.0	59.5	59.9
TiO_2	0.71	0.78	0.74	0.75	0.74	0.88	0.82	0.77	0.82	0.82	0.79	0.55	0.46	0.52
Al_2O_3	19.0	17.9	17.9	18.4	17.7	17.0	16.8	16.6	16.7	17.5	17.6	17.3	18.8	18.1
Fe_2O_3	7.75	7.75	7.29	8.02	7.43	7.54	8.37	4.81	9.05	7.44	7.71	5.45	3.46	3.55
FeO	0.76	2.21	1.94	1.66	2.01	3.45	2.65	4.92	0.59	0.66	0.12	0.57	1.34	1.26
MnO	0.18	0.16	0.17	0.17	0.18	0.21	0.30	0.19	0.15	0.16	0.15	0.18	0.12	0.17
MgO	2.85	3.35	3.40	3.45	3.31	4.21	4.23	3.37	3.39	2.89	2.88	2.00	1.15	1.57
CaO	9.36	8.72	8.28	7.84	8.02	8.71	9.48	7.63	6.83	6.14	5.96	3.97	2.33	2.93
Na_2O	5.01	2.77	3.39	2.93	3.15	2.96	2.89	2.92	3.12	3.43	3.42	4.04	1.95	3.83
K_2O	2.74	2.77	2.88	2.73	3.09	2.99	2.84	4.37	3.81	4.31	4.42	5.05	3.49	5.11
P_2O_5	0.43	0.36	0.40	0.35	0.39	0.31	0.28	0.46	0.37	0.40	0.40	0.24	0.20	0.21
Ba	780	817	850	797	873	896	935	1123	910	929	934	1100	1069	n.a.
Ce	83	67	81	73	84	71	70	106	102	115	115	99	118	n.a.
Co	n.a.	28	30	32	34	34	42	34	26	n.a.	n.a.	9	4	n.a.
Cr	10	12	n.a.	16	14	19	17	n.a.	n.a.	0	0	n.a.	n.a.	n.a.
La	42	40	41	36	53	52	37	60	59	50	51	53	49	n.a.
Nb	6	11	10	9	6	6	9	20	14	12	13	20	21	n.a.
Ni	16	17	24	21	22	25	22	16	6	7	6	10	7	n.a.
Pb	n.a.	11	11	11	11	13	12	25	13	n.a.	n.a.	45	24	n.a.
Rb	27	26	24	31	57	59	69	129	106	132	133	167	134	n.a.
Sr	1178	1284	1310	1221	1348	1136	1431	1348	1245	1175	1156	1113	866	n.a.
V	191	264	243	273	265	349	293	268	187	158	144	78	63	n.a.
Y	27	30	28	25	29	26	26	26	26	27	29	35	30	n.a.
Zr	95	102	99	99	97	140	104	144	146	157	153	196	212	n.a.

Wd, welded scoriae. ***Supplementary Material*** *– Core-to-rim compositional profiles on 23 selected plagioclase crystals.*

Soligo et al., 2000) are the best preserved and most voluminous. The deposits of this eruption are widely distributed on the eastern parts of the island, following the shape of the eastern rims of the "Il Piano" and "La Fossa" calderas (**Figure 1**).

The most voluminous and best-preserved flow units are located at the intersection of these two caldera systems, in correspondence of the cliffs of "Punta di Capo Secco" (**Figures 1**, **2**, **5**). The base of this outcrop is constituted by 4 m of thickly bedded, planar to wavy and cross-laminated, thin (<10 cm) ash deposits (**Figures 2D,E**, **5**), carrying some lithics (up to 17–18 cm) and having bomb sags with a N110°E direction, that can be clearly attributed to a dilute PDC. These PDC deposits are typically characterized by a high frequency of thin layers rich in juvenile fragments and accretionary lapilli and of crustal xenoliths of leuco-monzogabbro (cf. Faraone et al., 1986) up-to-25 cm in size. Such features suggest that these PDC could have a phreatomagmatic origin, in which country rocks have been carried out at the surface together with the magmatic component. Toward the top, these deposits (**Figures 2E**, **5**) end with a 0.5 m thick layer very rich in brecciated lithics (crustal and volcanics) and juvenile bombs (up to 10 cm; **Figure 2E**) generating bomb-sags with a N110°E direction of provenance. Due to these features, this layer can be interpreted as an opening breccia.

The main portion of the SL is constituted by a 25 m thick massive layer made up by mildly welded to strongly welded or "lava-like," scoriaceous deposits (**Figures 2**, **5**). The degree of welding clearly varies with the thickness of the deposit. Following the cliff of this outcrop from "Punta di Capo Secco" to "Capo Secco" promontory (from north to south; **Figure 1**), the deposit changes progressively from "lava-like" (up to 25 m of thickness) to strongly welded in the intermediate portions (ca. 15 m of thickness) and finally to mildly or weakly welded where thickness is lower than 10 m. Vitric, elongated structures, interpreted by Keller (1980) as fiammae, were recognized in the basal and top portion of the deposit. Conversely, our field evidence suggests that "fiammae-like" structures found at the bottom and the top of SL are the agglutinated surfaces of each bomb, stretched and ripped off by the growing thickness of the deposit. In the upper part of "Punta di Capo Secco" outcrop, at about 5 m from the top, a 1 m thick deposit of fine and lithic-rich ash is interbedded in the welded scoriae of SL. It corresponds to the "epiclastic breccia layer" of De Astis et al. (2013), and it has been also found in the Grotta dei Pisani area (**Figures 1**, **5**), at highest elevation, where the dimensions of brecciated lithics are larger. At "Punta di Capo Secco" the succession is closed by the brecciated deposits of the Lentia domes (ca. 15 kyrs; De Rosa et al., 2003).

The SL deposits also crop out on the high western flank of Mt. Saraceno (**Figures 1**, **2F,G**), on a 25° steep slope. Here, above the cross-laminated PDCs deposits, two portions can be identified (**Figure 5**). The lowermost portion is constituted by a 1 m thick layer of mildly to strongly welded scoriae and bombs, where the single ballistic fragments can still be recognized (**Figure 2G**). The uppermost is a 5–8 m thick "lava-like" deposit very similar to those of "Punta di Capo Secco" (**Figure 2F**). The stratigraphic and topographic position, joined to the depositional features, lead to consider these deposits as proximal. These two layers are separated by a very thin (<1 cm) deposit of fine ash, also outcropping in the "Grotta dei Pisani" area (**Figure 5**), and corresponding to the inter-layered epiclastic breccia deposits recognized by De Astis et al. (2013) in the SL succession.

Quadrara Formation (Qu)

The Quadrara Formation (21.3 ± 3.4 kyrs; Soligo et al., 2000) crops out on the southernmost portion of the "Il Piano" caldera, mantling the outer border of the volcanic edifice (**Figures 1**, **4**). This Formation, related to a single eruptive event, starts with few centimeters of fine ash laminated beds rich in lithics followed by 1 m thick layer of inversely graded and biotite-bearing white pumices (**Figure 4**). Although at "Faro Vecchio" it seems that white pumices progressively grade into the overlying mildly to strongly welded blackish scoria deposit, at "Quadrara" and "Timpone del Corvo" areas a layer of very fine unsorted and ungraded ash separates the pumice layer from the upper scoria deposit (**Figure 5**).

WHOLE ROCK GEOCHEMISTRY

Whole rock geochemistry of the analyzed welded scoriae at Vulcano island confirms that all the products belong to the shoshonitic series, coherently with literature data for rocks of these eruptive epochs (Keller, 1980; De Astis et al., 1997; De Astis et al., 2013; Nicotra et al., 2018). On the whole (**Figure 6A**), the considered samples mainly plot into the shoshonitic basalt and shoshonite fields, with only the pumice of Qu and some samples of SL which show latitic composition.

It is worth of note that whole rock composition of samples of SL at Capo Secco (**Figures 1**, **2**, **5**) tends to be slightly less evolved from the base to the top of the succession (**Figure 6C** and **Table 1**). A significant variation is also shown by some trace elements, such as Ba and Nb, which, from the bottom to the top of the succession, decrease and increase, respectively. By contrast, the SL samples of the western flank of Mt. Saraceno (VL18-43/45/44; **Table 1**) show fairly constant compositions, similar to those of the deposits at the base of Capo Secco succession (K_2O = 3.2–3.4 wt%). Within the sequence of Quadrara, the white pumices at the base of the succession show the most evolved compositions, being classified as latite (**Figure 6A**). Conversely, in the dark scoriae above the cm-thick epiclastic layer, whole rock compositions tend to be gradually more basic. The diluted PdC deposit at the base of Monte Luccia is slightly less evolved and Ca-rich than the overlying scoriae (**Figures 6A,B**).

Spider diagram normalized to Primordial Mantle (**Figure 6D**) shows a superimposition of the patterns of all the samples, with only the Quadrara latites slightly more enriched in Rb, Ba, Nb, K, Zr, and depleted in P and Ti.

PETROGRAPHY AND MINERAL CHEMISTRY

Petrographic analysis has been carried out on most representative samples of the considered formations, including also the dilute

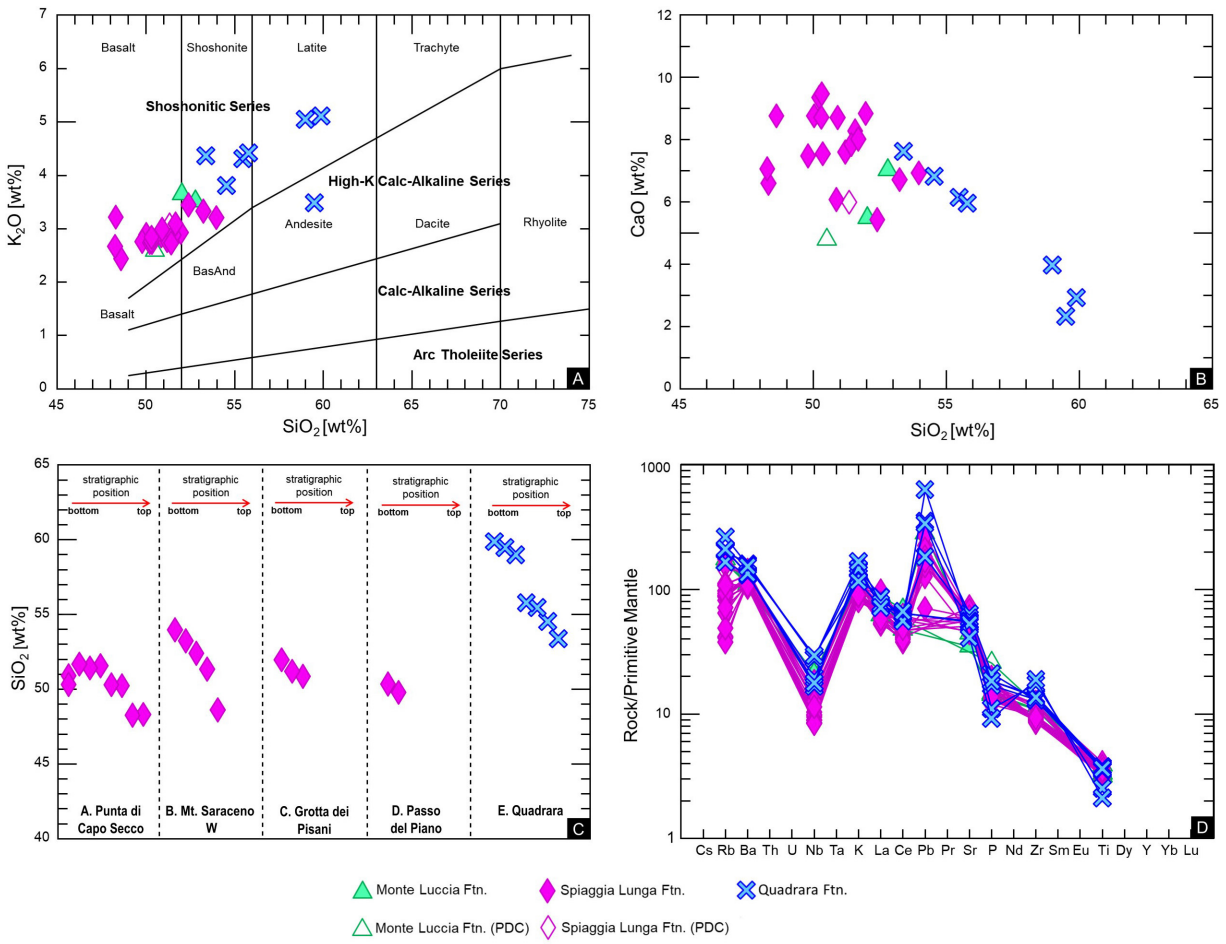

FIGURE 6 | Whole rock diagrams for the collected rock samples. **(A)** Peccerillo and Taylor (1976) classificative diagram; **(B)** CaO vs. SiO_2 variation; **(C)** variation of SiO_2 content with stratigraphic height in the different sampled outcrops; **(D)** primordial mantle- normalized (Sun and McDonough, 1989) spider diagram of incompatible elements contents.

PDCs and pumice samples which preceded the emplacement of welded scoriae.

One of the most intriguing features is that the most welded part of each formation, especially in the central portion of SL, exhibits a "lava-like" texture also at microscopic scale. Less welded deposits have a more scoriaceous structure, often characterized by the unique presence of rapidly chilled and highly vesiculated glass. Although characterized by a strong vesiculation due to syn- and post-eruptive degassing, the most welded deposits generally have a porphyritic structure, with a variable porphyritic index (P.I. in vol%) that ranges from 5 to 45% (ML = 10–15%; SL = 35–45%; Qu = 5–15%). Groundmass varies from hypo-crystalline to aphanitic and from micro- to crypto-crystalline; it is often intersertal, with only some small portions having a fluidal displacement of their micro-crystals.

The mineral assemblage is that typical of basaltic products, with phenocrysts of plagioclase (0–57 vol%), clinopyroxene (10–57 vol%), olivine (3–25 vol%), and opaque oxides (3–8 vol%). The pumice and scoriae of Qu deposits have also biotite phenocrysts (up to 10 vol%), whose content decreases from the bottom to the top of the succession. The presence of cumulitic aggregates of clinopyroxene (± plagioclase ± olivine) has been detected especially in the SL formation, with a maximum size of approximately 2400 μm in samples VL18-5 (at the bottom of the volcano-stratigraphic succession).

Plagioclase phenocrysts are generally euhedral, with normal zoning and always twinned. Within the considered volcano-stratigraphic units, only SL presents plagioclase phenocrysts in equilibrium with the surrounding melt. Plagioclase is absent in Quadrara deposits, whereas in the ML scoriae only rare (<5 vol%) relicts of deeply altered (often with sericitization processes) and dissolved plagioclase were found (i.e., xenocrysts). SL deposits also present rare (<5 vol%) xenocrysts or xenocrystic cores, especially in the samples at the bottom of the welded scoriae succession (VL18-5 and SL2 samples; **Figure 5**). Numerous broken plagioclases have been observed within the VL18-5 and SL2 samples, which are two bombs deforming the underlying PDCs dilute deposits (**Figure 5**).

Clinopyroxene crystals are mostly euhedral, ranging between 0.5 and 2 mm in dimensions; they are augitic in composition

and often show several layers of melt inclusions aligned along crystallographic directions. Olivine occurs as euhedral to subhedral phenocrysts, with small grain size (up to 1 mm), and often characterized by iddingsitic post-emplacement alteration. Biotite in Qu Formation is clearly euhedral in the lower white pumice layer, whereas it occurs as antecrysts surrounded by vesiculated colorless glass in the overlying scoriaceous grayish deposits.

PLAGIOCLASE TEXTURAL AND COMPOSITIONAL FEATURES

Despite core-to-rim profiles on plagioclases of SL present a wide compositional interval [An_{43-80} (**Supplementary Material**)], if the whole length of the transects is considered (ca. 16,629 μm; cf. **Supplementary Material**) most of it (ca. 71%, 11,750 μm) show a main composition ranging An_{60-65} (e.g., **Figure 7A**). This feature highlights the occurrence of a population of An_{60-65} plagioclases crystallizing from the same magma reservoir, with the remaining ca. 30% of crystals being perturbed by the magma dynamics occurring prior and during the eruptive event. For SL eruption, these processes, and the related eruptive scenarios, have been studied through the integration of textural investigations and core-to-rim compositional profiles of plagioclase crystals (**Figure 7**). Such analysis led to the identification of four main plagioclase textures, often coexisting in the same crystal, namely (**Figure 7**): (I) Oscillatory Zoning (OZ); (II) Resorbed Cores/Crystals (RC); (III) Envelopes of Resorption (ER); (IV) crystals with alignments of Melt Inclusions (MI). For each sample, textures of all the plagioclase crystals with an apparent length of the c-axis greater than 500 μm (ca. 2000 crystals) were also identified and classified (**Figure 8**).

Plagioclases with oscillatory zoning (OZ) are characterized by small oscillations of the An content in the compositional interval An_{58-65}, as also suggested by the optical features of the crystal. Core-to-rim compositional profiles have evidenced the presence of two different amplitudes of oscillation of the An content, ranging from $\sim\Delta An_{1-3}$ and $\sim\Delta An_{5-7}$ (**Figure 7**). On the whole, the FeO content exhibits a flat, saw-tooth pattern with very narrow variations (up to 0.3 wt%), which remains constant for the whole profile (**Figure 7A**). Phenocrysts with OZ as unique texture are generally rare, and limited to crystals having a maximum length of 600–700 μm. More frequently, this texture represents only a portion of the crystal. The average compositions of OZ segments range in the narrow interval An_{58-65} (cf. **Supplementary Material** and **Figure 7**), resulting in more or less flat profiles interrupted by peaks or bands of more anorthitic compositions related to other textures (**Figure 7**). In some crystals (e.g., VL18-9 Pl 20; **Figure 7A**), although oscillatory zoning presents very little variations (ΔAn_{1-2}), the final transects present a total decrease of ΔAn_8. The frequency of crystals with only OZ in the whole sequence of SL ranges between 5 and 27%, with an apex reached at the base of the welded layer (VL18-6 and VL18-44 samples) and a progressive decrease toward the top of the succession (**Figure 8**).

Resorbed crystals (RC) of plagioclase are characterized by the resorption of the entire crystals or of most of their cores (**Figure 7B**) and re-crystallization of glass. The degree of resorption is very variable, and results in different textures, from small (10–20 μm) pockets of glass (**Figure 7C**) aligned along the *c*-axis direction, to crystals entirely resorbed and deeply fractured (**Figure 7B**). At the end of the event of resorption, plagioclase texture is again OZ, often super-imposed by other growth/dissolution textures. In the residual portions of the crystal, compositional profiles show a marked saw-tooth pattern of the An content at fairly constant FeO, with variation in the order of ΔAn_{7-10} with respect to the normal An_{60-65} range (**Figures 7B,C**). Although in the considered successions this texture presents a wide range of frequency (2–75%; **Figure 8**), it is dominant only within a bomb at the base of the SL sequence (SL-2 sample, up to 75%). Conversely, it is stable at 20–30% in the upper part of the stratigraphic succession (**Figure 8**), and below 10% in the sequence of Mt. Saraceno East.

Plagioclases affected by the development of Envelopes of Resorption (ER) are characterized by levels (up to 80 μm thick) of dusty sieve-textures arranged along the plagioclase growth planes. In correspondence of the micrometric-sized isolated and/or interconnected "pockets" of glass, compositional variations of An and FeO contents are observed (**Figure 7C**). The envelopes of resorption are located at various regions of the crystal, often proportionally to the size of the crystal: in general, the bigger the crystal, the more internal the envelope. Core-to-rim compositional profiles of plagioclase with ER are generally characterized by an increase of ΔAn_{10-12}, which generates An peaks up to An_{72-79}. FeO content could have a concordant increase (up to 0.6 wt%) or remaining fairly constant. In all the considered volcano-stratigraphic successions, the abundance of this texture increases (from 10 to 35%) from the bottom to the top of the deposit (**Figure 8**).

Oscillatory zoning is often super-imposed by alignments of Melt Inclusion (MI) (**Figure 7D**). These layers are characterized by thin (few micrometers) alignments of inclusion of melt, presenting different shapes and arranged along crystallographic directions parallel to the growth planes of the crystal (**Figure 7D**). In correspondence of the alignment of MI a strong increase in the An content (up to ΔAn_{15}) at constant FeO (**Figure 7E**) is observed. When MI alignments and ER textures occur in the same crystal, MI are always in more internal position. Furthermore, more than one envelope of MI can be found within a single crystal (up to 7 in VL18-6 and VL18-51 samples). This texture is by-far the more abundant within all the considered samples (**Figure 8**). In particular, it is dominant in the samples at the bottom of the succession (up to 79%) and tends to decrease its abundance toward the top of the deposit (**Figure 8**).

DISCUSSION

Plagioclase Textures vs. Pre-eruptive Dynamics

During the last 20 years, the technological advancement of microanalytical investigations of volcanic products shed

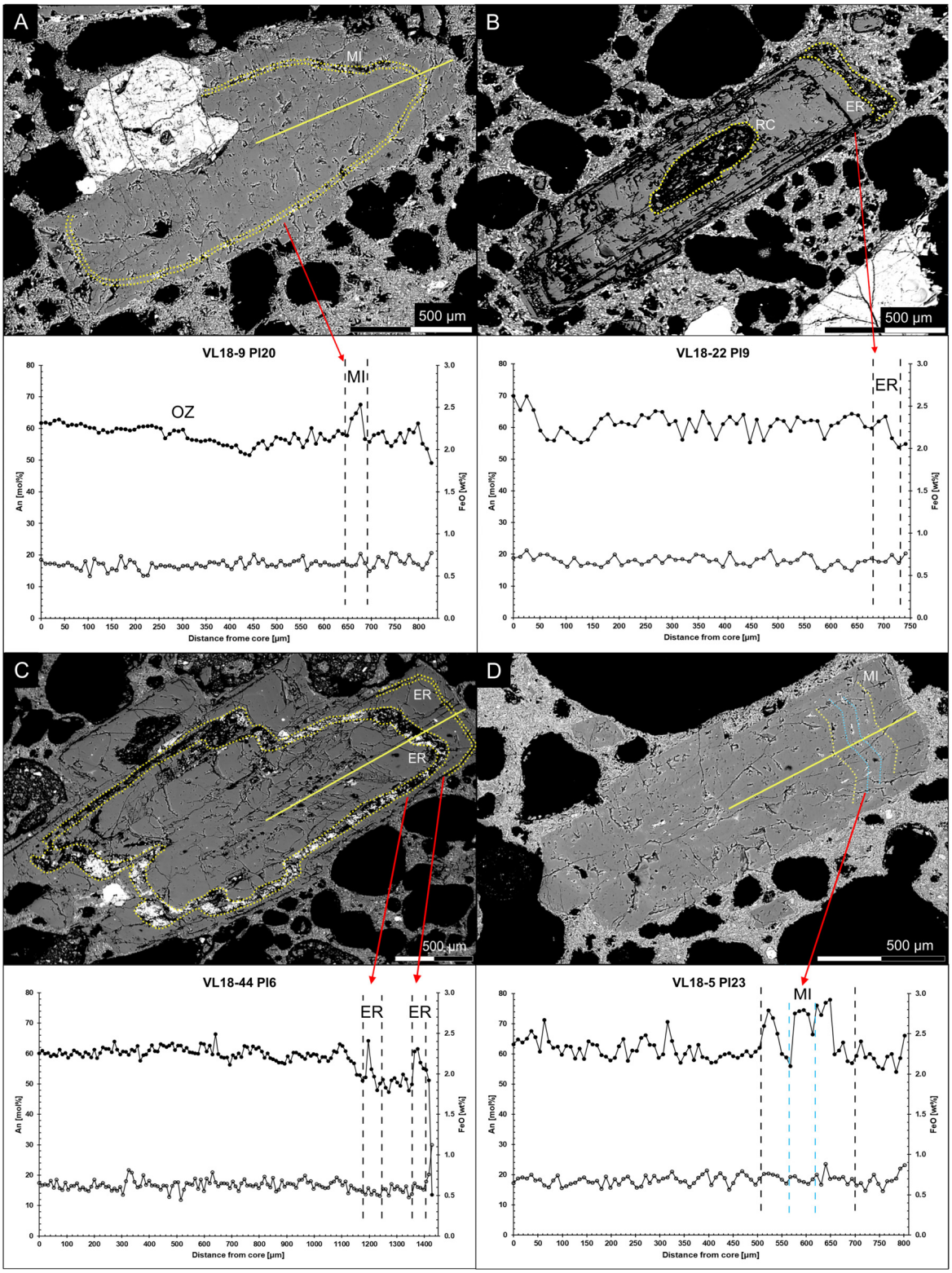

FIGURE 7 | High-contrast and back-scattered images of some representative plagioclase crystals, together with their core-to-rim EMPA/WDS profiles (steps of 5–10 µm). **(A)** Oscillatory zoned (OZ) plagioclase with Melt Inclusion Layers (MIL): in correspondence of the inclusions a peak of $\sim\Delta An_{10}$ is registered, at fairly constant FeO. **(B)** Plagioclase showing a Totally Resorbed Core (TRC) and Enveloped Rims (ER) textures. **(C)** Mildly resorbed Plagioclase crystals (MRC) with a coarsely sieved core, characterized by two layers of ER. **(D)** Plagioclase crystal with three layers of melt inclusions toward the rim of the crystal.

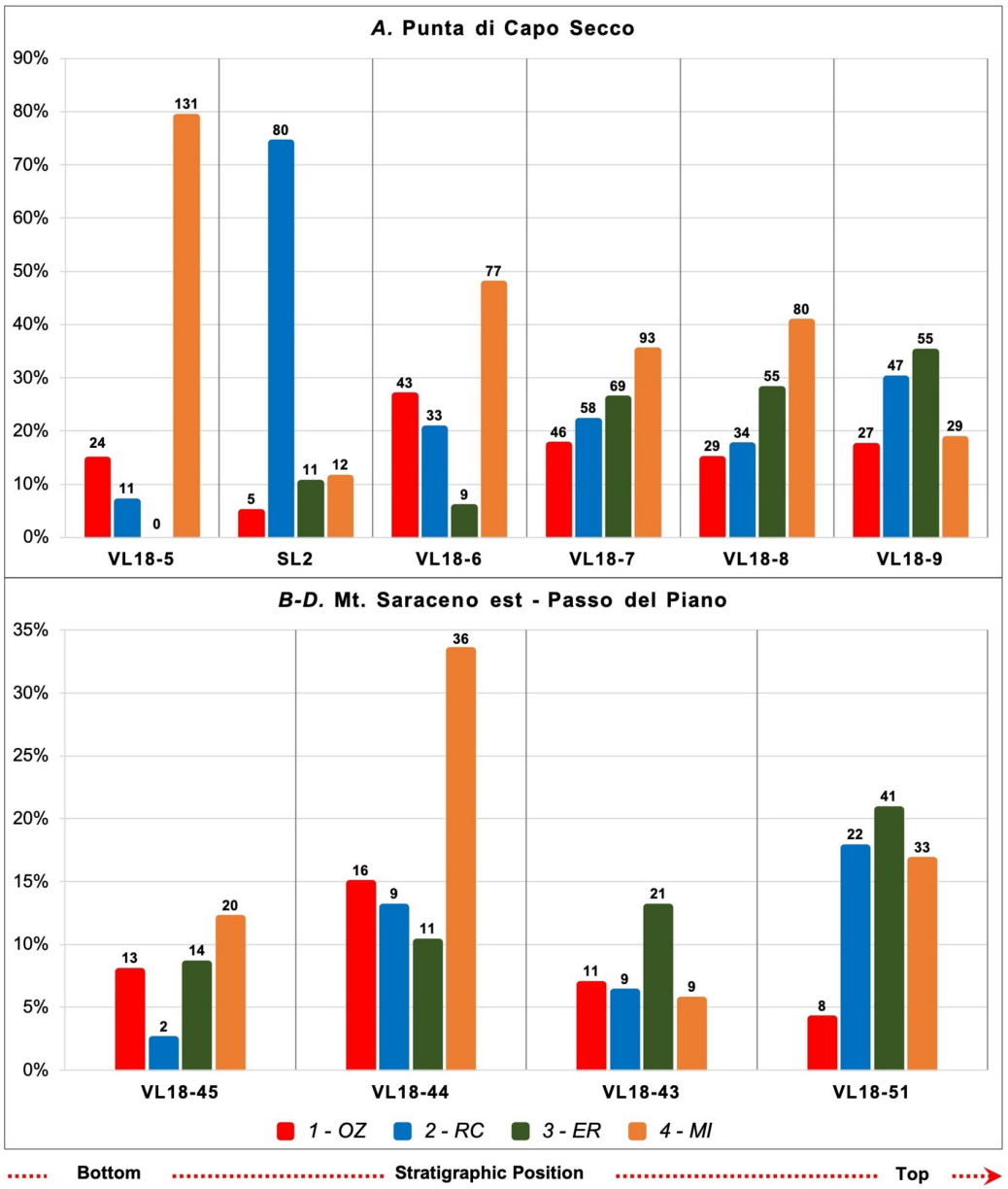

FIGURE 8 | Frequency of phenocrysts (>500 μm) plagioclase textures in the samples of each eruptive unit. Numbers above each histogram represent the number of counted crystals.

light on the way of how magmas store, rise up and interact with other magmas prior and during an eruption (Nelson and Montana, 1992; Pearce, 1994; Singer et al., 1995; Davidson and Tepley, 1997; Clynne, 1999; Streck, 2008; Viccaro et al., 2010, 2016; Kahl et al., 2013; Di Muro et al., 2014; Nicotra et al., 2014, 2018; Ubide and Kamber, 2018; Di Stefano et al., 2020). Indeed, the main phenocrystic phases such as plagioclase, clinopyroxene, olivine, and oxides develop specific textures as a response to any little change of physical and chemical conditions of melts (P-T-X-H_2O) in which they are crystallizing (Anderson, 1984; Kawamoto, 1992; Nelson and Montana, 1992; Pearce, 1994; Singer et al., 1995; Davidson and Tepley, 1997; Clynne, 1999; Tepley et al., 1999; Streck, 2008; Viccaro et al., 2010, 2016; Kahl et al., 2013; Nicotra and Viccaro, 2012a,b; Nicotra et al., 2014, 2018; Ubide and Kamber, 2018). Although a lot of work is still needed, the *routinary* utilization of this microanalytical investigation within the process of analysis of an eruptive event could give an important effort to the assessment and mitigation of volcanic risk. In this paper we use textural and compositional analysis on plagioclase crystals in order to relate the volcanological features observed in the SL welded scoriae at Vulcano island with the pre- and syn-eruptive processes leading

to their formation. Textural and compositional analysis on the welded scoriae of Spiaggia Lunga allowed the identification of four main plagioclase textures (**Figure 7**), namely: (I) Oscillatory Zoning; (II) Resorbed crystals; (III) Envelopes of resorption; (IV) Crystals with alignments of melt inclusion.

Oscillatory zoning (OZ) in plagioclase crystals is characterized by small oscillations of the An content ($<\Delta An_7$) at fairly constant FeO (**Figure 7A**). In the welded scoriae of SL, two different patterns of oscillations have been found ($\sim\Delta An_{2-3}$ and $\sim\Delta An_{5-7}$). The development of this growth texture in plagioclase does not automatically imply significant modifications in chemical and physical parameters of the magmatic system (Allègre et al., 1981; Ortoleva, 1990; Streck, 2008; Nicotra and Viccaro, 2012b). Small amplitude oscillations can be attributed to crystallization kinetics at the crystal/melt interface within a system not affected by significant changes in chemical and physical conditions (cf. Allègre et al., 1981; Ortoleva, 1990; Streck, 2008). Oscillations characterized by larger amplitude (at the same wavelengths) can be instead associated to small changes of the physical and chemical conditions of the magmatic system, but not sufficient to develop major dissolution episodes (Cashman, 1990; Ortoleva, 1990; Pearce and Kolisnik, 1990; Streck, 2008; Viccaro et al., 2010, 2012; Nicotra and Viccaro, 2012a,b; Nicotra et al., 2018). This type of oscillatory zoning is typical of magma reservoirs with small physical (chiefly temperature) and chemical (chiefly H_2O concentrations) gradients, which can trigger fast (but limited) movements of the crystal within the system, and then the development (sometimes) of crenulated surfaces attributed to minor episodes of dissolution (cf. Pearce and Kolisnik, 1990; Singer et al., 1995; Nicotra and Viccaro, 2012a). Summarizing, OZ is a plagioclase texture which can be related to "quiet" conditions of crystallization. The OZ profile of plagioclase VL18-9 Pl20 (in the high part of the SL sequence; **Figures 5**, **7A**), suggests that the magma reservoir in which plagioclase crystallized was not significantly recharged by more primitive magma coming from depth for most of its crystallization history. This is testified by the almost constant decrease from An_{65} to An_{57} in the first half of the profile (**Figure 7A**), with a constant rate ($<\Delta An_{1-2}$). So, for half of its crystallization history, this plagioclase crystallized with compositions ranging An_{57-65} in a magma reservoir which was cooling at fairly constant P-T-X-H_2O conditions.

When magma reservoirs experience major physical perturbations, plagioclase registers the changes of the system through the development of disequilibrium textures, sometimes coupled with compositional changes (Nelson and Montana, 1992; Singer et al., 1995; Davidson and Tepley, 1997; Streck, 2008). Experimental petrology has shown that increased ascent rates reduce the stability field of plagioclase at water-undersaturated and isothermal conditions, provoking its resorption (Nelson and Montana, 1992; Pearce et al., 1987; Streck, 2008). In the welded scoriae of SL, resorbed crystals (RC) of plagioclase could be therefore attributed to a more or less rapid transfer of their host magma within water-undersaturated portions of the plumbing system, and without significant loss of heat during the ascent. Considering that at Vulcano island, for similar whole rock composition, plagioclase would start to crystallize at a depth of 11 km (310–290 MPa; Nicotra et al., 2018), and that the depth of exsolution of H_2O has been calculated at 5 km (130 MPa) by Mandarano et al. (2016), RC plagioclase of SL would have acquired their resorption texture in this pressure interval. Our data do not allow to be more precise about the depth of the mid-crustal reservoir, so we will consider it located between 5 and 11 km of depth. In addition, the observed variability of the degree of dissolution/resorption within the RC plagioclase should be directly proportional to the different ascent rates experienced by the host magma (cf. Nelson and Montana, 1992 and below in the text). The observed coexistence, within the same rock sample of SL, of a wide variability of resorption textures in plagioclase crystals supports the idea of different inputs of fresh magma at different ascent rates from the reservoir located at 11–5 km of depth toward a shallower one. Plagioclase crystals characterized by resorption core surrounded by OZ texture growth (**Figure 7B**) suggest that, prior to the eruption, magma stopped and ponded in the shallow (ca. 5 km b.s.l.) reservoir.

Relationships between the resorption of plagioclase and the ascent rate have been experimentally investigated by Nelson and Montana (1992). These authors empirically related the decompression underwent by magmas at undersaturated-water conditions with the approximate percentages of resorption (i.e., resorption channel and formation of coarse glassy pockets and sieve-textures) observed in plagioclase. If the resorption areas scales with crystal size, considering that: (I) the sizes of SL phenocrysts are about 10–15 times greater than that of the experimental ones, (II) the resorption occurs in an interval of pressure between 300 and 130 MPa, and (III) the approximate area of resorption represents 10–35% of the entire crystal, it could be inferred, using the formulae of Nelson and Montana (1992), that RC texture is acquired within an interval of 2–3 days. Magmas would have rose up between 11 and 5 km with an ascent rate ranging 0.023–0.034 m/sec. Although this range of ascent rates is only indicative, it seems reasonable considering the eruptive scenario of SL and similar results obtained in other tectonic contexts (cf. Browne and Szramek, 2015).

Plagioclase of SL show also Envelopes of Resorption (ER) characterized by layers of dusty sieve-textures (**Figure 7**). Compositional core-to-rim profiles have highlighted that the Envelopes of Resorption correspond to a concordant increase of An and FeO or only an increase of An (ΔAn_{10-12}) at fairly constant FeO. This texture is related to sudden changes in the chemical and physical conditions of the host magma, and is classically associated with the injection of hotter magma, with similar or slightly more basic composition (e.g., Tsuchiyama, 1985; Nakamura and Shimakita, 1998; Streck, 2008; Nicotra and Viccaro, 2012a,b). Therefore, plagioclase with an increase of An and FeO contents in correspondence of the sieve texture envelopes (**Figure 7C**) experienced the injection and mixing of a slightly more basic magma from depth, able to change the FeO content, which typically reflects changes in composition of the system. When the increase of An is accompanied by fairly constant FeO content, the magma that is intruding and mixing with the residing one presents a rather similar composition (as in the case of the SL eruption; cf. **Figure 4**), but its higher volatile elements content and temperature lead to the crystallization of

more An-rich layers of plagioclase: such process is known in literature as cryptic mixing (Nicotra and Viccaro, 2012a; Nicotra et al., 2018; Pizarro et al., 2019). ER textures in plagioclase of SL are usually followed by a OZ "shell," suggesting that the ingress of a new magma into the SL system cannot be considered the trigger of the eruptive event itself. Conversely, the injected magma had enough time to mix with the resident one and be progressively erupted.

One of the most abundant textures within SL plagioclase is that characterized by alignment of Melt Inclusions (MI), super-imposed to oscillatory zoning and presenting a strong increase in the An content (up to ΔAn_{15}) at constant FeO (**Figure 7D**). Present-day literature is still not exhaustive about the mechanisms of entrapment of melt inclusion in plagioclase in such arrangements. This is mainly due to the fact that each inclusion can have different shapes, each with a different petrologic significance (Bennett et al., 2019). In the SL welded scoriae plagioclase, at least two different magma dynamics could be associated to the observed compositional changes in correspondence of MI alignments: (I) a sudden depressurization event in the magma reservoir in which plagioclase were crystallizing (cf. Ustunisik et al., 2014); (II) gas-flushing of the magma chamber where plagioclase were crystallizing, with the gas phase coming from a more deep-seated reservoir. Both processes of decrease of pressure (P) and increase of the water content (P_{H2O}) are able to raise up the An content in the crystallizing envelopes of plagioclase (Yoder and Tilley, 1962; Nielsen et al., 1995; Bennett et al., 2019). We put forward the idea that the An increase, and the relative MI entrapment, could be attributed to a rapid decompression underwent by the magma reservoir where SL plagioclases were crystallizing. Indeed, MI are ever parallel to the growth planes of the crystals, suggesting that such arrangements are related to phases of rapid crystal growth, able to incorporate small drops of melt (Nielsen et al., 1995; Nicotra and Viccaro, 2012b; Cashman and Blundy, 2013; Bennett et al., 2019). The very fact that up to seven parallel alignments of MI have been found in some crystals (VL18-6 and VL18-51 samples), suggests that the magma plumbing system experienced the same number of decompression events. No evidences have been found about gas flushing, usually preceding the upcoming a more deep-seated magma, into the upper crystallizing magma reservoir. In water-undersaturated portions of the plumbing system, the uprising gas phase is able to be re-dissolved into the ponding shallow magma reservoir, finally leading to the selective enrichment of some elements in the encountered portion (e.g., K, Ti, Fe, Rb, Ba, F, Cl). This process, usually called "volatile-induced differentiation" and also observed in some basaltic s.l. volcanic systems (Rittmann, 1962; Burnham, 1979; Caroff et al., 1997; Greenough et al., 1999; de Hoog and van Bergen, 2000; Ferlito et al., 2008; Nicotra et al., 2010; Mazziotti Tagliani et al., 2012; Nicotra and Viccaro, 2012a), is able to produce visible modification in the whole rock composition of magmas, which is also reflected in the crystallizing mineralogical phase. In the plagioclase case, volatile-induced differentiation would have significantly modified the FeO (for effect of the increased fO_2) content in correspondence of the MI alignments, a feature which is never observed in the SL samples. Furthermore, whole rock compositions at SL are clearly not selectively enriched in some elements, but they are concordant with the observed processes of magma rejuvenation.

How a Caldera-Forming Event Can Develop at Vulcano Island

Multidisciplinary investigations, integrating volcanological field survey, geochemistry, mineral chemistry, and petrology, on the ML-SL-Qu welded scoria deposits at Vulcano island have highlighted some common peculiar features which develop during these events, all occurring along the borders of the caldera of "Il Piano." Although the considered volumes for each eruption are very low (up to 0.1 km^3 for the most voluminous eruptive event; De Rosa et al., 1988), their deposits have been able to mantle specific areas of the calderas, giving some hints about their eruptive mechanisms.

Beyond their location along the volcano-tectonic structures of the island, all the considered eruptions are communed by the similarity of their deposits, represented by basic scoriae blankets from poorly to strongly welded. Volcanological survey has also highlighted the presence, at their base, of an alternance of cross-laminated tuff layers, deposited from dilute PDCs, minor and thin fall layers with accretionary lapilli and a high frequency of country crustal rocks (i.e., leuco-monzogabbro; Faraone et al., 1986), features which relate these deposits to a phreatomagmatic event (cf. Schmincke, 2004). These deposits are all strictly related to the successive (in terms of stratigraphic column; **Figure 5**) welded scoriae, as witnessed by the occurrence, in their upper portion, of bombs and blocks which plastically deformed the soft tuffs. These clasts can be either juvenile bombs or also, in the case of SL, pieces of crustal country rocks carried up during the opening of the eruptive fissure. The location of these eruptive events along the rims of "Il Piano" caldera suggests that magmas, after the initial magma-water interaction phase, were able to reach the surface through the newly formed or re-activated ring faults of this caldera (**Figure 9A**).

Once that the initial phases of the caldera-forming eruptions have been outlined, a deeper insight into the geochemical and petrographic features of the erupted magmas suggests distinctive pre- and syn-eruptive dynamics for each of the analyzed welded scoriae deposits.

Deep Magma Ascent at Monte Luccia (ML)

The welded scoriae of ML (48 kyrs; De Astis et al., 1989) cover the northern and central areas of the island, bordering the northernmost subaerial termination of the "Il Piano" caldera. Field survey suggests that they are produced by a low-intensity strombolian-to-hawaiian activity, with some phases of sustained lava fountaining. A small density-driven scoria flow was also emplaced along the northern flanks over the underlying Primordial Vulcano unit. Unfortunately, the lack of plagioclase crystals in equilibrium with the host magmas did not allow information on the pre-eruptive dynamics of this eruption. Nonetheless, this suggests that the ML welded basaltic scoriae derive from a magma coming from a depth higher than those of nucleation of plagioclase. At Vulcano island, this depth has been calculated at ca. 11 km for magmas with shoshonitic

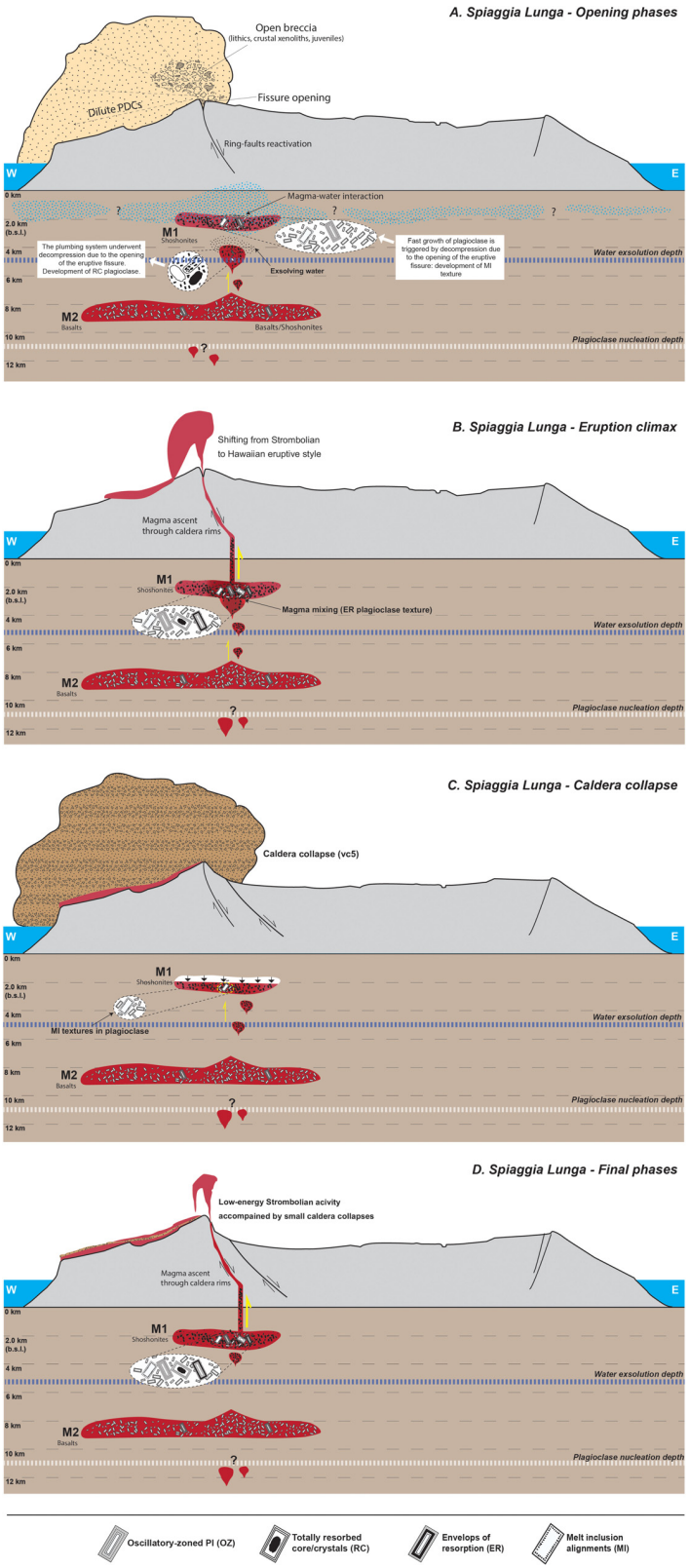

FIGURE 9 | Cartoon showing the different phase of evolution of the Spiaggia Lunga eruption. **(A)** The SL event starts with an phreatomagmatic eruption, where a shallow residing and zoned magma reservoir with shoshonitic/latitic composition interacts with ground- or sea-water. This causes the deposition of the dilute PDCs,

(Continued)

FIGURE 9 | Continued
the formation of the accretionary lapilli, and leads to the opening the eruptive fissure. The magma involved in this initial phase has a shoshonitic composition (M1). The decompression on the system provokes the starting of magma ascent from a water-undersaturated portion of the feeding system (M2, basaltic in composition). During this ascent, RC texture is acquired by plagioclase crystals. **(B)** Onset of the purely magmatic eruption, which starts with a Strombolian eruptive style. The M2 basaltic magma enters into the shallow M1, and efficiently mixes with it. The ingress of a slightly hotter, volatile-rich and more basic magma causes the development of ER texture in plagioclase crystals. The arrival of this new magma at the surface is probably related to the shifting of eruptive style from Strombolian to Hawaiian. The decompression on the system leads to the formation of the MI texture in plagioclase. **(C)** The emptying of the shallow reservoir triggers the collapse of the southern border of the caldera of "Il Piano" (vc5 in De Astis et al., 2013). The deposits of this collapse are evident along the southern flanks of Vulcano island, interlayered within the SL welded scoriae. Such decompression event leads to fast growth of plagioclase and formation of plagioclase with MI textures. **(D)** After the major event, small minor collapses are registered by plagioclase crystals. Eruptive activity turns into strombolian until the end of the eruption.

affinity by means of MELTS simulations (cf. Nicotra et al., 2018). The presence of a deep basaltic/shoshonitic reservoir active throughout the entire eruptive history of Vulcano island has been proposed by several authors, which located it close to the Moho discontinuity (18–21 km b.s.l.; e.g., Zanon et al., 2003; Davì et al., 2009; De Astis et al., 2013; Nicotra et al., 2018). At this stage it is not possible to have more insights about the mechanisms which triggered the ascent of this deep-seated magma. Nonetheless, the similar eruptive dynamics with SL and Qu events (starting with phreatomagmatic eruptions and ascent of magma through the ring-faults of "Il Piano" caldera) can lead to the speculation of a fast magma ascent due to a sudden event of decompression of the plumbing system, similarly to what happened during the SL eruption (see below). However, a hypothesis of eruptive event as response of the ascent of a deep-seated magma (similar to what observed by Nicotra et al., 2018, for the present-day magma at "La Fossa") cannot be ruled out for ML eruption. The area of Monte Luccia (**Figure 1**) was successively cut by the vc4 volcano-tectonic collapse of De Astis et al. (2013).

Spiaggia Lunga as Archetype Caldera-Forming Event at Vulcano

The eruptive event of SL is by far the archetype of the caldera-forming eruptions at Vulcano island, mainly thanks to the higher volume of erupted products (0.1 km^3) and the good exposure of its deposits. In addition, the occurrence of an important and plagioclase-dominated crystal cargo (P.I. 35 vol%) allowed the reconstruction of the pre- and syn-eruptive scenarios of this event. As testified by the geological survey, the first phase of the eruption is represented by a phreatomagmatic phase (**Figure 9A**): at "Punta di Capo Secco" (**Figures 1**, **3**, **5**), the associated dilute PDCs deposits reach 4 m of thickness, which can be related to a medium-energy event. The cross-laminated structure of the deposits is studded, at its top, by a great amount (about 30 vol%) of bomb-sags, made up by juvenile and xenolitic (crustal and volcanic) clasts. They give a direction of provenance of 110°E, which points toward the southwestern-most rim of the "Il Piano" caldera. Among the crustal xenoliths, those with leuco-monzogabbroic composition are the most abundant: given their very shallow position into the crustal portion beneath Vulcano island [ca. 1350 m b.s.l.; Faraone et al. (1986)], these products can be considered as a breccia related to vent opening. We put forward the idea that the magma reservoir activated and involved into these initial stages (M1 in **Figure 9A**) had a shoshonitic composition (**Figure 6** and **Table 1**) and would be located at ca. 2 km b.s.l. of depth, i.e., the depth of provenance of the lithics of leuco-monzogabbros (Faraone et al., 1986). So, the onset of the eruption would be provoked by the interaction of magma residing at ca. 2 km b.sl. and phreatic water, generating a phreatomagmatic event along the pre-existing fractures/faults of the caldera of "Il Piano."

The vent opening-breccia deposits could be related to a second more energetic phase of the SL eruption, in which the eruptive fissure suddenly widened as a consequence of the re-activation of the ring-faults of the "Il Piano" caldera (**Figure 9A**). This volcano-tectonic event would be able to provoke a decompression wave propagating downward in the magmatic plumbing system (**Figure 9A**), as testified by the formation of MI texture on the An_{60-65} plagioclase, which was crystallizing in the shallow shoshonitic M1 reservoir (**Figure 9A**). The rapid decompression event was registered by the plagioclase of the shoshonitic ballistic bombs producing bomb-sags at the top of the dilute PDC deposits (MI = 79% in VL18-5 sample; **Figures 5**, **8**).

The opening of the eruptive fissure would have also provoked the ascent of a more basic magma which was residing in a reservoir, located between 5 km (the exsolution depth of water; cf. Mandarano et al., 2016) and 11 km (plagioclase nucleation depth; Nicotra et al., 2018; M2 in **Figure 9A**). The ascent of magma from the M2 reservoir, at water under-saturated conditions, would have been able to form the RC texture in the plagioclase of SL eruption (RC = 74% in SL2 sample; **Figures 8**, **9A**). The M1 shoshonitic magma then reached the surface with the onset of a low-energy strombolian activity of lava fountaining (**Figure 9B**).

The gradual involvement, within the course of the eruption, of a deeper reservoir (M2) with magmas of more mafic compositions, hotter and richer in volatiles, is testified by numerous factors. Firstly, the evidence of a gradual increase (from 6 to 35%) of dusty sieve-textured plagioclase (ER texture; **Figures 7C**, **8**) from the bottom to the top of the SL stratigraphic column of "Punta Capo di Secco" (**Figure 5**). As previously stated, ER texture is related to the ingress of a slightly more basic, hotter and volatile-rich magma (the M2 in this case) into the system (**Figure 9B**), able to increase both An and FeO content in the plagioclase compositional profiles (**Figure 7**). Secondly, the whole rock compositions at Punta Capo di Secco (**Figure 6C**) outlining that: (i) the SL eruption starts with the emission of shoshonitic products (SiO_2 = 50.3–50.9 wt%, K_2O = 2.84–2.99 wt%; **Figure 6C** and **Table 1**); (ii) the eruption continues without changing the compositions of the magmas up to the main phase of the eruption, which produced the welded central part of the succession (VL18-6, VL18-7, and VL18-8; SiO_2 = 51.4–51.7 wt%, K_2O = 2.73–3.09 wt%; **Figure 6C** and **Table 1**), and (iii) only in

the final stage of the eruption the more basic (basaltic) magma is emitted forming the upper portion of the SL deposits ($SiO_2 < 49$ wt%, $K_2O < 2.8$ wt%; **Figure 6C** and **Table 1**). This suggests that the M2 basaltic magma entered into the system during the course of the eruption and efficiently mixed with the residing M1 (**Figure 9B**), leading to a progressive shifting of whole rock compositions toward more basic terms (**Figure 6C**). Such magma recharge/rejuvenation from the bottom to the top of the succession has been already evidenced by De Rosa et al. (1988). The efficient mixing, and subsequent arrival at the surface of this hotter and more basic magma probably led to the craterization of the eruptive fissure (as proposed by De Rosa et al., 1988) and determined the change of eruptive style from Strombolian to Hawaiian, with an increase of the emission rate witnessed by the extreme welding of the ejected spatter and bombs (**Figure 9B**).

The involvement of the M2 reservoir seems therefore to be related to the occurrence of shallow volcano-tectonic processes, which re-activated, at least, a portion of the plumbing system beneath Vulcano island. This is the opposite of what found by Nicotra et al. (2018) who, analyzing the volcanic activity of the last 1000 years at "La Fossa" and "Vulcanello," have highlighted that the initial trigger of the processes leading to eruptions would be related to the ascent of "fresh" basaltic/shoshonitic magma from the Moho. Nonetheless, the plumbing systems of "La Fossa" and "Il Piano" present very different features, mainly due to a temporal evolution of the systems, which are able to deeply change the dynamics of magma ascent and storage. At "La Fossa," several authors highlighted the occurrence of a polybaric and rather articulated plumbing system, formed by (at least) four different reservoirs located at different depths (cf. Clocchiatti et al., 1994; Zanon et al., 2003; De Astis et al., 2013; Mandarano et al., 2016; Nicotra et al., 2018); each magma reservoir would have a different composition within the range between basalts and rhyolites (cf. Nicotra et al., 2018 and references therein). The "Il Piano" plumbing system is certainly less evolved than "La Fossa" one, at least in terms of the compositions of magmas involved between 48 and 21 kyrs (latites are the most differentiated erupted products). In our reconstruction (**Figure 9**) latitic magmas would be located within the shallow M1 reservoir (2 km b.s.l.), which at "La Fossa" is actually occupied by a degassed rhyolitic magma. The plumbing system of "Il Piano" would be also slightly less articulated, as one of the four reservoirs of "La Fossa" would lack (cf. Clocchiatti et al., 1994; Zanon et al., 2003; De Astis et al., 2013; Mandarano et al., 2016; Nicotra et al., 2018).

Within the stratigraphic column of SL, the main caldera-forming event is testified by 1 m thick layer of chaotic breccia (**Figure 5**), found (with variable thickness) all over the western flank of the "Il Piano" Caldera. The trigger of the caldera collapse is inferred to be the partial emptying of the M1 shallow magma reservoir (**Figure 9C**). Considering the stratigraphic position of the epiclastic deposits occurring at the top of the stratigraphic succession and above the strongly welded deposits (**Figure 5**), we suggest that the caldera collapse can be due to several concurring causes, involving (I) the possible high eruption rate of the "lava-like" Hawaiian phase of the SL eruption and (II) the absence of correlation of this phase with the input of fresh mafic magma from the deeper reservoir. After this major event of collapse along the ring faults of the "Il Piano" caldera, the eruption continued with a decreasing output rate and a shifting toward low-energy strombolian activity (**Figure 9D**). This is testified by the lower degree of welding of the last-emitted products in correspondence of "Capo Secco" (**Figures 3A,D**). During the last phases of SL eruption, small decompression events of fissure opening (**Figure 9D**) are registered by plagioclase crystals, with the development of up to 3 layers of melt inclusions (ever after the envelop of resorption; **Figure 7D**).

Late Re-activation of "Il Piano" Caldera at Quadrara

Quadrara eruptive event (ca. 21 kyrs; Soligo et al., 2000) shows different eruptive dynamics with respect to the Monte Luccia and Spiaggia Lunga eruptions. Although Quadrara's eruption also begins with a phreatomagmatic phase (**Figure 4**), it continues with a thin (0.2–1 m) layer of fall-deriving and biotite-bearing white pumices having latitic compositions (**Figure 6**). The presence of biotite implies the occurrence of an isolated magma reservoir, where the increase of volatile pressure allowed the crystallization of this hydrous mineral phase and where the magma evolved to latitic compositions (**Figure 6**). On the basis of the stratigraphic and physical continuity of the PDC dilute deposits and the overlying pumices, we hypothesize that the onset of the shallow phreatomagmatic activity would have led to the self-activation of the plumbing system. The latitic magma would have been able to rise up through the old ring faults of the Caldera of "Il Piano," giving rise to a typical fall eruption and the deposition of white-to-grayish pumices. The occurrence of a small caldera collapse is here evidenced by a cm-thick epiclastic layer, followed by a grayish-to-black scoria blanket with compositions ranging from latitic to shoshonitic toward the top of the deposit. Such variation could be related, as in the SL eruption, to the retrieval of a basaltic deep magma from the Moho discontinuity, which mixed with the latitic residing one.

CONCLUSION

The integration of a detailed volcanological field survey with geochemistry and textural and compositional investigations on plagioclase crystals allowed to shed light on the pre- and syn-eruptive dynamics of some eruptive events producing welded scoriae associated to small caldera collapses at Vulcano island.

The main points to be remarked are:

I. Between 48 and 21 kyrs the ring-faults and fissures of the caldera of "Il Piano" were the main locus of volcanic activity at Vulcano island. The three most important eruptions of this period [Monte Luccia (ML), Spiaggia Lunga (SL), and Quadrara (Qu)] are characterized by the emplacement of blankets of strongly welded scoriae.
II. All the three considered eruptions started with a phreatomagmatic phase, able to deposit some dilute PDCs and thin fall layers. At the end of this phase, open-breccia deposits and juvenile bombs deformed these underlain still soft deposits.

III. At Monte Luccia, the oldest among the studied eruption, the phreatomagmatic phase and, probably, the widening of the northern caldera faults would have enhanced the ascent of a shoshonitic magma from a reservoir located below the nucleation depth of plagioclase (ca. 11 km at Vulcano). However, a hypothesis of a direct ascent of a deep-seated magma as trigger of the eruptive events cannot be ruled out for ML eruption. This magma rose up directly to the surface, producing Hawaiian to Strombolian eruptive activity.

IV. At Spiaggia Lunga, magmas involved into the phreatomagmatic phase (M1) had a shoshonitic compositions and were residing at 2 km b.s.l., generating plagioclase with OZ texture and An_{60-65} compositions. The decompression due to the volcano-tectonic event formed the MI alignment textures in plagioclase of the M1 reservoir, and caused the ascent of a deep-seated (5–11 km) magma (M2) of basaltic composition. During the ascent, Resorbed Crystal texture formed in plagioclases.

The M2 basaltic magma progressively entered into the M1 reservoir, and gradually mixed with it, as testified the formation of the Envelope of Resorption (ER) texture in plagioclase and by the tendency of whole rock compositions to be more basic from the bottom to the top of the eruptive sequence. The involvement of such more basic magma is also suggested in the shifting of the eruptive style of the eruption, from a low-energy Strombolian to a Hawaiian.

The collapse of the south-western border (vc5 in De Astis et al., 2013) of the "Il Piano" caldera would be therefore the effect of a rapid emptying of the shallow M1 magma reservoir, due to possible high eruption rates during the "lava-like" phase not accompanied by a new input of magma coming from the M2 deep reservoir, which would have been able to re-pressurize the system.

V. At the base of the Quadrara deposits, the occurrence of white latitic pumices layer containing biotite suggests that the eruption started from a shallow, isolated reservoir, where the increase of volatile pressure allowed the crystallization of hydrous phases. A deeper shoshonitic magma was then involved in the last stages on the eruption, forming a scoria level at the top of the sequence.

Results of our study also highlight that the textural and compositional investigations on plagioclase crystals, but also of other phenocrystic phases like pyroxene and olivine, integrated with volcanological s.l. observations and with petrologic monitoring, can contribute to the evaluation and mitigation of volcanic risk through the understanding of how an eruptive scenario will develop.

DATA AVAILABILITY STATEMENT

All datasets generated for this study are included in the article/**Supplementary Material**.

AUTHOR CONTRIBUTIONS

MM executed the textural investigations and compositional profiles of plagioclase crystals, with the scientific support of EN. EN elaborated the resulting data, conceived the model of evolution of the eruptive events. EN wrote the manuscript with the contribution of PD and MM (figures and tables). RD found and managed the funds which allowed this research, and contributed in the elaboration of the model of evolution of the considered eruptive events. All authors performed the volcanological survey and associated rock sampling.

FUNDING

This work was supported by the 2012–2014 DPC-INGV V3 Project grant no. INGV-V3/UR5 (Project Coordinator RD). EN was supported by a *post doc* fellowship from the University of Calabria, title "Dynamics and timescales of magma ascent and storage processes in the Lipari and Vulcano feeding system."

ACKNOWLEDGMENTS

We thank Prof. Mauro Rosi, Dr. Fabio Speranza, Arianna Beatrice Malaguti, and Ilaria Tubia for their help and useful discussions during the field work. We are grateful to Dr. Giancarlo Niceforo and Mariano Davoli for their precious help in the XRF and EMPA analyses, respectively. We also thank the Guest Associate Editor Marc-Antoine Longprè, and two reviewers for their appropriate and useful comments to the first version of the manuscript.

SUPPLEMENTARY MATERIAL

The Supplementary Material for this article can be found online at: https://www.frontiersin.org/articles/10.3389/feart.2020.00223/full#supplementary-material

REFERENCES

Albert, P. G., Giaccio, B., Isaia, R., Costa, A., Niespolo, E. M., Nomade, S., et al. (2019). Evidence for a large-magnitude eruption from Campi Flegrei caldera (Italy) at 29 ka. *Geology* 47, 595–599. doi: 10.1130/g45805.1

Allègre, C. J., Provost, A., and Jaupart, C. (1981). Oscillatory zoning: a pathological case of crystal growth. *Nature* 294, 223–228. doi: 10.1038/294223a0

Andersen, N. L., Singer, B. S., Jicha, B. R., Beard, B. L., Johnson, C. M., and Licciardi, J. M. (2017). Pleistocene to holocene growth of a large upper crustal rhyolitic magma reservoir beneath the active laguna del maule Volcanic field, Central Chile. *J. Petrol.* 58, 85–114. doi: 10.1093/petrology/egx006

Anderson, A. T. (1984). Probable relations between plagioclase zoning and magma dynamics, Fuego volcano, Guatemala. *Am. Mineral.* 69, 660–676.

Annen, C., and Sparks, R. S. (2006). Effects of repetitive emplacement of basaltic intrusions on thermal evolution and melt generation in the crust. *Earth Planet. Sci. Lett.* 203, 937–955. doi: 10.1016/s0012-821x(02)00929-9

Barberi, F., Gandino, A., Gioncada, A., La Torre, P., Sbrana, A., and Zenucchini, C. (1994). The deep structure of the Eolian arc (Filicudi-Panarea-Vulcano sector)

in light of gravity, magnetic and volcanological data. *J. Volcanol. Geoth. Res.* 61, 189–206. doi: 10.1016/0377-0273(94)90003-5

Barberi, F., Innocenti, F., Ferrara, G., Keller, J., and Villar, L. (1974). Evolution of aeolian Arc volcanism (southern Tyrrhenian Sea). *Earth Planet. Sci. Lett.* 21, 269–276. doi: 10.1016/0012-821x(74)90161-7

Bennett, E. N., Lissenberg, C. J., and Cashman, K. V. (2019). The significance of plagioclase textures in mid-ocean ridge basalt (Gakkel Ridge, Arctic Ocean). *Contrib. Mineral. Petr.* 174, 49.

Browne, B., and Szramek, L. (2015). "Rates of magma ascent and storage," in *The Encyclopedia of Volcanoes*, 2nd Edn, eds H. Sigurdsson, B. Houghton, S. McNutt, H. Rymer, and J. Stix (London: Academic Press), 203–214. doi: 10.1016/b978-0-12-385938-9.00009-2

Burnham, C. W. (1979). "Magmas and hydrothermal fluids," in *Geochemistry of Hydrothermal Ore Deposits*, 2nd Edn, ed. H. L. Barnes (Hoboken, NJ: John Wiley and Sons), 71–136.

Caroff, M., Ambrics, C., Maury, R. C., and Cotten, J. (1997). From alkali basalt to phonolite in hand-size samples: vapor-differentiation effects in the Bouzentes lava flow (Cantal, France). *J. Volcanol. Geoth. Res.* 79, 47–61. doi: 10.1016/s0377-0273(97)00023-1

Cashman, K., and Blundy, J. (2013). Petrological cannibalism: the chemical and textural consequences of incremental magma body growth. *Contrib. Mineral. Petr.* 166, 703–729. doi: 10.1007/s00410-013-0895-0

Cashman, K. V. (1990). "Textural constraints on the kinetics of crystallization of igneous rocks," in *Modern Methods of Igneous Petrology: Understanding Magmatic Processes Rev*, Vol. 24, eds J. Nicholls and J. K. Russell (Chantilly, VA: Mineralogical Society of America), 259–314.

Cashman, K. V., and Giordano, G. (2014). Calderas and magma reservoirs. *J. Volcanol. Geoth. Res.* 288, 28–45. doi: 10.1016/j.jvolgeores.2014.09.007

Clocchiatti, R., Del Moro, A., Gioncada, A., Joron, J. L., Mosbach, M., Pinarelli, L., et al. (1994). Assessment of a shallow magmatic system: the 1888–1890 eruption, Vulcano Island, Italy. *Bull. Volcanol.* 56, 466–486. doi: 10.1007/s00445005 0056

Clynne, M. A. (1999). A complex magma mixing origin for rocks erupted in 1915, Lassen Peak, California. *J. Petrol.* 40, 105–132. doi: 10.1093/petroj/40.1.105

Coltelli, M., Del Carlo, P., and Vezzoli, L. (1998). Discovery of a Plinian basaltic eruption of Roman age at Etna volcano, Italy. *Geology* 26, 1095–1098.

Crisci, G. M., De Rosa, R., Esperanca, S., Mazzuoli, R., and Sonnino, M. (1991). Temporal evolution of a three components system: the island of Lipari (Aeolian Arc, southern Italy). *Bull. Volcanol.* 53, 207–221. doi: 10.1007/bf0030 1231

Davì, M., De Rosa, R., Donato, P., Vetere, F., Barca, D., and Cavallo, A. (2009). Magmatic evolution and plumbing system of ring-fault volcanism: the Vulcanello Peninsula (Aeolian Islands, Italy). *Eur. J. Mineral.* 21, 1009–1028. doi: 10.1127/0935-1221/2009/0021-1955

Davì, M., De Rosa, R., and Holtz, F. (2010). Mafic enclaves in the rhyolitic products of Lipari historical eruptions; relationships with the coeval Vulcano magmas (Aeolian Islands, Italy). *Bull. Volcanol* 72, 991–1008. doi: 10.1007/s00445-010-0376-5

Davidson, J. P., and Tepley, F. J. (1997). Recharge in Volcanic systems: evidence from isotope profiles of phenocrysts. *Science* 275, 826–829. doi: 10.1126/science.275.5301.826

De Astis, G., Frazzetta, G., and La Volpe, L. (1989). I depositi di riempimento della caldera del Piano ed i depositi della Lentia. *Bollett. G. N. V.* 2, 763–778.

De Astis, G., La Volpe, L., Peccerillo, A., and Civetta, L. (1997). Volcanological and petrological evolution of Vulcano Island (Aeolian Arc, southern Tyrrhenian Sea). *J. Geophys. Res.* 102, 8021–8050. doi: 10.1029/96jb03735

De Astis, G., Lucchi, F., Dellino, P., La Volpe, L., Tranne, C. A., Frezzotti, M. L., et al. (2013). "Geology, volcanic history and petrology of Vulcano (central Aeolian archipelago)," in *The Aeolian Islands Volcanoes*, Vol. 37, eds F. Lucchi, A. Peccerillo, J. Keller, C. A. Tranne, and P. L. Rossi (London: Geological Society of London), 281–349. doi: 10.1144/m37.11

de Hoog, J., and van Bergen, M. (2000). Volatile-induced transport of HFSE, REE, Th and U in arc magmas: evidence from zirconolite-bearing vesicles in potassic lavas of Lewotolo volcano (Indonesia). *Contrib. Mineral. Petr.* 139, 485–502. doi: 10.1007/s004100000146

De Ritis, R., Ravat, D., Ventura, G., and Chiappini, M. (2013). Curie isotherm depth from aeromagnetic data constraining shallow heat source depths in the central Aeolian Ridge (Southern Tyrrhenian Sea, Italy). *Bull. Volcanol.* 75:710.

De Rosa, R., Guillou, H., Mazzuoli, R., and Ventura, G. (2003). New unspiked K-Ar ages of volcanic rocks of the central and western sector of the Aeolian Islands: reconstruction of the volcanic stages. *J. Volcanol. Geoth. Res.* 120, 161–178. doi: 10.1016/s0377-0273(02)00369-4

De Rosa, R., Mazzuoli, R., Frazzetta, G., and La Volpe, L. (1988). The spiaggia lunga scoriae deposits: an example of fissural type eruption at Vulcano (Aeolian Islands, Italy). *Rend. Soc. Ital. Mineral. Petrol.* 43, 1059–1068.

Del Moro, A., Gioncada, A., Pinarelli, L., Sbrana, A., and Joron, J. L. (1998). Sr, Nd, and Pb isotope evidence for open system evolution at Vulcano, Aeolian Arc, Italy. *Lithos* 43, 81–106. doi: 10.1016/s0024-4937(98)00008-5

Di Muro, A., Métrich, N., Vergani, D., Rosi, M., Armienti, P., Fougereox, T., et al. (2014). The shallow plumbing system of Piton de la Fournaise volcano (La Réunion Island, Indian Ocean) revealed by the major 2007 caldera forming eruption. *J. Petrol.* 55, 1287–1315. doi: 10.1093/petrology/egu025

Di Stefano, F., Mollo, S., Ubide, T., Petrone, C. M., Caulfield, J., Scarlato, P., et al. (2020). Mush cannibalism and disruption recorded by clinopyroxene phenocrysts at Stromboli volcano: new insights from recent 2003–2017 activity. *Lithos* 360–361:105440. doi: 10.1016/j.lithos.2020.105440

Ellam, R. M., Hawkesworth, C. J., Menzies, M. A., and Rogers, N. W. (1989). The volcanism of southern Italy: role of subduction and the relationships between potassic and sodic alkaline magmatism. *J. Geophys. Res.* 94, 4589–4601. doi: 10.1029/jb094ib04p04589

Esperança, S., Crisci, G. M., De Rosa, R., and Mazzuoli, R. (1992). The role of the crust in the magmatic evolution of the Island of Lipari (Aeolian Islands, Italy). *Contrib. Mineral. Petr.* 112, 450–462. doi: 10.1007/bf00310777

Fabbro, G. N., Druitt, T. H., and Scaillet, S. (2013). Evolution of the crustal magma plumbing system during the build-up to the 22-ka caldera-forming eruption of Santorini (Greece). *Bull. Volcanol.* 75, 1–22.

Faraone, D., Silvano, A., and Verdiani, G. (1986). The monzogabbroic intrusion in the island of Vulcano, Aeolian Archipelago, Italy. *Bull. Volcanol.* 48, 299–307. doi: 10.1007/bf01081758

Ferlito, C., Viccaro, M., and Cristofolini, R. (2008). Volatile-induced differentiation in the plumbing system of Mt. Etna volcano (Italy): evidence from glass and tephra of the 2001 eruption. *Bull. Volcanol.* 70, 455–473. doi: 10.1007/s00445-007-0149-y

Fontaine, F. R., Roult, G., Michon, L., Barruol, G., and Di Muro, A. (2014). The 2007 eruptions and caldera collapse of the Piton de la Fournaise volcano (La Réunion Island) from tilt analysis at a single very broadband seismic station. *Geophys. Res. Lett.* 41, 2803–2811. doi: 10.1002/2014gl059691

Frezzotti, M. L., Peccerillo, A., Zanon, V., and Nikogosian, I. (2004). Silica-rich melts in quartz xenoliths from Vulcano Island and their bearing on processes of crustal anatexis and crust–magma interaction beneath the Aeolian Arc, Southern Italy. *J. Petrol.* 45, 3–26. doi: 10.1093/petrology/egg080

Gasparini, C., Iannaccone, G., Scandone, P., and Scarpa, R. (1982). Seismotectonics of the Calabrian Arc. *Tectonophysics* 82, 267–286. doi: 10.1016/0040-1951(82)90163-9

Gioncada, A., and Sbrana, A. (1991). La Fossa Caldera, Vulcano: inferences from deep drillings. *Acta Vulcanol.* 1, 115–126.

Greenough, J., Lee, C., and Fryer, B. (1999). Evidence for volatile-influenced differentiation in a layered alkali basalt flow, Penghu Islands, Taiwan. *Bull. Volcanol.* 60, 412–424. doi: 10.1007/s004450050241

Gudmundsson, A. (2012). Magma chambers: formation, local stresses, excess pressures, and compartments. *J. Volcanol. Geoth. Res.* 237-238, 19–41. doi: 10.1016/j.jvolgeores.2012.05.015

Gvirtzman, Z., and Nur, A. (1999). The formation of Mount Etna as the consequence of slab rollback. *Nature* 401, 782–785. doi: 10.1038/44555

Harpp, K. S., and Geist, D. J. (2018). The Evolution of Galápagos Volcanoes: an alternative prospective. *Front. Earth Sci.* 6:50. doi: 10.3389/feart.2018.00050

Jellinek, A., and de Paolo, D. (2003). A model for the origin of large silicic magma chambers: precursors of caldera-forming eruptions. *Bull. Volcanol.* 65, 363–381. doi: 10.1007/s00445-003-0277-y

Kahl, M., Chakraborty, S., Costa, F., Pompilio, M., Liuzzo, M., and Viccaro, M. (2013). Compositionally zoned crystals and real-time degassing data reveal changes in magma transfer dynamics during the 2006 summit eruptive episodes of Mt. Etna. *Bull. Volcanol.* 75:692.

Kawamoto, T. (1992). Dusty and honeycomb plagioclase: indicators of processes in the Uchino stratified magma chamber, Izu Peninsula, Japan. *J. Volcanol. Geoth. Res.* 49, 191–208. doi: 10.1016/0377-0273(92)90014-5

Keller, J. (1980). The island of Vulcano. *Rend. della Soc. Ital. di Mineral. Petrogr.* 3, 369–414.

Kennedy, B., Holohan, E. P., Stix, J., Gravley, D. M., Davidson, J. R. J., and Cole, J. W. (2018). Magma plumbing beneath collapse caldera volcanic systems. *Earth Sci. Rev.* 177, 404–424. doi: 10.1016/j.earscirev.2017.12.002

Mandarano, M., Paonita, A., Martelli, M., Viccaro, M., Nicotra, E., and Millar, I. L. (2016). Revealing magma degassing below closed-conduit active volcanoes: geochemical features of volcanic rocks versus fumarolic fluids at Vulcano (Aeolian Islands, Italy). *Lithos* 248-251, 272–287. doi: 10.1016/j.lithos.2016.01.026

Marsh, B. D. (1996). Solidification fronts and magmatic evolution. *Mineral. Mag.* 60, 5–40. doi: 10.1180/minmag.1996.060.398.03

Mazziotti Tagliani, S., Nicotra, E., Viccaro, M., and Gianfagna, A. (2012). Halogen-dominant mineralization at Mt. Calvario dome (Mt. Etna) as a response of volatile flushing into the magma plumbing system. *Miner. Petrol.* 106, 89–105. doi: 10.1007/s00710-012-0215-9

Nakamura, M., and Shimakita, S. (1998). Dissolution origin and syn-entrapment compositional changes of melt inclusions in plagioclase. *Earth Planet. Sci. Lett.* 161, 119–133. doi: 10.1016/s0012-821x(98)00144-7

Nelson, S. T., and Montana, A. (1992). Sieve-textured plagioclase in volcanic rocks produced by rapid decompression. *Am. Mineral.* 77, 1242–1249.

Nicotra, E., Giuffrida, M., Viccaro, M., Donato, P., D'Oriano, C., Paonita, A., et al. (2018). Timescales of pre-eruptive magmatic processes at Vulcano (Aeolian Islands, Italy) during the last 1000 years. *Lithos* 316-317, 347–365. doi: 10.1016/j.lithos.2018.07.028

Nicotra, E., and Viccaro, M. (2012a). Transient uprise of gas and gas-rich magma batches fed the pulsating behaviour of the 2006 eruptive episodes at Mt. Etna volcano. *J. Volcanol. Geoth. Res.* 22, 102–118. doi: 10.1016/j.jvolgeores.2012.03.004

Nicotra, E., and Viccaro, M. (2012b). Unusual magma storage conditions at Mt. Etna (Southern Italy) as evidenced by plagioclase megacryst-bearing lavas: implications for the plumbing system geometry and summit caldera collapse. *Bull. Volcanol.* 74, 795–815. doi: 10.1007/s00445-011-0566-9

Nicotra, E., Viccaro, M., De Rosa, R., and Sapienza, M. (2014). Volcanological evolution of the Rivi-Capo Volcanic complex at Salina, Aeolian Islands: magma storage processes and ascent dynamics. *Bull. Volcanol.* 76, 840–864.

Nicotra, E., Viccaro, M., Ferlito, C., and Cristofolini, R. (2010). Influx of volatiles into shallow reservoirs at Mt. Etna volcano (Italy) responsible for halogen-rich magmas. *Eur. J. Mineral.* 22, 121–138. doi: 10.1127/0935-1221/2010/0022-1991

Nielsen, R. L., Crum, J., Bourgeois, R., Hascall, K., Forsythe, L. M., Fisk, M. R., et al. (1995). Melt inclusions in high−an plagioclase from the Gorda Ridge: an example of the local diversity of MORB parent magmas. *Contrib. Mineral. Petr.* 122, 34–50. doi: 10.1007/s004100050111

Ortoleva, P. J. (1990). Role of attachment kinetic feedback in the oscillatory zoning of crystal grown from melts. *Earth Sci. Rev.* 29, 3–8. doi: 10.1016/0012-8252(90)90023-o

Pearce, T. H. (1994). "Recent work on oscillatory zoning in plagioclase," in *Feldspars and Their Reactions*, ed. I. Parsons (Dordrecht: Kluwer Academic Publisher), 313–349. doi: 10.1007/978-94-011-1106-5_8

Pearce, T. H., and Kolisnik, A. M. (1990). Observations of plagioclase zoning using interference imaging. *Earth Sci. Rev.* 29, 9–26. doi: 10.1016/0012-8252(0)90024-p

Pearce, T. H., Russel, J. K., and Wolfson, I. (1987). Laser-interference and Nomarski interference imaging of zoning profiles in plagioclase phenocrysts from the May 18, 1980, eruption of Mount St. Helens, Washington. *Am. Mineral.* 72, 1131–1143.

Peccerillo, A., Donati, C., Santo, A. P., Orlando, A., Yirgu, G., and Ayalew, D. (2007). Petrogenesis of silicic peralkaline rocks in the Ethiopian rift: geochemical evidence and volcanological implications. *J. Afr. Earth Sci.* 48, 161–173. doi: 10.1016/j.jafrearsci.2006.06.010

Peccerillo, A., and Frezzotti, M. L. (2015). Magmatism, mantle evolution and geodynamics at the converging plate margins of Italy. *J. Geol. Soc. Lond.* 172, 407–427. doi: 10.1144/jgs2014-085

Peccerillo, A., and Taylor, S. R. (1976). Geochemistry of eocene calc-alkaline volcanic rocks from the Kastamonu Area, Northern Turkey. *Contrib. Mineral. Petr.* 58, 63–81. doi: 10.1007/bf00384745

Pizarro, C., Parada, M. A., Contreras, C., and Morgado, E. (2019). Cryptic magma recharge associated with the most voluminous 20th century eruptions (1921, 1948 and 1971) at Villarrica Volcano. *J. Volcanol. Geoth. Res.* 384, 48–63. doi: 10.1016/j.jvolgeores.2019.07.001

Rittmann, A. (1962). *Volcanoes and Their Activity*. New York, NY: John Wiley & Sons, 305.

Ruch, J., Vezzoli, L., De Rosa, R., Di Lorenzo, R., and Acocella, V. (2016). Magmatic control along a strike-slip volcanic arc: the central Aeolian arc (Italy). *Tectonics* 35, 407–424. doi: 10.1002/2015tc004060

Sainz-Maza Aparicio, S., Martí, J., Montesinos, F. G., Borreguero Gómez, A., Pereda de Pablo, J., Vaquero Fernández, P., et al. (2019). Gravimetric study of the shallow basaltic plumbing system of Tenerife, Canary Islands. *Phys. Earth Planet. Inter.* 297, 106319. doi: 10.1016/j.pepi.2019.106319

Schmincke, H. (2004). *Volcanism*. Berlin: Springer-Verlag, 324.

Singer, B. S., Dungan, M. A., and Layne, G. D. (1995). Textures and Sr, Ba, Mg, Fe, K and Ti compositional profiles in volcanic plagioclase: clues to the dynamics of calc-alkaline magma chamber. *Am. Mineral.* 80, 776–798. doi: 10.2138/am-1995-7-815

Soligo, M., De Astis, G., Delitala, M. C., La Volpe, L., Taddeucci, A., and Tuccimei, P. (2000). Uranium-series disequilibria in the products from Vulcano Island (Sicily, Italy): isotopic chronology and magmatological implications. *Acta Vulcanol.* 12, 49–59.

Streck, M. J. (2008). "Mineral textures and zoning as evidence for open system processes," in *Minerals, Inclusions and Volcanic Processes. Reviews in Mineralogy and Geochemistry*, Vol. 69, eds K. D. Putirka and F. J. III Tepley (Chantilly, VA: Mineralogical Society of America), 595–622. doi: 10.1515/9781501508486-016

Sun, S. S., and McDonough, W. F. (1989). "Chemical and isotopic systematics of oceanic basalts: implications for mantle composition and processes," in *Magmatism in Ocean Basins*, Vol. 42, eds A. D. Saunders and M. J. Norry (London: Geological Society of London), 313–345. doi: 10.1144/gsl.sp.1989.042.01.19

Tepley, F. J. III, Davidson, J. P., and Clynne, M. A. (1999). Magmatic interactions as recorded in plagioclase phenocrysts of Chaos Crags, Lasses volcanic center, California. *J. Petrol.* 40, 787–806. doi: 10.1093/petroj/40.5.787

Tsuchiyama, A. (1985). Dissolution kinetics of plagioclase in the melt of the system diopside-albite-anorthite, and the origin of dusty plagioclase in andesites. *Contrib. Mineral. Petr.* 89, 1–16. doi: 10.1007/bf01177585

Ubide, T., and Kamber, B. S. (2018). Volcanic crystals as time capsules of eruption history. *Nat. Commun.* 9:326.

Ustunisik, G., Kilinc, A., and Nielsen, R. L. (2014). New insights into the processes controlling compositional zoning in plagioclase. *Lithos* 200–201, 80–93. doi: 10.1016/j.lithos.2014.03.021

Ventura, G. (2013). "Kinematics of the Aeolian volcanism (Southern Tyrrhenian Sea) from geophysical and geological data," in *The Aeolian Islands Volcanoes*, Vol. 37, eds F. Lucchi, A. Peccerillo, J. Keller, C. A. Tranne, and P. L. Rossi (London: Geological Society of London), 3–11. doi: 10.1144/m37.2

Ventura, G., Vilardo, G., and Bruno, P. P. (1999). The role of flank collapse in modifying the shallow plumbing system of volcanoes: an example from Somma–Vesuvius, Italy. *Geophys. Res. Lett.* 26, 3681–3684. doi: 10.1029/1999gl005404

Viccaro, M., Barca, D., Bohrson, W. A., D'Oriano, C., Giuffrida, M., Nicotra, E., et al. (2016). Crystal residence time from trace element zoning in plagioclase reveal changes in magma transfer dynamics at Mt. Etna during the last 400 years. *Lithos* 248–251, 309–323. doi: 10.1016/j.lithos.2016.02.004

Viccaro, M., Giacomoni, P. P., Ferlito, C., and Cristofolini, R. (2010). Dynamics of magma supply at Mt. Etna volcano (Southern Italy) as revealed by textural and compositional features of plagioclase phenocryst. *Lithos* 116, 77–91. doi: 10.1016/j.lithos.2009.12.012

Viccaro, M., Giuffrida, M., Nicotra, E., and Ozerov, A. Y. (2012). Magma storage, ascent and recharge history prior to the 1991 eruption at Avachinsky Volcano, Kamchatka, Russia: inferences on the plumbing system geometry. *Lithos* 140–141, 11–24. doi: 10.1016/j.lithos.2012.01.019

Wang, C. Y., Hwang, W. T., and Shi, Y. (1989). Thermal evolution of a rift basin: the Tyrrhenian Sea. *J. Geophys. Res.* 94, 3991–4006. doi: 10.1029/jb094ib04p03991

Yoder, H. S., and Tilley, C. E. (1962). Origin of basalt magmas: an experimental study of natural and synthetic rock systems. *J. Petrol.* 3, 342–532. doi: 10.1093/petrology/3.3.342

Zanella, E., De Astis, G., and Lanza, R. (2001). Paleomagnetism of welded, pyroclastic-fall scoriae at Vulcano, Aeolian Archipelago. *J. Volcanol. Geoth. Res.* 107, 71–86. doi: 10.1016/s0377-0273(00)00298-5

Zanon, V., Frezzotti, M. L., and Peccerillo, A. (2003). Magmatic feeding system and crustal magma accumulation beneath Vulcano Island (Italy): evidence from CO_2 fluid inclusions in quartz xenoliths. *J. Geophys. Res.* 108:2298. doi: 10.1029/2002JB002140

Conflict of Interest: The authors declare that the research was conducted in the absence of any commercial or financial relationships that could be construed as a potential conflict of interest.

frontiers in Earth Science

ORIGINAL RESEARCH
published: 10 July 2020
doi: 10.3389/feart.2020.00256

Zoned Pyroxenes as Prospectivity Indicators for Magmatic Ni-Cu Sulfide Mineralization

Louise Schoneveld[1], Stephen J. Barnes[1], Hannu V. Makkonen[2], Margaux Le Vaillant[1], David J. Paterson[3], Valentina Taranovic[1], Kai-Yuan Wang[4,5] and Ya-Jing Mao[6]*

[1] Mineral Resources, Australian Resources Research Centre, CSIRO, Kensington, WA, Australia, [2] Boliden FinnEx Oy, Sodankylä, Finland, [3] Australian Synchrotron, ANSTO, Clayton, VIC, Australia, [4] State Key Laboratory of Ore Deposit Geochemistry, Institute of Geochemistry, Chinese Academy of Sciences, Guiyang, China, [5] University of Chinese Academy of Sciences, Beijing, China, [6] Key Laboratory of Mineral Resources, Institute of Geology and Geophysics Chinese Academy of Sciences, Beijing, China

Small intrusions dominated by olivine- and pyroxene-rich cumulates are well known to be favorable hosts to magmatic Ni-Cu-(Platinum Group Element—PGE) sulfide mineralization. Such intrusions are common in a variety of settings around the world, but only a very small proportion contain economically exploitable sulfides; these tend to be of conduit or chonolith style. If prospectivity could be discriminated from sparse sampling at early exploration stages, then the discovery rate for deposits of this type could be improved. To this end, a number of pyroxene-bearing samples from small intrusions containing magmatic sulfide deposits have been investigated including the Noril'sk-Talnakh camp in Siberia, the Kotalahti nickel belt in Finland, Ntaka Hill in Tanzania, Nova-Bollinger in the Albany-Fraser Orogen of Australia, Savannah in the Halls Creek Orogen of Australia, Jinchuan in central China, Xiarihamu in Tibet and Huangshanxi in the east Tianshan Ni province of NW China. To compare, samples from unmineralized intrusions in four of these regions were also investigated along with four mafic intrusions from other localities that are not associated with any known economic sulfide mineralization. Using fine-scale (<5 μm/pixel) chemical imaging on the Australian Synchrotron, complex zoning in chromium was found in cumulate and poikilitic pyroxenes within the strongly mineralized intrusions. The zoning patterns can be separated into three distinct types: (1) abrupt zoning: a single change in trace element concentration with a sharp boundary; (2) sector zoning: hourglass style zonation; and (3) oscillatory zoning: small scale oscillations that are usually cyclic. Zoning of all three types can be present in a single grain. The presence of cumulus orthopyroxene with a combination of abrupt zoning, sector zoning and resorbed olivine inclusions has so far only been detected in mineralized intrusions. This combination of zoning patterns is postulated to be an indication of high magma flux and fluctuating cooling rates that accompany wall rock assimilation in dynamic conduits where sulfide liquid forms and accumulates. The distinctive zoning patterns reported here can, in many cases, be easily imaged using desktop microbeam XRF mapping techniques and may provide a useful fertility indicator for the exploration of new magmatic Ni-Cu-(PGE) deposits.

Keywords: clinopyroxene, orthopyroxene, chromium, zoning, XRF, sulfide, exploration

OPEN ACCESS

Edited by:
Maurizio Petrelli, University of Perugia, Italy

Reviewed by:
Cristina Perinelli, Sapienza University of Rome, Italy
Leonid Danyushevsky, University of Tasmania, Australia

****Correspondence:***
Louise Schoneveld
louise.schoneveld@csiro.au

Specialty section:
This article was submitted to Petrology, a section of the journal Frontiers in Earth Science

Received: *30 January 2020*
Accepted: *09 June 2020*
Published: *10 July 2020*

Citation:
Schoneveld L, Barnes SJ, Makkonen HV, Le Vaillant M, Paterson DJ, Taranovic V, Wang K-Y and Mao Y-J (2020) Zoned Pyroxenes as Prospectivity Indicators for Magmatic Ni-Cu Sulfide Mineralization. Front. Earth Sci. 8:256. doi: 10.3389/feart.2020.00256

INTRODUCTION

Magmatic Ni-Cu-sulfide mineralization is often associated with conduit-style or chonolith-style intrusions (Ripley and Li, 2011; Barnes et al., 2017a; Barnes and Robertson, 2019) that contain pyroxenites or other pyroxene-rich cumulates. These pyroxenites, such as those described in Huangshanxi, China (Mao et al., 2019) and Ntaka, Tanzania (Barnes et al., 2016b), commonly contain large, sometimes poikilitic pyroxenes that trap early cumulus olivine and chromite and preserve zoning of Cr (Barnes et al., 2019a). Chromium is highly compatible in pyroxene (Ewart et al., 1973; Barnes, 1986; Hart and Dunn, 1993; Lundstrom et al., 1998; Frei et al., 2009; Schoneveld, 2017) which allows Cr zoning patterns to track changes in magma chemistry during pyroxene growth. Pyroxenes generally have fast growth rates (10^{-7}-10^{-8} cm/s) (Ubide and Kamber, 2018) which has allowed zoning in pyroxenes in volcanic systems to be a useful proxy to record changes in magmatic conditions (Welsch et al., 2016; Ubide and Kamber, 2018; Ubide et al., 2019). As the diffusion of Cr is extremely slow (Cherniak and Dimanov, 2010), Cr-zonation in pyroxenes is an effective time capsule that can reveal cryptic cooling and crystallization histories in mafic-ultramafic magmatic systems. Potentially, this gives us a tool to compare the magmatic histories of mineralized and unmineralized systems.

In this contribution we discuss and compare the various types of Cr-zonation of pyroxenes in the mineralized intrusions from a number of economic Ni-Cu magmatic sulfide deposits around the world. These intrusions differ in age, geological setting and metal tenor, but have all been found to display various chemical zonation in pyroxenes. We test the potential application of pyroxene zoning as a prospectivity indicator by comparing the zoning patterns from mineralized (as far as we know), unmineralized or very weakly mineralized intrusions, and intrusions not associated with mineralization from a range of localities.

ZONING IN PYROXENES

As the pyroxene mineral group has a very large stability field, it usually nucleates early during solidification and can continue to grow for much of the lifetime of mafic-ultramafic intrusions. This allows these minerals to capture the changes in magmatic history within its crystal structure in the form of variable zonation patterns and inclusions. Minor element zonations within both clinopyroxene and orthopyroxene are complex but can be separated into distinct types (**Figure 1**); (1) normal zoning and reverse zoning (2) sector/hour-glass zoning (3) abrupt zoning (4) oscillatory zoning and finally (5) complex zoning which can incorporate any combination of the previous. Here we discuss the magmatic histories that are indicated by each type of zonation with emphasis on chromium due to its high partitioning and slow diffusion rate in both orthopyroxene and clinopyroxene.

Normal Zonation

Normal zonation is indicated by a diffuse reduction in chromium (and other compatible elements) concentration toward grain rims (**Figure 1A**) with a correlated increase in incompatible elements such as Ti (Bernstein, 2006). Chromium is one of the most compatible elements within both types of pyroxene (Barnes, 1986; Bédard, 2014) which causes it to be depleted as the system evolves. Occasionally, this zonation is reversed to the typical normal zonation, where the concentration of chromium increases toward the rims.

Sector Zoning

Sector zoning is sometimes referred to as hour-glass or bow-tie zoning due to its characteristic shape (**Figure 1B**). This type of zonation is common in natural terrestrial (Hollister and Gancarz, 1971; Downes, 1974; Leung, 1974; Welsch et al., 2016), lunar (Hargraves et al., 1970; Hollister et al., 1971) and experimental pyroxene (Lofgren et al., 2006; Schwandt and McKay, 2006).

These sector zones represent differences in chemistry of a crystal due to kinetic effects at the growth surface, whereby elements are incorporated into the structure at different rates along different crystallographic surfaces, rather than changes in chemistry or conditions of the surrounding magma (Hollister and Gancarz, 1971). There are at least four controlling factors for the creation of sector zones, as explained by Hollister and Gancarz (1971); "(1) size and composition of ionic complexes added to the crystal as it grows, (2) rate of addition of material, (3) rate of equilibration of the new material with the matrix at the surfaces of growth steps, and (4) rate of re-equilibration of surface layers with the matrix by exchange of ions perpendicular to the crystal faces." Therefore, these crystals grew fast enough to outrun diffusive equilibration between adjacent growth sectors.

In clinopyroxene, the M1 and T sites are exposed on the (010) crystal face whereas either the M1 or the T sites are exposed on the (100) face (Hollister and Gancarz, 1971). This different exposure of the vacant sites on different faces of the clinopyroxene grains means that the partition coefficients on each face will be different. In the case of the pyroxenes present here, there is a difference in the partitioning of chromium that creates visible sector zoning within both clinopyroxene and orthopyroxene grains. Sector zoning in pyroxenes can lead to false abrupt zoning when viewed in a two dimensional section through the c-axis as illustrated in Welsch et al. (2016) and displayed in **Figure 1**.

Abrupt Zoning

Abrupt zoning is characterized by a large change in chemistry over a short distance of crystal growth (**Figure 1C**). This type of zoning is indicative of two stages of growth. This could indicate either a change in growth environment of the pyroxenes, or a change in chemistry of the magma, where the budget of chromium has been exhausted or the chromium has changed to a less favorable cation (i.e., Cr^{3+} over Cr^{2+}) resulting in a sudden change to a lower partition coefficient (Barnes, 1986). A likely cause of abrupt zoning is a change from crystallization on the liquidus from freely convecting magma to equilibrium crystallization in a restricted closed system in the intercumulus pore space of an orthocumulate, following incorporation of the crystal into a cumulus pile or mush.

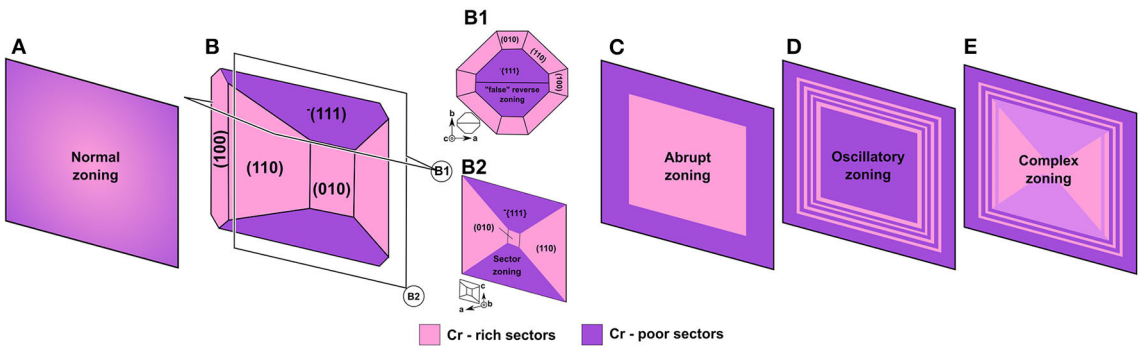

FIGURE 1 | Types of zonation visible in pyroxene. A schematic illustration using Cr content in clinopyroxene to illustrate the zoning types. Normal zoning **(A)** is common in unmineralized/barren intrusions and is characterized by a diffuse reduction in chromium (and other compatible elements) concentration toward the rims. **(B)** Sector zoning, hourglass style zonation in Cr concentration in the core of the pyroxene, Modified from Welsch et al. (2016). Cross sections through the b and c axis give; (B2) hourglass sector-zoned clinopyroxene and (B3) a false-reverse zoned clinopyroxene. **(C)** Abrupt zoning: a rapid change in the trace element chemistry between the core and rim **(D)** oscillatory zoning: repetitive cycles of chemistry change within the crystal. **(E)** Complexly zoned pyroxene can be made up of a combination of **(B–D)**.

Oscillatory Zoning

Oscillatory zoning is the repetitive or cyclic change in chemistry of the crystal during growth. There are two possible causes for the formation of oscillations of chemistry during crystal growth as outlined by Fowler and Shore (1996); (1) extrinsic causes such as changes in pressure (P), temperature (T) or magma composition (X) or (2) intrinsic causes such as fluctuations between diffusive and advective supply of cations in a melt boundary layer immediately adjacent to the growing crystal.

Fowler and Shore (1996) suggest that oscillatory zoning is favored in silicates of "moderately rapid growth" i.e., growing between 10^{-11} and 10^{-13} m/s.

Complexly Zoned Pyroxenes

A complexly zoned pyroxene in the context of this manuscript is any combination of sector, abrupt and oscillatory zoning of chromium within a clinopyroxene or orthopyroxene.

SAMPLES

We investigate samples from eleven economically mineralized magmatic Ni-Cu sulfide intrusions from regions including; the Noril'sk-Talnakh camp in Siberia, the Kotalahti nickel belt in Finland, Ntaka Hill in Tanzania, Nova-Bollinger in the Albany-Fraser Orogen of Australia, Savannah in the Halls Creek Orogen of Australia, Jinchuan in central China, Xiarihamu in Tibet, and Huangshanxi in the east Tianshan Ni province of NW China (**Table 1**).

In addition to these significantly mineralized intrusions, we compare intrusions within the same region that contain "weak" (usually sparsely disseminated) mineralization to those that show no evidence of magmatic sulfides ("barren").

Finally, we investigate four mafic intrusive bodies that are not associated with any known economic mineralization to determine "background" textural and chemical features that are not specifically relatable to mineralization. These samples include the Ngunala (previously referred to as Caroline) intrusion and the Wanka Wanka dyke in the East Musgrave province of Central Australia, the Archean Ora Banda sill and the Proterozoic Jimberlana Dyke, both in the East Yilgarn Craton of Australia. It should be noted that a possibility exists for "false negatives" in that some of the bodies sampled and placed in the "weak" or "barren" categories have not been extensively explored and could subsequently tun out to contain economic mineralization at depth; this problem is endemic to this kind of study and we can only use the information currently available.

More details of these samples are included in **Table 1** and full details and references for the deposits, intrusions and samples are included in the **Supplementary Material**.

METHODS

The samples were fashioned into 30 or 100 μm thin sections, mounted on either quartz or standard petrographic glass slides.

Synchrotron, Maia Mapper, and Desktop X-Ray Fluorescence Imaging

Multiple experiments on the XFM beamline at the Australian Synchrotron, operated by ANSTO were carried out between 2015 and 2019. The common method used in these experiments is scanning with a pixel size of 4 * 4 μm, a movement speed of 5 mm/s and a dwell of 0.8 ms, though this method varied depending on target area, grain size and available time. The images were collected on a Maia 384 detector array using the Kirkpatrick Baez mirror microprobe end-station. We used a monochromatic 2 μm beam spot size for at an energy of 18,500 eV. The collected spectra were then processed by the *GeoPIXE* software into element concentrations presented as maps of quantified element concentrations with spectral overlap, pileup and background removed using the Dynamic Analysis (DA) method for real-time spectral deconvolution (Ryan, 2000; Kirkham et al., 2010; Ryan et al., 2014).

To increase the detection limit for Cr and Ti via XRF, we also reduced the energy of the synchrotron X-rays to 7,050 eV which

TABLE 1 | Representative samples from each intrusion.

Location	Intrusion	Sample	Rock type	Category	Primocryst cumulus phase*	Oikocrysts	Chadacrysts	Zoning CPX	Zoning OPX	Comment
Iberian pyrite belt, Spain	Aguablanca	AB-NA1	Pyroxenite breccia	ED-S	Clinopyroxene, sulfide liquid			Reverse zoning	Exsolution	Disaggregated pyroxenite in magmatic sulfide liquid matrix
East kunlun orogenic belt, tibet	Xiarihamu	QX14-23-14	Lherzolite	ED-M	Olivine, chromite, opx			NA	Abrupt, osc.	Small olivine inclusions in cumulus opx
East Tianshan Ni province, NW China	Huangshanxi	06-18-908	Harzburgite	ED-S	Olivine/orthopyroxene, chromite	opx	Chromite, olivine	Sector, abrupt	Sector, abrupt, reverse rim	Small olivine inclusions in cumulus opx
Kotalahti Ni belt—Raahe-ladoga belt (Svecofennian), Finland	Majasaari	KU27906	plagioclase - peridotite	Barren	Olivine, chromite			Weak sector, normal	Weak sector, normal	
	Kekonen	KU07018	peridotite (+ serpentine)	ED-S	Olivine, opx			Normal (cpx at the expense of opx)	Sector, abrupt	Small olivine inclusions in cumulus opx
	Rytky	KU30024	Peridotite	ED-S	Olivine, sulfide liquid			Abrupt, osc., sector	Abrupt, osc.	
		KU30025	Peridotite	ED-S	Olivine	cpx	Olivine	Abrupt, osc., sector	Abrupt, osc.	
		KU30063	Pyroxenite	ED-S	Orthopyroxene	cpx	opx	Sector, osc., normal	Sector, abrupt	
	Niinimaki	KU23620	Serpentinite	Minor	Olivine, chromite	opx	Chromite, olivine	None	Normal	
	Saarijarvi	KU06937	Peridotite—lherzolite	Minor	Olivine/chromite	opx	Chromite, olivine	None	Normal	
	Ylivieska	KU25187	Olivine gabronorite	Minor	Olivine, plagioclase		Olivine, plagioclase	Normal	NA	
	Saarela	KU30145	Norite	Minor	Orthopyroxene			None	Weak sector, abrupt	
Longshoushan terrane, gansu, China	Jinchuan	JII-II	Lherzolite	ED-M	Olivine/orthopyroxene			Sector	Sector, abrupt, osc.	
Norilsk region, siberia	Kharealakh	KH-2_map1	Picro-gabbrodolerite	ED-M	Olivine	cpx	Olivine	Sector, normal	NA	
	Norilsk-1	N1-24-93.6	"Taxite" - contaminated gabbro, dolerite	ED-M	Chromite/olivine			Sector, adrupt, weak osc.	NA	
		NOR1-1A	Gabbro, olivine gabbro, wehrlite ("picrogabbrodolerite")	ED-M	Olivine	cpx	Olivine	Normal	Normal	
	Kharealakh	VZU-3B		ED-M	Olivine			Abrupt, osc.	NA	
	AlloreRiver	BX2_2438.7		Minor	Plagioclase	cpx	Plagioclase	Weak sector, abrupt	NA	
	Lower Talnakh	TR31_797.4		Minor	Olivine	cpx	Olivine, plagioclase	Weak sector, normal	NA	
		TR31_798.7		Minor	Olivine			Weak sector, abrupt	NA	
	Chernogorsk	UK35-229.9		Minor	Olivine	cpx	Plagioclase	Weak sector, normal	NA	
Albany fraser orogen	Nova	N614-5	Lherzolite	ED-S	Olivine	opx	Olivine	Sector, osc.	Sector	

(Continued)

TABLE 1 | Continued

Location	Intrusion	Sample	Rock type	Category	Primocryst cumulus phase*	Oikocrysts	Chadacrysts	Zoning CPX	Zoning OPX	Comment
		SFRD0111-169		ED-S	Olivine, Cr-spinel, opx	opx	Olivine	Adrupt	Sector	
		SFRD0272-390		ED-S	Olivine, Cr-spinel, orthopyroxene			Normal	Sector, abrupt	Extensive olivine-plagioclase reaction coronas (amph-spinel symplectites)
	Upper Nova	SFRD0017_49	Peridotite	Minor	Olivine, Cr-spinel	cpx	Olivine	Normal	Normal	Extensive olivine-plagioclase reaction coronas (amph-spinel symplectites)
Mozambique mobile belt	Ntaka hill	Ntaka-8321	Harzburgite	ED-S	Orthopyroxene			None	Reverse abrupt	Small olivine inclusions in cumulus opx
		Ntaka-8386	Harzburgite	ED-S	Orthopyroxene			None	Sector, abrupt, osc.	Small olivine inclusions in cumulus opx
Halls creek orogen	Turkey creek	TCDM01	Gabbronorite	Barren	Plagioclase, opx			Exsolution, normal	Exsolution, normal	Probably non-cumulate
	Savannah	EK2366	Norite	ED-S	Orthopyroxene			None	Exsolution, normal	
INTRUSIONS UNRELATED TO NI-SULFIDE MINERALIZATION										
East musgrave province (S Australia)	Ngunala (Caroline)	DD10W0D002-131	Pyroxenite	VMD	Orthopyroxene	cpx	opx	None	None	
Widgiemooltha dike swarm	Jimberlana	A65	Pyroxenite	VMD	Orthopyroxene	cpx	opx	Normal	Weak sector, normal	
Kalgoorlie terrane (Archean Yilgarn Craton)	OraBanda	OB1	Pyroxenite	VMD	Orthopyroxene	cpx	opx	Abrupt, normal	Normal	
East musgrave province (S Australia)	WankaWanka	WW3_150	Lherzolite	Barren	Olivine	cpx, opx	olivine	osc., normal	osc., normal	
Bushveld complex	Bushveld	BV9		VMD	Orthopyroxene, chromite	cpx	Chromite, opx	Normal	None	

*Oscillatory zoning abbreviated to osc. NA is "not applicable" which indicates the phase is not present. *Euhedral to subidiomorphic habit, usualy forming framework of touching grains, with small proportion of inclusions, or no inclusions (Irvine, 1982); magmatic sulfide is also a cumulus phase in some of these samples, but occurs as interstitial aggregates. Mineralization code: ED-S, economic deposit, small; ED-M, economic deposit, major; Minor, minor disseminated, sub-economic; VMD, trace to very minor disseminated sulfide, not economic. Data sources (Keays and Campbell, 1981; Chai and Naldrett, 1992; Witt, 1995; Makkonen, 1996; Mäkinen and Makkonen, 2004; Makkonen and Mursu, 2004; Li et al., 2005; Song et al., 2012; Makkonen et al., 2017). This table is extended in the **Supplementary Material** to include the method for the synchrotron data and details of the intrusions.*

is below the absorption edge for Fe. This increases the resolution of these zoning patterns significantly as shown in Barnes et al. (2020).

The major element data obtained via the synchrotron XRF is in good agreement ($r^2 = 0.97$) with the data obtained by electron probe microanalyzer (EPMA) for the same regions on sample KU30024 (**Figure 2**), however, the high energy scans have high errors for trace Cr concentrations due to noise in the X-ray signal. Comparing a traverse across the same grain (KU27906) from the high energy experiment (18,500 eV) and the low energy experiment (7,050 ev) the data is within error, with the low energy results giving much higher precision than the high energy experiment.

Desktop microbeam XRF mapping was also used to determine if these zoning patterns can be observed using more widely available technology. The XRF mapping was conducted using a Bruker desktop microbeam XRF mapper—M4 Tornado™, at CSIRO Mineral Resources, Western Australia. The device is equipped with a rhodium X–ray tube which was set to 50 kV and 500 nA and an XFlash® silicon drift X–ray detector. Maps were created using a 40 µm spot size on a 40 µm raster with dwell times of 5 ms per pixel. Element maps represent the unquantified background corrected peak height data for Kα peaks for each element, scaled either linearly or logarithmically between minimum and maximum measured counts over the sample. The elements were then stacked in red-green-blue (RGB) colored images. It should be noted that minor element maps generated using the Tornado device are highly susceptible to diffraction artifacts, causing spurious appearances of high concentrations due to crystal orientations relative to source and detector that correspond to Bragg angles. As this is extremely common, they have been included and clearly labeled in this manuscript (for an example see **Figure 6B**) in an attempt to avoid misinterpretation of these features. Use of the multi-detector Maia array overcomes this problem.

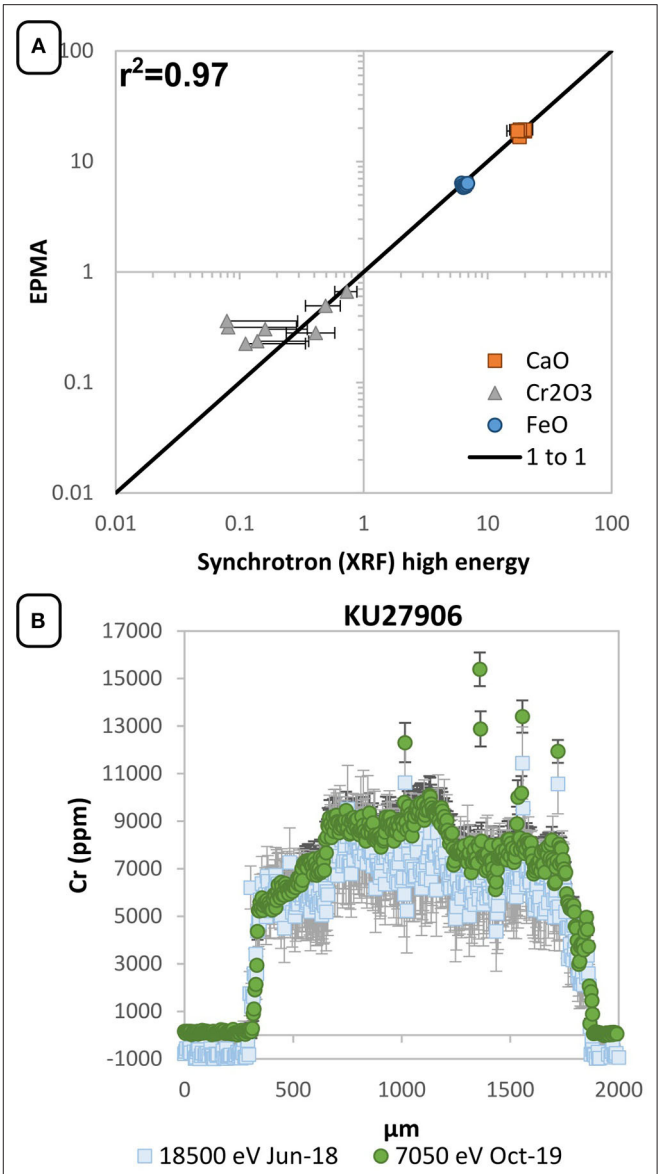

FIGURE 2 | (A) A comparison between the major elements calculated from the Synchrotron Maia Detector from the high energy experiment (18,500 eV) with the EPMA analysis from sample KU30024. **(B)** Sample KU27906 (**Figure 7**) was measured in both the 18,500 eV experiment and the low energy (7,050 ev) experiment and the results are comparable, with Cr precision increasing using the low energy technique.

MINERALIZED INTRUSIONS

The Rytky intrusion of the Kotalahti Ni-belt in Finland (Makkonen, 2015) has both orthopyroxenes and clinopyroxenes that are very large (∼1 cm) and both show significant abrupt zonation. The clinopyroxene grain examined in **Figure 3A** has distinct sector zoning and oscillations in Cr in the rims and contains olivine inclusions. The traverse through this clinopyroxene grain shows core values of ∼4000–6000 ppm Cr near the olivine inclusions with a rapid decrease to near zero (**Figure 4A**) in the Cr-poor rims. The outer zones display oscillations in Cr; however, these are of much lower concentration (<1,000 ppm) than the core. Both Mn and Ti increase in the outer 1,000 µm of this clinopyroxene grain. Orthopyroxenes from this intrusion also display abrupt changes from core to rim and oscillations in Cr content in the rims (**Figure 5**). The abrupt change from core to rim is difficult to quantify as the crystals are different sizes and we are analyzing traverses through a random cross section of the crystal, therefore the relative distance that the crystal changes from high to low concentrations can change greatly (**Figure 5**).

The Ntaka Hill intrusion was described in detail in Barnes et al. (2016b, 2019b). Sample Ntaka-8,321 is a harzburgite and shows abrupt zoning of Cr in all the large (∼4 mm) orthopyroxenes (**Figure 3B**). There are also fine scale oscillations throughout the core of the grains and slight sector zonation. Ntaka Hill pyroxenites and harzburgites also show widespread abrupt zonation, where partially resorbed olivine inclusions are preferentially located at the edges of the Cr-enriched cores

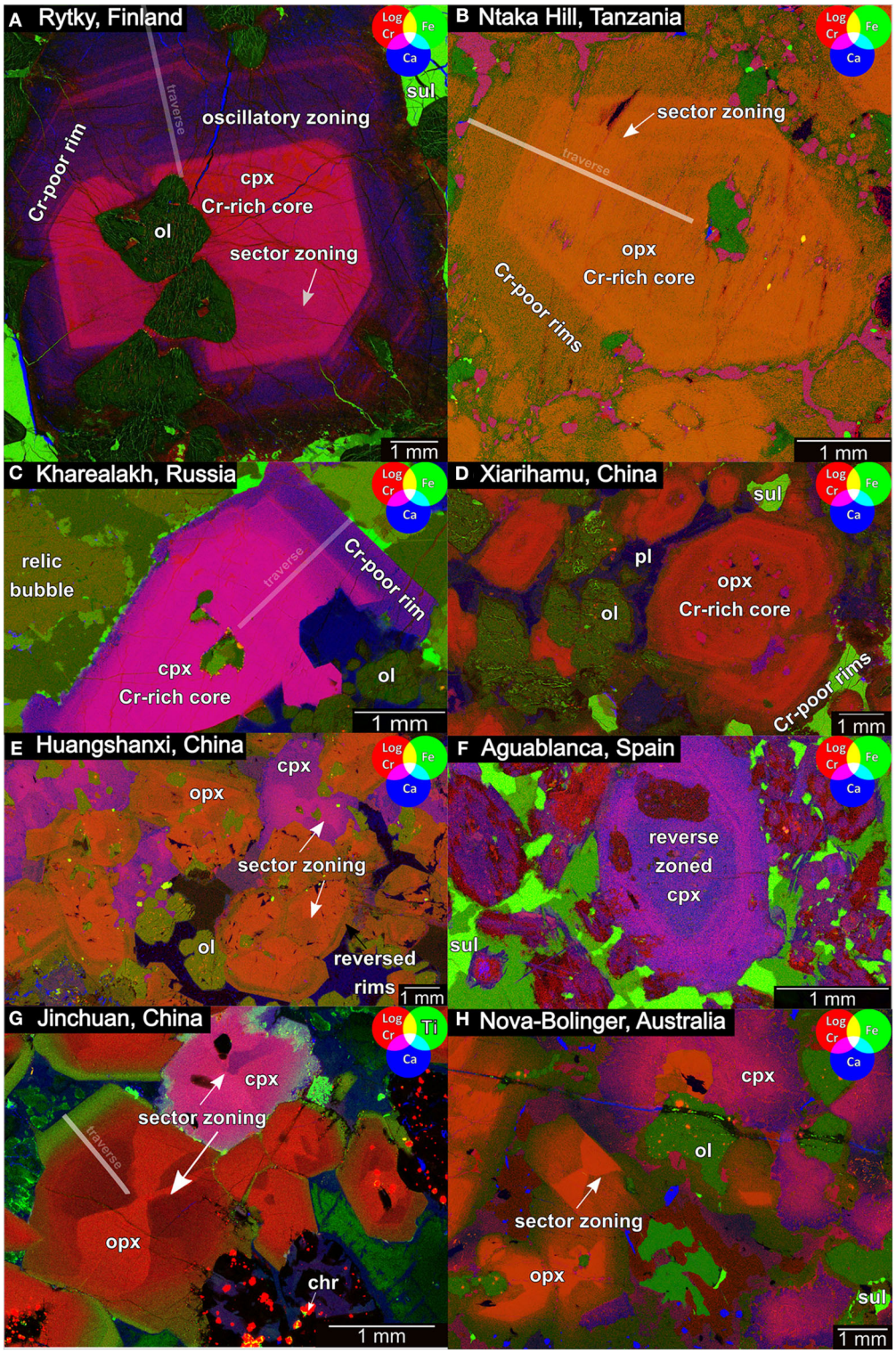

FIGURE 3 | X-ray Fluorescence (XRF) images collected from the Australian Synchrotron of zoned pyroxenes in Ni-Cu magmatic sulfide deposits from around the world. **(A)** Rytky, **(B)** Ntaka Hill, **(C)** Kharealakh (Talnakh), **(D)** Xiarihamu, **(E)** Huangshanxi, **(F)** Aguablanca, **(G)** Jinchuan, and **(H)** Nova-Bollinger. Stacked false color (RGB) image of logged chromium concentration in red, iron or titanium in green and calcium in blue. Clinopyroxene [$Ca(Mg,Fe)Si_2O_6$] is displayed in pink (Cr-rich) to purple (Cr-poor) while orthopyroxene [$(Mg,Fe)SiO_3$] is orange (Cr-rich) to green (Cr-poor) in colouration. Mineral abbreviations: cpx, clinopyroxene; ol, olivine; opx, orthopyroxene; pl, plagioclase; S, sulfide.

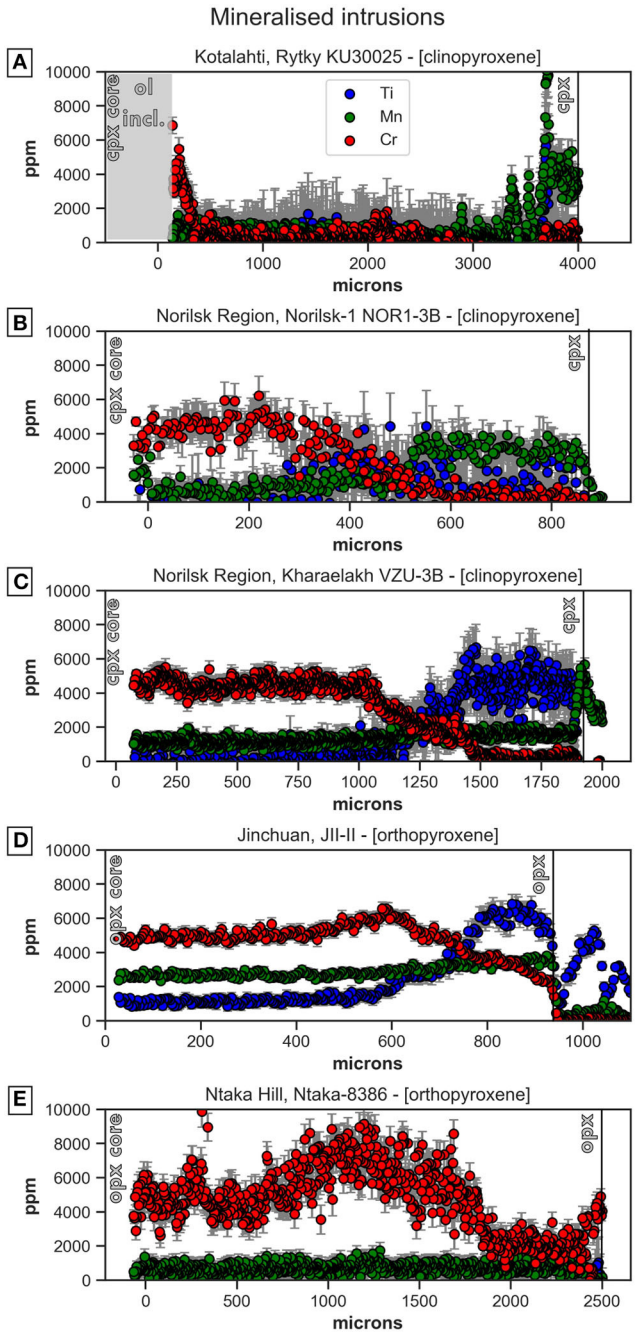

FIGURE 4 | Traverses across clinopyroxene and orthopyroxene from core to rim in mineralized intrusions. **(A)** Traverse through clinopyroxene from the Rytky intrusion, Kotalahti Ni-belt (**Figure 3A**). **(B)** Clinopyroxene from the Norilsk-1 intrusion of the Norilsk-Talnkah region. **(C)** Clinopyroxene from the Kharaelakh intrusion of the Norilsk-Talnakh region (**Figure 3C**). **(D)** An orthopyroxene from Jinchuan intrusion (**Figure 3G**). **(E)** An orthopyroxene from the Ntaka Hill intrusion in Tanzania (**Figure 3B**).

(Barnes et al., 2016b), and less common reverse zoning toward Cr-enriched rims. A traverse along an orthopyroxene grain was undertaken in a high energy scan on the synchrotron (lower precision in these minor elements than the low energy scans) and shown in **Figure 4E**. An enrichment in Cr is observed from the core toward the abrupt zone (∼4,000–8,000 ppm), which drops to the Cr poor rims (∼2000 ppm).

The intrusions of the Norilsk-Talnakh region: Kharaelakh, Talnakh and Norilsk 1, are known to be anomalously orthopyroxene-poor. Examining one of the clinopyroxene grain from the Kharaelakh intrusion (**Figure 3C**), there is an abrupt zonation between the Cr-rich core (∼4,500 ppm) and the Cr-poor (near zero) rim (**Figure 4C**). Clinopyroxenes in this sample commonly host olivine and chromite inclusions which represent the first phases crystallizing in this system (Schoneveld et al., 2020). This sample was included in the detailed investigation of blebby sulfides from Norilsk of Barnes et al. (2019a) and Le Vaillant et al. (2017).

The intrusions of the Xiarihamu deposit were discussed in detail in Wang et al. (2019). The Cr-rich core of the orthopyroxene grain in **Figure 3D** shows oscillations and also contains small clinopyroxene inclusions.

The samples from both Huangshanxi and Aguablanca display examples of "reverse zoning" where the concentration of chromium increases in the outer mantle of the grains. The sample from Huangshanxi (**Figure 3E**) was discussed in detail in Mao et al. (2019). The sample is made up of mostly sector zoned orthopyroxenes and clinopyroxenes with some plagioclase, olivine and sulfide. The orthopyroxene grains examined in **Figure 3E** show a mantle of lower Cr values which is not reflected in the adjacent clinopyroxene grains. Both pyroxenes contain small olivine inclusions. The sample from Aguablanca (**Figure 3F**) was discussed in Barnes et al. (2018). This sample is made up of mostly sulfides and many clinopyroxenes with reverse and oscillatory zoning; where the core of the clinopyroxene grains are low in Cr and there is a Cr rich mantle which reduces to a Cr-poor rim.

The sample from Jinchuan (**Figure 3G**) shows strong sector zoning in both pyroxene types with an abrupt Cr-poor, Ti-rich rim in the orthopyroxenes. General information on the crystal growth in these intrusions is included in Mao et al. (2018). A traverse along one of these orthopyroxene grains (**Figure 4D**) shows a slight increase in Cr (4,500–6,000 ppm) then a rapid decrease in to 2,000 ppm over outer 300 μm of the rim. This latter decrease in Cr is correlated to an increase in Ti from ∼1,000–6,000 ppm.

The sample from the mineralized Lower Intrusion at Nova-Bollinger (Barnes et al., in press) (**Figure 3H**) contains sector zoned orthopyroxenes with sharply-defined rims that reduce to near zero Cr concentrations. The Cr-rich orthopyroxene cores commonly contain olivine inclusions. The clinopyroxenes exhibit a diffuse change from core to rim. This sample is also host to olivine-plagioclase reaction coronas that include a second generation of orthopyroxenes forming symplectite intergrowths with spinel.

In addition to these large, complexly zoned pyroxenes, many of the mineralized intrusions have clinopyroxene or orthopyroxene oikocrysts (Barnes et al., 2016b, 2019a). These are very large (>5 mm) single crystals that enclose many

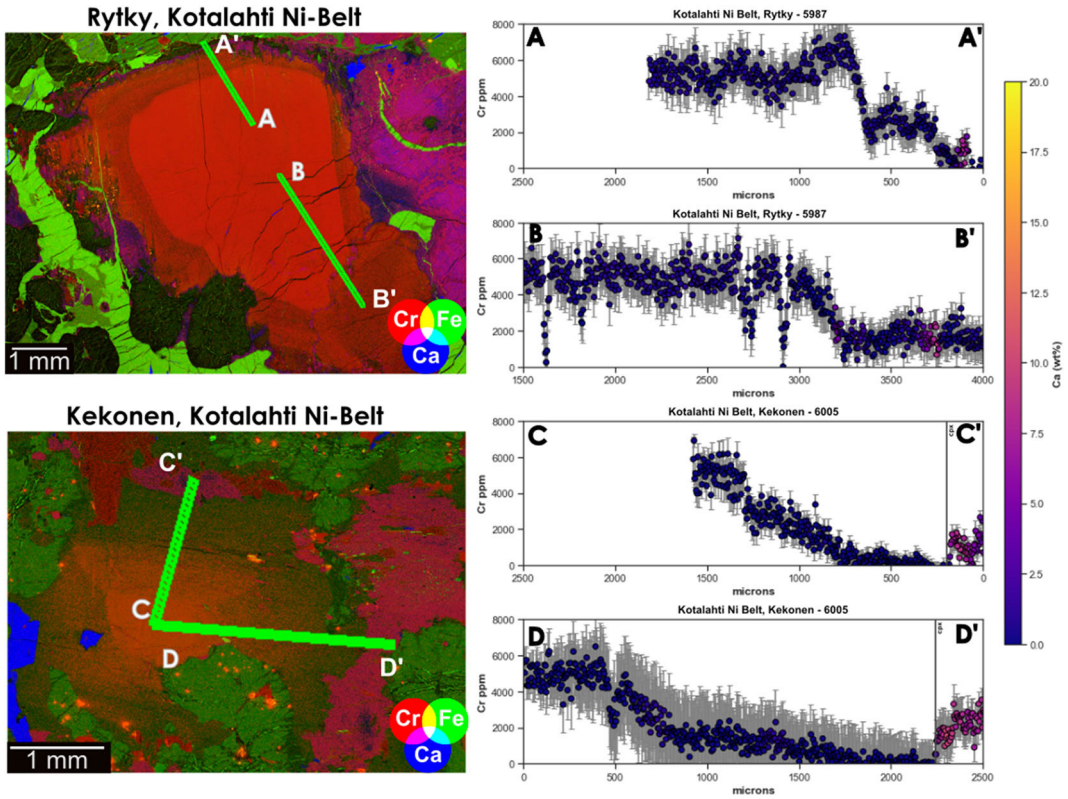

FIGURE 5 | Traverses through abrupt zonation in orthopyroxene (opx) grains. Traverse **(A,B)** are on an orthopyroxene from Rtyky while **(C,D)** are from the Kekonen intrusion. Both samples are from Kotalahti Ni-belt. The degree of abrupt zonation may depend on crystal orientation. The sector zoning in the second grain represents looking down the **(C)** axis. Therefore **(C,D)** are traverses approximately along with **(A,B)** axis. Each traverse is cropped to a total of 2,500 um and presented as core to rim traverses so we can directly compare between traverses. Color scheme is wt% Ca content of the analysis to ensure orthopyroxene composition with no inclusions.

small crystals; usually either pyroxene (**Figure 6A**) or olivine (**Figure 6B**). These oikocrysts also display Cr sector zoning.

In general, these mineralized intrusions are all made up of olivine, pyroxene and plagioclase with additional phases including chromite and sulfide. The pyroxenes are generally large (>1 mm), commonly host olivine inclusions and have abrupt zoning of Cr and usually sector zoning.

UNMINERALIZED INTRUSIONS

The "unmineralized" classification of intrusions represent both intrusions with no sulfides present (barren) as well as intrusions that contain a small quantity of sulfides (weakly mineralized).

In general, these intrusions have less orthopyroxene than their mineralized counterparts (with the exception of Norilsk-Talnakh where the mineralized intrusions are unusually orthopyroxene-poor) and gradational normal zonation in Cr in both pyroxene species. This normal zonation is characterized by the gradual increase of incompatible trace elements toward the crystal edges which represents gradual depletion of highly compatible Cr during progressive equilibrium crystallization from the trapped liquid. The low energy method (Barnes et al., 2020) allows observation at high sensitivities for Cr and Ti to distinguish very subtle changes in chemistry. Pyroxenes from the unmineralized or weakly mineralized intrusions display weak sector zonation that is only visible in the low energy scanning mode as the differences in the concentration between the zones is minimal.

A number of intrusions were investigated from the Kotalahti Ni-belt (Makkonen, 2015) which range from barren (Majasaari, **Figure 7A**), some indications of mineralization (Saarela, **Figure 7B**) to weakly mineralized (Saarijarvin, **Figure 7C**). The barren Majasaari intrusion is made up of olivine, plagioclase and chromite with large (>3 mm) clinopyroxene and orthopyroxene grains. The pyroxenes enclose small olivine and chromite grains and the clinopyroxene displays faint sector zoning, as displayed by the grain in **Figure 7A**. The Saarela intrusion samples are predominantly plagioclase-rich cumulates with some clinopyroxene and orthopyroxene grains. The orthopyroxenes are ∼1 mm in size and have an enrichment of chromium throughout some of the grains. The weakly mineralized Saarijarvin intrusion has very large (>8 mm) normally zoned orthopyroxenes that enclose olivine chadacrysts (**Figure 7C**). The concentration of Ti in the orthopyroxene grain in **Figure 7C** increases from 2,400 ppm in the core to ∼5,000 ppm toward the rims while Cr decreases from 6,800 to ∼3,000 ppm toward the rims (**Figure 8**).

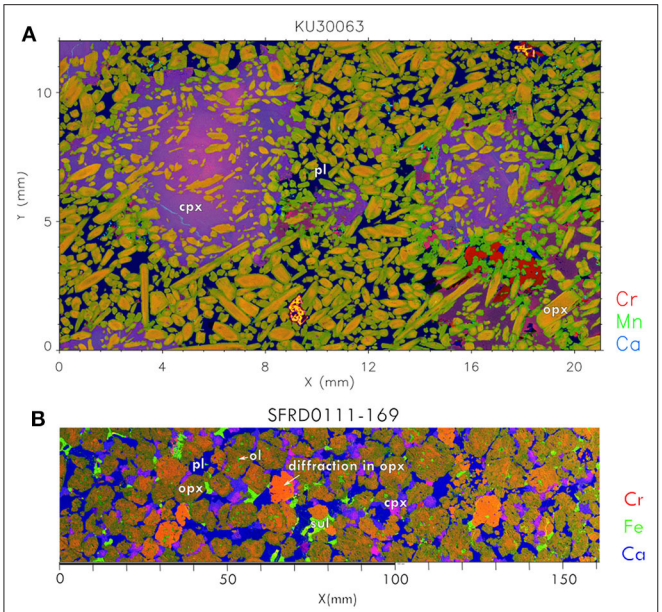

FIGURE 6 | (A) Large clinopyroxene (cpx) oikocrysts enclosing small orthopyroxene (opx) chadacrysts and surrounded by orthopyroxene in the Rytky intrusion from the Kotalahti Nickel Belt. Sector zoning visible in the core of the large clinopyroxene with all grains displaying normal zonation of Cr. **(B)** Tornado XRF image, large sector zoned orthopyroxene cumulate oikocrysts containing small olivine chadacrysts. Sample SFRD0111-169 from the Nova intrusion. Sample shows the common feature of diffraction artifacts which is a known disadvantage of the desktop XRF mapping techniques. These artifacts give a false high Cr concentration for an entire grain that is due to the crystal orientation, displayed in the image as solid orange opx.

The Turkey Creek intrusion (near Savannah) and the upper Nova intrusion show limited Cr zoning in pyroxene oikocrysts. The Upper Intrusion at Nova shows a good example of normal zonation in both clinopyroxene and orthopyroxene grains (**Figures 7E**, **8**). The Turkey Creek sample shows large clinopyroxene grains with smaller orthopyroxene exsolutions in their cores (**Figure 7D**).

The unmineralized intrusions from Norilsk-Talnakh show weak sector zoning in the cores of the clinopyroxenes which also contain plagioclase inclusions. These intrusions also show a diffuse zonation between the Cr-rich cores and the Cr-poor rims (**Figures 7**, **8**).

There is a small possibility that these "barren" intrusions are under-explored and may eventually turn out to contain significant mineralization following further exploration; therefore, we also investigate pyroxenes from mafic intrusions that are not associated with any known mineralization (other than minor marginal disseminations) on a regional scale.

MAFIC INTRUSIONS

These intrusions are associated with the presence of at most very minor, uneconomic magmatic sulfides, however, the pyroxenes within these intrusions still exhibit zonation from which we can infer their magma history.

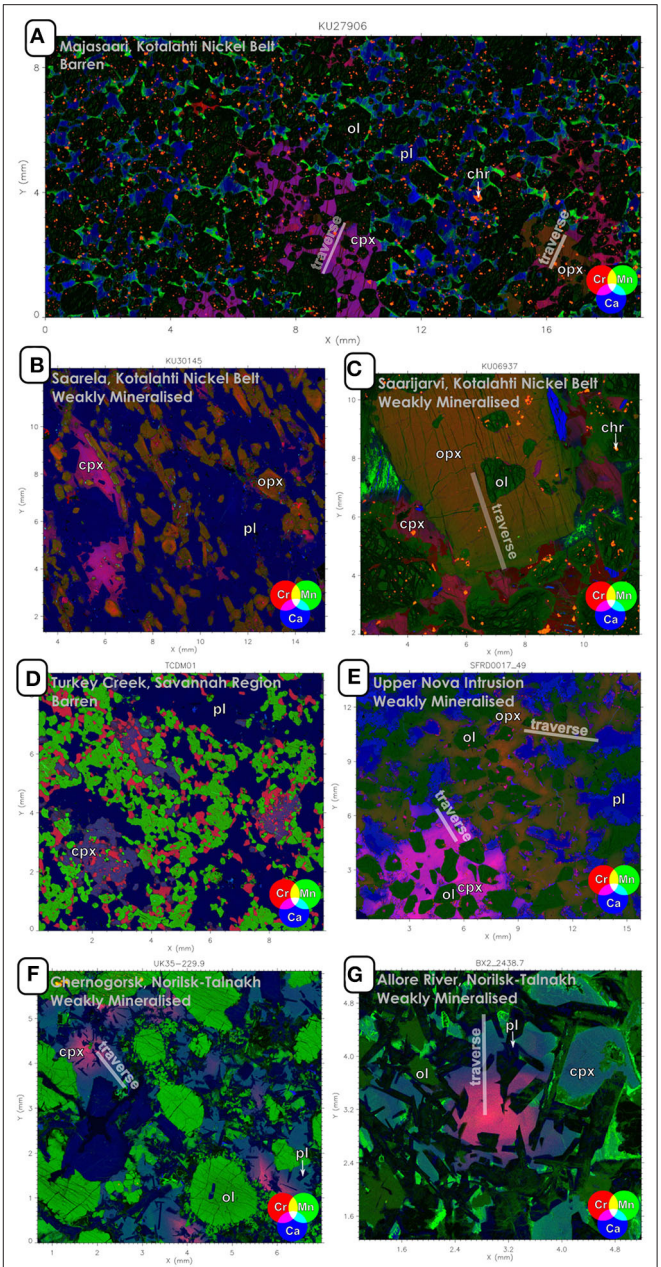

FIGURE 7 | Concentric normal zonation (Cr-rich core, Cr-poor rim) in pyroxene from reactions with the trapped liquid during crystallization. Note lack of abrupt step between cores and rims. X-ray Fluorescence (XRF) images collected from the Australian Synchrotron using low energy (7,050 eV) method (Barnes et al., 2020) Stacked false color (RGB) image of chromium concentration in red, manganese in green and calcium in blue. Mineral abbreviations: cpx, clinopyroxene; ol, olivine; opx, orthopyroxene; pl, plagioclase.

The Wanka Wanka Dyke (**Figures 9A**, **10C,D**) is a small (150 m wide and 15 km long) zoned dyke with an ultramafic core and mafic margin and is considered to likely represent part of the feeder system of the Giles Complex layered intrusions in central Australia. Both the clinopyroxene and orthopyroxene grains (**Figure 9B**) exhibit a diffuse reduction in the Cr concentration, then a sudden return to original Cr

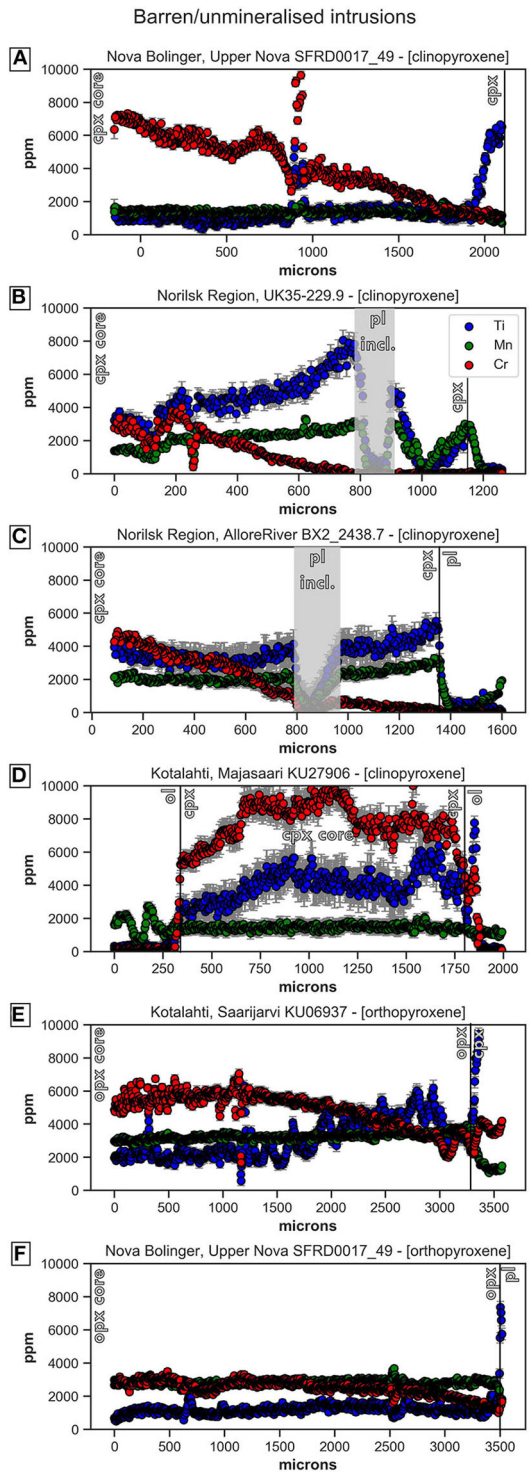

FIGURE 8 | Traverses across clinopyroxene and orthopyroxene from core to rim in barren and unmineralized intrusions. **(A)** Clinopyroxene from Upper Nova intrusion (**Figure 7E**), **(B)** clinopyroxene from Chernogorsk, Norilsk Region (**Figure 7F**), **(C)** clinopyroxene from the Allore River intrusion, Norilsk Region (**Figure 7G**), **(D)** a traverse from clinopyroxene edge to edge through core from the Majassaari intrusion of the Kotalahti Ni Belt (**Figure 7A**), and **(E)** core to rim traverse through an orthopyroxene of the Saarijarvi intrusions, Kotalahti Ni-belt (**Figure 7C**). **(F)** An orthopyroxene from Upper Nova intrusion (**Figure 7E**).

concentrations with an embayed boundary which is repeated (in this case 3 times; **Figure 10C**). This is an example of magma recharge into a mafic system during pyroxene growth which is discussed further below. This intrusion contains no known sulfide accumulations.

The Jimberlana Dyke contains minor disseminated sulfides in orthocumulate layers close to its margins but no economic concentrations. The cumulus orthopyroxenes within the Jimberlana intrusion show extremely faint sector zoning while the clinopyroxene oikocrysts are dominated by faint normal zoning (**Figures 9D**, **10E,F**). The Ora Banda Sill contains traces of centrally-disposed platinum group element enriched sulfides within orthopyroxenites. In the Ora Banda Sill, both pyroxenes show normal zonation toward the rims (**Figures 9E,F**, **10G**) with the exception of the orthopyroxene chadacrysts, within the core of the clinopyroxene oikocrysts, which are smaller and do not display normal zonation. The Ngunala (Caroline) intrusion has homogenous levels of Cr throughout all the orthopyroxene and clinopyroxene grains (**Figures 10A,B**).

DISCUSSION

A common feature of the pyroxenes in the mineralized intrusions is abrupt normal zonation, whereby chromium rich cores zone abruptly to chromium poor rims (**Figures 3A–D,G**), whereas the unmineralized intrusions are dominated by smooth normal zonation. The most plausible explanation for abrupt zonation is that the Cr-enriched core represents open-system cumulus growth at the liquidus temperature of the magma, where the growing crystal remains in contact with flowing magma in a chamber or conduit, while the rim represents diffusion-limited post-cumulus growth from trapped intercumulus liquid within a crystal mush. In this situation, the trapped liquid becomes progressively depleted in Cr due to the high compatibility of Cr in pyroxenes.

Samples from Aguablanca, Spain (**Figure 3F**) display "reverse zoned" clinopyroxenes, with chromium poor cores, a chromium rich mantle then a chromium poor rim. Samples from Huangshanxi, China (**Figure 3E**) display "reversed rimmed" orthopyroxenes where the concentration of chromium is high in the core, surrounded by a mantle of low concentrations of chromium and returning to high concentrations at the rims. These patterns cannot be explained by a simple two-stage history (cumulus followed by postcumulus) and imply some kind of multi-stage reworking in a dynamic crystallization environment.

In general, the value for Cr within orthopyroxene cores in the mineralized intrusions is fairly consistent (6,800 ± 1,700 ppm), probably reflecting equilibrium with magma saturated in chromite (Barnes et al., 2016b). The unmineralized intrusions are variable, ranging from clinopyroxene cores with values as high as 7,900 ± 1300 ppm (Majasaari, Kotalahti) to 2,000 ± 100 ppm (Ngunala—Caroline). In the same sample, the concentrations are similar between both clinopyroxene and orthopyroxene. This suggests the partition coefficient

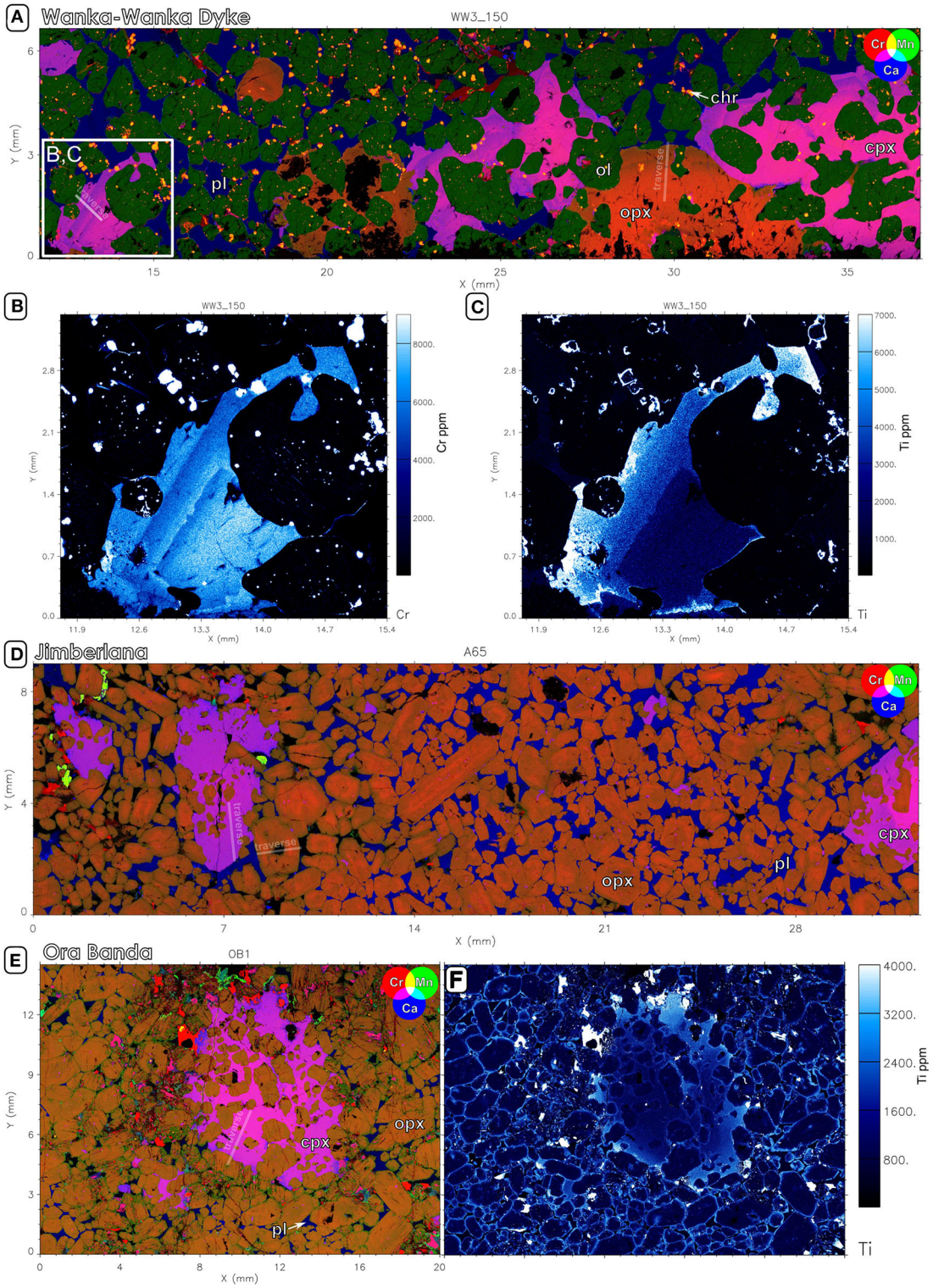

FIGURE 9 | Pyroxene textures in mafic intrusions that are not associated with mineralization (other than localized minor disseminations). **(A)** Wanka Wanka Dyke with inset of **(B,C)**. **(B)** Cr map of clinopyroxene; oscillatory zoning. **(C)** Ti map of clinopyroxene; normal zoning. **(D)** Jimberlana; large clinopyroxene oikocryst that contains small orthopyroxene chadacrysts in a matrix of weakly sector zoned orthopyroxene and plagioclase. **(E)** Ora Banda; large clinopyroxene oikocrysts with orthopyroxene chadacrysts in an orthopyroxene and plagioclase matrix. **(F)** Normal zonation in Ora Banda pyroxene with an increased in incompatible elements (such as Ti) in the rims. X-ray Fluorescence (XRF) images collected from the Australian Synchrotron using low energy (7,050 eV) method (Barnes et al., 2020) Stacked false color (RGB) image of chromium concentration in red, manganese in green and calcium in blue. Mineral abbreviations: cpx, clinopyroxene; ol, olivine; opx, orthopyroxene; pl, plagioclase.

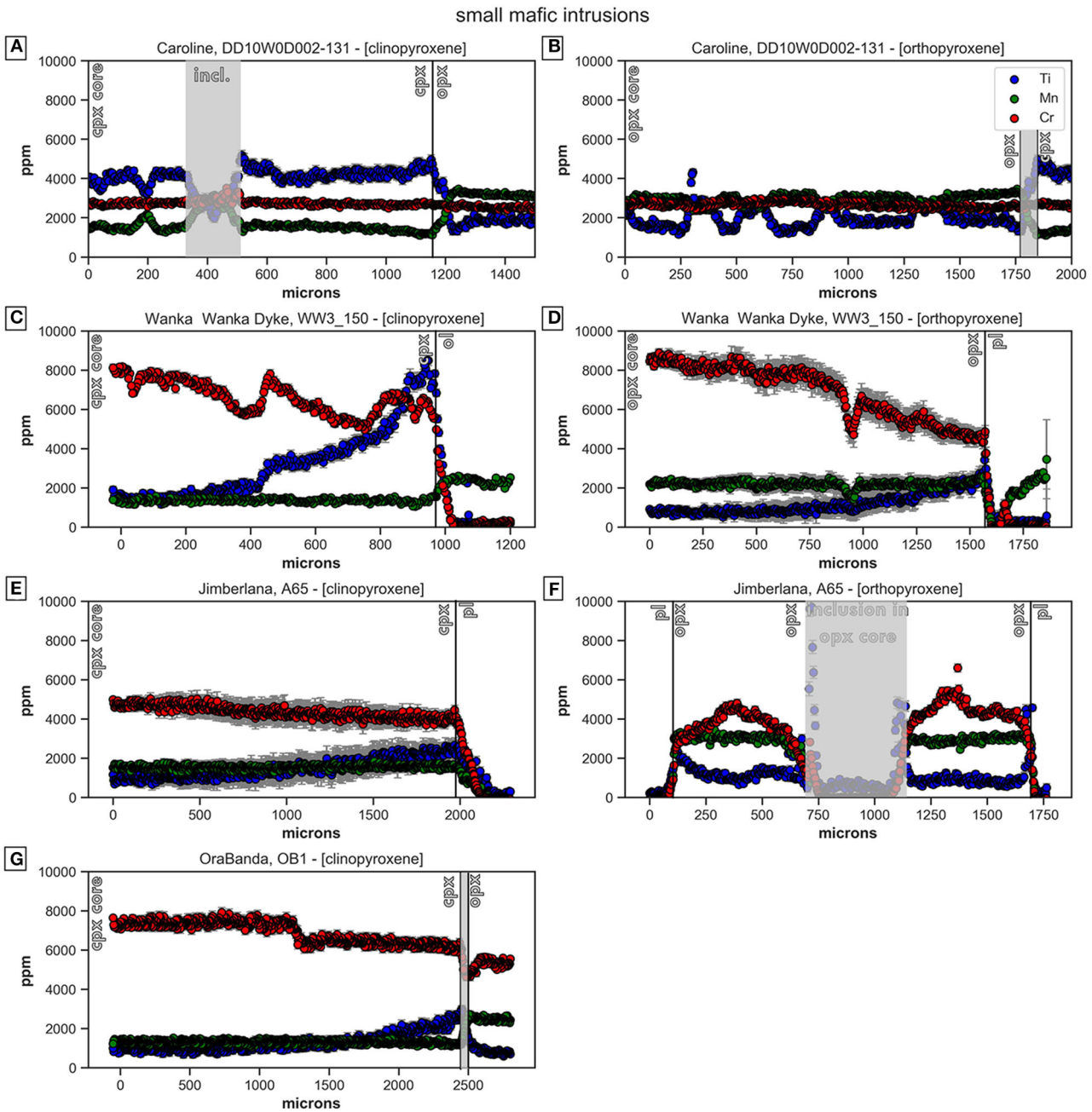

FIGURE 10 | Traverses across clinopyroxene and orthopyroxene from core to rim in mafic intrusions. **(A,B)** A clinopyroxene and orthopyroxene traverses from the Ngunala (Caroline) intrusion, **(C,D)** clinopyroxene and orthopyroxene traverses from the Wanka Wanka Dyke (**Figure 9A**), **(E,F)** clinopyroxene and orthopyroxene traverse from the Jimberlana intrusion (**Figure 9D**), and **(G)** a traverse through the large clinopyroxene oikocryst of the Ora Banda intrusion (**Figure 9E**).

for chromium is similar in both phases, however, as sector zoning is visible, the partitioning is slightly different within each sector.

We compared the concentration of adjacent sector zones in orthopyroxene grains in a number of samples and calculated the Cr enrichment factor (high concentration over low concentration) between the sectors. The enrichment factors in the ore grade samples range from 1.1 to 1.8 with an average ($n = 83$) of 1.6 ± 0.2 times enrichment between the sectors (**Figure 11**). The unmineralized intrusions (Jimberlana and Kotalahti) have enrichment factors between sectors within orthopyroxene grains of 1.4 ± 0.2 ($n = 34$) which is within a standard deviation of the mineralized intrusions. The average enrichment factor for Cr measured in these intrusive orthopyroxene grains is similar to those measured between sectors

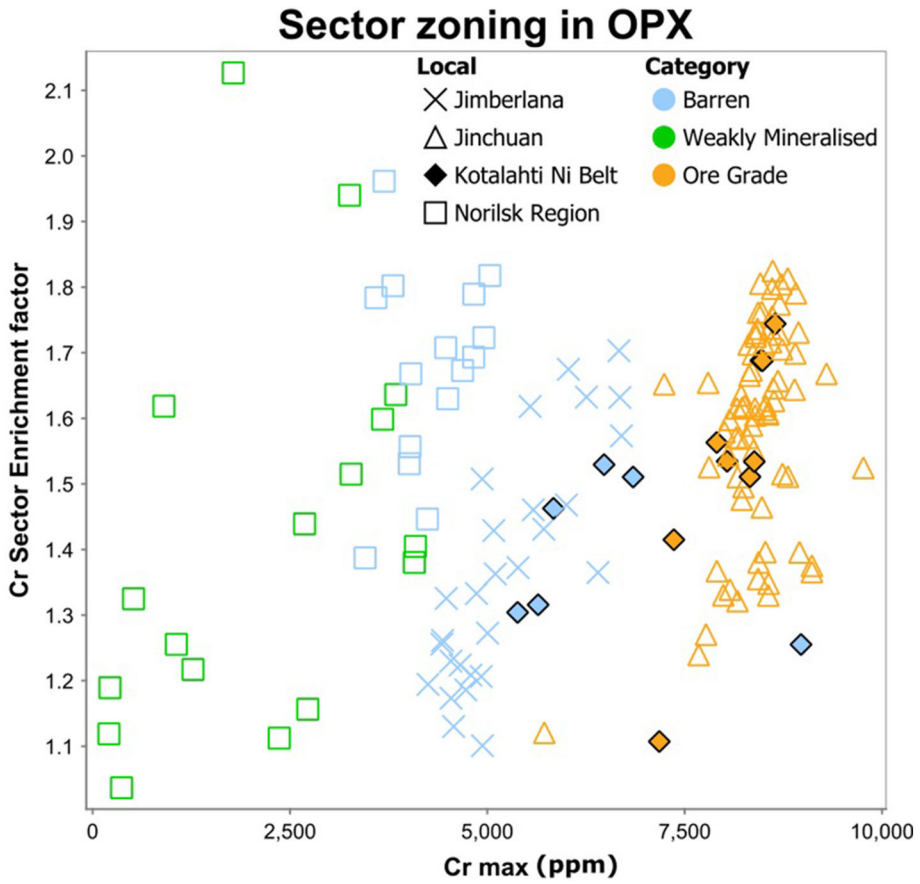

FIGURE 11 | The sector zone enrichment factor for Cr (high concentration sector over low concentration sector) for orthopyroxene (opx) in samples taken from the Australian Synchrotron μXRF maps. Average for each category is Barren = 1.4, weakly mineralized = 1.5, ore grade = 1.6.

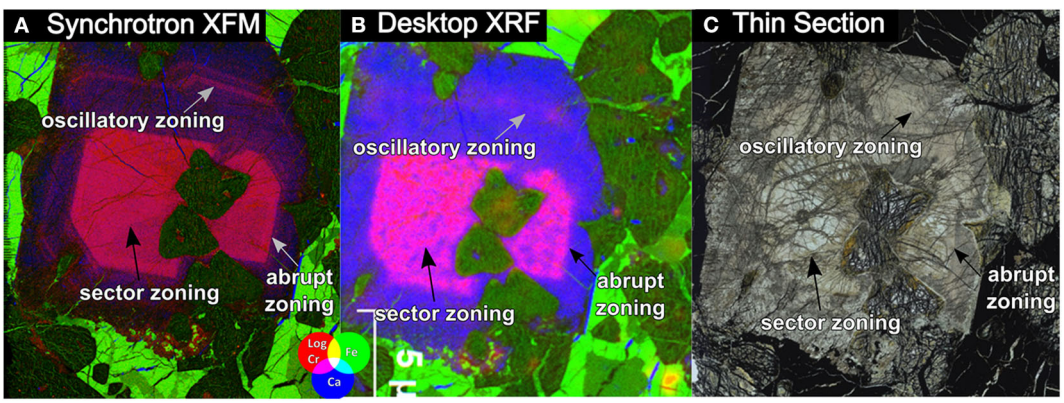

FIGURE 12 | Sample KU30024 imaged by **(A)** μXRF on the Australian synchrotron, **(B)** a Bruker desktop microbeam XRF mapper—M4 Tornado™, **(C)** and plane polarized light image of the thin section. The abrupt zoning can be observed very well with a desktop XRF system and can sometimes be distinguished in thin section. The sector zoning is also visible in thin section.

in volcanic clinopyroxenes (1.4 times) in Ubide et al. (2019).

Partitioning of trace elements is dependent on many extrinsic variables, such as pressure, temperature and melt composition (Ewart et al., 1973; Barnes, 1986; Hart and Dunn, 1993; Lundstrom et al., 1998; Frei et al., 2009; Schoneveld, 2017) and the partitioning between the sectors in pyroxenes may also be dependent on these variables. Few experimental studies have been conducted looking at the partitioning between sectors in minerals (Kouchi et al., 1983; Schwandt and McKay, 2006) but

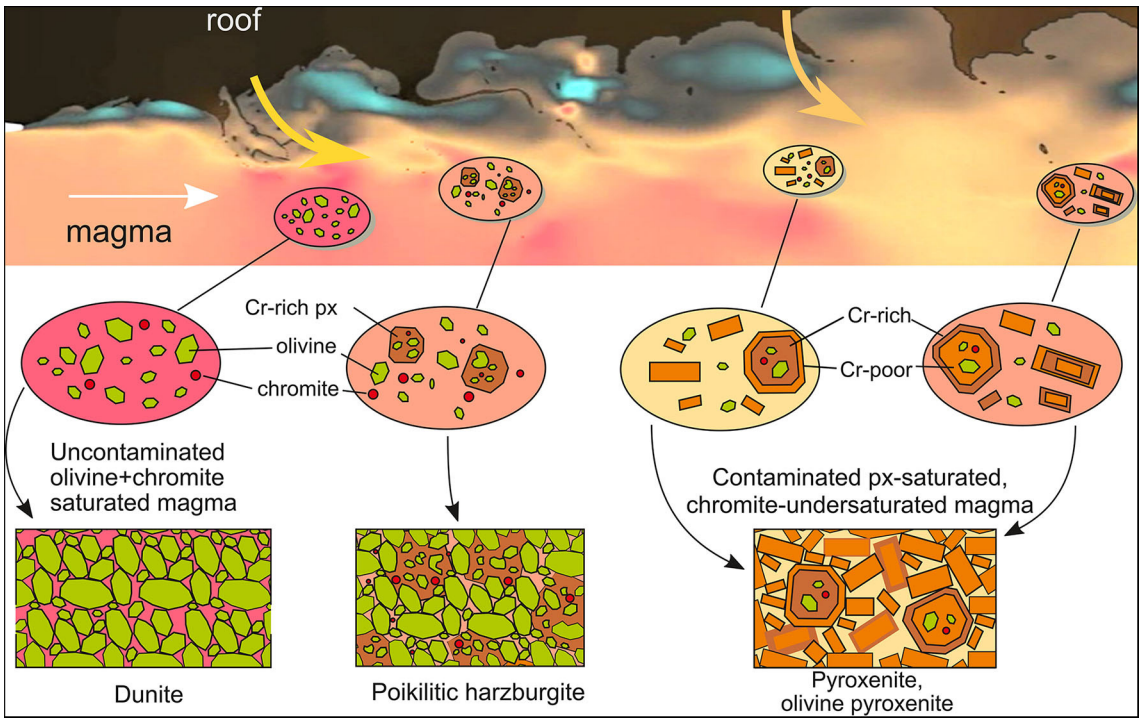

FIGURE 13 | The flowing magma assimilates the surrounding material, causing short-range transient fluctuations in composition, silica activity and redox state in poorly mixed magma. This allows for complex zoning of the mineral phases. sulfide mineralization can occur due to the assimilation of country rocks, therefore these zoning patterns can indicate high magma volumes required to form sulfide mineralization. Diagram modified from Barnes et al. (2016b).

this partitioning may prove to provide insights into the magmatic histories. The main problem with using partition coefficients for magma history determinations is not being certain of the melt composition, which is usually not amenable to direct sampling. If extrinsic variables can be determined from partitioning between sectors in a single crystal, the melt becomes less relevant.

The Wanka Wanka dyke contains a good example of a clinopyroxene grain recording the extrinsic change of the system (**Figure 9B**). The Cr concentration profile exhibits a sawtooth pattern (**Figure 10C**) with a gradual concentration decrease followed by a rapid and significant increase after an embayed boundary (**Figure 9B**). This embayment, along with the oscillation in Cr content is a strong indication of dissolution due to magma recharge (Ubide and Kamber, 2018). The Ti concentration in this sample displays normal zoning, with an increase in Ti concentration after the first magma recharge (**Figure 9C**). As titanium can be an order of magnitude less compatible in clinopyroxenes than chromium (Bédard, 2014; Schoneveld, 2017), it does not record the small recharge in magma chemistry but does record the distinct change in chemistry between cumulus and post cumulus growth. Interestingly, the sawtooth-patterned clinopyroxene grain here appears to be an oikocryst, as discussed further in the next section.

Oscillatory zoning of Cr can also be observed throughout the mineralized intrusions, although these oscillations are usually at much finer scale (**Figure 3**). Examined at high spatial resolution (**Figure 3A**), these oscillations in chemistry can be observed in both the cores and rims of ortho- and of clinopyroxenes (**Figure 4**), although the variations are usually on the scale of 10–100 ppm. In contrast, the increase in Cr concentration in the clinopyroxene grains of the Wanka Wanka sample reaches ∼2,000 ppm. Oscillatory zoning is thought to occur in clinopyroxenes that grow moderately rapidly [10^{-11} and 10^{-13} m/s; Fowler and Shore (1996)] which suggests the clinopyroxene grain in the Rytky intrusion of Kotalahti (**Figure 3A**) took anywhere from ∼10 to 1,000 years to grow the outer, oscillated rims. If we could refine growth speed calculations further, this would be a great asset in determining the formation timescale of the "long lived" intrusions.

FORMATION OF OIKOCRYSTS

Pyroxene oikocrysts are common in mafic intrusions both small and large (Wager et al., 1960; Wager and Brown, 1969; Barnes et al., 2016b, 2019b; Mao et al., 2019) creating what is known as poikilitic textures (**Figure 6**). These pyroxene oikocrysts can be multi-centimeter in scale with inclusions (chadacrysts) of smaller phases (usually olivine, pyroxene or chromite). All of the intrusion types (mineralized, unmineralized, and those not associated with mineralization) can display poikilitic textures (**Figures 6**, **7A**, **9E**). These grains characteristically trap the early cumulus phases which allows us to analyse the evolution of the chemistry of the system as well as the evolution of the

texture. The small chadacrysts within pyroxene oikocrysts can either represent the first stage of nucleation or remnant grains following peritectic dissolution. By performing detailed crystal size distribution (CSD) analysis we are able to make some inferences of the formation of the systems (Berger et al., 2011; Kaufmann et al., 2018; Mao et al., 2018; Schoneveld et al., 2020).

There are two main theories for the formation of oikocrysts in these systems (Kaufmann et al., 2018): (1) the post-cumulus model: formation *in-situ* in the cumulate pile from the intercumulus trapped liquid (Wager et al., 1960); (2) The cumulus model: growth during the formation of the cumulate (Campbell, 1968; Mathison, 1987; Tegner and Wilson, 1995; Barnes et al., 2016b), with the poikilitic texture arising from differential nucleation and growth rates of the poikilitic and enclosed (chadacryst) phases (McBirney and Noyes, 1979).

By using the Cr-zoning we have outlined in this manuscript, we can make further inferences on the formation of these textures. The smooth normal zonation that characterizes the unmineralized intrusions (**Figure 7A**) would be aligned with the post-cumulate theory of formation, with the steady decrease in chromium indicating a closed system where early-formed cumulus phases are undergoing reaction with trapped intercumulus liquid. The sector zoning and oscillations in the oikocrysts in mineralized intrusions (**Figure 6**) represent rapid growth in a still actively forming and crystallizing cumulate without this steady depletion in Cr from the post-cumulate reactions.

We can use the zonation of different elements to infer combinations of cumulate and post-cumulate growth such as those outlined from the Wanka Wanka Dyke (**Figure 9**) where Cr contents suggest there was a magma recharge event during oikocryst growth. This may have been possible by (1) growth from intercumulus liquid within a crystal mush in the presence of advecting or convecting intercumulus liquid communicating with the main magma source (Kerr and Tait, 1985, 1986); (2) rapid crescumulate growth due to supersaturation in a boundary layer at the mush-magma interface (Campbell, 1968; McBirney and Noyes, 1979; Mathison, 1987; Godel et al., 2013; Barnes et al., 2016b, 2018; Mao et al., 2018), or (3) growth within the mush by peritectic reaction between cumulus crystals and upward-migrating evolved liquid derived from crystal mush beneath (Kaufmann et al., 2018). Given that the Wangka Wankga sample represents a cumulate from the center of a relatively small (∼100 m wide) dike, the first and third interpretations are unlikely, and we prefer the second.

CR ZONATION IN PYROXENES AS AN EXPLORATION TOOL

Commonly, economic Ni-Cu sulfide deposits are found within a small proportion of the intrusions within a given magmatic province. Excellent examples of this are the Norilsk-Talnakh region of Siberia (Naldrett, 2004) or the Halls Creek Orogen of Western Australia (Mole et al., 2018; Le Vaillant et al., 2020). Our results suggest that, while they might not be strictly diagnostic, zoning patterns in pyroxenes might be useful indicators (along with other factors) for ranking relative prospectivity of mafic-ultramafic intrusions where limited sampling is available, for example at the early stages of a regional exploration program. Our results are primarily based on synchrotron data, not readily available in an exploration context. However, most of the important features can be recognized with lab-based microbeam XRF mapping (**Figure 12**).

Desktop XRF mappers are becoming more affordable and more widely utilized in exploration. The technology is becoming faster to use and cheaper to acquire with the data obtained from these XRF mappers giving elemental and textural data on minimally prepared drill core samples. With some geological knowledge, this data can readily be transformed into to mineralogical information. Sample preparation requires only a flat saw-cut surface, which is a significant reduction in time when compared to the creation of thin section or drilled and polished rounds/mounts for other microanalytical techniques. Although these technologies may never replace detailed petrography and electron-beam microanalysis, they are a useful intermediate step to ensure sampling of representative or key areas for microanalysis, to give context to these analysis (Barnes et al., 2017b; Pearce et al., 2017), and to provide valable textural and mineralogical evidence on processes operating at cm or dm scales not recognizable in thin sections (e.g., Barnes et al., 2020).

Comparing the same sample (KU30024) collected using both the Australian Synchrotron XRF and a desktop XRF, many of the features can be observed using both techniques. The important distinguishing features; poikilitic textures, abrupt zonation and sector zoning are visible using the desktop techniques. The zoning patterns observed in the unmineralized intrusions are of much lower concentrations and are only readily visible using complex, low energy and higher resolution techniques using the Australian Synchrotron. Therefore, the unmineralized samples do not show any of these zonation patterns when examined with the desktop XRF mapping techniques.

Limitations

Thus, far we have mostly investigated samples from within the sulfide rich zone of the mineralized intrusion. Future research is needed to systematically investigate how far these signals propagate through the magma conduit away from the sulfide. Quantification of the limits on growth rate imposed by preservation of sector and other zoning types will be vital in extracting more information from these intriguing textures.

CONCLUSIONS

In summary, we have observed a suite of possible zoning patterns in pyroxenes that may be observed when examining mafic intrusions.

1. Abrupt zoning (Cr)—a zone of low Cr concentration around a Cr rich (∼ >5,000 ppm) core, with a steep concentration gradient defining the core-rim boundary;
2. Sector zoning (Cr)—hour-glass style of zonation in the core of pyroxene grains and/or;

3. Cumulate poikilitic pyroxenes—large pyroxene grains enclosing smaller olivine, pyroxene or chromite grains, commonly showing abrupt zoning toward sharply Cr-depleted rims.

To date, our studies indicate that sector zoning in pyroxenes, both clearly cumulus and poikilitic, is almost ubiquitous in small intrusions with relatively rapid cooling rates (but much less evident in large intrusions such as the Bushveld Complex). Abrupt zoning is most commonly observed in mineralized intrusions while smooth gradual zoning toward Cr-poor rims is more characteristic of unmineralized bodies.

The presence of sector zoning within oikocryst cores is noted in several localities, both mineralized (e.g., Norilsk-Talnakh) and unmineralized (Majasaari) and is of particular interest from the point of view of the origin of poikilitic textures. It tends to favor a model for simultaneous growth of both oikocryst and chadacryst phases with the poikilitic phase growing faster from fewer nucleation sites.

One particular combination of characteristics has so far only been observed within mineralized intrusions: poikilitic pyroxenes (particularly orthopyroxene) with abrupt, in some cases oscillatory, zoning which have euhedral Cr-rich cores containing olivine inclusions. Following Barnes et al. (2016b) we suggest that this combination of features arises from reactive transport of olivine and orthopyroxene grains within variably contaminated magma in dynamic conduit systems (**Figure 13**). Orthopyroxene grows as a result of peritectic reaction between suspended olivine and locally Si-saturated contaminated magma. Where the magma is initially chromite-saturated, the high Cr content of the growing orthopyroxene cores is buffered by equilibrium with chromite. Such dynamic flow conditions coupled with the necessity of assimilation of externally derived sulfur (Ripley and Li, 2013; Barnes et al., 2016a) are essential to the origin of magmatic Ni-Cu-PGE sulfide ores in conduit settings.

As revealed by XRF-based mapping technique, it appears that zoning in pyroxenes may actually be as widespread and complex as the more familiar zoning patterns in plagioclases and zircons.

DATA AVAILABILITY STATEMENT

The datasets generated for this study are available on request to the corresponding author.

AUTHOR CONTRIBUTIONS

LS and SB wrote and edited the manuscript as well as collected and analyzed the data and created all the figures. HM, VT, K-YW, and Y-JM provided samples and expertise on their mineral deposits. ML, DP, and VT assisted in collecting and analyzing the data. All authors contributed to the article and approved the submitted version.

ACKNOWLEDGMENTS

This research is a collection of data obtained over the last 5 years as small parts of experiments 8941, 8965, 10023, 11667, and 14304 and as the focus of experiments 13405 and 15166 on the X-ray fluorescence microscopy beamline at the Australian Synchrotron, part of ANSTO. We would like to thank everyone who collected, lent, and prepared the samples used in this study as well as all those who helped with their technical expertise to enable the researchers to collect this data. In particular, we thank IGO Ltd. for access to the Nova-Bollinger deposit. Teresa Ubide is thanked for suggesting this manuscript be submitted to this research topic and her assistance with experiment 15,166 on the Australian Synchrotron. This manuscript benefitted from suggestions from Belinda Godel and Siyu Hu before submission. The manuscript was also improved by two reviewers and Catherine Annen. MP is thanked for the editorial handling of this manuscript.

SUPPLEMENTARY MATERIAL

The Supplementary Material for this article can be found online at: https://www.frontiersin.org/articles/10.3389/feart.2020.00256/full#supplementary-material

REFERENCES

Barnes, S., Le Vaillant, M., Godel, B., and Lesher, M. (2019a). Droplets and bubbles: solidification of sulphide-rich vapour-saturated orthocumulates in the Norilsk-Talnakh Ni-Cu-PGE ore-bearing intrusions. *J. Petrol.* 60, 269–300. doi: 10.1093/petrology/egy114

Barnes, S. J. (1986). The distribution of chromium among orthopyroxene, spinel and silicate liquid at atmospheric pressure. *Geochim. Cosmochim. Acta* 50, 1889–1909. doi: 10.1016/0016-7037(86)90246-2

Barnes, S. J., Cruden, A. R., Arndt, N., and Saumur, B. M. (2016a). The mineral system approach applied to magmatic Ni–Cu–PGE sulphide deposits. *Ore Geol. Rev.* 76, 296–316. doi: 10.1016/j.oregeorev.2015.06.012

Barnes, S. J., Holwell, D. A., and Le Vaillant, M. (2017a). Magmatic sulfide ore deposits. *Elements* 13, 91–97. doi: 10.2113/gselements.13.2.89

Barnes, S. J., Mole, D. R., Hornsey, R., and Schoneveld, L. E. (2019b). Nickel-copper sulfide mineralization in the ntaka hill ultramafic complex, nachingwea region, tanzania. *Econ. Geol.* 114, 1135–1158. doi: 10.5382/econgeo.4677

Barnes, S. J., Mole, D. R., Le Vaillant, M., Campbell, M., Verrall, M., Roberts, M., et al. (2016b). Poikilitic textures, heteradcumulates and zoned orthopyroxenes in the Ntaka Ultramafic Complex, Tanzania: implications for crystallisation mechanisms of oikocrysts. *J. Petrol.* 57, 1171–1198. doi: 10.1093/petrology/egw036

Barnes, S. J., Mungall, J. E., Le Vaillant, M., Godel, B., Lesher, C. M., Holwell, D., et al. (2017b). Sulfide-silicate textures in magmatic Ni-Cu-PGE sulfide ore deposits: disseminated and net-textured ores. *Am. Mineral.* 102, 473–506. doi: 10.2138/am-2017-5754

Barnes, S. J., Paterson, D., Ubide, T., Schoneveld, L., Ryan, C., and Le Vaillant, M. (2020). Imaging trace-element zoning in pyroxenes using synchrotron XRF mapping with the Maia detector array: benefit of low-incident energy. *Am. Mineral.* 105, 136–140. doi: 10.2138/am-2020-7228

Barnes, S. J., Piña, R., and Le Vaillant, M. (2018). Textural development in sulfide-matrix ore breccias in the Aguablanca Ni-Cu deposit, Spain, revealed by X-ray fluorescence microscopy. *Ore Geol. Rev.* 95, 849–862. doi: 10.1016/j.oregeorev.2018.03.004

Barnes, S. J., and Robertson, J. C. (2019). Time scales and length scales in magma flow pathways and the origin of magmatic Ni–Cu–PGE ore deposits. *Geosci. Front.* 10, 77–87. doi: 10.1016/j.gsf.2018.02.006

Barnes, S. J., Taranovic, V., Miller, J. M., Boyce, G., and Beresford, S. W. (in press). Sulfide emplacement and migration in the Nova-Bollinger Ni-Cu-Co deposit, Albany-Fraser Orogen, Western Australia. *Econ. Geol.*

Bédard, J. H. (2014). Parameterizations of calcic clinopyroxene—Melt trace element partition coefficients. *Geochem. Geophys. Geosyst.* 15, 303–336. doi: 10.1002/2013GC005112

Berger, A., Herwegh, M., Schwarz, J.-O., and Putlitz, B. (2011). Quantitative analysis of crystal/grain sizes and their distributions in 2D and 3D. *J. Struct. Geol.* 33, 1751–1763. doi: 10.1016/j.jsg.2011.07.002

Bernstein, S. (2006). In situ fractional crystallization of a mafic pluton: microanalytical study of a Palaeogene gabbronorite plug in East Greenland. *Lithos* 92, 222–237. doi: 10.1016/j.lithos.2006.03.034

Campbell, I. H. (1968). The origin of heteradcumulate and adcumulate textures in the Jimberlana Norite. *Geol. Mag* 105, 378–383. doi: 10.1017/S0016756800054431

Chai, G., and Naldrett, A. J. (1992). The Jinchuan ultramafic intrusion: cumulate of a high-Mg basaltic magma. *J. Petrol.* 33, 277–304. doi: 10.1093/petrology/33.2.277

Cherniak, D. J., and Dimanov, A. (2010). Diffusion in pyroxene, mica and amphibole. *Rev. Mineral. Geochem.* 72, 641–690. doi: 10.2138/rmg.2010.72.14

Downes, M. J. (1974). Sector and oscillatory zoning in calcic augites from M. Etna, Sicily. *Contrib. Mineral. Petrol.* 47, 187–196. doi: 10.1007/BF00371538

Ewart, A., Bryan, W. B., and Gill, J. B. (1973). Mineralogy and Geochemistry of the Younger Volcanic Islands of Tonga, S.W. Pacific. *J. Petrol.* 14, 429–465. doi: 10.1093/petrology/14.3.429

Fowler, A. D., and Shore, M. (1996). Oscillatory zoning in minerals; a common phenomenon. *Canad. Mineral.* 34, 1111–1126.

Frei, D., Liebscher, A., Franz, G., Wunder, B., Klemme, S., and Blundy, J. (2009). Trace element partitioning between orthopyroxene and anhydrous silicate melt on the lherzolite solidus from 1.1 to 3.2 GPa and 1,230 to 1,535°C in the model system Na2O–CaO–MgO–Al2O3–SiO2. *Contribut. Mineral. Petrol.* 157, 473–490. doi: 10.1007/s00410-008-0346-5

Godel, B. M., Barnes, S. J., Gurer, D., Austin, P., and Fiorentini, M. L. (2013). Chromite in komatiites: 3D morphologies with implications for crystallization mechanisms. *Contribut. Mineral. Petrol.* 165, 173–189. doi: 10.1007/s00410-012-0804-y

Hargraves, R. B., Hollister, L. S., and Otalora, G. (1970). Compositional zoning and its significance in pyroxenes from three coarse-grained lunar samples. *Science* 167, 631–633. doi: 10.1126/science.167.3918.631

Hart, S. R., and Dunn, T. (1993). Experimental cpx/melt partitioning of 24 trace elements. *Contribut. Mineral. Petrol.* 113, 1–8. doi: 10.1007/BF00320827

Hollister, L. S., and Gancarz, A. J. (1971). Compositional sector-zoning in clinopyroxene from the Narce area, Italy. *Am. Mineral.* 56, 959.

Hollister, L. S., Trzcienski, W. E. Jr., Hargraves, R. B., and Kulick, C. G. (1971). Petrogenetic significance of pyroxenes in two Apollo 12 samples. *Geochim. Cosmochim. Acta* 2, 529–557.

Irvine, T. N. (1982). Terminology for layered intrusions. *J. Petrol.* 23, 127–162. doi: 10.1093/petrology/23.2.127-a

Kaufmann, F., Vukmanovic, Z., Holness, M., and Hecht, L. (2018). Orthopyroxene oikocrysts in the MG1 chromitite layer of the Bushveld Complex: implications for cumulate formation and recrystallisation. *Contribut. Mineral. Petrol.* 173, 1–20. doi: 10.1007/s00410-018-1441-x

Keays, R. R., and Campbell, I. H. (1981). Precious metals in the Jimberlana Intrusion, Western Australia: implications for the genesis of platiniferous ores in layered intrusions. *Econ. Geol.* 76, 1118–1141. doi: 10.2113/gsecongeo.76.5.1118

Kerr, R. C., and Tait, S. R. (1985). Convective exchange between pore fluid and an overling reservoir of dense fluid: a postcumulus process in layered intrusions. *Earth Planet. Sci. Lett.* 75, 147–156. doi: 10.1016/0012-821X(85)90097-4

Kerr, R. C., and Tait, S. R. (1986). Crystallisation and compositional convection in a porous medium with application to layered igneous intrusions. *J. Geophys. Res.* 91, 3591–3608. doi: 10.1029/JB091iB03p03591

Kirkham, R., Dunn, P., Kuczewski, A., Siddons, D., Dodanwela, R., Moorhead, G., et al. (2010). The Maia spectroscopy detector system: engineering for integrated pulse capture, low-latency scanning and real-time processing. *Proc. Aust. Inst. Phys.* 1234, 240–243. doi: 10.1063/1.3463181

Kouchi, A., Sugawara, Y., Kashima, K., and Sunagawa, I. (1983). Laboratory growth of sector zoned clinopyroxenes in the system CaMgSi2O6-CaTiAl2O6. *Contribut. Mineral. Petrol.* 83, 177–184. doi: 10.1007/BF00373091

Le Vaillant, M., Barnes, S. J., Mungall, J. E., and Mungall, E. L. (2017). Role of degassing of the Noril'sk nickel deposits in the Permian-Triassic mass extinction event. *Proc. Natl. Acad. Sci. U.S.A.* 114, 2485–2490. doi: 10.1073/pnas.1611086114

Le Vaillant, M., Barnes, S. J., Mole, D. R., Fiorentini, M. L., LaFlamme, C. K., Denyszyn, S., et al. (2020). Multidisciplinary study of a complex magmatic system: the Savannah Ni-Cu-Co Camp, Western Australia. *Ore Geol. Rev.* 117:102392. doi: 10.1016/j.oregeorev.2019.103292

Leung, I. S. (1974). Sector-zoned titanaugites morphology, crystal chemistry, and growth. *Am. Mineral.* 59, 127–138.

Li, X. H., Su, L., Chung, S. L., Li, Z. X., Liu, Y., Song, B., et al. (2005). Formation of the jinchuan ultramafic intrusion and the world's third largest ni-cu sulfide deposit: associated with the similar to 825 ma south china mantle plume? - Art. No. Q11004. *Geochem. Geophys. Geosyst.* 6:11004. doi: 10.1029/2005GC001006

Lofgren, G. E., Huss, G. R., and Wasserburg, G. J. (2006). An experimental study of trace-element partitioning between Ti-Al-clinopyroxene and melt: equilibrium and kinetic effects including sector zoning. *Am. Mineral.* 91, 1596–1606. doi: 10.2138/am.2006.2108

Lundstrom, C. C., Shaw, H. F., Ryerson, F. J., Williams, Q., and Gill, J. (1998). Crystal chemical control of clinopyroxene-melt partitioning in the Di-Ab-An system: implications for elemental fractionations in the depleted mantle. *Geochim. Cosmochim. Acta* 62, 2849–2862. doi: 10.1016/S0016-7037(98)00197-5

Mäkinen, J., and Makkonen, H. (2004). Petrology and structure of the Palaeoproterozoic (1.9 Ga) Rytky nickel sulphide deposit, Central Finland: a comparison with the Kotalahti nickel deposit. *Intern. J. Geol. Mineral. Geochem. Mineral Deposits* 39, 405–421. doi: 10.1007/s00126-004-0413-4

Makkonen, H., and Mursu, J. (2004). *Tutkimustyöselostus Pielaveden Kunnassa Valtausalueilla Saarela 1 ja 2 (kaiv.rek.nrot 7294/1 ja 7572/1) Suoritetuista Nikkelimalmitutkimuksista Vuosina 1999-2003. Geological Survey of Finland, archive report M06/3314/2004/1/10.*

Makkonen, H. V. (1996). 1.9 Ga tholeiitic magmatism and related Ni-Cu deposition in the Juva area, SE Finland. *Geol. Survey Finland Bull.* 386, 101.

Makkonen, H. V. (2015). "Nickel deposits of the 1.88 Ga kotalahti and vammala belts," in *Mineral Deposits of Finland,* eds W. D. Maier, R. Lahtinen and H. O' Brien (Elsevier), 253–287. doi: 10.1016/B978-0-12-410438-9.00010-8

Makkonen, H. V., Halkoaho, T., Konnunaho, J., Rasilainen, K., Kontinen, A., and Eilu, P. (2017). Ni-(Cu-PGE) deposits in Finland – Geology and exploration potential. *Ore Geol. Rev.* 90, 667–696. doi: 10.1016/j.oregeorev.2017.06.008

Mao, Y.-J., Barnes, S. J., Qin, K.-Z., Tang, D., Martin, L., Su, B., et al. (2019). Rapid orthopyroxene growth induced by silica assimilation: constraints from sector-zoned orthopyroxene, olivine oxygen isotopes and trace element variations in the Huangshanxi Ni–Cu deposit, Northwest China. *Contribut. Mineral. Petrol.* 174, 33. doi: 10.1007/s00410-019-1574-6

Mao, Y.-J., Barnes, S. J., Duan, J., Qin, K.-Z., Godel, B. M., and Jiao, J. (2018). Morphology and particle size distribution of olivines and sulphides in the Jinchuan Ni-Cu sulphide deposit: evidence for sulphide percolation in a crystal mush. *J. Petrol.* 59, 1701–1730. doi: 10.1093/petrology/egy077

Mathison, C. I. (1987). Pyroxene oikocrysts in troctolitic cumulates — evidence for supercooled crystallisation and postcumulus modification. *Contribut. Mineral. Petrol.* 97, 228–236. doi: 10.1007/BF00371242

McBirney, A. R., and Noyes, R. M. (1979). Crystallization and layering in the Skaergaard Intrusion. *J. Petrol.* 20, 487–554. doi: 10.1093/petrology/20.3.487

Mole, D. R., Barnes, S. J., Taylor, R. J. M., Kinny, P. D., and Fritz, H. (2018). A relic of the Mozambique Ocean in south-east Tanzania. *Precambrian Res.* 305, 386–426. doi: 10.1016/j.precamres.2017.10.009

Naldrett, A. J. (2004). *Magmatic Sulfide Deposits: Geology, Geochemistry and Exploration*. Heidelberg: Springer.

Pearce, M. A., Godel, B. M., Fisher, L. A., Schoneveld, L. E., Cleverly, J. S., Oliver, N. H. S., et al. (2017). Microscale data to macroscale processes: a review of

microcharacterization applied to mineral systems. *Geol. Soc. London Special Publicat.* 453:SP453.3. doi: 10.1144/SP453.3

Ripley, E. M., and Li, C. (2011). "A review of conduit-related ni-cu-(pge) sulfide mineralization at the voisey's bay deposit, labrador, and the eagle deposit, northern michigan," in *Magmatic Ni-Cu and PGE Deposits: Geology, Geochemistry and Genesis. Reviews in Economic Geology, Vol. 17*, eds C. Li and E. M. Ripley (Littleton: Society of Economic Geologists), 181–197.

Ripley, E. M., and Li, C. (2013). Sulfide saturation in mafic magmas: is external sulfur required for magmatic Ni-Cu-(PGE) ore genesis? *Econ. Geol.* 108, 45–58. doi: 10.2113/econgeo.108.1.45

Ryan, C. G. (2000). Quantitative trace element imaging using pixe and the nuclear microprobe. *J. Imaging Syst. Technol.* 11, 219–230. doi: 10.1002/ima.1007

Ryan, C. G., Siddons, D. P., Kirkham, R., Li, Z. Y., de Jonge, M. D., Paterson, D. J., et al. (2014). Maia X-ray fluorescence imaging: Capturing detail in complex natural samples. *J. Phys. Conf. Ser.* 499:012002.

Schoneveld, L. E. (2017). Partitioning of trace elements between plagioclase, clinopyroxene and melt (Doctor of Philosophy). The Australian National University.

Schoneveld, L. E., Barnes, S. J., Williams, M., Le Vaillant, M., and Paterson, D. (2020). Silicate and oxide mineral chemistry and textures of the Norilsk-Talnakh Ni-Cu-PGE ore-bearing intrusions. *Econ. Geol.* doi: 10.5382/econgeo.4747

Schwandt, C. S., and McKay, G. A. (2006). Minor- and trace-element sector zoning in synthetic enstatite. *Am. Mineral.* 91, 1607–1615. doi: 10.2138/am.2006.2093

Song, X. Y., Danyushevsky, L. V., Keays, R. R., Chen, L.-M., and Wang, Y.-S. (2012). Structural, lithological, and geochemical constraints on the dynamic magma plumbing system of the Jinchuan Ni-Cu sulfide deposit, NW China. *Mineral. Dep.* 47, 277–297. doi: 10.1007/s00126-011-0370-7

Tegner, C., and Wilson, J. R. (1995). Textures in a poikilitic olivine gabbro cumulate: evidence for supercooling. *Mineral. Petrol.* 54, 161–173. doi: 10.1007/BF01162859

Ubide, T., and Kamber, B. (2018). Volcanic crystals as time capsules of eruption history. *Nat. Commun.* 9, 326–326. doi: 10.1038/s41467-017-02274-w

Ubide, T., Mollo, S., Zhao, J.-,x., Nazzari, M., and Scarlato, P. (2019). Sector-zoned clinopyroxene as a recorder of magma history, eruption triggers, and ascent rates. *Geochim. Cosmochim. Acta.* 251, 265–283. doi: 10.1016/j.gca.2019.02.021

Wager, L. R., and Brown, G. M. (1969). *Layered Igneous Rocks.* Edinburgh: Oliver and Boyd.

Wager, L. R., Brown, G. M., and Wadsworth, W. J. (1960). Types of igneous cumulates. *J. Petrol.* 1, 73–85. doi: 10.1093/petrology/1.1.73

Wang, K.-Y., Song, X.-Y., Yi, J.-N., Barnes, S. J., She, Y.-W., Zheng, W.-Q., et al. (2019). Zoned orthopyroxenes in the Ni-Co sulfide ore-bearing Xiarihamu mafic-ultramafic intrusion in northern Tibetan Plateau, China: implications for multiple magma replenishments. *Ore Geol. Rev.* 113:103082. doi: 10.1016/j.oregeorev.2019.103082

Welsch, B., Hammer, J., Baronnet, A., Jacob, S., Hellebrand, E., and Sinton, J. (2016). Clinopyroxene in postshield Haleakala ankaramite: 2. Texture, compositional zoning and supersaturation in the magma. *Contribut. Mineral. Petrol.* 171, 1–19. doi: 10.1007/s00410-015-1213-9

Witt, W. K. (1995). Tholeiitic and high-Mg mafic/ultramafic sills in the Eastern Goldfields Province, Western Australia: implications for tectonic settings. *Austral. J. Earth Sci.* 42, 407–422. doi: 10.1080/08120099508728211

Conflict of Interest: HM was employed by the company Boliden FinnEx Oy.

The remaining authors declare that the research was conducted in the absence of any commercial or financial relationships that could be construed as a potential conflict of interest.

frontiers in Earth Science

ORIGINAL RESEARCH
published: 31 July 2020
doi: 10.3389/feart.2020.00310

Defining Pre-eruptive Conditions of the Havre 2012 Submarine Rhyolite Eruption Using Crystal Archives

Joseph Knafelc[1], Scott E. Bryan[1], David Gust[1] and Henrietta E. Cathey[2]*

[1] School of Earth and Atmospheric Sciences, Queensland University of Technology, Brisbane, QLD, Australia, [2] Central Analytical Research Facility, Institute for Future Environments, Queensland University of Technology, Brisbane, QLD, Australia

The 2012 Havre eruption evacuated a crystal-poor rhyolite (~3–7% crystals) producing a volumetrically dominant (~1.4 km^3) pumice raft, as well as seafloor giant pumice (5–8%) and lavas (12–14%) at the vent (~0.1 km^3), both of which have subtly higher phenocryst contents. For crystal-poor rhyolites like the Havre pumice, it can often remain ambiguous as to whether the few phenocrysts present, in this case, plagioclase, orthopyroxene, clinopyroxene, Fe-Ti oxides ± quartz, are: (a) autocrysts crystallizing from the surrounding melt, (b) antecrysts being sourced from mush and the magma plumbing system, or (c) xenocrysts derived from source materials or chamber walls, or (d) possibly a combination of all of the above. In crystal-poor magmas, the few crystals present are strongly relied upon to constrain pre-eruptive conditions such as magmatic temperatures, pressures, water content and fO_2. A detailed textural and compositional analysis combined with a range of equilibrium tests and rhyolite-MELTS modeling provide the basis for distinguishing autocrystic vs inherited crystal populations in the Havre eruption. An autocrystic mineral assemblage of andesine plagioclase, enstatite and Fe-Ti oxides constrains the pre-eruptive conditions of the Havre rhyolite magma: magmatic temperatures of 890 ± 27°C, crystallization pressures at 2–4 kbars, oxygen fugacity of NNO + 0.4 and water concentrations (5.6 ± 1.1 wt.%). Inherited phases not in equilibrium with the host melt composition are clinopyroxene, An-rich plagioclase (> An_{53}) and quartz. Rhyolite-MELTs modeling indicates the clinopyroxene and quartz have most likely been sourced from cooler, silicic mush zones in the Havre magmatic system. This study demonstrates that even in crystal-poor rhyolites it cannot be assumed that all crystals are autocrystic and can be used to constrain pre-eruptive magmatic conditions.

Keywords: crystal-poor rhyolite, Havre 2012 eruption, pumice raft, Rhyolite-MELTS, autocryst, antecryst

OPEN ACCESS

Edited by:
Chiara Maria Petrone, Natural History Museum, United Kingdom

Reviewed by:
Mike Cassidy, University of Oxford, United Kingdom
Ben S. Ellis, ETH Zürich, Switzerland

****Correspondence:***
Joseph Knafelc
joseph.knafelc@hdr.qut.edu.au;
knafelc.joseph@gmail.com

Specialty section:
This article was submitted to Petrology, a section of the journal Frontiers in Earth Science

Received: *07 April 2020*
Accepted: *30 June 2020*
Published: *31 July 2020*

Citation:
Knafelc J, Bryan SE, Gust D and Cathey HE (2020) Defining Pre-eruptive Conditions of the Havre 2012 Submarine Rhyolite Eruption Using Crystal Archives. Front. Earth Sci. 8:310. doi: 10.3389/feart.2020.00310

INTRODUCTION

Crystal Cargo

Identifying the origins of crystals in magmatic systems is critical to understanding the inner workings of these systems, in particular, magma petrogenesis and pre-eruptive conditions that then place constraints on eruption dynamics. The past 20 years has seen an evolution in understanding of the origin of crystals from the generally held assumption that all phenocrysts were autocrysts

nucleated and grown from the erupted magma to being a potentially complex mixture of autocrysts, xenocrysts (e.g., quartz, K-feldspars in basalts, and ancient zircon in granites and rhyolites) and antecrysts that record related, but earlier phases of magmatism (Charlier et al., 2005; Gill et al., 2006; Charlier et al., 2007; Davidson et al., 2007; Hildreth and Wilson, 2007; Jerram and Martin, 2008; Bryan et al., 2008). The recycling of crystals into new magma batches can result from magma recharge events, the mobilization of, and entrainment from, crystal mush zones, remelting of recently formed subsolidus materials, or unmelted remains (restite) of partially melted source materials (e.g., Bachmann and Bergantz, 2004, 2008a,b; Hildreth and Wilson, 2007; Bryan et al., 2008; Deering et al., 2011; Deering and Bachmann, 2010; Huber et al., 2012; Cooper and Kent, 2014; Lubbers et al., 2020). The crystal population or 'cargo' (dependent on the mineral suite) can therefore potentially record magmatic conditions (i.e., temperature, fO_2, water content, pressure) of contrasting domains of a magma system (e.g., magma storage chambers, conduit or deeper cumulate piles). Autocrysts provide information on the pre-eruptive conditions of the magma chamber, microlites on conduit and ascent conditions, whereas antecrysts can provide valuable information on other domains of prior crystallization in the magmatic system.

For crystal-poor rhyolites, the task of determining the origins of crystal populations is often more difficult as the low crystal content typically yields a limited range in mineralogy that is combined with limited whole-rock/melt chemical variation. The Havre 2012 submarine eruption is typical of such rhyolites – it is crystal-poor (generally < 8%) and has a relatively restricted crystal assemblage of plagioclase, two pyroxenes and Fe-Ti oxides (Carey et al., 2018). This assemblage is consistent with the observed mineralogy in other low- to medium-K rhyolites from the Tonga-Kermadec arc (e.g., Wright et al., 2006; Barker et al., 2013). The state of the Havre magmatic system remains unconstrained because the eruptive history and previous eruption products are poorly known due to its remote and deep-water (900 mbsl) location.

Here we undertake the first petrologic study of the Havre 2012 eruption to critically assess the origins of the crystal cargo of the rhyolite. Phenocryst is used here as a non-genetic term, describing relatively large (0.1-1 cm), conspicuous crystals in igneous rocks (MacKenzie et al., 1982; Neuendorf, 2005). Each phenocrystic phase has the potential to be autocrystic, antecrystic, or xenocrystic, where a single phenocryst can contain domains of contrasting genetic origins (e.g., a xenocrystic or antecrystic core enveloped in an autocrystic rim). We therefore use textural and size information coupled with mineral chemistry to discriminate autocrystic from inherited and recycled (antecrystic or xenocrystic) mineral phases. Chemical equilibrium tests (e.g., Bacon and Hirschmann, 1988; Putirka, 2008; Mollo et al., 2013) are important tools to distinguish autocrysts that can then be used confidently to estimate pre-eruptive magmatic temperatures and pressures of crystallization. Rhyolite-MELTs models (Gualda et al., 2012; Ghiorso and Gualda, 2015) estimate initial conditions (i.e., water concentrations and oxygen fugacity) to confirm the observed petrographic relationships and act as an independent and predictive check of what the autocrystic mineral assemblage is under those magmatic conditions. The results presented here are a first-step in understanding the magmatic plumbing system of the Havre volcano, and provide insight into the processes involved in the generation and pre-eruptive storage conditions of a significant volume of crystal-poor rhyolite in an island arc setting.

Havre 2012 Submarine Eruption and Sampling Locations

The Havre 2012 eruption provides a valuable opportunity to examine the crystal populations of a large volume (∼1.5 km^3), crystal-poor rhyolite produced in an island arc-setting. The Havre volcano is located within the Kermadec arc approximately halfway between New Zealand and Tonga. Havre is a ∼1 km high edifice with a summit elevation 900 m below sea level (9.6 MPa), and the volcano is capped by a summit caldera ∼3 km wide with the caldera floor residing at 1520 m below sea level (Wright et al., 2006). Reconnaissance sampling of the summit of Havre volcano revealed the presence of basaltic andesite and dacite-rhyolite lavas that are slightly less evolved than the 2012 Havre rhyolite in composition (Wright et al., 2006). The pre-2012 and dredged samples from Havre (**Figure 1**) are utilized here as starting compositions in Rhyolite-Melts models to assess the role of crystal fractionation in producing the large volume of crystal-poor rhyolite.

In July 2012, a new submarine silicic eruption occurred at Havre, and was estimated to have evacuated ∼1.5 km^3 DRE of magma, representing the largest known historic submarine silicic eruption (Carey et al., 2014, 2018). Satellite images constrain eruption timing to July 19, 2012 (Carey et al., 2014; Jutzeler et al., 2014). The main raft was visible in MODIS images over the next four months as it dispersed over an area of 550,000 km^2 by which time the raft was dispersed in way that it was no longer visible in MODIS images (Jutzeler et al., 2014). Pumice raft material successively arrived along the shores of Tonga, New Zealand and Australia in the following months, where stranded pumice was collected and characterized for this study (**Figure 1**). In 2015, a more substantial and detailed study of the Havre summit was undertaken (Mapping, Exploration and Sampling at Havre or MESH) using autonomous underwater vehicles (AUV) and remotely operated vehicles (ROV) to collect high-resolution multibeam data and sample seafloor products of the eruption at Havre. The MESH cruise identified new eruptive products from the 2012 eruption including; (1) a series of 14 chemically distinct lava flows/domes fed from a lengthy fissure along the southern caldera rim (cumulative eruptive volume of ∼0.005 km^3; see Carey et al., 2018; Ikegami et al., 2018), (2) A layer of giant pumice ranging in size from ∼1 to 9 m in diameter and covering > 35 km^2 of the caldera floor (Carey et al., 2018; Manga et al., 2018a; Mitchell et al., 2018); and (3) A thin layer of ash (< 0.1 km^3; Carey et al., 2018) that has been divided into four subunits differentiated by contrasting ash morphologies, some of which suggests that part of the Havre magma fragmented without

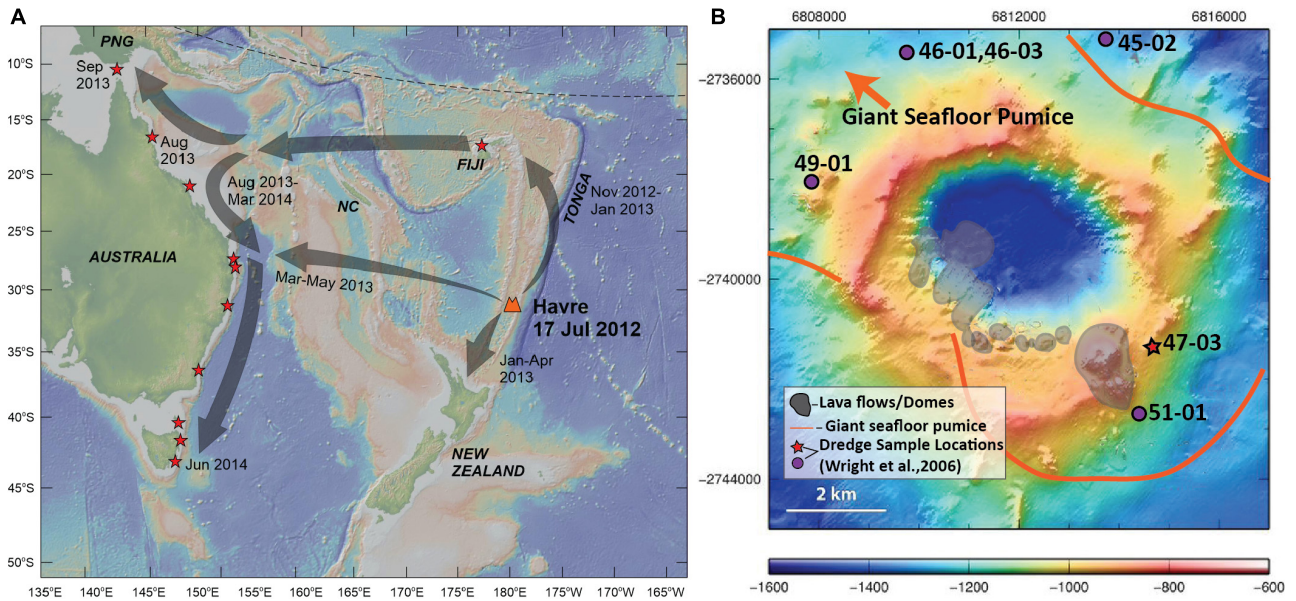

FIGURE 1 | Sampling locations of Havre 2012 eruptive products. **(A)** Map of southwest Pacific showing source location of Havre volcano with eruption timing, the regional dispersal of the pumice raft (gray arrows) and arrival timing of raft material for Tonga, New Zealand and the Eastern Coast of Australia. Red stars denote locations where stranded pumice raft material has been collected for this study. Basemap is derived from the Global Multi-Resolution Topography synthesis (Ryan et al., 2009) generated by GeoMapApp (http://www.geomapapp.org/). Abbreviations: NC, New Caledonia; PNG, Papua New Guinea. **(B)** Havre volcano bathymetry map (modified from Carey et al., 2014) showing the locations of summit lava flows and domes produced in the 2012 eruption (Carey et al., 2018), the depositional area of giant seafloor pumice, and location of dredged lava samples which pre-date the Havre 2012 eruption (Wright et al., 2006). Red star marks the location of the dredge sample that is used in this study as a parental composition in Rhyolite-MELTS models. Grid coordinates are based on the World Geodetic System (WGS84).

direct water contact (Murch, 2018; Murch et al., 2019). The culmination of the many studies of the Havre eruption over the last five years is that there is a more complex eruptive history to the 2012 eruption rather than simply being entirely effusive or explosive.

To date the majority of studies on the Havre 2012 submarine eruption have focused on the limited volume (< 0.1 km^3 or 7% of the total eruptive material) seafloor eruptive products (e.g., Carey et al., 2014, 2018; Manga et al., 2018a,b; Ikegami et al., 2018; Mitchell et al., 2018, 2019; Murch et al., 2019). Studies on the volumetrically dominant pumice raft (∼1.4 km^3 or 93% of total eruptive material) has been at a reconnaissance level, examined limited material (e.g., Rotella et al., 2015; Manga et al., 2018b) and focused on raft dispersion (e.g., Jutzeler et al., 2014; Carey et al., 2014; Velasquez et al., 2018). One outcome of the seafloor-focused studies has been the interpretation that the giant seafloor pumice and pumice raft were erupted contemporaneously (Manga et al., 2018a,b) given near identical whole-pumice compositions, similar mineralogy (i.e., plagioclase, orthopyroxene, clinopyroxene and Fe-Ti oxides) and textural features (e.g., banded pumice, tubed pumice and bread crusting). This study takes a more in-depth examination of the volumetrically dominant raft pumice to further characterize the 2012 Havre eruption. The raft, given its erupted volume, provides a much larger sampling of the Havre magma chamber. The raft pumice has been insufficiently documented in previous studies and the results here provide an improved platform for comparison between the buoyant and widely dispersed raft and the near-vent deposits at Havre.

MATERIALS AND METHODS

Extensive sampling of pumice raft material has been undertaken of strand deposits of Havre pumice from across the SW Pacific (**Figure 1**), which has allowed us to capture the full textural and potential compositional diversity of pumiceous material produced in the eruption. Two pieces of the seafloor giant pumice and four samples of different lava flows from the summit of Havre have also been analyzed in this study, and in conjunction with previously published data (Manga et al., 2018a,b; Carey et al., 2018; Ikegami et al., 2018), are used to provide a more comprehensive petrological picture of the 2012 Havre eruption.

Whole-pumice and glass chemistry are used to constrain melt chemistry and identify any potential compositional diversity amongst eruptive products. Due to the overall low crystal contents, whole-pumice and glass chemistry are similar (see also Mitchell et al., 2019). Whole-pumice composition has been determined for 29 pumice raft and two giant seafloor samples (**Table 1**). Sample preparation initially involved the removal of seawater contamination as outlined in **Supplementary Material 1**. For XRF analysis an aliquot of the cleaned and powdered sample (*ca.* 0.5 g) was fused into a glass disk using a commercial lithium metaborate/lithium tetraborate flux (50:50 LiT:LiM, 0.5 wt% LiI) in a platinum crucible using

TABLE 1 | Havre 2012 pumice XRF whole-rock chemistry normalized to anhydrous totals.

Pumice Type	Sample ID	SiO_2	TiO_2	Al_2O_3	FeO(T)	MnO	MgO	CaO	Na_2O	K_2O	P_2O_5	LOI	Total	Mg#
White-Raft	*WP-1-HI*	72.3	0.4	13.9	3.1	0.1	0.7	2.7	5.1	1.5	0.1	0.5	98.6	31.5
	WP-2-MB	72.0	0.5	14.0	3.0	0.1	0.7	2.6	5.6	1.5	0.1	1.0	100.2	30.6
	WP-3-MB	72.3	0.5	14.0	3.0	0.1	0.7	2.6	5.3	1.5	0.1	1.6	99.5	30.4
	WP-4-MB	72.4	0.5	14.0	3.0	0.1	0.7	2.6	5.1	1.4	0.1	0.9	100.9	30.4
	Wp-1-FB	72.3	0.5	14.0	3.0	0.1	0.6	2.8	5.1	1.5	0.1	1.0	99.4	29.7
	WP-1-DMB	72.8	0.5	13.8	3.0	0.1	0.6	2.6	5.0	1.5	0.1	1.5	99.9	29.5
	WP-BH-1rst	72.1	0.5	13.7	2.9	0.1	0.6	2.6	6.0	1.5	0.1	2.0	100.4	30.9
	WP-3-MB	72.8	0.5	13.8	3.0	0.1	0.6	2.6	5.0	1.5	0.1	1.1	99.6	29.0
	PP-17-BB	72.5	0.5	14.0	3.0	0.1	0.7	2.6	5.1	1.5	0.1	1.2	99.8	31.5
	PP-16-CU	71.9	0.5	14.0	3.0	0.1	0.7	2.6	5.7	1.5	0.1	1.0	100.5	30.9
	PP-9-CB	72.7	0.4	14.1	3.0	0.1	0.7	2.5	5.0	1.5	0.1	1.1	101.0	30.9
Banded-Raft	*GP-3-BB*	72.9	0.5	13.9	2.9	0.1	0.6	2.5	5.1	1.5	0.1	2.2	99.3	30.1
	BP-2-MB	72.7	0.5	13.9	2.9	0.1	0.6	2.5	5.3	1.4	0.1	2.6	98.8	30.3
	BP-3-MB	72.2	0.5	14.0	3.0	0.1	0.7	2.6	5.3	1.4	0.1	2.5	99.6	30.9
	BP-4-MB	72.7	0.5	13.9	3.0	0.1	0.6	2.6	5.1	1.4	0.1	2.3	99.5	30.0
	BP-5-MB	72.4	0.5	13.9	2.9	0.1	0.6	2.5	5.6	1.5	0.1	2.6	100.4	29.5
	BP-6-MB	72.6	0.5	14.0	2.9	0.1	0.6	2.6	5.3	1.4	0.1	2.3	99.8	29.6
	BP-9-EG	72.8	0.5	13.8	3.0	0.1	0.6	2.6	5.0	1.5	0.1	2.7	99.4	30.1
	BP-1-CU	71.6	0.5	13.5	2.9	0.1	0.6	2.5	6.7	1.5	0.1	2.2	101.4	28.8
	BP-53-EG	72.3	0.5	13.7	3.1	0.1	0.8	2.6	5.3	1.5	0.1	0.7	98.3	32.9
	BP-1-NNP	73.1	0.4	13.8	2.9	0.1	0.6	2.5	5.0	1.5	0.1	2.3	99.7	29.0
	GP-1-MB	73.1	0.4	13.8	2.9	0.1	0.6	2.5	5.0	1.5	0.1	2.2	99.8	28.5
	GP-2-BB	73.0	0.5	13.8	2.9	0.1	0.6	2.5	5.0	1.5	0.1	2.4	98.5	27.7
Brown-Raft	*Brown-1-UN*	72.9	0.4	13.9	2.9	0.1	0.6	2.5	5.1	1.5	0.1	3.4	99.2	29.0
	Brown-1-MB	72.0	0.5	13.6	2.9	0.1	0.6	2.5	6.2	1.5	0.1	3.7	100.5	28.6
Breadcrust-Raft	*BC-1*	72.2	0.4	13.8	2.9	0.1	0.6	2.5	5.9	1.5	0.1	3.3	99.8	28.9
	BC-2	72.5	0.4	13.9	2.9	0.1	0.6	2.4	5.5	1.5	0.1	3.5	100.1	30.5
	BC-1-HI	73.0	0.4	13.8	2.9	0.1	0.6	2.5	5.1	1.5	0.1	4.0	99.7	28.2
	Br/BC-EB	73.0	0.4	13.8	2.9	0.1	0.6	2.5	5.1	1.5	0.1	3.7	99.2	28.4
Seafloor	*BGSFP-1*	72.9	0.4	13.8	3.0	0.1	0.6	2.6	5.0	1.5	0.1	1.0	99.3	28.9
	GGSFP-2	73.0	0.4	13.8	2.9	0.1	0.6	2.5	5.0	1.5	0.1	0.7	98.5	28.4

*Mg# is calculated on a molar basis so Mg#*100 = [Mg/(Fe^{2+} + Mg)] where Fe^{2+}/Fe^{3+} ratio = 0.889.*

an electric fusion furnace. The resultant disk was analyzed in a Wavelength Dispersive X-ray Fluorescence spectrometer (WD-XRF) under vacuum using a 1kW Rh X-ray tube. The spectrometer was calibrated using the WROXI calibration set utilizing a *quasi*-Lachance matrix correction. A separate LOI was determined gravimetrically by igniting an aliquot of each sample (*ca*. 0.1 g) in a high-alumina sintered silica crucible at 1050°C.

We have used whole-pumice chemistry to represent melt chemistry prior to eruption in thermobarometry calculations (e.g., glass-orthopyroxene, glass-clinopyroxene, and glass-plagioclase) and corresponding equilibrium tests for each mineral phase. This is for a number of reasons. First, glass data are not available for all pumice textural types and for all samples from which mineral compositions have been determined. However, whole-pumice chemistry is available for all samples with mineral chemical analyses and this permits a more consistent approach for evaluating mineral and magma chemistries. Second, reliable glass analyses are more difficult to obtain in the banded raft and seafloor pumice samples which are densely populated with microlites and nanolites (e.g., **Figure 2C**). Third, the relatively low-crystal content (3-7%) results in only a very minor shift between glass and whole-rock chemistry. However, glass compositions are distinctly more SiO_2-rich and evolved compared to whole-pumice compositions reflecting modification of glass chemistry by microlite and nanolite crystallization (Mitchell et al., 2019). Given microlite crystallization is a syn-eruptive process (Hammer et al., 1999; Cashman and Blundy, 2000; Toramaru et al., 2008; Mollo and Hammer, 2017), the glass chemistry is no longer reflective of the pre-eruptive melt chemistry which is the focus here.

To resolve the origin of the crystal cargo of the 2012 Havre rhyolite, a detailed study of mineral phase abundance, texture, chemistry and zonation patterns was undertaken, which can be particularly insightful in terms of recording pre-eruptive magma interactions and processes. Modal abundance data for twenty-two samples are presented in **Table 2**. Point counting of thin sections used a grid with a 0.5 mm spacing in the X direction and 1 mm step size in the Y direction allowing for an average of ∼1500 counts per standard thin section.

Textural variations from core to rim in minerals are a useful indication of equilibrium vs disequilibrium crystallization conditions from the time of nucleation (i.e., cores) to last stages of crystallization prior to eruption (i.e., rims). Anhedral crystals or internally resorbed/embayed textures can indicate chemical disequilibrium and can typically be marked by sharp compositional boundaries and changes. Therefore, the shape and compositional zoning (or lack thereof) present in crystals provides context on the origins of the crystal cargo or domains within crystals. A detailed petrographic review of all eruptive products was completed through backscatter electron (BSE) imaging of each mineral phase. BSE images reveal the typical range of crystal morphologies (i.e., anhedral vs euhedral) of each mineral phase and any zoning patterns. The extent of mineral chemical variation from core to rim provides information on different zoning vectors (i.e., normal vs reserve zoning) and provides context on conditions of crystallization over time in the magmatic system. Microlites and nanolite crystals in the glass record syn-eruptive conditions typically associated with degassing and decompression (Hammer et al., 1999; Cashman and Blundy, 2000; Toramaru et al., 2008; Mollo and Hammer, 2017).

In this study, *in situ* electron probe micro analysis (EPMA) was performed on the phenocryst assemblage of orthopyroxene, clinopyroxene, plagioclase and Fe-Ti oxides. Mineral chemistry and a select population of raft pumice glass analysis results are reported in **Supplementary Excel File 1** as wt.% oxides and ion proportions based on stoichiometric cation to oxygen ratios for each mineral phase. Core and rim single-spot EPMA were performed on individual crystals when a certain spot size was permitted (i.e., microphenocrysts and phenocrysts) to investigate zoning patterns and potential compositional variations for each mineral phase. Microlites due to their small size are only analyzed in one location. EPMA- 1-μm spatial resolution elemental maps reveal detailed compositional patterns of orthopyroxene and clinopyroxene. Elemental maps indicate the presence or lack thereof, of internal compositional variations and disequilibrium textures, which can be drawn upon to further interpret the magmatic processes and conditions that the pyroxene phases experienced.

Quantitative *in situ* spot analyses by wavelength dispersive spectrometry (WDS) of pumice glass and minerals in thin section, as well as quantitative, background-corrected elemental maps of pyroxenes, were performed using a JEOL JXA 8530f field emission microprobe equipped with five wavelength-dispersive spectrometers and using Probe Software applications (Probe for EPMA, Probe Image and CalcImage; Eugene, OR, United States). Thin sections were coated with 20 nm carbon prior to analysis. For spot analysis of glass, instrument conditions of 15 kV accelerating voltage, 10 nA beam current and a 10 μm-defocused beam were used, with X-ray counts for Si and Na collected first and concurrently in the element analysis order. The on-peak counting times were adjusted to provide detection limits $\leq$ 300 ppm for most elements with the exceptions of Ba (500 ppm), F (370 ppm), and Na (380 ppm) for which a 5 second on-peak counting time was used in order to minimize Na loss under the electron beam. An LDE1 analyzing crystal was used for F, as well an exponential fit to the continuum background and interference correction for Fe La on F Ka. A selection of commercially available and in-house natural and synthetic standards was used as calibration materials, including Astimex albite (Na), barite (Ba), plagioclase An_{59} (Al), hematite (Fe), rhodonite (Mn), tugtupite (Cl) and orthoclase (K); NBS synthetic glass standard K411 (Ca, Mg); and in-house celestite (Sr), topaz (F), rutile (Ti), and Lipari glass (Si). Oxygen was calculated by stoichiometry. Mafic minerals were analyzed in a separate session under conditions of 15 kV accelerating voltage, 30 nA beam current and a 3 μm-defocused beam. Similar standard assignments were used as for glass, with exceptions and additions being NBS K411 for Si, and Astimex standards

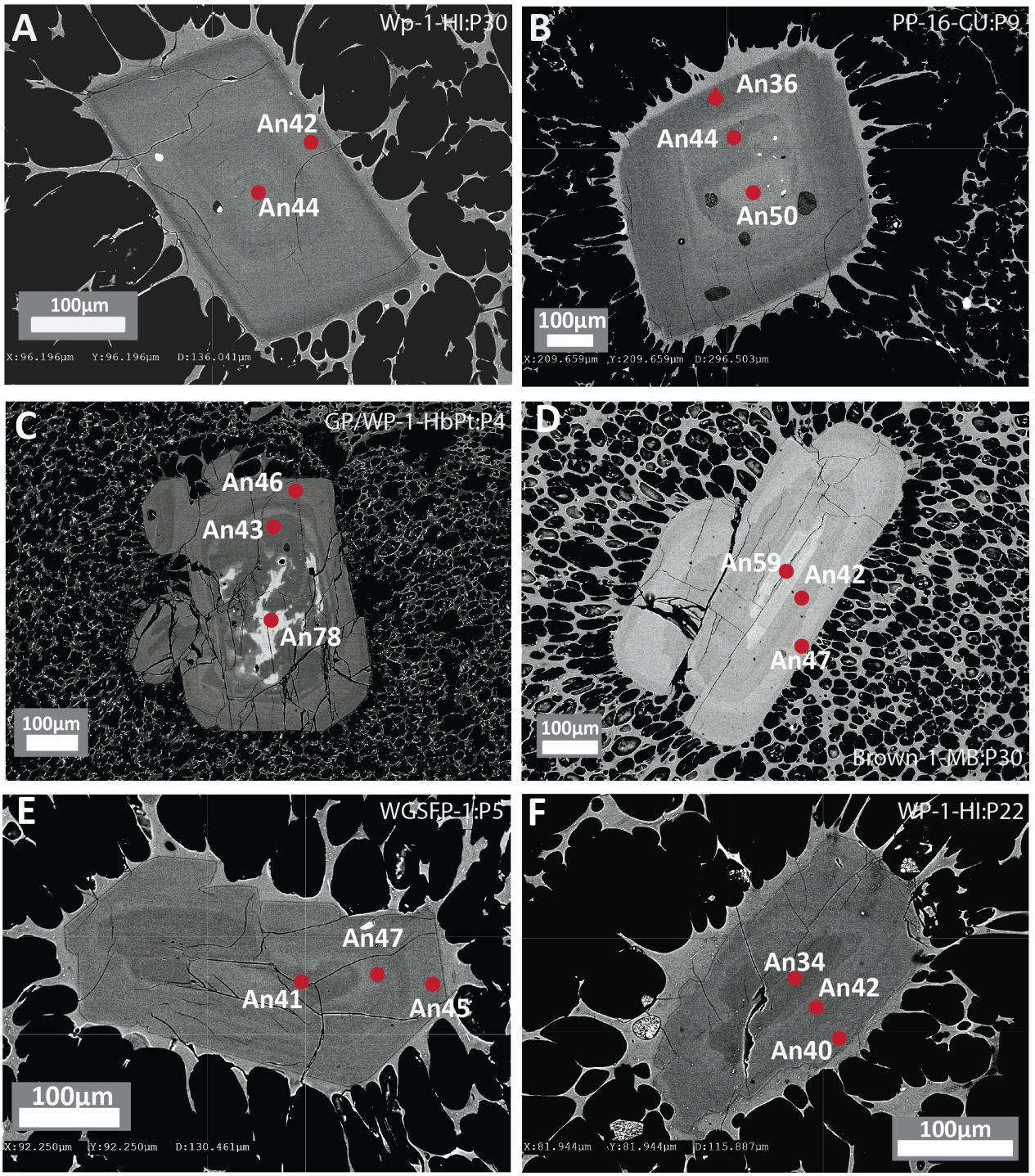

FIGURE 2 | Backscattered electron (BSE) images of plagioclase phenocrysts from white pumice raft samples with concentric zoning showing contrasting core to rim relationships. **(A,B)** Euhedral plagioclase phenocrysts showing normal compositional zoning with minor oscillations. **(C,D)** Euhedral plagioclase phenocrysts with compositionally distinct An-rich resorbed cores and oscillatory zoned overgrowths. **(E,F)** Subhedral plagioclase phenocrysts with partially resorbed sodic plagioclase cores. Red dots denote location of EPMA with corresponding An content.

Cr_2O_3 (Cr) and pentlandite (Ni). Detection limits for all elements in the mineral routines are $\leq$ 200 ppm. Analyzing crystals for glass on spectrometers 1-5 included: 1-LDE1 (F Ka), 2-PETL (Ca-K-Cl-S-P Ka, Sr La), 3-TAP (Si-Al Ka), 4-LIFH (Fe-Mn-Cr-Ti K, Ba La), 5-TAPH (Na-Mg Ka); and for pyroxenes 1-PETJ (Ca Ka), 2-LIFL (Ni-Cr Ka), 3-TAP (Si-Al Ka),

TABLE 2 | Modal abundances of Havre eruptive products.

Pumice Type	*Sample ID*	Glass and vesicle%	Crystal%	Plagioclase%	Opx%	Cpx%	Oxide%	Quartz%	Total counts
White-Raft	*WP-1-HI*	95	5	2	1	1	0	0	1560
	WP-2-HbPt	96	4	2	1	0	1	0	1795
	TWP-3-MB	94	6	3	1	1	1	0	1543
	PP-11-CB	96	4	2	0	0	1	0	1604
	PP-1-MB	96	4	2	1	0	1	0	1500
	PP-16-CU	97	3	2	1	0	0	0	1442
	Total counts	9053	391	227	78	36	50	0	9444
	Average% White	96	4	2	1	0	1	0	
Banded-Raft	*(Br/Bp-1-RB)*	95	5	3	1	1	1	0	524
	(Br/Bp-2-MB)	93	7	4	1	1	1	0	703
	BP-53-BB	94	6	4	1	0	1	0	1424
	BP-1-MB	95	5	3	1	1	0	0	1522
	BP-3-Mb	94	6	4	1	1	0	0	1544
	BP-2-MB	95	5	3	1	0	0	0	1688
	GP/Wp-1-HbPt	94	6	3	1	1	1	0	1515
	Total counts	8406	513	304	96	56	54	4	8920
	Average% Banded	94	6	3	1	1	1	0	
Brown-Raft	*Brown-1-UN*	94	6	4	1	1	1	0	1498
	(Br/Bp-1-RB)	94	6	4	0	1	1	0	765
	(Br/Bp-2-MB)	89	11	6	3	1	1	0	524
	Total counts	2591	196	119	35	17	25	0	2787
	Average% Brown	93	7	4	1	1	1	0	
Seafloor Pumice	*GSFP-1*	93	7	5	1	1	0	0	1548
	GSFP-2	93	7	5	1	1	1	0	1506
	Total counts	2840	214	144	24	21	21	4	3054
	Average% Seafloor	93	7	5	1	1	1	0	
Lavas	*HVR-009*	88	12	8	2	1	1	0	1554
	HVR-0010	88	12	8	2	1	1	0	1547
	HVR-0012	86	14	9	2	1	2	0	1784
	HVR-015	86	14	9	2	1	1	0	1507
	Total counts	5561	831	553	116	70	80	12	6392
	Average% Lavas	87	13	9	2	1	1	0	

The matrix% is the modal abundance of glass and vesicle components combined; lava vesicularity varies from < 5 modal% to > 50 modal% (Ikegami et al., 2018) and raft pumice has a mean vesicularity of 78% (Rotella et al., 2015; Carey et al., 2018).

4-LIFH (Fe-Mn-Cr-Ti Ka, 5-TAPH (Na-Mg Ka). Data quality control was monitored during all analytical runs using in-house secondary standards including separate sessions for mineral and pumice glass analysis.

In order to achieve a 1-μm spatial resolution for detailed elemental mapping of pyroxene, the selection of analytical conditions was informed by Monte-Carlo simulations of electron beam trajectories in pyroxene using *CASINO* software (Université de Sherbrooke, Québec, Canada). A reduced accelerating voltage of 10 kV, beam current of 100 nA and 500 ms dwell time were used, with a 1-μm defocused beam to match the step size. The mean atomic number (MAN) background method was used for map acquisition, which permits two passes over the map area to yield background corrected data for 10 elements (Si, Ti, Al, Cr, Fe, K, Mn, Mg, Ca, Na). In order to illuminate the interfaces between pyroxene and glass, K was included in the setup. Map data were acquired using Probe Image and processed using CalcImage softwares (Eugene, OR, United States), and output to Surfer (Golden Software) for visualization. Oxygen is calculated by stoichiometry, with standards identical to those for pyroxenes described above.

RESULTS

Havre Pumice Textural Diversity

Previous studies (Carey et al., 2014, 2018; Manga et al., 2018a,b; Mitchell et al., 2019) have focused primarily on the seafloor giant pumice and lava flows (< 7% by volume). Through our extensive sampling of beach stranded raft pumice, we observe a wider variety of pumice textural types than has been recognized from the Havre summit and seafloor deposits including a subpopulation of white pumice with secondary pink coloration and a 'brown' pumice with bread crusted surfaces (**Supplementary Material 2**). Of note is that the brown pumice textural type is observed to be in direct contact with white and banded raft pumice textural types within individual clasts confirming that it was an additional pumice

type produced in the 2012 eruption. Although the majority of the pumice raft material has a heterogenous vesicle size and shape distribution and typically lacks vesicles < 20 μm (e.g., Rotella et al., 2015; Manga et al., 2018a); the brown and other bread crusted pumice types are distinctive in having a much more homogeneous vesicle size and shape distribution with nearly spherical vesicles typically 20–40 μm in size (**Figure 2D**).

Havre Pumice Chemistry

Major element chemistry of the Havre pumice is presented in **Table 1** and represents a more extensive set of chemical analyses of the raft pumice (i.e., white, banded, brown and bread crusted pumice textural types) than previously published (Rotella et al., 2015; Carey et al., 2018). Whole-pumice chemistry shows some difference to glass chemistry determined by EPMA (**Supplementary Excel File 1**; see also Mitchell et al., 2019) despite the overall low crystal contents of the Havre pumice. For example, FeO(t) displays the most prominent difference of the major oxides from ∼2.9 wt.% (whole-pumice) to 2.2 wt.% in the glass. These differences are most likely due to plagioclase and Fe-Ti oxide microlite (see glass domains in **Figure 2**) and nanolite crystallization upon eruption/ascent. On the basis of major element chemistry, the Havre eruption appears to have evacuated a sizeable, relatively chemically homogenous volume (∼1.5 km^3) of metaluminous, medium-K calc-alkaline rhyolite.

Mineralogy

Havre pumice raft samples contain the phenocryst/microphenocryst assemblage of plagioclase, orthopyroxene (enstatite), clinopyroxene (augite), and Fe-Ti oxides (titanomagnetite, ilmenite), with plagioclase being the dominant phenocryst phase in all erupted products. Trace occurrences of apatite, quartz and pyrrhotite were observed in some samples (**Table 2**). The plagioclase-two pyroxene assemblage is characteristic of pumice materials from other volcanoes in the Tonga-Kermadec arc (e.g., Bryan, 1970; Bryan et al., 2004; Wright et al., 2006; Barker et al., 2013). Most mineral phases occur as phenocrysts (0.5–3 mm), microphenocrysts (0.2–0.5 mm), microlites (< 0.2 mm) and as components of polymineralic glomerocrysts. Glomerocrysts typically consist of plagioclase, orthopyroxene and Fe-Ti oxides (ilmenite and/or titanomagnetite), where rare glomerocrysts contain clinopyroxene. Modal abundance data indicate subtle differences in crystal content between the raft pumice, the giant seafloor pumice and lavas (**Table 2**). This is consistent with the observations of Carey et al. (2018) who reported slightly higher abundances of plagioclase (3–5%) and orthopyroxene (1–2%), and less Fe-Ti oxides (< 1%) in the giant seafloor pumice compared to the raft pumice such that giant seafloor pumice has slightly higher overall phenocryst contents. When considering all the erupted products from the 2012 Havre eruption, a spectrum exists in terms of crystal content from very crystal-poor rhyolite (white raft pumice, ∼3–6%) through banded raft pumice and giant seafloor pumice (4–7%) to more phenocrystic lavas (up to 15%) that are distinctly more plagioclase-rich (**Table 2**).

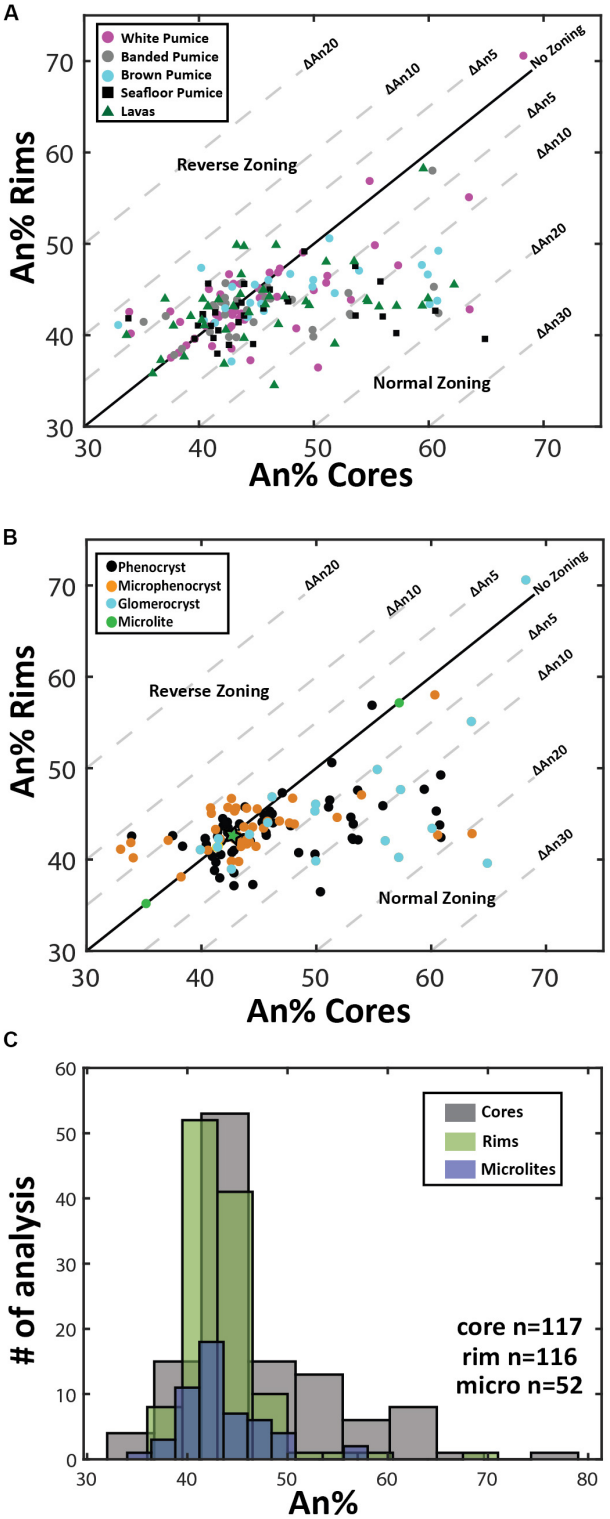

FIGURE 3 | Plagioclase compositional variation. **(A)** and **(B)** Zoning patterns of plagioclase where core and rim analyses are plotted to illustrate growth history of individual phenocrysts. Plagioclase zoning patterns are discriminated by eruptive product **(A)** and crystal size **(B)**. Plagioclase phenocrysts tend toward lower anorthite contents during fractional

(Continued)

FIGURE 3 | Continued
crystallization of rhyolite magma under closed-system conditions, resulting in normal compositional zoning; normal zoning is most pronounced in the phenocrysts and glomerocrystic plagioclase. Note that microlite compositions are based on 1 analysis per crystal as microlite size prevented paired core-rim analyses being obtained from each microlite. The maximum and minimum An content of microlites is plotted on the one-one line as green circles and the mean of all microlite analyses is plotted as a green star at $An_{43.5}$. **(C)** Histograms comparing microlite compositions with plagioclase core and rim phenocryst compositions. Note the larger spread of plagioclase core compositions and the overlap of rim and microlite compositions that are An_{40-45}. Note in C the normal distribution of the cores is shifted to the right by $\sim An_5$ relative to microlite distribution, while a normal distributions of the phenocryst rim and microlite An content are nearly identical. The number of single spot EPMA for plagioclase cores, rims, and microlites are 116, 117, and 52, respectively.

Plagioclase

Plagioclase is the most abundant mineral phase in all Havre 2012 eruptive products and is observed as phenocrysts, microphenocrysts, microlites and in glomerocrysts often containing inclusions of titanomagnetite and/or ilmenite. Plagioclase microlites and microphenocrysts are typically euhedral to subhedral whereas plagioclase phenocrysts and glomerocrysts are more subhedral showing some rounding and truncation of zoning bands (**Figure 2**). Internally, zoning is common in the larger plagioclase, and distinct resorbed or rounded core domains can also be distinguished (**Figure 2**).

Overall, plagioclase compositions range from An_{33} to An_{79} and can be classified as sodic andesine to calcic labradorite with minimal orthoclase content ($< Or_1$). The range of An content is observed in plagioclase from all eruptive products (**Figure 3A**), but when discriminated on the basis of crystal size (**Figure 3B**), high-An plagioclase compositions ($> An_{50}$) are mostly present as cores to phenocrysts and glomerocrysts (**Figures 2B,C**). In contrast, plagioclase rim and microlite compositions are much more uniform in composition and show little compositional variation (mostly An_{40-45}; **Figure 3C**). As observed in BSE images (**Figure 2**), zoning is most pronounced in the plagioclase phenocrysts and glomerocrysts. Despite the optical evidence for zonation, a significant proportion of plagioclase shows only minor compositional zonation of $< An_5$ when paired core and rim analyses from single plagioclase crystals are compared (**Figure 3A**). However, plagioclase phenocrysts and particularly glomerocrysts tend to exhibit relatively strong normal zoning with up to An_{30} difference between core and rim compositions (**Figure 3B**). Some plagioclase microphenocrysts and phenocrysts show a weak reverse zonation with up to An_{10} difference between core and rim compositions.

Orthopyroxene and Clinopyroxene

Two pyroxenes are present in all the Havre eruptive products, but orthopyroxene is typically more modally abundant than clinopyroxene (**Table 2**). Modal abundance estimates indicate subtle differences in relative abundances across the erupted products. In the volumetrically dominant white raft pumice, orthopyroxene is twice as abundant as clinopyroxene while in the giant seafloor and some banded pumice their proportions are subequal. Highest clinopyroxene abundances are recorded from the lavas (**Table 2**). These results, however, cannot be compared with the study of the Havre 2012 lavas by Ikegami et al. (2018) as ortho- and clinopyroxene were not distinguished. Like plagioclase, orthopyroxene occurs as phenocrysts, microphenocrysts and microlites in the pumice glass, as well as in small glomerocrysts associated with plagioclase, titanomagnetite or ilmenite, and rarely clinopyroxene. Clinopyroxene crystals are mainly microphenocrysts < 200 μm in size, but are rarely > 0.5 mm. Orthopyroxene is more euhedral and zoning is less frequently observed when compared to the subhedral to anhedral clinopyroxene that often shows zoning and resorption textures (**Figure 4**).

End-member compositions (i.e., Wo, En, Fs) have been calculated using the Lindsley and Andersen (1983) projection scheme considering minor constituents that readily replace major cations (i.e., Ti, Cr, Al) in pyroxene. Augite compositions range from $En_{39}Fs_{23}Wo_{37}$ to $En_{54}Fs_6Wo_{40}$. However, at least two distinct compositional groups can be distinguished with most clinopyroxenes having En_{40-45} and a minor population at En_{50-55} (**Figure 5**). This compositional variation is observed for phenocryst core, phenocryst rim and small anhedral crystals < 200 μm, although rim compositions are mostly restricted to En_{40-45} (**Figure 6B**).

Orthopyroxene compositions range from $En_{53}Fs_{44}Wo_3$ to $En_{63}Fs_{34}Wo_3$ and can be classified as enstatite with minimal wollastonite content ($< Wo_5$). In contrast to clinopyroxene, orthopyroxene has a much more uniform composition with little variation in mean En values ($\sim En_{42-43}$) observed from core to rim, as well as between phenocrysts and microlites (**Figure 6C**). In contrast to plagioclase, both clinopyroxene and orthopyroxene show very subtle to no compositional zonation with most crystals exhibiting $< En_5$ variation between core and rim (**Figure 6A**). This is consistent with only faint traces of zonation visible in SEM backscatter images (**Figure 4**) and elemental maps (**Figures 7**, **8**).

Pyroxene elemental maps are used in this study to assess several aspects of the magmatic history of the 2012 Havre eruption. First, the zoning patterns for enstatite and augite can provide valuable records of the magmatic history because elemental diffusion is relatively slow (Costa and Morgan, 2011; Müller et al., 2013) thereby preserving a more protracted record (e.g., Ubide and Kamber, 2018). Second, pyroxene is present across much of the spectrum of magma compositions erupted in the Tonga-Kermadec arc (e.g., Haase et al., 2002; Wright et al., 2006; Smith et al., 2010) and can crystallize across the entire crustal column at varying pressures, temperatures, and water contents (Putirka, 2008). Third, the zoning patterns of enstatite and augite are compared to see if they record similar zonation patterns and thus record similar magmatic conditions and histories indicating their co-existence during crystallization.

Orthopyroxene elemental EPMA mapping (**Figure 7**) indicates many enstatite minerals are generally unzoned, consistent with evidence from EPMA spot analysis and core-rim relationships (**Figure 6A**). Some orthopyroxene was found to exhibit concentric zoning with some oscillations in Fe^{+2} and

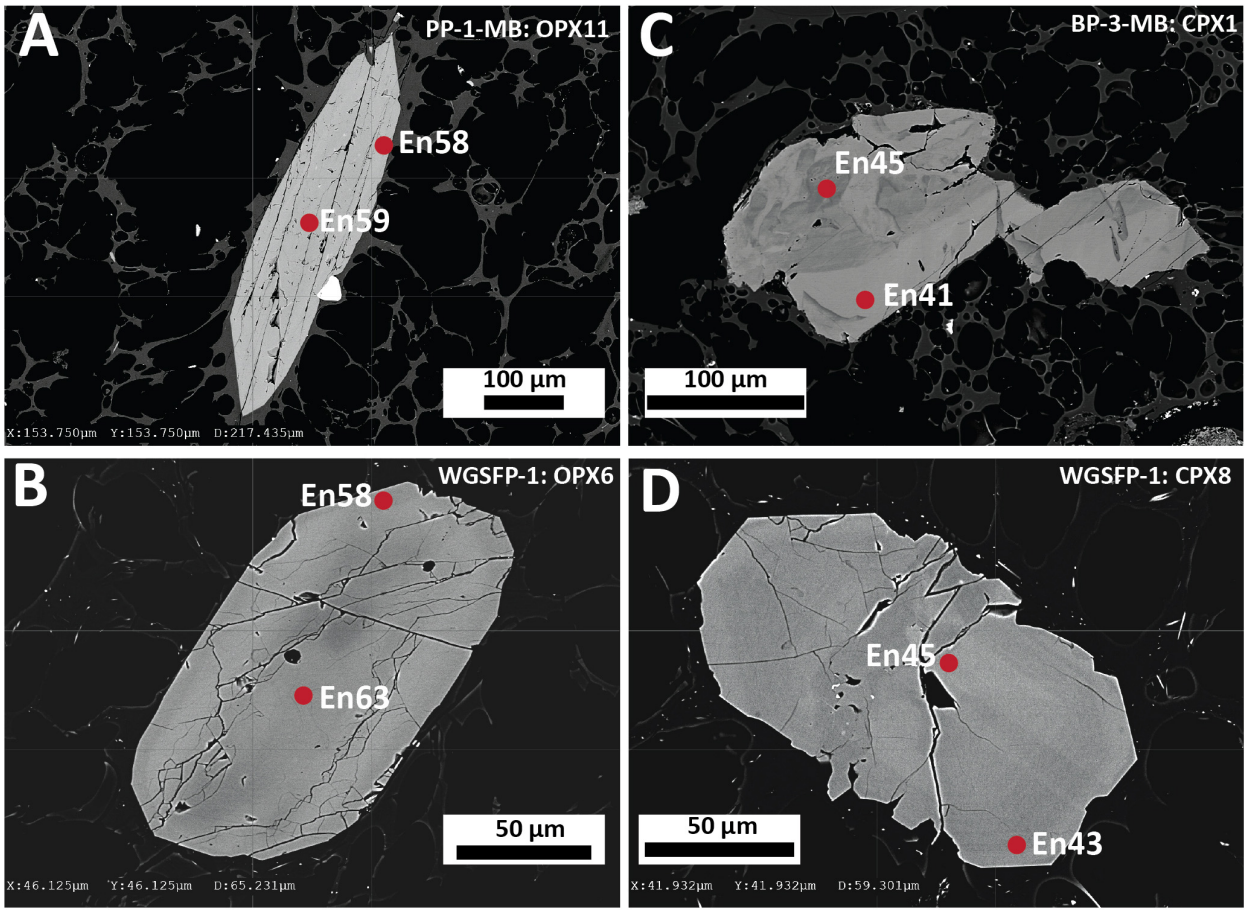

FIGURE 4 | Representative backscattered electron images of orthopyroxene and clinopyroxene highlighting the main textural features of orthopyroxene and clinopyroxene in the Havre 2012 eruptive products. **(A)** Euhedral orthopyroxene phenocryst with an intergrown Fe-Ti oxide crystal from a white raft pumice sample PP-1-MB. **(B)** Euhedral orthopyroxene microphenocryst from a giant seafloor pumice sample WGSFP-1. **(C)** Subhedral clinopyroxene microphenocryst displaying a patchy zoning pattern from a banded raft pumice sample BP-2-MB. **(D)** Weakly subhedral clinopyroxene microphenocryst displaying faint concentric zoning and embayed rims from a giant seafloor pumice sample WGSPF-1.

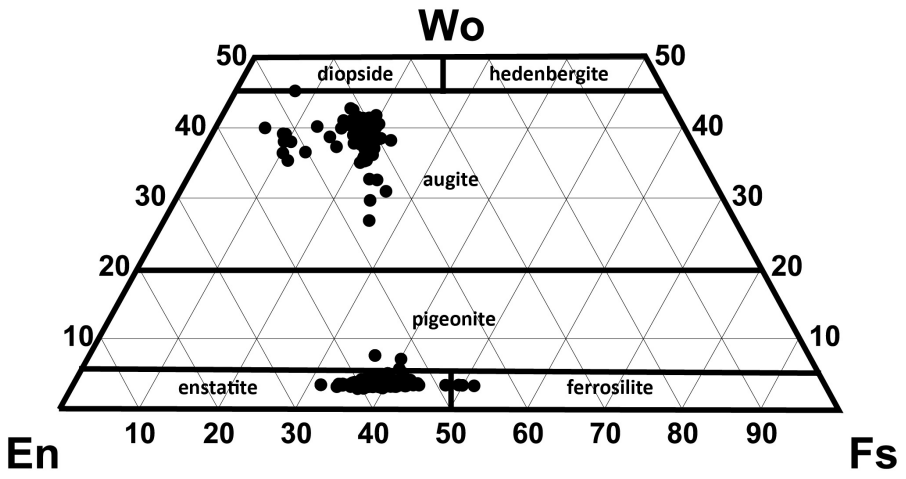

FIGURE 5 | Pyroxene quadrilateral diagram for all orthopyroxene (n = 195) and clinopyroxene (n = 138) analyses (projection scheme of Lindsley and Andersen, 1983).

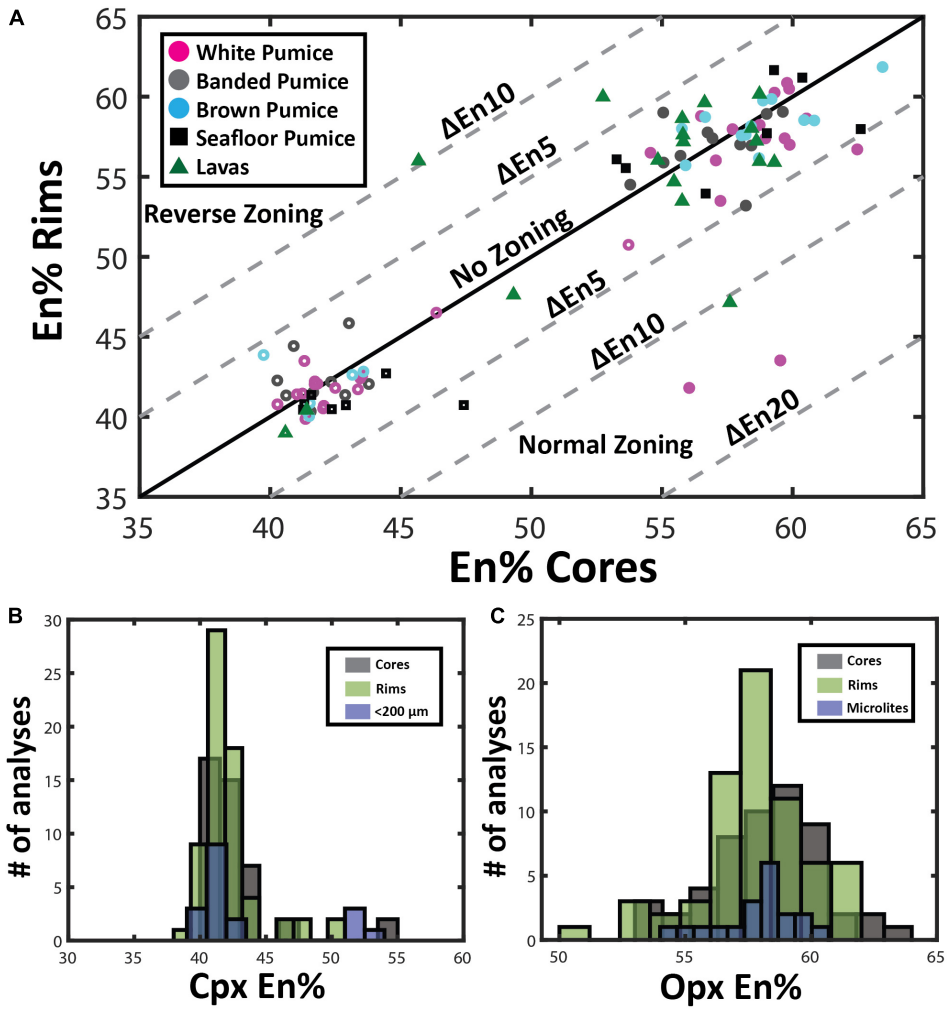

FIGURE 6 | Pyroxene compositional variation. **(A)** Zoning patterns of pyroxene where core and rim analyses are plotted to illustrate growth history of individual phenocrysts discriminated by eruptive product. Pyroxene phenocrysts tend toward lower enstatite contents during fractional crystallization of rhyolite magma under closed-system conditions, resulting in normal compositional zoning. Open symbols are clinopyroxene, and filled symbols, orthopyroxene compositions. **(B)** and **(C)** Histograms comparing microlite compositions with pyroxene rim and core compositions in clinopyroxene **(B)** and orthopyroxene **(C)**.

Mg^{2+} (**Figure 7A**). Where significant zoning was observed (e.g., **Figure 7A**), rim compositions overlap compositions of the euhedral microlites (**Figure 7B**).

New element maps for clinopyroxene confirm the presence of two compositionally distinct populations in terms of Fe-Mg content (**Figures 8A,B**). The low-En augite exhibits subtle zonation where the outer crystal boundary truncates compositional bands. The high-En augite shows strikingly different compositional zonation patterns and crystal forms (**Figures 8C,D**). The majority of the high-En augite are enriched in Mg and Al but are enveloped by a thin, relatively Fe-, Ti-rich and Al-poor rim, and where sector zoning is also present (**Figure 8C**). The sector zoned augite follows similar enrichment and depletion trends in the hourglass to prism sectors as observed in Mount Etna clinopyroxene where increased Al^{+3} is considered to record increasing degrees of undercooling (Ubide et al., 2019). The small (< 100 µm), slightly more Ca-rich augite exhibits strongly embayed forms (**Figure 8D**) and contrast with the euhedral shape of equivalent-sized orthopyroxene microlites. Cr in clinopyroxene follows sector zoning where present (**Figure 8C**) as well as concentric oscillatory zoning, primarily in the mantle of the crystal, independent of hourglass and prism zoning. However, in general, both the low- and high-En augites contain relatively low Cr contents and lack Cr-rich zones indicating augite growth has largely occurred in the absence of new injections of basaltic magma directly into the Havre rhyolite magma chamber (Streck, 2008; Ubide et al., 2019).

Titanomagnetite and Ilmenite

Small, euhedral titanomagnetite and ilmenite grains (**Figures 9C,D**) are often incorporated as inclusions in pyroxene, plagioclase and also occur in glomerocrysts. Both Fe-Ti oxide minerals are found in all pumice textural types, although ilmenite appears to be more abundant in the giant seafloor pumice and

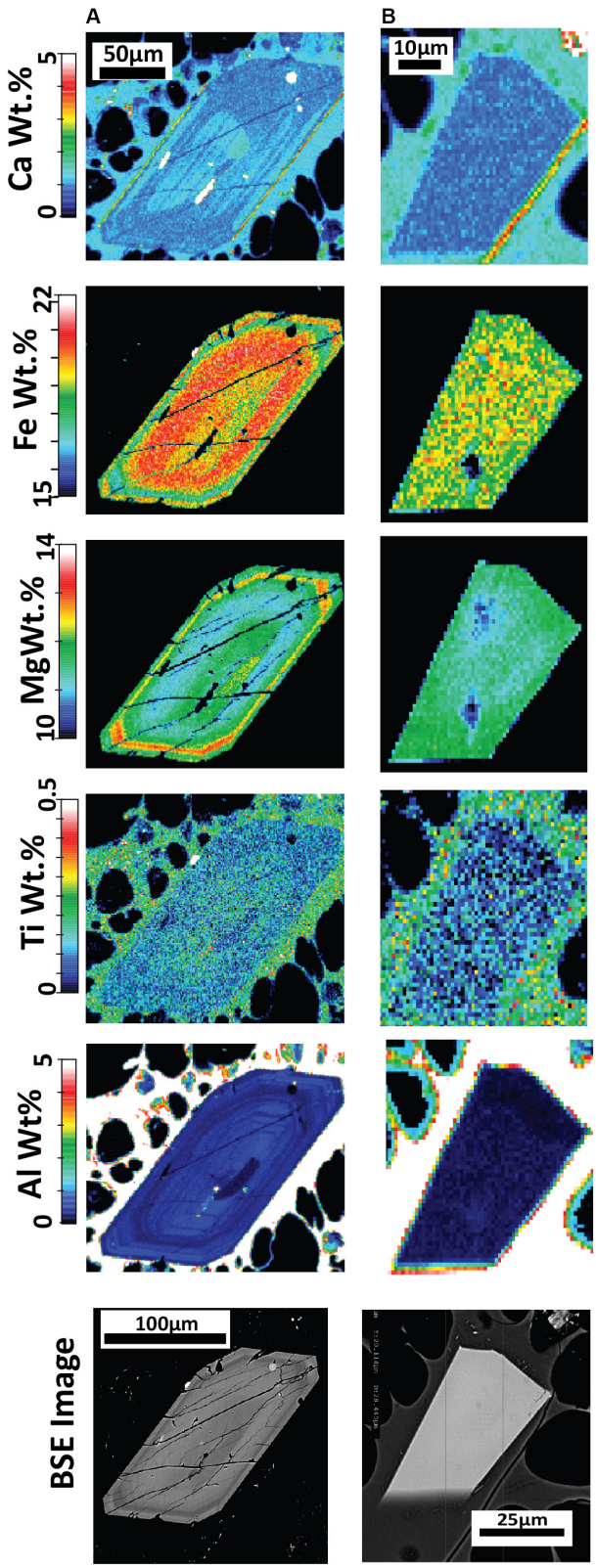

FIGURE 7 | Quantitative major element compositional maps acquired by EPMA for orthopyroxene **(A,B)** with corresponding backscattered electron *(Continued)*

FIGURE 7 | Continued
(BSE) images from pumice raft samples. The maps represent background-corrected, fully quantitative analytical results acquired at 10 kV accelerating voltage with a 1 um step size and spatial resolution and are semiquantitative for the surrounding glass groundmass. **(A)** Orthopyroxene with concentric zoning from banded pumice sample BP-53-BB; **(B)** A homogeneous orthopyroxene microlite from white raft pumice sample WP-1-HI. The elemental maps reveal an overlap in composition between the microlites and phenocryst/microphenocryst rims, such as in **(A)**.

is least abundant in the white raft pumice. Overall, Fe-Ti oxide modal abundance (**Table 2**) is lowest in the white raft pumice (∼0.5 wt%), slightly higher in banded and giant seafloor pumice (∼0.7%) and highest in the Havre lavas (∼1.2%). Fe-Ti oxide microlites and nanolites are observed frequently throughout all eruptive products with banded and seafloor pumice containing the greatest density of Fe-oxide microlites (see glass domains in **Figure 9**).

Ulvospinel solid-solution cation proportions are estimated following the method of Carmichael and Nicholls (1967). Cation proportions are then used to estimate Mol% of Usp in titanomagnetite and Mol% of Ilmenite-Hematite (Ilm-Hmt) following calculations from Lindsley and Spencer (1982). Titanomagnetite ranges from Usp_{35} to Usp_{38}, whereas ilmenite shows a restricted compositional range (Ilm_{86-89}). The Fe-Ti oxides have moderate enrichments in minor elements with ∼1.9 to 2 wt% Al_2O_3 and ∼1.36 to 1.5 wt% MgO. No compositional differences in Fe-Ti oxide compositions are apparent between the different erupted products.

Other Accessory Phases

Trace amounts of quartz (< 1%) have previously been reported from the giant seafloor pumice and some raft pumice (Carey et al., 2018). In a more extensive analysis of the raft pumice in this study, only trace amounts of quartz (∼0.1%) have been observed in the banded raft pumice, and quartz has not been observed in the volumetrically dominant white and volumetrically minor brown pumice types (**Table 1**). Where quartz is present, it is small (< 200 µm), has anhedral forms and shows evidence of some resorption (**Figures 9A,B**). Apatite has so far only been observed as 1–20 µm inclusions in orthopyroxene, and Ikegami et al. (2018) also reported apatite being present in the rhyolite lavas and domes. Rare, euhedral to subhedral grains of pyrrhotite are observed but appear restricted to the white raft pumice.

Geothermometry and Geobarometry

The observed phenocryst/microphenocryst assemblage permits the application of a number of geothermometers and geobarometers to constrain pre-eruptive magmatic temperatures, pressures of crystallization as well as fO_2 and water concentrations. A previous temperature estimate of 850 ± 20°C for the Havre rhyolite magma was given by Manga et al. (2018a), and this was based on the clinopyroxene-orthopyroxene Fe–Mg exchange geothermometer (Putirka, 2008), but was reported without mineral chemistry data or equilibrium tests. Therefore, previous Havre 2012 clinopyroxene-orthopyroxene temperature

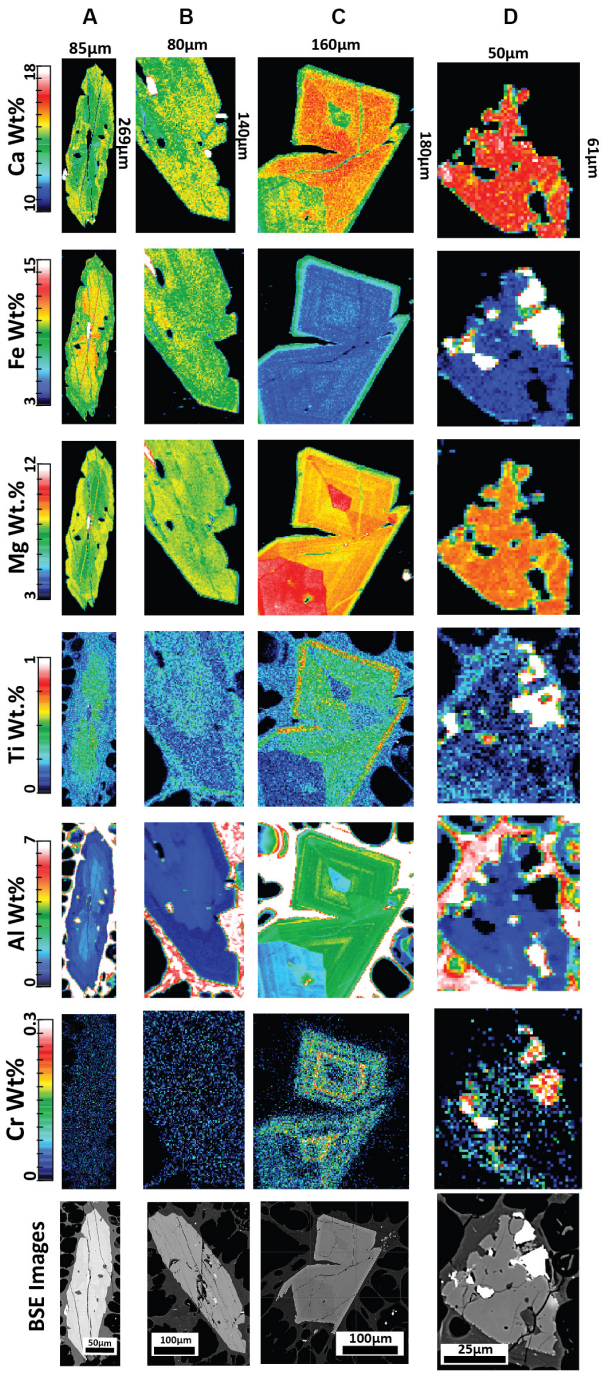

FIGURE 8 | Quantitative elemental compositional maps acquired by EPMA for low-En augite **(A,B)** and high-En augite **(C,D)** with corresponding backscattered electron (BSE) images from pumice raft samples. The maps represent background-corrected, fully quantitative analytical results acquired at 10 kV accelerating voltage with a 1um step size and spatial resolution and are semiquantitative for the surrounding glass groundmass. **(A)** Clinopyroxene with an embayed rim displaying slight reverse zoning; banded pumice sample BP-53-BB. **(B)** Clinopyroxene with near homogenous composition from giant seafloor pumice sample GSFP-2 **(C)** A clinopyroxene microphenocryst displaying sector zoning from white raft pumice sample WP-1-HI; **(D)** Resorbed clinopyroxene with Fe-Ti oxide inclusions from giant seafloor pumice sample GSFP-2.

estimates have assumed the two pyroxenes are in equilibrium and co-crystallized from the Havre rhyolite melt prior to eruption.

Based on the observed mineralogy, we use and compare the following geothermometers to constrain pre-eruptive magmatic temperatures: (1) plagioclase-melt geothermometer of Putirka (2005); (2) paired clinopyroxene-orthopyroxene as well as orthopyroxene-melt and clinopyroxene-melt geothermometers of Putirka (2008); and (3) compositions of coexisting Fe–Ti oxides (Carmichael and Nicholls, 1967) for ilmenite-magnetite geothermometry (Lepage, 2003) and fO_2 (Spencer and Lindsley, 1981). Pressure estimates are also obtainable using plagioclase- and orthopyroxene-melt compositions and assuming an initial magmatic water content of 5.8 wt% determined from plagioclase-hosted melt inclusions from giant seafloor pumice (Manga et al., 2018a). Titanomagnetite–ilmenite pairs were checked for Mg/Mn equilibrium (Bacon and Hirschmann, 1988), 'Rhodes diagrams' for clinopyroxene-orthopyroxene pairs (Rhodes et al., 1979), and plagioclase-melt using $K_D(Ab\text{-}An)^{plag-liq}$ exchange (Putirka, 2005) to give confidence to temperature estimates.

Fe-Ti Oxide Geothermometry

The Fe–Ti oxide temperature estimates are thought to approximate those when the titanomagnetite–ilmenite–liquid equilibrium was quenched by the eruption (e.g., Bryan et al., 2002). Although titanomagnetite and ilmenite are not observed as touching pairs, they are observed to be present within the same thin section and pumice clast. Therefore ilmenite-titanomagnetite compositions analyzed from the same thin section are inputted into Eq.17 and Eq.18 from Spencer and Lindsley (1981) to estimate temperatures, and oxygen fugacity, respectively. The Mg/Mn ratios of ilmenite-magnetite pairs fall within the error range of the Mg/Mn plot (Bacon and Hirschmann, 1988), confirming equilibrium between the coexisting oxide phases in the Havre rhyolite melt (**Supplementary Material 3**). Temperature and fO_2 estimates using equations 17 and 18 of Spencer and Lindsley (1981) give a temperature range of 871–915°C and an oxygen fugacity of 0.307–0.533 above the NNO (nickel–nickel oxide) buffer.

Plagioclase-Whole-Rock/Melt Geothermometry and Geobarometry

The $K_D(Ab\text{-}An)^{plag-liq}$ exchange between a plagioclase crystal and melt will be 0.1 ± 0.05 for crystals in equilibrium at temperatures < 1050°C (Putirka, 2005). According to the $K_D(Ab\text{-}An)^{plag-liq}$ between plagioclase and the melt, all plagioclase rim and microlite compositions are in chemical equilibrium with the whole-pumice chemistry, whereas core compositions > An_{53} are out of equilibrium, which is consistent with textural observations of resorption of high-An core domains in the plagioclase (**Figure 2**). Plagioclase crystallization temperatures are calculated using Eq.26 of Putirka (2005), which uses the plagioclase and corresponding whole-pumice chemistry, and the water content of 5.8 wt.% (Manga et al., 2018a) to take into account the effect water will have on the plagioclase crystallization temperature (± 37°C uncertainty). Based on the available compositions, the-plagioclase-melt geothermometer yielded a temperature range from 877 to 909°C (1 s.d. = 5.6°C) and a mean of 890 ± 37°C.

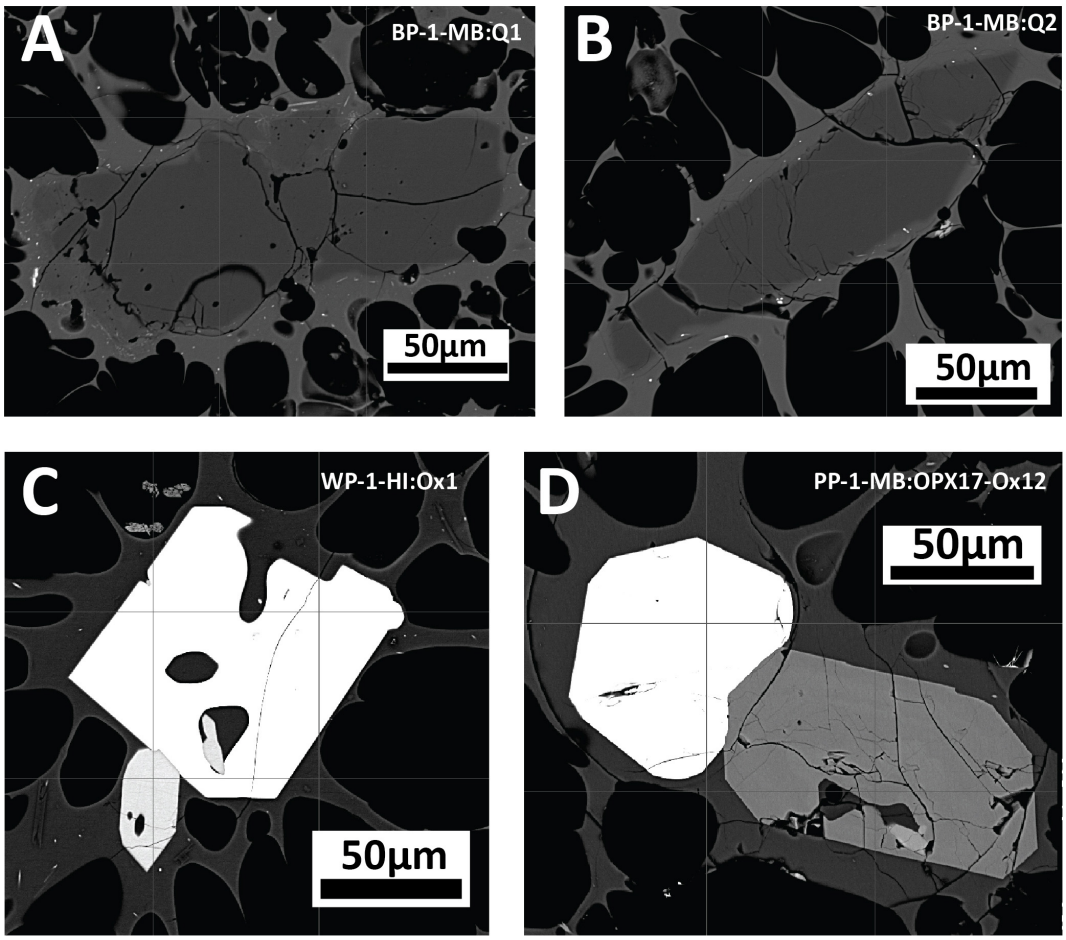

FIGURE 9 | Backscatter images of accessory phases of anhedral quartz **(A,B)** in banded pumice sample BP-1-MB, and Fe-Ti oxides and orthopyroxene intergrowths displaying euhedral crystal faces **(C,D)** in white pumice raft samples WP-1-HI and PP-1-MB.

Crystallization depths can be estimated using Equation 25a of Putirka (2005), which considers the effect of water on the pressure or crystallization depth of plagioclase. The plagioclase-melt geobarometer yields pressures ranging from 0.7 to 5.5 kbars (mean of 2.64 kbars, equivalent to 9.8 km depth). The resulting pressures are taken cautiously as the errors are significant (± 3.8 kbars). However, the majority of geobarometer estimates are between 2 and 4 kbars.

Pyroxene Geothermometry

The two-pyroxene geothermometer has previously been used to constrain a magmatic temperature of 850°C for the 2012 Havre eruption (Manga et al., 2018a). The geothermometer is ideal for estimating pre-eruptive temperatures of a melt when both mineral phases are touching or in very close proximity and can be shown to be in chemical equilibrium with each other and the surrounding melt (Putirka, 2008). Equilibrium tests (**Figures 10**, **11A**) were undertaken for augite and enstatite compositions following the method of Rhodes et al. (1979), which revealed the augite to not be in equilibrium with both the melt composition and co-existing enstatite in the same pumice samples. Orthopyroxene-clinopyroxene pairs that are in equilibrium have K_D $(Fe\text{-}Mg)^{opx-cpx}$ values between 1.09 ± 0.14. However, the orthopyroxene and clinopyroxene phases present in all the Havre pumice show a range in K_D $(Fe\text{-}Mg)^{opx-cpx}$ from 0.6 to 0.89 (**Supplementary Excel File**). When a clinopyroxene crystal is in chemical equilibrium with the surrounding melt, the $K_D(Fe\text{-}Mg)^{cpx-liq}$ will be 0.27 ± 0.3 (Putirka, 2008). The 'Rhodes diagram' helps illustrate this disequilibrium (**Figure 10A**), which plots the Mg number of clinopyroxene vs the Mg number of the melt constrained from whole-pumice chemistry, and is subsequently compared with $K_D(Fe\text{-}Mg)^{cpx-liquid}$ values (0.27 ± 0.3) determined experimentally (Rhodes et al., 1979). The Mg number of Havre augite ranges from 62 to 85, much higher than predicted from the host melt composition, and thus almost all Havre augite plot outside the equilibrium field. A comparison of the predicted vs observed Diopside-Hedenbergite (DiHd; Putirka et al., 1996; Mollo et al., 2013) and EnFs (Putirka, 1999) components of the augite (**Figures 10B,C**) further support the conclusion that the clinopyroxene is an out of equilibrium phase in the Havre melt. Consequently, we have not pursued

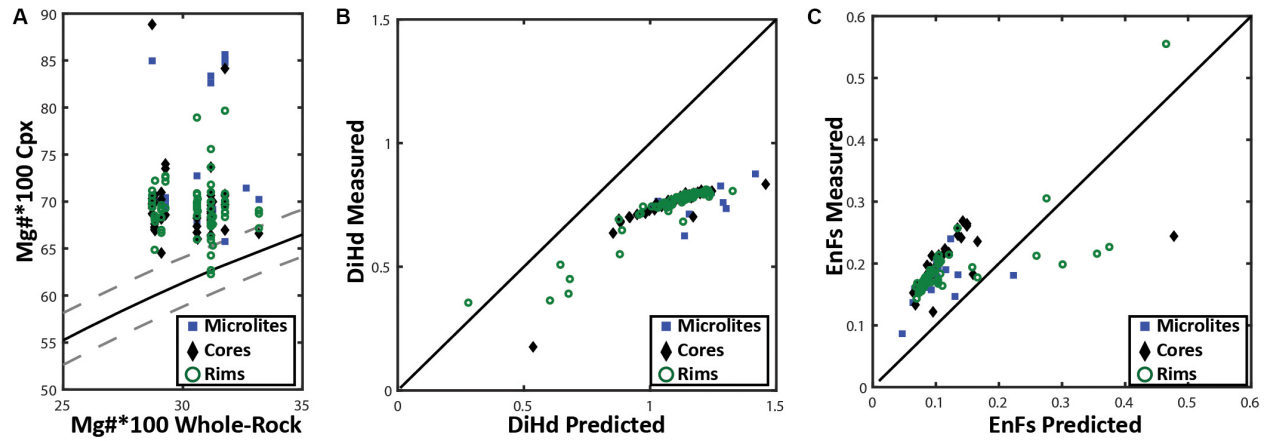

FIGURE 10 | (A) | Rhodes diagram following Rhodes et al. (1979) for clinopyroxene- whole rock chemistry distinguished by analysis location. The *X*-axis is the 100*Mg# of whole rock and the *Y*-axis represents the 100*Mg# of a corresponding clinopyroxene crystal. The solid black line is the ideal $K_D(Fe\text{-}Mg)^{cpx-liquid}$ for chemical equilibrium (0.26), where the dashed lines on either side of this line represent possible $K_D(Fe\text{-}Mg)^{cpx-liquid}$ range from 0.23 to 0.29 that is acceptable for clinopyroxene to be considered to be in chemical equilibrium with the whole rock/melt chemistry. **(B)** Plotting the predicted vs measured DiHd (Diopside-Hedenbergite) and **(C)** EnFs (Ferrosilite-Enstatite) clinopyroxene components as a secondary test for clinopyroxene-melt equilibrium. Here DiHd observed and predicted components are calculated by using the normative scheme from Putirka et al. (1996), Mollo et al. (2013) and Eq.3.1a (Putirka, 1999), respectively. The black line in **(B)** and **(C)** defines a 1-1 line between the measured and predicted clinopyroxene components; plotting further away from this line indicates the clinopyroxene is less likely to be in equilibrium with the melt.

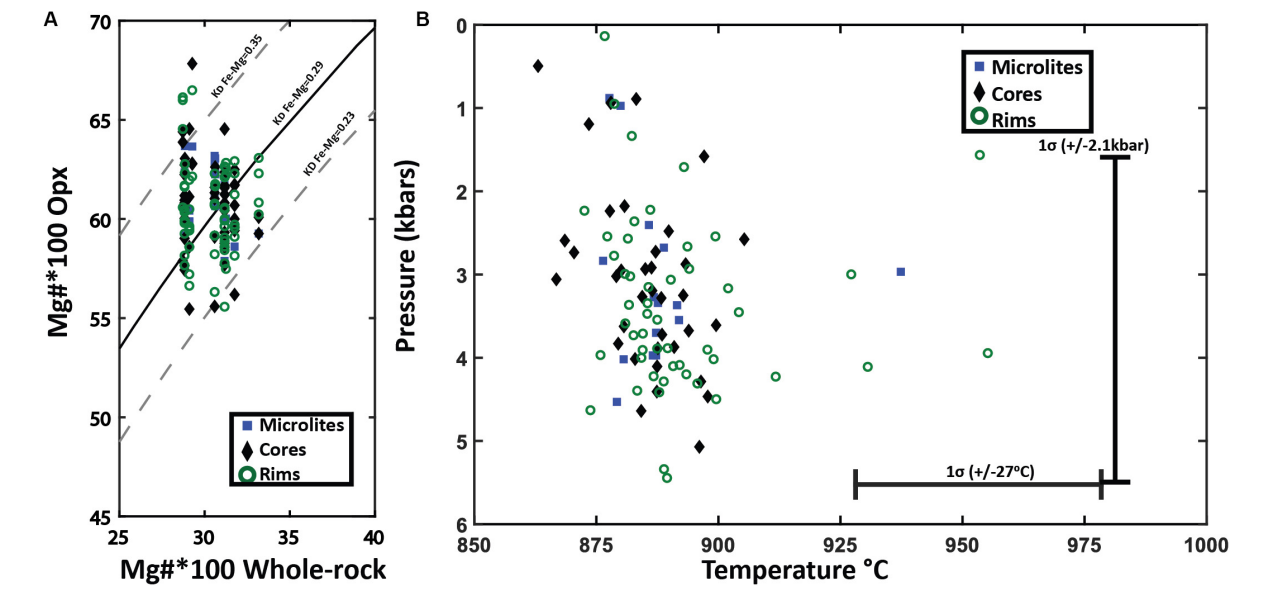

FIGURE 11 | Orthopyroxene-whole pumice/melt equilibrium test and thermobarometry. **(A)** Fe-Mg chemical equilibrium test between analyzed orthopyroxene and whole pumice chemistry for Havre raft pumice. Rhodes diagram (Rhodes et al., 1979) for orthopyroxene-whole pumice chemistry for all orthopyroxene crystals plotted by analysis location. The *X*-axis is the 100*Mg# = (Mg/Mg + Fe)*100 of the whole pumice and the *Y*-axis is the corresponding 100*Mg# for an orthopyroxene crystal. The solid black line is the ideal $K_D(Fe\text{-}Mg)^{Opx-liquid}$ for chemical equilibrium (0.29), where the dashed lines on either side represent the range of $K_D(Fe\text{-}Mg)^{Opx-liquid}$ from 0.23 to 0.35 that indicate chemical equilibrium with the melt chemistry. **(B)** Orthopyroxene-whole rock/melt thermobarometry plotted by analysis spot location. Orthopyroxene chemistry and corresponding whole-rock XRF chemistry are inputted into Putirka, 2008 Eq.28a to yield temperature estimates (± 27°C uncertainty) with a magmatic water content of 5.8 wt.% H_2O. Temperature estimates are then used in Eq.29b of Putirka (2008) to calculate pressures (± 2.1 kbars uncertainty).

temperature estimates based on augite compositions using Putirka (2008).

The enstatite was similarly assessed for equilibrium with the Havre melt composition. The $K_D(Fe\text{-}Mg)^{Opx-liq}$ will be 0.29 ± 0.06 if an orthopyroxene is in chemical equilibrium with the melt (Putirka, 2008). The Mg number of the Havre enstatite ranges from 53 to 67 and when plotted against Mg numbers of corresponding whole-rock/melt chemistry,

almost all analyzed enstatite plots within the equilibrium field (**Figure 11A**). The equilibrium tests for orthopyroxene and melt chemistry, therefore, provide confidence that the Havre orthopyroxene-liquid thermobarometry equations of Putirka (2008) can be utilized to constrain pre-eruptive temperatures and pressures of the Havre magmatic system (**Figure 11B**). The orthopyroxene-melt geothermometer (Equation 28a of Putirka, 2008 with ± 27°C uncertainty), yielded a temperature range from 857 to 1001°C (mean temperature of 890°C). These temperature estimates are consistent with those obtained from the coexisting Fe-Ti oxide and plagioclase-melt geothermometers.

H_2O Melt Concentrations and Water Saturation

Pre-eruptive water concentrations of the Havre 2012 rhyolite have been determined previously from plagioclase-hosted melt inclusions from the giant seafloor pumice (∼5.8 ± 0.7 wt.%; Manga et al., 2018a). A subsequent study that analyzed a different set, and a larger number of melt inclusions hosted in plagioclase and quartz from both raft and giant seafloor pumice reported a slightly lower water content of 4.9 ± 0.8 wt.% for the Havre rhyolite (Manga et al., 2018b). However, the host mineral phase was not identified for each melt inclusion analysis. When the melt inclusion data for the giant seafloor pumice from the two studies are combined, the average water content is 5.4 wt.% (n = 29) and higher than the average water content reported from the raft pumice samples only (4.8 wt.%; n = 26).

In this study, Equation 25b of Putirka (2008) provides an independent assessment of water contents in the melt, and the corresponding plagioclase and melt compositions indicate pre-eruptive water contents of 5.1 to 6.2 wt.% H_2O (mean of 5.6 ± 1.1 wt.% H_2O). Water content in the melt has also been calculated using Waters and Lange (2015) plagioclase-melt hygrometer assuming temperatures estimated from Putirka (2005) plagioclase-melt geothermometer (∼890°C), and a pressure of 2 kbars yields slightly lower water contents of 4.5 ± 0.35 wt.%. These estimates are within error of the water concentrations measured from melt inclusions (Manga et al., 2018a,b).

As a melt evolves through crystal fractionation the water content of the melt typically increases proportionally with the degree of crystallization until water saturation is reached. The program MagmSat (following H_2O-CO_2 mixed fluid saturation models from Ghiorso and Gualda, 2015) is used here to estimate at what H_2O^{melt} concentrations the Havre rhyolite would become water saturated. Inputted variables of whole-rock composition (PP-16-CU; **Table 1**), CO_2 estimates (80 ppm) from plagioclase-hosted melt inclusions (Manga et al., 2018a), pressure (2 kbars) and temperature (890°C) are kept constant, while melt water concentrations were increased incrementally until the magmatic system reached water saturation. The Havre 2012 rhyolite becomes water saturated when the melt contains > 6.04 wt.% H_2O at these conditions; consistent with $H2O^{melt}$ concentration values reported here and from plagioclase-melt inclusions (Manga et al., 2018a). Water saturation criteria are sensitive to pressure, where at low pressures (1.5 kbars) the melt becomes water saturated at lower water contents (> 5.05 wt.%), and at higher pressure (3 kbars) the melt only becomes water saturated at significantly higher water concentrations (> 8.45 wt.%).

DISCUSSION

It is increasingly realized that crystal populations present in magmas are not grown solely from the host melt in which they are resident on emplacement (Jerram and Martin, 2008). In particular, arc magmas have been shown to have prolific crystal cargoes, and much of the assembly of crystals can occur in the final stages of emplacement (e.g., Kent et al., 2010; Zellmer et al., 2014). Magmas commonly have a range of crystals where a combination of textural and microgeochemical analysis can be used to distinguish different genetic origins of crystals. However, for crystal-poor rhyolites like the Havre pumice, it can be difficult to determine whether the few phenocrysts present truly represent autocrysts crystallizing from the surrounding melt, are antecrysts due to mush remobilization, or even xenocrysts derived from source materials or chamber walls, or possibly a combination of all of the above. Previous studies on the historic 2012 submarine eruption have assumed all phenocryst present are autocrystic (e.g., Manga et al., 2018a,b). Importantly then, the few crystals present are strongly relied upon to constrain pre-eruptive conditions such as magmatic temperatures, pressures, water content and fO_2.

The textural and chemical characterization of the Havre mineral phases highlights some potential issues with assuming all phases are autocrystic and have co-existed and co-precipitated from the host silicic melt. Some phases are mostly euhedral (plagioclase, Fe-Ti oxides, orthopyroxene), whereas resorption, truncation of compositional banding and subhedral to anhedral shapes are evident in other phases (clinopyroxene, quartz). Geochemical tests reveal that some mineral phases are also not in equilibrium with the host melt composition (high-An plagioclase, clinopyroxene). This raises the question: what mineral phases are in or out of equilibrium with the host melt? The answer to this question will determine what mineral phases are autocrystic and can inform us on the host rhyolite melt and its conditions immediately prior to eruption, and those mineral phases that are inherited into the melt (either antecrysts or xenocrysts) and provide complementary information on the magmatic system and its architecture beneath the Havre volcano.

Crystal Cargo Components of the Havre Rhyolite

Autocryst Assemblage

Plagioclase is the dominant phenocryst and microlite phase in the Havre pumice, and phenocrysts are typically euhedral in form. Phenocryst rim compositions strongly overlap with microlite compositions (andesine, An_{40-50}). Calculated $K_D(An\text{-}Ab)^{plag-liq}$ values between the melt and plagioclase compositions demonstrate that phenocryst and glomerocryst core compositions with > An_{53} are not in chemical equilibrium

with the host melt. This is consistent with the rounded to resorbed boundaries of these high-An core domains to plagioclase phenocrysts (**Figure 2**). Consequently, the labradorite to rare bytownite plagioclase components are excluded from the autocrystic mineral assemblage of the Havre rhyolite.

Nearly all orthopyroxene crystals, including core and rim domains, and microlites, are in equilibrium with the host melt composition based on $K_D(Mg\text{-}Fe)^{opx-liq}$ exchange between the orthopyroxene and melt (**Figure 11A**). This is supported by the generally euhedral shape observed for all orthopyroxene crystals. Enstatite compositions are relatively restricted and overlapping between core, rim and microlites (En_{55-60}), and consistent with all orthopyroxene crystallization occurring from the host melt. However, subtle textural variations and the presence of relatively homogenous and unzoned to zoned phenocrysts (**Figures 6A,C**) suggests some orthopyroxene phenocrysts may contain inherited components that record earlier crystallization histories in the Havre magmatic system. The equilibrium tests and restricted composition suggests this earlier crystallization of orthopyroxene was from compositionally similar (i.e., silicic) magma.

Both Fe-Ti oxides are shown to be in chemical equilibrium based on the Mg/Mn partitioning test (Bacon and Hirschmann, 1988), and is consistent with their general euhedral form. Abundant, euhedral Fe-Ti oxide micro- and nanolites are also observed in the pumice glass and are particularly prevalent in the banded and giant seafloor pumice samples (e.g., **Figure 2**). Apatite is observed as inclusions in both orthopyroxene and clinopyroxene crystals and is typically euhedral in shape and therefore is interpreted as an early crystallizing phase in the Havre rhyolite.

Inherited/Antecrystic Assemblage

Two key, and somewhat unexpected, mineral phases are identified here as not being autocrystic, and are interpreted to have been mobilized into the Havre rhyolite melt prior to eruption. The main mineral phase is augite, and a number of features are consistent with augite phenocrysts and microphenocrysts not being in equilibrium. As with plagioclase, a wider, and slightly bimodal range of compositions are observed for augite core domains ($En_{40}Fs_{19}Wo_{41}$ to $En_{54}Fs_6Wo_{40}$). Augite is always subordinate to enstatite, and typically shows more subhedral to anhedral forms (e.g., **Figure 4**). Pyroxene elemental maps reveal a greater diversity of augite zonation patterns and confirm the existence of two discrete compositional populations characterized by relatively lower and higher Mg, Ca (**Figure 8**). All chemical equilibrium tests (i.e., $K_D(Fe\text{-}Mg)^{opx-cpx}$: $K_D(Fe\text{-}Mg)^{cpx-liq}$; predictive vs observed pyroxene components; **Figure 11**) further indicate the augite is not in equilibrium with the melt or co-existing enstatite and is therefore, not autocrystic.

The second mineral phase interpreted to be inherited is quartz. Given the silicic melt composition, quartz crystallization would be expected. However, quartz is rare and principally observed in the erupted products with higher phenocryst contents – the banded and giant seafloor pumice and lavas/domes (**Table 2**). The few quartz crystals present are small and subhedral to anhedral (**Figures 9A,B**). The recycled origin for quartz is examined further with Rhyolite-MELTS modeling in the following section.

Rhyolite-MELTS Models

Modeling to Constrain the Origins of the Havre Crystal Cargo

To further test if the main mineralogy observed in the Havre rhyolite (i.e., plagioclase, enstatite, augite, titanomagnetite, and ilmenite ± quartz) is all autocrystic and can be produced by closed system fractional crystallization, a matrix of Rhyolite-MELTS (Gualda et al., 2012; Ghiorso and Gualda, 2015) models were calculated. Two starting compositions (see **Supplementary Excel File**) were used: (1) one of the Havre rhyolite raft pumice (sample PP-16-CU), and (2) a low-K dacite lava collected prior to the 2012 eruption from the flanks of Havre volcano (Dredge Sample 47-03 from Wright et al., 2006; **Figure 1B**). The later sample is chosen as a parental composition given it is less evolved and derived from the same magma system as the eruptive material from the Havre 2012 eruption.

All Rhyolite-MELTS models are calculated at fO_2 = NNO (or QFM + 0.4) based on oxygen fugacity estimates from co-existing Fe-Ti oxides. Slightly different starting values have been used for Rhyolite-MELTS modeling using the Havre raft pumice or Havre flank lava as parental compositions. For the models using the raft pumice as the starting composition, the initial water content of 5.8 wt% is consistent with plagioclase hygrometer constraints from this study (i.e., Putirka, 2005) and plagioclase hosted melt inclusion data from the giant seafloor pumice (Manga et al., 2018a).We do not use water concentrations of 4.9 wt.% (Manga et al., 2018b) as this includes measurements from quartz-hosted melt inclusions, which is now suspected of being antecrystic; in this case, water concentrations measured from quartz will not record the water concentrations of the host melt (i.e., Havre rhyolite). Pressure is varied in models from 1.5 to 5 kbars based on opx-whole-rock geobarometer results. The initial parameters for Rhyolite-MELTS models using the Havre flank dacite starting composition are: fO_2 = NNO and 4 wt.% H_2O with 4 isobaric models generated at 1 kbar increments from 1–4 kbars. Models using an initial water content of 4 wt.% are presented here because at higher water contents, the melt quickly becomes water saturated with crystallization. A less evolved starting composition in the Rhyolite-MELTS models also provides a test for the origins of the mineral phases observed in the Havre pumice, as the mineral suite observed in nature is predicted to be derived from crystallization of a slightly less evolved melt composition than the final eruptive products. However, the Havre flank is only a proxy for a parental magma to the Havre 2012 crystal poor-rhyolite, and is used here because there is no evidence for a more primitive parental source of magma (i.e., basaltic enclaves, or magma mixing signatures). Therefore, this study does not speculate on the extent of prior crystallization and/or partial melting needed to produce the Havre flank composition from a more primitive melt or country rock.

All Rhyolite-MELTS models for each starting composition are run from a temperature slightly higher than the calculated liquidus (e.g., the temperature of the first crystallizing phase of each pressure dependent model; ∼910–960°C) down to 750–760°C in 10°C increments. For each 10°C increment, Rhyolite-MELTS provides the proportion of liquid to crystals (**Figures 12C,D**), the composition of the evolving liquid

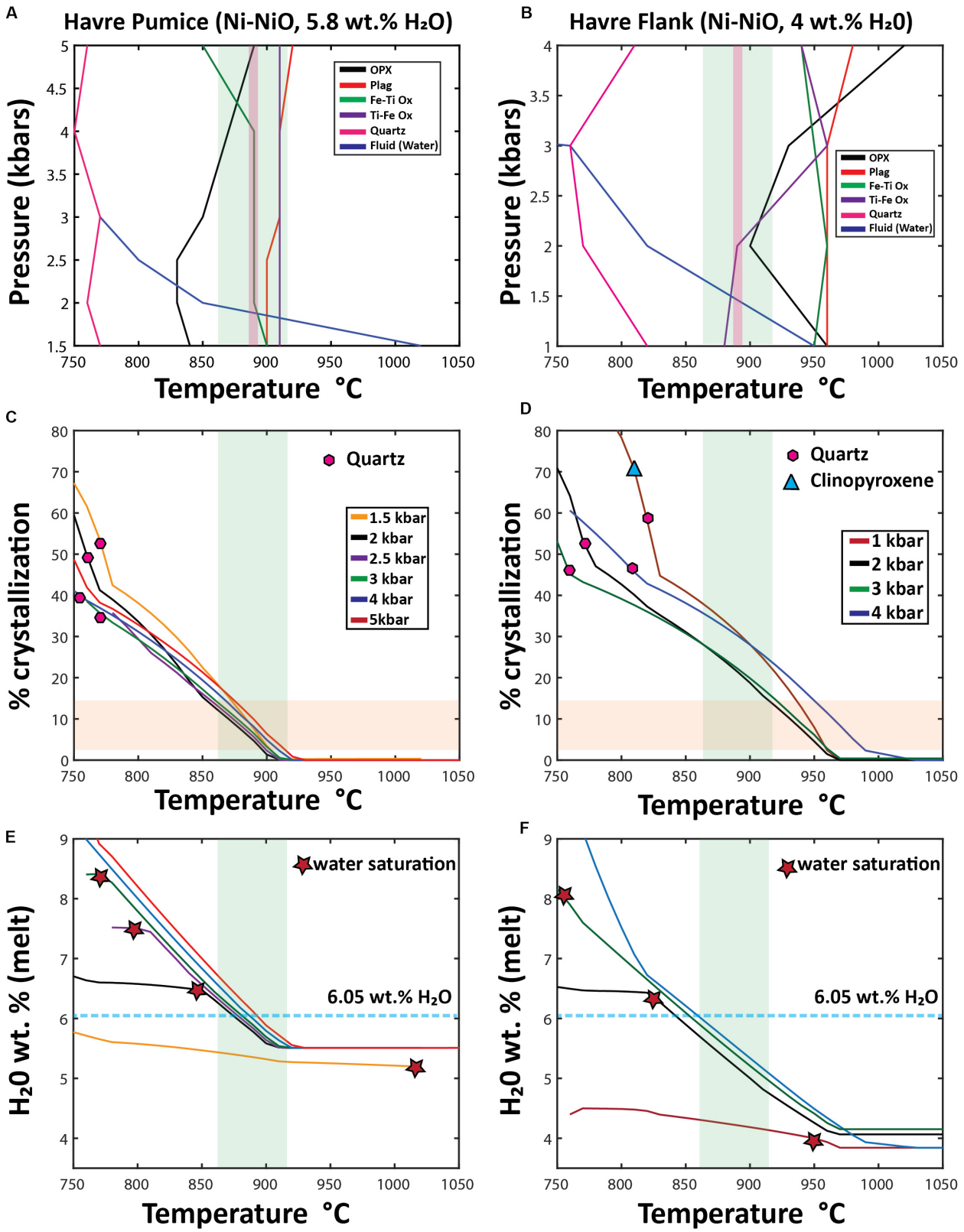

FIGURE 12 | Outcomes of Rhyolite MELTS modeling using two different starting compositions: Havre pumice raft (PP-16-CU), and a pre-2012 Havre flank dacite lava (Wright et al., 2006). Starting compositions for both Rhyolite-MELTS models are given in the **Supplementary Excel File 1**. **(A,B)** "synthetic" phase

(Continued)

FIGURE 12 | Continued
diagrams; **(C,D)** Crystallization**%** vs temperature **(E,F)** H_2O^{melt} vs temperature, In the temperature vs. pressure phase diagrams **(A,B)** produced from multiple Rhyolite-MELTS models, each line is the result of combining the liquidus temperature of an individual crystallizing phase at different pressures; the blue line shows the calculated temperature and pressure at which the melt becomes water saturated. The green band represents the orthopyroxene-melt geothermometry results (890 ± 27°C) of the Havre pumice in all diagrams **(A–F).** In **(A,B)**, the pink shaded field represents geothermometry results of Fe-Ti oxide pairs (~885–890°C). In the% crystallization vs temperature diagrams **(C,D)**, the horizontal orange field denotes the range of crystal contents (3–15%) observed throughout all Havre 2012 eruptive products. The first appearance of quartz (pink hexagons) and clinopyroxene (light blue triangles) is shown for each pressure model run. The H_2O^{melt} vs temperature diagrams **(E,F)** are used to show when the melt becomes water saturated (red stars) and the estimated concentration of water in the melt needed for the Havre rhyolite to be water saturated (light blue dashed line at 6.05 wt.% H_2O, 100 ppm CO_2) calculated from Ghiorso and Gualda (2015) fluid mixing models. In all rhyolite-MELTS models crystallization continues in the presence of an exsolved/exsolving fluid phase following water saturation.

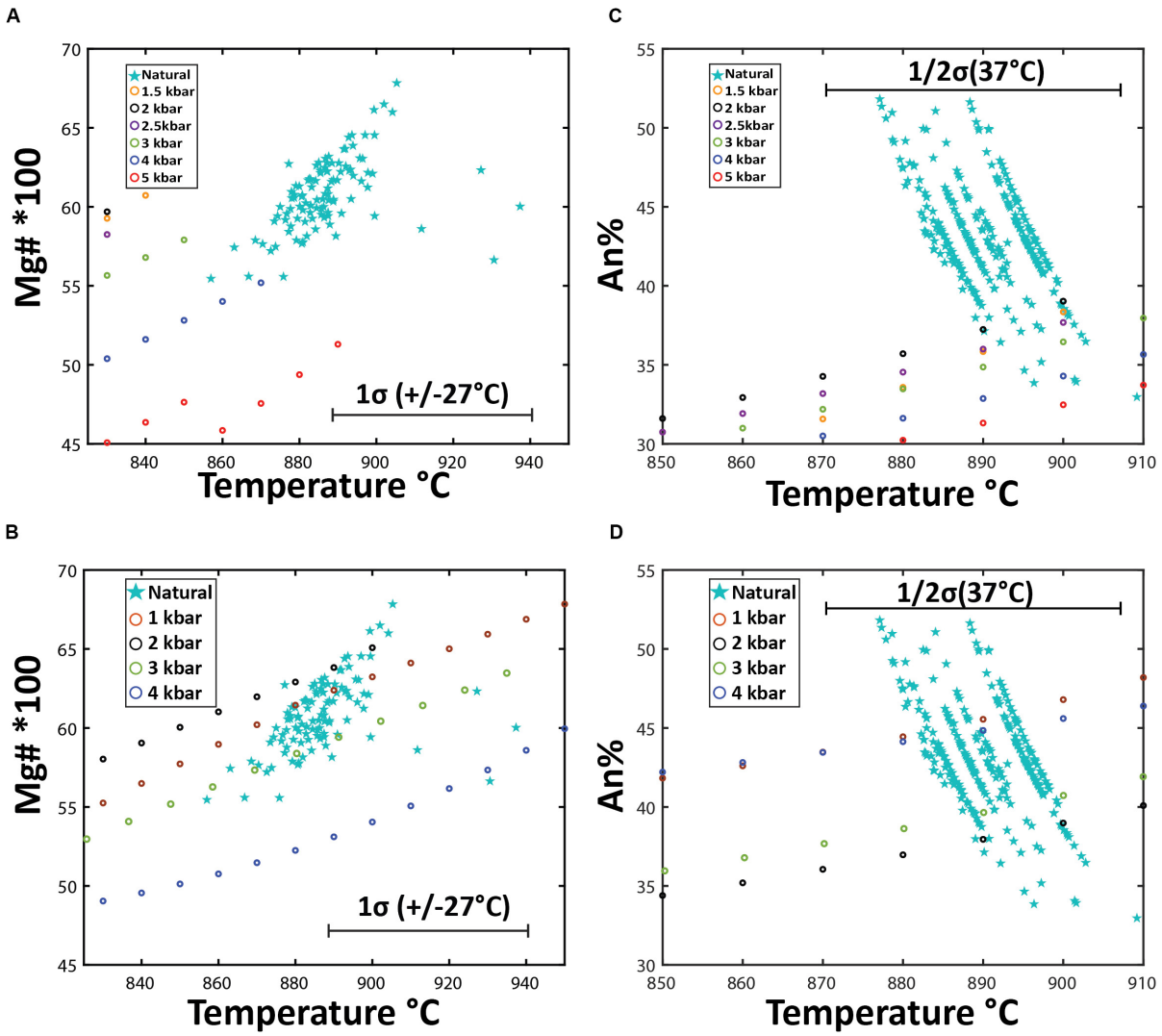

FIGURE 13 | Mineral chemistry outcomes of Rhyolite-MELTS modeling using two different starting compositions**: (A,C)** Havre pumice raft (PP-16-CU), and **(B,D)** a pre-2012 Havre flank dacite lava (Wright et al., 2006). **(A,B)** are a comparison of measured vs Rhyolite-MELTS calculated orthopyroxene compositions where temperatures (± 27°C uncertainty) for measured orthopyroxene compositions are calculated from eq. 28a of Putirka (2008) assuming 5.8% H_2O magmatic water content. **(C,D)** compares measured vs Rhyolite-MELTS calculated plagioclase compositions where temperatures (± 37°C uncertainty) for measured plagioclase are calculated based on eq. 26 of Putirka (2005) for in equilibrium plagioclase based on Ab-An exchange criteria.

(**Figures 12E,F**) and each crystallizing phase (**Figure 13**). We use multiple isobaric pressure models, conducted at constant fO_2 and water concentrations, to produce synthetic phase diagrams in T-P space based on both starting compositions (**Figures 12A,B**). A suite of models at varying conditions of water were also conducted, where reducing the water content does not greatly affect the sequence or composition of crystallizing phases and only slightly increases the liquidus temperature of each phase.

Rhyolite-MELTS Crystallization Sequence

Rhyolite-MELTS isobaric models calculated at 1–4 kbar pressure using the Havre pumice (PP-16-CU) as a parental composition predict a crystallization sequence from first to last crystallizing phase of ilmenite, plagioclase, titanomagnetite, orthopyroxene and quartz (**Figure 12A**). At > 4 kbars, plagioclase replaces ilmenite as the liquidus phase, and orthopyroxene crystallizes before titanomagnetite (**Figure 12A**). Clinopyroxene is never produced under any pressures. Quartz is only crystallized when the melt reaches 750–770°C, and after 35 to 53% of the melt has crystallized (**Figure 12C**).Water saturation can be reached at high temperatures (1020°C) and low pressures (1.5 kbar), whereas at slightly higher pressures (2–3 kbars), water saturation is not reached until the melt has cooled to lower temperatures from 860 to 770°C (**Figure 12A**). However, at pressures in excess of 3 kbars, the melt remains water undersaturated. Water saturation is reached at lower H_2O^{melt} concentrations (∼5.2 wt.%) in the melt for lower pressure models (1.5 kbars) but at higher pressures from 2 to 3 kbars, the melt does not reach water saturation until the melt has accumulated ∼6.5 to 8.4 wt.% H_2O (**Figure 12E**). Modifying the starting composition of the 2 kbar rhyolite-MELTS model to include 80 ppm CO_2 (as indicated from melt inclusions, Manga et al., 2018a), alters the temperature (880°C) and $H2O^{melt}$ concentrations (6.14 wt.%) at which water saturation is reached.

Rhyolite-MELTS modeling using the dacite flank lava as the parental composition predicts the following crystallization sequence at low pressures (1–3 kbar): plagioclase, ilmenite, orthopyroxene, and magnetite. The first crystallizing phase changes at progressively higher-pressure conditions of crystallization with ilmenite and plagioclase (3 kbar) and orthopyroxene (4 kbar) being the liquidus phase (**Figure 12B**). Clinopyroxene only crystallizes in 1 kbar pressure models as a near solidus phase at 810°C and only after ∼70% of the melt has already crystallized (**Figure 12D**). Quartz crystallizes in all pressure models from 750 to 820°C after 45 to 58% of the system has crystallized (**Figures 12B,D**). Water saturation occurs at 950°C in lower pressure (1 kbar) models and at 760°C at 3 kbars; water saturation is not reached when crystallization occurs at 4 kbar (**Figures 12B,F**). Water saturation is reached at a H_2O melt concentration of ∼4 wt.% in lower pressure (1 kbar) models; at ∼6.4 wt.% in the 2 kbar model; and at ∼8.2 wt.% in the 3 kbar model (**Figure 12F**).

Comparison of Rhyolite-MELTS and Observed Crystallizing Assemblages

In addition to the crystallization sequence, the Rhyolite-MELTS modeling allows comparison of the crystallization temperatures of each phase and the mineral chemistry of the calculated and observed mineral assemblage (**Figure 13**). Comparisons of orthopyroxene compositions (**Figures 13A,B**) are based on the measured and calculated Mg number and corresponding pyroxene-melt temperatures (Putirka, 2008; eq.28) with Rhyolite-MELTS calculated temperatures of crystallization at different pressures. Measured Havre orthopyroxene compositions, crystallization temperatures, and pressure are consistent with the Havre flank Rhyolite-MELTS model results for orthopyroxene at 1–3 kbars (**Figure 13B**). For example, the temperature at which orthopyroxene crystallizes (890–900°C) in Rhyolite-MELTS models over 2–3.5 kbars is consistent with temperature and pressure estimates calculated by orthopyroxene-melt thermobarometry of 890 ± 27°C and 2–4 kbars, respectively. In contrast, much less consistency is observed for the Havre pumice Rhyolite-MELTS model that in general, does not produce the same orthopyroxene composition and crystallization temperature at any pressure (**Figure 13A**). Natural Havre pumice orthopyroxene have higher Mg numbers and calculated temperatures (∼890°C) where the Rhyolite-MELTS models predict orthopyroxene crystallization at lower temperatures (< 863°C).

Figures 13C,D compare measured An content of plagioclase with calculated plagioclase compositions crystallizing from the two starting melt compositions over a pressure range from 1–4 kbars. The Havre rhyolite pumice Rhyolite-MELTS model produces plagioclase compositions of An_{35} at low pressures (1–2 kbars), which overlaps only with the most sodic andesine analyzed from the Havre pumice (**Figure 13C**). In contrast, measured Havre plagioclase compositions, and calculated temperatures and pressures using the plagioclase-liquid geobarometer of Putirka (2005) are consistent with Rhyolite-MELTS calculated plagioclase compositions in the Havre dacite (flank) models at all pressures from 1–4 kbars (**Figure 13D**). Of note is that the Rhyolite-MELTS calculated plagioclase liquidus temperature is much greater than plagioclase-melt thermobarometer estimates, however, plagioclase continuously crystallizes throughout all the Rhyolite-MELTS models (**Figures 12A,B**).

In the Havre flank (dacite) Rhyolite-MELTS model (**Figure 12B**), ilmenite and titanomagnetite are both predicted to crystallize at high temperatures (940–970°C) and at higher pressures (> 2 kbars), whereas at lower pressures, titanomagnetite crystallizes out at a higher temperature (∼940–950°C) and does not coexist with ilmenite until lower temperatures (880–900°C). These calculated crystallization temperatures are therefore consistent with results from Fe-Ti oxide geothermometry (∼885–890°C). Similarly, Havre pumice Rhyolite-Melts models indicate ilmenite and titanomagnetite to co-exist at 890°C at pressures < 4 kbars, where ilmenite is shown to be the first crystallizing oxide at 910°C in all pressure models (**Figure 12B**).

Implications of Rhyolite-MELTS Models

Several implications arise from the Rhyolite-MELTS modeling and through comparison with the observed mineral assemblage, compositions and phase relationships. First, as indicated from textural relationships, clinopyroxene rarely appears as a crystallizing phase, and quartz does not appear as a crystallizing phase until near solidus temperatures (750–820°C). Clinopyroxene is only produced from these silicic melt compositions at low temperatures, at near-solidus conditions (> 70% crystallization; **Figure 12D**), and at low pressures (1 kbar). Second, Rhyolite-MELTS modeling confirms the autocrystic phases being co-existing Fe-Ti oxides, sodic plagioclase and orthopyroxene (**Figures 12A,B**). The crystallization order can be subtly changed with increasing

pressure of crystallization. Third, given the relatively high initial water content, the Rhyolite-MELTS models are sensitive to pressure as well as to when the magma reached fluid saturation (**Figures 12E,F**). Water saturation of a melt potentially can be a trigger for eruption and terminate crystallization unrelated to decompression and degassing (e.g., Sparks, 1978; Melnik, 2000). If crystallization occurred at shallow depths (< 1.5–2.25 kbars) then fluid saturation occurs before any other phase has crystallized (**Figures 12A,B,E,F**). This could then imply the entire crystal cargo is inherited or that crystallization was occurring in the presence of an exsolved fluid phase. However, when pressure is > 2 kbars in Havre pumice models (**Figure 12A**) and > 1.5 kbars in Havre flank models (**Figure 12B**), then crystallization of plagioclase, orthopyroxene and Fe-Ti oxides can occur prior to any water saturation. The H_2O^{melt} concentration at which water saturation occurs in each model provides the conditions (i.e., temperature and crystal content) required for volatile exsolution (**Figures 12C–F**). Water saturation needs to follow H_2O^{melt} concentrations in breaching water saturation criteria (> 6.04 wt.% H_2O^{melt}) for models to truly represent a scenario where the eruption could be triggered by a pressure build-up in the crystallizing, water-supersaturated Havre magma (e.g., Tait et al., 1989). This is the case for 2 kbars models that reach water saturation of ∼6.4 wt.% H_2O at ∼860°C (**Figure 12E**). While, the addition of a small amount of CO_2 dissolved in the magma (80 ppm from plagioclase-hosted melt inclusions; Manga et al., 2018a) raises the temperature at which the magma reaches fluid saturation (e.g., 880°C at 6.14 wt.% H_2O), it does not cause any substantive change in the crystallization sequence. Fourth, Rhyolite-MELTS calculated melt compositions overlap observed Havre pumice compositions after ∼7.5–14% crystallization (**Figures 12C,E**), and this is consistent with the observed low crystal contents in the 2012 Havre erupted products (**Table 2**). Fifth, Rhyolite-MELTS models and using the Havre flank lava starting composition run at moderate pressures (2–3 kbars), best replicate the observed mineralogy, crystallization sequence as informed by enclosing relationships and relative modal abundances, and pressure estimates from the different geobarometers (**Figures 12A–D**, **13**).

Assembly and Pre-eruptive Conditions of the Havre Rhyolite Magma

The combination of textural and microgeochemical analysis with Rhyolite-MELTS modeling provides valuable insights into the assembly of the crystal cargo of the Havre rhyolite magma and improved constraints on the pre-eruptive conditions.

The autocrystic mineral assemblage of the Havre rhyolite is concluded to be andesine plagioclase, magnetite, ilmenite, enstatite and accessory apatite. This is supported by the generally euhedral forms of these mineral phases, and their common occurrence in small crystal aggregates or glomerocrysts. Phenocryst/microphenocryst rim compositions typically overlap with euhedral microlite compositions in the pumice glass (**Figures 3**, **6**). This crystallizing assemblage is replicated after low degrees of crystallization (7–15%) in a range of Rhyolite-MELTS models using slightly different silicic melt starting compositions, pressures and initial water contents. Liquidus temperatures are interpreted to be recorded by the co-existing Fe-Ti oxides at ∼940°C. Eruptive temperatures appear to be slightly lower at ∼890-900°C based on plagioclase-melt, orthopyroxene-melt, and co-existing Fe-Ti oxide geothermometry. The consistency in temperature estimates by these three different geothermometers gives confidence to the results. Rhyolite-MELTS models and geobarometry estimates from orthopyroxene-melt and plagioclase-melt compositions indicate final magma storage and crystallization at depths of ∼2–3 kbar.

We conclude that augite, the calcic plagioclase (labradorite-bytownite) components of plagioclase phenocrysts and trace quartz are inherited crystal components into the Havre rhyolite magma. The exact origin of these mineral phases remains unclear and could be better constrained if more was known on the pre-eruptive history of the Havre magmatic system.

At least two compositionally and texturally distinct augites are present (**Figures 6**, **8**) suggesting an ultimate derivation from crystal mush zones in the Havre plumbing system. Sector zoning in clinopyroxene (**Figure 8C**) has been attributed to slow, near-equilibrium crystallization kinetics associated with low degrees of undercooling (< 40°C; Ubide et al., 2019; Masotta et al., 2020). The low degrees of undercooling can be explained by clinopyroxene subjected to slow magma ascent, or gradual recharge of a crystal mush zone (Ubide et al., 2019). While, most major elements partition into sectors (i.e., Mg^{+2} and Si^{+4} in hourglass sectors and Ca^{+}, Ti^{+4} and Al^{+3} in prism sectors), Cr and Fe^{+2} in contrast, follow concentric zoning patterns, with enriched Cr zones recording mafic recharge events (e.g., Ubide and Kamber, 2018). Enriched Cr rims of sector zoned clinopyroxene are consistent with a mafic recharge event triggering eruptions at Mount Etna (e.g., Ubide and Kamber, 2018); however, at Havre, Cr enrichment is only observed in crystal interiors, and most likely recording older recharge events perhaps in a crystal mush zone somewhere at depth in the Havre magmatic plumbing system. The implication of the rhyolite-MELTS models for clinopyroxene to appear only after extended crystallization (> 70%; **Figure 12D**) is consistent with low temperature crystallization of clinopyroxene in a crystal mush zone. Preserving sector zoning then requires rapid cooling and/or quenching of the pyroxene upon eruption where decompression and degassing induced crystallization is recorded in Al^{+3} and Ti^{+4} enriched rims (**Figure 8**) relative to the clinopyroxene mantle (e.g., Ubide et al., 2019).

The occurrence of quartz suggests some mush zones are very silicic. Melts models indicate quartz is a likely antecryst incorporated into the erupted melt from a cooler/dryer crystal-rich mush zone (> 50%) or margins of the reservoir. The spectrum of crystal contents observed between Havre eruptive products could also be explained by a crystal-poor rhyolite cap immediately overlying a crystal-rich zone where greater entrainment of crystals occurs on eruption as a result of withdrawal dynamics. A similar process could occur near the margin of the magma reservoir where the magma system would be progressively crystal-rich and cooled from the center to margins of the system. Crystal entrainment from cooler parts of the magma system is consistent with higher counts of antecryst (e.g., quartz and clinopyroxene; **Table 2**) in the seafloor eruptive

products compared to the pumice raft. However, the more calcic plagioclase may be sourced from more mafic-intermediate compositions or during partial melting of source material. The occurrence of thin rim overgrowths (10–100 μm) to phenocrysts (e.g., **Figures 2**, **7**A) with compositions that overlap microlites suggests the inherited crystal components resided in the Havre rhyolite melt for a brief period prior to eruption. The H_2O-rich and CO_2-poor (< 200 ppm) compositions of the plagioclase-hosted melt inclusions (Manga et al., 2018a) would also be consistent with some magma storage prior to eruption (e.g., Cashman and Sparks, 2013).

The discrimination of these mineral phases into autocrystic and inherited components is significant. Although the proportion of inherited crystal material is low, and does not materially change the bulk rock texture or composition, it shows that even in crystal-poor magmas, crystal cannibalization from other source materials can occur, and that the mineral phases added to the crystal cargo may not be obviously out of equilibrium (e.g., quartz in rhyolite). Previous studies presented pre-eruptive H_2O melt concentrations from plagioclase-hosted melt inclusions (Manga et al., 2018a) as well as quartz-hosted melt inclusions (Manga et al., 2018b). Plagioclase with An < 53 is shown to be in equilibrium in this study, however quartz is a likely antecrystic or xenocrystic phase, and therefore the melt inclusion data incorporating quartz-hosted melt inclusion compositions (Manga et al., 2018b) are less likely to accurately record the pre-eruptive conditions and water concentrations in the host melt. This study considers water concentrations of 5.8 ± 0.7 wt.% from only plagioclase-hosted melt inclusions (Manga et al., 2018a) to more accurately record the pre-eruptive melt water concentrations and these concentrations are consistent with the plagioclase-melt hygrometer estimates reported here.

The clinopyroxene has previously been relied upon to constrain the pre-eruptive temperature of the Havre rhyolite magma. Manga et al. (2018a) derived a temperature estimate of 850 ± 20°C using the coupled orthopyroxene-clinopyroxene geothermometer of Putirka (2005). Several lines of evidence have been presented here to show the clinopyroxene is not in equilibrium, and the geothermometer yields low temperature estimates compared to a range of other geothermometers underpinned by equilibrium tests.

The 2012 Havre eruption has been somewhat controversial in terms of whether the eruption was explosive or effusive. This is due to the water depth of ∼900 m for the summit of Havre volcano, and modeled eruption parameters and observed products at the vent indicating an overall effusive style of eruption (Manga et al., 2018a), yet a large volume and buoyant pumice raft was produced and textural features to some ash deposits related to the eruption suggest some magma-driven explosivity (Carey et al., 2014; Murch et al., 2019). Models used to simulate the Havre eruption (e.g., magma ascent conduit model of Manga et al., 2018a) are sensitive to changes in eruption temperature. For example, more than a four-fold increase in ascent rate results if an eruption temperature of 890°C is used, and ascent rates > 200 m s^{-1} can result for magmatic temperatures of 1000°C. Rhyolite-MELTS models demonstrate that the magma remains fluid undersaturated at high pressures (> 2.5 kbars), crystallizing all inferred autocrystic phases (plagioclase, Fe-Ti oxides, and orthopyroxene) in agreement with geothermometry estimates. However, the magma is primed for fluid saturation and volatile exsolution at lower pressures (< 2 kbars) suggesting subsurface fragmentation was possible during the pumice raft-producing phase of the Havre eruption. We conclude that considerable uncertainty exists as to whether an entirely effusive eruption (Manga et al., 2018a) produced the voluminous pumice raft of the 2012 Havre eruption.

CONCLUSION

A detailed petrographic and compositional study of the Havre pumice mineralogy, coupled with Rhyolite-MELTS modeling have identified complexities in the crystal cargo of a relatively large volume, crystal-poor and apparently chemically homogenous rhyolite magma. While the mineral assemblage is not diverse or unusual for a subduction-related rhyolite magma, a range of different but complementary approaches were able to distinguish autocrystic from inherited crystal components. The autocrystic assemblage crystallizing just prior to eruption was plagioclase (An_{40-45}), enstatite, Fe-Ti oxides and accessory apatite. Inherited crystal components include An-rich (> An_{53}) plagioclase, augite and quartz. Rhyolite-MELTS modeling and geothermometric indicators suggest the quartz and augite are antecrystic and derived from cooler, silicic mush zones in the Havre magmatic system as quartz was found to crystalize at 750–820°C, and clinopyroxene only crystallized at low pressures and as a near-solidus phase (> 70% crystallization). When the entire eruptive sequence is considered, a subtle trend emerges of increasing crystal content and inherited crystal cargo from the volumetrically dominant white raft pumice to the volumetrically minor and late-erupted summit lava flows (Carey et al., 2018; Murch et al., 2019).

Discriminating autocrystic from inherited crystal components is critical when attempting to constrain the pre-eruptive characteristics of the magma body. Even when crystal contents are low, phenocryst assemblages are restricted and phases may be broadly consistent with melt or whole-rock compositions, it should not automatically be assumed all mineral phases present are autocrystic. Equilibrium tests confirmed clinopyroxene was not in equilibrium with host melt or co-existing orthopyroxene compositions, and temperature estimates using clinopyroxene (Manga et al., 2018a) have been found to be low. A range of different thermometers validated by equilibrium tests yielded consistent pre-eruptive temperature estimates for the Havre rhyolite: 890 ± 27°C (orthopyroxene-melt; Putirka, 2008); 890 ± 37°C (plagioclase-melt, Putirka, 2008), and 890-900°C (Fe-Ti oxides; Spencer and Lindsley, 1981). Oxygen fugacity constrained by ilmenite and titanomagnetite pairs indicate the magma was not strongly oxidizing (QFM + 0.4 ∼NNO). Corresponding plagioclase and melt compositions indicate pre-eruptive water contents of 5.1 to 6.2 wt% H_2O (mean of 5.6 ± 1.1 wt.% H_2O) and are consistent with magmatic water contents previously determined from plagioclase melt inclusions (Manga et al., 2018a). Moderate crystallization

depths of 2–4 kbars are also indicated from plagioclase-melt compositions (Putirka, 2008). The consistency of results for the different mineral-based geothermometers gives confidence that plagioclase, orthopyroxene and Fe-Ti oxides were co-crystallizing in the Havre rhyolite magma immediately prior to eruption.

The lack of strong mafic recharge signals (e.g., reverse compositional zoning, Cr-rich rims in clinopyroxene) suggest mafic recharge did not directly trigger the eruption. Given the relatively high initial water content, the Rhyolite-MELTS models are sensitive to pressure and timing of when magma reached fluid saturation. The observed mineral phase relationships and Rhyolite-MELTS modeling results are most consistent with some crystallization occurring at pressures $>$ 2 kbar prior to eruption and that the Havre magma was primed for volatile exsolution on decompression and ascent to the surface. Rhyolite-Melts modeling suggests limited fractionation from a dacitic parental composition can successfully produce the erupted Havre melt composition and observed autocrystic mineralogy.

DATA AVAILABILITY STATEMENT

All datasets presented in this study are included in the article/**Supplementary Material**.

AUTHOR CONTRIBUTIONS

This manuscript is a result of JK's Ph.D. research, where sample preparation, chemical analyses, data analysis, and production of figures was completed by JK with the guidance/training of QUT's Central Analytical Research Facility (CARF) staff and Ph.D. supervisors SB, DG, and HC. SB is JK's principle Ph.D. supervisor with expertise in volcanology, pumice raft-producing eruptions, and igneous petrology. He provided guidance on petrographic and mineral chemistry interpretations and had a major role in writing and editing the manuscript. DG with his expertise in petrology and mineralogy provided guidance in mineral chemistry calculations and interpretations presented in this study. DG also conducted a suite of Rhyolite-MELTS models presented here. HC with her expertise in EPMA performed routine EPMA set up and standardization for EPMA of glass and mineral chemistry for all single spot and pyroxene spatial elemental map sessions. All authors contributed to the article and approved the submitted version.

FUNDING

JK was supported by a QUT PRA scholarship and an AINSE postgraduate research scholarship.

ACKNOWLEDGMENTS

We acknowledge the Central Analytical Research Facility (CARF) at Queensland University of Technology for EPMA and XRF chemical analyses. Thank you to Rebecca Carey for kindly providing samples of the 2012 Havre lavas and giant seafloor pumice included in this study that initially formed the basis of a QUT vacation research experience project to Daniel Franks. The two reviewers are thanked for their constructive reviews and comments which have greatly improved the manuscript. Thank you to Teresa Ubide for presenting the opportunity to be a part of this special issue and providing constructive feedback during the research process.

SUPPLEMENTARY MATERIAL

The Supplementary Material for this article can be found online at: https://www.frontiersin.org/articles/10.3389/feart.2020.00310/full#supplementary-material

MATERIAL S1 | XRF desalination methods.

MATERIAL S2 | Unique Havre raft pumice types.

MATERIAL S3 | Mn/Mg Fe-Ti oxide pairs equilibrium test.

MATERIAL S4 | Excel files of mineral chemistry (plagioclase, orthopyroxene, clinopyroxene, magnetite & ilmenite), EPMA glass chemistry, orthopyroxene-clinopyroxene equilibrium test results, and starting compositions of MELTS models.

REFERENCES

Bachmann, O., and Bergantz, G. W. (2004). On the origin of crystal-poor rhyolites: extracted from batholithic crystal mushes. *J. Petrol.* 45, 1565–1582. doi: 10.1093/petrology/egh019

Bachmann, O., and Bergantz, G. W. (2008a). Rhyolites and their source mushes across tectonic settings. *J. Petrol.* 49, 2277–2285. doi: 10.1093/petrology/egn068

Bachmann, O., and Bergantz, G. (2008b). The magma reservoirs that feed supereruptions. *Elements* 4, 17–21. doi: 10.2113/gselements.4.1.17

Bacon, C. R., and Hirschmann, M. M. (1988). Mg/Mn partitioning as a test for equilibrium between coexisting Fe-Ti oxides. *Am. Mineral.* 73, 57–61.

Barker, S. J., Wilson, C. J. N., Baker, J. A., Millet, M. A., Rotella, M. D., Wright, I. C., et al. (2013). Geochemistry and petrogenesis of silicic magmas in the intra-oceanic Kermadec arc. *J. Petrol.* 54, 351–391. doi: 10.1093/petrology/egs071

Bryan, S. E., Cook, A., Evans, J. P., Colls, P. W., Wells, M. G., Lawrence, M. G., et al. (2004). Pumice rafting and faunal dispersion during 2001-2002 in the Southwest Pacific: record of a dacitic submarine explosive eruption from Tonga. *Earth Planet. Sci. Lett.* 227, 135–154. doi: 10.1016/j.epsl.2004.08.009

Bryan, S. E., Ferrari, L., Reiners, P. W., Allen, C. M., Petrone, C. M., Ramos-Rosique, A., et al. (2008). New insights into crustal contributions to large-volume rhyolite generation in the mid-Tertiary Sierra Madre Occidental province. Mexico, revealed by U–Pb geochronology. *J. Petrol.* 49, 47–77. doi: 10.1093/petrology/egm070

Bryan, S. E., Marti, J., and Leosson, M. (2002). Petrology and geochemistry of the Bandas del Sur formation, Las Cañadas edifice, Tenerife (Canary Islands). *J. Petrol.* 43, 1815–1856. doi: 10.1093/petrology/43.10.1815

Bryan, W. B. (1970). Mineralogy of Coral Sea drift pumice. *Carnegie Institute Washington Yearbook.* 68, 187–190.

Carey, R., Soule, S. A., Manga, M., White, J. D., McPhie, J., Wysoczanski, R., et al. (2018). The largest deep-ocean silicic volcanic eruption of the past century. *Sci. Adv.* 4:e1701121. doi: 10.1126/sciadv.1701121

Carey, R. J., Wysoczanski, R., Wunderman, R., and Jutzeler, M. (2014). Discovery of the largest historic silicic submarine eruption. *Eos Trans. Am. Geophys. Union* 95, 157–159. doi: 10.1002/2014eo190001

Carmichael, I. S. E., and Nicholls, J. (1967). Iron-titanium oxides and oxygen fugacities in volcanic rocks. *J. Geophys. Res.* 72, 4665–4687. doi: 10.1029/jz072i018p04665

Cashman, K., and Blundy, J. (2000). Degassing and crystallization of ascending andesite and dacite. *Philos. Trans. R. Soc. Lon. Ser. AMath. Phys. Eng. Sci.* 358, 1487–1151.

Cashman, K., and Sparks, R. S. J. (2013). How volcanoes work: a 25 year perspective. *Geol. Soc. Am. Bull.* 125, 664–690. doi: 10.1130/b30720.1

Charlier, B. L. A., Bachmann, O., Davidson, J. P., Dungan, M. A., and Morgan, D. J. (2007). The upper crustal evolution of a large silicic magma body: evidence from crystal-scale Rb–Sr isotopic heterogeneities in the Fish Canyon magmatic system. Colorado. *J. Petrol.* 48, 1875–1894. doi: 10.1093/petrology/egm043

Charlier, B. L. A., Wilson, C. J. N., Lowenstern, J. B., Blake, S., Van Calsteren, P. W., and Davidson, J. P. (2005). Magma generation at a large, hyperactive silicic volcano (Taupo, New Zealand) revealed by U–Th and U–Pb systematics in zircons. *J. Petrol.* 46, 3–32. doi: 10.1093/petrology/egh060

Cooper, K. M., and Kent, A. J. (2014). Rapid remobilization of magmatic crystals kept in cold storage. *Nature* 506, 480–483. doi: 10.1038/nature12991

Costa, F., and Morgan, D. (2011). "Time constraints from chemical equilibration in magmatic crystals," in *Timescales of Magmatic Processes: From Core to Atmosphere*, eds S. P. Turner, J. A. Van-Orman, and A. Dosset (Chichester: Wiley), 125–159. doi: 10.1002/9781444328509.ch7

Davidson, J. P., Morgan, D. J., Charlier, B. L. A., Harlou, R., and Hora, J. (2007). Tracing magmatic processes and timescales through mineral-scale isotopic data. *Annu. Rev. Earth Planet. Sci.* 35, 273–311.

Deering, C. D., and Bachmann, O. (2010). Trace element indicators of crystal accumulation in silicic igneous rocks. *Earth Planet. Sci. Lett.* 297, 324–331. doi: 10.1016/j.epsl.2010.06.034

Deering, C. D., Bachmann, O., Dufek, J., and Gravley, D. M. (2011). Rift-related transition from andesite to rhyolite volcanism in the Taupo Volcanic Zone (New Zealand) controlled by crystal–melt dynamics in mush zones with variable mineral assemblages. *J. Petrol.* 52, 2243–2263. doi: 10.1093/petrology/egr046

Ghiorso, M. S., and Gualda, G. A. R. (2015). An H2O-CO2 mixed fluid saturation model compatible with rhyolite-MELTS. *Contribut. Mineral. Petrol.* 169:53.

Gill, J., Reagan, M., Tepley, F., and Malavassi, E. (2006). Arenal volcano, costa rica: magma genesis and volcanological processes. *J. Volcanol. Geoth. Res.* 157, 1–8.

Gualda, G. A. R., Ghiorso, M. S., Lemons, R. V., and Carley, T. L. (2012). Rhyolite-MELTS: a modified calibration of MELTS optimized for silica-rich, fluid-bearing magmatic systems. *J. Petrol.* 53, 875–890. doi: 10.1093/petrology/egr080

Haase, K. M., Worthington, T. J., Stoffers, P., Garbe-Schönberg, D., and Wright, I. (2002). Mantle dynamics, element recycling, and magma genesis beneath the Kermadec Arc-Havre Trough. *Geochem. Geophy. Geosyst.* 3, 1–22. doi: 10.1029/2002gc000335

Hammer, J. E., Cashman, K. V., Hoblitt, R. P., and Newman, S. (1999). Degassing and microlite crystallization during pre-climactic events of the 1991 eruption of Mt. Pinatubo, Philippines. *Bull. Volcanol.* 60, 355–380. doi: 10.1007/s004450050238

Hildreth, W., and Wilson, C. J. (2007). Compositional zoning of the Bishop Tuff. *J. Petrol.* 48, 951–999. doi: 10.1093/petrology/egm007

Huber, C., Bachmann, O., and Dufek, J. (2012). Crystal-poor versus crystal-rich ignimbrites: a competition between stirring and reactivation. *Geology* 40, 115–118. doi: 10.1130/g32425.1

Ikegami, F., McPhie, J., Carey, R., Mundana, R., Soule, A., and Jutzeler, M. (2018). The eruption of submarine rhyolite lavas and domes in the deep ocean–Havre 2012. Kermadec Arc. *Front. Earth Sci.* 6:147. doi: 10.3389/feart.2018.00147

Jerram, D. A., and Martin, V. M. (2008). Understanding crystal populations and their significance through the magma plumbing system. *Geol. Soc. Lon. Special Publ.* 304, 133–148. doi: 10.1144/sp304.7

Jutzeler, M., Marsh, R., Carey, R. J., White, J. D., Talling, P. J., and Karlstrom, L. (2014). On the fate of pumice rafts formed during the 2012 Havre submarine eruption. *Nat. Communi.* 5, 1–10.

Kent, A. J., Darr, C., Koleszar, A. M., Salisbury, M. J., and Cooper, K. M. (2010). Preferential eruption of andesitic magmas through recharge filtering. *Nat. Geosci.* 3, 631–636. doi: 10.1038/ngeo924

Lepage, L. D. (2003). ILMAT: an Excel worksheet for ilmenite-magnetite geothermometry and geobarometry. *Comput. Geosci.* 29, 673–678. doi: 10.1016/S0098-3004(03)00042-6

Lindsley, D. H., and Andersen, D. J. (1983). A two-pyroxene thermometer. *J. Geophys. Res. Solid Earth* 88, A887–A906. doi: 10.1029/JB088iS02p0A887

Lindsley, D. H., and Spencer, K. J. (1982). Fe-Ti oxide geothermometry: reducing analyses of coexisting Ti-magnetite (Mt) and ilmenite (Ilm). *EOS Transactions, American Geophysical Union* 63:471.

Lubbers, J., Deering, C., and Bachmann, O. (2020). Genesis of rhyolitic melts in the upper crust: fractionation and remobilization of an intermediate cumulate at Lake City caldera, Colorado, USA. *J. Volcanol. Geoth. Res.* 392:106750. doi: 10.1016/j.jvolgeores.2019.106750

MacKenzie, W. S., Donaldson, C. H., and Guilford, C. (1982). *Atlas of Igneous Rocks and Their Textures*, Vol. 12. London: Longman.

Manga, M., Fauria, K. E., Lin, C., Mitchell, S. J., Jones, M., Conway, C. E., et al. (2018a). The pumice raft-forming (2012) Havre submarine eruption was effusive. *Earth Planet. Sci. Lett.* 489, 49–58. doi: 10.1016/j.epsl.2018.02.025

Manga, M., Mitchell, S. J., Degruyter, W., and Carey, R. J. (2018b). Transition of eruptive style: pumice raft to dome-forming eruption at the Havre submarine volcano, southwest Pacific Ocean. *Geology* 46, 1075–1078. doi: 10.1130/g45436.1

Masotta, M., Pontesilli, A., Mollo, S., Armienti, P., Ubide, T., Nazzari, M., et al. (2020). The role of undercooling during clinopyroxene growth in trachybasaltic magmas: Insights on magma decompression and cooling at Mt. Etna volcano. *Geochim. Cosmochim. Acta* 268, 258–276. doi: 10.1016/j.gca.2019.10.009

Melnik, O. (2000). Dynamics of two-phase conduit flow of high-viscosity gas-saturated magma: large variations of sustained explosive eruption intensity. *Bull. Volcanol.* 62, 153–170. doi: 10.1007/s004450000072

Mitchell, S. J., Houghton, B. F., Carey, R. J., Manga, M., Fauria, K. E., Jones, M. R., et al. (2019). Submarine giant pumice: a window into the shallow conduit dynamics of a recent silicic eruption. *Bull. Volcanol.* 81:42.

Mitchell, S. J., McIntosh, I. M., Houghton, B. F., Carey, R. J., and Shea, T. (2018). Dynamics of a powerful deep submarine eruption recorded in H2O contents and speciation in rhyolitic glass: the 2012 Havre eruption. *Earth Planet. Sci. Lett.* 494, 135–147. doi: 10.1016/j.epsl.2018.04.053

Mollo, S., and Hammer, J. E. (2017). Dynamic crystallization in magmas. *EMU Notes Mineral.* 16, 373–418.

Mollo, S., Putirka, K., Misiti, V., Soligo, M., and Scarlato, P. (2013). A new test for equilibrium based on clinopyroxene–melt pairs: clues on the solidification temperatures of Etnean alkaline melts at post-eruptive conditions. *Chem. Geol.* 352, 92–100. doi: 10.1016/j.chemgeo.2013.05.026

Müller, T., Dohmen, R., Becker, H. W., Ter Heege, J. H., and Chakraborty, S. (2013). Fe–Mg interdiffusion rates in clinopyroxene: experimental data and implications for Fe–Mg exchange geothermometers. *Contribut. Mineral. Petrol.* 166, 1563–1576. doi: 10.1007/s00410-013-0941-y

Murch, A. (2018). *Ash Generation in the 2012 Eruption of Havre Volcano, Kermadec Arc: The Largest Deep Subaqueous Eruption of the Last Century*. Doctoral dissertation, University of Otago, Dunedin.

Murch, A. P., White, J. D., and Carey, R. J. (2019). Characteristics and deposit stratigraphy of submarine-erupted silicic ash, Havre volcano, Kermadec Arc, New Zealand. *Front. Earth Sci.* 7:1. doi: 10.3389/feart.2019.00001

Neuendorf, K. K. (2005). *Glossary of Geology*. Berlin: Springer Science & Business Media.

Putirka, K. (1999). Clinopyroxene+ liquid equilibria to 100 kbar and 2450 K. *Contribut. Mineral. Petrol.* 135, 151–163. doi: 10.1007/s004100050503

Putirka, K., Johnson, M., Kinzler, R., Longhi, J., and Walker, D. (1996). Thermobarometry of mafic igneous rocks based on clinopyroxene-liquid equilibria, 0–30 kbar. *Contribut. Mineral. Petrol.* 123, 92–108. doi: 10.1007/s004100050145

Putirka, K. D. (2005). Igneous thermometers and barometers based on plagioclase+ liquid equilibria: tests of some existing models and new calibrations. *Am. Mineral.* 90, 336–346. doi: 10.2138/am.2005.1449

Putirka, K. D. (2008). Thermometers and barometers for volcanic systems. *Rev. Mineral. Geochem.* 69, 61–120. doi: 10.1515/9781501508486-004

Rhodes, J. M., Dungan, M. A., Blanchard, D. P., and Long, P. E. (1979). Magma mixing at mid-ocean ridges: evidence from basalts drilled near 22 N on the Mid-Atlantic Ridge. *Tectonophysics* 55, 35–61. doi: 10.1016/0040-1951(79)90334-2

Rotella, M. D., Wilson, C. J., Barker, S. J., Schipper, C. I., Wright, I. C., and Wysoczanski, R. J. (2015). Dynamics of deep submarine silicic explosive eruptions in the Kermadec arc, as reflected in pumice vesicularity textures. *J. Volcanol. Geoth. Res.* 301, 314–332. doi: 10.1016/j.jvolgeores.2015.05.021

Ryan, W. B., Carbotte, S. M., Coplan, J. O., O'Hara, S., Melkonian, A., Arko, R., et al. (2009). Global multi-resolution topography synthesis. *Geochem. Geophys. Geosyst.* 10. doi: 10.1029/2008GC002332

Smith, I. E., Stewart, R. B., Price, R. C., and Worthington, T. J. (2010). Are arc-type rocks the products of magma crystallisation? Observations from a simple oceanic arc volcano: raoul Island, Kermadec Arc, SW Pacific. *J. Volcanol. Geoth. Res.* 190, 219–234. doi: 10.1016/j.jvolgeores.2009.05.006

Sparks, R. S. J. (1978). The dynamics of bubble formation and growth in magmas: a review and analysis. *J. Volcanol. Geoth. Res.* 3, 1–37. doi: 10.1016/0377-0273(78)90002-1

Spencer, K. J., and Lindsley, D. H. (1981). A solution model for coexisting iron–titanium oxides. *Am. Mineral.* 66, 1189–1201.

Streck, M. J. (2008). Mineral textures and zoning as evidence for open system processes. *Rev. Mineral. Geochem.* 69, 595–622. doi: 10.1515/9781501508486-016

Tait, S., Jaupart, C., and Vergniolle, S. (1989). Pressure, gas content and eruption periodicity of a shallow crystallizing magma chamber. *Earth Planet. Sci. Lett.* 92, 107–123. doi: 10.1016/0012-821x(89)90025-3

Toramaru, A., Noguchi, S., Oyoshihara, S., and Tsune, A. (2008). MND (microlite number density) water exsolution rate meter. *J. Volcanol. Geoth. Res.* 175, 156–167. doi: 10.1016/j.jvolgeores.2008.03.035

Ubide, T., and Kamber, B. S. (2018). Volcanic crystals as time capsules of eruption history. *Nat. Commun.* 9, 1–12.

Ubide, T., Mollo, S., Zhao, J. X., Nazzari, M., and Scarlato, P. (2019). Sector-zoned clinopyroxene as a recorder of magma history, eruption triggers, and ascent rates. *Geochim. Cosmochim. Acta* 251, 265–283. doi: 10.1016/j.gca.2019.02.021

Velasquez, E., Bryan, S. E., Ekins, M., Cook, A. G., Hurrey, L., and Firn, J. (2018). Age and area predict patterns of species richness in pumice rafts contingent on oceanic climatic zone encountered. *Ecol. Evol.* 8, 5034–5046. doi: 10.1002/ece3.3980

Waters, L. E., and Lange, R. A. (2015). An updated calibration of the plagioclase-liquid hygrometer-thermometer applicable to basalts through rhyolites. *Am. Mineral.* 100, 2172–2184. doi: 10.2138/am-2015-5232

Wright, I. C., Worthington, T. J., and Gamble, J. A. (2006). New multibeam mapping and geochemistry of the 30–35 S sector, and overview, of southern Kermadec arc volcanism. *J. Volcanol. Geoth.. Res.* 149, 263–296. doi: 10.1016/j.jvolgeores.2005.03.021

Zellmer, G. F., Sakamoto, N., Iizuka, Y., Miyoshi, M., Tamura, Y., Hsieh, H. H., et al. (2014). Crystal uptake into aphyric arc melts: insights from two-pyroxene pseudo-decompression paths, plagioclase hygrometry, and measurement of hydrogen in olivines from mafic volcanics of SW Japan. *Geol. Soc. Lon. Special Publ.* 385, 161–184. doi: 10.1144/sp385.3

Conflict of Interest: The authors declare that the research was conducted in the absence of any commercial or financial relationships that could be construed as a potential conflict of interest.

frontiers in Earth Science

ORIGINAL RESEARCH
published: 28 August 2020
doi: 10.3389/feart.2020.00352

Insights Into Magma Chamber Processes From the Relationship Between Fabric and Grain Shape in Troctolitic Cumulates

Marian B. Holness[1], Charlotte Morris[1], Zoja Vukmanovic[1] and Dan J. Morgan[2]*

[1] Department of Earth Sciences, University of Cambridge, Cambridge, United Kingdom, [2] School of Earth and Environment, University of Leeds, Leeds, United Kingdom

The strength of foliations defined by shape preferred orientation of plagioclase in troctolitic cumulates from the Layered Series of the Skaergaard intrusion, and the Rum Eastern Layered Intrusion, increases as the grains become more tabular, due either to the greater propensity of highly non-equant grains to be re-arranged by magmatic currents or tectonic disruption of poorly consolidated mush, or by the effects of a pre-existing shape preferred orientation on final grain shape in fully solidified rocks. The stratigraphic evolution of grain shape, microstructures and fabrics in the lowest 320 m of the Skaergaard Layered Series records the progressive inflation of the chamber to its final size. During the earliest stages of solidification, the extent of *in situ* nucleation and growth on the chamber floor decreased upward through the stratigraphy, due to the development of a thermally insulating blanket of mush on the floor. An upward increase in foliation strength as the chamber inflated to its final size was a result of the increasing strength of convection of the bulk magma and an increasing contribution to the floor mush of crystals derived from the walls of the enlarging magma chamber. Plagioclase in the troctolites in the open-system magma chamber of the Rum Eastern Layered Intrusion is generally more equant than that in the Skaergaard intrusion, perhaps related to the slower crystal growth on the margins of the continuously replenished Rum chamber. Significant sub-solidus modification of original igneous microstructures is observed in Rum troctolites from parts of the stratigraphy recording frequent replenishment events.

Keywords: fabric, cumulate, grain shape, Skaergaard intrusion, Rum (NW Scotland)

OPEN ACCESS

Edited by:
David A. Neave,
The University of Manchester,
United Kingdom

Reviewed by:
Stearns Anthony Morse,
University of Massachusetts Amherst,
United States
Eric C. Ferre,
University of Louisiana at Lafayette,
United States

****Correspondence:***
Marian B. Holness
marian@esc.cam.ac.uk

Specialty section:
This article was submitted to Petrology, a section of the journal Frontiers in Earth Science

Received: *20 January 2020*
Accepted: *29 July 2020*
Published: *28 August 2020*

Citation:
Holness MB, Morris C, Vukmanovic Z and Morgan DJ (2020) Insights Into Magma Chamber Processes From the Relationship Between Fabric and Grain Shape in Troctolitic Cumulates. Front. Earth Sci. 8:352. doi: 10.3389/feart.2020.00352

INTRODUCTION

Fabrics formed by a preferred grain orientation in igneous rocks potentially preserve valuable information about processes occurring during solidification. Here we focus on fabrics defined by a shape-preferred orientation (SPO) of plagioclase in mafic cumulates. Such shape-preferred fabrics were initially thought to result from settling of non-equant grains from a stagnant magma (Hess, 1960; Jackson, 1961) but, following Grout (1918), it has since been strongly argued that fabrics are a consequence of deposition from, or re-working of crystals by, flowing magma or of

tectonic re-working of dis-aggregated mushes (e.g., Wager and Deer, 1939; Brothers, 1964; Wager and Brown, 1968; Higgins, 1991; Vukmanovic et al., 2018): they can therefore be classified as primary or secondary fabrics according to the scheme of Holness et al. (2017). However, there is a considerable literature arguing that all fabrics observed in mafic cumulates form during recrystallisation associated with gravitationally driven compaction of relatively melt-poor crystal mushes (e.g., Young and Donaldson, 1985; Boudreau and McBirney, 1997; Boorman et al., 2004): these are the tertiary fabrics of Holness et al. (2017). These two fabric-forming mechanisms can be differentiated using evidence for recrystallisation during deformation, by the spatial distribution of any compositional zoning, from the relationship between the SPO and any crystallographic-preferred orientation (CPO), and by a direct assessment of the extent of deformation by either dislocation creep or dissolution-reprecipitation (Holness et al., 2017).

In this contribution we concentrate on fabrics formed by crystal re-arrangement in melt-rich environments and demonstrate how detailed examination of the relationship between plagioclase grain shape and grain orientation, as viewed in thin section, provides information about the thermal history of a magma body. We show how microstructures can be used to demonstrate the progressive decrease in heat loss through the chamber floor during the early history of a deep, closed-system, magma chamber. We also assess the importance of sub-solidus microstructural modification by textural equilibration. By concentrating on samples with the same primocryst assemblage (troctolitic cumulates) we reduce the number of variables that might be controlling the microstructure.

PREVIOUS WORK

Grain Shape

Despite recent advances in 3D tomographic techniques (e.g., Denison et al., 1997; Jerram et al., 2010), the most accessible way to determine grain shape in rocks dominated by a single mineral remains microscopic examination of thin sections. However, thin sections provide a 2D slice through 3D material, introducing uncertainty in the true 3D shape or range of shapes present in a rock. Progress has been made by computing the range of shapes of grain intersections expected for an idealized shape (Higgins, 1994; Morgan and Jerram, 2006), calculated for the two endmembers of completely random orientations and an entirely foliated fabric (Higgins, 1994). The grains in real rocks, however, are likely to have a range of shapes (Duchêne et al., 2008), requiring a more sophisticated treatment involving the determination of the crystallographic orientation of each grain (Farr et al., 2018).

The shape of plagioclase grains is a sensitive function of cooling and crystallization rates (Lofgren, 1974; Sato, 1995). At cooling rates typical of dolerites and gabbros, Ca-rich plagioclase growth is interface-controlled: unimpeded growth results in tabular grains with the large faces parallel to (010). The tablets may be elongated along the *c*-axis but are more commonly elongate along the *a*-axis (see discussion in Smith and Brown, 1988). Holness (2014) demonstrated that in mafic rocks in which the plagioclase grains are randomly oriented, the arithmetic mean, or average, apparent aspect ratio as viewed in thin section, AR [a parameter also used by Meurer and Boudreau (1998) and Boorman et al. (2004)], is a function of cooling rate: the slower the cooling, the lower the value of AR. This method of quantifying grain shape is independent of the range of shapes present in the rock.

Fabrics in Igneous Rocks

The classification scheme of Holness et al. (2017) divides igneous fabrics into three categories: primary (formed during crystal nucleation and growth, or during accumulation of crystals mobilized by gravity or magmatic currents); secondary (forming post-accumulation, during slumping or mechanical re-arrangement of crystal-rich material in the transition between suspension flow and solid state); and tertiary (formed by recrystallization of low-porosity mush). In order to decode magmatic behavior, we must therefore exclude rocks with tertiary fabrics.

Tertiary fabrics, formed in low-porosity mush, require grains to change shape during plastic deformation. Plastic deformation by dislocation creep leaves a clearly identifiable microstructural signature. Tertiary fabrics may also form during plastic deformation by pressure solution mechanisms, potentially leaving clues in the spatial distribution of compositional zoning (Svahnberg and Piazolo, 2013). However, the commonly observed relationship between SPO and CPO in mafic igneous rocks solidified in tectonically inactive regions (i.e., the long, short and intermediate axes of the plagioclase grains are generally oriented in the same way relative to the crystal structure) can only occur if there is anisotropy of either dissolution, precipitation (e.g., Svahnberg and Piazolo, 2013) or grain boundary sliding (Miyazaki et al., 2013). Although little is known about anisotropy of plagioclase behavior in the super-solidus, in hydrous sub-solidus systems the anisotropy of dissolution is such that it would result in grain elongation perpendicular to the (010) faces (Heidelbach et al., 2000; Arvidson et al., 2004; Svahnberg and Piazolo, 2013). Plagioclase in mafic cumulates is almost invariably tabular parallel to (010), as is that grown as isolated grains in melt, suggesting that cumulate SPO fabrics are highly unlikely to be tertiary dissolution-reprecipitation fabrics.

Shape-preferred orientation fabrics formed during *in situ* nucleation and growth at the magma-mush interface (i.e., involving no grain mobilization) are confined to systems in which grain growth is controlled by steep gradients in either composition or temperature, leading to comb layering defined by the growth of elongate grains along the gradient. Examples include the harrisites of Rum (Donaldson, 1974), spinifex-textured olivine in komatiite flows (*ibid.*), and the perpendicular feldspar rock of Skaergaard (Wager and Deer, 1939). If, however, the temperature and/or compositional gradients driving crystallization are shallow, *in situ* crystal nucleation and growth does not result in fabric formation: instead, grains nucleate with random orientations and grow until they impinge against adjacent grains. The dominance of heterogeneous nucleation on pre-existing grains is likely to create a strongly cohesive mush

which cannot undergo the extensive disaggregation necessary for grain re-arrangement and secondary fabric formation.

Thus, microstructures formed during *in situ* nucleation and growth with no subsequent mobilization of grains, and in the absence of strong compositional or temperature gradients, are characterized by the absence of an SPO. They are furthermore characterized by the prevalence of irregular grain boundaries that are not generally parallel to expected growth faces, by the presence of small mineral inclusions on the irregular grain boundaries [termed "impingement lenses" by Holness et al. (2007a)], by a wide range of grain sizes indicative of an extended nucleation period and the absence of hydrodynamic sorting (Holness et al., 2019), by the absence of any correlation between the location of compositional zoning and crystallographic orientation, and by the presence of partially included grains of the same phase as the enclosing grain (Holness et al., 2019) (**Figure 1a**). Within a group of samples from the same body, the average apparent aspect ratio of plagioclase will have a negative correlation with the median value of the clinopyroxene-plagioclase-plagioclase dihedral angle, Θ_{cpp} (Holness, 2015). Any oikocrysts enclose chadacrysts of a wide range of sizes (McBirney and Hunter, 1995) (**Figure 1a**).

Conversely, primary and secondary fabrics are commonly created by grain alignment during mobilization, transport and accumulation of crystals grown elsewhere. The strength and nature of fabrics formed by grain re-arrangement in a current are a function not only of grain shape, but also depend on particle concentration and the extent to which particles interact during transport (Rust, 1972; Mainprice and Nicolas, 1989; Iso et al., 1996; Yamamoto and Matsuoka, 1996). In high Reynolds number systems typical of sedimentary rocks, elongate clasts can be either aligned parallel to the shear direction (Rust, 1972; Davies and Walker, 1974; Yamamoto and Matsuoka, 1996), or aligned parallel to the vorticity axis and perpendicular to the flow direction (Rust, 1972; Iso et al., 1996; Yamamoto and Matsuoka, 1996). A different behavior may pertain, however, in igneous systems in which grains are cohesive and the particle Reynolds number is much lower, but little is known about this.

Rocks with SPO fabrics formed by significant mass transport and crystal re-distribution are characterized by distinct microstructural features. They contain abundant euhedral grains bounded by growth faces, and grain boundaries are commonly planar and formed by the juxtaposition of euhedral grains (**Figure 1b**). Grain boundaries defined by the juxtaposition of planar growth faces are not commonly associated with compositional zoning, which is instead confined to crystal margins adjacent to interstitial phases (unless, of course, the grains were zoned before they were brought into contact during re-distribution). There is no correlation between overall plagioclase grain shape and Θ_{cpp} (Holness, 2015). There may be a rather narrow range of grain sizes, indicative of hydrodynamic sorting before accumulation.

It is important to note here that cumulates formed by re-distribution of crystals grown elsewhere may have no fabric if the accumulated grains were not given a preferred orientation either during primary deposition or by re-working, or if the accumulation was formed of poorly packed grain clusters (Jackson, 1961; Campbell et al., 1978). Such accumulations might acquire a (secondary) fabric if the framework collapses during compaction (pure shear) as a consequence of gravitational loading (Gray et al., 2003; Philpotts and Philpotts, 2005), during slumping (simple shear) of an unstable crystal pile (e.g., O'Driscoll et al., 2007), or by seismically induced fluidization (e.g., Davis et al., 2007; Bergantz et al., 2017). Although theoretical models suggest there is no fixed volume fraction representing lock-up if the crystal mush is subjected to shearing during,

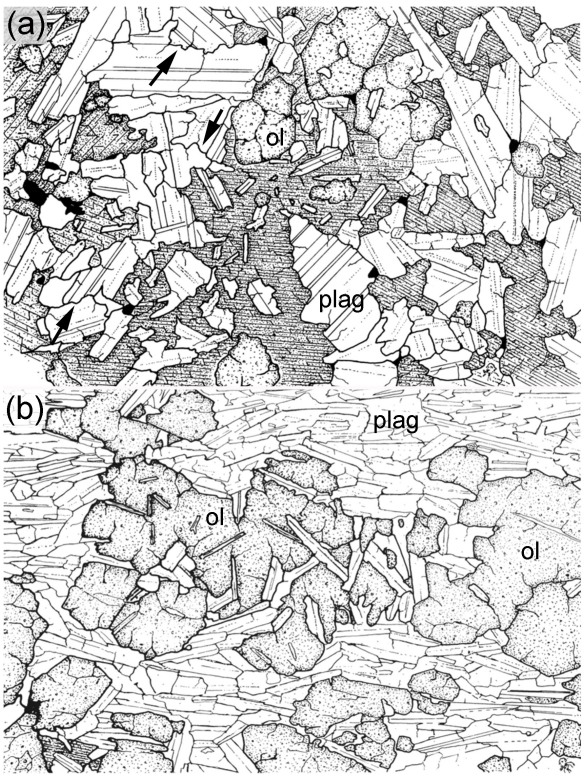

FIGURE 1 | Line drawings of troctolitic cumulates, reproduced with permission from Journal of Geology, from McBirney and Hunter (1995). The cleavage of pyroxene and the twinning of plagioclase are idealized, olivine is stippled and the opaque phase is Fe-Ti oxide. No scale bars were provided in the original drawings, but this absence does not detract from the value of the images, in which the (scale-invariant) grain shape, size distribution, and morphology of grain boundaries are the main points of interest. **(a)** Troctolitic cumulate from LZa of the Skaergaard, with poikilitic interstitial pyroxene, and a microstructure indicative of *in situ* nucleation and growth. Note the absence of a shape preferred orientation of the plagioclase, the wide range of grain sizes (pointing to a prolonged period of nucleation, with no hydrodynamic sorting), and the irregular grain boundaries commonly at high angles to expected growth faces typical of growth to impingement (examples are arrowed). In such rocks, minerals commonly have compositional zoning adjacent to interstitial grains (not shown). **(b)** A troctolite from the Eastern Layered Series of Rum, with the expected microstructure for a crystal mush formed predominantly by the accumulation of crystals grown elsewhere. The strong lamination is defined by a shape preferred orientation of euhedral, unzoned, plagioclase. Grain boundaries are generally planar, formed by juxtaposition of euhedral grains bounded by growth faces. The narrow range of grain sizes is consistent with hydrodynamic sorting. Plagioclase grains enclosed by olivine are generally more elongate and randomly oriented, preserving an early stage of mush history.

e.g., seismic activity, slumping due to slope instability, magma re-injection or bubble nucleation (e.g., Petford and Koenders, 2003; Petford, 2009; Bergantz et al., 2017; Petford et al., 2020), secondary fabrics can only form by such mechanisms if the mush does not contain sufficient strong grain boundaries to prevent disaggregation. Philpotts et al. (1996) find there is only a limited window at ∼33 vol.% solid for secondary fabric formation by gravitational loading of a basaltic mush in bodies of ∼100 m height: the mush clearly becomes too strong at lower porosities to permit disruption by gravitational loading alone.

If randomly oriented accumulations retain their high initial porosity [e.g., if the grain population is dominated by elongate or highly tabular grains which do not pack efficiently at random orientations (Williams and Philipse, 2003)], the final microstructure might be difficult to distinguish from one created entirely by *in situ* nucleation and growth as the only points of difference might be the absence of a wide range of grain sizes, the absence of partially included grains of the same phase, and the lack of intrusion-scale correlation between overall plagioclase grain shape and Θ_{cpp}.

Reported Examples of the Relationship Between Fabric and Grain Shape

Fabric strength and grain shape are commonly positively correlated in cumulates. A strong relationship between fabric and the shape of feldspars is found in the alkaline layered intrusions of the Gardar Province, South Greenland, in which foliation formed by a feldspar SPO is almost perfect in nepheline syenites containing wafer-thin alkali feldspar grains, but is weak or absent in syenitic cumulates containing almost equant feldspar (Upton et al., 1996). Since the packing of the feldspars in the latter is highly inefficient compared to that in the former, this relationship leads to an associated correspondence between modes of interstitial phases and the fabric strength.

Higgins (1991) found that the plagioclase in a sample of laminated anorthosite from the Sept Iles intrusion was less equant than that in a sample of closely associated massive anorthosite from the same intrusion. Followed by Higgins and Chandrasekharam (2007); Higgins (1991) attributed the difference to changes in the chemical potential gradient in the liquid surrounding the growing crystals, citing Kouchi et al. (1986) to argue that the less equant crystals in the laminated anorthosite were a consequence of them growing from relatively strongly flowing magma. However, Kouchi et al. (1986) demonstrated that, at any given undercooling, crystals in a stirred liquid grow with shapes indicative of a smaller undercooling of a static liquid, i.e., the transition from interface-controlled growth to diffusion-limited growth requires a greater undercooling in stirred, compared to static, liquid. Since plagioclase becomes less equant as the undercooling is increased (e.g., Shea and Hammer, 2013), the relatively less equant crystals in the laminated anorthosite are unlikely be a consequence of magma flow.

Meurer and Boudreau (1998) also report a positive correlation between foliation strength and plagioclase shape in plagioclase-rich cumulates (anorthosites, troctolites, and gabbros) from the Stillwater Complex, Montana. However, they argue that it was caused by recrystallisation during gravitationally driven compaction [i.e., a tertiary fabric according to the scheme of Holness et al. (2017)]. In agreement with Boudreau and McBirney (1997), Holness et al. (2017) pointed out that such a hypothesis requires a strong anisotropy of dissolution in plagioclase perpendicular to that seen in hydrous systems (Heidelbach et al., 2000; Arvidson et al., 2004; Svahnberg and Piazolo, 2013). Demonstration of fabric formation by recrystallization during compaction is possible using careful microstructural examination, since it would result in the truncation of both original growth faces and intra-crystalline compositional zonation in rocks dominated by the accumulation of crystals grown elsewhere: no evidence has yet been presented in support of this.

Modification of Grain Shape in the Sub-Solidus

Microstructures formed during crystal growth from a melt may be modified subsequently during either super- or sub-solidus textural equilibration driven by the minimization of interfacial energies. Such equilibration can result in the loss of primary grain shape and SPO, and the truncation of any concentric compositional zoning formed during solidification. A close approach to textural equilibrium results in smooth grain boundary curvature (and hence rounding of planar growth faces and the attainment of equant grain shapes), the establishment of equilibrium dihedral angles at the corners of any melt-filled pores and at all three- and four-grain junctions, and grain growth. Textural equilibration is fastest in the super-solidus (Ikeuye and Smith, 1949), but in the sub-solidus is fastest in monomineralic domains, where it involves only grain boundary migration, rather than diffusion along grain boundaries (Hunter, 1996).

The first stage of textural equilibration is the attainment of the equilibrium geometry in the immediate vicinity of all melt–solid–solid and three- and four-grain junctions. The relatively slow rate of sub-solidus equilibration at poly-phase junctions means that the geometry of clinopyroxene-plagioclase-plagioclase three-grain junctions is generally unmodified in gabbros from all layered intrusions investigated to date (e.g., Holness et al., 2012), whereas this is not expected to be the case for three-grain junctions involving only one phase (i.e., monomineralic junctions). Further progression of sub-solidus textural equilibration involves grain boundary migration as all interfaces attain constant mean curvature, creating a granular microstructure with equant grains. The final stage of equilibration involves grain growth by a combination of Ostwald ripening in poly-mineralic domains and normal grain growth in monomineralic domains. Textural equilibration therefore results in a reduction in average apparent aspect ratio, the loss of SPO fabrics, and an increase in grain size. Note, however, that the crystallographic orientation of individual grains remaining after grain growth (and therefore any CPO fabric) remains essentially unchanged, providing the opportunity to detect the presence of an original magmatic SPO.

For rocks which have undergone only the minimal amount of textural equilibration (i.e., they retain the original igneous

geometry of both two-phase three-grain junctions and grain boundaries) the only indication of sub-solidus textural equilibration will be found in the geometry of three-grain junctions in monomineralic domains. Although the median and average value of the dihedral angle at junctions between three grains of the same mineral are necessarily 120°, regardless of the extent to which equilibrium has been approached, any textural equilibration will be recorded by a change in the standard deviation of the population of dihedral angles (Kretz, 1994).

For monomineralic systems in which there is no anisotropy of interfacial energies, the standard deviation of a population of dihedral angles is zero. However, all minerals of geological interest are anisotropic to some extent, so a fully texturally equilibrated microstructure has a finite value of standard deviation of dihedral angle populations (Kretz, 1966). For example, the standard deviation of a population of plagioclase–plagioclase–plagioclase junctions in a high-grade metamorphic rock presumed to be in, or very close to, textural equilibrium is in the range 9.1–13° (Vernon, 1968, 1970). Little is known about the likely range of dihedral angles in monomineralic silicates that have undergone no sub-solidus equilibration. Elliott et al. (1997) created artificial 3D microstructures by permitting randomly positioned grains to grow to impingement and found that the population of dihedral angles measured in 2D slices through the fully solidified 3D aggregate was similar to that expected for one with a standard deviation of 20° of the true 3D dihedral angles. However, these artificial microstructures did not include the effects of growth anisotropy: plagioclase grows as facetted grains, commonly leading to the high-angle impingement of grain boundaries against planar (010) plagioclase faces in gabbros with no fabric (e.g., Kretz, 1966; Vernon, 1968). We might thus expect a standard deviation >20° for populations of plagioclase–plagioclase–plagioclase dihedral angles in unequilibrated igneous rocks containing randomly oriented plagioclase.

A Regime Diagram

Any correlations between grain shape and the strength of primary igneous SPO fabrics result from a complex interplay of two-way interactions between shape and fabric in a liquid-rich environment. The microstructures resulting from super-solidus processes may then be modified in the sub-solidus during textural equilibration. These interactions can be illustrated using a simple regime diagram (**Figure 2**) relating the average apparent aspect ratio, AR, to the alignment factor, AF, for which a value of 100 denotes perfect alignment to form a foliation and one of 0 denotes perfectly random orientation.

Particle shape affects fabric strength because highly non-equant particles will be more strongly aligned by magmatic currents than more equant particles. Conversely, the extent to which non-equant grains are aligned in a solidifying mush can affect grain shape as solidification progresses, since growth cannot occur on the faces of crystals in contact with their neighbors. This means that crystals in an accumulation with an original SPO fabric [e.g., an accumulation of tabular plagioclase crystals predominantly touching on their (010) faces] will become increasingly non-equant with continued solidification since they can only grow on faces adjacent to melt (Brown, 1956). In this case, the early development of an SPO controls the final shape of the constituent grains, resulting in a decrease in the slope of a positive correlation between AF and AR created by current action (**Figure 2A**). [As an aside, this effect of fabric on final grain shape means that AR in a foliated dolerite or gabbro cannot be mapped straightforwardly onto cooling rates in the way it can be for those with randomly oriented plagioclase (Holness, 2014)].

As a consequence of this two-way interaction, for the simplest case in which particles can assume any shape, we would expect a positive correlation between AF and AR, with a zero value of AF (perfect random orientation) for equant grains (AR = 1), and a slope dependent on the balance between the effects of grain rotation by currents and post-accumulation overgrowth (**Figure 2B**). For the particular case of minerals of geological

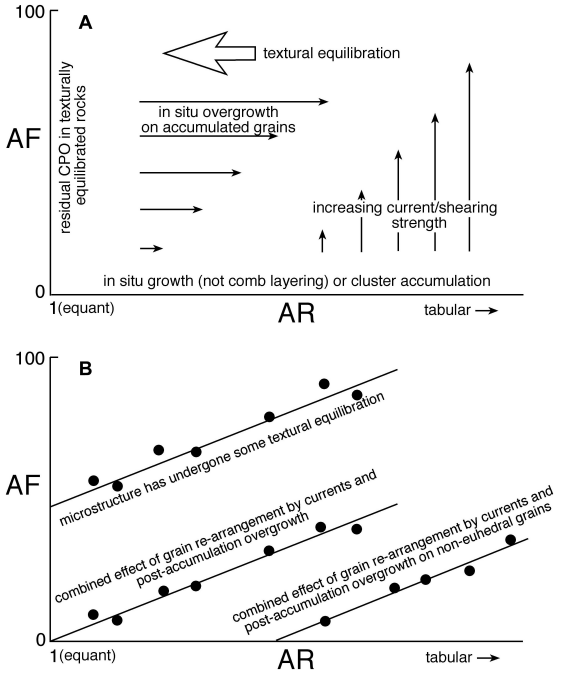

FIGURE 2 | Schematic diagrams of the relationship between fabric strength defined by a shape preferred orientation (SPO, quantified by the alignment factor, AF, which has a value of 0 for randomly aligned grains and a maximum value of 100 for perfectly aligned grains) and the average apparent aspect ratio (AR). **(A)** Rocks with no preferred shape orientation (AF = 0) form predominantly during *in situ* nucleation and growth, or by the accumulation of grain clusters. Positive correlations between alignment factor (AF) and average apparent aspect ratio (AR) can be achieved in two ways: firstly, an increasing fabric strength in a melt-bearing mush results in an increased AR during subsequent solidification, since no growth can occur on faces in contact with other grains (Brown, 1956); secondly, for any given strength of current, particles with higher AR will be re-arranged and aligned to form a stronger preferred alignment. Rocks with entirely equant grains (AR = 1), but with a residual SPO recorded by a crystallographic preferred orientation (i.e., with AF > 0 if defined using CPO), must have undergone extensive textural equilibration. **(B)** Positive correlations between alignment factor (AF) and average apparent aspect ratio (AR) pass through the origin for systems in which particles are free to take any primary shape. Those passing through the *y*-axis must have undergone some textural equilibration, whereas those cutting the *x*-axis are realistic for natural systems in which any mineral grain has a limited range of shapes.

TABLE 1 | Details of troctolitic samples from the Cambridge 1966 drill core through the lower part of the Skaergaard Layered Series.

Sample	Height (m)	Zone	Mineral modes (vol.%)					AR average	AR min	AR max	Plag average length (mm)	AF	Number of grains	Bulk P_2O_5 (wt.%)
			Plag	Ol	Fe-Ti Oxides	Augite	Ca-poor pyroxene							
115′ 9″	163.8	LZa	45.4	36.3	1.6	10.7	6.0	3.10	3.03	3.19	1.408	49.33	213	
211′ 11″	134.4	LZa	74.9	11.0	0.4	10.1	3.6	3.21	3.13	3.29	1.292	53.53	289	0.13
317′ 6.5″	*102.2*	*LZa*	*67.3*	*14.3*	*0.7*	*10.0*	*6.7*	*3.30*	*3.23*	*3.37*	*1.326*	*55.79*	*311*	
351′ 7″	91.8	LZa	67.6	12.5	0.7	14.6	4.6	3.10	3.03	3.17	1.089	47.27	265	0.11
371′ 7″	*85.7*	*LZa*	*71.8*	*18.9*	*0.3*	*6.2*	*2.8*	*3.03*	*2.95*	*3.10*	*0.942*	*55.63*	*451*	*0.12*
438′ 4″	65.4	LZa	65.1	16.3	0.5	14	4.1	3.34	3.25	3.41	1.087	59.64	332	0.11
481′ 1″	52.4	LZa	59.4	18.9	0.8	14.2	6.7	3.06	2.91	3.25	1.302	51.66	251	0.11
511′ 10″	43.2	LZa	65.0	20.5	0.7	9.9	3.9	3.18	3.09	3.26	1.133	56.03	332	0.13
522′ 1″	39.9	LZa	66.9	20.3	0.4	9.6	2.8	3.37	3.30	3.44	1.368	70.88	252	0.08
571′ 4″	24.8	LZa	88.3	5.5	1.2	2.0	3.0	2.81	2.74	2.85	0.933	39.93	323	0.14
621′ 2″	9.7	LZa	74.1	7.5	0.2	15.6	2.7	2.65	2.49	2.78	0.889	39.85	384	0.08
651′ 2″	*0.5*	*LZa*	*74.8*	*12.9*	*0.9*	*7.7*	*3.7*	*2.84*	*2.77*	*2.91*	*1.076*	*40.31*	*303*	*0.08*
671′1 ″	−5.5	HZ	74.1	19.0	0.9	4.9	1.1	2.47	2.41	2.53	0.616	35.29	338	0.04
681′ 1″	−8.6	HZ	57.6	36.6	1.3	2.8	1.7	2.48	2.43	2.54	0.706	55.31	377	0.04
730′ 9″	−23.7	HZ	79.0	10.6	0.7	6.5	3.2	3.09	3.02	3.17	0.987	47.89	381	0.18
760′7 ″	−31.56	HZ	76.3	7.0	2.3	12.4	2.0	2.83	2.69	2.96	0.862	34.51	296	0.09
800′5 ″	−45.0	HZ	76.3	11.7	0.0	9.0	3.0	2.80	2.65	2.94	0.977	30.60	271	0.09
842′ 3″	−57.7	HZ	71.8	14.1	3.7	7.1	3.3	2.44	2.38	2.50	1.047	28.94	280	0.13
867′ 3″	−65.3	HZ	29.8	54.7	2.0	12.9	0.6	2.29	2.23	2.35	0.692	29.96	301	0.13
887′10 ″	−71.6	HZ	77.0	12.7	2.7	4.0	3.6	2.82	2.67	2.90	1.017	31.89	285	0.13
930′2 ″	−84.5	HZ	80.6	8.0	1.7	6.7	3.1	2.53	2.42	2.66	1.191	29.60	220	0.16
933′	−85.4	HZ	77.9	8.6	0.3	3.8	9.4	2.63	2.50	2.74	1.129	17.35	241	0.13
940′6 ″	−87.7	HZ	67.7	21.8	0.4	7.5	2.7	2.56	2.44	2.66	0.943	25.85	227	0.05
979′ 11″	*−99.7*	*HZ*	*62.8*	*25.4*	*0.5*	*7.7*	*3.6*	*2.95*	*2.89*	*3.02*	*0.919*	*33.92*	*320*	*0.10*
987′ 11″	*−102.1*	*HZ*	*70.4*	*12.2*	*0.4*	*15.1*	*1.9*	*2.79*	*2.73*	*2.85*	*1.020*	*35.82*	*338*	
1060′ 1″	−124.1	HZ	72.6	15.3	0.9	5.8	5.4	2.81	2.72	2.86	0.921	21.35	346	0.17
1091′6″	−133.7	HZ	70.9	3.8	0.3	23.8	1.2	2.57	2.52	2.62	1.107	15.03	245	0.06
1122′4 ″	−143.1	HZ	71.0	5.7	2.1	17.6	3.6	2.25	2.14	2.35	0.972	8.10	177	0.09
1145′2 ″	−150.1	HZ	77.0	2.7	3.7	5.6	11.0	2.31	2.20	2.41	0.964	12.82	171	0.10

The sample number gives the depth in feet and inches in the core. HZ, Hidden Zone; LZa, Lower Zone a. Bulk rock P_2O_5 data are from Holness et al. (2015). Mineral modes are either from Holness et al. (2015) or determined as part of the present study. Those samples in italics are those for which AR was previously reported by Holness (2015).

interest, it is rare for grain shape in a suite of related rocks to range from perfectly equant to highly non-equant, so any positive correlation is likely to cut the *x*-axis in **Figure 2B** at some value higher than 1. For the case of plagioclase, the lowest value of AR is likely to be found in those members of a sample suite in which growth was predominantly *in situ* and at random orientations, or in the slowest-cooled members of a sample suite. If the positive correlation between AF and AR cuts the *y*-axis [i.e., a finite value of AF (defined in this case by a CPO, rather than an SPO) is seen when AR = 1], the original microstructure must have been modified by sub-solidus textural equilibration (**Figure 2B**).

CHOICE OF SAMPLES

The Skaergaard Intrusion, East Greenland

The Skaergaard Intrusion formed from the injection of a large (8 km × 11 km × 4 km, Nielsen, 2004) body of relatively evolved tholeiitic basaltic magma into a fault-bounded (Irvine et al., 1998) space forming on the extending margin of East Greenland during the opening of the North Atlantic Ocean, at the unconformity between underlying Precambrian gneisses and an overlying sequence of Eocene plateau lavas (Wager and Deer, 1939). Once the chamber had been filled by a series of magma pulses (Holness et al., 2007b, 2015) it remained closed both to further magma replenishment and to eruption, crystallizing inward from the margins to form one of the world's best examples of progressive fractionation of a basaltic magma.

The least evolved cumulates on the floor of the chamber are troctolitic, forming the Hidden Zone (HZ) and Lower Zone a (LZa) of the Layered Series (Wager and Deer, 1939): they contain primocrysts of olivine and plagioclase with interstitial clinopyroxene, Ca-poor pyroxene (inverted pigeonite), Fe-Ti oxides, apatite and minor quartz, K-feldspar and biotite. The top of LZa, and base of Lower Zone b (or LZb), is marked by clinopyroxene joining the liquidus assemblage. Holness (2015) demonstrated that the average apparent aspect ratio of plagioclase

changes systematically through the Layered Series, with a weakly defined increase in AR through the lowest 950 m, and a well-defined decrease through the overlying stratigraphy to a minimum at ∼2,400 m stratigraphic height.

We chose 29 troctolites from the Cambridge 1966 drill core which covers the lowest 350 m of the floor cumulates, including 150 m of HZ (described in Holness et al., 2015), avoiding samples with strongly poikilitic interstitial pyroxene. In the drill core, the base of LZb is ∼180 m above the top of HZ. Mineral modes are reported in **Table 1**. Bulk rock geochemical analyses of 26 of our samples are reported by Holness et al. (2015). The stratigraphic positions of the samples are shown in **Figure 3** (the zero point of the stratigraphy in this figure is the base of the current exposure, i.e., the division between HZ and LZa). Thin sections from the drill core are oriented parallel to the length of the core (which is presumed to have intersected the paleohorizontal at a steep angle). The plagioclase grain shape has already been reported for a sub-set of our Skaergaard sample suite by Holness (2015): we re-measured grain shape in these samples for consistency.

It has been argued that the lower half of the Cambridge drill core records the progressive inflation of the Skaergaard chamber (Holness et al., 2015). The lowermost few tens of meters sampled by the drill core are thought to have crystallized from a small sill-like injection of basaltic magma that formed at the contact between the Precambrian gneiss and the overlying sequence of lavas. Well before it crystallized fully, this initial intrusion was inflated by the arrival of successive magma batches to become the Skaergaard magma chamber.

The increase in Mg number at −120 m (**Figure 3**) is not associated with modal banding or grain size reduction but is accompanied by localized polymodal olivine populations (Holness et al., 2015) together with an increase in Θ_{cpp} indicative of decreased super-solidus cooling rates. These observations are consistent with the early inflation of the growing magma chamber by the arrival of at least three relatively small batches of hot, buoyant, olivine-phyric magma that were not chilled sufficiently to result in a high nucleation rate (Holness et al., 2015). We examine three samples from this part of the core.

The decrease in Mg number at −89 m (**Figure 3**), associated with no change in either Θ_{cpp} or grain size, has been argued to indicate the arrival of a small batch of cool, evolved, relatively dense, liquid which ponded on the chamber floor before progressively mixing with the overlying, more primitive bulk magma (Holness et al., 2015). We examined three samples from this part of the core.

The olivine-rich layer at −65 m (**Figure 3**) marks the arrival of a small batch of primitive magma which was quickly and thoroughly mixed with the resident magma (Holness et al., 2015): we examined two samples from this part of the core.

The region of the core between −24 and 40 m records major changes of microstructure, modal mineralogy and trace element composition, indicative of the arrival of a substantial volume of hot and primitive magma and the inflation of the chamber to its final size (Holness et al., 2015). The interval between −2.5 m and about 50 m is marked by a zone of fairly well-defined modal layering that might mark the onset of vigorous convection and mixing in the newly enlarged chamber. The olivine-rich layer at -8.8m is fine-grained (*ibid.*) and may have formed by accumulation from an olivine-phyric magma that rapidly mixed with the resident magma, with little opportunity to develop either a geochemically distinct ponded layer on the chamber floor or a distinct layer of entrained grains of forsterite-rich olivine. We examined two samples from this region of the stratigraphy.

The plagioclase in the Skaergaard samples is highly non-equant (**Figures 4A,B**). Plagioclase-plagioclase grain boundaries in samples with a weak fabric are commonly irregular (**Figure 4A**), whereas those in samples with a stronger fabric are generally smooth, commonly planar, and predominantly parallel to (010) growth faces of one or both grains (**Figure 4B**). Compositional zoning is common: many grains have normally zoned margins whereas some also have highly irregular internal zoning (Maaløe, 1976).

The Rum Eastern Layered Intrusion, Scotland

The Rum Central Complex is part of the British Palaeogene Igneous Province, an area of intense igneous activity formed during continental attenuation prior to opening of the North Atlantic Ocean, and has been dated at 60.53 ± 0.08 Ma (Hamilton et al., 1998). The pre-Palaeogene rocks of Rum mainly comprise a thick succession of Proterozoic (Torridonian) sandstones with the gneissic Archean basement locally exposed within the uplifted parts of the Complex (Emeleus et al., 1996; Emeleus, 1997). Igneous activity on Rum comprised an early, relatively minor, salic stage and a later, wholly mafic to ultramafic stage. The latter forms the Rum Central Complex, which is divisible into the mafic/ultramafic Western, Central and Eastern Layered Intrusions. The contemporaneous Long Loch Fault, running through the center of the island, has been suggested as the prime magma conduit feeding the growing complex (Emeleus et al., 1996).

The Rum Eastern Layered Intrusion was built from numerous replenishments of a shallow sub-volcanic sill-like chamber by variously basaltic (Renner and Palacz, 1987) and picritic (McClurg, 1982; Greenwood et al., 1990; Upton et al., 2002) magma (Emeleus et al., 1996; Holness and Winpenny, 2009). The Eastern Layered Intrusion comprises 16 macro-scale cyclic units comprising a lower peridotite with upper allivalite horizons (a local term describing troctolites or gabbros). This relatively coarse sub-division disguises a great complexity in the modal layering, with the majority of the allivalites containing many subsidiary peridotite horizons (Emeleus et al., 1996; Holness and Winpenny, 2009), ranging in thickness from several meters down to ∼1 cm.

The Unit 10 allivalite is notable for evidence of downward infiltration of picritic magma at the top (Tait, 1984, 1985) and upward infiltration of relatively evolved magma at the base (Holness, 2007; Holness et al., 2012). The bulk geochemistry of a subset of the Unit 10 samples is reported by Tait (1984, 1985). Much of the Unit 10 allivalite is gabbroic, with troctolites confined to the lowest few meters: we chose five samples from the lowest 2 m of the traverse collected by Tait (1984) [denoted Traverse D by Holness et al. (2012)] of which the uppermost is a gabbro. These samples record evidence of

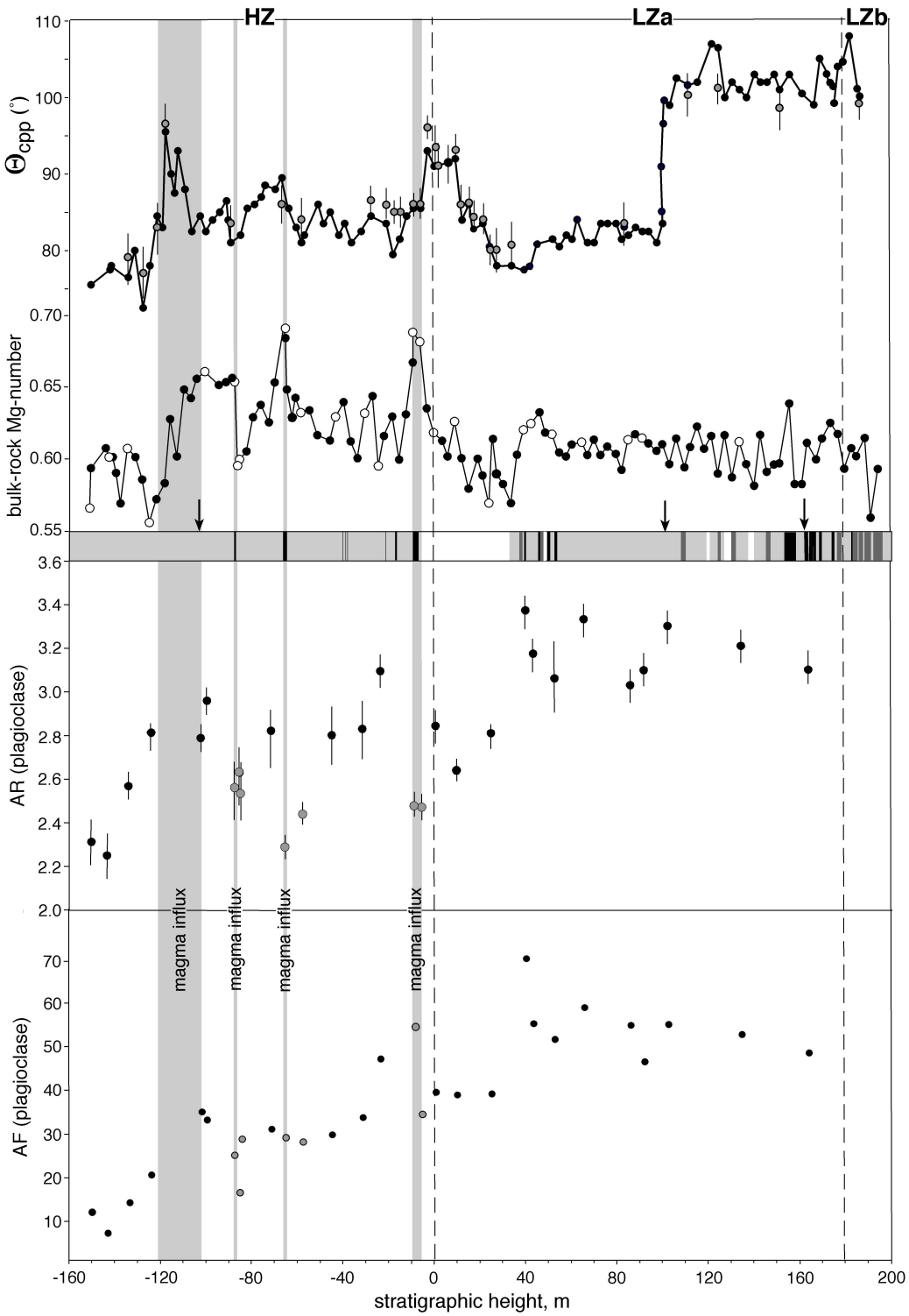

FIGURE 3 | Microstructural and compositional variation through the 1966 Cambridge drill core, sampling the lowest 350 m of the Skaergaard Layered Series. The schematic log shows olivine-rich bands as black, average compositions as gray and leucocratic bands as white [see Holness et al. (2015) for further details]. The stratigraphic variation of clinopyroxene-plagioclase–plagioclase dihedral angle, Θ_{cpp}, and the bulk rock Mg-number are shown [from Holness et al. (2007c, 2015)]. The dotted lines show the divisions into HZ, LZa, and LZb. The vertical gray bands show the regions of stratigraphy identified by Holness et al. (2015) as recording the input of magma into the inflating chamber. Samples described in the present study are shown as open circles in the Mg-number plot if compositional data is available, with the position of the three samples for which no compositional data is available shown as arrows on the schematic log. The variation of plagioclase AF and AR are shown. Those samples denoted by a gray circle are those closely associated with the points marking magma influx and chamber inflation.

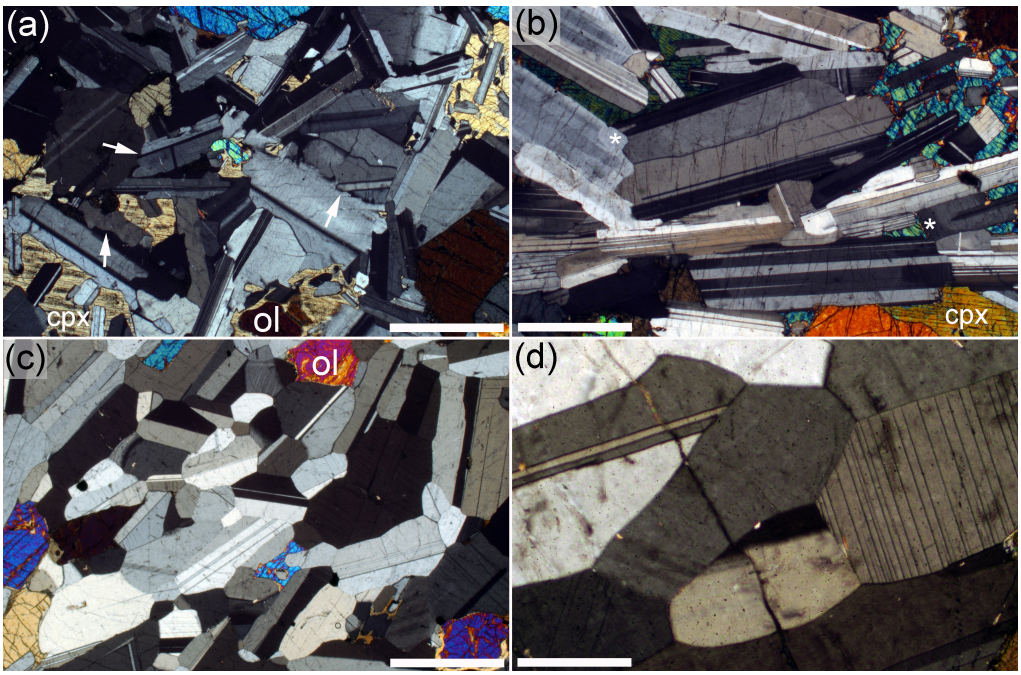

FIGURE 4 | photomicrographs of Skaergaard and Rum troctolites, all photographed under crossed polars. **(a)** Sample from lower part of HZ, containing primocrysts of olivine and plagioclase with interstitial clinopyroxene. There is no preferred alignment of elongate plagioclase. Note the irregularity of the grain boundaries (examples are arrowed) that are not parallel to expected growth faces in the two grains on either side. Scale bar is 1mm long. **(b)** LZa sample from the upper part of the 1966 drill core, in which plagioclase primocrysts show a well-developed shape preferred orientation. Grains are commonly bounded by expected growth faces parallel to (010). Compositional zoning is confined to the ends of the elongate laths (examples are shown by asterisks), demonstrating that grain boundaries parallel to the large (010) faces were formed as equant grains were brought together mechanically. Scale bar is 1 mm long. **(c)** Troctolite from Unit 12 of the Rum Eastern Layered Series. Note the rounded grain boundaries in the plagioclase-rich regions, with significant modification of the original euhedral shape of these primocrysts. Scale bar is 1mm long. **(d)** Plagioclase-rich region of Rum Unit 12 troctolite demonstrating the almost granular microstructure indicative of extensive sub-solidus textural equilibration. Scale bar is 200 μm long.

significant, post-accumulation, upward infiltration of evolved magma derived from the underlying peridotite.

The Unit 12 allivalite is predominantly troctolitic with several subsidiary peridotite horizons interpreted as the record of replenishment events (Holness and Winpenny, 2009). No bulk rock geochemical data are available for the Unit 12 samples, although mineral compositions are reported by Holness and Winpenny (2009). We chose four samples of Unit 12 troctolitic cumulates, located sufficiently far from the subsidiary peridotites that they are unlikely to have been affected by changes in cooling rate due to the presence of nearby hot picritic magma (Holness and Winpenny, 2009). Sections were cut perpendicular to any fabrics.

The Rum troctolites are dominated by olivine and plagioclase, with several of our samples close to perfectly adcumulate (**Table 2**). Minor quantities of interstitial clinopyroxene are present, commonly forming thin rims separating olivine and plagioclase primocrysts, although clinopyroxene forms oikocrysts in several of the Unit 10 troctolites. The median clinopyroxene-plagioclase-plagioclase dihedral angle, Θ_{cpp}, in the Rum troctolites unaffected by late-stage infiltration is 80–85° (Holness, 2007; Holness and Winpenny, 2009). Cr-spinel may be present in small quantities (<2 vol.%). Evolved phases such as apatite, low-Ca pyroxene and Fe-Ti oxides are absent. The plagioclase in the Rum troctolites is slightly elongate (as viewed in thin section) and is characterized by smooth plagioclase-plagioclase grain boundaries (**Figure 4C**), with a granular microstructure (i.e., almost equant grains) developed in relatively finer-grained plagioclase-only regions (**Figure 4D**). In comparison with the Skaergaard troctolites, very few grain boundaries are planar and parallel to the (010) faces of the adjacent grains. There is no evidence of plastic deformation by dislocation creep. Weak intra-crystalline plagioclase compositional zoning is locally present.

MATERIALS AND METHODS

Plagioclase apparent aspect ratio in natural samples was measured using either photomicrographs or a high-quality scan of entire thin sections under crossed polars. Thin sections were oriented perpendicular to any foliation where visible, and parallel to the drill core (and hence, to the best of our knowledge, perpendicular to the paleo-horizontal). The long and short axis of each grain intersection were drawn on by hand and the aspect ratio was calculated using the Feret diameter tool of ImageJ. Previous work on the shapes and orientations of plagioclase enclosed in pyroxene oikocrysts has demonstrated that there are

TABLE 2 | Details of samples from the Rum Eastern Layered Intrusion.

Sample	Height (m)	Mineral modes (vol.%)				AR	AR Min	AR Max	Plag length (mm)	AF	*n*
		Plag	Ol	Augite	Cr-spinel						
Unit 10											
146196	0.1	69.2	27.8	1.5	1.5	2.23	2.18	2.27	0.668	20.77	351
146197	0.4	60.1	21.9	18.0	0.0	2.32	2.28	2.36	0.732	35.72	403
146198	0.6	68.1	14.5	16.9	0.5	2.62	2.58	2.69	0.719	56.79	280
146199	0.7	57.6	34.9	7.5	0.0	2.44	2.39	2.49	0.822	44.16	267
146200	1.9	56.5	11.4	32.1	0.0	2.37	2.32	2.41	0.914	32.04	275
Unit 12											
R12-J7	6.40	72.5	23.5	1.5	2.5	2.10	2.06	2.14	0.873	47.00	322
R12-J13	11.40	74.0	18.1	5.5	2.4	2.27	2.23	2.31	1.015	56.53	293
R12-J16	14.27	75.8	19.6	1.3	3.3	2.36	2.31	2.40	1.084	59.92	259
R12-J30	7.95	72.9	25.2	1.5	0.4	2.18	2.15	2.21	0.867	56.81	289

*Abbreviations as for **Table 1**.*

commonly systematic differences between enclosed plagioclase and that outside oikocrysts, with the enclosed grains thought to preserve the early structure of the mush (**Figure 1B**; Mathison, 1987; Higgins, 1991, 1998). Some of our samples contain a few grains of poikilitic pyroxene, and for consistency, we avoided analyzing plagioclase grains enclosed in oikocrysts: every other visible plagioclase grain was analyzed in each image or scan. Between 171 and 451 grains were measured for each sample. The 2σ confidence interval on the average aspect ratio was constrained using bootstrap sampling: a method suitable for populations of measurements for which the shape of the underlying distribution is unknown. Results are reported in **Tables 1**, 2.

Our values of AR for the sub-set of Skaergaard samples measured by Holness (2015) are consistently lower than previously reported: we suggest this is because we used higher resolution images for the present study, permitting the inclusion of the complete grain population in each thin section. The alignment factor, AF, was calculated according to the method of Meurer and Boudreau (1998), by which a value of 100 denotes perfect alignment to form a foliation and one of 0 denotes perfectly random orientation.

Plagioclase–plagioclase–plagioclase dihedral angles were measured using a 4-axis Leitz universal stage mounted on a James Swift monocular microscope fitted with a 32× long working distance objective. 33 randomly chosen individual three-grain junctions were measured for each sample, resulting in a population of 99 dihedral angles (though note that only 2/3 of this population represents independent values). We report the standard deviation of this population.

The apparent aspect ratio of 3D cuboid grains cut by randomly oriented planes was calculated according to the method of Morgan and Jerram (2006), using two endmembers. The first assumes a completely random orientation of crystals of a given shape and size, whereas the other assumes a perfect foliation. For comparison with the natural samples, we calculated the shape and cross-sectional area of 2,000 grain intersections for the two endmembers for the seven different grain shapes 1:1.5:2, 1:2:3, 1:2:4, 1:2:6, 1:3:7, 1:4:7, and 1:5:8, when viewed perpendicular to foliation. The aspect ratio of each grain intersection was calculated using the fit ellipse function of ImageJ. Note that in creating these synthetic populations, no allowance was made for space-filling constraints which prevent crystals attaining these idealized cuboids when forming a poly-crystalline aggregate.

RESULTS

Skaergaard and Rum Grain Shapes and Fabrics

There is a well-defined increase in plagioclase alignment factor (AF) with increasing stratigraphic height in the lower part of the Skaergaard stratigraphy, with a region of approximately constant AF between −100 and 0 m stratigraphic height, followed by an increase to higher, but rather scattered, values at 40 m stratigraphic height (**Figure 3**). AR also broadly increases with stratigraphic height (**Figure 3**), but with a sharp increase in the lower part of the stratigraphy, a region of broadly constant AR between −100 and 20 m height, and then a region of higher but variable AR in the upper part of the core. Notably, locally low values of AR are closely associated with three of the episodes of magma influx identified by Holness et al. (2015) (at −89, −65, and −8 m). We identified seven samples with anomalously low values of AR (shown as gray symbols in **Figure 3**). Three of these seven samples contain finer-grained plagioclase than the rest of the suite (**Table 1**).

The microstructural data from the main group of samples form a positive correlation on a plot of AF against AR (the Skaergaard main trend), while the seven samples with lower than expected AR form an almost AR-invariant group, albeit with a lot of scatter (the Skaergaard second trend) (**Figure 5**). Extrapolation of the best-fit line through the data points forming the main trend gives an AR of 2.10 for fully random samples (AF = 0) and 4.05 for perfectly foliated samples (AF = 100).

The Rum samples from the two allivalite units form two clearly distinct groups on a plot of AR against AF (**Figure 5**), each with a positive slope, but offset to lower AR than the Skaergaard main trend. The single gabbroic sample from Unit 10 is indistinguishable from the Unit 10 troctolites on this plot.

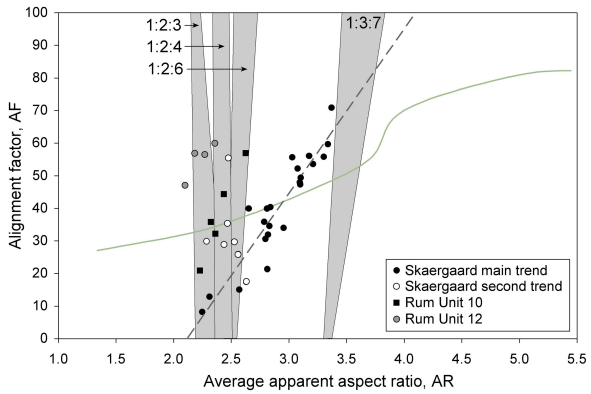

FIGURE 5 | The variation of alignment factor (AF) as a function of average apparent aspect ratio (AR) for the Skaergaard and Rum troctolites. The continuous green line shows the trend reported by Meurer and Boudreau (1998) for Stillwater cumulates. The shaded boxes show the range of correlations expected for rocks containing grains of a constant (cuboid) shape (see labels). The left-side of each box is that calculated without the 5% smallest grain intersections, and the right-side of the box is that calculated without the 20% smallest grain intersections. In all cases, the calculated trend for the synthetic systems with constant grain shape is steeper than that observed for the natural samples, suggesting that the trend in the natural samples is caused at least in part by less equant grains in samples with stronger fabrics. The dashed line shows the best fit through the main group of Skaergaard samples.

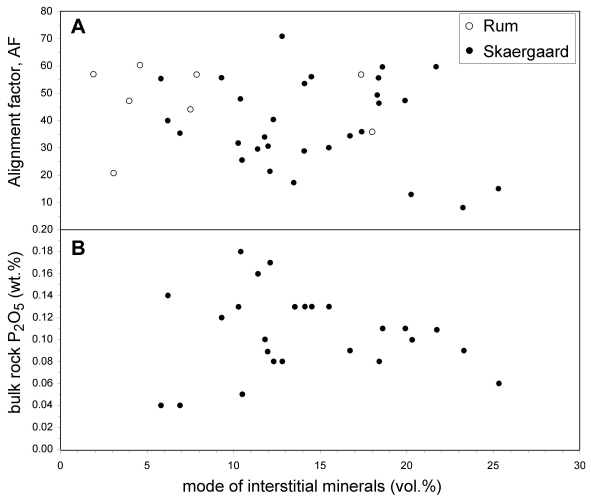

FIGURE 6 | (A) The variation of alignment factor (AF) as a function of the volumetric proportion of interstitial phases (i.e., all phases other than plagioclase and olivine) in the Skaergaard and Rum troctolites. **(B)** The variation of bulk rock P_2O_5 [reported by Holness et al. (2015) and shown in **Table 1**] as a function of the volumetric proportion of interstitial phases in the Skaergaard troctolites.

In agreement with McBirney and Hunter (1995), we find no correlation between the volumetric proportion of interstitial minerals and fabric strength (**Figure 6A**) in either the Rum or the Skaergaard troctolites. Similarly, there is no correlation between the amount of interstitial minerals and the bulk rock P_2O_5 concentration in the Skaergaard troctolites (**Figure 6B**).

Apparent Grain Shapes and Fabrics in Synthetic Systems

A population of randomly chosen grain intersections through isolated perfect cuboids includes many very small slices, commonly with high aspect ratio (Higgins, 1994). Such small slices are not observed in natural samples of plutonic rocks, because of the constraints placed on grain shape by the necessity of space-filling. Additionally, one might expect that the overall grain size of the natural samples would control the observed population of grain intersections, with the chance of observing a slice with an extreme aspect ratio increasing with increasing overall grain size. However, this effect will be modified by the effects of the overall thickness of the thin section, which makes detecting slices cut <30 μm from the grain edge difficult. The problems associated with the absence of detailed modeling either of the way the effective cut-off changes with grain size, or of the effect of space-filling constraints on the shape corners and edges of crystals in fully solidified rocks, are minimized if the 2D grain shape is parameterized by the mode of the population of apparent aspect ratios (e.g., Higgins, 1994). However, to permit direct comparison with previous studies of the plagioclase grain shape in natural examples (Meurer and Boudreau, 1998; Holness, 2014), we chose to use the average apparent aspect ratio.

To permit comparison of our populations of intersections of isolated cuboids with the cumulates, we calculated the way the average aspect ratio of the synthetic population changes with progressive exclusion of the smallest grain intersections (quantified by area) (**Figure 7**). For all cuboid shapes, once the smallest ∼50 grain intersections are ignored the average apparent aspect ratio in the perfectly foliated population is higher than that in the population with randomly oriented cuboids (**Figure 7**). The difference between AR in the perfectly foliated and that in the population with random cuboid orientation generally increases with greater exclusion of the smaller intersections. We do not consider, however, the populations involving only the few hundred largest intersections (i.e., those parts of the curves toward the right in **Figure 7**) to be comparable to the natural samples.

The average apparent aspect ratios for the cuboid shapes 1:4:7 and 1:5:8 lie entirely outside the range 2.25–3.37 (i.e., that range observed for the Skaergaard main trend, **Table 1**), while that for 1:1.5:2 lies in that range only if almost all the small interactions are included (**Figure 7**). These three shapes are therefore unlikely to be similar to those found in the Skaergaard cumulates forming the main trend on the plot of AR vs. AF.

For the shapes 1:2:3, 1:2:4, and 1:2:6, the average apparent aspect ratio of populations containing all but the smallest 5% of the intersections and of populations containing all but the smallest 20% intersections (i.e., those populations likely to most closely approximate natural samples), fall in the range 2.25–3.37. Intersections of cuboids with the shape 1:3:7 have a generally higher aspect ratio than observed in the Skaergaard samples,

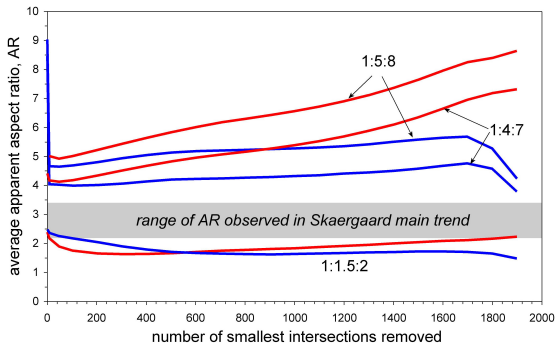

FIGURE 7 | The variation of average apparent aspect ratio (AR) for synthetic rocks comprising grains of constant shape (either 1:1.5:2, 1:4:7, or 1:5:8) as a function of the completeness of the population of grain intersections. The shape of a total of 2,000 intersections was calculated, and AR was calculated by omitting progressively more of the smallest intersections. For each of the three shapes, the red line shows the variation of AR in a perfectly foliated system while the blue line shows that for entirely randomly oriented grains. The horizontal gray box shows the range of AR found in the main group of Skaergaard troctolites (shown in **Figure 5**).

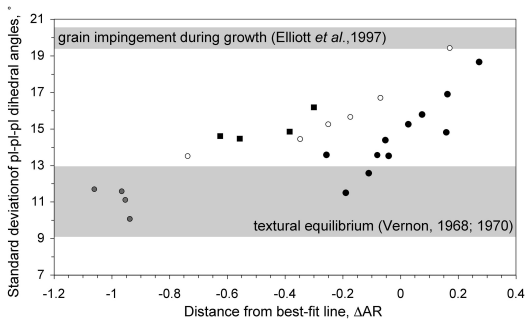

FIGURE 8 | The standard deviation of populations of plagioclase–plagioclase–plagioclase dihedral angles in the Skaergaard and Rum troctolites as a function of the difference, ΔAR, between the observed AR and the expected AR were the sample to fall on the line of best fit through the main group of Skaergaard data (shown in **Figure 5**). Symbols as in **Figure 5**. The horizontal gray boxes show the reported values of standard deviation for fully texturally equilibrated samples (from Vernon, 1968, 1970) and that consistent with random impingement of growing grains (from Elliott et al., 1997).

but fall into the range if they are randomly oriented. The range of likely average apparent aspect ratios in rocks containing plagioclase grains with these four shapes is shown in **Figure 5**. As the grain shape becomes increasingly less equant, the difference in AR between the random and the foliated microstructures increases, but in none of the four cases does it increase as much as is observed for the Skaergaard main trend and the two suites of Rum samples (**Figure 5**).

The Extent of Sub-Solidus Textural Equilibration

The standard deviation of plagioclase–plagioclase–plagioclase dihedral angle populations in a selection of samples from Skaergaard and Rum is shown in **Figure 8**. Since progressive textural equilibration is expected to change grain shape without having much effect on crystallographic orientation, we plotted standard deviation of the dihedral angles as a function of the difference between the actual observed AR and the expected AR were the sample to fall precisely on the best-fit line through the main grouping of Skaergaard data. Thus, a positive ΔAR is calculated for samples falling on the right of the dashed line in **Figure 5**, and a negative ΔAR is calculated for those falling on the left.

The data fall into three well-defined groups. The analyzed subset of the main Skaergaard trend (comprising samples covering the full range of observed ΔAR) shows a steeply decreasing standard deviation, from values close to those expected for impingement (Elliott et al., 1997) to those expected for textural equilibrium (Vernon, 1968, 1970), as ΔAR decreases. The Skaergaard second group (represented by six of the seven samples) also show this correlation, but with a shallower slope and offset to more negative values of ΔAR; the Rum Unit 10 samples fall very close to this group. The final group comprises the Rum Unit 12 samples, which form a tight cluster with standard deviations indicative of textural equilibrium.

DISCUSSION

Comparison With Previous Work

Our observations demonstrate a greater sensitivity of the strength of fabrics to plagioclase grain shape in troctolites than that originally proposed by Meurer and Boudreau (1998) for cumulates from Stillwater (**Figure 5**). It is unlikely that this difference is a consequence of different plagioclase modes in the two sets of samples, since the Meurer and Boudreau (1998) samples all appear to have a similar range of mineral modes to that in the cumulates analyzed here. A major difference between our study of the Rum and Skaergaard cumulates and Meurer and Boudreau's (1998) work on Stillwater is that the latter did not include all plagioclase grains in their measurement populations, whereas we measured all those grains which were visible in each photomicrograph.

The relationship between AR and AF found by Meurer and Boudreau (1998) (**Figure 5**) is that expected for samples that have undergone significant textural equilibration, since it can be extrapolated to finite values of AF for fully equant grains (**Figure 2**). It would be instructive to re-examine their samples and measure the standard deviation of plagioclase–plagioclase–plagioclase dihedral angles to determine how closely they have approached textural equilibrium.

Grain Shape and Fabric Strength

A comparison of the variation in the calculated average apparent aspect ratio as a function of fabric strength in the synthetic rocks and in the samples from Rum and the Skaergaard main trend demonstrates that the positive correlation between AR and AF observed in the natural samples is highly unlikely to

be an artifact created by the fabric itself. Instead, a comparison of the data derived from the synthetic systems suggest that the observed increase in AR with increasing alignment factor in the main group of Skaergaard samples is associated with a change in general grain shape from something in the range 1:2:3–1:2:6 to 1:3:7 (**Figure 5**). It should be remembered, however, that it is unlikely that the natural samples contain only a single grain shape and that the observed trend is most probably a result of the entire range of shapes becoming less equant.

That the strongest fabrics (highest AF) correlate with high AR is due to some combination of fabric creation being easier for more elongate plagioclase grains in either flowing magma or in a mush undergoing seismic activity (i.e., AR is the controlling factor), and the limitations on growth caused by the impingement of (010) faces (i.e., AF is the controlling factor). Working out which of these two processes is dominant is not straightforward.

The strong correlation between position relative to the best fit line on the AR vs. AF plot (**Figure 5**) and the extent of textural equilibration of the plagioclase–plagioclase–plagioclase three-grain junctions (**Figure 8**), suggests that the scatter of both the main and the second group of Skaergaard samples, and the cumulates from Rum Unit 10 from their respective lines of best fit, is at least partly a consequence of variable extents of textural equilibration: those samples in which sub-solidus cooling rates were sufficiently slow to permit the completion of the first stage of textural equilibration (and therefore a low standard deviation) have a relatively low AR. Such sub-solidus reduction in average aspect ratio of the original grains grown during solidification is likely to be most pronounced for the smaller plagioclase grains in the sample, although we do not have sufficient grains in our thin sections to test this hypothesis.

Figure 8 also demonstrates that the lower AR found in the second group of Skaergaard samples and the Rum Unit 10 cumulates cannot be a result of a comparatively close approach to textural equilibrium, since the standard deviation of dihedral angles at plagioclase triple junctions in these samples is too high. Instead, the original plagioclase grains in these samples must have been more equant than those in the main Skaergaard group, perhaps with shapes in the range 1:2:3–1:2:6 (**Figure 5**). The different shape probably accounts for the more shallow slope for these samples in **Figure 8**: the choice of abscissa in **Figure 8** is only meaningful for the Skaergaard main group of data.

The troctolites in the Rum Unit 12 have a similar range of alignment factor as those from Unit 10, but lower aspect ratio (**Figure 3**). This lower aspect ratio is associated with plagioclase three-grain junction geometry that appears to be in, or very close to, textural equilibrium (**Figure 8**). The complete Rum data set forms a well-defined positive correlation on the plot of standard deviation vs. ΔAR (**Figure 8**), suggestive of a grain shape in Unit 12 originally indistinguishable from that in Unit 10 but with significant modification during sub-solidus textural equilibration (c.f. Vernon, 1970), consistent with slower sub-solidus cooling of the floor during and immediately after the formation of Unit 12. The Unit 12 allivalite records seven replenishment events after the arrival of the magma that forms the base of the allivalite (Holness and Winpenny, 2009) and we suggest that this continuous replenishment of the open-system magma chamber prevented significant cooling of the recently solidified cumulates, leading to extensive sub-solidus textural equilibration.

Changes in Fabric Strength Through the Lower Part of the Skaergaard Stratigraphy

The well-defined general increase in fabric strength with increasing stratigraphic height in the Skaergaard Layered Series troctolites (**Figure 3**) is associated not only with an increasingly non-equant plagioclase grain shape but also with a progression from microstructures indicative of *in situ* nucleation and growth (**Figures 1A**, **4A**) to those expected for mushes in which accumulated crystals have been re-arranged by magmatic currents (**Figures 1B**, **4B**). We suggest that these changes record the early inflation of the Skaergaard chamber and the changing location of crystallization as cooling proceeded subsequent to full inflation.

The formation of a horizontal tabular intrusion splits the geotherm, ensuring that cooling is fastest at the roof (Morse, 1986), leading to convection [both thermal and two-phase (e.g., Grout, 1918)]. Because the change in temperature of the liquidus and adiabat with increasing pressure are different, down-welling magma in an intrusion of km-scale height becomes super-cooled, driving nucleation and crystal growth in the down-welling plumes and ensuring that crystallization occurs near the chamber floor (Irvine, 1970). The resulting predominance of crystallization near the floor, amplified by the accumulation of crystals nucleated at the roof and walls and brought down by convection currents, means that crystal accumulation is greatest on the floor of the magma chamber, with the stratigraphic position of the most evolved floor cumulates closer to the roof than the base of the stratigraphy. This asymmetry of crystal accumulation amplifies the asymmetry of cooling by creating an insulating blanket of mush on the floor, made more effective by the release of latent heat during the solidification of interstitial liquid. The insulating floor blanket prevents the large undercooling required for *in situ* nucleation of crystals from the bulk magma (i.e., primocrysts) at the floor itself. Morse (1988) suggests that ∼100 m of floor blanket is required to make a discernible difference to the location of crystal nucleation and growth from the bulk magma. Thus it is only possible to nucleate primocrysts directly on the chamber floor in an intrusion of km-scale height immediately after magma emplacement, with crystals supplied to the floor during the later stages of solidification by migration of those nucleated at the roof and walls. Microstructures in the floor cumulates are thus dominated by those indicative of *in situ* nucleation and growth only in the lowermost parts of the stratigraphy, being replaced by those indicative of crystal transport and re-arrangement by magmatic currents higher in the stratigraphy.

Note, however, that this scenario applies only to bodies created by a single magma batch, or by a series of batches that are sufficiently closely spaced in time to be treated as effectively one single batch. The location of crystal nucleation and growth in open systems replenished by batches of super-heated magma will be different (e.g., Latypov et al., 2017).

The Skaergaard chamber filled progressively, likely beginning as a sill, with full inflation marked by the arrival of a major magma injection once ∼150 m of the stratigraphy had formed. The microstructural evidence points to a transient initial period of *in situ* nucleation on the chamber floor, both because the chamber in its earliest stages was a thin sill, and because the thermal blanket on the floor had not developed, allowing enough heat loss through the floor to create sufficient undercooling to permit nucleation on the floor itself. As the chamber inflated, the increased height promoted convection both because cooling through the roof dominated over that at the floor, and because of an increased contribution to cooling at the increasingly extensive vertical walls. The onset of convection would lead not only to a substantial increase in the amount of material brought to the chamber floor, a decrease of *in situ* heterogeneous nucleation on the chamber floor itself, and also to the creation of fabrics as the convection currents aligned the accumulated grains, evident as increasingly well-developed SPO fabrics upward in the Skaergaard stratigraphy.

We suggest that the stratigraphic variation of AF observed in the lower 320m of the Skaergaard stratigraphy (**Figure 3**) is consistent with the conclusions of Holness et al. (2015): a rapid inflation of an initial sill-like body is recorded in the core between −120 and −100 m depth, followed by a period in which the chamber inflated only by a small amount following injections of magma at −89 and −65 m. The chamber attained its final height with the major injection recorded in the drill core at −8 m. The two events which significantly changed the height of the chamber are associated with step-wise increases in AF. We suggest these increases are due to step-wise increases in convective strength, due to the greater influence of cooling at the increasingly important vertical walls and the greater asymmetry of cooling at the roof and floor.

Note that Campbell (1978), following an assessment of the various ways in which adcumulates may form, argues for *in situ* heterogeneous nucleation throughout the development of floor cumulates, with only minimal contribution to the floor mush of crystals nucleated and grown elsewhere in the chamber. However, the concentration of clear microstructural evidence for *in situ* nucleation and growth only in the lowest part of the stratigraphy suggests that this was not the case in the Skaergaard. Above the first few tens of meters of stratigraphy, the crystal pile on the chamber floor grew by the accumulation of significant quantities of crystals either sourced elsewhere, nucleated just above the magma-mush interface in downwelling plumes (e.g., Morse, 1986), or formed in a floor mush that could be easily disaggregated to form secondary fabrics.

While the above explanation can account for the observed stratigraphic variation in fabric strength and the extent of microstructural evidence for *in situ* grain growth, we have not yet discussed the associated changes in grain shape. Although we cannot yet unambiguously differentiate which of the two primary drivers for the positive correlation between AR and AF is dominant, we ought to consider what might be causing an upward increase in AR in the absence of any effects of increasing AF.

The aspect ratio of non-equant minerals undergoing *in situ* growth is affected by the timing of impingement against adjacent grains, with early impingement resulting in a lower aspect ratio (Martin et al., 1987). Thus, the marked increase in AR observed in the lowermost 40m of the stratigraphy (**Figure 3**) could be a consequence of a decreasing significance of *in situ* nucleation and growth as the insulating floor blanket developed. An increase in plagioclase aspect ratio can also be achieved by an increase in the cooling rate (Holness, 2014). However, the rate of cooling through the floor, and the overall rate of heat loss from the intrusion, decrease with time. A cooling-rate-controlled increase in AR can therefore only be recorded in the floor cumulates if they have an increasing component of accumulated crystals sourced from rapidly cooling parts of the chamber such as the roof and walls.

During the earliest history of the Skaergaard intrusion, the wall mush was relatively strong, with only localized evidence for tearing and disruption caused by collapse. As solidification proceeded, the mush developed diffuse patches of coarse-grained, relatively evolved material interpreted to have formed during the collapse and tearing of a progressively weaker and more poorly consolidated mush (Humphreys and Holness, 2010). This decreasing coherence would have been associated with an increase in the amount of crystals lost from the inner margin of the mush and therefore an increase in the rate of supply of sediment to the floor. Since the plagioclase formed at the rapidly cooling wall is likely to be less equant than that grown at the more slowly cooled floor, an increase in the contribution of the wall mush to the floor cumulates would be recorded in an increase in AR upward through the stratigraphy.

Localized Departures From the Main Skaergaard Trend

Three of the four regions of the stratigraphy associated with evidence for magma influx are marked by relatively equant plagioclase (**Figure 3**), with a narrow range of AR, despite a wide range of alignment factor (**Figure 5**). Two of these three replenishment events, those at −65 and −8 m, involved the arrival of hot primitive magma (Holness et al., 2015). The cumulates at these points in the stratigraphy are relatively fine-grained and have low AR compared to nearby samples (**Table 1** and **Figure 3**). The fine grain size is likely to be a consequence of chilling of the incoming magma, leading to a high nucleation rate. The relatively low AR may be a consequence of early impingement (consequent to the high nucleation rate) or because the growth rate of the plagioclase slowed on the arrival of hotter magma. That cooling rate may have been a dominant influence on plagioclase shape is suggested by the observation that AF is not unusually low in these samples, indicating no significant increase of *in situ* nucleation and growth on the chamber floor.

The arrival of magma recorded at −89 m stratigraphic height is associated with a reduction of Mg#, denoting evolved cool magma (**Figure 3**; Holness et al., 2015). The associated reduction in AR is not particularly marked (**Figure 3**) and there is no change in the grain size (**Table 1**). We suggest that the relatively small decrease in AR (compared to the influxes at −65 and −8 m) was

a result of an increase in the contribution of *in situ* nucleation to the growth of the floor mush as the temperature of the magma chamber decreased, consistent with the single sample from this region of the core with weak fabric.

The prolonged magma injection event recorded between about −120 and −100 m depth in the core, which increased the chamber height sufficiently to create a step-wise increase in convective strength (recorded in an increase in AF) is not associated with lower than expected values of AR (**Figure 3**). We suggest that the relatively long duration of this event, involving at least three batches of magma (Holness et al., 2015), did not result in discrete chilling events that could be detected on the length scale of our sampling. We suggest that a closer sampling strategy through this part of the core might pick up localized excursions in grain size and shape.

Comparison of Rum and Skaergaard Troctolites

The main fabric-forming mechanisms in the Rum and Skaergaard chambers are likely to have been different. There is no evidence of vertical walls in the generally tabular Rum chamber, and none of the roof is preserved *in situ*. However, abundant evidence of slumping attests to frequent tectonic disturbance (O'Driscoll et al., 2007) and we suggest that the fabrics in the Rum troctolites are due to the disaggregation and re-arrangement of the mush by external tectonic events (e.g., Davis et al., 2007), rather than the strong convection currents active in the Skaergaard chamber [i.e., that the Rum fabrics are secondary, rather than primary, according to the classification scheme of Holness et al. (2017)].

The values of Θ_{cpp} in the troctolites of the Rum Eastern Layered Intrusion that are not affected by late-stage infiltration are similar to those reported for troctolites in the Skaergaard intrusion (Holness, 2015), consistent with similar solidification rates of the floor mush in the two intrusions. That the original grain shape of plagioclase in the Rum troctolites is generally more equant than that seen in most of the Skaergaard samples (**Figure 3**), suggests that growth rates of plagioclase at the roof of the open-system, continually replenished, sill-like Rum chamber was slower than at the roof and walls of the closed-system Skaergaard chamber.

The Effect of Fabric on Mush Structure and Adcumulus Status

Following Wager (1963), the most commonly used parameter to determine adcumulus status is the bulk rock concentration of incompatible elements such as P_2O_5. Accordingly, there should be a correlation between the bulk rock concentration of highly incompatible elements and the mode of minerals grown from the interstitial liquid, but this is not generally observed (McBirney and Hunter, 1995; Meurer and Meurer, 2006; Karykowski and Maier, 2017). As pointed out by McBirney and Hunter (1995), and verified here, there is no such correlation between bulk rock P_2O_5 and the mode of interstitial minerals in the Skaergaard troctolites (**Figure 6B**), due perhaps to the progressive loss or addition of interstitial liquids during solidification (Karykowski and Maier, 2017), or to difficulties in nucleating apatite which ends up crystallizing in channels through which late-stage liquids flowed (Meurer and Meurer, 2006). Thus, bulk rock P_2O_5 concentrations are unlikely to be a good measure of the extent to which cumulates contain late-stage liquids.

Although one might perhaps expect adcumulate rocks to develop from a mush in which the accumulated crystals were efficiently packed with a low initial porosity, we found no correlation between the strength of foliation and the mode of interstitial minerals for either the Rum or Skaergaard troctolites (**Figure 6A**). This is in agreement with the findings of McBirney and Hunter (1995), and also with Wager (1963) who stated that "the effect on the phosphorus content of variation in the initial packing is considered slight, compared with the effects of adcumulus growth." Thus the development of adcumulates requires processes other than efficiently packed grains in a strongly foliated rock.

CONCLUSION

The strength of foliations defined by shape preferred orientation of plagioclase in troctolitic cumulates from both the Rum Eastern Layered Intrusion and the Skaergaard intrusion increases as the grains become more tabular, due either to the greater propensity of highly non-equant grains to be re-arranged by magmatic currents or tectonic disruption of poorly consolidated mush, or by the effects of a pre-existing fabric on final grain shape in fully solidified rocks. The stratigraphic evolution of grain shape, microstructures and fabrics in the lower part of the Skaergaard Layered Series records the progressive inflation of the chamber to its final size. Our microstructural observations are consistent with a decrease in the extent of *in situ* nucleation and growth on the chamber floor as the gradually thickening crystal pile created an insulating blanket and to an increasing contribution of both convection and the accumulation of crystals derived from the walls of the expanding magma chamber, as predicted by Irvine (1970) and Morse (1988). That the overall plagioclase grain shape becomes more equant at higher levels in the stratigraphy than those examined here (Holness, 2015) is likely to be primarily a consequence of decreasing cooling rates. The convective strength would likely remain high for most of the remaining stratigraphy, until crystallization had proceeded sufficiently to decrease the height of the remaining magma and as the country rocks heated up appreciably.

Igneous microstructures can be modified during slow sub-solidus cooling: although alignment factor is likely to remain constant (leading eventually to a CPO in a granular rock), textural equilibration leads to a decrease in grain aspect ratio and an approach to equilibrium geometry of three-grain junctions. This is clearly evident in the Unit 12 troctolites of the open-system magma chamber of the Rum Eastern Layered Intrusion. The observation that the standard deviation of plagioclase–plagioclase–plagioclase dihedral angles varies in a systematic manner with the average grain shape suggests that this might

be a useful new parameter to quantify the thermal history of cumulates. More work should be done to explore this variation.

DATA AVAILABILITY STATEMENT

The datasets generated for this study are available on request to the corresponding author.

AUTHOR CONTRIBUTIONS

MH wrote the manuscript and collected some of the data. CM and ZV collected some of the data. DM did the numerical analysis of grain intersections in synthetic systems. All authors contributed to the article and approved the submitted version.

FUNDING

This work was supported by a grant from the Natural Environment Research Council (grant number NE/N009894/1). ZV was supported by a Marie Skłodowska-Curie Fellowship (grant number 708131-EFOX). CM was supported by the Robert Wright Fund of Trinity College, Cambridge, and the John Muir Foundation.

ACKNOWLEDGMENTS

We are grateful to Eric Ferre and Tony Morse for helpful and insightful reviews, and to Michael Higgins and Rais Latypov for their helpful comments on an early version of the manuscript. All remaining misconceptions are our own.

REFERENCES

Arvidson, R. S., Beig, M. S., and Luttge, A. (2004). Single-crystal plagioclase feldspar dissolution rates measured by vertical scanning interferometry. *Am. Mineral.* 89, 51–56. doi: 10.2138/am-2004-0107

Bergantz, G. W., Schleicher, J. M., and Burgisser, A. (2017). On the kinematics and dynamics of crystal-rich systems. *J. Geophys. Res. Solid Earth* 122, 6131–6159. doi: 10.1002/2017jb014218

Boorman, S., Boudreau, A., and Kruger, F. J. (2004). The lower zone – critical zone transition of the bushveld complex: a quantitative textural study. *J. Petrol.* 45, 1209–1235. doi: 10.1093/petrology/egh011

Boudreau, A. E., and McBirney, A. R. (1997). The Skaergaard Layered Series. Part III. Non-dynamic layering. *J. Petrol.* 38, 1003–1020. doi: 10.1093/petroj/38.8.1003

Brothers, R. N. (1964). Petrofabric analyses of Rhum and Skaergaard layered rocks. *J. Petrol.* 5, 255–274. doi: 10.1093/petrology/5.2.255

Brown, G. M. (1956). The layered ultrabasic rocks of rhum, inner hebrides. *Philos. Trans. R. Soc. Lond. Ser. B* 240, 1–53. doi: 10.1098/rstb.1956.0011

Campbell, I. H. (1978). Some problems with the cumulus theory. *Lithos* 11, 311–321.

Campbell, I. H., Roeder, P. L., and Dixon, J. M. (1978). Plagioclase buoyancy in basaltic liquids as determined with a centrifuge furnace. *Contrib. Mineral. Petrol.* 67, 369–377. doi: 10.1007/bf00383297

Davies, I. C., and Walker, R. G. (1974). Transport and deposition of re-sedimented conglomerates: the Cap Enrage formation, Cambro-Ordovician, Gaspe, Quebec. *Sediment. Res.* 44, 1200–1216.

Davis, M., Koenders, M. A., and Petford, N. (2007). Vibro-agitation of chambered magma. *J. Volcanol. Geothermal Res.* 167, 24–36. doi: 10.1016/j.jvolgeores.2007.07.012

Denison, C., Carlson, W. D., and Ketcham, R. A. (1997). Three-dimensional quantitative textural analysis of metamorphic rocks using high-resolution computed X-ray tomography: part I. *Methods Tech. J. Metamorphic Geol.* 15, 29–44. doi: 10.1111/j.1525-1314.1997.00006.x

Donaldson, C. H. (1974). Olivine crystal types in harrisitic rocks of the Rhum pluton and in Archean spinifex rocks. *Geol. Soc. Am. Bull.* 85, 1721–1726.

Duchêne, S., Pupier, E., Le Carlier de Veslud, C., and Toplis, M. J. (2008). A 3D reconstruction of plagioclase crystals in a synthetic basalt. *Am. Mineral.* 93, 893–901. doi: 10.2138/am.2008.2679

Elliott, M. T., Cheadle, M. J., and Jerram, D. A. (1997). On the identification of textural equilibrium in rocks using dihedral angle measurements. *Geology* 25, 355–358.

Emeleus, C. H. (1997). *Geology of Rum and the Adjacent Islands. Memoir for 1:50 000 Geological Sheet 60 (Scotland)*. London: HM Stationery Office.

Emeleus, C. H., Cheadle, M. J., Hunter, R. H., Upton, B. G. J., and Wadsworth, W. J. (1996). "The rum layered suite," in *Layered Intrusions*, ed. R. G. Cawthorn, (Netherlands: Elsevier), 403–439. doi: 10.1016/s0167-2894(96)80014-5

Farr, R. S., Vukmanovic, Z., Holness, M. B., and Griffiths, E. (2018). Reconstructing grain-shape statistics from electron back-scatter diffraction microscopy. *Phys. Rev. Mater.* 2:073804. doi: 10.1103/PhysRevMaterials.2.073804

Gray, N. H., Philpotts, A. R., and Dickson, L. D. (2003). Quantitative measures of textural anisotropy resulting from magmatic compaction illustrated by a sample from the Palisades sill, New Jersey. *J. Volcanol. Geotherm. Res.* 121, 293–312. doi: 10.1016/s0377-0273(02)00463-8

Greenwood, R. C., Donaldson, C. H., and Emeleus, C. H. (1990). The contact zone of the Rhum ultrabasic intrusion; evidence of peridotite formation from magnesian magmas. *J. Geol. Soc.* 147, 209–212. doi: 10.1144/gsjgs.147.2.0209

Grout, F. F. (1918). Internal structures of igneous rocks: their significance and origin with special reference to the Duluth gabbro. *J. Geol.* 26, 439–458. doi: 10.1086/622605

Hamilton, M. A., Pearson, D. G., Thompson, R. N., Kelley, S. P., and Emeleus, C. H. (1998). Rapid eruption of Skye lavas inferred from precise U-Pb and Ar-Ar dating of the Rum and Cuillin plutonic complexes. *Nature* 394, 260–263. doi: 10.1038/28361

Heidelbach, F., Post, A., and Tullis, J. (2000). Crystallographic preferred orientation in albite samples deformed experimentally by dislocation and solution precipitation creep. *J. Struct. Geol.* 22, 1649–1661. doi: 10.1016/s0191-8141(00)00072-9

Hess, G. B. (1960). Stillwater igneous complex, Montana: a quantitative mineralogical study. *Geol. Soc. Am. Memoir* 80:230.

Higgins, M. D. (1991). The origin of laminated and massive anorthosite, Sept Iles layered intrusion, Quebec, Canada. *Contrib. Mineral. Petrol.* 106, 340–354. doi: 10.1007/bf00324562

Higgins, M. D. (1994). Numerical modelling of crystal shapes in thin sections: estimation of crystal habit and true size. *Am. Mineral.* 79, 113–119.

Higgins, M. D. (1998). Origin of anorthosite by textural coarsening: quantitative measurements of a natural sequence of textural development. *J. Petrol.* 39, 1307–1323. doi: 10.1093/petroj/39.7.1307

Higgins, M. D., and Chandrasekharam, D. (2007). Nature of sub-volcanic magma chambers, Deccan Province, India: evidence from quantitative textural analysis of plagioclase megacrysts in the Giant Plagioclase Basalts. *J. Petrol.* 48, 885–900. doi: 10.1093/petrology/egm005

Holness, M. B. (2007). Textural immaturity of cumulates as an indicator of magma chamber processes: infiltration and crystal accumulation in the rum Eastern Layered Intrusion. *J. Geol. Soc. Lond.* 164, 529–539. doi: 10.1144/0016-76492006-021

Holness, M. B. (2014). The effect of crystallization time on plagioclase grain shape. *Contrib. Mineral. Petrol.* 168:1076. doi: 10.1007/s00410-014-1076-5

Holness, M. B. (2015). Plagioclase growth rates control three-grain junction geometry in dolerites and gabbros. *J. Petrol.* 56, 2117–2144. doi: 10.1093/petrology/egv065

Holness, M. B., Anderson, A. T., Martin, V. M., Maclennan, J., Passmore, E., and Schwindinger, K. (2007a). Textures in partially solidified crystalline nodules: a window into the pore structure of slowly cooled mafic intrusions. *J. Petrol.* 48, 1243–1264. doi: 10.1093/petrology/egm016

Holness, M. B., Nielsen, T. F. D., and Tegner, C. (2007b). Textural maturity of cumulates: a record of chamber filling, liquidus assemblage, cooling rate and large-scale convection in mafic layered intrusions. *J. Petrol.* 48, 141–157. doi: 10.1093/petrology/egl057

Holness, M. B., Humphreys, M. C. S., Sides, R., Helz, R. T., and Tegner, C. (2012). Toward an understanding of disequilibrium dihedral angles in mafic rocks. *J. Geophys. Res.* 117:B06207.

Holness, M. B., Stock, M. J., and Geist, D. (2019). Magma chambers versus mush zones: constraining the architecture of sub-volcanic plumbing systems from microstructural analysis of crystalline enclaves. *Philos. Trans. R. Soc. A* 377:20180006. doi: 10.1098/rsta.2018.0006

Holness, M. B., Tegner, C., Namur, O., and Pilbeam, L. (2015). The earliest history of the skaergaard magma chamber: a textural and geochemical study of the cambridge drill core. *J. Petrol.* 56, 1199–1227. doi: 10.1093/petrology/egv034

Holness, M. B., Tegner, C., Nielsen, T. F. D., Stripp, G., and Morse, S. A. (2007c). A textural record of solidification and cooling in the Skaergaard intrusion, East Greenland. *J. Petrol.* 48, 2359–2377. doi: 10.1093/petrology/egm064

Holness, M. B., Vukmanovic, Z., and Mariani, E. (2017). Assessing the role of compaction in the formation of adcumulates: a microstructural perspective. *J. Petrol.* 58, 643–674.

Holness, M. B., and Winpenny, B. (2009). The Unit 12 allivalite, Eastern Layered Intrusion, Isle of Rum: a textural and geochemical study of an open-system magma chamber. *Geol. Magaz.* 146, 437–450. doi: 10.1017/s0016756808005797

Humphreys, M. C. S., and Holness, M. B. (2010). Melt-rich segregations in the Skaergaard Marginal Border Series: tearing of a vertical silicate mush. *Lithos* 119, 181–192. doi: 10.1016/j.lithos.2010.06.006

Hunter, R. H. (1996). Texture development in cumulate rocks. *Dev. Petrol.* 15, 77–101. doi: 10.1016/s0167-2894(96)80005-4

Ikeuye, K. K., and Smith, C. S. (1949). Studies of interface energies in some aluminium and copper alloys. *J. Miner. Metals Mater. Soc.* 1, 762–768. doi: 10.1007/BF03398934

Irvine, T. N. (1970). Heat transfer during solidification of layered intrusions. I. Sheets and sills. *Can. J. Earth Sci.* 7, 1031–1061. doi: 10.1139/e70-098

Irvine, T. N., Andersen, J. C. Ø, and Brooks, C. K. (1998). Included blocks (and blocks within blocks) in the Skaergaard intrusion: geological relations and the origins of rhythmic modally graded layers. *Geol. Soc. Am. Bull.* 110, 1398–1447.

Iso, Y., Cohen, C., and Koch, D. L. (1996). Orientation in simple shear flow of semi-dilute fiber suspensions 2. Highly elastic fluids. *J. Non Newt. Fluid Mech.* 62, 135–153. doi: 10.1016/0377-0257(95)01405-5

Jackson, E. D. (1961). "Primary textures and mineral associations in the ultramafic zone of the stillwater complex," in *Paper Presented at the Geological Survey Professional Paper 358*, (Washington: U.S Government Printing Office).

Jerram, D. A., Davis, G. R., Mock, A., Charrier, A., and Marsh, B. D. (2010). Quantifying 3D crystal populations, packing and layering in shallow intrusions: a case study from the Basement Sill, Dry Valleys, Antarctica. *Geosphere* 6, 537–548. doi: 10.1130/ges00538.1

Karykowski, B. T., and Maier, W. D. (2017). Microtextural characterisation of the Lower Zone in the western limb of the Bushveld Complex, South Africa: evidence for extensive melt migration within a sill complex. *Contrib. Mineral. Petrol.* 172:60. doi: 10.1007/s00410-017-1380-y

Kouchi, A., Tsuchiyama, A., and Sunagawa, I. (1986). Effect of stirring on crystallisation kinetics of basalt: texture and element partitioning. *Contrib. Mineral. Petrol.* 93, 429–438. doi: 10.1007/bf00371713

Kretz, R. (1966). Interpretation of the shape of mineral grains in metamorphic rocks. *J. Petrol.* 7, 68–94. doi: 10.1093/petrology/7.1.68

Kretz, R. (1994). *Metamorphic Crystallisation*. Chichester: John Wiley and Sons.

Latypov, R., Chistyakova, S., Barnes, S. J., and Hunt, E. J. (2017). Origin of platinum deposits in layered intrusions by in situ crystallisation: evidence from undercutting Merensky Reef of the Bushveld Complex. *J. Petrol.* 58, 715–762.

Lofgren, G. (1974). An experimental study of plagioclase crystal morphology: isothermal crystallization. *Am. J. Sci.* 274, 243–273. doi: 10.2475/ajs.274.3.243

Maaløe, S. (1976). The zoned plagioclase of the Skaergaard Intrusion, East Greenland. *J. Petrol.* 17, 398–419. doi: 10.1093/petrology/17.3.398

Mainprice, D., and Nicolas, A. (1989). Development of shape and lattice preferred orientations: application to the seismic anisotropy of the lower crust. *J. Struct. Geol.* 11, 175–189. doi: 10.1016/0191-8141(89)90042-4

Martin, D., Griffiths, R. W., and Campbell, I. H. (1987). Compositional and thermal convection in magma chambers. *Contrib. Mineral. Petrol.* 96, 465–475. doi: 10.1007/bf01166691

Mathison, C. I. (1987). Pyroxene oikocrysts in troctolitic cumulates – evidence for supercooled crystallization and postcumulus modification. *Contrib. Mineral. Petrol.* 97, 228–236. doi: 10.1007/bf00371242

McBirney, A. R., and Hunter, R. H. (1995). The cumulate paradigm reconsidered. *J. Geol.* 103, 114–122. doi: 10.1086/629727

McClurg, J. (1982). *Petrology and Evolution of the Northern Part of the Rhum Ultrabasic Complex*. Ph.D. thesis, University of Edinburgh, Edinburgh.

Meurer, W. P., and Boudreau, A. E. (1998). Compaction of Igneous cumulates Part II: compaction and the development of igneous foliations. *J. Geol.* 106, 293–304. doi: 10.1086/516023

Meurer, W. P., and Meurer, M. E. S. (2006). Using apatite to dispel the "trapped liquid" concept and to understand the loss of interstitial liquid by compaction in mafic cumulates: an example from the Stillwater Complex, Montana. *Contrib. Mineral. Petrol.* 151, 187–201. doi: 10.1007/s00410-005-0054-3

Miyazaki, T., Sueyoshi, K., and Hiraga, T. (2013). Olivine crystals align during diffusion creep of Earth's upper mantle. *Nature* 502, 321–326. doi: 10.1038/nature12570

Morgan, D. J., and Jerram, D. A. (2006). On estimating crystal shape for crystal size distribution analysis. *J. Volcanol. Geotherm. Res.* 154, 1–7. doi: 10.1016/j.jvolgeores.2005.09.016

Morse, S. A. (1986). Convection in aid of adcumulus growth. *J. Petrol.* 27, 1183–1214. doi: 10.1093/petrology/27.5.1183

Morse, S. A. (1988). Motion of crystals, solute, and heat in layered intrusions. *Can. Mineral.* 26, 209–224.

Nielsen, T. F. D. (2004). The shape and volume of the Skaergaard Intrusion, Greenland: implications for mass balance and bulk composition. *J. Petrol.* 45, 507–530. doi: 10.1093/petrology/egg092

O'Driscoll, B., Hargraves, R. B., Emeleus, C. H., Troll, V. R., Donaldson, C. H., and Reavy, R. J. (2007). Magmatic lineations inferred from anisotropy of magnetic susceptibility fabrics in Units 8, 9, and 10 of the Rum Eastern Layered Series, NW Scotland. *Lithos* 98, 27–44. doi: 10.1016/j.lithos.2007.01.009

Petford, N. (2009). Which effective viscosity? *Mineral. Magaz.* 73, 167–191. doi: 10.1180/minmag.2009.073.2.167

Petford, N., and Koenders, M. A. (2003). Shear-induced pressure changes and seepage phenomena in a deforming porous layer – I. *Geophys. J. Int.* 155, 857–869. doi: 10.1111/j.1365-246x.2003.02076.x

Petford, N., Koenders, M. A., and Clemens, J. D. (2020). Igneous differentiation by deformation. *Contrib. Min. Pet.* 175:45. doi: 10.1007/s00410-020-1674-3

Philpotts, A. R., Carroll, M. R., and Hill, J. M. (1996). Crystal-mush compaction and the origin of pegmatitic segregation sheets in a thick flood-basalt flow in the mesozoic hartford basin, connecticut. *J. Petrol.* 37, 811–836. doi: 10.1093/petrology/37.4.811

Philpotts, A. R., and Philpotts, D. E. (2005). Crystal-mush compaction in the Cohassett flood-basalt flow, Hanford, Washington. *J. Volcanol. Geotherm. Res.* 145, 192–206. doi: 10.1016/j.jvolgeores.2005.01.008

Renner, R., and Palacz, Z. (1987). Basaltic replenishment of the Rhum magma chamber - Evidence from Unit 14. *J. Geol. Soc. Lond.* 144, 961–970. doi: 10.1144/gsjgs.144.6.0961

Rust, B. R. (1972). Pebble orientation in fluvial sediments. *J. Sediment. Res.* 42, 384–388.

Sato, H. (1995). Textural difference between pahoehoe and aa lavas of Izu-Oshima volcano, Japan – an experimental study on population density of plagioclase. *J. Volcanol. Geotherm. Res.* 66, 101–113. doi: 10.1016/0377-0273(94)00055-l

Shea, T., and Hammer, J. E. (2013). Kinetics of cooling- and decompression-induced crystallsiation in hydrous mafic-intermediate magmas. *J. Volcanol. Geotherm. Res.* 260, 127–145. doi: 10.1016/j.jvolgeores.2013.04.018

Smith, J. V., and Brown, W. L. (1988). *Feldspar Minerals. Volume I: Crystal Structures, Physical, Chemical and Microtextural Properties*. Berlin: Springer-Verlag.

Svahnberg, H., and Piazolo, S. (2013). Interaction of chemical and physical processes during deformation at fluid-present conditions: a case study from

an anorthosite-leucogabbro deformed at amphibolite facies conditions. *Contrib. Mineral. Petrol.* 165, 543–562. doi: 10.1007/s00410-012-0822-9

Tait, S. R. (1984). *Fluid Dynamical Processes in The Formation of Layered Igneous Rocks*. Ph.D. thesis, University of Cambridge, Cambridge, MA.

Tait, S. R. (1985). Fluid dynamic and geochemical evolution of cyclic unit 10, Rhum, Eastern layered series. *Geol. Magaz.* 122, 469–484. doi: 10.1017/s0016756800035391

Upton, B. G. J., Parsons, I., Emeleus, C. H., and Hodson, M. E. (1996). "Layered alkaline igneous rocks of the Gardar Province, South Greenland," in *Layered Intrusions*, ed. R. G. Cawthorn, (Elsevier), 331–363. doi: 10.1016/s0167-2894(96)80012-1

Upton, B. G. J., Skovgaard, A. C., McClurg, J., Kirstein, L., Cheadle, M., Emeleus, C. H., et al. (2002). Picritic magmas and the Rum ultramafic complex, Scotland. *Geol. Magaz.* 139, 437–452. doi: 10.1017/s0016756802006684

Vernon, R. H. (1968). Microstructures of high-grade metamorphic rocks at Broken Hill, Australia. *J. Petrol.* 9, 1–22. doi: 10.1093/petrology/9.1.1

Vernon, R. H. (1970). Comparative grain-boundary studies of some basic and ultrabasic granulites, nodules and cumulates. *Scottish J. Geol.* 6, 337–351. doi: 10.1144/sjg06040337

Vukmanovic, Z., Holness, M. B., Monks, K., and Andersen, J. C. Ø (2018). The Skaergaard trough layering: sedimentation in a convecting magma chamber. *Contrib. Mineral. Petrol.* 173:43. doi: 10.1007/s00410-018-1466-1

Wager, L. R. (1963). The mechanism of adcumulus growth in the layered series of the Skaergaard intrusion. *Mineral. Soc. Am. Spec. Pap.* 1, 1–9.

Wager, L. R., and Brown, G. M. (1968). *Layered Igneous Rocks*. Edinburgh: Oliver and Boyd.

Wager, L. R., and Deer, W. A. (1939). *Geological Investigations in East Greenland Part III-The Petrology of the Skaergaard intrusion, Kangerdlussuaq, East Greenland*. Copenhagen: Meddelelser om Grønland.

Williams, S. R., and Philipse, A. P. (2003). Random packings of spheres and spherocylinders simulated by mechanical contraction. *Phys. Rev. E* 67:051301.

Yamamoto, S., and Matsuoka, T. (1996). Dynamic simulation of microstructure and rheology of fiber suspensions. *Polymer Eng. Sci.* 36, 2396–2403. doi: 10.1002/pen.10638

Young, I. M., and Donaldson, C. H. (1985). Formation of granular-textured layers and laminae within the Rhum crystal pile. *Geol. Magaz.* 122, 519–528. doi: 10.1017/s0016756800035433

Conflict of Interest: The authors declare that the research was conducted in the absence of any commercial or financial relationships that could be construed as a potential conflict of interest.

frontiers in Earth Science

ORIGINAL RESEARCH
published: 29 September 2020
doi: 10.3389/feart.2020.531911

Magma Pressure-Temperature-Time Paths During Mafic Explosive Eruptions

Megan E. Newcombe[1], Terry Plank[2], Youxue Zhang[3], Megan Holycross[4], Anna Barth[2], Alexander S. Lloyd[2,5], David Ferguson[6], Bruce F. Houghton[7] and Erik Hauri[8†]*

[1] Department of Geology, University of Maryland, College Park, College Park, MD, United States, [2] Lamont-Doherty Earth Observatory, Palisades, NY, United States, [3] Earth and Environmental Sciences, University of Michigan, Ann Arbor, MI, United States, [4] National Museum of Natural History, Smithsonian Institution, Washington, WA, United States, [5] The Hun School of Princeton, Princeton, NJ, United States, [6] School of Earth and Environment, University of Leeds, Leeds, United Kingdom, [7] School of Ocean and Earth Science and Technology, University of Hawai'i at Mānoa, Honolulu, HI, United States, [8] Department of Terrestrial Magnetism, Carnegie Institution for Science, Washington, WA, United States

We have constrained syneruptive pressure-temperature-time (P-T-t) paths of mafic magmas using a combination of short-timescale cooling and decompression chronometers. Recent work has shown that the thermal histories of crystals in the last few seconds to hours of eruption can be constrained using concentration gradients of MgO inside olivine-hosted melt inclusions, produced in response to syneruptive cooling and crystallization of olivine on the inclusion walls. We have applied this technique to the study of melt inclusions erupted by arc and ocean island volcanoes, including the 1974 subplinian eruption of Fuego volcano; the 1977 fire-fountain eruption of Seguam volcano; and three eruptions of Kilauea volcano (episode 1 of the 1959 Kilauea Iki fire-fountain eruption, the 1500 CE vigorous fire-fountain eruption, and the 1650 CE subplinian eruption). Of the eruptions studied so far, melt inclusions from the 1959 Kilauea Iki eruption record the highest syneruptive cooling rates (3–11°C/s) and the shortest cooling durations (4–19 s), while inclusions from the 1974 Fuego eruption record the slowest cooling rates (0.1–1.7°C/s) and longest cooling durations (21–368 s). The high cooling rates inferred for the Kilauea Iki and Seguam fire fountain eruptions are consistent with air quenching over tens of seconds during and after fragmentation and eruption. Melt inclusions sampled from the interiors of small (~6 cm diameter) volcanic bombs at Fuego are found to have cooled more slowly on average than inclusions sampled from ash (with particle diameters < 2 mm) during the same eruption, as expected based on conductive cooling models. We find evidence for a systematic relationship between cooling rates and decompression rates of magmas, in which rapidly ascending gas-bearing magmas experience slower cooling during ascent and eruption than slowly ascending magmas. Our magma P-T-t constraints for the Kilauea Iki eruption are in broad agreement with isentropic models that show that the dominant driver of cooling in the conduit is adiabatic expansion of a vapor phase; however, at Fuego and Seguam, our results suggest a significant role for latent heat production and/or open-system degassing (both of which violate assumptions required for isentropic ascent). We thereby caution against the application of isentropic

OPEN ACCESS

Edited by:
Teresa Ubide, The University of Queensland, Australia

Reviewed by:
Takeshi Kuritani, Hokkaido University, Japan
Adam Kent, Oregon State University, United States

***Correspondence:**
Megan E. Newcombe
newcombe@umd.edu

† Deceased

Specialty section:
This article was submitted to Petrology, a section of the journal Frontiers in Earth Science

Received: *01 February 2020*
Accepted: *12 August 2020*
Published: *29 September 2020*

Citation:
Newcombe ME, Plank T, Zhang Y, Holycross M, Barth A, Lloyd AS, Ferguson D, Houghton BF and Hauri E (2020) Magma Pressure-Temperature-Time Paths During Mafic Explosive Eruptions. Front. Earth Sci. 8:531911. doi: 10.3389/feart.2020.531911

conduit models to magmas containing relatively high initial water concentrations (e.g., arc magmas containing ∼4 wt% water). We note that several processes that have been inferred to occur in volcanic conduits such as magma stalling, magma mingling, open- and closed-system degassing, vapor fluxing, and vapor accumulation (in foam layers or as slugs of gas) are associated with different implied vapor volume fractions during syneruptive ascent. Given the sensitivity of magma P-T-t paths to vapor volume fraction, the syneruptive thermometer presented here may be a means of identifying these processes during the seconds to hours preceding the eruption of mafic magmas.

Keywords: syneruptive magma ascent, diffusion, melt inclusions, olivine, thermal histories, conduit processes

INTRODUCTION

The temperature of magma during ascent through the volcanic conduit exerts an important control on magma crystallinity and viscosity, which in turn affect magma rheology and ascent dynamics (Costa et al., 2007; Vona et al., 2011; Shea and Hammer, 2013; La Spina et al., 2016; Bamber et al., 2020). A recent numerical modeling effort by La Spina et al. (2015) found that "a temperature variation of 30 K at the base of the conduit has a bigger effect on mass discharge rate than an increase of 1 wt% in water content," thereby highlighting the impact of seemingly small temperature variations on the vigor of explosive basaltic eruptions. Temperature variations during ascent and eruption also influence the speciation and oxygen fugacity of exsolved vapor (Oppenheimer et al., 2018; Moussallam et al., 2019). Recently developed real-time monitoring tools for gas geochemistry are now providing continuous records of volcanic gas emissions (Aiuppa et al., 2005; Shinohara, 2005; Aiuppa et al., 2007; de Moor et al., 2016), but in order to interpret and harness the information provided by these records, we must decipher the relationships between the dynamics of magma degassing and escape, magma temperature, and vapor speciation.

In addition to the importance of syneruptive temperature changes as a control on eruption dynamics and outgassed vapor speciation, the syneruptive cooling rate of tephra is also a key parameter for accurately determining pre-eruptive CO_2 and H_2O concentrations of melt inclusions, which are widely used to estimate magma storage depths (e.g., Métrich and Wallace, 2008; Ruth et al., 2018; Rasmussen et al., 2019). CO_2 may effectively partition into vapor bubbles during post-entrapment cooling, thereby compromising the utility of melt inclusions as magma barometers (Hartley et al., 2014; Moore et al., 2015). This challenge has been met by the development of several analytical (Hartley et al., 2014; Moore et al., 2015), modeling (Wallace et al., 2015; Maclennan, 2017; Tucker et al., 2019; Rasmussen et al., 2020) and experimental (Mironov et al., 2015; Rasmussen et al., 2020) approaches to correct for diffusion of CO_2 from melt inclusions into their vapor bubbles. Syneruptive cooling rate sets the time available for CO_2 diffusion within melt inclusions: Eruptive deposits that cool slowly allow extensive loss of CO_2 into vapor bubbles, while rapidly cooled melt inclusions pass through a higher closure temperature for CO_2 diffusion and allow less diffusion of CO_2 into vapor bubbles. One of the largest sources of error in the models that have been developed to account for diffusion of CO_2 into vapor bubbles is uncertainty in estimates of the syneruptive cooling rate (Maclennan, 2017; Tucker et al., 2019; Rasmussen et al., 2020). Similarly, it is widely recognized that olivine-hosted melt inclusions are susceptible to syneruptive and post-eruptive water loss via diffusion of water through the host olivine (Massare et al., 2002; Gaetani et al., 2012; Bucholz et al., 2013; Lloyd et al., 2013; Le Voyer et al., 2014). Melt inclusions from pyroclasts that cool slowly suffer more extensive water loss than those sampled from rapidly quenched pyroclasts, demonstrating the strong control of syneruptive cooling rate on the extent of post-eruptive water loss from melt inclusions.

Despite the importance of the thermal evolution of magma as a control on eruptive processes (Costa et al., 2007; Vona et al., 2011; Shea and Hammer, 2013; La Spina et al., 2016; Bamber et al., 2020) and the post-entrapment evolution of melt inclusion volatile contents, petrologic studies of magma temperature changes during ascent and eruption are limited. Blundy et al. (2006) used plagioclase-melt thermometry to infer temperature increases of ∼100°C over several months of magma ascent during dome-building eruptions of Mount Saint Helens and Shiveluch volcanoes. Plagioclase-melt thermometry also reveals apparent temperature increases during magma ascent at Soufrière Hills, Mount Unzen, and Izu Oshima (Humphreys et al., 2016); however, Humphreys et al. (2016) suggest that post-entrapment water loss and/or disequilibrium crystallization could explain some or all of the apparent temperature increases during magma ascent inferred by plagioclase-melt thermometry. Other authors have exploited changes in water speciation during quenching (Zhang et al., 1997) and calorimetry (Wilding et al., 2000; Gottsmann and Dingwell, 2002; Potuzak et al., 2008; Nichols et al., 2009) to infer cooling rates of silicate melts as they pass through the closure temperature for water diffusion or the glass transition temperature, respectively.

The techniques listed above are not sensitive to temperature changes over the minute-to-hour timescales of magma ascent during explosive eruptions. Newcombe et al. (2014) developed a technique that uses MgO concentration gradients in olivine-hosted melt inclusions to constrain multi-stage thermal histories of magmas during the last few seconds to hours of ascent and syneruptive quenching, potentially providing a means to bridge the gap in timescales accessible with previously developed methods. So far, this technique has been applied to melt inclusions from submarine lavas, a sub-aerial hornito eruption, olivine-bearing sand from Papakaloa Beach (Hawaii), sand from

the Kilauea Iki crater, and olivines from martian meteorite Yamato 980459 (Newcombe et al., 2014; Saper and Stolper, 2020). The application of this technique to explosive basaltic-to-intermediate systems that exhibit a range of eruptive styles could reveal systematics of temperature changes during late-stage magma ascent, eruption, and quenching. Additionally, constraints of cooling rates from individual olivine-hosted melt inclusions will allow more accurate reconstruction of pre-eruptive volatile contents using published models of vapor bubble formation (Maclennan, 2017; Tucker et al., 2019; Rasmussen et al., 2020).

In this study, we apply recently developed magma temperature and ascent chronometers in concert to determine P-T-t paths of magmas erupted at arc and ocean island volcanoes. The studied eruptions exhibited a variety of eruptive styles [their volcanic explosivity indices (VEI) range from 1 to 4] and their pre-eruptive magmas contained variable water concentrations (from ∼0.5 to ∼4 wt% H_2O). Previously published determinations of magma decompression rates for the eruptions considered in this study indicate a range of linear decompression rates from ∼0.05 to 0.4 MPa/s (Lloyd et al., 2014; Ferguson et al., 2016; Newcombe et al., 2020). There is increasing evidence that the decompression rate of mafic magmas correlates with eruption explosivity (Ferguson et al., 2016; Cassidy et al., 2018; Barth et al., 2019); however, links between syneruptive T-t and P-t paths have not previously been investigated via petrologic methods. By exploring a range of magma properties and eruptive styles, we aim to identify the dominant controls on syneruptive magma P-T-t paths that can be used to guide future conduit modeling efforts.

Background: Why Would the Temperature of Magma Change During Ascent?

During ascent from depth to the surface, magma experiences an increase in its gravitational potential energy and an increase in its kinetic energy. In order to satisfy conservation of energy, these energy increases must be balanced by a decrease in the internal energy of the magma. Whether or not this decrease in the magma's internal energy is associated with a decrease in temperature depends on the extent to which the system (i.e., the ascending parcel of magma) is open to transfer of heat, work, and mass. If a parcel of magma ascends rapidly enough to prevent significant melt-vapor segregation and conduction of heat across the conduit walls, then its ascent may closely follow an adiabatic path (i.e., the system is closed to transfer of heat and mass). If, furthermore, this parcel of magma experiences minimal syneruptive crystallization, irreversible gas exsolution (Sahagian and Proussevitch, 1996), or viscous heating, then its ascent may be considered approximately isentropic. During isentropic decompression of a melt-vapor mixture, expansion of the magma (which is dominated by expansion of the vapor phase) does work against its surroundings, and this is compensated by a decrease in the enthalpy and temperature of the magma. Isentropic ascent is an endmember scenario that produces maximal cooling (Mastin and Ghiorso, 2001). Temperature changes expected during adiabatic ascent of magma along both isentropic and isenthalpic paths are considered in detail by Mastin and Ghiorso (2001).

A parcel of magma that ascends slowly enough to allow significant loss of heat and/or mass through the conduit walls cannot be approximated as an adiabatic system. Loss of vapor from the magma may trigger degassing-driven crystallization which produces latent heat (Blundy and Cashman, 2005). Irreversible processes such as viscous heating and irreversible vapor exsolution also lead to heat production during magma ascent (Fujii and Uyeda, 1974; Sahagian and Proussevitch, 1996; Koyaguchi, 2005; Mastin, 2005; Vedeneeva et al., 2005; Costa et al., 2007). If minimal expansion or lifting work is done by the magma (e.g., slow-moving magma extruded during a dome-building eruption), and if heat production is able to exceed heat loss by conduction through the conduit walls, then the temperature of the magma may increase during ascent (Blundy et al., 2006; Glazner, 2019).

Here, we consider magma ascent during explosive eruptions of mafic magmas. These magmas have lower viscosities and higher decompression rates (Lloyd et al., 2014; Ferguson et al., 2016; Newcombe et al., 2020) than the andesitic magmas of the dome-building eruptions considered by Blundy et al. (2006) that were inferred to experience syneruptive heating. Conduit models typically neglect to account for temperature variations during ascent (Sahagian, 2005), but the small subset of models that explicitly consider temperature variations during magma ascent do so either by considering the contributions of both adiabatic vapor expansion and latent heat of crystallization to the temperature evolution of the magma (Kavanagh and Sparks, 2009; La Spina et al., 2015), or by making the assumption that the ascending magma follows an isentropic path (Mastin and Ghiorso, 2000; Mastin and Ghiorso, 2001; Campagnola et al., 2016; Kilinc, 2018). In particular, the popular Conflow and Confort models that calculate temperature changes of magmas undergoing isentropic ascent often predict tens of degrees of syneruptive cooling in the conduit (Mastin and Ghiorso, 2000; Campagnola et al., 2016). However, the assumptions of isentropic models are easily violated, e.g., if the magma crystallizes or stalls on ascent, or if melt-vapor segregation occurs. Given the many challenges of numerically reproducing the complex and dynamic conduit environment, we turn instead to the development of syneruptive magma thermometers that can more directly assess syneruptive P-T-t paths of magmas with fewer *a priori* assumptions.

Samples

Olivine phenocrysts containing melt inclusions and/or melt embayments were selected from the 1974 subplinian eruption of Fuego volcano; the 1977 fire-fountain eruption of Seguam volcano; and three eruptions of Kilauea volcano (episode 1 of the 1959 Kilauea Iki fire-fountain eruption, the 1500 CE vigorous fire-fountain eruption, and the 1650 CE subplinian eruption). These samples were selected primarily because their syneruptive ascent histories have been previously constrained using volatile concentration gradients in melt embayments (Lloyd et al., 2014; Ferguson et al., 2016; Newcombe et al., 2020), volatile loss from olivine-hosted melt inclusions (Lloyd et al., 2013), and

concentration gradients of water preserved in olivine and/or clinopyroxene phenocrysts (Lloyd et al., 2016a; Newcombe et al., 2020). These previous studies of syneruptive magma ascent will allow us to examine potential relationships between thermal histories and ascent histories of magmas in the last few seconds to hours of their transport to the surface. The studied eruptions span a range of eruptive styles, from the low-intensity fire-fountain eruptions of Seguam and Kilauea Iki to the high-intensity subplinian eruption of Fuego. Further details of the studied eruptions are provided below.

Samples From the October 1974 Eruption of Volcán de Fuego (Guatemala)

We selected 19 olivine-hosted melt inclusions from the same airfall samples studied by Lloyd et al., (2013, 2014, 2016a). These samples erupted on 17th October, 1974, and were collected during the eruption by S. Bonis of the Instituto Geográphico Nacional, Guatemala City and provided by William Rose (IGSN: ASL000001, ASL000002 and ASL000003). Olivine from this phase of the eruption ranges in composition from Fo_{72} to Fo_{78} (Lloyd et al., 2013). Of the melt inclusions selected, four were previously characterized for major, minor, and volatile element concentrations by Lloyd et al. (2013) (sample names 127-1, 132-2, 136-9, and 134D-R7). The melt inclusions were derived from tephra with a range of clast sizes, and therefore they likely experienced a range of post-eruptive thermal conditions: Twelve of the melt inclusions were derived from ash (particles with diameter < 2 mm; Lloyd et al., 2013); one inclusion was derived from a lapillus (sample 136-9 of Lloyd et al., 2013; lapilli range in size from 2 to 64 mm); and six were derived from the outer rim of a volcanic bomb (sample 134D-R7 of Lloyd et al., 2013; volcanic bombs are classified here as clasts with diameters > 64 mm).

The 17th October event had a volcanic explosivity index (VEI) of 4 and its eruptive column is estimated to have reached a height of ∼15 km (Rose et al., 1978). The average decompression rate of magma erupted during the 17th October subplinian event was estimated by modeling the generation of volatile concentration gradients in olivine-hosted melt embayments. The H_2O, CO_2 and S profiles in four embayments yielded decompression rates between 0.3 and 0.5 MPa/s for magma that ascended from its pre-eruptive storage region (at a depth of ∼10 km) over a time period of 8–12 min and at a velocity of 11–17 m/s (Lloyd et al., 2014). Shapes of water concentration gradients measured across clinopyroxene phenocrysts from this eruption are consistent with the timescales of magma ascent derived from the olivine-hosted melt embayments (Lloyd et al., 2016a).

Samples From the 1977 Eruption of Seguam Volcano (Central Aleutian Arc)

We selected 12 olivine-hosted melt inclusions from a rapidly quenched tephra sample (sample SEG-07-06 of Zimmer et al., 2010). Melt inclusions from this sample were previously reported to contain 3.3 ± 0.33 wt% water and their olivine hosts have compositions that range from Fo_{80} to Fo_{85} (Zimmer et al., 2010). Lloyd et al. (2016a) report water concentrations of clinopyroxene phenocrysts and associated melt inclusions from tephra sample SEG-07-06 and from a coevally erupted lava flow, for which they developed a model of post-eruption water loss from the lava samples during slow cooling. Newcombe et al. (2020) report best-fit decompression rates for the Seguam 1977 eruption spanning 0.02 to 0.23 MPa/s, based on fitting volatile concentration gradients in olivine-hosted melt embayments and fitting water concentration gradients along the crystallographic "a" axis of olivine phenocrysts. Plateaus in sulfur concentration observed along the profiles of melt embayments from Seguam suggest pre-eruptive stalling and/or crystallization of the Seguam magma at a range of depths. Best-fit decompression histories derived from Seguam melt embayments suggest magma ascent durations of 9–320 min from initial pressures of 61–308 MPa (Newcombe et al., 2020).

Samples From Kilauea Volcano (Hawaii)

We selected olivine-hosted melt inclusions from three contrasting summit eruptions of Kilauea volcano, Hawaii, which were previously studied by Ferguson et al. (2016), who used volatile concentration gradients in olivine-hosted melt embayments to determine magma ascent rates during each eruption. A brief description of the three eruptions is provided below.

Episode 1 of the 1959 Kilauea Iki Fire-Fountain Eruption

The Kilauea Iki fire-fountain eruption began on November 14, 1959, and its 16 main eruptive episodes spanned 36 days (Richter et al., 1970; Mueller et al., 2019). Each eruptive episode began with a phase of pyroclastic fountaining and coeval filling of a lava lake, followed by the abrupt cessation of fountaining and subsequent draining of part of the lava lake back into the vent (Eaton et al., 1987). For this reason, magma erupted during every eruptive episode after episode 1 suffered from mixing with lava that drained back into the vent during the previous eruptive episode(s) (Eaton et al., 1987; Wallace and Anderson, 1998; Sides et al., 2014). In order to avoid potential complexities in the ascent and thermal histories of magmas that have mixed with degassed and cooled drainback lava in the conduit, we focus on tephra from episode 1 of the eruption which was the least affected by lava drainback and shallow storage. Fire fountains from episode 1 of the Kilauea Iki eruption reached a maximum height of ∼380 m and produced $\sim 30 \times 10^6$ m^3 of lava over 7 days (Richter et al., 1970; Eaton et al., 1987).

We selected six olivine-hosted melt inclusions from tephra layer ρ17 of Stovall et al. (2011) collected and provided by Bruce Houghton. Tephra from this layer is relatively coarse, with a mean maximum clast size of ∼55 mm (Stovall et al., 2011). The host olivine phenocrysts range in composition from Fo_{86} to Fo_{89} and the inclusions contain 0.65–0.81 wt% water [D. Ferguson, unpublished data; see also Sides et al. (2014)]. Ferguson et al. (2016) used volatile concentration gradients along an olivine-hosted melt embayment from this sample to constrain a magma decompression rate of $\sim 0.05 \pm 0.005$ MPa s^{-1} from 110 MPa (∼4 km depth) during episode 1, corresponding to an ascent duration of ∼36 min at an average velocity of ∼2 ms^{-1}.

The Keanakāko'i Basal Reticulite of the c. 1500 CE Vigorous Fire-Fountain Eruption

The basal reticulite of the Keanakāko'i tephra is thought to have erupted c. 1500 CE from widely spaced vents around the rim of Kilauea's caldera (Swanson et al., 2012; May et al., 2015). The Keanakāko'i basal reticulite forms in a thick layer (up to ∼65 cm) along much of the caldera rim (Swanson et al., 2012). The deposition of reticulite so close to its vent is consistent with its eruption in a high fire fountain (estimated to be >600 m) from a deep caldera (estimated to be ∼200–300 m deep), such that any denser pumice and scoria fell back into the caldera, thereby allowing the preservation of the delicate reticulite along the caldera rim (Swanson et al., 2012). The reticulite is golden-brown in color with clast diameters from <1 cm to ∼20 cm, and it exhibits a distinctive open-cell polyhedral structure (i.e., similar to honeycomb) with vesicularities of ∼95–98 vol.% (May et al., 2015). The formation of this distinctive and delicate texture is thought to require rapid ascent and late vesiculation of supersaturated melt, followed by a period of textural maturation by Ostwald ripening in the eruptive fountain, which is estimated to occur in <20 s (Mangan and Cashman, 1996). Given these textural constraints, we might expect the syneruptive thermal history of the reticulite to be consistent with rapid ascent along a liquid adiabat followed by quenching in air over a timescale on the order of 10 s.

We have analyzed two olivine-hosted melt inclusions from the 1500 CE reticulite also collected by Bruce Houghton. Their host olivine crystals range in composition from Fo_{87} to Fo_{89} and the inclusions contain ∼0.6 wt% water. Ferguson et al. (2016) report magma decompression rates for the basal reticulite of 0.1–0.32 ± 0.02 MPa s^{-1} from an initial pressure of 40 MPa (∼1.5 km depth), based on diffusion modeling of volatile concentration gradients in melt embayments.

The 1650 CE Subplinian Eruption

The 1650 CE subplinian layer 6 deposit of the Keanoakāko'i tephra is a widely dispersed and conspicuously coarse layer of fall scoria (McPhie et al., 1990). The deposit can be mapped to the coast, ∼20 km from the vent, and its dispersal in a southeasterly direction suggests that the eruptive plume reached the jet stream, thereby implying plume heights of ∼10–20 km (Swanson et al., 2012). The layer 6 deposit is thought to be the product of a small-volume, explosive eruption with no evidence for groundwater involvement (McPhie et al., 1990). The compositions of glasses in layer 6 juvenile clasts exhibit linear trends on MgO variation diagrams of TiO_2 and K_2O that are consistent with magma mixing, possibly involving three endmember components (Garcia et al., 2018).

We have analyzed one olivine-hosted melt inclusion from the scoriaceous component of the 1650 CE layer 6 deposit collected by Don Swanson. The olivine host of this melt inclusion has a composition of Fo_{89}, and the inclusion contains 0.6 wt% water. Ferguson et al. (2016) report a magma decompression rate for the layer 6 deposit of 0.45 ± 0.01 MPa s^{-1} from an initial pressure of 60 MPa (∼2 km depth), based on diffusion modeling of volatile concentration gradients in an olivine-hosted melt embayment.

MATERIALS AND METHODS

Analytical Techniques

Melt inclusions and their host olivine phenocrysts were analyzed for major, minor, and trace elements using a Cameca SX100 microprobe (EMP) at the American Museum of Natural History (AMNH). We analyzed linear traverses along the diameters of the melt inclusions (beginning and ending in the adjacent host olivine), with each analysis along the traverse being spaced ∼2 μm apart (see also Newcombe et al., 2014). The traverses were analyzed using a 10 nA beam current and a 15 kV accelerating potential with a focused beam (nominal beam diameter ∼1 μm). On-peak counting times for major elements varied between 5 s (Na), 20 s (Mg, Si, K Ca, Al, and Fe), and 40 s (Mn, Ti, and P). Background counting times for the elements were set to 50% of their on-peak counting times. All analyses were corrected for inter-run calibration offsets using factors determined by replicate analyses of in-house, hydrous basaltic glass standards FR:ND-60-01 and MR:ND-70-01 (Lloyd et al., 2013; Ferguson et al., 2016). Raw data, corrected data, accepted compositions of glass standards, and correction factors are provided in the **Supplementary Data Tables**. Replicate analyses of glass standards FR:ND-60-01 and MR:ND-70-01 yielded average RSDs of <1% for SiO2, <2% for Al2O3 and MgO, and <3% for FeO and CaO. We note that use of a focused beam on hydrous glasses is known to cause sodium loss (London, 2005). We aimed to minimize this effect while maximizing the spatial resolution and precision of our major element analyses by reducing the on-peak counting time for Na to 5s and by analyzing sodium during the first pass of analyses.

Concentrations of volatiles (H_2O, CO_2, S, Cl, and F) in 11 melt inclusions from Seguam volcano were characterized using the Cameca NanoSIMS 50L at the Department of Terrestrial Magnetism, Carnegie Institute of Washington, following previously developed analytical protocols (Hauri et al., 2002, 2011; Lloyd et al., 2014; Ferguson et al., 2016). Samples were mounted in dental resin; polished to 0.25 μm; cleaned in ultrasonic baths of toluene, acetone and isopropanol; baked in a vacuum oven at ∼110°C for several days; pressed into indium mounts; coated in gold; and placed into the sample exchange chamber of the nanoSIMS 1–3 days prior to the beginning of the analytical session. The Cs^+ primary beam was tuned to achieve an approximate beam diameter of ∼5 μm and a current of ∼4 nA, with charge compensation provided by an electron gun. Prior to data collection, the sample area was pre-sputtered for 120 s in order to remove the gold coat and surface contamination. The primary beam was rastered over a 10 × 10 μm area. During data collection, electronic gating was applied to ensure the collection of ions from only the inner 14% of the measurement area (corresponding to an area of 3.7 × 3.7 μm). Negatively charged ions of $^{12}C^-$, $^{16}O^1H^-$, $^{19}F^-$, $^{30}Si^-$, $^{32}S^-$, and $^{35}Cl^-$ were detected simultaneously using six electron multipliers. $^{30}Si^-$ was used as a denominator of all reported ion intensity ratios, and the mass resolution power was sufficient to resolve $^{16}O^1H^-$ from ^{17}O. A selection of basaltic and basaltic andesitic glasses with well-characterized major element and volatile contents were used as standards (see

Supplementary Data Tables). 35 replicate analyses of basaltic andesite standard glass MR:ND-70-01 yielded relative standard deviations (100*standard deviation/mean) of 4.4% for CO_2, 4.5% for H_2O, 2.8% for F, 6.0% for S, and 16.1% for Cl.

We also provide in the **Supplementary Data Tables** analyses of volatile concentrations in five olivine-hosted melt inclusions from Seguam volcano that were measured using the Cameca IMS 6f SIMS at the Department of Terrestrial Magnetism, Carnegie Institute of Washington. The sample preparation protocols and analytical standards were the same as used for the nanoSIMS analyses described above. Analytical protocols and measurements of secondary standards are provided in Newcombe et al. (2020).

Constraint of Syneruptive Thermal Histories Using MgO Zonation in Olivine-Hosted Melt Inclusions

During syneruptive cooling, olivine-hosted melt inclusions typically crystallize a thin rim (on the order of ∼1 μm) on their walls. Rapid crystallization of this olivine rim results in the production of a diffusive boundary layer in the adjacent melt that is depleted in elements that are compatible in olivine (e.g., Mg and Fe) and enriched in incompatible elements (e.g., Al, Ca, Na, K, and Ti). If cooling and crystallization are sufficiently slow, this boundary layer will diffusively propagate toward the center of the melt inclusion. Newcombe et al. (2014) characterized chemical zonation in olivine-hosted melt inclusions from MORB and OIB settings, and they developed a numerical method for using the shape of the MgO zonation in the inclusions to constrain the rate and duration of syneruptive cooling from the liquidus to the temperature corresponding to the lowest measured MgO in the melt. A calculation to demonstrate the expected evolution of MgO zonation in an olivine-hosted melt inclusion in response to cooling and syneruptive crystallization is provided in **Figure 1**. We have applied the method of Newcombe et al. (2014) to olivine-hosted melt inclusions from arc and OIB settings with well constrained ascent histories with the aim of determining syn- and post-eruptive thermal histories of melt inclusions from explosive eruptions of basaltic and basaltic andesitic magmas containing up to ∼4 wt% water. The consideration in this study of hydrous melts warrants reexamination of parameterizations adopted by the model of Newcombe et al. (2014) to account for changes in the physical and chemical properties of basaltic melts resulting from water addition.

Effect of Water Addition and Major Element Composition on the Diffusivity of MgO in Basaltic Melt

The model of Newcombe et al. (2014) applies a temperature-dependent, effective binary MgO diffusivity based on experiments by Chen and Zhang (2008) of olivine dissolution in basaltic melt from the Juan de Fuca (JDF) Ridge. The consideration in this study of melt compositions that are significantly different (particularly in terms of their water concentrations) to JDF basalt raises the question of the extent to which MgO diffusivity (D_{MgO}) varies with melt composition. Natural silicate melts are multicomponent systems, and the diffusion of any one component depends on the concentration gradients of all of the other components. Full treatment of the development of boundary layers within olivine-hosted melt inclusions would require knowledge of the multicomponent diffusion matrix for basaltic and basaltic andesitic melts. While much progress has been made (Kress and Ghiorso, 1995; Liang, 2010; Guo and Zhang, 2016, 2018, 2020), multicomponent diffusion matrices are still only available for dry haplobasaltic and basaltic melts at a few temperatures. Effective binary treatment of MgO diffusion during olivine dissolution has been shown to work well experimentally (Chen and Zhang, 2008) and multicomponent diffusion calculations are consistent with effective binary calculations for MgO (Guo and Zhang, 2020). The advantage of multicomponent diffusion treatment is the ability to simultaneously model diffusion profiles of other major oxides, but the temperature dependence of the multicomponent diffusion matrices are less well constrained than that of the effective binary diffusivity of MgO. Hence, the effective binary treatment is better suited for inferring thermal histories (Newcombe et al., 2014), which is our goal here.

The experimental studies described above constrain D_{MgO} in nominally anhydrous melts; however, no experimental studies are currently available that constrain the effect of H_2O on D_{MgO} in basaltic melts. In order to address this uncertainty in our model, we performed an experiment to determine D_{MgO} in hydrous arc basaltic melt. Our experimental setup is similar to that of the olivine dissolution experiments performed by Chen and Zhang (2008), except that a hydrous arc basalt composition (synthesized using reagent-grade powdered oxides; the composition of the starting material is provided in the **Supplementary Data Tables**) was used in place of JDF basalt, and ∼3.8 wt% water was added to the mixture as $Al(OH)_3$. The powdered starting material was placed in a Ni capsule containing a polished piece of San Carlos olivine. The Ni capsule was placed in a 3/4-inch pyrex-NaCl assembly and was held at 10 kbar and 1225°C in a piston cylinder apparatus (at the Smithsonian Institution) for 2400 s, at which point the experiment was quenched by shutting off the power. The quenched experimental charge was cut and polished along its diameter, and major and minor elements were analyzed by electron microprobe along a traverse normal to the olivine-glass interface. The electron microprobe traverse across the quenched melt reveals that olivine dissolution took place during the experiment, producing diffusive boundary layers that propagated into the adjacent melt (see **Supplementary Figure S1**). In order to assess the likely effect of water addition on D_{MgO}, we have applied the approach of Chen and Zhang (2008) to constrain $D_{MgO} = 3.13(\pm 0.15) \times 10^{-11}$ m^2s^{-1} in our experimental melt at 1225°C, which is a factor of 3.44 higher than D_{MgO} calculated at 1225°C using the parameterization of Chen and Zhang (2008) for dry basalt. Based on this result, when fitting MgO data in melt inclusions containing hydrous arc basaltic melts (i.e., inclusions from Fuego and Seguam) we reduce our cooling timescales (calculated using the Chen and Zhang (2008) parameterization of D_{MgO}) by multiplying by a factor of 0.29 [i.e., we assume the relationship $x \propto \sqrt{D_{MgO}t}$, where x is the characteristic diffusion length-scale and t is time, such that an increase in D_{MgO} by a factor of 3.44 must be

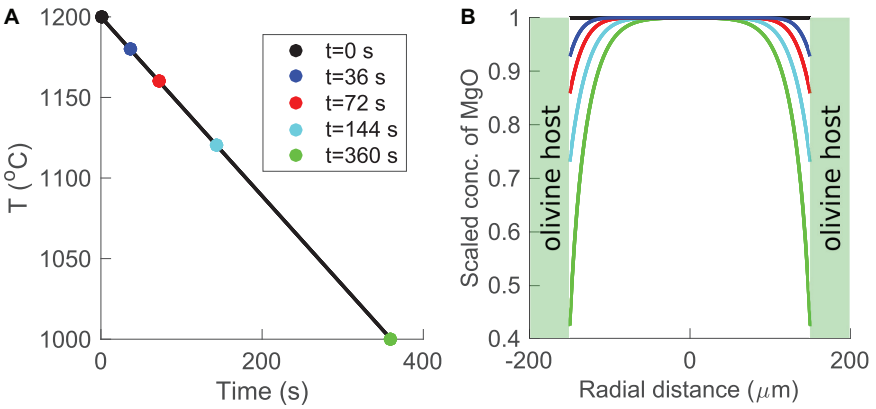

FIGURE 1 | Forward model of the generation of MgO zonation in an olivine-hosted melt inclusion subjected to cooling from 1200 to 1000°C at a rate of 0.6°C/s (based on Figure 7 of Newcombe et al., 2014). **(A)** Temperature-time path imposed by the forward model. Colored circles indicate "snapshots" of the thermal history that are plotted in **(B)**. **(B)** Development of MgO zonation in a 150-μm radius melt inclusion in response to the temperature-time path displayed in **(A)**. The inclusion is assumed to have an initially homogenous composition (black line). As the temperature decreases, the MgO concentration in the melt at the edge of the inclusion evolves according to the temperature-dependent partition coefficient of MgO between melt and olivine (Newcombe et al., 2014). In response to the cooling and crystallization-induced decrease of MgO at the inclusion edges, MgO diffuses from the center to the edges of the inclusion. Blue, red, cyan, and green curves show snapshots of the evolution of MgO zonation in the melt inclusion after 36, 72, 144, and 360 s, respectively. The green shaded regions are olivine. Note that the position of the olivine-melt interface is assumed to be fixed. Mass balance calculations indicate that the width of the olivine growth rim produced during syneruptive cooling is typically ~1% of the radius of the inclusion such that the movement of the olivine-melt boundary can safely be neglected (Newcombe et al., 2014).

compensated by a decrease in t by a factor of 1÷3.44 (which is equal to 0.29)].

We have also assessed potential uncertainties in our modeled timescales associated with the application of the Chen and Zhang (2008) parameterization of D_{MgO} to our Kilauea melt inclusions. These inclusions contain slightly higher water concentrations (~0.65–0.81 wt% H_2O) than JDF basalt (~0.3 wt% H_2O), and they have different major element compositions (e.g., Kilauea basalts are depleted in Al_2O_3 and FeO and enriched in MgO compared to JDF basalts). Zhang et al. (2010) proposed a parameterization of D_{MgO} as a function of anhydrous melt composition, and application of this parameterization suggests that D_{MgO} in anhydrous Kilauea melt could be ~1.5 times D_{MgO} in JDF melt, such that our modeled cooling durations at Kilauea could be off by a factor of ~0.7 (i.e., 1÷1.5) if we assume the Chen and Zhang (2008) parameterization of D_{MgO}. We note that this offset is within the uncertainty of the D_{MgO} parameterization of Zhang et al. (2010), which is able to reproduce experimental data within a factor of ~2, so we consider the Chen and Zhang (2008) parameterization of D_{MgO} to be acceptable for our Kilauea melt inclusions.

Impact of Water Addition on Olivine-Liquid Thermometry

A key component of the model of Newcombe et al. (2014) is the assumption of a simple relationship between temperature and MgO concentration of silicate melt in equilibrium with olivine. Many such olivine-liquid thermometers have been proposed (e.g., Roeder and Emslie, 1970; Ford et al., 1983; Beattie, 1993; Sugawara, 2000; Chen and Zhang, 2008; Putirka, 2008). The original model of Newcombe et al. (2014) adopted a thermometer developed by Chen and Zhang (2008), which was calibrated using dissolution experiments of Fo_{90} San Carlos olivine in basaltic melt from the Juan de Fuca Ridge. Here, we instead adopt the olivine-liquid thermometer of Sugawara (2000), which has the advantages of being calibrated over a wider range of olivine and melt compositions than the thermometer of Chen and Zhang (2008) and of being easy to implement due to the simplicity of the parameterization for which temperature and liquid MgO content are the only variables. We have adapted the Sugawara (2000) thermometer to account for the effect of water on the liquidus temperature of olivine-saturated melt by adding a water-dependent temperature offset based on the results of Médard and Grove (2008):

$$\Delta T_{H_2O} = 40.4^{*}H_2O - 2.97^{*}H_2O^2 + 0.0761^{*}H_2O^3 \quad (1)$$

$$T\,(\mathrm{K}) = 1316 + (12.95/0.68)^{*}\mathrm{MgO} - \Delta T_{H_2O} \quad (2)$$

In equations (1) and (2), T is temperature in Kelvin, ΔT_{H_2O} is degrees by which the liquidus temperature is depressed due to water addition, and H_2O and MgO are in wt%. Temperatures calculated for our Fuego and Seguam melts using equation (2) are up to ~50°C lower than temperatures calculated using the model of Putirka et al. (2007). We have tested the effect of this temperature offset on our modeled thermal histories and we find that increasing our temperatures by ~50°C results in an increase in our best-fit cooling rates by a factor of ~2 (see **Supplementary Material**). We note that, while the choice of thermometer affects absolute values of temperatures and cooling rates calculated by our model, our focus here is on relative changes in temperature and cooling rate during syneruptive magma cooling, and we expect relative differences between thermal histories of the melt inclusions to be preserved with the consistent application of any thermometer.

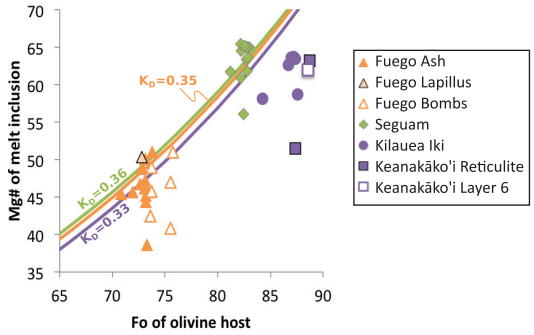

FIGURE 2 | Mg# [molar Mg/(Mg + Fe^{2+})] of melt inclusions against forsterite content of their host olivine crystals. $Fe^{3+}/(Fe^{3+} + Fe^{2+})$ in the melt is assumed to be 0.2 at Fuego (Lloyd et al., 2013), 0.23 at Seguam (Zimmer et al., 2010), and 0.18 at Kilauea (Helz et al., 2017). The colored curves indicate equilibrium between olivine and melt, assuming the composition-dependent model for K_D proposed by Toplis (2005) (Fuego in green, Seguam in orange, and Kilauea in purple). Note that all Kilauea melt inclusions and the majority of Fuego melt inclusions have undergone some amount of post-entrapment crystallization of olivine (i.e., their measured compositions lie below the equilibrium curve), while several of the Seguam inclusions appear to have undergone post-entrapment melting (i.e., their compositions are too Mg-rich to be in equilibrium with their olivine hosts).

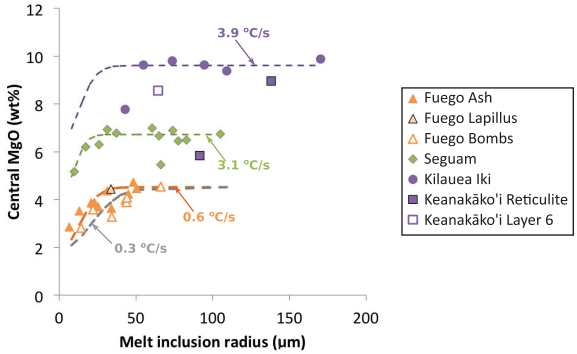

FIGURE 3 | MgO concentration measured in the centers of melt inclusions (not corrected for post-entrapment crystallization) plotted against inclusion radius. Each point represents an average of ~5 MgO measurements. Inclusions from Fuego with radii <~50 μm and inclusions from Seguam with radii <~30 μm are depleted in MgO in their centers due to the propagation of a diffusive boundary layer of MgO depletion produced during syneruptive olivine crystallization on the inclusion walls. Colored dashed curves show relationships between central MgO concentrations and inclusion radii calculated by a one-stage linear cooling model. The initial MgO concentration and cooling rate for each model were set to the average best-fit values determined by fitting MgO concentration gradients in individual melt inclusions from Fuego ash and bombs, Seguam, and Kilauea Iki (see **Figure 4**). The purple curve uses an initial MgO of 9.6 wt% and a cooling rate of 3.9°C/s (designed to match the Kilauea Iki melt inclusions); the green curve uses an initial MgO of 6.7 wt% and a cooling rate of 3.1°C/s (to match the Seguam inclusions); the orange curve uses an initial MgO of 4.5 wt% and a cooling rate of 0.6°C/s; and the gray curve uses an initial MgO of 4.5 wt% and a cooling rate of 0.3°C/s (to match the Fuego bombs).

Choice of Initial and Final Temperatures for Thermal History Modeling

The starting temperature for the thermal history modeling is calculated based on an estimate of the pre-eruptive MgO concentration of each melt inclusion, and the final temperature considered by the model is the temperature corresponding to the lowest measured MgO concentration at the edge of the melt inclusion. For the Fuego melt inclusions (in Fo_{71-76} olivine hosts), we estimated the pre-eruptive MgO concentration of the inclusions by calculating the liquid MgO concentration that would be in equilibrium with the far-field olivine host (**Figure 2**), assuming an Fe-Mg exchange coefficient (K_D) of 0.35 (Toplis, 2005; Lloyd et al., 2013) and a molar Fe^{3+}/Fe^{2+} ratio of 0.20 (Lloyd et al., 2013). Four of the largest Fuego melt inclusions (VF-127-1; VF-132-2; FuegoNL-7; and VF-136-6) were found to contain slightly higher MgO concentrations than implied by equilibrium with their host olivine crystals (see **Figure 2** and **Supplementary Data Tables**); for these inclusions the average of the central ~5 measurements of MgO concentration were adopted as the initial MgO concentration. The Fuego melt inclusions exhibit a clear relationship between their central MgO concentrations and the size of the inclusions (**Figure 3**): On average, the smallest inclusions have the lowest central MgO concentrations and vice versa. This trend is consistent with the idea that the post-entrapment crystallization of this suite of inclusions occurred syneruptively rather than during long-timescale magma chamber processing (i.e., the boundary layer of MgO depletion produced during syneruptive olivine crystallization is able to propagate to the centers of the small inclusions in the suite, while this boundary layer is confined to the edges of the large inclusions such that their central MgO concentrations are unmodified).

For the Seguam melt inclusions (in Fo_{82-83} hosts), calculation of the liquid MgO concentration implied by equilibrium with the far-field olivine [using the model of Toplis (2005) to calculate a K_D of 0.34 and assuming a molar Fe^{3+}/Fe^{2+} ratio of 0.23 (Zimmer et al., 2010)] reveals that several of the melt inclusions have MgO concentrations that lie above their expected equilibrium values (**Figure 2**). This suggests that several of the inclusions may have undergone a small amount of post-entrapment melting prior to eruption. For these inclusions, we assume an initial MgO concentration equal to the average of ~5 MgO measurements from their center. For the few inclusions that appear to have undergone syneruptive post-entrapment crystallization (Seg1-MI2; Seg6-MI2; Seg6-MI3), we assume an MgO concentration implied by equilibrium with their olivine host. Notably, those inclusions for which diffusion has reached the inclusion centers are the smallest in diameter in the Seguam suite (**Figure 3**).

For the Kilauea melt inclusions (in Fo_{83-88} hosts), calculation of the liquid MgO concentration implied by equilibrium with the far-field olivine [using the model of Toplis (2005) to calculate a K_D of 0.33 and assuming a molar Fe^{3+}/Fe^{2+} ratio of 0.18 (Helz et al., 2017)] reveals that all of the melt inclusions in this suite have undergone extensive post-entrapment crystallization (9.25–25%; see **Figure 2**). The Kilauea inclusions are all relatively large (radii range from 43 to 170 μm; see **Figure 3** and **Supplementary Data Tables**), and many of the inclusions exhibit long central plateaus of approximately constant MgO, Al_2O_3,

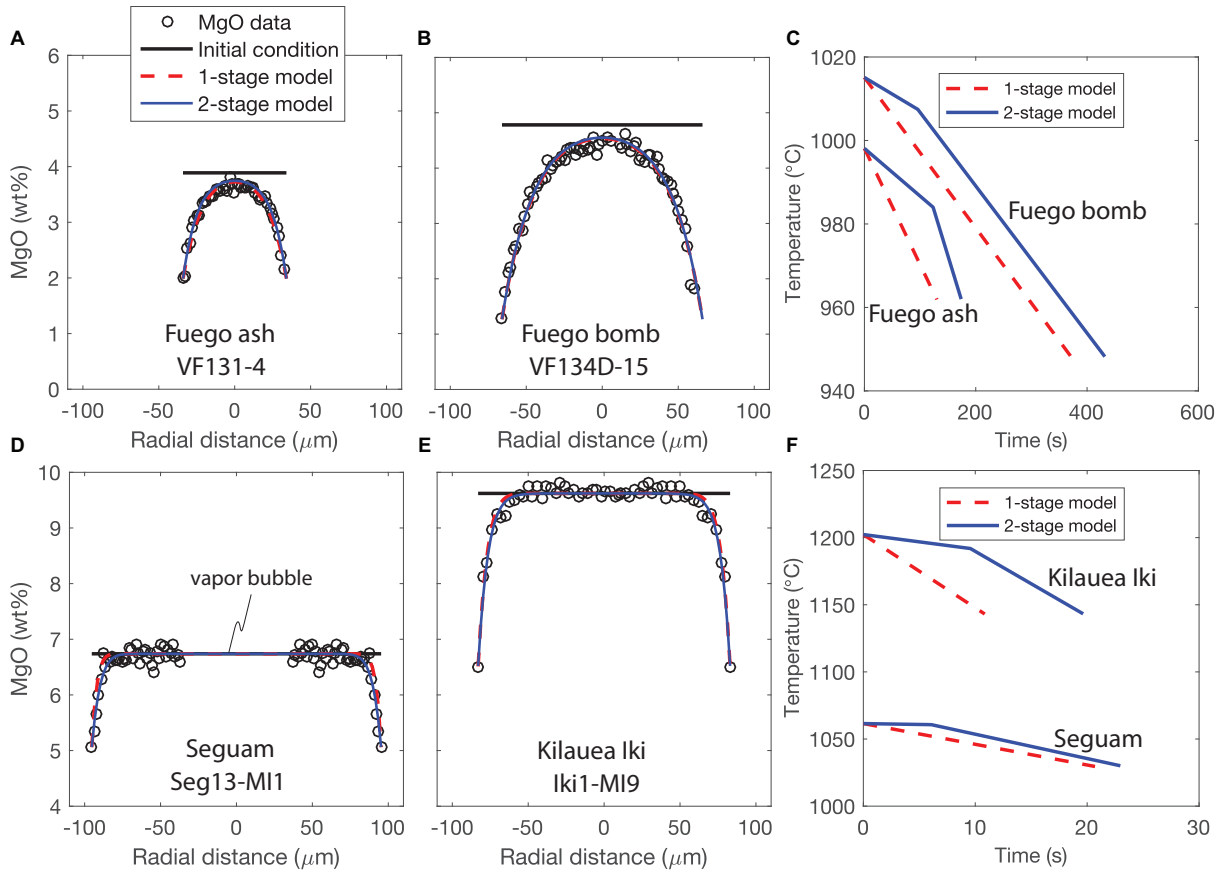

FIGURE 4 | Results of thermal history fitting to MgO concentration gradients in melt inclusions using the model of Newcombe et al. (2014), modified as described in section "Constraint of Syneruptive Thermal Histories Using MgO Zonation in Olivine-Hosted Melt Inclusions." One representative melt inclusion is shown for Fuego ash and volcanic bombs, Seguam, and Kilauea Iki. Data and model fits for all melt inclusions are provided in the Supplement. MgO data from each inclusion have been fit to both one- and two-stage linear thermal histories. MgO data and best-fit thermal history model curves for **(A)** Fuego ash inclusion VF131-4, **(B)** Fuego bomb inclusion VF134D-15, **(D)** Seguam inclusion Seg13-MI1, and **(E)** Kilauea inclusion Iki1-MI9. Best-fit one- and two-stage thermal histories for **(C)** Fuego inclusions VF131-4 and VF134D-15 and **(F)** Seg13-MI1 and Iki1-MI9. Note difficult scales for **(C,F)**.

CaO and SiO_2 concentrations (**Figure 4** and **Supplementary Data Tables**). The existence of central plateaus in MgO and other major element concentrations in these inclusions indicates that the post-entrapment crystallization that impacted the central compositions of the inclusions must have happened long enough prior to ascent and syneruptive quenching that the inclusions had time to diffusively re-homogenize. The minimum timescale required for re-homogenization of a $\sim 10^2$ μm diameter inclusion at magmatic temperatures is only $\sim 10^2$ min (Newcombe et al., 2014), much shorter than the hours to years available for melt re-homogenization during residence of the inclusion in a magma chamber (Danyushevsky et al., 2000, 2002; Lynn et al., 2017; Rasmussen et al., 2018). Once re-homogenized, information about the timescale of post-entrapment crystallization is lost from the melt inclusion, although information concerning the timescale of crystallization may be derived from chemical gradients in the surrounding host olivine (Danyushevsky et al., 2002). The focus of this study is on syneruptive thermal histories of olivine-hosted melt inclusions, so we have used the average of the central ∼5 MgO measurements in each of the Kilauea melt inclusions as the initial MgO concentration for the thermal history modeling. We note that this choice of initial condition does not consider the pre-eruptive magmatic histories of these melt inclusions in the hours to years prior to ascent and eruption, but instead focuses on temperature changes during the seconds to hours of magma ascent and syneruptive quenching.

RESULTS

Characteristics of Chemical Zonation in the Melt Inclusions

We measured major element concentration gradients across a total of 40 olivine-hosted melt inclusions: 19 from Fuego (12 inclusions from ash, 6 inclusions from bomb interiors, and 1 inclusion from lapilli), 12 from Seguam, and 9 from Kilauea (6 inclusions from Kilauea Iki, 2 inclusions from the 1500 CE reticulite, and 1 inclusion from the 1650 CE subplinian deposit). Every melt inclusion analyzed exhibits chemical zonation consistent with that described by Newcombe et al. (2014). All of

the inclusions have regions of MgO depletion at their edges, indicative of rapid crystallization of olivine on the inclusion walls in response to syneruptive cooling. Interestingly, some of the Seguam inclusions (Seg4-MI1, Seg5-MI1, Seg6-MI1, and Seg7-MI1; see **Supplementary Material**) exhibit subtle hints of concave-up concentration gradients of MgO across their centers, which may reflect a period of heating prior to quenching on eruption. This would be consistent with the observation that these inclusions have melt compositions that are too primitive to be in equilibrium with their host olivine (**Figure 2**), which could be explained if they had undergone a small amount of post-entrapment melting prior to eruption. Alternatively, the concave-up MgO profiles could be a consequence of multicomponent diffusion effects (Saper and Stolper, 2020) or they could conceivably be an artifact of melt advection during growth of the large vapor bubbles observed in the majority of these inclusions.

There are some other notable characteristics of the MgO zonation observed in melt inclusions from each eruption. For example, the largest of the melt inclusions erupted during the Seguam and Kilauea Iki fire-fountain eruptions exhibit long plateaus of approximately constant MgO across their centers and sharp decreases in MgO that are confined to the outer ∼10–20 μm of the inclusions (e.g., Seg4-MI1, Seg5-MI1, Seg7-MI1, Seg13-MI1, Seg15-MI1, Iki-MI6, Iki-MI7, and Iki-MI9; see **Figure 4** and **Supplementary Material**). These narrow zones of MgO depletion indicate that the syneruptively generated boundary layer was unable to reach the centers of these melt inclusions before they cooled below the closure temperature for MgO diffusion through the melt. In contrast, syneruptively generated MgO concentration gradients in the Fuego melt inclusions appear to have propagated to the centers of even the largest inclusions in this sample suite.

Results of Thermal History Modeling

We have used the model of Newcombe et al. (2014), modified as described in section "Constraint of Syneruptive Thermal Histories Using MgO Zonation in Olivine-Hosted Melt Inclusions," to find one- and two-stage linear thermal histories that are best able to reproduce the shapes of the MgO concentration gradients measured in our olivine-hosted melt inclusions. A Monte Carlo approach is used to find the best-fit cooling rates and the uncertainties associated with these cooling rates for each melt inclusion (details of this approach are described in Newcombe et al., 2014). Our code is freely available on Github[1], the best-fit thermal histories and fits to the data are provided in the **Supplementary Material**, and the results of fitting the MgO gradients to the one-stage model are summarized in **Figure 5**. Melt inclusions from the 1959 Kilauea Iki fire fountain eruption record the highest syneruptive cooling rates (3–11°C/s) and the shortest cooling durations (4–19 s), while inclusions from the 1974 subplinian eruption of Fuego volcano record the lowest cooling rates (0.1–1.7°C/s) and longest cooling durations (21–368 s) of the studied eruptions (**Figure 5**). Our best-fit cooling rates for Kilauea Iki are in excellent agreement with best-fit cooling rates for this eruption determined by Saper and Stolper (2020). Notably, the inclusions sampled from the interiors of small (∼6 cm diameter) volcanic bombs at Fuego are found to have cooled more slowly on average than inclusions sampled from ash (with particle diameters < 2 mm) during the same eruption (see discussion in section "Influence of Clast Size on Post-Eruptive Thermal Histories").

In addition to fitting MgO concentration gradients in individual melt inclusions, we have also examined trends between the central MgO concentration of the inclusions and the radii of the inclusions (**Figure 3**). Our expectation is that, for a given cooling rate, there will be a critical melt inclusion radius above which the leading edge of the diffusive boundary layer produced during syneruptive olivine crystallization will not be able to propagate to the center of the inclusion, thereby leaving the centers of all inclusions that are larger than this critical radius unmodified from their pre-eruptive compositions. Inclusions smaller than this critical radius should exhibit a trend of decreasing central MgO with decreasing inclusion size (assuming that all inclusions in a suite experience similar cooling rates and have similar initial MgO concentrations). Such a trend was observed in melt inclusions from the Siqueiros transform fault and was successfully reproduced by a syneruptive cooling model (Figure 5 of Newcombe et al., 2014). Similar trends are observed here at Seguam and Fuego, and these trends can also be reproduced by single-stage linear cooling models (see curves on **Figure 3**). At Seguam, the critical radius above which the central compositions of the inclusions are unmodified from their pre-eruptive values is ∼30 μm, while at Fuego, the critical radius is ∼40 μm for the ash-derived melt inclusions and >60 μm for the bomb-derived melt inclusions (i.e., all of the bomb-derived inclusions have compositions that appear to have been modified by the propagation of syneruptive boundary layers to their centers). We note that inclusion Seg4-MI1 appears to be an outlier of the central MgO vs. melt inclusion radius relationship observed at Seguam; however, this particular inclusion is hosted in lower forsterite ($Fo_{81.2}$) olivine than other inclusions in this suite, and despite the relatively low MgO content of this inclusion, its central composition does not appear to have been modified by syneruptive boundary layer propagation (see **Supplementary Material** and **Data Tables**). This inclusion may have been picked up from a cooler, more evolved part of the magmatic system during ascent.

The model curves on **Figure 3** were generated using the average best-fit cooling rate determined by fitting MgO profiles across individual inclusions from each deposit: the Fuego ash cooling model assumes a cooling rate of 0.6°C/s; the Fuego bomb cooling model assumes a cooling rate of 0.3°C/s; and the Seguam cooling model assumes a cooling rate of 3.1°C/s.

Unlike the Seguam and Fuego inclusions, melt inclusions from Kilauea do not exhibit clear trends between their central MgO concentrations and inclusion size. The majority of these inclusions have plateaus of approximately constant MgO across their centers, with narrow zones of MgO depletion confined to the outer few tens of microns of the inclusions. All of the inclusions from Kilauea have undergone large amounts (∼10–25%) of post-entrapment olivine crystallization (see **Supplementary Data Tables**). The central plateaus of MgO concentration across these inclusions

[1] doi: 10.5281/zenodo.3998246

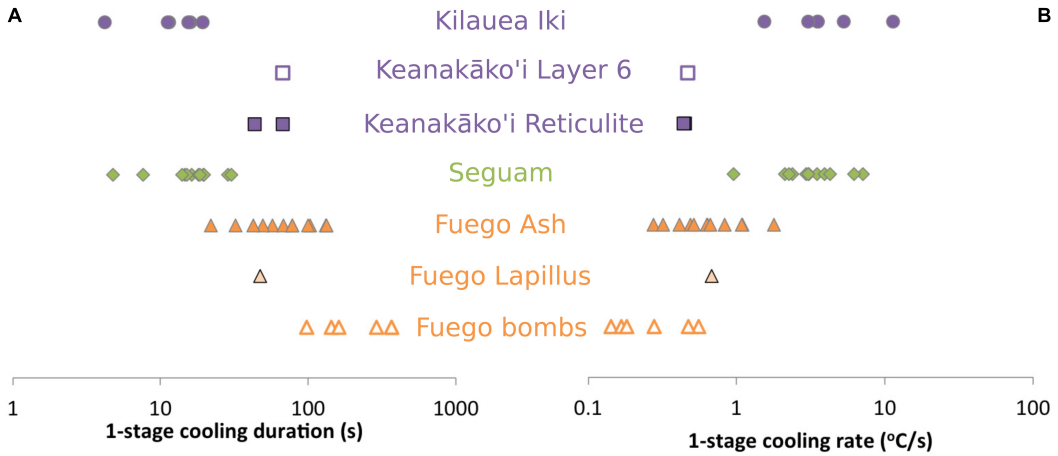

FIGURE 5 | Results of thermal history modeling **(A)** Best-fit cooling durations obtained by fitting MgO concentration gradients in olivine-hosted melt inclusions to a one-stage linear cooling model. **(B)** Best-fit cooling rates obtained by fitting MgO concentration gradients in olivine-hosted melt inclusions to a one-stage linear cooling model. Estimated errors on best-fit parameters are provided in the **Supplementary Data Tables**.

indicate that this post-entrapment cooling and crystallization occurred long enough prior to eruption that the inclusion compositions were able to re-homogenize before the generation of syneruptive boundary layers. The relatively uniform central MgO concentrations of the Kilauea Iki inclusions is consistent with a model of rapid syneruptive cooling (the Kilauea cooling model curve on **Figure 3** assumes a cooling rate of 3.9°C/s) such that only inclusions with radii <30 μm (i.e., smaller than any of the inclusions analyzed) would have their center compositions modified by boundary layer diffusion.

In summary, we find significant differences between best-fit thermal histories of melt inclusions from Fuego ash, Fuego bombs, Seguam, and Kilauea. These differences can be distinguished by fitting MgO concentration gradients in individual melt inclusions from each deposit, but they can also be discerned by examining trends in central MgO versus inclusion size.

Relationship Between Syneruptive Cooling Rates and Syneruptive Decompression Rates

We observe a negative correlation between syneruptive magma decompression rates and cooling rates (**Figure 6**). Magmas erupted during fire-fountain-style eruptions (Seguam, Kilauea Iki, and the Keanakāko'i reticulite) decompressed relatively slowly (Ferguson et al., 2016; Newcombe et al., 2020) and experienced relatively rapid cooling over relatively short durations, while magmas erupted during subplinian eruptions (Fuego and the Keanakāko'i layer 6 deposit) decompressed relatively rapidly (Lloyd et al., 2014; Ferguson et al., 2016) and experienced relatively slow cooling over relatively long durations. The origins of the correlation observed in **Figure 6** are discussed in section "Causes of Variations in Best-Fit Thermal Histories Among Different Eruptions."

DISCUSSION

Influence of Clast Size on Post-eruptive Thermal Histories

A recent study by Lloyd et al. (2013) characterized water concentrations of olivine-hosted melt inclusions from clasts of different sizes (fine-grained ash, lapilli, and bombs) erupted at Fuego on 17th October, 1974, and they found that those inclusions from the interiors of the large bomb clasts had lost more water than the inclusions derived from the fine-grained ash. This finding is consistent with the longer expected durations of post-eruptive cooling of large versus small clasts based on simple conductive cooling models.

Conductive cooling models are relatively straightforward to implement and they provide estimates of the thermal histories experienced by volcanic clasts as a function of clast diameter and distance from the cooling surface. However, many parameters required by these models are poorly constrained (see analysis by Birnie and Dyar, 1986) and the models make many simplifying assumptions (e.g., the easiest models to implement are analytical solutions to the heat equation that assume a constant boundary temperature) such that they cannot capture the complexities of syn- and post-eruptive thermal histories of real volcanic clasts. For example, pyroclasts likely break up and change shape during eruptions; grains may migrate from center to edge of a pyroclast (or vice versa) during eruption; tephra may suffer comminution in the conduit; lavas may experience drain-back and re-eruption; clasts may be re-heated by subsequent eruptive events; or post-depositional processing may dislodge individual grains from large clasts. Given the many simplifying assumptions and limitations of most conductive cooling models, and the importance of cooling rate as a control on physical properties of erupting magma (and the ability of olivine-hosted melt inclusions to preserve pre-eruptive water concentrations), much effort has been made to develop techniques for directly measuring

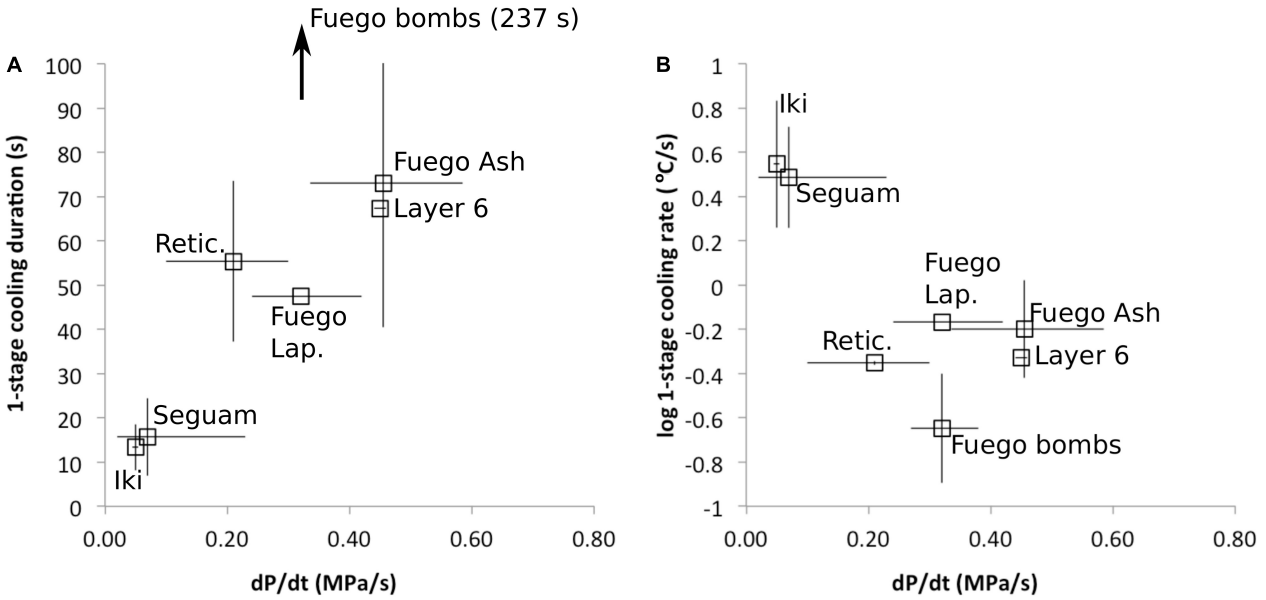

FIGURE 6 | Average best-fit cooling durations and cooling rates versus best-fit decompression rates for each eruption. Decompression rates (and associated error bars) are from the one-stage ascent models of Lloyd et al. (2014), Ferguson et al. (2016), and Newcombe et al. (2020). **(A)** Average best-fit cooling durations are positively correlated with magma decompression rate. Melt inclusions from the subplinian eruptions (Fuego and the Keanakāko'i layer 6 deposit) experienced longer durations of syneruptive cooling and higher magma decompression rates on average than inclusions from the fire-fountain eruptions (Seguam, Kilauea Iki, and the Keanakāko'i Reticulite). **(B)** Average best-fit cooling rates are negatively correlated with magma decompression rate. Inclusions from the subplinian eruptions experienced slower cooling, consistent with cooling during ascent in the conduit just prior to quenching on eruption (and/or cooling in the volcanic plume), while inclusions from the fire-fountain eruptions experienced rapid cooling, consistent with sub-aerial quenching, but not consistent with significant cooling in the conduit just prior to eruption.

syn-eruptive cooling rates of pyroclasts (Zhang et al., 1997, 2000; Gottsmann and Dingwell, 2002; Xu and Zhang, 2002; Potuzak et al., 2008; Nichols et al., 2009; Newcombe et al., 2014; Saper and Stolper, 2020).

The technique developed by Newcombe et al. (2014) of using MgO concentration gradients in olivine-hosted melt inclusions to constrain their syneruptive thermal histories provides a direct record of syn- and post-eruptive magma temperatures during cooling from liquidus temperature to the temperature corresponding to the lowest measured MgO in the melt. This record could potentially be used to identify slowly cooled inclusions, and thereby assess the likelihood of syn- or post-eruptive water loss from the inclusions prior to making expensive and time-consuming measurements of their volatile contents. Additionally, syneruptive cooling rates determined from MgO zonation in melt inclusions can be used to estimate the closure temperature for CO_2, which is an important parameter for assessing the extent of CO_2 diffusion into melt inclusion vapor bubbles (Maclennan, 2017; Tucker et al., 2019; Rasmussen et al., 2020). To our knowledge, it is the only technique currently available that enables multi-stage syneruptive thermal histories of magma to be constrained.

We have tested the ability of this technique to resolve variations in post-eruptive thermal histories by applying it to the same Fuego ash, lapilli, and bomb samples considered by Lloyd et al. (2013). We observe that the mean duration of cooling experienced by inclusions derived from the bomb clasts is longer (up to ∼6 min; see **Figure 5A**) than the mean duration of cooling experienced by inclusions derived from ash (up to ∼2 min; **Figure 5A**), confirming expectations of their relative cooling durations based on conductive cooling models [e.g., Lloyd et al. (2013) use the model of Recktenwald (2006) to estimate post-eruptive cooling durations from ∼1030 to ∼450°C of ∼10 min in the interior of the Fuego bombs and <1 s for the fine-grained ash].

It is notable that the best-fit cooling durations for the ash-derived melt inclusions are significantly longer than the <1 s post-eruptive cooling duration calculated by the conductive cooling model employed by Lloyd et al. (2013). In part, this is due to the assumption made by this conductive cooling model of a constant ambient temperature surrounding the pyroclasts of 30°C, while models of the temperature evolution of fire fountains and volcanic plumes suggest that the ambient temperature experienced by pyroclasts as they exit the conduit decreases from the eruption temperature to temperatures below the closure temperatures for H_2O and MgO diffusion over time periods of $\sim 10^1$ s (Hort and Gardner, 2000; Porritt et al., 2012; Ayris et al., 2014). In addition to post-fragmentation cooling, it is likely that the magma experienced cooling in the conduit prior to fragmentation in response to adiabatic expansion of vapor bubbles, thereby further increasing the durations of cooling recorded by MgO zonation in the ash-derived melt inclusions.

Assessment of the Contribution of Syneruptive Water Loss to Apparent Temperature Decreases Recorded by Olivine-Hosted Melt Inclusions

In addition to post-eruptive water loss from melt inclusions derived from large clasts, Lloyd et al. (2013) discuss the possibility that water could be diffusively lost from olivine-hosted melt inclusions during magma ascent and degassing in the conduit. This raises the question of the extent to which water loss (which is known to drive olivine crystallization) could be contributing to the apparent temperature decreases inferred from MgO zonation in the Fuego inclusions. In order to address this question, we have calculated the expected diffusive water loss from melt inclusions with radii of 10–80 μm, positioned 110 μm away from the nearest edge of their host olivine crystal, during magma ascent from 220 MPa to the surface (**Figure 7A**). Model setup and parameters are provided in the caption to **Figure 5**. For ascent durations of 10 min (Lloyd et al., 2014), we calculate that melt inclusions with radii as small as 10 μm would lose < 2% of their initial water. This water loss would drive an amount of olivine crystallization equivalent to a temperature decrease of < 4°C [assuming an initial water concentration of 4.2 wt% and the H_2O-liquidus temperature function of Médard and Grove (2008)]. Thus, we consider cooling rather than water loss to be the dominant driver of syneruptive crystallization in our Fuego ash melt inclusions.

It is apparent on **Figure 7B** that the bomb-derived melt inclusions have higher calculated amounts of cooling than the ash-derived inclusions, consistent with the lower closure temperature for MgO afforded by slower cooling of these inclusions (see further discussion in the **Supplementary Material**), and also consistent with some amount of post-eruptive water loss from the bomb-derived inclusions prior to passing through the closure temperature for MgO. The total amount of post-eruptive water loss from the bomb-derived inclusions is estimated to be ∼1 wt% (Lloyd et al., 2013). If this water loss happened above the closure temperature for MgO, it would drive crystallization equivalent to a temperature drop of 37.5°C. However, the temperature drop recorded by the bomb melt inclusions is only ∼20°C greater than recorded by the ash inclusions, suggesting that much of the post-eruptive water loss happened after the cessation of post-entrapment olivine crystallization and diffusion of MgO through the melt. This makes sense given the higher diffusivity, and hence lower closure temperature, of H_2O.

Causes of Variations in Best-Fit Thermal Histories Among Different Eruptions

Figures 5, **6** demonstrate variations in best-fit thermal histories among our studied eruptions. Some of this variability can be explained as a result of variable clast sizes; e.g., the slower cooling experienced by Fuego bombs versus ash (section "Influence of Clast Size on Post-Eruptive Thermal Histories"). However, clast size is not responsible for all of the observed variation; e.g., our Fuego ash-derived melt inclusions record slower cooling than our Kilauea Iki inclusions despite the smaller average grain size of Fuego ash compared with the average grain size of the Kilauea Iki tephra. Instead, it appears that eruptive style may play a role in controlling the thermal histories recorded by our melt inclusions

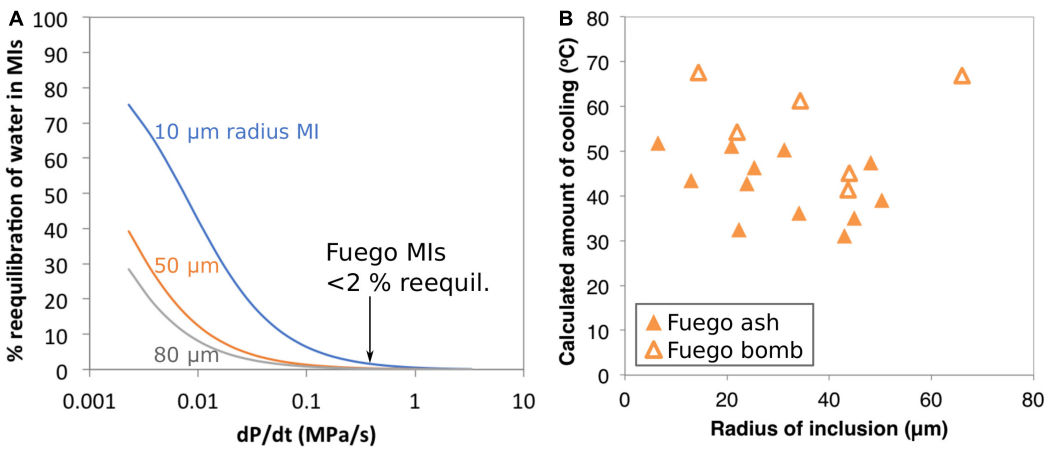

FIGURE 7 | (A) Model of diffusive water loss from olivine-hosted melt inclusions during syneruptive magma decompression. Calculations are shown for melt inclusions with radii of 10, 50, and 80 μm, positioned 110 μm away from the nearest edge of their host olivine crystal. The magma is assumed to ascend from 220 MPa to the surface and to contain an initial water concentration of 4.2 wt%. Parameters for this calculation are chosen based on observations of Fuego olivine-hosted melt inclusions and embayments (Lloyd et al., 2013, 2014). Water diffusivity through olivine is 2.45×10^{-11} m^2s^{-1} based on the Arrhenius relationship from Barth et al. (2019) and assuming 1D diffusion along the crystallographic 'a' direction at 1030°C. The partition coefficient for water between melt and olivine is assumed to be 0.001 and the external magma is assumed to follow a closed-system degassing path (Newman and Lowenstern, 2002). At a magma decompression rate of ∼0.4 MPa/s (Lloyd et al., 2014) we expect very little water loss (<2%) from the Fuego melt inclusions during ascent. **(B)** Calculated amount of cooling (i.e., the temperature implied by the maximum measured MgO minus the temperature implied by the minimum measured MgO in each melt inclusion) versus inclusion radius. The lack of a clear negative correlation between these variables supports the conclusion of the calculations in **(A)** that the Fuego inclusions lose minimal water during magma ascent. The bomb-derived inclusions have higher calculated temperature drops on average than the ash-derived inclusions, consistent with slower cooling of the bomb-derived inclusions to a lower MgO closure temperature and/or post-eruptive water-loss-driven olivine crystallization.

(**Figure 6**); e.g., tephra from the Kilauea Iki and Seguam fire fountain eruptions experienced more rapid cooling than tephra from the higher VEI eruptions that generated ash clouds (Fuego and the Keanakāko'i layer 6 deposit).

Why would tephra from the more explosive eruptions experience slower cooling? One possibility is that post-fragmentation cooling of tephra in subplinian ash columns could be slower than post-fragmentation cooling in fire-fountain plumes. Several models of the temperature evolution of volcanic plumes suggest that tephra rapidly cools below the closure temperature of MgO within $\sim 10^1$ s in both fire-fountain plumes (Porritt et al., 2012) and during Plinian eruptions (Sparks, 1986; Hort and Gardner, 2000). Models and experiments by Ayris et al. (2014) suggest that HCl adsorption by volcanic glasses at temperatures of ∼200–800°C can occur over minute timescales in volcanic plumes, although we note that these adsorption reactions occur below the closure temperature for MgO diffusion. Based on these modeling efforts, we consider it unlikely that the longer thermal histories we observe for our subplinian eruptions are a result of slower post-fragmentation cooling.

Another possibility for explaining the longer cooling durations recorded by melt inclusions from our more explosive eruptive deposits is that the carrier magma for these melt inclusions contained a high vapor fraction in the shallow conduit that drove cooling via adiabatic decompression during the last few minutes of magma ascent in the conduit (considered in greater detail below). We cannot definitively rule out either endmember scenario described above (or indeed, a hybrid model in which the subplinian tephras experienced slower cooling than the fire-fountain tephras both pre- and post-fragmentation). However, regardless of which scenario is correct, the following observations allow us to place constraints on the pre-eruptive P-T-t paths of these magmas during their ascent through the conduit:

- Our largest Fuego and Seguam melt inclusions have central MgO concentrations that are approximately in equilibrium with their far-field olivine hosts (**Figures 2**, **3**). This requires the net temperature change between melt inclusion entrapment and the onset of syneruptive cooling to be minimal (see section "Do the MgO Plateaus Observed in Our Kilauea and Seguam Melt Inclusions Require Approximately Isothermal Magma Ascent, or Are More Complex Thermal Histories Possible").
- Our largest Seguam and Kilauea Iki melt inclusions have plateaus of MgO across their centers and narrow zones of MgO depletion at their edges that are consistent with approximately isothermal ascent followed by quenching on eruption (although we note that such profiles may not *require* isothermal ascent; see section "Do the MgO Plateaus Observed in Our Kilauea and Seguam Melt Inclusions Require Approximately Isothermal Magma Ascent, or Are More Complex Thermal Histories Possible").

In the following sections, we use these constraints and our best-fit thermal histories to assess the validity of syneruptive temperature variations calculated by conduit models.

Comparison of Estimated Magma P-T-t Paths With Expectations Based on the Isentropic "Conflow" Model

The observations described in section "Characteristics of Chemical Zonation in the Melt Inclusions" and section "Results of Thermal History Modeling" suggest that magmas erupted during the Kilauea Iki and Seguam fire-fountain eruptions ascended approximately isothermally, while magmas represented by the 1974 Fuego Ash, the Keanakāko'i basal reticulite, and the Keanakāko'i layer 6 deposit underwent net cooling during the last ∼minute of ascent and eruption. As described in the Introduction, the most reasonable process responsible for driving magma cooling on ascent is adiabatic expansion of a vapor phase. In this section, we compare the thermal histories we have determined using MgO concentration gradients in olivine-hosted melt inclusions to results of calculations using the conduit model "Conflow" (Mastin and Ghiorso, 2000; Mastin and Ghiorso, 2001; Campagnola et al., 2016) to explore the meaning and implications of the syneruptive thermal histories experienced by each of the magmas erupted at Fuego, Seguam, and Kilauea.

The Conflow model is used here to calculate the expected changes in temperature, pressure, velocity, and vapor volume fraction during syneruptive ascent of magmas at Fuego, Seguam, and Kilauea volcanoes. This model is one of few existing conduit models that consider temperature changes of magma during ascent (Sahagian, 2005). Assumptions made by the Conflow model include: (1) the magma-gas mixture is treated as a homogeneous fluid (i.e., there is no relative movement between gas and liquid during ascent); (2) gas exsolution is assumed to follow equilibrium solubility laws; (3) the conduit is assumed to be vertical and cylindrical; (4) flow properties are uniform across the radius of the conduit (i.e., the model is one-dimensional); (5) flow is assumed to be steady-state; (6) no heat is transferred across the conduit walls; (7) gas, melt, and crystals are at thermal equilibrium; (8) H_2O is the only vapor species; (9) no vapor escapes across the conduit walls; (10) no crystallization occurs during ascent; and (11) magma ascent is assumed to be adiabatic and reversible (i.e., the magma-gas mixture follows an isentropic path). The model is designed to be most applicable to sustained eruptions of rapidly ascending magmas (e.g., basaltic fire-fountain eruptions like the eruptions of Seguam and Kilauea Iki, and Plinian or subplinian eruptions like the Fuego 1974 eruption), and justifications and limitations of the above listed model assumptions are provided in Mastin and Ghiorso (2000). In addition to the assumptions listed above, we further assume a constant conduit diameter of 10 m (Barth et al., 2019), zero crystallinity, and a fragmentation criterion of 0.75 vapor volume fraction. Additional input parameters and model outputs are provided in the **Supplementary Data Tables**.

The Conflow model calculates the temperature change of ascending magma by applying the following expression of energy conservation (Mastin and Ghiorso, 2001):

$$dh + udu + gdz = 0 \quad (3)$$

where h is specific enthalpy of the magma-gas mixture, u is velocity, z is depth, and g is gravitational acceleration. Integration of equation (3) gives the following expression (Mastin and Ghiorso, 2000):

$$h = h_1 + \left(u_1^2 - u^2\right) + g(z_1 - z) \quad (4)$$

where h_1 is the enthalpy of the melt-vapor mixture at the base of the conduit, u_1 is the velocity at the base of the conduit, and z_1 is the depth at the base of the conduit. The enthalpy of a crystal-free melt-vapor mixture can be calculated as follows (Mastin and Ghiorso, 2000):

$$h = m_g h_g + m_M h_M \quad (5)$$

where m_g and m_M are the mass fractions of gas and melt, respectively, and h_g and h_M are the specific enthalpies of gas and melt. The specific enthalpy of water vapor is a function of pressure and temperature and can be calculated using the method of Haar et al. (1984). Similarly, the specific enthalpy of the melt is a function of temperature, pressure and composition, and can be calculated using the method of Ghiorso and Sack (1995). As the model magma ascends through the conduit, its enthalpy at each pressure is calculated using equation (2). The temperature of the magma is then adjusted until the enthalpy of the melt-vapor mixture calculated by equation (3) is in agreement with the enthalpy prescribed by equation (2) (Mastin and Ghiorso, 2000). We note that the assumption made by the Conflow model of isentropic ascent produces maximal cooling because the model neglects to account for heat-producing processes such as crystallization and also prevents the loss of vapor from the system (Mastin and Ghiorso, 2001). As such, ascent-driven temperature decreases predicted by Conflow calculations should be considered upper bounds.

Figure 8 shows a comparison between temperature-time paths calculated by Conflow and best-fit temperature-time paths determined by fitting MgO concentration gradients in olivine-hosted melt inclusions. For each eruption, we plot an overall best-fit thermal history determined by averaging the best-fit parameters for all of the individually fit melt inclusions.

At Kilauea Iki, Conflow predicts that the magma undergoes very little cooling on ascent (**Figure 8**). This is consistent with our thermal history modeling based on MgO zonation in the olivine-hosted melt inclusions from this eruption: Several of the inclusions exhibit plateaus of MgO concentration across their centers that are consistent with approximately isothermal magma ascent. The lack of adiabatic cooling experienced by Kilauea Iki magma is likely a result of the low initial water concentration of the magma. The relatively dry Kilauea Iki magma exsolves water vapor very late in its ascent history (**Figure 9A**), so the magma follows a liquid-only adiabat for most of its ascent. Significant cooling begins just a few hundred meters from the surface when water vapor rapidly exsolves, driving fragmentation, greater adiabatic expansion and cooling. Short durations ($\sim 10^1$ s) of cooling implied by MgO decreases in the outer $\sim 10^1$ μm of the melt inclusions are consistent with expected durations of sub-aerial quenching in a fire fountain (Porritt et al., 2012). We note that the lack of evidence of cooling during ascent of the Kilauea Iki magma is consistent with the rise-speed-dependent model for fire-fountain eruptions in which vapor bubbles are retained in the magma in which they formed (Parfitt and Wilson, 1995). On the other hand, our Kilauea Iki results may be in conflict with the collapsing foam model (Jaupart and Vergniolle, 1989) in which fire-fountain eruptions are driven by the ascent of a CO_2-rich foam through the conduit. In this case we would expect much longer durations of cooling in the conduit, driven by adiabatic

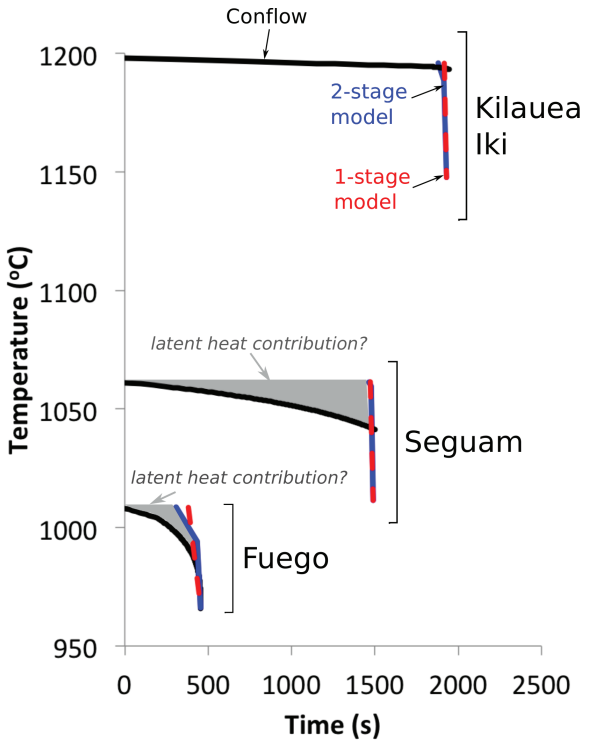

FIGURE 8 | Thermal histories of syneruptive magmas from Fuego, Seguam, and Kilauea Iki, as determined by fitting melt inclusion MgO concentration gradients to one-stage (red dashed lines) and two-stage (blue lines) cooling models, and as calculated by the 'Conflow' model (Mastin and Ghiorso, 2000; Campagnola et al., 2016) (black curves). At Kilauea Iki, the Conflow model suggests that the magma cooled very little during ascent through the conduit. We interpret the ~10 s of cooling recorded by the inclusions to represent quenching in the fire-fountain. At Seguam and Fuego, we do not find good agreement between our inclusion-derived thermal histories and the Conflow calculation: Conflow predicts 20–40°C of magma cooling during ascent, while the MgO concentrations in the centers of our Seguam and Fuego inclusions are approximately in equilibrium with their olivine hosts, which suggests that they did not experience net cooling during ascent. One- and two-stage cooling model parameters are averages of parameters obtained by fitting individual melt inclusions from a given eruption (see **Supplementary Data Tables**). Values of input parameters for the Conflow model curves (e.g., initial ascent velocity, initial pressure and magma composition) are provided in the **Supplementary Data Tables**. Initial ascent velocities for Seguam and Kilauea Iki are based on ascent histories derived from volatile concentration gradients along melt embayments; the choice of initial velocity and initial pressure determines the duration of the calculated ascent history for each of these eruptions. For the subplinian Fuego eruption, we assume that the magma reaches sonic velocity at the surface (i.e., the theoretical maximum velocity). Application of this assumption for the Conflow calculation results in magma ascent velocities that are comparable to those obtained by fitting volatile concentration gradients in melt embayments (Lloyd et al., 2014).

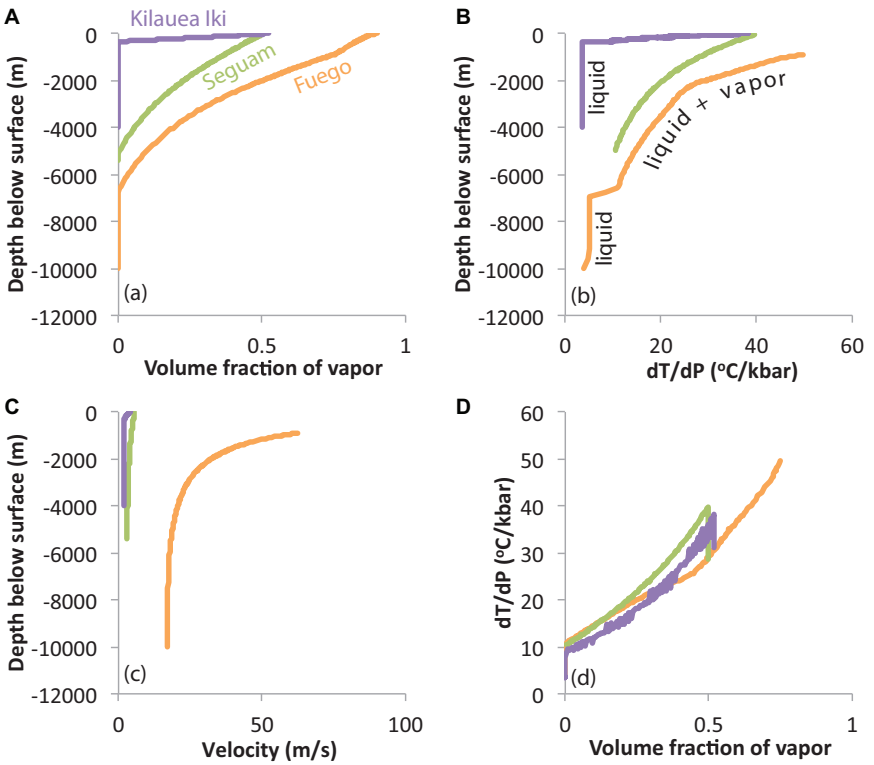

FIGURE 9 | Results of Conflow modeling of the Fuego, Seguam, and Kilauea Iki eruptions. **(A)** Relationships between volume fraction of exsolved vapor and depth in the conduit. Fuego and Seguam magmas each begin their ascent histories with ∼4 wt% water, so these magmas exsolve a vapor phase at greater depths than the relatively dry (∼0.75 wt%) magma erupted at Kilauea Iki. **(B)** Variations in the slope of the adiabat (dT/dP) with depth. Prior to exsolution of a vapor phase, dT/dP of silicate liquid is relatively low (≤5°C/kbar). Following the exsolution of vapor dT/dP rapidly increases in response to adiabatic expansion and cooling of the vapor (which has a much higher thermal expansivity than the silicate liquid). **(C)** Variations in magma ascent velocity with depth. **(D)** Relationship between dT/dP and volume fraction of vapor in the magma. Despite significant differences among our studied eruptions for all other parameters explored in this figure, the relationships between dT/dP and vapor volume fraction are approximately identical, illustrating that vapor volume fraction is the dominant control on dT/dP during adiabatic magma ascent.

expansion of the vapor-rich foam. It is possible that the collapsing foam model could apply to the Keanakāko'i basal reticulite and the Keanakāko'i layer 6 deposit, both of which exhibit longer cooling durations (∼44–67 s) than those observed at Kilauea Iki; however, as noted in section "Samples From Kilauea Volcano (Hawaii)," the formation of reticulite is estimated to occur in <20 s (Mangan and Cashman, 1996), so textural constraints suggest that expansion of a foam layer in the conduit may not be a viable explanation for the relatively long thermal histories observed for the Keanakāko'i basal reticulite. An alternative explanation for the longer cooling durations observed for the Keanakāko'i basal reticulite is the effect of clast size (see section "Influence of Clast Size on Post-Eruptive Thermal Histories"). We do not have constraints on the size of the specific clasts from which our reticulite melt inclusions were derived, but we note that clasts of up to ∼20 cm have been observed in the Keanakāko'i basal reticulite (May et al., 2015). Clast sizes of just a few cm could explain the slower cooling rates experienced by our reticulite-derived melt inclusions.

At Seguam and Fuego, we do not find good agreement between the Conflow model and our thermal histories determined from modeling of MgO gradients in olivine-hosted melt inclusions. Conflow predicts cooling of ∼20°C during ascent of the Seguam magma over a time period of ∼40 min (**Figure 8**), while plateaus of MgO concentration across the centers of the largest Seguam melt inclusions are suggestive of approximately isothermal magma ascent. As described in section "Characteristics of Chemical Zonation in the Melt Inclusions," some inclusions exhibit hints of concave-up MgO profiles across their centers that could be indicative of a small amount of magma heating during ascent, but the Conflow model predicts monotonic cooling. As observed at Kilauea, MgO decreases in the outer $\sim 10^1$ μm of Seguam melt inclusions are consistent with expected durations ($\sim 10^1$ s) of sub-aerial quenching in a fire-fountain plume and thus do not appear to require any cooling in during ascent in the conduit.

Our best-fit thermal histories for Fuego melt inclusions provide an excellent match to the overall amount of cooling predicted by Conflow, but we find shorter durations of cooling than the Conflow model [Conflow predicts cooling of ∼40°C over ∼8 min during ascent of the Fuego magma, while our thermal history modeling of Fuego ash-derived melt inclusions

suggests cooling of ∼40°C over 0.4–2.2 min]. Our Fuego melt inclusion MgO zonation profiles do not enable us to constrain the ascending magma's thermal history prior to the final couple of minutes of syneruptive ascent and quenching; however, the fact that the centers of our largest Fuego inclusions are approximately in equilibrium with their olivine hosts (**Figures 2**, **3**) suggests minimal *net* change in temperature from entrapment until the final couple of minutes of ascent and eruption.

The mismatch between the Conflow model and our best-fit thermal histories at Fuego and Seguam suggest that the assumption of isentropic ascent made by the Conflow model may be inappropriate for these eruptions. Unlike the relatively dry Kilauea magma, Fuego and Seguam magmas contain ∼4 wt% water. Degassing of this water begins at ∼300 MPa (Newcombe et al., 2020) and likely triggers crystallization (Blundy and Cashman, 2005). We note that clinopyroxenes from the Seguam eruption display textures and melt inclusions compositions consistent with rapid growth conditions during magma ascent (Lloyd et al., 2016b). Latent heat produced by crystallization on ascent would act to counter (to some extent) the cooling effect of vapor expansion. Conflow does not account for latent heat production, so it is therefore unsurprising that the Conflow model overestimates the extent (at Seguam) and duration (at Seguam and Fuego) of cooling experienced by wet magmas undergoing degassing-driven crystallization.

Another potential issue with the application of the Conflow model to hydrous arc magmas is the likelihood of vapor loss from the magma during ascent (i.e., open-system degassing), which would violate the closed system assumption of the isentropic model. Slow ascent of hot, basaltic magma may allow migration and escape of vapor bubbles, thereby reducing the adiabatic cooling experienced by the magma (which is dominated by the expansion of the vapor phase). This process could potentially produce a systematic relationship between magma temperature change and syneruptive ascent rate, in which fast-ascending magmas (in which vapor bubbles are more efficiently retained) experience more net cooling than slow-ascending magmas (in which vapor bubbles may migrate and escape). This idea is explored further in section "Systematics of Magma Temperature Changes During Ascent."

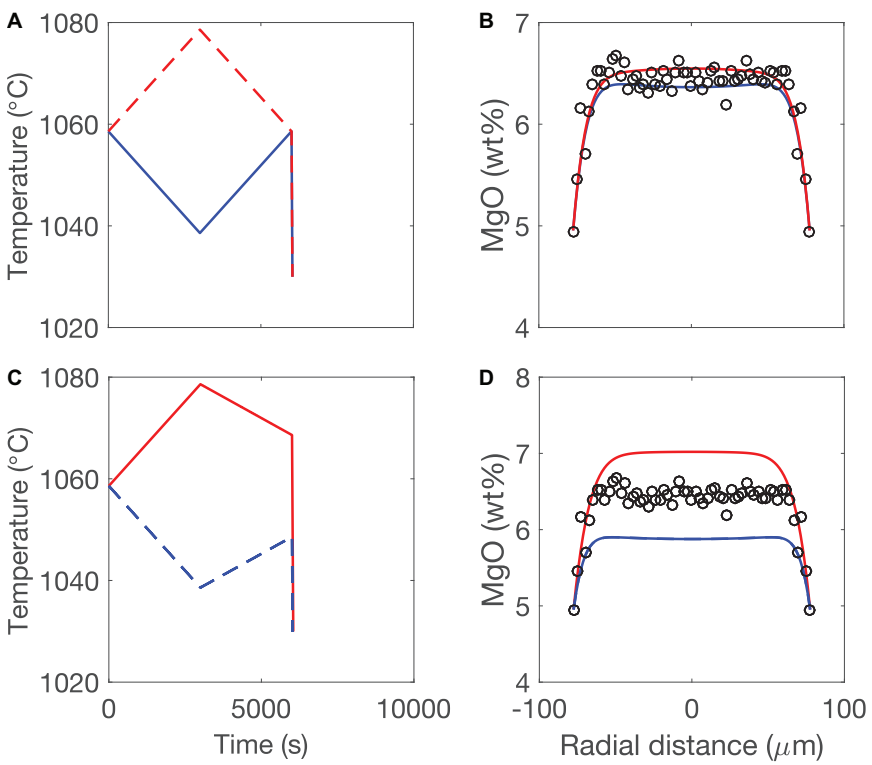

FIGURE 10 | Forward modeling to calculate the effects of temperature variations of ± 20°C on the generation of MgO zonation in inclusion Seg5-MI1. **(A)** Two separate thermal histories are imposed: one in which the temperature increases and decreases by 20°C over a period of 100 min before quenching at 0.9°C/s (red dashed lines); and one in which the temperature first decreases and then increases by 20°C over a period of 100 min before quenching at 0.9°C/s (blue lines). **(B)** Modeled MgO zonation in melt inclusion Seg5-MI1 in response to the thermal histories imposed in **(A)**. Both models (red and blue curves) provide a reasonably good match to the data (black circles). In these examples, the imposed temperature variations occur over a long enough duration that MgO variations are able to approximately homogenize by diffusion, thereby erasing the evidence of the prior thermal histories. **(C)** Imposed thermal histories used to generate the model curves in **(D)**. Note that in these examples, there is a *net* temperature change of ±10°C between the initial temperature and the temperature reached just prior to quenching. **(D)** Modeled MgO zonation in melt inclusion Seg5-MI1 in response to the thermal histories imposed in **(C)**. Thermal histories in which we impose a net 10°C increase (red curve) or net 10°C decrease (blue curve) in temperature prior to quenching are unable to match our Seg5-MI1 data. This demonstrates the sensitivity of MgO zonation in Seguam melt inclusions to *net* temperature changes during magma ascent.

Do the MgO Plateaus Observed in Our Kilauea and Seguam Melt Inclusions Require Approximately Isothermal Magma Ascent, or Are More Complex Thermal Histories Possible?

As discussed in section "Characteristics of Chemical Zonation in the Melt Inclusions," several Kilauea Iki and Seguam melt inclusions exhibit plateaus of approximately constant MgO across their centers. The simplest interpretation of these MgO plateaus is that the Kilauea and Seguam magmas ascended the conduit approximately isothermally prior to quenching on eruption. However, it seems likely that the Seguam magma, which underwent significant crystallization and degassing of ∼4 wt% water during ascent, may have experienced periods of both cooling and heating in the conduit. This assertion is supported by the results of conduit modeling by La Spina et al. (2015) that accounts for latent heat production. La Spina et al. (2015) find evidence for ∼20°C of cooling followed by ∼20°C of heating during magma ascent just prior to the 2007 effusive eruption of Stromboli, Italy (e.g., their **Figure 1**). We have conducted some simple forward models to test whether the MgO plateaus observed in our Seguam melt inclusions are consistent with the kinds of temperature variations predicted by the La Spina et al. (2015) model (**Figure 10**). We impose thermal histories with durations of ∼100 min (chosen to match the average duration of magma ascent determined via modeling of volatile diffusion in melt embayments; Newcombe et al., 2020) in which the temperature varies by up to ± 20°C prior to quenching on eruption. Models in which the *net* temperature change during magma ascent is 0°C (prior to quenching) provide a reasonably good match to the MgO profile measured in Seg5-MI1 (**Figures 10A,B**). However, models in which the net temperature change during magma ascent is 10°C (prior to quenching) are unable to match the MgO profile (**Figures 10C,D**). We conclude from this exercise that it is possible to erase the effects of temperature variations of tens of °C on MgO zonation in our Seguam melt inclusions. This behavior is more likely to occur in wet magmas in which D_{MgO} is enhanced (see section "Effect of Water Addition and Major Element Composition on the Diffusivity of MgO in Basaltic Melt") and in magmas that ascend slowly enough to provide time for MgO variations to diffusively homogenize. However, the fact that the central MgO concentrations of our Seguam melt inclusions are approximately in equilibrium with their olivine hosts requires minimal *net* temperature change during magma ascent (we estimate a maximum net temperature change of ∼4°C can be tolerated by our Seg5-MI1 data). We note that the thermal histories imposed in **Figure 10** are highly non-unique. The incorporation into our model of chemical zonation of oxides other than MgO could narrow the range of viable thermal histories (Saper and Stolper, 2020); e.g., we note that concave-up profiles of CaO across our Seguam inclusions likely rule out thermal histories with prolonged cooling prior to quenching (such as the thermal history plotted in red in **Figure 10A**). Future efforts are needed to constrain the families of possible thermal histories that satisfy major element zonation data in olivine-hosted melt inclusions, perhaps by coupling with models of magma ascent based on thermodynamic and fluid dynamic principles; however, such efforts are beyond the scope of this work.

Systematics of Magma Temperature Changes During Ascent

We have used MgO concentration gradients in olivine-hosted melt inclusions to constrain syneruptive temperature changes of magmas during five basaltic eruptions. The syneruptive magmas involved in these eruptions had variable decompression rates (Fuego > Keanakāko'i layer 6 > Keanakāko'i reticulite > Seguam > Kilauea Iki) and contained different initial water concentrations (Fuego > = Seguam > > Kilauea). What are the underlying processes and controls driving temperature changes during these eruptions?

Thermodynamic models of adiabatic magma ascent (Mastin and Ghiorso, 2000; Mastin and Ghiorso, 2001) support the idea that the dominant control on adiabatic cooling is the volume fraction of vapor in the magma: Kilauea Iki, Seguam, and Fuego magmas experienced very different ascent histories (e.g., **Figures 9A–C**), but relationships between the slope of the adiabat (dT/dP) and the volume fraction of vapor calculated by Conflow are almost identical for all three magmas (**Figure 9D**).

The clear importance of vapor volume fraction as a driver of syneruptive magma cooling suggests that we may be able to explain the systematics of magma temperature changes in terms

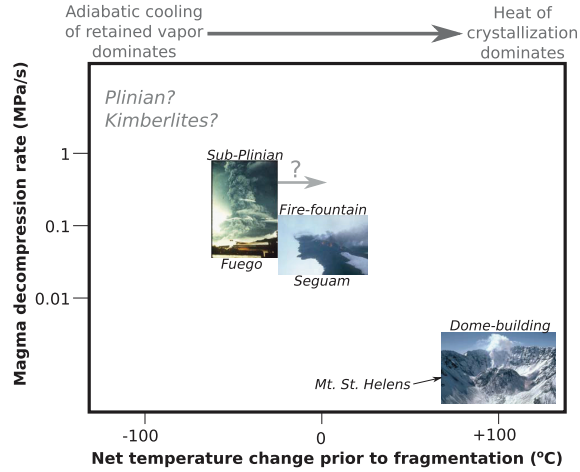

FIGURE 11 | Hypothesized trend between magma decompression rate and temperature change during ascent. We find evidence that the Seguam 1977 magma experienced a net temperature change of ∼0°C during syneruptive ascent and the Fuego 1974 magma experienced a net temperature change between ∼–40°C (if our best-fit thermal histories reflect cooling in the conduit) and ∼0°C (if our best-fit thermal histories reflect cooling in the volcanic plume). Blundy et al. (2006) report a temperature increase of ∼100°C accompanying slow extrusion of magma during dome-building eruptions at Mount Saint Helens and Shiveluch volcanoes. Together, these results are suggestive of a negative correlation between decompression rate and temperature change during ascent, which likely relates to higher degrees of melt-vapor segregation and more crystallization in slower ascending magmas. Studies of ascent and syneruptive temperature changes at volcanoes with a wider variety of eruptive styles (e.g., Plinian eruptions) and magma compositions will be required to test the validity of this hypothesized trend. Photo credit: USGS.

of a magma's ability to produce and retain vapor bubbles during ascent. As described in the previous section, magmas erupted at Fuego and Seguam both initially contained ∼4 wt% water such that the volume fraction of vapor exsolved by each magma must have been approximately equal; however, rapid magma ascent at Fuego (Lloyd et al., 2014) allowed this magma to retain its vapor, while slower ascent at Seguam (Newcombe et al., 2020) likely led to melt-vapor segregation and crystallization on ascent. The lower initial volatile content of the Kilauea Iki magma resulted in delayed (i.e., shallower) vapor exsolution from this magma compared to the magmas erupted at Fuego and Seguam, thereby explaining the lack of cooling in the conduit inferred from MgO gradients in the melt inclusions from Kilauea.

Several studies have been conducted of pre- and syn-eruptive temperature changes during andesitic dome-building eruptions. Blundy et al. (2006) used plagioclase-melt thermometry to infer temperature increases of ∼100°C of andesitic magmas leading up to dome-building eruptions of Shiveluch and Mount Saint Helens volcanoes. Blundy et al. (2006) proposed that this temperature increase was a result of latent heat production during degassing-driven crystallization. Additionally, several studies of dome-building eruptions at Soufriere Hills (Devine et al., 1998; Rutherford and Devine, 2003) have found evidence for heating events just prior to and/or during magma ascent and eruption (much of this heating was attributed to recharge of hot basaltic magma, but some of the heating could conceivably be a result of syneruptive degassing-driven crystallization). Placing these results in the context of our findings at Fuego, Seguam, and Kilauea, we hypothesize that there may be a direct relationship between magma ascent rate and temperature change during magma ascent, with the slowest ascending magmas experiencing net temperature increases during ascent due to crystallization and vapor loss, and the fastest ascending magmas experiencing net temperature decreases during ascent due to retention and adiabatic expansion of exsolved vapor (**Figure 11**).

The application of olivine-hosted melt inclusion thermometry to the study of syneruptive temperature changes during explosive basaltic eruptions suggests that thermal histories of hydrous arc magmas are not well-reproduced by isentropic models of magma ascent, likely due to the occurrence of open-system degassing and/or degassing-driven crystallization, so we caution against the use of isentropic conduit models for arc magmas. Future work (e.g., application of this technique to kimberlitic magmas and effusively erupted magmas) will further elucidate the systematics of pressure-temperature-time conditions experienced by syneruptive basaltic magmas. Similar techniques could be applied to silicic systems (e.g., Blundy et al., 2006; Myers et al., 2018), where higher melt viscosities may produce different behaviors on magma ascent (e.g., higher shear heating and increased vapor retention).

CONCLUSION

- We have used MgO concentration gradients in olivine-hosted melt inclusions to estimate syneruptive T-t paths of mafic magmas erupted at Fuego, Seguam, and Kilauea volcanoes. By combining our syneruptive T-t constraints with previously determined decompression histories for these magmas, we are able to place constraints on the P-T-t paths of basaltic magmas during ascent and eruption.
- Melt inclusions from the 1959 Kilauea Iki fire fountain eruption record the highest syneruptive cooling rates (3–11°C/s) and the shortest cooling durations (4–19 s), while inclusions from the 1974 subplinian eruption of Fuego volcano record the lowest cooling rates (0.1–1.7°C/s) and longest cooling durations (21–368 s) of the studied eruptions.
- A comparison of bomb- and ash-derived melt inclusions from Fuego demonstrates the importance of clast size as a control on syneruptive cooling rates. Melt inclusions sampled from the interiors of small (∼6 cm diameter) volcanic bombs at Fuego are found to have cooled more slowly on average than inclusions sampled from ash (with particle diameters < 2 mm) during the same eruption, as expected based on conductive cooling models. The effects of clast size may also explain the relatively long durations of cooling recorded by melt inclusions from the Keanakāko'i basal reticulite.
- Our constraints on the P-T-t paths of magmas erupted at Kilauea Iki are consistent with the predictions of conduit models that assume isentropic magma ascent and little degassing-driven crystallization.
- Our P-T-t constraints at Seguam and Fuego (both containing initial water concentrations of ∼4 wt%) reveal less cooling than predictions of isentropic magma ascent models, and may indicate the importance of open-system degassing and/or degassing-driven crystallization in the minutes to hours preceding these eruptions.
- We find evidence for a systematic relationship between magma thermal history and decompression rate, in which rapidly ascending gas-bearing magmas experience slower cooling during ascent and eruption than slowly ascending magmas. This relationship may be rationalized by thermodynamic models that show that the dominant driver of cooling in the conduit is adiabatic expansion of a vapor phase, because a corollary of these models is that, in order to drive syneruptive cooling, the magma must ascend rapidly enough to prevent significant melt-vapor separation.

Given the expected sensitivity of magma P-T-t paths to vapor volume fraction, it may be possible to use the syneruptive ascent chronometers and thermometers presented here as a means of identifying processes that are otherwise difficult to constrain, such as magma stalling, open- and closed-system degassing, vapor fluxing, and vapor accumulation during syneruptive ascent of mafic magmas.

DATA AVAILABILITY STATEMENT

All datasets generated for this study are included in the article/**Supplementary Material**. Code developed over the course

of this study is freely available on Github (doi: 10.5281/zenodo.3998246).

AUTHOR CONTRIBUTIONS

MN and TP designed the study. BFH collected Kilauea samples. MN, ASL, DF, and EH performed geochemical analyses. MN performed the thermal history modeling with guidance from YZ. MH ran the piston cylinder experiment. YZ fit the results of the piston cylinder experiment. AB modeled syneruptive water loss from Fuego melt inclusions. MN wrote the manuscript with input from all co-authors.

FUNDING

This work was funded by NSF GeoPRISMS award 1551868.

ACKNOWLEDGMENTS

We are grateful to Adrian Fiege at the American Museum of Natural History for his help with the electron microprobe analyses, and to Jianhua Wang at the Carnegie Institution for Science for his help with the SIMS and nanoSIMS analyses. Philipp Ruprecht is thanked for his support and mentorship. We thank Bill Rose and Don Swanson for sharing their samples of the Fuego and Kilauea eruptions, and we thank Lee Saper and Edward Stolper for sharing the results of their controlled cooling experiments. We greatly appreciate AK and TK for their insightful reviews, and TU for her thoughtful editorial handling.

SUPPLEMENTARY MATERIAL

The Supplementary Material for this article can be found online at: https://www.frontiersin.org/articles/10.3389/feart.2020.531911/full#supplementary-material

REFERENCES

Aiuppa, A., Federico, C., Giudice, G., and Gurrieri, S. (2005). Chemical mapping of a fumarolic field: La Fossa Crater, Vulcano Island (Aeolian Islands, Italy). *Geophys. Res. Lett.* 32, doi: 10.1029/2005gl023207

Aiuppa, A., Moretti, R., Federico, C., Giudice, G., Gurrieri, S., Liuzzo, M., et al. (2007). Forecasting Etna eruptions by real-time observation of volcanic gas composition. *Geology* 35, 1115–1118. doi: 10.1130/g24149a.1

Ayris, P. M., Delmelle, P., Cimarelli, C., Maters, E. C., Suzuki, Y. J., and Dingwell, D. B. (2014). HCl uptake by volcanic ash in the high temperature eruption plume: mechanistic insights. *Geochim. Cosmochim. Acta* 144, 188–201. doi: 10.1016/j.gca.2014.08.028

Bamber, E. C., Arzilli, F., Polacci, M., Hartley, M. E., Fellowes, J., Di Genova, D., et al. (2020). Pre- and syn-eruptive conditions of a basaltic Plinian eruption at Masaya Volcano, Nicaragua: the Masaya Triple Layer (2.1 ka). *J. Volcanol. Geotherm. Res.* 392, 106761. doi: 10.1016/j.jvolgeores.2019.106761

Barth, A., Newcombe, M. E., Plank, T., Gonnermann, H., Hajimirza, S., Soto, G. J., et al. (2019). Magma decompression rate correlates with explosivity at basaltic volcanoes – constraints from water diffusion in olivine. *J. Volcanol. Geotherm. Res.* 387, 106664. doi: 10.1016/j.jvolgeores.2019.106664

Beattie, P. (1993). Olivine-melt and orthopyroxene-melt equilibria. *Contrib. Mineral. Petrol.* 115, 103–111. doi: 10.1007/bf00712982

Birnie, D. P., and Dyar, M. D. (1986). Cooling rate calculations for silicate glasses. *J. Geophys. Res. Solid Earth* 91, 509–513. doi: 10.1029/JB091iB04p0D509

Blundy, J., and Cashman, K. (2005). Rapid decompression-driven crystallization recorded by melt inclusions from Mount St. Helens volcano. *Geology* 33, 793–796. doi: 10.1130/g21668.1

Blundy, J., Cashman, K., and Humphreys, M. (2006). Magma heating by decompression-driven crystallization beneath andesite volcanoes. *Nature* 443, 76–80. doi: 10.1038/nature05100

Bucholz, C. E., Gaetani, G. A., Behn, M. D., and Shimizu, N. (2013). Post-entrapment modification of volatiles and oxygen fugacity in olivine-hosted melt inclusions. *Earth Planet. Sci. Lett.* 374, 145–155. doi: 10.1016/j.epsl.2013.05.033

Campagnola, S., Romano, C., Mastin, L., and Vona, A. (2016). Confort 15 model of conduit dynamics: applications to Pantelleria Green Tuff and Etna 122 BC eruptions. *Contrib. Mineral. Petrol.* 171:60.

Cassidy, M., Manga, M., Cashman, K., and Bachmann, O. (2018). Controls on explosive-effusive volcanic eruption styles. *Nat. Commun.* 9:2839.

Chen, Y., and Zhang, Y. (2008). Olivine dissolution in basaltic melt. *Geochim. Cosmochim. Acta* 72, 4756–4777. doi: 10.1016/j.gca.2008.07.014

Costa, A., Melnik, O., and Vedeneeva, E. (2007). Thermal effects during magma ascent in conduits. *J. Geophys. Res. Solid Earth* 112, doi: 10.1029/2007jb004985

Danyushevsky, L. V., Della-Pasqua, F. N., and Sokolov, S. (2000). Re-equilibration of melt inclusions trapped by magnesian olivine phenocrysts from subduction-related magmas: petrological implications. *Contrib. Mineral. Petrol.* 138, 68–83. doi: 10.1007/pl00007664

Danyushevsky, L. V., Sokolov, S., and Falloon, T. J. (2002). Melt inclusions in olivine phenocrysts: using diffusive re-equilibration to determine the cooling history of a crystal, with implications for the origin of olivine-phyric volcanic rocks. *J. Petrol.* 43, 1651–1671. doi: 10.1093/petrology/43.9.1651

de Moor, J. M., Aiuppa, A., Pacheco, J., Avard, G., Kern, C., Liuzzo, M., et al. (2016). Short-period volcanic gas precursors to phreatic eruptions: insights from Poás Volcano, Costa Rica. *Earth Planet. Sci. Lett.* 442, 218–227. doi: 10.1016/j.epsl.2016.02.056

Devine, J. D., Murphy, M. D., Rutherford, M. J., Barclay, J., Sparks, R. S. J., Carroll, M. R., et al. (1998). Petrologic evidence for pre-eruptive pressure-temperature conditions, and recent reheating, of andesitic magma erupting at the Soufriere Hills Volcano, Montserrat, W.I. *Geophys. Res. Lett.* 25, 3669–3672. doi: 10.1029/98GL01330

Eaton, J. P., Richter, D. H., and Krivoy, H. L. (1987). Cycling of magma between the summit reservoir and Kilauea Iki lava lake during the 1959 eruption of Kilauea volcano. *US Geol. Surv. Prof. Pap.* 1350, 1307–1335.

Ferguson, D. J., Gonnermann, H. M., Ruprecht, P., Plank, T., Hauri, E. H., Houghton, B. F., et al. (2016). Magma decompression rates during explosive eruptions of Kīlauea volcano, Hawaii, recorded by melt embayments. *Bull. Volcanol.* 78:71.

Ford, C., Russell, D., Craven, J., and Fisk, M. (1983). Olivine-liquid equilibria: temperature, pressure and composition dependence of the crystal/liquid cation partition coefficients for Mg, Fe2+, Ca and Mn. *J. Petrol.* 24, 256–266. doi: 10.1093/petrology/24.3.256

Fujii, N., and Uyeda, S. (1974). Thermal instabilities during flow of magma in volcanic conduits. *J. Geophys. Res.* 79, 3367–3369. doi: 10.1029/JB079i023p03367

Gaetani, G. A., O'Leary, J. A., Shimizu, N., Bucholz, C. E., and Newville, M. (2012). Rapid reequilibration of H2O and oxygen fugacity in olivine-hosted melt inclusions. *Geology* 40, 915–918. doi: 10.1130/g32992.1

Garcia, M. O., Mucek, A. E., Lynn, K. J., Swanson, D. A., and Norman, M. D. (2018). Geochemical evolution of Keanakāko'i Tephra, Kīlauea Volcano, Hawai 'i. *Field Volcanol.* 538:203.

Ghiorso, M. S., and Sack, R. O. (1995). Chemical mass transfer in magmatic processes IV. A revised and internally consistent thermodynamic model for the interpolation and extrapolation of liquid-solid equilibria in magmatic systems at elevated temperatures and pressures. *Contrib. Mineral. Petrol.* 119, 197–212. doi: 10.1007/s004100050036

Glazner, A. F. (2019). The ascent of water-rich magma and decompression heating: a thermodynamic analysis. *Am. Mineral.* 104, 890–896. doi: 10.2138/am-2019-6925

Gottsmann, J., and Dingwell, D. (2002). The thermal history of a spatter-fed lava flow: the 8-ka pantellerite flow of Mayor Island, New Zealand. *Bull. Volcanol.* 64, 410–422. doi: 10.1007/s00445-002-0220-7

Guo, C., and Zhang, Y. (2016). Multicomponent diffusion in silicate melts: SiO2–TiO2–Al2O3–MgO–CaO–Na2O–K2O System. *Geochim. Cosmochim. Acta* 195, 126–141. doi: 10.1016/j.gca.2016.09.003

Guo, C., and Zhang, Y. (2018). Multicomponent diffusion in basaltic melts at 1350° C. *Geochim. Cosmochim. Acta* 228, 190–204. doi: 10.1016/j.gca.2018.02.043

Guo, C., and Zhang, Y. (2020). Multicomponent diffusion in a basaltic melt: temperature dependence. *Chem. Geol.* 549, 119700. doi: 10.1016/j.chemgeo.2020.119700

Haar, L., Gallagher, J. S., and Kell, G. S. (1984). *NBS/NRC Steam Tables: Thermodynamic and Transport Properties and Computer Programs for Vapor and Liquid States of Water in SI Units*. Washington, DC: Hemisphere Publishing Corporation, 320.

Hartley, M. E., Maclennan, J., Edmonds, M., and Thordarson, T. (2014). Reconstructing the deep CO2 degassing behaviour of large basaltic fissure eruptions. *Earth Planet. Sci. Lett.* 393, 120–131. doi: 10.1016/j.epsl.2014.02.031

Hauri, E., Wang, J., Dixon, J. E., King, P. L., Mandeville, C., and Newman, S. (2002). SIMS analysis of volatiles in silicate glasses: 1. Calibration, matrix effects and comparisons with FTIR. *Chem. Geol.* 183, 99–114. doi: 10.1016/S0009-2541(01)00375-8

Hauri, E. H., Weinreich, T., Saal, A. E., Rutherford, M. C., and Van Orman, J. A. (2011). High pre-eruptive water contents preserved in lunar melt inclusions. *Science* 333, 213–215. doi: 10.1126/science.1204626

Helz, R. T., Cottrell, E., Brounce, M. N., and Kelley, K. A. (2017). Olivine-melt relationships and syneruptive redox variations in the 1959 eruption of Kīlauea Volcano as revealed by XANES. *J. Volcanol. Geotherm. Res.* 33, 1–14. doi: 10.1016/j.jvolgeores.2016.12.006

Hort, M., and Gardner, J. (2000). Constraints on cooling and degassing of pumice during Plinian volcanic eruptions based on model calculations. *J. Geophys. Res. Solid Earth* 105, 25981–26001. doi: 10.1029/2000jb900186

Humphreys, M. C., Edmonds, M., and Klöcking, M. S. (2016). The validity of plagioclase-melt geothermometry for degassing-driven magma crystallization. *Mineral. Soc. Am.* 101, 769–779. doi: 10.2138/am-2016-5314

Jaupart, C., and Vergniolle, S. (1989). The generation and collapse of a foam layer at the roof of a basaltic magma chamber. *J. Fluid Mech.* 203, 347–380. doi: 10.1017/s0022112089001497

Kavanagh, J. L., and Sparks, R. S. J. (2009). Temperature changes in ascending kimberlite magma. *Earth Planet. Sci. Lett.* 286, 404–413. doi: 10.1016/j.epsl.2009.07.011

Kilinc, A. (2018). "Temperature variations in isentropic (Adiabatic) uprise of Magma," in *Proceedings of the AGU Fall Meeting Abstracts*, Washington, DC.

Koyaguchi, T. (2005). An analytical study for 1-dimensional steady flow in volcanic conduits. *J. Volcanol. Geotherm. Res.* 143, 29–52. doi: 10.1016/j.jvolgeores.2004.09.009

Kress, V. C., and Ghiorso, M. S. (1995). Multicomponent diffusion in basaltic melts. *Geochim. Cosmochim. Acta* 59, 313–324. doi: 10.1016/0016-7037(94)00286-u

La Spina, G., Burton, M., de' Michieli, and Vitturi, M. (2015). Temperature evolution during magma ascent in basaltic effusive eruptions: a numerical application to Stromboli volcano. *Earth Planet. Sci. Lett.* 426, 89–100. doi: 10.1016/j.epsl.2015.06.015

La Spina, G., Burton, M., Vitturi, MdM, and Arzilli, F. (2016). Role of syn-eruptive plagioclase disequilibrium crystallization in basaltic magma ascent dynamics. *Nature communications* 7, 13402.

Le Voyer, M., Asimow, P. D., Mosenfelder, J. L., Guan, Y., Wallace, P. J., Schiano, P., et al. (2014). Zonation of H2O and F concentrations around melt inclusions in olivines. *J. Petrol.* 55, 685–707. doi: 10.1093/petrology/egu003

Liang, Y. (2010). Multicomponent diffusion in molten silicates: theory, experiments, and geological applications. *Rev. Mineral. Geochem.* 72, 409–446. doi: 10.1515/9781501508394-010

Lloyd, A., Plank, T., Ruprecht, P., Hauri, E., and Rose, W. (2013). Volatile loss from melt inclusions in pyroclasts of differing sizes. *Contrib. Mineral. Petrol.* 165, 129–153. doi: 10.1007/s00410-012-0800-2

Lloyd, A. S., Ferriss, E., Ruprecht, P., Hauri, E. H., Jicha, B. R., and Plank, T. (2016a). An assessment of clinopyroxene as a recorder of magmatic water and magma ascent rate. *J. Petrol.* 57, 1865–1886. doi: 10.1093/petrology/egw058

Lloyd, A. S., Newcombe, M. E., and Plank, T. (2016b). "Constraining magma ascent and degassing paths with olivine- and clinopyroxene-hosted melt inclusions: evidence for multiple depths of crystallization and boundary-layer entrapment," in *Proceedings of the AGU Fall Meeting on 2016*, San Francisco, CA.

Lloyd, A. S., Ruprecht, P., Hauri, E. H., Rose, W., Gonnermann, H. M., and Plank, T. (2014). NanoSIMS results from olivine-hosted melt embayments: Magma ascent rate during explosive basaltic eruptions. *J. Volcanol. Geotherm. Res.* 283, 1–18. doi: 10.1016/j.jvolgeores.2014.06.002

London, D. (2005). Effect of current density on the electron microprobe analysis of alkali aluminosilicate glasses. *Am. Mineral.* 90, 1131–1138. doi: 10.2138/am.2005.1769

Lynn, K. J., Garcia, M. O., Shea, T., Costa, F., and Swanson, D. A. (2017). Timescales of mixing and storage for Keanakāko'i Tephra magmas (1500–1820 C.E.), Kīlauea Volcano, Hawai'i. *Contrib. Mineral. Petrol.* 172, 76. doi: 10.1007/s00410-017-1395-4

Maclennan, J. (2017). Bubble formation and decrepitation control the CO2 content of olivine-hosted melt inclusions. *Geochem. Geophys. Geosyst.* 18, 597–616. doi: 10.1002/2016gc006633

Mangan, M. T., and Cashman, K. V. (1996). The structure of basaltic scoria and reticulite and inferences for vesiculation, foam formation, and fragmentation in lava fountains. *J. Volcanol. Geotherm. Res.* 73, 1–18. doi: 10.1016/0377-0273(96)00018-2

Massare, D., Métrich, N., and Clocchiatti, R. (2002). High-temperature experiments on silicate melt inclusions in olivine at 1 atm: inference on temperatures of homogenization and H2O concentrations. *Chem. Geol.* 183, 87–98. doi: 10.1016/s0009-2541(01)00373-4

Mastin, L. G. (2005). The controlling effect of viscous dissipation on magma flow in silicic conduits. *J. Volcanol. Geotherm. Res.* 143, 17–28. doi: 10.1016/j.jvolgeores.2004.09.008

Mastin, L. G., and Ghiorso, M. S. (2000). *A Numerical Program for Steady-State Flow of Magma-Gas Mixtures Through Vertical Eruptive Conduits*. Vancouver, WA: U.S. Geological Survey.

Mastin, L. G., and Ghiorso, M. S. (2001). Adiabatic temperature changes of magma–gas mixtures during ascent and eruption. *Contrib. Mineral. Petrol.* 141, 307–321. doi: 10.1007/s004100000210

May, M., Carey, R. J., Swanson, D. A., and Houghton, B. F. (2015). "Reticulite-producing fountains from ring fractures in Kilauea Caldera ca. 1500 CE," in *Hawaiian Volcanoes: From Source to Surface*, Vol. 208, eds R. Carey, V. Cayol, M. Poland, and D. Weis (Hoboken, NJ: John Wiley and Sons).

McPhie, J., Walker, G. P. L., and Christiansen, R. L. (1990). Phreatomagmatic and phreatic fall and surge deposits from explosions at Kilauea volcano, Hawaii, 1790 a.d.: Keanakāko'i Ash Member. *Bull. Volcanol.* 52, 334–354. doi: 10.1007/bf00302047

Médard, E., and Grove, T. L. (2008). The effect of H2O on the olivine liquidus of basaltic melts: experiments and thermodynamic models. *Contrib. Mineral. Petrol.* 155, 417–432. doi: 10.1007/s00410-007-0250-4

Métrich, N., and Wallace, P. J. (2008). Volatile abundances in basaltic magmas and their degassing paths tracked by melt inclusions. *Rev. Mineral. Geochem.* 69, 363–402.

Mironov, N., Portnyagin, M., Botcharnikov, R., Gurenko, A., Hoernle, K., and Holtz, F. (2015). Quantification of the CO2 budget and H2O–CO2 systematics in subduction-zone magmas through the experimental hydration of melt inclusions in olivine at high H2O pressure. *Earth Planet. Sci. Lett.* 425, 1–11.

Moore, L. R., Gazel, E., Tuohy, R., Lloyd, A. S., Esposito, R., Steele-MacInnis, M., et al. (2015). Bubbles matter: an assessment of the contribution of vapor bubbles to melt inclusion volatile budgets. *Am. Mineral.* 100, 806–823. doi: 10.2138/am-2015-5036

Moussallam, Y., Oppenheimer, C., and Scaillet, B. (2019). On the relationship between oxidation state and temperature of volcanic gas emissions. *Earth Planet. Sci. Lett.* 520, 260–267.

Mueller, S. B., Houghton, B. F., Swanson, D. A., Poret, M., and Fagents, S. A. (2019). Total grain size distribution of an intense Hawaiian fountaining event: case study of the 1959 Kīlauea Iki eruption. *Bull. Volcanol.* 81:43. doi: 10.1007/s00445-019-1304-y

Myers, M. L., Wallace, P. J., Wilson, C. J., Watkins, J. M., and Liu, Y. (2018). Ascent rates of rhyolitic magma at the onset of three caldera-forming eruptions. *Mineral. Soc. Am.* 103, 952–965.

Newcombe, M. E., Fabbrizio, A., Zhang, Y., Ma, C., Le Voyer, M., Guan, Y., et al. (2014). Chemical zonation in olivine-hosted melt inclusions. *Contrib. Mineral. Petrol.* 168, 1–26. doi: 10.1007/s00410-014-1030-6

Newcombe, M. E., Plank, T., Asimow Paul, D., Barth, A., and Hauri, E. (2020). Water-in-olivine magma ascent chronometry: every crystal is a clock. *J. Volcanol. Geotherm. Res.* 398:106872.

Newman, S., and Lowenstern, J. B. (2002). VolatileCalc: a silicate melt–H2O–CO2 solution model written in visual basic for excel. *Comput. Geosci.* 28, 597–604. doi: 10.1016/S0098-3004(01)00081-4

Nichols, A. R. L., Potuzak, M., and Dingwell, D. B. (2009). Cooling rates of basaltic hyaloclastites and pillow lava glasses from the HSDP2 drill core. *Geochim. Cosmochim. Acta* 73, 1052–1066. doi: 10.1016/j.gca.2008.11.023

Oppenheimer, C., Scaillet, B., Woods, A., Sutton, A. J., Elias, T., and Moussallam, Y. (2018). Influence of eruptive style on volcanic gas emission chemistry and temperature. *Nat. Geosci.* 11, 678–681.

Parfitt, E., and Wilson, L. (1995). Explosive volcanic eruptions—IX. The transition between Hawaiian-style lava fountaining and Strombolian explosive activity. *Geophys. J. Int.* 121, 226–232.

Porritt, L., Russell, J., and Quane, S. (2012). Pele's tears and spheres: examples from Kilauea Iki. *Earth Planet. Sci. Lett.* 333, 171–180.

Potuzak, M., Nichols, A. R. L., Dingwell, D. B., and Clague, D. A. (2008). Hyperquenched volcanic glass from Loihi Seamount. Hawaii. *Earth Planet. Sci. Lett.* 270, 54–62. doi: 10.1016/j.epsl.2008.03.018

Putirka, K. D. (2008). Thermometers and barometers for volcanic systems. *Rev. Mineral. Geochem.* 69, 61–120.

Putirka, K. D., Perfit, M., Ryerson, F., and Jackson, M. G. (2007). Ambient and excess mantle temperatures, olivine thermometry, and active vs. passive upwelling. *Chem. Geol.* 241, 177–206.

Rasmussen, D. J., Plank, T. A., and Roman, D. C. (2019). "Magmatic water content controls Magma storage depth," in *Proceedings of the American Geophysical Union Fall meeting 2019*, San Francisco, CA.

Rasmussen, D. J., Plank, T. A., Roman, D. C., Power, J. A., Bodnar, R. J., and Hauri, E. H. (2018). When does eruption run-up begin? Multidisciplinary insight from the 1999 eruption of Shishaldin volcano. *Earth Planet. Sci. Lett.* 486, 1–14.

Rasmussen, D. J., Plank, T. A., Wallace, P. J., Newcombe, M. E., and Lowenstern, J. B. (2020). Vapor bubble growth in olivine-hosted melt inclusions. *Am. Mineral.* doi: 10.2138/am-2020-7377

Recktenwald, G. (2006). *Transient, One-Dimensional Heat Conduction in a Convectively Cooled Sphere*. Portland, OR: Portland State University.

Richter, D. H., Eaton, J. P., Murata, K. J., Ault, W. U., and Krivoy, H. L. (1970). *Chronological Narrative of the 1959-60 Eruption of Kilauea Volcano, Hawaii*. Reston, VA: United States Geological Survey.

Roeder, P., and Emslie, R. (1970). Olivine-liquid equilibrium. *Contrib. Mineral. Petrol.* 29, 275–289.

Rose, W. I., Anderson, A. T., Woodruff, L. G., and Bonis, S. B. (1978). The October 1974 basaltic tephra from Fuego volcano: description and history of the magma body. *J. Volcanol. Geotherm. Res.* 4, 3–53. doi: 10.1016/0377-0273(78)90027-6

Ruth, D. C., Costa, F., de Maisonneuve, C. B., Franco, L., Cortés, J. A., and Calder, E. S. (2018). Crystal and melt inclusion timescales reveal the evolution of magma migration before eruption. *Nat. Commun.* 9, 1–9.

Rutherford, M. J., and Devine, J. D. (2003). Magmatic conditions and Magma ascent as indicated by Hornblende phase equilibria and reactions in the 1995–2002 Soufrière Hills Magma. *J. Petrol.* 44, 1433–1453. doi: 10.1093/petrology/44.8.1433

Sahagian, D. (2005). Volcanic eruption mechanisms: insights from intercomparison of models of conduit processes. *J. Volcanol. Geotherm. Res.* 143, 1–15. doi: 10.1016/j.jvolgeores.2004.12.006

Sahagian, D. L., and Proussevitch, A. A. (1996). Thermal effects of magma degassing. *J. Volcanol. Geotherm. Res.* 74, 19–38. doi: 10.1016/S0377-0273(96)00047-9

Saper, L., and Stolper, E. (2020). Controlled cooling-rate experiments on olivine-hosted melt inclusions: chemical diffusion and quantification of eruptive cooling-rates on Hawaii and Mars. *Geochem. Geophys. Geosyst.* 21:e2019GC008772. doi: 10.1029/2019GC008772

Shea, T., and Hammer, J. E. (2013). Kinetics of cooling- and decompression-induced crystallization in hydrous mafic-intermediate magmas. *J. Volcanol. Geotherm. Res.* 260, 127–145. doi: 10.1016/j.jvolgeores.2013.04.018

Shinohara, H. (2005). A new technique to estimate volcanic gas composition: plume measurements with a portable multi-sensor system. *J. Volcanol. Geotherm. Res.* 143, 319–333. doi: 10.1016/j.jvolgeores.2004.12.004

Sides, I., Edmonds, M., Maclennan, J., Houghton, B., Swanson, D., and Steele-MacInnis, M. (2014). Magma mixing and high fountaining during the 1959 Kīlauea Iki eruption, Hawai 'i. *Earth Planet. Sci. Lett.* 400, 102–112.

Sparks, R. (1986). The dimensions and dynamics of volcanic eruption columns. *Bull. Volcanol.* 48, 3–15.

Stovall, W. K., Houghton, B. F., Gonnermann, H., Fagents, S. A., and Swanson, D. A. (2011). Eruption dynamics of Hawaiian-style fountains: the case study of episode 1 of the Kīlauea Iki 1959 eruption. *Bull. Volcanol.* 73, 511–529. doi: 10.1007/s00445-010-0426-z

Sugawara, T. (2000). Empirical relationships between temperature, pressure, and MgO content in olivine and pyroxene saturated liquid. *J. Geophys. Res.* 105, 8457–8472.

Swanson, D. A., Rose, T. R., Fiske, R. S., and McGeehin, J. P. (2012). Keanakāko'i Tephra produced by 300years of explosive eruptions following collapse of Kīlauea's caldera in about 1500CE. *J. Volcanol. Geotherm. Res.* 215, 8–25. doi: 10.1016/j.jvolgeores.2011.11.009

Toplis, M. J. (2005). The thermodynamics of iron and magnesium partitioning between olivine and liquid: criteria for assessing and predicting equilibrium in natural and experimental systems. *Contrib. Mineral. Petrol.* 149, 22–39. doi: 10.1007/s00410-004-0629-4

Tucker, J. M., Hauri, E. H., Pietruszka, A. J., Garcia, M. O., Marske, J. P., and Trusdell, F. A. (2019). A high carbon content of the Hawaiian mantle from olivine-hosted melt inclusions. *Geochim. Cosmochim. Acta* 254, 156–172.

Vedeneeva, E. A., Melnik, O. E., Barmin, A. A., and Sparks, R. S. J. (2005). Viscous dissipation in explosive volcanic flows. *Geophys. Res. Lett.* 32, doi: 10.1029/2004gl020954

Vona, A., Romano, C., Dingwell, D. B., and Giordano, D. (2011). The rheology of crystal-bearing basaltic magmas from Stromboli and Etna. *Geochim. Cosmochim. Acta* 75, 3214–3236. doi: 10.1016/j.gca.2011.03.031

Wallace, P. J., and Anderson, A. T. Jr. (1998). Effects of eruption and lava drainback on the H 2 O contents of basaltic magmas at Kilauea Volcano. *Bull. Volcanol.* 59, 327–344.

Wallace, P. J., Kamenetsky, V. S., and Cervantes, P. (2015). Melt inclusion CO2 contents, pressures of olivine crystallization, and the problem of shrinkage bubbles. *Am. Mineral.* 100, 787–794. doi: 10.2138/am-2015-5029

Wilding, M., Dingwell, D., Batiza, R., and Wilson, L. (2000). Cooling rates of hyaloclastites: applications of relaxation geospeedometry to undersea volcanic deposits. *Bull. Volcanol.* 61, 527–536. doi: 10.1007/s004450050003

Xu, Z., and Zhang, Y. (2002). Quench rates in air, water, and liquid nitrogen, and inference of temperature in volcanic eruption columns. *Earth Planet. Sci. Lett.* 200, 315–330.

Zhang, Y., Jenkins, J., and Xu, Z. (1997). Kinetics of the reaction $H_2O + O \rightarrow 2$ 2OH in rhyolitic glasses upon cooling: geospeedometry and comparison with glass transition. *Geochim. Cosmochim. Acta* 61, 2167–2173.

Zhang, Y., Ni, H., and Chen, Y. (2010). Diffusion data in silicate melts. *Rev. Mineral. Geochem.* 72, 311–408.

Zhang, Y., Xu, Z., and Behrens, H. (2000). Hydrous species geospeedometer in rhyolite: improved calibration and application. *Geochim. Cosmochim. Acta* 64, 3347–3355.

Zimmer, M. M., Plank, T., Hauri, E. H., Yogodzinski, G. M., Stelling, P., Larsen, J., et al. (2010). The role of water in generating the calc-alkaline trend: new volatile data for Aleutian Magmas and a new tholeiitic index. *J. Petrol.* 51, 2411–2444. doi: 10.1093/petrology/egq062

Conflict of Interest: The authors declare that the research was conducted in the absence of any commercial or financial relationships that could be construed as a potential conflict of interest.

frontiers in Earth Science

ORIGINAL RESEARCH
published: 15 January 2021
doi: 10.3389/feart.2020.584371

Experimental Constraints on Homogenization of Plagioclase-Hosted Melt Inclusions From Plagioclase Ultraphyric Basalts

Kristen R. Lewis[1], *Gokce K. Ustunisik*[1,2]* *and Roger L. Nielsen*[1,3]

[1]Department of Geology and Geological Engineering, South Dakota School of Mines and Technology, Rapid City, SD, United States, [2]Department of Earth and Planetary Sciences, American Museum of Natural History, New York, NY, United States, [3]College of Earth, Ocean, and Atmospheric Sciences, Oregon State University, Corvallis, OR, United States

Study of melt inclusions (MIs) is a commonly applied method for defining the composition of magmas present at depth prior to mixing, fractionation, and degassing. Our ability to use data from MIs is complicated by post-entrapment processes (PEP) that can modify their composition during transport and eruption. Many of the PEP can be reversed by heating the MIs to temperatures near those at which the MI and its host were formed. However, the process of reversing PEP by homogenization may introduce changes in MI compositions, making interpretation difficult. We present a series of low and high pressure homogenization experiments on plagioclase-hosted MIs from Plagioclase Ultraphyric Basalts (PUBs) designed to develop a methodology for recovering the composition at the time of entrapment of plagioclase-hosted MIs. These experiments included low pressure (1 bar) homogenization experiments conducted as a time series for 30 min, 4 h, 1 day, 4 days, and 8 days), and at 7.5 kbar for 2 and 4 days. The 7.5 kbar pressure used for the high pressure experiments was based on the CO_2-based entrapment pressures determined from MI from this sample. Experiments run at low pressure and run times of 4 and 8 days exhibited compositional drift, most notably in the form of increasing MgO in MIs. This drift was not observed at 7.5 kbars or for the shorter run time 1 atm experiments. These results are consistent with a model where drift in composition with time is caused by crystal relaxation driven by the high internal pressure within the MI (the pressure at which the MI formed), together with the lower confining pressure during homogenization (1 bar). Therefore, MI homogenization will produce the least amount of drift if runs are made for short time periods (~30 min) or at the pressure of entrapment.

Keywords: PUBs, Plagioclase, melt inclusions, MORB, trace elements

OPEN ACCESS

Edited by:
Marc-Antoine Longpré, Queens College (CUNY), United States

Reviewed by:
Takeshi Kuritani, Hokkaido University, Japan
Jason Peter Coumans, Durham University, United Kingdom

***Correspondence:**
Gokce K. Ustunisik
Gokce.Ustunisik@sdsmt.edu

Specialty section:
This article was submitted to Petrology, a section of the journal Frontiers in Earth Science

Received: *17 July 2020*
Accepted: *04 December 2020*
Published: *15 January 2021*

Citation:
Lewis KR, Ustunisik GK and Nielsen RL (2021) Experimental Constraints on Homogenization of Plagioclase-Hosted Melt Inclusions From Plagioclase Ultraphyric Basalts. Front. Earth Sci. 8:584371. doi: 10.3389/feart.2020.584371

INTRODUCTION

Mid-ocean ridge basalts (MORBs) are frequently used as proxies for understanding the physical and chemical characteristics of the mantle as well as developing models for the formation of oceanic crust. However, as magmas are transported from the site of generation to eruption, multiple processes modify their physical and chemical characteristics (Coogan, 2014). These processes include fractionation, magma mixing/mingling, assimilation, and degassing (Maclennan, 2008; Rubin et al., 2009; Shorttle et al., 2015). Therefore, the lavas erupted on the seafloor may no longer be

representative of the melts initially derived from the mantle (O'Hara, 1977; Langmuir, 1989; Michael and Shilling, 1989; Lissenberg and Macleod, 2016; O'Neill and Jenner, 2016).

One method commonly used to define the characteristics of the array of primitive melt compositions that existed prior to and during mixing, degassing, and fractionation is the study of melt inclusions (MIs) trapped in early crystallizing phases (Kohut and Nielsen, 2004; Kent and Putirka, 2008). In general, it is assumed that MIs are closed systems, in that they preserve geochemical information of the magmas at the time of entrapment. Under ideal circumstances, crystals forming from a suite of magmas will trap the suite of evolving liquids as they undergo processes such as mixing, fractionation, and degassing during storage and their transport to the surface. However, during transport, storage, and eruption, MIs undergo post-entrapment modification such as crystallization or diffusive re-equilibration (Danyuschevsky et al., 2002; Kent and Putirka, 2008). Here we use post-entrapment crystallization as a term that includes both the formation of daughter crystals within the MI as well as host growth at the crystal melt interface (Tait, 1992; Danyuschevsky et al., 2002). In many cases, MIs require homogenization to remove the post-entrapment crystals, and that homogenization process also can affect the composition of MIs (Schiavi et al., 2016; Drignon et al., 2019). This is particularly true of plagioclase megacrysts in plagioclase ultraphyric basalts (PUBs) that are carried to the surface in magmas that are significantly more evolved than the magmas from which anorthitic megacrysts form (Lange et al., 2013a; Lange et al., 2013b). This results in up to 100°C undercooling and thus pervasive post-entrapment crystallization prior to eruption. Nevertheless, the primitive character of those megacrysts and their MIs make such crystals a fertile source of otherwise unobtainable information on magma diversity and volatile contents.

Post-entrapment processes affect the evolution of the MI composition and cause the MI to deviate from the melt composition at the time of entrapment. It is important to note that homogenization parameters are determined differently for plagioclase-hosted MIs as compared to olivine-hosted ones. Olivine-hosted MIs are often heated using a heating stage and homogenization temperature is determined by the disappearance of the vapor bubble (Danyushevsky et al., 2000; Danyushevsky et al., 2002). Vapor bubbles may be present due to relaxation of the host and may persist through heating. Thus, using the vapor bubble as a means to determine the homogenization temperature has been documented as an imprecise method. In addition, changes in the crystal as a function of heating time can cause the homogenization temperature to differ from the entrapment temperature (Schiavi et al., 2016; Drignon et al., 2019).

Plagioclase-hosted MIs have an additional constraint due to the fact that primitive MIs are saturated with both plagioclase and olivine (plagioclase-olivine cotectic) (Bryan, 1983; Nielsen, 2011). As such, we can apply calculated phase equilibria (e.g. MELTs Ghiorso et al., 2002), the presence of olivine daughter crystals, and the assumption that the liquids are on the plagioclase-olivine cotectic to determine the homogenization parameters rather than the temperature at which the vapor bubble disappears (Roedder, 1979; Sinton et al., 1993; Nielsen, 2011). Additionally, post-entrapment processes can be dealt with computationally by adding or subtracting the composition of the host crystal. However, primitive plagioclase-hosted MIs contain multiple phases (olivine, plagioclase) which do not grow in cotectic proportions thus making computation difficult (Danyushevsky et al., 2002; Lange et al., 2013a; Lange et al., 2013b; Neave et al., 2017). To apply this method, one needs to know the precise compositions of the daughter crystals, which are often too small to analyze.

To see through the effects of post-entrapment and homogenization processes, we must understand how constraints such as duration of heating and pressure used during the homogenization process, could modify the composition of MIs and/or host mineral. This question therefore has at least three parts. First, one needs to understand the characteristics of the post-entrapment modification that happens prior to quench. Second, if we want to use homogenization to recreate the melt at the time of entrapment, we need an independent measure for what to expect (e.g. what does successful homogenization look like). Finally, we need to understand what happens to both the physical characteristics and composition of both MI and its host during homogenization. To the first order, heating provides the conditions where the post-entrapment crystals are incorporated back into the MI therefore producing a homogenous glass that represents the melt at the time of entrapment. The temperature and pressure at which the inclusions are homogenized should be those of MI entrapment (Nielsen, 2011). Therefore, experimental conditions for homogenization are based on the observed phase equilibria (Nielsen, 2011) and the volatile abundances contained within the MIs, which together can be used to calculate the temperature and pressure of entrapment (Ghiorso and Gualda, 2015). However, there is evidence that heating at pressures that are not that of entrapment can cause changes in the mineral structure and melt composition (Schiavi et al., 2016; Drignon et al., 2019).

The goal of this research is to understand how sensitive melt inclusion compositions are to the temperature, pressure, and time of homogenization and develop a methodology to recreate the melt composition at the time of entrapment. Constraining the major, trace, and volatile element characteristics within the MI compositions as a function of temperature, pressure, and time will also help to better understand the nature of processes that modified the initial melt composition en route to the surface.

We focused this work on experimentally heating plagioclase megacrysts from plagioclase ultraphyric basalts (PUBs), a component of the array of MORB lavas. PUBs are characterized by abundant (>15%), large (~2 mm–2 cm) plagioclase megacrysts with a high anorthite content ($An_{80–94}$) (Lange et al., 2013a; Lange et al., 2013b). Based on their texture and composition, these anorthitic feldspars are not in equilibrium with the host glass (Kohut and Nielsen, 2004). Their high and relatively narrow range of anorthitic content and wide range of trace element composition suggests that they formed prior to fractionation and mixing, and therefore are a means for improving our understanding of the magmas formed in the mantle. The fact that these anorthitic megacrysts are large and

comparatively easy to work with, have abundant MIs, and have been well characterized in a number of previous studies (Sinton et al., 1993; Nielsen et al., 1995; Lange et al., 2013a; Lange et al., 2013b; Drignon et al., 2019) help us to set boundary conditions for this work (e.g. pressure of entrapment, range of An content, constraints on homogenization temperature).

BACKGROUND

Melt Inclusions as Proxies

Melt inclusions have been studied as a source of geochemical information on primitive melts for over 40 years (e.g. Anderson and Wright, 1972; Dungan and Rhodes, 1978; Roedder, 1979; Sobolev and Shimizu, 1993; Sobolev, 1996). However, it was the development of micro-analytical tools (e.g., Secondary Ion Mass Spectrometry-SIMS) capable of analyzing trace elements in MIs and their adjacent hosts that enabled the increased attention to and application of MI data. A further increase in interest in MIs resulted from additional technical developments in microanalysis, as well as improved understanding of the solubility of volatiles as a function of temperature, pressure, and composition (Kent and Putirka, 2008; Ghiorso and Gualda, 2015).

Most of the existing MI research on basaltic systems focuses on olivine-hosted MIs (Sobolev and Shimizu, 1993; Wanless and Shaw, 2012; Le Voyer et al., 2017). The rationale for a focus on olivine is that it is perceived to be the first mineral to crystalize from basaltic magmas and are therefore a source of information on the character of magmas early in the evolution of a suite of magmas. Further, olivine-hosted MIs have been preferred over plagioclase because it is thought plagioclase-hosted MIs are susceptible to leakage along cleavage planes. However, the recent work by Drignon et al. (2018), Drignon et al. (2019) has shown that CO_2 does not diffuse through plagioclase on the timescale of days. Diffusion of H out of plagioclase-hosted MIs is significant and occurs on the timescale of hours (Gaetani et al., 2012). Nevertheless, the rate of H loss is much slower than is the case for olivine-hosted MIs, that occurs in less than an hour at temperatures near ~1,250°C (Gaetani et al., 2012; Ferris et al., 2018). Therefore, plagioclase-hosted MIs are an important additional source of data on the chemical characteristics and the depth of formation of primitive MORB magmas (Drignon et al., 2018). Additionally, plagioclase is an abundant host that can be found in magmas ranging from basalt to rhyolite, whereas olivine is commonly restricted to basalts.

Volatile (CO_2 and H_2O) contents measured from MIs can be used to estimate the pressure and therefore depth of plagioclase formation (Ghiorso and Gualda, 2015; Coumans et al., 2016). Establishing the pressure of entrapment is essential for experimental homogenization. Drignon et al. (2018) reported crystallization pressures between 2.3 and 9.1 kbars, with the majority between 3 and 7 kbars, for plagioclase megacrysts from PUBs sampled from the Blanco Fracture Zone. Each of those pressure estimates have errors of ~1.5 kbar and are as high or higher than the pressure estimates based on data from olivine-hosted MIs from other ocean floor basalts (Bennett et al., 2019; Kotash et al., 2019). An understanding of the range of values requires an accurate estimate for the total CO_2 content of MIs. In turn, the CO_2 estimate is subject to knowledge of the homogenization parameters such as heating rate and run time, as well as the details of how CO_2 is distributed in the MI.

Drignon et al. (2019) reported the results of a series of homogenization experiments run on plagioclase megacrysts from PUBS samples from the Blanco Fracture Zone. Experimental run times were 30 min, 4 h, 1 day, and 4 days. They observed a systematic drift in the melt inclusion MgO composition with time, which was attributed to crystal deformation/relaxation and pressure loss within the MI. During homogenization at 1 bar, the internal pressure of the MI drops in response to the deformation of the host crystal (Schiavi et al., 2016). It is thought that host deformation is a plastic process, as MIs and vapor bubbles grow with heating and do not return to their original size with cooling (Danyushevsky et al., 2000, Danyushevsky et al., 2002). Deformation of the crystal occurs when the internal pressure within the MI (which begins at the pressure of entrapment) pushes outward on the crystal at the same time as heating at 1 bar (reduced confining pressure) allows the crystal to respond to lower internal pressure in the MI (Schiavi et al., 2016). In effect, plagioclase deforms as it "relaxes" in order to eliminate the pressure differential between the MI and the confining pressure on the host. The compositional drift of melt inclusion MgO with experimental heating time reported by Drignon et al. (2019) was attributed to a drop in the Mg plagioclase/melt partition coefficient during homogenization that could be related to a drop in pressure. However, the partitioning database for Mg plagioclase/melt partitioning is insufficiently precise to affirm that the Mg partition coefficient is pressure or temperature dependent (Nielsen et al., 2017). In addition, even if our understanding of the compositional, temperature, and pressure dependence of Mg partitioning between plagioclase and melt were more precise, we must recognize that equilibrium is rarely achieved during the process of MI homogenization. Within the timeframe of such experiments, the crystal will continue to deform, the internal pressure will change, and diffusive exchange will move towards equilibrium, which is a moving target. In the face of the documented change in melt inclusion MgO content as a function of time, it is important for us to understand if other elements behave similarly, and if the observed trends are dependent on MI or host composition. This knowledge is required if we are to understand the geochemical signals evident in plagioclase-hosted MIs, particularly the heterogeneity of their trace element signal (Lange et al., 2013a; Lange et al., 2013b; Nielsen et al., 2020).

To understand how the composition within and around the MI change during homogenization, we conducted a series of experiments that expand on the work of Drignon et al. (2019). The objective of this new research is to answer the question: Does confining pressure influence the major and trace element partitioning behavior between the plagioclase host and its MIs? In effect, we expanded the scope of the previous research to include the behavior of trace elements, different host compositions and experimental confining pressure.

We Tested Two Scenarios

(1) Assuming equilibrium at the time of entrapment, the progressive diffusive exchange of major and trace components between the host plagioclase and the MI is caused by crystal relaxation and resultant reduction in pressure within the MI.
(2) Host plagioclase and MIs are not in equilibrium at the time of entrapment. During the heating process, the crystal and MI are driven towards equilibrium, and produce the compositional profiles seen at the MI/host interface.

Before we experimentally test which scenario describes the driving forces for compositional drift, we will describe some of the boundary conditions and terminology we will be applying.

Crystal Relaxation

For the purpose of this investigation, we will use the term "crystal relaxation" for the phenomenon where the crystal deforms in response to the pressure differential between the pressurized MI, and the host crystal or in response to lower confining pressure. As previously noted, it is thought that the plagioclase host deformation is plastic (Danyushevsky et al., 2002). The degree to which the MI and surrounding host composition responds to the relaxation is unknown, as well as the driving mechanism (e.g. changes in partition coefficients, diffusion rate, etc.). The utility of MIs as a source of information on evolving magma suites is based on the assumption that they preserve melt compositions unmodified by late stage process such as fractionation or mixing, as well as preserve information about temperature and pressure of formation. This assumption is only true if post-entrapment processes can be reversed and the MI remains isolated from the rest of the melt and is not significantly modified by reaction with the host crystal (e.g. diffusive exchange). For example, if a MI is breached, it is no longer a closed system and cannot be interpreted as such. Although MIs undergo compositional changes during magma ascent and crystallization due to post-entrapment processes, it has been presumed that decompression and resultant physical deformation of the host is minimal (Zhang, 1998).

Schiavi et al. (2016) conducted experiments on olivine-hosted MIs to determine pressure, temperature, and volume (of the inclusion) constraints on MI homogenization. These experiments documented that homogenization at 1 bar results in an increase in the volume of the MI due to deformation of the host crystal. This deformation was inferred to occur as a result of the pressure differential between the MI and the host. During reheating, the host crystal relaxes in response to pressure re-equilibration between itself and the initially pressurized MI (Danyushevsky et al., 2002; Schiavi et al., 2016; Drignon et al., 2019). Schiavi et al. (2016) suggested that the method for avoiding crystal relaxation is to apply external pressure to the crystal host during homogenization.

Entrapment Under Disequilibrium Conditions

Trace element analysis taken from core to rim of plagioclase crystals from PUBs were studied by previous researchers to investigate melt evolution. These analyses yielded no progressive trend (e.g. normal or reverse zoning—Adams et al., 2011; Nielsen et al., 2020). This suggests that the plagioclase megacrysts formed from a series of different liquids that were not linked by any simple mixing or fractionation process. Although the major element variation is minimal in comparison to trace element variation, rejuvenation events (new magma pulses), different magma sources, or magma mixing/mingling are consistent with the observed range of composition. The lack of correlation of major and trace element signatures throughout the growth of the crystals supports the conclusions of Lange et al. (2013a), Lange et al. (2013b) that the plagioclase megacrysts formed via sidewall crystallization within conduits that transported magma from the mantle to the ocean floor. Therefore, it is possible that melt trapped as inclusions during plagioclase growth is not representative of the initial magma, but rather different magmas that the crystal has come into contact with, depending on when entrapment occurred. Kohut and Nielsen (2004) demonstrated that, for a system similar to the one we investigated the rate of diffusion in the melt is typically, but not always, faster than the rate of crystal growth related to MI formation. If the melt trapped as a MI came from a different magma source (for example following a mixing related rapid crystallization event), the extent of disequilibrium between the host plagioclase and the MI must be assessed if we are to use MI information to understand processes active in the regions where the anorthitic megacrysts form. This approach was applied to evaluate host/MI equilibria by Nielsen et al. (2017), who reported that the ratio of the concentration in the host to that in the homogenized MI was within error of the experimentally determined partition coefficients for those elements. However, those comparisons were made for MI that had been homogenized for 30 min.

EXPERIMENTAL PROCEDURES

Experimental Design

We designed a set of homogenization (heating and subsequent quenching) experiments at 1 bar and 7.5 kbars completed in the form of a time series (30 min, 4 h, 1 day, 4 days, and 8 days) to evaluate the effect of confining pressure and the duration of heating on MI composition. We analyzed major and trace element compositions for both low and high pressure experiments to measure differences that could be tied to whether or not confining pressure has an effect on the MI and host plagioclase composition. 1 bar represents the surface pressure, while 7.5 kbars was chosen because it represents a pressure near the maximum of the calculated pressure of plagioclase crystallization based on MI CO_2, which represent minimum entrapment pressures (Drignon et al., 2018).

Sample Selection and Characteristics

Two PUB samples, D23-2 from the West Valley of the Juan de Fuca Ridge and A91-1R1 from the Blanco Fracture Zone (BFZ) were selected for this study. In addition to being characterized by high phenocryst content (>20% in both cases), the crystal cargo of each was characterized by a relatively narrow range of anorthite content as well as average anorthite contents that were distinctly different from one another (A91-1R1: 84 ± 2%; D23-2: 88 ± 2%). The ~4% An difference between the average megacryst composition was judged to be sufficiently large that we could use any differences in the results to evaluate the role of host composition. It is important to note that the total range of anorthite content in PUBs is 86–92% (Lange et al., 2013a; Lange et al., 2013b).

Plagioclase megacrysts were extracted from each sample by crushing and hand picking. Sample A91-1R1 was the same sample that was the subject of Drignon et al. (2019) where the drift of MgO within MI as a function of heating time was first identified. The melt inclusions hosted within the plagioclase megacrysts range in radius from 2 to >100 μm. Plagioclase-hosted MIs tend to have tabular or disc-shaped morphology with two long axes and one shorter axis. Prior to homogenization they are characterized by side-wall post-entrapment crystallization at the MI-plagioclase interface and by minute daughter crystals (plagioclase and olivine) within the MI as well as a vapor bubble (Drignon et al., 2019). These samples were chosen in part due to the fact that the MIs exhibit a relatively narrow range of major element compositions associated with comparatively heterogeneous trace element composition in the plagioclase host and MI within each sample (Nielsen, 2011; Lange et al., 2013a; Lange et al., 2013b; Nielsen et al., 2020). However, these are natural samples, thus there is some initial variability in post-entrapment crystallization prior to homogenization.

Experimental Details

Low Pressure Homogenization Experiments

Low pressure homogenization experiments were conducted at 1 bar using the vertical quench furnace at South Dakota School of Mines and Technology (SDSM&T). Experiments were performed in air without measurement of fO_2. This decision was based on previous work that determined fO_2 to be near Fayalite-Magnetite-Quartz buffer (FMQ), as well as the fact that oxygen does not diffuse through feldspar at the timescale of these experiments (Drignon et al., 2019; Dygert et al., 2020). The entrapment temperature of 1,230°C was determined using observation of batches of MIs heated sequentially (as per Nielsen et al., 1995). In detail, batches of crystals were heated to temperatures just below our estimate of the entrapment temperature and examined for presence of daughter crystals and the degree to which the MI lay at or near the olivine-plagioclase cotectic. If daughter crystals or sidewall crystals were present in the MI, another batch of crystals were heated to a temperature 10°C above the initial batch. This process was continued until the MI compositions departed from the olivine-plagioclase cotectic on to a plagioclase control line. These temperatures were then confirmed by heating stage (Lange et al., 2013a; Lange et al., 2013b; Drignon et al., 2019).

Depending on the size of the megacryst up to six crystals were placed in Pt-foil boats wrapped in fine Pt-quench wire (0.003 inches) and suspended from a thicker Pt-suspension wire (0.024 inches). The run assembly was then lowered into the furnace to the hot spot at 1,230°C for the duration of each experiment. At the end of designated times the sample was quenched by running an electric current through the Pt-quench wire causing it to vaporize. This allowed the boat containing the sample to drop into water in the quench chamber. For plagioclase-hosted inclusions, this rapid quench is necessary because crystallization within the MI can happen even during the removal of the assembly from the furnace if the sample is quenched in air. Previous work showed that 3–5 s between the removal of the run assembly from the furnace and quench could cause percent level changes in the Al and Ca concentrations of the MI (Nielsen et al., 1995). Following the homogenization experiments, probe sections were prepared by exposing the MIs at the surface of before the final polish.

It is important to note here that a major advantage of a vertical quench furnace is the minimal sample preparation required before the experiments are run. One needs only separate crystals from the host and place them in a Pt-foil boat. Up to six crystals can be run at a time, then examined to evaluate the degree to which the effects of post-entrapment crystallization had been reversed. Crystals that did not satisfy those conditions (e.g. remaining daughter crystals at low temperature end to liquids on a plagioclase alone control line) were eliminated from further study. Note that plagioclase control line refers to the process vector describing addition or subtraction of plagioclase to the melt.

High Pressure Homogenization Experiments

High pressure homogenization experiments were conducted using an end-loaded piston-cylinder apparatus at Lamont–Doherty Earth Observatory (LDEO). End loads of 150 tons were applied to the 1/2″ pressure vessel of Boyd-England design. Piston loading by a 3″ ram to reach 5 kbar of 198 bars oil pressure used the calibration for $BaCO_3$ of Fram and Longhi (1992). Experiments were run at 7.5 kbar and 1275°C for run times of 2 and 4 days. The temperature for high pressure runs was based on the results of a set of phase equilibria experiments on PUB compositions (Ustunisik et al., 2020). Similar to low pressure experiments, fO_2 was not measured on the assumption that oxygen does not diffuse any quicker at high pressure than it does at low pressure.

Runs were performed in a ½ inch (″) inside diameter Boyd-England compound pressure vessel with cylindrical Pb-wrapped $BaCO_3$/MgO pressure medium (0.487″, 0.313″, 1.25″), graphite furnace (0.312″, 0.25″, 1.25″), high-density Al_2O_3 sleeve (0.248″, 0.181″, 0.25″), one-hole and solid MgO spacers (0.5″), MgO wafer (0.078″), and platinum capsule, with continuous external H_2–N_2 (5% H_2, 95% N_2) flow to protect the thermocouple from oxidation.

Plagioclase phenocrysts (2–3 depending on size) were loaded in platinum capsules packed with cesium iodide, which is compressible therefore avoiding the destruction of crystals. Experiments were pressurized cold then heated incrementally

to 850°C for over an hour after which the assembly was left at 850°C overnight to stabilize and close porosity in the pressure media. After repressurization, temperature was raised in 50°C steps of approximately 20 min to the run temperature, repressurized after 20 min, left for the experiment duration and quenched by turning off the electric power. Cooling to less than 400°C took approximately 5 s. Run products were mounted in epoxy then sectioned and polished for petrographic and geochemical analysis.

ANALYTICAL TECHNIQUES

Electron Microprobe Analysis

Backscattered electron (BSE) images and major element abundances for plagioclase and glass from the experimental runs were obtained using the Cameca SX100 electron microprobe (EMP) at Oregon State University (OSU). BSE images were used to map out the location and size of each melt inclusion analyzed.

Major element data were obtained both as point analysis of MIs and traverses from the plagioclase host into individual MIs. The criteria used to determine if MI were breached were based on the findings of Nielsen et al. (1995), Nielsen et al. (1998) with a focus on the MI morphology and the sulfur content. In their findings, breached or decrepitated MIs lost all of their sulfur in less than 30 min heating time. MIs that fell off the sulfur saturation curve by 2σ were considered breached and therefore discarded based on the assumption that MORB lavas are sulfide saturated (Wallace and Carmichael, 1992; Nielsen et al., 1998; Drignon et al., 2019). Point analysis were done at the center of the MI in order avoid overlap with the host plagioclase. Traverses were taken from the plagioclase host to the MI with a step size of 2 μm. Traverses also approached the MI from different directions in order to address the possibility of diffusional anisotropy, whether diffusion profiles vary or not along different crystallographic axes.

Calibration for glass was performed using VG-2 (NMNH 111240-52) for Si, Ti, Al, Fe, Mg, Ca; fluorapatite (NMNH 104021) for P, Lake County labradorite (NMNH 115900) for Na, microcline (NMNH 143966) for K. Na and K were analyzed first to reduce the volatile loss due to the electron beam. Electron beam conditions for glass were: 15 kV accelerating voltage, 30 nA beam current, with a 5 μm diameter electron beam. Standards for plagioclase were Lake County labradorite for Na, Al, Si and Ca, VG-2 basaltic glass for Mg, Fe, Ti and microcline for K. Peak counting times were 5s for Na, 10 s for Si, Al, Ca, K; 30 s for Ti; and 60 s for Fe, and Mg. Microprobe analysis conditions for plagioclase were: 15 kV accelerating voltage, 30 nA beam current with a 2 μm diameter electron beam. Tests on several standards were performed throughout the analytical sessions to verify that calibrations did not drift more that 1% relative.

Trace Element Analysis

Laser ablation trace element analysis were completed at the W.M. Keck Collaboratory for Plasma Spectrometry at the College of Earth, Ocean, and Atmospheric Sciences (CEOAS) at Oregon State University using a Teledyne/Photon Machines Analyte G2 ArF Excimer laser coupled to a ThermoElemental iCAP-RQ quadrupole inductively coupled plasma mass spectrometer. Run products were analyzed for Li, Mg, Ca, Ti, Sr, Y, Zr, Nb, Ba, La, Ce, Nd, Sm, Eu, Gd, Dy, Er, Yb, Hf, Ta and Pb to determine whether the systematic drift in composition observed by Drignon et al. (2018) was constrained to only major elements, or the same pattern was also observed in trace elements. These elements were selected for the variation in their diffusion rates and partition coefficients to test whether the partitioning behavior or diffusion rate elements were affected differently by the process creating the previously observed trend.

The Helex 100 sample cell configuration on this unit was designed to hold up to nine standard 1″ microprobe rounds and is typically configured to hold six or seven "unknown" rounds with the remaining two to three positions used to hold rounds containing standard reference materials. The samples were isolated in a helium atmosphere and helium gas was used to carry the ablated particulates through Teflon tubing to the mass spectrometer. The helium gas (with transported particulates) was mixed with argon gas within the torch-box housing using a small nylon-T, just prior to introduction to the ICP torch. All ablated material was carried via ultrapure He gas flowing at 0.8 L/min and is mixed with Ar-nebulizer gas at a flow rate between 0.95 and 1.0 L/min. Beam diameters ranged between 10 and 30 μm depending on inclusion size, a laser repetition rate of 8 Hz was used for all analyses and laser fluence was set to 6.35 J/cm^2.

A typical analysis begins with a 30 s background reading followed by a 70 s acquisition period. The data are collected using time resolved analysis in peak hopping mode using a single point per peak, with 10 ms dwell time on each analyte. Under these conditions individual acquisitions typically lead to between 30 and 40 second-long stable, signal plateaus resulting in ~0.75–1.25 s of count time per analyte.

For some inclusions, due their morphology, the laser ablates through the inclusion into the plagioclase. To correct for this, all of the data were back calculated using electron microprobe MgO abundances to minimize the effect of plagioclase contamination. This was done by assuming the Mg measured via LA-ICP-MS should have a 1:1 ratio with Mg measured by EMPA. The MI composition was calculated by projecting to the known MgO abundances of the MI and the host as per Nielsen et al. (2017). Sr and Ba concentrations for the MI were estimated using the plagioclase/melt partition coefficients calculated using the constraints of Nielsen et al. (2017) based on the measured An content of the host and 1,230°C. Inclusions that required more than 30% correction were discarded (10% of analyses performed).

RESULTS

Major Element Variation With Heating Time

Changes in melt inclusion composition as a function of time were measured for both the Blanco Fracture Zone and Juan de Fuca Ridge samples for five time intervals including 30 min, 4 h, 1 day, 4 days, and 8 days (**Figures 1**, **2**). Mg and Si in MI increases with

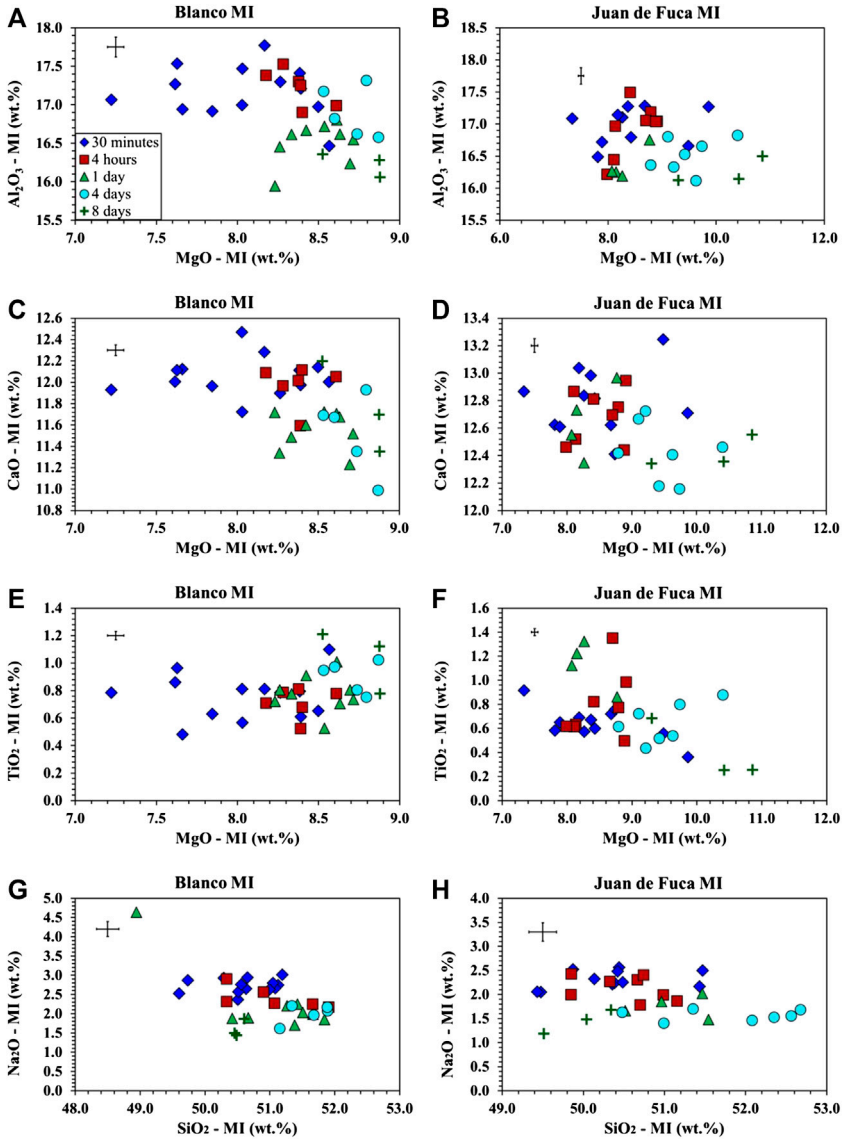

FIGURE 1 | Major element analysis of MIs from the Juan de Fuca Ridge (D23-2) and the Blanco Fracture Zone (A91-1R1) samples following homogenization at 1 bar. Symbols for run time is consistent across all major element plots with 30 min as blue diamonds, 4 h as red squares, 1 day as green triangles, 4 days as aqua circles, and 8 days as dark green crosses. Error bars are located in the upper left hand corner of each plot. **(A)** Al_2O_3 vs. MgO for A91-1R1 (Blanco Fracture Zone) shows a decrease in Al_2O_3 and an increase in MgO with time. **(B)** Al_2O_3 vs. MgO for D23-2 (Juan de Fuca) shows a decrease in Al_2O_3 and an increase in MgO with time. **(C)** CaO vs. MgO for A91-1R1 (Blanco Fracture Zone) shows a decrease in CaO and an increase in MgO. **(D)** CaO vs. MgO for D23-2 (Juan de Fuca) shows a decrease in CaO and an increase in MgO. **(E)** TiO_2 vs. MgO for A91-1R1 (Blanco Fracture Zone) correlating TiO_2 and MgO. **(F)** TiO_2 vs. MgO for the D23-2 (Juan de Fuca) correlating TiO_2 and an increase in MgO. **(G)** Na_2O vs. SiO_2 for A91-1R1 (Blanco Fracture Zone) shows a decrease in Na_2O and an increase in SiO_2 outside of 8 days experiments. **(H)** Na_2O vs. SiO_2 for D23-2 (Juan de Fuca) shows a decrease in Na_2O and an increase in SiO_2 outside of 8 days experiments.

time while Ca, Al, and Na decrease. The exception is the 8-day runs which do not follow the trend of increasing Si. Ti shows compositional change with time, but the trends are different for each sample. Ti increases with time for MIs in plagioclase from the Blanco sample, but decreases with time for MIs in plagioclase from the sample of the West Valley of the Juan de Fuca. Regardless of this, longer periods of homogenization are tied to compositional drift. Similar trends are observed for inclusions in both the Blanco Fracture Zone and Juan de Fuca samples.

Major Element Profiles

Traverses of EMPA analyses from the plagioclase host into the MI (**Figures 3A–C**, **4A–B**) show that the area around MIs are lower in Mg compared to the host (away from MI/far-field host) in the longest (4- and 8-day) experiments. It is important to note that the zone of excitation of the electron beam is 2 μm and thus the values reported are minima. Similar patterns are not seen in the shorter (30 min, 4 h, and 1 day) experiments. As noted in **Electron Microprobe Analysis**, two traverses were done on

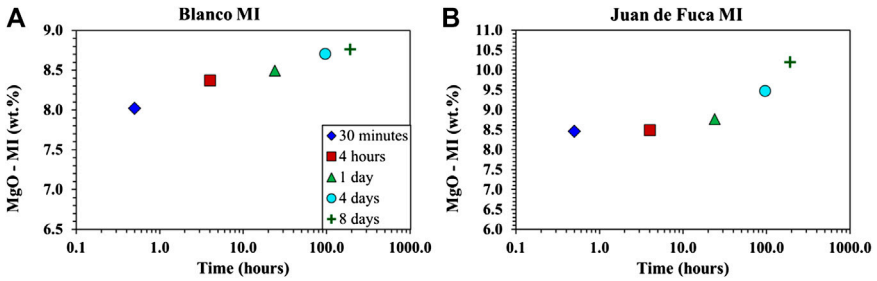

FIGURE 2 | Averaged point analysis per time group for low pressure samples. Symbols include 30 min average as a blue diamond, 4 hours average as a red square, 1 day average as a green triangle, 4 days average as an aqua circle, and 8-days average as a dark green cross. **(A)** Time vs. MgO for the Blanco fracture zone (A91-1R1) averaged time groups. **(B)** Time vs. MgO for the Juan de Fuca Ridge (D23-2) averaged time groups.

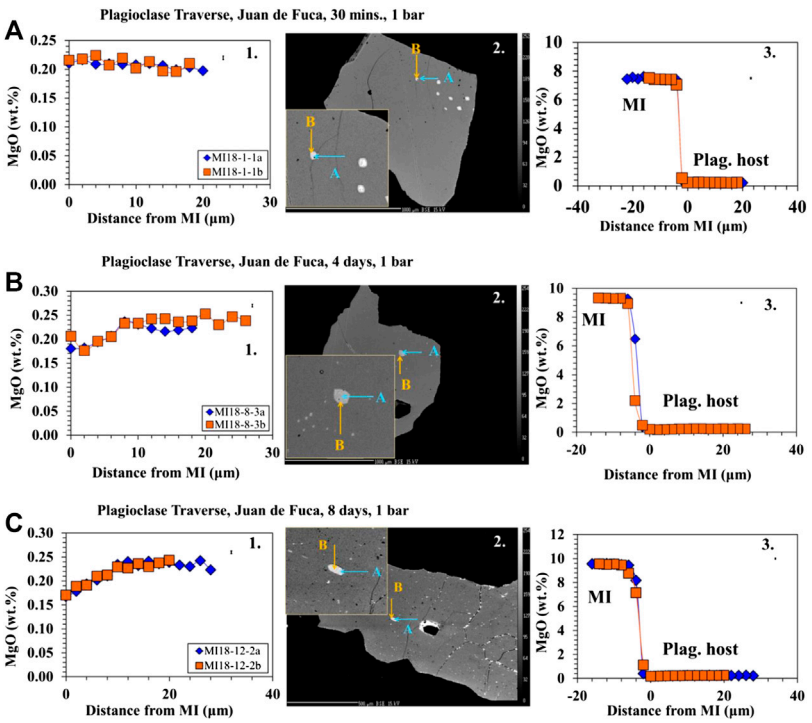

FIGURE 3 | Major element profiles between the host plagioclase and the MIs for low pressure experiments. 1) The profile from the plagioclase host (right) into the MI (left) marked by an increase in MgO. Error bars are located in the upper right corner. 2) BSE images showing the direction and location of traverses. 3) Profile within the plagioclase host as it approaches the boundary of the MI (marked by 0 distance from MI). **(A)** Profiles and BSE on a 30 minute-low pressure Juan de Fuca sample-D23-2. Results show no change in MgO as the traverse approaches the MI boundary. **(B)** Profiles and BSE on 4 days Juan de Fuca-D23-2 low pressure sample. Results show a decrease in MgO as the traverse approaches the MI boundary. **(C)** Profiles and BSE on 8 days-low pressure Juan de Fuca-D23-2 sample. Results show a decrease in MgO as the traverse approaches the MI boundary. Error (1σ) in MgO is smaller than the symbols and was determined on the basis of counting statistics.

each MI from different directions to assess the possible influence of crystallographic orientation. The two different traverses are set at 90° to each other. We did not determine the crystallographic orientation prior to analysis, but as there were minimal differences between the two traverses on all analysis, crystallographic orientation was determined to be inconsequential.

The morphology of MI in these samples is highly variable. Most small inclusions are spherical, with increasing numbers of disc-shaped inclusions among the larger MI population (see BSE images of MIs—**Figure 3**). In addition, MI occur as isolated bodies or in bands associated with zoning patterns. Two phase melt inclusions are restricted to spinel + melt and vapor + melt – olivine is never found as part of a binary phase MI (as reported by Nielsen et al., 2020). However, small olivine daughter crystals (<5 microns) are common in MIs that have not been heated (naturally quenched – see images in Drignon et al., 2019). This is consistent with previous observations of MIs in

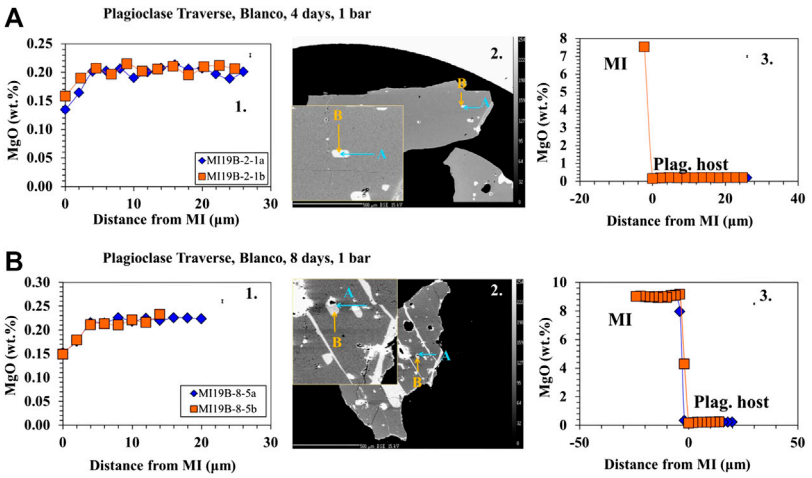

FIGURE 4 | Major element profiles between the host plagioclase and the MI for low pressure experiments. 1) The profile from the plagioclase host (right) into the MI (left) marked by an increase in MgO. Error bars are located in the upper right corner. 2) BSE images showing the direction and location of traverses. 3) Profile within the plagioclase host as it approaches the boundary of the MI (marked by 0 distance from MI). **(A)** Profiles and BSE on 4-day Blanco-A91-1R1 low pressure sample. Results show a decrease in MgO as the traverse approaches the MI boundary. **(B)** Profiles and BSE on 8-day low pressure Blanco-A91-1R1 sample. Results show a decrease in MgO as the traverse approaches the MI boundary. The bands of melt (light grey) across the crystal (medium grey) represent melt present along fractures, presumably cleavage planes. A number of other breached MIs are present in the same image.

plagioclase megacrysts (see compilation of plagioclase-hosted MI images in Nielsen et al., 2017). The increased tendency for irregular (non-spherical) morphologies in plagioclase-hosted inclusions is consistent with the observations of the MI formation experiments of Kohut and Nielsen (2004). The shape of MIs is a complex function of degree of undercooling and crystal growth rate.

The results from the traverses between the plagioclase host and MI for Juan de Fuca and Blanco samples (**Figures 3A–C**, **4A–B**) document that in the 4- and 8-days runs, MgO in the plagioclase drops by ~25% in the 5–10 microns closest to the inclusion. This drop in MgO near the inclusion is not observed for the shorter run experiments. The width of the zone of lower MgO in the 4-days experiments varies for different MIs. We did not assess the possible influence of the third dimension. The resultant profiles depend on the angle between the polished surface and the MI/plagioclase interface. If the MI/host interface intersects the surface orthogonally, one would expect a narrower profile to be sampled compared to the case where the MI/host interface intersected the surface at a high angle. There is minimal difference between the two traverses in all cases regardless of run time, thus the change in MgO is not controlled by crystallographic orientation. Experiments with a large change in melt inclusion MgO content show a significant Mg depletion halo at the MI/host interface. This profile is observed primarily in the 4- and 8- days experiments is consistent with a model where Mg diffuses "uphill" from the plagioclase host into the MI (**Figures 3B,C**, **4A–B**). While the compositional drift also occurs in 4-hour and 1-day runs as seen in the MI point analysis, the profile from the plagioclase into the MI is not large enough to be observed in the traverses. As diffusion does not have an effect on 30 min run products, no trends are found to be visible (**Figure 3A**).

Trace Element Profiles

The results of the major element analysis document a drift in composition with time primarily observed in MgO (~1–1.5 wt% **Figures 1**, **2**). This leads to the question of whether the trace elements contents are affected by heating time and whether or not the heterogeneity in MI and megacrysts compositions reported in earlier investigations can be attributed to the homogenization process (Nielsen et al., 1995; Sours-Page et al., 1999; Cottrell et al., 2002). As mentioned earlier, several different trace elements were selected on the basis of differing partitioning behavior between plagioclase and basaltic glass (MI) (Zr, Nb—lowest; Ti, Mg, Ce—low; Ba—medium; Sr—high) (Bindeman et al., 1998) and diffusion rates (Zr, Nb—slowest; Ce, Ti—slow; Ba—medium; Sr, Mg—fast) (Cherniak and Watson, 2020; Nielsen et al., 2020).

We expected to observe one of two possible outcomes. The first is a mirrored phenomenon of what is observed in the major element results; that there is compositional drift with increasing homogenization time. The second is a cone of equilibration where trace element variability decreases with increasing homogenization time. The only trace element noted to show any correlation with run time is Ti (**Figures 5A**,**B**). Ti exhibits decreasing abundance with time in the Juan de Fuca Ridge sample, while exhibiting a slight increase in Ti for Blanco Fracture Zone sample (**Figures 5A**,**B**). However, the range of Ti for any specific run time remains the same (e.g. not convergence). Sr, Nb, Ba, Ce, and Zr (**Figures 5C–F**, **6A–F**) exhibit no systematic change as a function of run time, and more important, exhibit no convergence as a function of run time. Such a convergence is what was predicted by Nielsen et al. (1995) and documented for compatible elements in plagioclase hosted MI by Cottrell et al. (2002). The wide range of highly incompatible, slowly diffusing trace elements is common in plagioclase-hosted inclusions (Nielsen et al., 1995; Nielsen et al., 2017; Nielsen et al.,

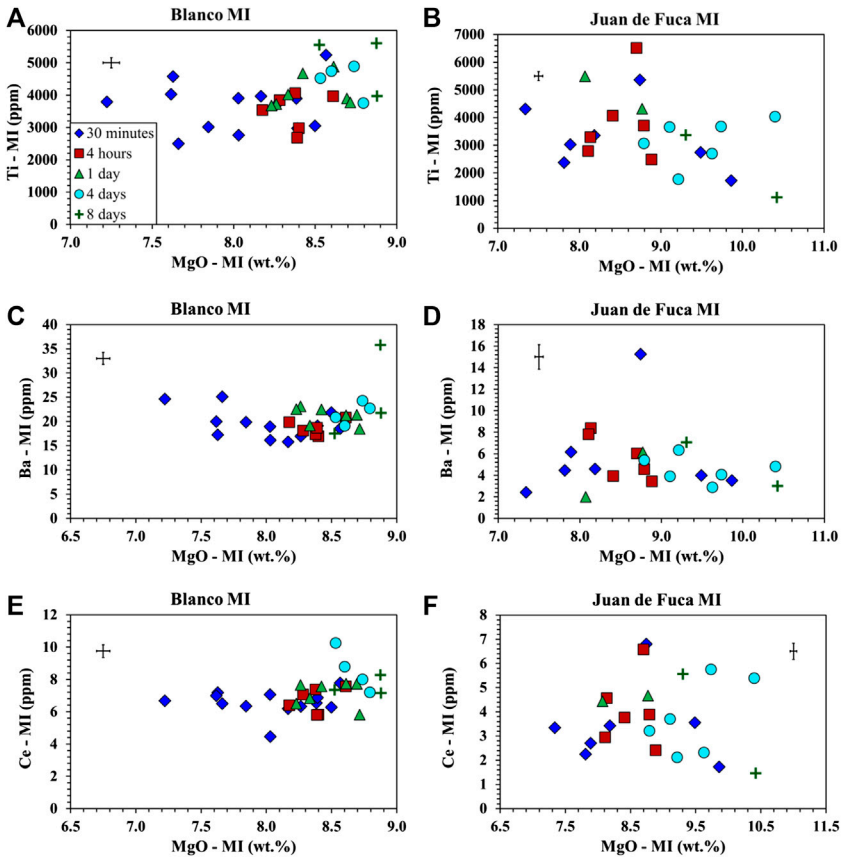

FIGURE 5 | Trace element analysis of MI obtained by LA-ICP-MS following homogenization at 1 bar for samples from the Juan de Fuca Ridge (D23-2) and the Blanco Fracture Zone (A91-1R1). Symbols as in **Figure 1**. Error bars are located in the upper left or right corner of each plot. **(A)** Ti vs. MgO for A91-1R1 (Blanco Fracture Zone) shows an increase in Ti and an increase in MgO with time. **(B)** Ti vs. MgO for D23-2 (Juan de Fuca) shows a decrease in Ti and an increase in MgO with time. **(C)** Ba vs. MgO for A91-1R1 (Blanco Fracture Zone) shows no trend in Ba and an increase in MgO. **(D)** Ba vs. MgO for D23-2 (Juan de Fuca) shows no trend in Ba and an increase in MgO. **(E)** Ce vs. MgO for A91-1R1 (Blanco Fracture Zone) shows a slight increase in Ce and an increase in MgO. **(F)** Ce vs. MgO for D23-2 (Juan de Fuca) shows no trend in Ce and an increase in MgO.

2020). The absence of either a convergent or divergent pattern supports the contention that the concentration of such elements (e.g. Zr, Nb) in MI represents a primary signal (Nielsen et al., 2017, Nielsen et al., 2020).

Role of Pressure on Homogenization

Two sets of high pressure experiments were completed at 7.5 kbar with run times of 2 and 4 days for both the Juan de Fuca Ridge and Blanco Fracture Zone samples. Analyses of Cs and I were done on the charges to evaluate whether or not the packing medium of cesium iodide was suitable for plagioclase (i.e. diffusion did not occur between the packing material and crystal) and to validate the experimental parameters (temperature, time, etc). The results showed that Cs and I were below the detection limits for the EMP, and therefore there was no evidence of diffusive exchange with the packing materials. One 4-day high pressure experiment using crystals from the Blanco fracture zone yielded melt inclusions characterized by a homogeneous glass center with ~ 5–10 μm quench crystallization within the MI along the MI/host interface. This quench growth occurred in spite of the fact that the assembly cooled to less than 400°C within 5 s. The quench crystals were too small to analyze individually but appear dark in the BSE images and were therefore assumed to be plagioclase. Growth of these crystals caused the melt at the MI/host to become enriched in Mg and Fe compared to the MI core (**Figure 7**). The 2- and 4-day high pressure experiments did not exhibit the trend of higher Mg in the MI, nor the lower Mg in the host as one approached the MI interface that are found in the 1 bar, 4- and 8-day experiments (**Figure 7**).

Size Dependency

Based on the observation that the MI/host traverses exhibit trends of different magnitudes, we examined a number of parameters that could be linked to the size of the depletion halo around the MI, as well as the average increase in melt inclusion Mg content as a function of experimental run time. If the migration of Mg into the MI was dependent on MI surface area, one might expect a

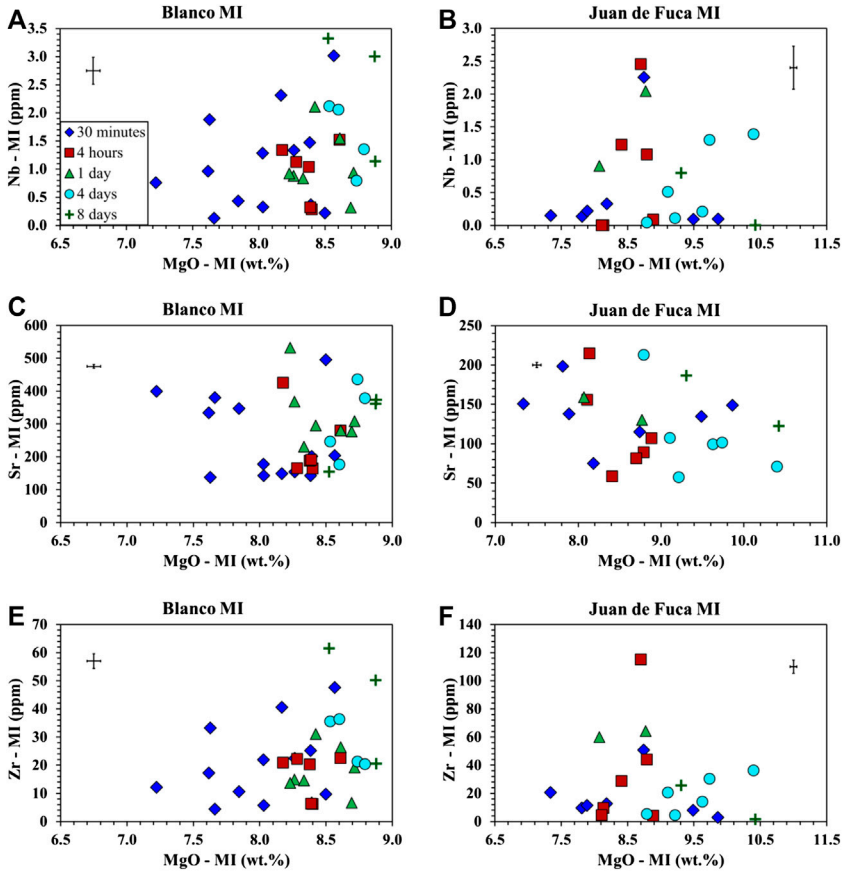

FIGURE 6 | Trace element analysis of MI following homogenization at 1 bar for samples from the Juan de Fuca Ridge (D23-2) and the Blanco Fracture Zone (A91-1R1). Symbols as in **Figure 1**. Error bars are located in the upper left or right corner of each plot. **(A)** Nb vs. MgO for A91-1R1 (Blanco Fracture Zone) shows no trend in Nb and an increase in MgO. **(B)** Nb vs. MgO for D23-2 (Juan de Fuca) shows no trend in Nb and an increase in MgO. **(C)** Sr vs. MgO for A91-1R1 (Blanco Fracture Zone) shows no trend in Sr and MgO. **(D)** Sr vs. MgO for D23-2 (Juan de Fuca) shows no trend in Sr and an increase in MgO. **(E)** Zr vs. MgO for A91-1R1 (Blanco Fracture Zone) shows no trend in Zr and an increase in MgO with time. **(F)** Zr vs. MgO for D23-2 (Juan de Fuca) shows no trend in Zr and an increase in MgO with time.

negative correlation of Mg change with inclusion radius because the surface area to volume ratio decreases with increasing MI radius, and thus each unit volume of liquid would have less host with which to interact. In contrast, if the migration of Mg was dependent on the extent of deformation, increase in inclusion volume and resultant pressure drop, then one might expect a positive correlation. This is because surface area is square function of radius while volume is a cube function (Tait, 1992; Zhang, 1998). For the purpose of this comparison, we calculated ΔMg based on the difference between the average Mg for the 30 min run time experiments, with the MI Mg for each individual MI from the 4 h run time experiments. This ΔMg value used the average MI composition from the 30-min runs as the base line. Note that volume increased as a cube function of radius, while surface area was a squared function. Our results (**Figure 8**) exhibit a positive correlation of the MI radius and the change in Mg among individual 4-days inclusions and the averaged 30-min Mg value, consistent with greater extent of deformation for larger inclusions. Again, this is consistent with the predictions of Tait (1992).

DISCUSSION

There are several factors that must be taken into consideration when homogenizing melt inclusions if we are to produce accurate constraints on the magmas from which the crystals form. Temperature, time, pressure, host composition, melt inclusion size, etc. all play an important role. Since the goal of homogenization is to re-create the composition of entrapment, it is important that the process does not cause progressive changes in the MI composition.

Drift in MI MgO content is correlated with experimental run time. The extent of change in MI MgO content and the magnitude of the depletion zone at the MI/host interface are dependent on time and therefore most evident in long run time experiments (4 and 8 days). Most major and trace elements exhibit similar or no correlation with time in each of the two samples. The sole exception is Ti, which increases in Blanco Fracture Zone samples (A91-1R1) but decreases in the Juan de Fuca Ridge as a function of run time (D23-2) (**Figures 1E–F**, **5A–B**). This suggests that the partitioning behavior may be different for the different MIs

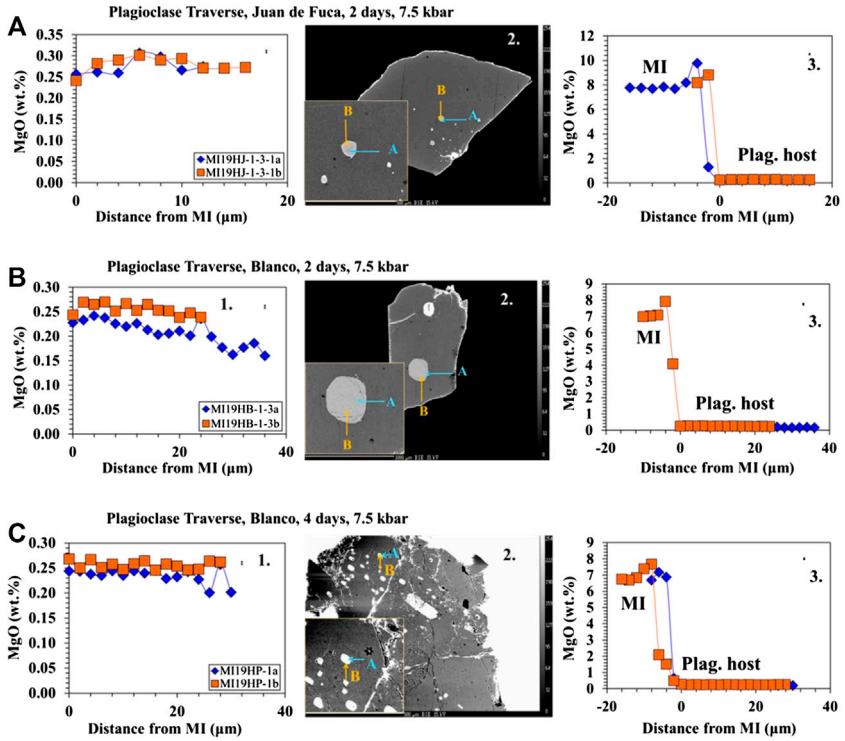

FIGURE 7 | Major element profiles between the host plagioclase and the MI for high pressure experiments. 1) The profile from the plagioclase host (right) into the MI (left) marked by an increase in MgO. Spike in MgO within the MI is a result of quench crystallization. Error bars are located in the upper right corner. 2) BSE images showing the direction and location of traverses. 3) Profile within the plagioclase host as it approaches the boundary of the MI (marked by 0 distance from MI). **(A)** Profiles and BSE on 2-day high pressure experiments for Blanco and Juan de Fuca samples. Results show no change in MgO as the traverse approaches the MI boundary, but an increase in MgO at the inner boundary of the MI. **(B)** Profiles and BSE on 4-day high pressure experiments for Blanco sample. Results show a no change in MgO as the traverse approaches the MI boundary, but an increase in MgO at the inner boundary of the MI.

and host compositions, or even small differences in temperature. It has been documented that plagioclase-melt partition coefficients for Ba, Sr, Ti, Zr, and the REEs are negatively correlated with both temperature and An content (D increases as temperature and anorthite content of plagioclase decreases) (Blundy and Wood, 1991; Dohman and Blundy, 2014; Nielsen et al., 2017). As noted in **Melt Inclusions as Proxies**, the precision and amount of plagioclase/melt partitioning data available at elevated pressure is insufficient to model partitioning in plagioclase quantitatively. If the experimental temperature and pressure were representative of the conditions at the time of entrapment, there should be no changes in MI or host composition as a function of experimental run time. As described in **Low Pressure Homogenization Experiments**, all crystals in this study were heated to 1,230°C at low pressure and 1,275°C at high pressure, which was determined using phase equilibria calculations, experimental results and the disappearance of the daughter crystals (Blundy and Wood, 1991; Lange et al., 2013a; Lange et al., 2013b; Drignon et al., 2019). If either of those constraints on entrapment temperature were off by as much at 10–15°C, one might expect a change in partitioning behavior (Dohman and Blundy, 2014; Nielsen et al., 2017). This may explain the different results for Ti in the two different samples. In particular, both samples, while differing in anorthite content, were homogenized at the same temperature—again based on both phase equilibria and independent heating stage work. It is believed, based on the behavior of Ti, that the Juan de Fuca samples may have been underheated. In addition, repeated heating and cooling will result in crystal relaxation. When homogenization temperatures are determined by heating stage, it is not uncommon for the temperature at which the bubble disappears to increase as the MI is reheated (Danyushevsky et al., 2000; Drignon et al., 2019). This will lead to erroneously high estimates for entrapment temperature, and potentially increase the rate of compositional drift.

Over or underheating may change the behavior of certain major and trace elements thus effecting the overall composition. This could be the potential cause of the opposite trends for Ti in the Juan de Fuca and Blanco samples present in the EMP and LA-ICP-MS data. These two samples are compositionally distinct but were both homogenized at the same temperature (1,230°C). Given the results, it is reasonable to conclude that each sample should be homogenized at different temperatures depending on composition. While phase equilibria and heating stage gave the same temperature for both samples, it is only accurate to within 10–15°C. Thus, it is possible that the Juan de Fuca samples were underheated. It is important to note here that plagioclase megacrysts are typically not in equilibrium with the magma in which they are transported to the surface (Lange et al., 2013a; Lange et al., 2013b). Therefore, during transport, they may reside for

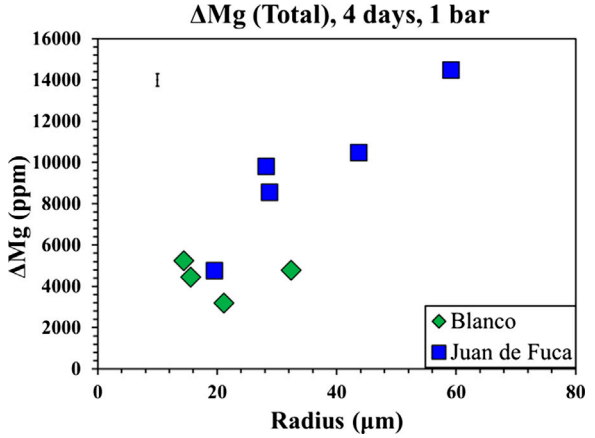

FIGURE 8 | The change in Mg between individual 4-day MIs and the averaged 30-min Mg value plotted against radius. Blue squares represent 4-day low pressure Juan de Fuca samples, while the green diamonds represent 4-day low pressure Blanco Fracture Zone samples. The plot shows an increase in the change in Mg with increasing MI size.

hours, days, weeks or more in magmas at much higher or lower temperature than that representative of their formation. Thus, understanding the sensitivity of MI composition to temperature is not just relevant to the effects of homogenization in the laboratory but also has implications for the conditions that megacrysts that are exposed to during transport.

The homogenization experiments were run at two different pressures to constrain the causes of compositional drift, which has previously been attributed to crystal relaxation (Schiavi et al., 2016; Drignon et al., 2019). Low pressure experiments (1 bar) are representative of the surface pressure while the high pressure experiments (7.5 kbars) represent the pressure of the upper mantle/lower crust. We selected the 7.5 kbars for the high pressure experiments because that value falls within the range of entrapment pressures calculated by Drignon et al. (2018) based on CO_2 contents in MI. To evaluate whether or not crystal relaxation or disequilibrium is causing compositional drift, the 1 bar and 7.5 kbars results were compared. The high pressure runs did not exhibit drift or the MgO profile displayed in the long (4- and 8-day) low pressure runs. If the MI were out of equilibrium at the time of entrapment, both low- and high pressure experiments would show the same profile caused by equilibration between the plagioclase host and MI. As the traverse profiles of the high pressure experiments are similar to those displayed in the 30 min low pressure experiments, our results are consistent with the interpretation that crystal relaxation is the main cause for compositional drift. During homogenization at low pressure, the crystal deforms in response to the internal pressure of the MI (Tait, 1992) and the lower (1 bar) confining pressure. As per the conclusions of Drignon et al. (2019), this may cause changes in the partitioning behavior of certain elements allowing for compositional drift to occur. Further, large inclusions have greater internal pressure drop as the crystal deforms (Tait, 1992; Zhang, 1998), potentially resulting in greater pressure related compositional drift.

TABLE 1 | Experimental conditions for melt inclusion homogenization experiments for Blanco fracture zone and Juan de Fuca ridge samples.

	# of Melt	Pressure	Temperature	Duration
Composition	Inclusions	(P)	(T)	(*t*)
Blanco (A91-1R1)				
MI19B-1	6	1 bar	1,230°C	30 min
MI19B-2	5	1 bar	1,230°C	4 days
MI19B-3	4	1 bar	1,230°C	1 day
MI19B-4	5	1 bar	1,230°C	4 h
MI19B-5	1	1 bar	1,230°C	4 h
MI19B-6	5	1 bar	1,230°C	1 day
MI19B-7	7	1 bar	1,230°C	30 min
MI19B-8	3	1 bar	1,230°C	8 days
MI19HB-1	3	7.5 kbars	1,275°C	2 days
MI19HP	2	7.5 kbars	1,275°C	4 days
Juan De Fuca (D23-2)				
MI18-1	1	1 bar	1,230°C	30 min
MI18-2	2	1 bar	1,230°C	4 h
MI18-3	1	1 bar	1,230°C	1 day
MI18-4	2	1 bar	1,230°C	4 days
MI18-5	0	1 bar	1,230°C	30 min
MI18-6	0	1 bar	1,230°C	4 h
MI18-7	3	1 bar	1,230°C	1 day
MI18-8	2	1 bar	1,230°C	4 days
MI18-9	2	1 bar	1,230°C	30 min
MI18-10	6	1 bar	1,230°C	4 h
MI18-11	3	1 bar	1,230°C	4 days
MI18-12	3	1 bar	1,230°C	8 days
MI18-13	8	1 bar	1,230°C	30 min
MI19HJ-1	5	7.5 kbars	1,275°C	2 days

Low (1 bar) pressure experiments were conducted in platinum (Pt) foil, and high pressure (7.5 kbars) experiments were conducted in Pt capsules. Reported oxygen fugacity refers to the fO_2 experienced by plagioclase host at the time of entrapment but not to furnace atmosphere. Based on the Eu anomaly measured for the melt inclusions and the plagioclase host for similar experiments of ours on the same composition by Dygert et al., 2020, the fO_2 was determined as within a half a log unit below FMQ.

During homogenization at high pressure, the experimental pressure is closer to the pressure of entrapment, hence the absence of compositional drift. These findings imply that homogenization should be done at the pressure of MI entrapment. Our high pressure results were not quenched quickly enough for the glass to be homogenous and without the formation of post-entrapment crystals along the side-wall of the MI. In order to utilize these findings, a faster quenching method is necessary. Some of the other issues arise from high pressure experiments include fracturing of crystals regardless of packing material of cesium iodide. Until these issues are addressed, homogenization at short run times (30 min) at 1 bar is an accommodating method which allows for removal of post-entrapment crystallization, rapid quenching, and lack of compositional drift as the crystal has not had time to relax.

While we ascribe crystal relaxation in the form of plastic deformation as the primary mechanism driving compositional drift, it is possible that local disequilibrium is still a factor. Although the major elements show consistent behavior, specific trace elements (Nb, Sr, Zr) are variable and show no drift or convergence with homogenization time. Adams et al. (2011), Lange et al. (2013a), Lange et al. (2013b), and Nielsen et al. (2020) attributed the observed wide range of trace element compositions in plagioclase megacrysts and their inclusions to

the trapping of melts from different mantle source regions while reaction with the wall rock resulted in buffering the major element compositions. Nb, Sr, Zr show this variability, while other trace elements show weak correlations. This may be a factor of element compatibility as elements will re-equilibrate quickly when compatible in plagioclase (Cottrell et al., 2002) in addition to the diffusion rate of the element. However, comparison of MI compositions with the composition of the hosts near the MI (in the form of MI/host partition coefficients) yields values close to experimental values (Nielsen et al., 2017).

Another factor to consider when analyzing homogenized MIs is the size of those inclusions. Compositional drift is larger in larger inclusions (**Figure 8**). In a study of the selective preservation of melt inclusions, Tait (1992) concluded that smaller inclusions will preferentially withstand rupture and that, for most naturally occurring inclusions sizes, the host will function as an infinite reservoir. Our results may be interpreted to indicate that the internal pressure within the inclusion, a function of volume (Tait, 1992; Zhang, 1998), is more important than surface area of the inclusion in controlling the observed compositional drift. In addition, the fact that larger inclusions did not rupture (as determined by their S contents—Nielsen et al., 1998), but rather exhibited greater compositional change, may be interpreted as an indication that the deformation of the plagioclase was plastic (not brittle) and that smaller inclusions will exhibit less deformation than larger inclusions.

An important implication of these results pertains to how analysts select inclusions for analysis. Most analysts prefer large MIs as they are easier to identify and to obtain uncontaminated analyses of glass. To minimize the effect of compositional drift, one would choose to analyze small inclusions. However, this may be difficult for certain analytical methods. Current limits of LA-ICP-MS analysis are a beam size of 10–30 μm. This is similar to the lower end of the range of most melt inclusions particularly in feldspar (**Figure 8**). If homogenization is restricted to 30 min in plagioclase-hosted inclusions, MI size should not be an issue as crystal relaxation will not yet modify the composition. This holds true for our experiments on plagioclase-hosted MIs but may not be the case for olivine-hosted ones (Schiavi et al., 2016) due to the comparatively rapid rate of deformation for olivine. The observed correlation of MI radius with the extent of compositional drift may be interpreted to mean that the pressure differential between the pressurized MI and the plagioclase host plays an important role in the observed compositional drift.

The observed drift in MI composition leads to the question of the source of the components. For example, MgO in the MI increases as a function of experimental run time and is correlated with the development of the MgO depletion zone in the plagioclase host for run times of 4 and 8 days. Based on the absence of such depletion in the high pressure experiments, we attribute this behavior to crystal relaxation driven by the internal pressure within the MI, which causes a change in the partitioning behavior of Mg. The observed trend of decreasing MI Al_2O_3 and Na_2O paired with increasing SiO_2 and MgO (**Figure 1**) is inconsistent with the addition or subtraction of a feldspar component (e.g. the MIs are not on a plagioclase control line).

CONCLUSION

To interpret information from MIs it is important to assess how post-entrapment processes, and the methodology that we apply to remove their effects may influence our understanding of the magmatic evolution of the systems of interest. Time, temperature, pressure, host composition, and MI size all need to be considered while interpreting data from homogenized MIs. Longer homogenization run times (up to 8 days), correlate with progressive changes in MI composition. Those observations of composition drift cannot be attributed to the addition of plagioclase components as this is not evident in the trends of decreasing Na_2O and increasing SiO_2 and MgO. While these findings suggest that experiments should be completed at the pressure of entrapment, in our case 30 min low pressure experiments were the most effective method as they are long enough to remove post-entrapment crystallization yet are short enough to prevent diffusive exchange with the host. Longer homogenization times cause drift in both the Juan de Fuca and Blanco Fracture Zone samples. Thus, the controlling process is not dependent on the plagioclase composition. However, it is important to have caution when homogenizing different compositions (different An-content of plagioclase megacrysts) at the same temperature. It is likely that this will lead to over or underheating, thus showing different results for specific major and trace elements. While certain trace elements showed weak compositional drift, the incompatible elements such as Zr, Nb and compatible element Sr showed heterogeneity despite the homogenization process. This suggests that the heterogeneity is a primary signal possibly caused by local disequilibrium or trace element compatibility (Cottrell et al., 2002). When analyzing homogenized MIs, we found that the most accurate results will be obtained from small inclusions pending the analysis type. Small inclusions are more difficult to accurately measure trace elements in as the beam size is often too large.

Further work at a range of experimental pressures as well as on other samples contain crystals formed as a range of entrapment pressures is necessary to broaden our understanding of the influence of confining pressure. Homogenization is a deceptively complex process; a number of parameters such as heating rate, pressure of entrapment, extent of post-entrapment crystallization, volatile content, heating time, size of MI, location of MI within the host and others need to be assessed and understood in order to re-create the composition that represents the composition of the melt at the time of entrapment. Here we have developed a methodology effective in removing post-entrapment processes and minimizing compositional drift during MI homogenization in plagioclase. This methodology will be critical in assessing the compositions of the array of magmas forming at depth that can be used as proxies for understanding mantle processes.

Based on our results, MI up to 500 microns in diameter will homogenize in 30 min or less. Further, there is no evidence that the concentration of highly incompatible elements ($D < 0.01$ e.g. Zr, Nb) in MI will be changed by homogenization. They therefore are most likely to represent the composition of the magmas present at depth. Elements characterized by higher rates of

diffusion in plagioclase (e.g. Mg, Sr, Ba) may exhibit narrower ranges in composition due to diffusive exchange between the MI and host. If rapid quench is possible, and the entrapment pressure can be approximated, homogenization at that pressure is ideal. However, our experience suggests that homogenization at high pressure results in more issues than it solves—including inadequate quench speed, crushing of the crystal, and difficulty in assessing the temperature at which daughter crystals melt as well as the pressure of entrapment. Therefore, we recommend homogenization for short times (~30 min) at low pressure for basaltic systems. In assessing results from MI, it is important to note that the compositional changes correlated with experimental run time described here are relevant to any natural system where the crystals have been moved from their place of origin. Storage of crystals formed at high pressure in a shallow reservoir will be subjected to the same composition effects we describe here from controlled experiments.

DATA AVAILABILITY STATEMENT

The original contributions presented in the study are included in the article. EMP and LA-ICP-MS data of the phases from all run products are provided under Supplementary Material. Further inquiries can be directed to the corresponding author.

AUTHOR CONTRIBUTIONS

This work was carried out by M.Sc. KL under the guidance of major thesis advisor GU as part of her thesis research. RLN provided constant intellectual support during the process. The homogenization experiments, sample preparation, and polishing were carried out by KL at SDSM&T in GU's laboratory where she is trained by GU to do the experiments. High pressure homogenization experiments were done by David Walker at Lamont Doherty Earth Observatory (LDEO) and prepped by KL with the help of GU who is a research associate at AMNH/LDEO. Analytical protocols for LA-ICP-MS and EMP and analysis were completed at Oregon State University by KL under the guidance of RN, GU, Frank Tepley and Chris Russo. RLN and GU accompanied to KL during EMPA visits for help with data collection. Data interpretation and composure of manuscript was done by KL under the advice and editing of GU and RLN.

FUNDING

Support for this work was provided by the National Science Foundation under grant number OCE-1634206 and OCE-163421 to RLN together with the NASA South Dakota Space Consortium grant to KL and SD Board of Reagents grant (441946, MA2000006) to GU.

ACKNOWLEDGMENTS

The authors thank M. A. Longpré, T. Kuritani, J. Coumans, and two anonymous reviewer for detailed and thoughtful input that greatly helped to improve the quality and clarity of the manuscript. The authors are also grateful to M. A. Longpré for the editorial handling of this manuscript. Authors would also like to acknowledge the scientific input and laboratory assistance from David Walker, Frank Tepley, and Chris Russo.

REFERENCES

Adams, D. T., Nielsen, R. L., Kent, A. J., and Tepley, F. J. (2011). Origin of minor and trace element compositional diversity in anorthitic feldspar phenocrysts and melt inclusions from the Juan de Fuca Ridge. *Geochem. Geophys. Geosy.* 12, 12. doi:10.1029/2011GC003778

Anderson, A. T., and Wright, T. L. (1972). Phenocrysts and glass inclusions and their bearing on oxidation and mixing of basaltic magmas, Kilauea Volcano, Hawaii. *Am. Mineral.* 57, 188–216.

Bennett, E. N., Jenner, F. E., Millet, M. A., Cashman, K. V., and Lissenberg, C. J. (2019). Deep roots for mid-ocean-ridge volcanoes revealed by plagioclase-hosted melt inclusions. *Nature* 572 (7768), 235–239. doi:10.1038/s41586-019-1448-0

Bindeman, I. N., Davis, A. M., and Drake, M. J. (1998). Ion microprobe study of plagioclase-basalt partition experiments at natural concentration levels of trace elements. *Geochem. Cosmochim. Acta.* 62, 1175–1193.

Blundy, J. D., and Wood, B. J. (1991). Crystal-chemical controls on the partitioning of Sr and Ba between plagioclase feldspar, silicate melts, and hydrothermal fluids. *Geochem. Cosmochim. Acta.* 55, 193–209.

Bryan, W. B. (1983). Systematics of modal phenocryst assemblages in submarine basalts: petrologic implications. *Contrib. Mineral. Petrol.* 83 (1), 62–74.

Cherniak, D. J., and Watson, E. B. (2020). Ti diffusion in feldspar. *Am. Mineral.* 105, 1040–1050. doi:10.2138/am-2020-7272

Coogan, L. A. (2014). *The lower oceanic crust, treatise on geochemistry*. 2nd ed. Victoria, Canada: University of VictoriaElsevier Press, 497–541.

Cottrell, E., Spiegelman, M., and Langmuir, C. H. (2002). Consequences of diffusive reequilibration for the interpretation of melt inclusions. *Geochem. Geophys. Geosy.* 3 (4), 1–26. doi:10.1029/2002GC000502

Coumans, J. P., Stix, J., Clague, D. A., Minarik, W. G., and Layne, G. D. (2016). Melt-rock interaction near the Moho: evidence from crystal cargo in lavas from near-ridge seamounts. *Geochem. Cosmochim. Acta.* 191, 139–164. doi:10.1002/2016GL071327

Danyushevsky, L. V., Della-Pasqua, F. N., and Sokolov, S. (2000). Re-equilibration of melt inclusions trapped by magnesian olivine phenocrysts from subduction-related magmas: petrological implications. *Contrib. Mineral. Petrol.* 138 (1–2), 68–83. doi:10.1007/pl00007664

Danyushevsky, L. V., McNeill, A. W., and Sobolev, A. V. (2002). Experimental and petrological studies of melt inclusions in phenocrysts from mantle-derived magmas: an overview of techniques, advantages, and complications. *Chem. Geol.* 183 (1), 5–24. doi:10.1016/S0009-2541(01)00369-2

Dohmen, R., and Blundy, J. (2014). A predictive thermodynamic model for element partitioning between plagioclase and melt as a function of pressure, temperature, and composition. *Am. J. Sci.* 314 (9), 1319–1372. doi:10.2475/09.2014.04

Drignon, M. J., Nielsen, R. L., Tepley, F. J., III, and Bodnar, R. J. (2019). Re-equilibration processes occurring in plagioclase-hosted melt inclusions from Plagioclase Ultraphyric Basalts. *Geochem. Geophys. Geosy.* 20, 109–119. doi:10.46427/gold2020.1468

Drignon, M. J., Nielsen, R. L., Tepley, F. J., III, and Bodnar, R. J. (2018). Upper mantle origin of plagioclase megacrysts from plagioclase-ultraphyric mid-oceanic ridge basalt. *Geol.* 47 (1), 43–46. doi:10.1130/g45542.1

Dungan, M. A., and Rhodes, J. M. (1978). Residual glasses and melt inclusions in basalts from DSDP Legs 45 and 46: evidence for magma mixing. *Contrib. Mineral. Petrol.* 67 (4), 417–431.

Dygert, N., Draper, D. S., Rapp, J. F., Lapen, T. J., Fagan, A. L., and Neal, C. R. (2020). Experimental determinations of trace element partitioning between plagioclase, pigeonite, olivine, and lunar basaltic melts and an fO_2 dependent model for plagioclase-melt Eu partitioning. *Geochem. Cosmochim. Acta.* 279, 25–280. doi:10.1111/bre.12373

Ferriss, E., Plank, T., Newcombe, M., Walker, D., and Hauri, E. (2018). Rates of dehydration of olivines from San Carlos and Kilauea Iki. *Geochem. Cosmochim. Acta.* 242, 1017. doi:10.1016/j.gca.2018.08.050

Fram, M. S., and Longhi, J. (1992). Phase equilibria of dikes associated with Proterozoic anorthosite complexes. *Am. Mineral.* 77, 605–616.

Gaetani, G. A., O'Leary, J. A., Shimizu, N., Bucholz, C. E., and Newville, M. (2012). Rapid reequilibration of H_2O and oxygen fugacity in olivine-hosted melt inclusions. *Geol.* 40 (10), 915–918. doi:10.1130/g32992.1

Ghiorso, M. S., and Gualda, G. A. (2015). An H_2O–CO_2 mixed fluid saturation model compatible with rhyolite-MELTS. *Contrib. Mineral. Petrol.* 169, 6. doi:10.1007/s00410-015-1141-8

Ghiorso, M. S., Hirschmann, M. M., Reiners, P. W., and Kress, V. C., III (2002). The pMELTS: a revision of MELTS for improved calculation of phase relations and major element partitioning related to partial melting of the mantle to 3 GPa. *Geochem. Geophys. Geosy.* 3, 5. doi:10.1029/2001GC000217

Kent, A. J., and Putirka, K. D., (2008). "*Melt inclusions in basaltic and related volcanic rocks*III" in *Reviews in mineralogy and geochemistry* (Washington, D.C.: Geochemical Society Press), 273–331.

Kohut, E., and Nielsen, R. L. (2004). Melt inclusion formation mechanisms and compositional effects in high-An feldspar and high-Fo olivine in anhydrous mafic silicate liquids. *Contrib. Mineral. Petrol.* 147 (6), 684–704. doi:10.1007/s00410-004-0576-0

Kotash, A., Tepley, F. J., III, Nielsen, R., and Bodnar, R. J. (2019). CO_2 and H_2O in plagioclase-hosted melt inclusions from ocean-ridge lavas: an indicator of crystallization in the lower oceanic crust. Abstract retrieved from AGU Fall Meeting. (Abstract No. V13C-0172).

Lange, A. E., Nielsen, R. L., Tepley, F. J., III, and Kent, A. J. (2013a). The petrogenesis of plagioclase-phyric basalts at mid-ocean ridges. *Geochem. Geophys. Geosy.* 14, 8. doi:10.1002/ggge.20207

Lange, A. E., Nielsen, R. L., Tepley, F. J., III, and Kent, A. J. (2013b). Diverse Sr isotope signatures preserved in mid-oceanic-ridge basalt plagioclase. *Geology* 41 (2), 279–282. doi:10.1016/j.chemgeo.2020.119566

Langmuir, C. H. (1989). Geochemical consequences of *in situ* crystallization. *Nature* 340 (6230), 199–205.

Le Voyer, M., Kelley, K. A., Cottrell, E., and Hauri, E. H. (2017). Heterogeneity in mantle carbon content from CO_2-undersaturated basalts. *Nat. Commun.* 8, 1. doi:10.1038/ncomms14062

Lissenberg, C. J., and MacLeod, C. J. (2016). A reactive porous flow control on mid-ocean ridge magmatic evolution. *J. Petrol.* 57 (11), 2195–2220. doi:10.1093/petrology/egw074

Maclennan, J. (2008). Concurrent mixing and cooling of melts under Iceland. *J. Petrol.* 49 (11), 1931–1953. doi:10.1093/petrology/egn052

Michael, P. J., and Schilling, J. G. (1989). Chlorine in mid-ocean ridge magmas: evidence for assimilation of seawater-influenced components. *Geochem. Cosmochim. Acta.* 53 (12), 3131–3143.

Neave, D. A., Hartley, M. E., Maclennan, J., Edmonds, M., and Thordarson, T. (2017). Volatile and light lithophile elements in high-anorthite plagioclase-hosted melt inclusions from Iceland. *Geochem. Cosmochim. Acta* 205, 100–118.

Nielsen, R. L., Crum, J., Bourgeois, R., Hascall, K., Forsythe, L. M., Fisk, M. R., et al. (1995). Melt inclusions in high-An plagioclase from the Gorda Ridge: an example of the local diversity of MORB parent magmas. *Contrib. Mineral. Petrol.* 122, 34–50.

Nielsen, R. L., Michael, P. J., and Sours-Page, R. (1998). Chemical and physical indicators of compromised melt inclusions. *Geochem. Cosmochim. Acta.* 62 (5), 831–839.

Nielsen, R. L. (2011). The effects of re-homogenization on plagioclase-hosted melt inclusions. *Geochem. Geophys. Geosyst.* 12, 10. doi:10.1029/2011GC003822

Nielsen, R. L., Ustunisik, G., Lange, A. E., Tepley, F. J., III, and Kent, A. J. R. (2020). Trace element and isotopic characteristics of plagioclase megacrysts in plagioclase ultraphyric basalts (PUBs). *Geochem. Geophys. Geosyst.* 21. doi:10.1029/2019GC00863

Nielsen, R. L., Ustunisik, G., Weinsteiger, A. B., Tepley, F. J., Johnston, A. D., and Kent, A. J. (2017). Trace element partitioning between plagioclase and melt: an investigation of the impact of experimental and analytical procedures. *Geochem. Geophys. Geosyst.* 18, 3359–3384. doi:10.1002/2017GC007080

O'Hara, M. J. (1977). Geochemical evolution during fractional crystallization of a periodically refilled magma chamber. *Nature* 266 (5602), 503–507.

O'Neill, H. S. C., and Jenner, F. E. (2016). Causes of the compositional variability among ocean floor basalts. *J. Petrol.* 57 (11), 2163–2194. doi:10.1016/j.epsl.2018.10.002

Roedder, E. (1979). Origin and significance of magmatic inclusions. *Bull. Mineral.* 102 (5), 487–510.

Rubin, K. H., Sinton, J. M., Maclennan, J., and Hellebrand, E. (2009). Magmatic filtering of mantle compositions at mid-ocean-ridge volcanoes. *Nat. GeoSci.* 2 (5), 321–328. doi:10.1038/NGEO504

Schiavi, F., Provost, A., Schiano, P., and Cluzel, N. (2016). P–V–T–X evolution of olivine-hosted melt inclusions during high-temperature homogenization treatment. *Geochem. Cosmochim. Acta.* 172, 1–21. doi:10.1038/NGEO504

Shorttle, O., Moussallam, Y., Hartley, M. E., Maclennan, J., Edmonds, M., and Murton, B. J. (2015). Fe-XANES analyses of Reykjanes Ridge basalts: implications for oceanic crust's role in the solid Earth oxygen cycle. *Earth Planet Sci. Lett.* 427, 272–285. doi:10.1016/j.epsl.2015.07.017

Sinton, C. W., Christie, D. M., Coombs, V. L., Nielsen, R. L., and Fisk, M. R. (1993). Near-primary melt inclusions in anorthite phenocrysts from the Galapagos Platform. *Earth Planet Sci. Lett.* 119 (4), 527–537.

Sobolev, A. V. (1996). Melt inclusions in minerals as a source of principle petrological information. *Petrol.* 4 (3), 209–220.

Sobolev, A. V., and Shimizu, N. (1993). Ultra-depleted primary melt included in an olivine from the Mid-Atlantic ridge. *Nature* 363, 151–154.

Sours-Page, R., Johnson, K. T., Nielsen, R. L., and Karsten, J. L. (1999). Local and regional variation of MORB parent magmas: evidence from melt inclusions from the endeavour segment of the Juan de Fuca Ridge. *Contrib. Mineral. Petrol.* 134 (4), 342–363.

Tait, S. (1992). Selective preservation of melt inclusions in igneous phenocrysts. *Am. Mineral.* 77 (1), 146–155.

Ustunisik, G., Nielsen, R. L., and Walker, D. (2020). *The missing magmas of MOR*.Abstract retrieved from Goldschmidt Conference. (Goldschmidt2020 Abstract).

Wallace, P., and Carmichael, I. S. (1992). Sulfur in basaltic magmas. *Geochem. Cosmochim. Acta.* 56 (5), 1863–1874.

Wanless, V. D., and Shaw, A. M. (2012). Lower crustal crystallization and melt evolution at mid-ocean ridges. *Nat. GeoSci.* 5 (9), 651. doi:10.1186/1880-5981-66-81

Zhang, Y. (1998). Mechanical and phase equilibria in inclusion-host systems. *Earth Planet Sci. Lett.* 157 (3), 209–222.

Conflict of Interest: The authors declare that Frank Tepley (OSU), Adam Kent (OSU), Hanna Nekvasil (Stony Brook), David Walker (LDEO of Columbia University), Denton Ebel (AMNH), Francis McCubbin (NASA JSC) are the most recent collaborators of co-authors and review of this article by them could be considered as a potential conflict of interest.

Advantages of publishing in Frontiers

OPEN ACCESS
Articles are free to read for greatest visibility and readership

FAST PUBLICATION
Around 90 days from submission to decision

HIGH QUALITY PEER-REVIEW
Rigorous, collaborative, and constructive peer-review

TRANSPARENT PEER-REVIEW
Editors and reviewers acknowledged by name on published articles

Frontiers
Avenue du Tribunal-Fédéral 34
1005 Lausanne | Switzerland

Visit us: www.frontiersin.org
Contact us: frontiersin.org/about/contact

REPRODUCIBILITY OF RESEARCH
Support open data and methods to enhance research reproducibility

DIGITAL PUBLISHING
Articles designed for optimal readership across devices

FOLLOW US
@frontiersin

IMPACT METRICS
Advanced article metrics track visibility across digital media

EXTENSIVE PROMOTION
Marketing and promotion of impactful research

LOOP RESEARCH NETWORK
Our network increases your article's readership